

DTIC FILE COPY

1

AGARD-R-755

AGARD-R-755

AD-A 198 872

# AGARD

ADVISORY GROUP FOR AEROSPACE RESEARCH & DEVELOPMENT

7 RUE ANCELEE 92200 NEUILLY SUR SEINE FRANCE

AGARD REPORT No.755

**Special Course on  
Modern Theoretical and Experimental  
Approaches to Turbulent Flow  
Structure and its Modelling**

**DISTRIBUTION STATEMENT A**

Approved for public release  
Distribution Unlimited

DTIC  
ELECTE  
SEP 23 1988  
S & D

NORTH ATLANTIC TREATY ORGANIZATION



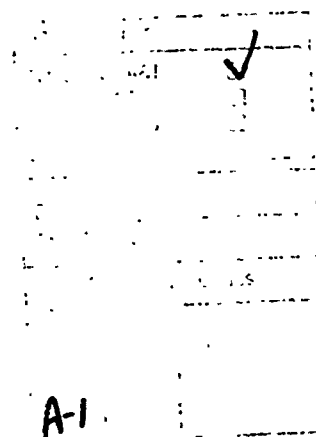
DISTRIBUTION AND AVAILABILITY  
ON BACK COVER

88 9 23 001

AGARD-R-755

NORTH ATLANTIC TREATY ORGANIZATION  
ADVISORY GROUP FOR AEROSPACE RESEARCH AND DEVELOPMENT  
(ORGANISATION DU TRAITE DE L'ATLANTIQUE NORD)

AGARD Report No.755  
SPECIAL COURSE ON  
MODERN THEORETICAL AND EXPERIMENTAL  
APPROACHES TO TURBULENT FLOW STRUCTURE  
AND ITS MODELLING



The material assembled in this book was prepared under the combined sponsorship of the Fluid Dynamics Panel, the von Kármán Institute and the Consultant and Exchange Programme of AGARD and was presented as an AGARD Special Course at the von Kármán Institute, Rhode-St-Genèse, Belgium on 16-20 March 1987.

## THE MISSION OF AGARD

The mission of AGARD is to bring together the leading personalities of the NATO nations in the fields of science and technology relating to aerospace for the following purposes:

- Exchanging of scientific and technical information;
- Continuously stimulating advances in the aerospace sciences relevant to strengthening the common defence posture;
- Improving the co-operation among member nations in aerospace research and development;
- Providing scientific and technical advice and assistance to the Military Committee in the field of aerospace research and development (with particular regard to its military application);
- Rendering scientific and technical assistance, as requested, to other NATO bodies and to member nations in connection with research and development problems in the aerospace field;
- Providing assistance to member nations for the purpose of increasing their scientific and technical potential;
- Recommending effective ways for the member nations to use their research and development capabilities for the common benefit of the NATO community.

The highest authority within AGARD is the National Delegates Board consisting of officially appointed senior representatives from each member nation. The mission of AGARD is carried out through the Panels which are composed of experts appointed by the National Delegates, the Consultant and Exchange Programme and the Aerospace Applications Studies Programme. The results of AGARD work are reported to the member nations and the NATO Authorities through the AGARD series of publications of which this is one.

Participation in AGARD activities is by invitation only and is normally limited to citizens of the NATO nations.

The content of this publication has been reproduced directly from material supplied by AGARD or the authors.

Published August 1987

Copyright © AGARD 1987  
All Rights Reserved

ISBN 92-835-0430-5



*Printed by Specialised Printing Services Limited  
40 Chigwell Lane, Loughton, Essex IG10 3TZ*

## PREFACE

This lecture series co-sponsored with the Fluid Dynamics Panel of AGARD, was held at the von Kármán Institute, Rhode-St-Genèse, Belgium, during the week March 16 to 20, 1986, as a follow-up to the continued involvement in the field of turbulent flows.

The intention was to make a presentation of the very latest developments in the domain of understanding and modelling of turbulent flow which in recent years has seen the development of some fairly new ideas and lines of approach.

It was for this reason that, together with the most advanced classical concepts of modelling such as direct simulation on super computers, large eddy simulation, solution of the Navier-Stokes equations in the spectral domain, some different approaches were presented. These included the concepts of strange attractors, bifurcations, spatial and temporal deterministic routes to chaos and lattice flow simulations. These concepts, already applied in some other domains of physics, may prove to be valuable tools in the attempt to understand some of the more complex features of turbulence, and may lead to models better adapted to the new generation of parallel computers.

Thanks to the efforts of an international body of well-known lecturers, the result was very successful and the meeting a source of lively and enriching discussions. I would like to take the occasion to present my thanks to all those who have contributed to the organization and the success of this lecture series.

\* \* \*

Ce cycle de conférences, organisé avec le support du Fluid Dynamics Panel de l'AGARD, a été tenu à l'Institut von Kármán, à Rhode-Saint-Genèse, la semaine du 16 au 20 mars 1986, comme une suite à toute une série de cours donnés les années précédentes dans le domaine de la mécanique de la turbulence.

Le but était de présenter les tout derniers développements dans les domaines de la description et la modélisation des écoulements turbulents, domaines dans lesquels on a assisté, ces dernières années, à la naissance et la mise en oeuvre d'un certain nombre d'idées nouvelles. Pour ces raisons le cycle était constitué de deux parties complémentaires. La première couvrait essentiellement les concepts les plus avancés dans le domaine de la modélisation classique, tels que la simulation directe sur super ordinateur, la simulation des grandes structures, la solution des équations de Navier Stokes dans le domaine spectral. Ensuite, on abordait une série de sujets en grande partie nouveaux, mais très prometteurs et ayant déjà fait leurs preuves dans d'autres domaines de la physique, tels que les concepts d'attracteurs étranges, de bifurcation, de routes déterministes, spatiales ou temporelles, vers le chaos et les gaz de réseau. Il semble possible que ces nouvelles approches puissent permettre une meilleure description de certaines propriétés de la turbulence et se révéler très bien adaptées au calcul à l'aide des nouveaux processeurs vectoriels. Grâce à l'effort d'un groupe de conférenciers de renommée internationale, ce cycle s'est révélé être une réussite et l'ensemble de la réunion une source de discussion très intéressantes et enrichissantes. Qu'il me soit permis ici de remercier tous ceux qui ont contribué à l'organisation et à la réussite de ce cycle de conférences.



#### DIRECTORS OF SPECIAL COURSE

Dr P. Berge  
Commissariat à l'Energie Atomique  
Direction de la Physique  
Serv. Phys. du Solide & Res. Magnétique  
Orme des Merisiers  
91191 Gif-sur-Yvette  
France

Professor D. Olivari  
Von Kármán Institute for Fluid Dynamics  
Chaussée de Waterloo 72  
1640 Rhode-Saint-Genèse  
Belgium

#### LECTURERS

Professor J.P. Boon  
Univ. Libre de Bruxelles  
Service de Chimie Physique 2  
Code Postal No. 231  
Bld du Triomphe  
1050 Bruxelles  
Belgium

Mr A. Noullez  
Univ. Libre de Bruxelles  
Service de Chimie Physique 2  
Code Postal No. 231  
Bld du Triomphe  
1050 Bruxelles  
Belgium

Dr B. Aupoix  
ONERA/CERT-DERAT  
2 Av. E. Belin  
31055 Toulouse Cedex  
France

Dr M. Dubois  
Commissariat à l'Energie Atomique  
Direction de la Physique  
Orme des Merisiers  
91191 Gif-sur-Yvette  
France

Dr D. Laurence  
E.D.F. (Electricité de France)  
Direction Etudes et Recherches  
Quai Watier — BP 49  
78401 Chatou Cedex  
France

Dr P. Manneville  
Commissariat à l'Energie Atomique  
Direction de la Physique  
Orme des Merisiers  
91191 Gif-sur-Yvette  
France

Dr S. Ciliberto  
Istituto Nazionale di Ottica  
Largo E. Fermi 6  
50125 Firenze  
Italy

Professor W.C. Reynolds  
Stanford University  
Mech. Engineering Dept.  
Stanford  
CA 93305  
USA

#### LOCAL COORDINATOR

Professor D. Olivari  
Von Kármán Institute for Fluid Dynamics  
Chaussée de Waterloo 72  
1640 Rhode-Saint-Genèse  
Belgium

#### AGARD REPRESENTATIVE

Mr M.C. Fischer  
Fluid Dynamics Panel Executive  
AGARD  
7 rue Anelle  
92200 Neuilly-sur-Seine  
France

# CONTENTS

	Page
PREFACE	iii
SPECIAL COURSE STAFF	iv
	Reference
FUNDAMENTALS OF TURBULENCE FOR TURBULENCE MODELING AND SIMULATION by W.C.Reynolds	1
TURBULENCE MODELLING THROUGH ONE POINT CLOSURES – APPLICATIONS – ENLIGHTENING BY LARGE EDDY SIMULATION by D.Laurence	2
HOMOGENEOUS TURBULENCE: TWO-POINT CLOSURES AND APPLICATIONS TO ONE-POINT CLOSURES by B.Aupoix	3
DYNAMICS AND ROUTES TO CHAOS FROM QUASIPERIODICITY by M.Dubois	4
A DETERMINISTIC APPROACH TO TURBULENCE: CHAOS IN RAYLEIGH-BENARD CONVECTION by P.Berge	5
TRANSITION TO TURBULENCE VIA SPATIO-TEMPORAL INTERMITTENCY by P.Manneville	6
DETERMINATION OF FRACTAL DIMENSION CONNECTION OF SPACE AND TMPORAL CHAOS AND APPLICATION TO EXPERIMENTAL RESULTS by S.Ciliberto	7
LATTICE GAS HYDRODYNAMICS by J.P.Boon and A.Noullez	8

# FUNDAMENTALS OF TURBULENCE FOR TURBULENCE MODELING AND SIMULATION

by

W.C.Reynolds  
Department of Mechanical Engineering  
Stanford University  
Stanford, CA 93305  
USA

## 1. FUNDAMENTALS OF FLUID MOTION

### 1.1 Introduction

This chapter presents a brief review of fluid flow fundamentals pertinent to turbulence. We expect them to be familiar to the reader, who may find our particular viewpoints, emphasis, and compact notation helpful and interesting.

We will make extensive use of the cartesian tensor summation convention, where repeated indices imply that the terms containing them must be summed over all possible coordinate indices. An overdot ( $\dot{\phantom{x}}$ ) will be used to denote a partial derivative with respect to time, and a subscript after a comma will denote partial differentiation with respect to the indicated coordinate direction; for example,

$$\dot{\rho} = \frac{\partial \rho}{\partial t} \quad P_{,i} = \frac{\partial P}{\partial x_i} \quad u_{i,j} = u_{1,1} + u_{2,2} + u_{3,3}.$$

We will also use the isotropic tensors  $\delta_{ij}$  and  $\epsilon_{ijk}$ , defined by

$$\delta_{ij} = \begin{cases} 1 & \text{if } i = j \\ 0 & \text{otherwise.} \end{cases}$$

and

$$\epsilon_{ijk} = \begin{cases} 1 & \text{if } ijk \text{ is from the sequence } 123123 \\ -1 & \text{if } ijk \text{ is from the sequence } 321321 \\ 0 & \text{otherwise} \end{cases}$$

Various contractions will be used frequently, including

$$\delta_{ii} = 3 \quad \epsilon_{ijk}\epsilon_{ipq} = \delta_{jp}\delta_{kq} - \delta_{jq}\delta_{kp}.$$

Tensors are entities that, in addition to being an array of elements identified by their subscripts, transform in a very special way when the coordinate system is transformed by rotation. A tensor that is totally unchanged by an arbitrary rotation of the coordinate system is called *isotropic*. Any second-order isotropic tensor must be a scalar times  $\delta_{ij}$ , and any third-order isotropic tensor must be a scalar times  $\epsilon_{ijk}$ . Moreover, any higher-order isotropic tensor must be expressible in terms of the various possible combinations of these two tensors, and hence they are fundamental building blocks in all sorts of physical modeling, including viscous flow and turbulence.

### 1.2 The basic equations

The basic equations are derived by application of basic principles to an elemental control volume (Fig. 1.2.1). The *conservation of mass* gives

$$\dot{\rho} + (\rho u_j)_{,j} = 0 \quad (1.2.1)$$

where  $\rho$  is the fluid density, and  $u_j$  is the fluid velocity component in the  $j^{\text{th}}$  direction. This is also called the *continuity equation*.

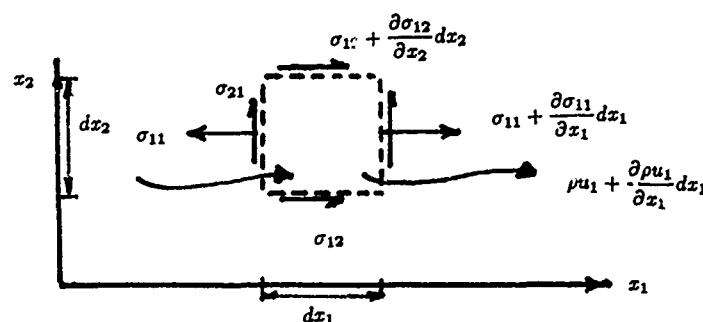


Figure 1.2.1 Control volume for basic equation derivation

The momentum equation is

$$(\rho \dot{u}_i) + (\rho u_j u_i)_{,j} = \sigma_{ji,i} + f_i \quad (1.2.2)$$

where  $\sigma_{ji}$  is the stress in the  $i^{\text{th}}$  direction on a control volume surface perpendicular to the  $j^{\text{th}}$  axis, and  $f_j$  is the body force (per unit volume) in the  $j^{\text{th}}$  direction.

The conservation of energy requires that

$$(\rho \dot{e}_0) + (\rho u_j e_0)_{,j} = (\sigma_{ji} u_i)_{,j} + f_i u_i - q_{j,j} \quad (1.2.3)$$

Here  $e_0 = e + \frac{1}{2} V^2$  is the total energy per unit mass, where  $e$  is the internal energy per unit mass and  $V^2 = u_i u_i$ , and  $q_j$  is the conduction heat flux (flow rate per unit area) in the  $j^{\text{th}}$  direction outward from the elemental control volume. The first term on the right represents the power input by the surface forces per unit volume, and the second that by the body forces.

The entropy balance is

$$(\rho \dot{s}) + (\rho u_j s)_{,j} = \varphi - (q_j/T)_{,j} \quad (1.2.4)$$

where  $s$  is the entropy per unit mass,  $T$  is the absolute temperature, and  $\varphi$  is the entropy production rate per unit volume. Here the term  $q_j/T$  represents the entropy flux associated with the heat flux  $q_j$ . The second law of thermodynamics requires that the entropy production be non-negative,

$$\varphi \geq 0. \quad (1.2.5)$$

These ideas are useful in assessing constitutive models for the stress tensor and heat flux vector, and in identifying the processes that produce entropy (dissipate energy) in viscous flows.

### 1.3 The stress tensor

The stress tensor  $\sigma_{ij}$  must be symmetric. This fact can be established by performing a *moment of momentum* analysis on the elemental control volume of Fig. 1.3.1. The torques of the stress terms are all of order  $dx_1 dx_2$ , and the moments of the momentum flows and body forces are all of higher order, hence  $\sigma_{12} = \sigma_{21}$ .

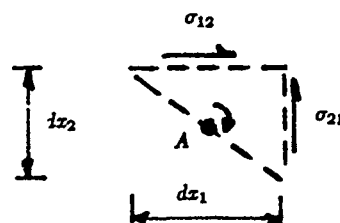


Figure 1.3.1 Control volume for stress tensor symmetry derivation

The tensor can be split into two parts:

$$\sigma_{ij} = -P \delta_{ij} + \tau_{ij} \quad (1.3.1)$$

The  $P$  term represents the isotropic component of the (inward) normal stress;  $\tau_{ij}$  is the deviations from this isotropic stress, attributed phenomenologically to *viscosity*. From a molecular point of view,  $\sigma_{ij}$  arises from molecular transport of momentum; the isotropic part  $P$  is determined by the average using the probability distribution for molecular velocities (e.g. Boltzmann), and  $\tau_{ij}$  arises from anisotropy in the probability distribution.

#### 1.4 Thermodynamic properties and concepts

The internal energy  $e$  reflects the randomly-oriented energy of molecular translation, rotation, vibration, and other microscopic energy modes (chemical bonds, etc.). In general,  $e$  depends upon the thermodynamic state (i.e.  $T$  and  $\rho$ ), but for idealized gas and incompressible liquid models depends only on temperature. It is sometimes called the *thermal energy*, and is all too frequently confused with *heat* ( $q$ ), which is the transport of energy by disordered molecular processes. The internal energy of an object can be increased by a transfer of energy as either heat or work, and the energy flowing as heat can come either from a source of internal energy or mechanical energy (kinetic, potential, or work). The internal energy is a thermodynamic property of matter, the heat transfer is not. The confusion between heat and internal energy is an unfortunate remnant of the caloric theory of heat, but perhaps understandable since the theory was discarded only about a century ago.

The entropy can be thought of as a measure of the degree of randomness at the molecular level, and in modern thermodynamic treatments the temperature is interpreted as a measure of the sensitivity of this randomness to changes in energy at constant density. Orderly microscopic exchanges of energy (e.g. as work or as bulk kinetic energy) have no associated entropy transport. But heat, the microscopically disordered transport of energy, does carry entropy with it, and it may be shown that this entropy transfer flux is  $q_j/T$ . For more discussion of these important thermodynamic concepts from this viewpoint, see Reynolds and Perkins (1977).

It is usually assumed that as far as the thermodynamic properties are concerned the fluid is in a state of local equilibrium, and hence that the usual relations between thermodynamic properties are valid. Thus, the *Gibbs equation* is used to relate entropy changes to energy and density changes,

$$Tds = de + Pd(1/\rho). \quad (1.4.1)$$

The enthalpy  $h$  is defined as

$$h = e + P/\rho \quad (1.4.2)$$

and represents the sum of the convected internal energy and flow work associated with the transport of a unit mass of fluid across a control volume boundary. We emphasize that it is the *internal energy* that appears in the basic energy balance equation.

An alternative form of the energy equation is obtained using (1.3.1) in (1.2.3), moving the pressure term to the left hand side;

$$(\rho \dot{e}_0) + (\rho u_j \dot{h}_0)_{,j} = (\tau_{ji} u_i)_{,j} + f_i u_i - q_{j,j}. \quad (1.4.3)$$

Here  $h_0 = h + \frac{1}{2}V^2$  is the stagnation enthalpy. Note that the *enthalpy* appears as the *convected* energy per unit mass (internal energy  $e$  plus flow work  $P/\rho$ ), but the *internal energy*  $e$  appears in the energy storage rate term. A common error is the use of enthalpy in *both* places.

#### 1.5 Kinematics of motion

Any deformation rate  $u_{i,j}$  can be decomposed into the sum of a strain rate  $S_{ij}$  and a rotation rate  $\Omega_{ij}$ ,

$$u_{i,j} = \frac{1}{2}(u_{i,j} + u_{j,i}) + \frac{1}{2}(u_{i,j} - u_{j,i}) = S_{ij} + \Omega_{ij}. \quad (1.5.1)$$

Note that the strain rate is a symmetric tensor and the rotation rate is antisymmetric. They play quite different roles in fluid mechanics, particularly in turbulence, and for this reason we prefer forms of the equations that make their presence or absence very clear.

#### 1.6 Mechanical and thermal energy equations

The fundamental equations may be combined to derive an equation describing the transport of macroscopic mechanical energy and another describing the transport of internal energy. The *mechanical energy equation* is derived by contracting the momentum equation with the velocity; multiplying (1.2.2)<sub>i</sub> by  $u_i$ ,

$$\left(\rho \frac{1}{2} V^2\right) + \left(\rho u_j \frac{1}{2} V^2\right)_{,j} = \sigma_{ji,j} u_i + f_i u_i. \quad (1.6.1)$$

The right hand side may be written as

$$(\sigma_{ij} u_i)_{,j} - \sigma_{ij} u_{i,j} + f_i u_i.$$

Then, using (1.3.1) to split the stress tensor and (1.5.1) in place of velocity gradients, and noting that  $\tau_{ij}\Omega_{ij} = 0$  since  $\tau_{ij}$  is symmetric and  $\Omega_{ij}$  is antisymmetric (sum over both repeated indices is implied), (1.6.1) can be rewritten as

$$\left(\rho \frac{1}{2} V^2\right) + (\rho u_j \frac{1}{2} V^2)_{,j} = PS_{jj} - (Pu_j)_{,j} + f_i u_i + (\tau_{ij} u_i)_{,j} - (\tau_{ij} S_{ij}). \quad (1.6.2)$$

The sum on the right represents the input of macroscopic mechanical energy to the control volume, which shows up as an increase in the kinetic energy of the flow. Two of these terms appear as power inputs in the thermal energy equation (1.6.4) but with opposite sign, and hence these terms represent exchanges between thermal and mechanical energy. The first is  $PS_{jj}$ , which is the rate of energy transfer, per unit volume, from thermal energy to mechanical energy due to expansion of the fluid. The second is  $\tau_{ij} S_{ij}$ , which represents the transfer of mechanical energy to thermal energy by viscous forces. This is the only viscous term involved in the entropy production equation (1.7.3), and hence this is the only viscous term properly termed *dissipation*. Since

$$\int (\tau_{ij} u_i)_{,j} d^3 \mathbf{x} = 0 \quad (1.6.3)$$

if the integral is taken over a volume where either the velocity or stress is zero on the boundaries, this viscous term has no global effect; it represents *reversible* viscous power input to the control volume from surrounding fluid. The term containing  $f_i$  is the power input from body forces, and the  $(Pu_j)_{,j}$  term represents power output by *flow work*.

The *thermal energy equation* is obtained by subtracting the mechanical energy equation (1.6.2) from the total energy equation (1.2.3), and is

$$(\rho e) + (\rho u_j e)_{,j} = -PS_{jj} + (\tau_{ij} S_{ij}) - q_{j,j}. \quad (1.6.4)$$

Here  $PS_{jj}$  represents the power output from thermal energy due to expansion of the fluid,  $\tau_{ij} S_{ij}$  is the power input to the thermal energy due to irreversible viscous effects, and  $q_{j,j}$  is the net power output due to heat conduction, all per unit volume.

Note that the enthalpy, which appeared in the alternate form of the *total energy equation* (1.4.3), does *not* appear in the thermal energy equation. We have derived the thermal energy equation correctly from first principles. One must be wary in reading literature where the thermal energy equation is developed from a "heat balance", because there is no such principle as the conservation of heat.

### 1.7 Irreversibility rate equation

Using the conservation of mass equation (1.2.1) in the Gibbs equation (1.4.1),

$$\rho T Ds = \rho De + PS_{ii} \quad (1.7.1)$$

where  $D$  denotes the substantial derivative

$$D() = \dot{() + u_j()_{,j}}. \quad (1.7.2)$$

Using the thermal energy equation (1.6.4) and the entropy balance (1.2.4), this yields an expression for the *irreversibility rate*,

$$T\varphi = -\frac{1}{T} q_j T_{,j} + \tau_{ij} S_{ij} \geq 0. \quad (1.7.3)$$

This clearly identifies the viscous dissipation term as discussed above, and provides a neat framework for evaluation of constitutive models for the heat flux or viscous stresses.

### 1.8 Constitutive equations

The theory of linear algebra is extremely helpful in developing constitutive models for the heat flux and viscous stresses, and also for developing turbulence models. We will use these ideas to review the constitutive equations so as to set the stage for later use of these ideas in developing turbulence models.

The most general vector  $f_i$  that is a function of *only one other vector*  $u_i$  is

$$f_i = C u_i \quad (1.8.1)$$

where the coefficient  $C$  can be a function of scalars, including the invariant of the vector (its magnitude  $u_k u_k$ ). Higher-order terms, such as  $u_i u_k u_k$ , need not be added since they are represented by allowing the coefficient to depend on the invariant of  $\mathbf{v}$ . Thus, if one assumes that the heat flux vector  $q_i$  is a function of the temperature gradient vector  $T_{,i}$ , the most general form is the familiar Fourier heat conduction law,

$$q_j = -kT_{,j} \quad (1.8.2)$$

where  $k$  is the *thermal conductivity*, which depends to first approximation on the temperature and may, in higher approximations, also depend on the scalar  $T_{,k}T_{,k}$ . It is generally believed that (1.8.2) describes heat conduction in fluids, except perhaps in regions of very strong temperature gradient such shock waves or combustion fronts.

The most general tensor  $a_{ij}$  that is a function of *only one other tensor*  $b_{ij}$ , is, in three dimensions,

$$a_{ij} = A\delta_{ij} + Bb_{ij} + Cb_{ij}^2 \quad (1.8.3)$$

where  $b_{ij}^2 = b_{ik}b_{kj}$ . The coefficients  $A$ ,  $B$  and  $C$  may depend on relevant scalars, including the three scalar invariants of the tensor  $b$ . Higher-order terms such as  $b_{ij}^3 = b_{ik}^2b_{kj}$  need not be added since, by the Cayley-Hamilton theorem, they can be expressed in terms of lower-order terms and the invariants of  $b$  and hence are already included in (1.8.3). Therefore, if it is assumed that the viscous stress tensor  $\tau_{ij}$  is a function of the local strain-rate tensor  $S_{ij}$ , this functional dependence must be of the form

$$\tau_{ij} = A\delta_{ij} + BS_{ij} + CS_{ij}^2 \quad (1.8.4)$$

where the coefficients may depend on scalars, such as temperature, density, or the invariants of  $S$ . This is called the *Stokes model* for viscous stresses.

The rms strain-rate  $S = (S_{ij}S_{ji})^{1/2}$  is a reciprocal time scale for the fluid deformation. If this time is long compared to molecular collision times, then the strain is considered weak and only linear terms in (1.8.4) are used. This leads to

$$\tau_{ij} = A\delta_{ij} + BS_{ij} \quad (1.8.5)$$

where  $A$  can depend at most linearly on the invariants of  $S$ , and  $B$  must be independent of  $S$ . If it further assumed that  $P = -\frac{1}{3}\sigma_{ii}$ , then by (1.3.1)

$$\tau_{kk} = 0 = 3A + BS_{kk}$$

so

$$A = -\frac{1}{3}BS_{kk}. \quad (1.8.6)$$

For a simple shearing flow where the only non-zero strain-rate elements are

$$S_{12} = S_{21} = \frac{1}{2} \frac{\partial u_1}{\partial x_2}$$

one defines the fluid viscosity  $\mu$  by

$$\tau_{12} = 2\mu S_{12} \quad (1.8.7)$$

from which, using (1.8.5), it follows that  $B = 2\mu$ . The resulting *Newtonian constitutive equation* is

$$\tau_{ij} = 2\mu S_{ij} - \frac{2}{3}\mu S_{kk}\delta_{ij}. \quad (1.8.8)$$

Note that the Newtonian constitutive equation assumes *only* that the viscous stress tensor is a trace-free linear function of the local strain rate; this assumption is believed to be quite adequate for many continuum fluid flows. The model fails in strong shock waves (normal stresses are incorrect) and in flow of polymers (rotation rates are also important).

Using (1.8.2) and (1.8.8) in (1.7.3), the irreversibility rate becomes

$$T\varphi = \frac{k}{T}T_{,i}T_{,i} + 2\mu(S_{ij}S_{ij} - \frac{1}{3}S_{ii}S_{kk}) \geq 0. \quad (1.8.9)$$

It is clear that the heat flux term is positive-definite. It is left as an exercise to demonstrate that the strain-rate term is also positive-definite (Hint: evaluate in the principal coordinates of  $S_{ij}$  by expressing the diagonal elements as the components of a vector in polar coordinates).

### 1.9 Vorticity

Vorticity is one of the most fundamental concepts in fluid mechanics, and probably the most important concept in turbulence. The vorticity vector  $\omega$  is defined by

$$\omega_i = \epsilon_{ijk}u_{k,j}. \quad (1.9.1)$$

Note that  $\epsilon_{ijk} u_{k,j} = 0$  and hence the vorticity, by definition, is *divergence free*,

$$\omega_{i,i} = 0. \quad (1.9.2)$$

By the definitions, the vorticity is related to the rotation rate,

$$\omega_i = \epsilon_{ijk} \Omega_{kj}. \quad (1.9.3)$$

Taking  $\epsilon_{pqi} \times (1.9.3)_i$ , one finds

$$\Omega_{qp} = \frac{1}{2} \epsilon_{pqi} \omega_i. \quad (1.9.4)$$

The vorticity field can be thought of as contributing to the velocity field. Forming  $\epsilon_{pqi} \times (1.9.1)_{i,q}$ , one finds

$$\epsilon_{pqi} \omega_{i,q} = \epsilon_{pqi} \epsilon_{ijk} u_{k,jq} = u_{q,ipq} - u_{p,iqq}$$

or

$$u_{i,kk} = -\epsilon_{ijk} \omega_{j,k} + (u_{k,k})_{,i}. \quad (1.9.5)$$

This is a *Poisson equation* for the velocity, analogous to the equation for temperature in a heat conducting medium with distributed sources. Eqn. (1.9.5) displays two "sources" of velocity, namely vorticity (more specifically vorticity *gradients*) and flow divergence (expansion or compression). In addition to the velocity generated by these sources, one can also have an additional component of velocity satisfying the *Laplace equation*  $u_{i,kk} = 0$ . From (1.9.5) we see that this component could be thought of as arising from *uniform vorticity* (a solid-body rotation) and *uniform irrotational expansion*, of which irrotational flow at constant density is a special case.

The part of the velocity field due to the vorticity gradients may be found using the general solution to the Poisson equation; at any instant in time, this solution is

$$u_i(\mathbf{x}) = - \int G(\mathbf{x}, \mathbf{x}') \epsilon_{ijk} \omega_{j,k}(\mathbf{x}') d^3 \mathbf{x}' \quad (1.9.6)$$

where  $G(\mathbf{x}, \mathbf{x}')$  is the *Green's function* for the Poisson solution in the flow domain, and  $d^3 \mathbf{x}'$  represents an element of volume for the integration over the flow domain. The Green's function for an infinite domain is

$$G(\mathbf{x}, \mathbf{x}') = \frac{-1}{4\pi \sqrt{(x_n - x'_n)(x_n - x'_n)}}. \quad (1.9.7)$$

Using this Green's function in (1.9.6), and integrating by parts to transfer the  $k$  differentiation from the vorticity to the Green's function, one finds

$$u_i(\mathbf{x}) = \int \epsilon_{ijk} \frac{(x_k - x'_k)}{4\pi [(x_n - x'_n)(x_n - x'_n)]^{3/2}} \omega_j d^3 \mathbf{x}'. \quad (1.9.8)$$

This is called the *Biot-Savart equation*. It gives that portion of the velocity field arising from vorticity, for an infinite flow domain. Computational methods in which markers track the motion of vorticity-bearing fluid use the Biot-Savart equation to compute the velocity field; this is an efficient calculation if the vorticity is highly concentrated and most of the fluid has negligible vorticity, and there are many interesting problems in turbulence that can be addressed in this manner.

We emphasize that all of the features of vorticity discussed thus far are *kinematic* in nature, and apply in either compressible or incompressible flows. In the next section we will address the *dynamic* of the vorticity.

### 1.10 Vorticity dynamics

Using the continuity equation (1.2.1) and the stress tensor split (1.3.1), the momentum equation (1.2.2) can be written as

$$\dot{u}_k + u_q u_{k,q} = \frac{1}{\rho} (\tau_{kq,q} - P_{,k} + f_k). \quad (1.10.1)$$

Taking  $\epsilon_{ijk} \times (1.10.1)_{k,j}$  one obtains

$$\dot{\omega}_i + u_j \omega_{i,j} = -\epsilon_{ijk} u_{q,j} u_{k,q} + \epsilon_{ijk} \left[ \frac{1}{2} (\tau_{kq,q} - P_{,k} + f_k) \right]_{,j}.$$

Using (1.5.1) and (1.9.4), the first term on the right is exactly

$$\omega_q S_{iq} - S_{q,i} \omega_i.$$



The pressure term can be expanded into two terms, one of which vanishes, and the vorticity equation becomes

$$\dot{\omega}_i + u_j \omega_{i,j} = \omega_j S_{ij} - S_{jj} \omega_i + \epsilon_{ijk} \left[ \left( \frac{1}{\rho} \tau_{kq,q} \right)_{,j} + \frac{1}{\rho^2} P_{,k} \rho_{,j} + \left( \frac{f_k}{\rho} \right)_{,j} \right]_{,i}. \quad (1.10.2)$$

Note that the left-hand side of (1.10.2) represents the rate of change of vorticity following a fluid particle. Thus, the terms on the right display the processes that can give rise to changes in vorticity of a fluid particle. The first term represents the straining of vortex filaments, and is a crucial term in turbulence; in a two-dimensional flow, this strain is always in planes perpendicular to the vorticity, and hence there is no vortex stretching in two-dimensional flow. The second term shows that fluid compression ( $S_{kk} < 0$ ) tends to amplify the vorticity, and expansion to attenuate it. The term containing  $\tau_{kq}$  represents viscous effects, including diffusion. The term containing pressure gradients and density gradients shows that these may combine to act as a source for vorticity, if these gradient vectors have a non-zero cross product: this term is important in the atmosphere. Body force gradients can also generate vorticity; but body forces are often *conservative*, i.e. of the form

$$f_k = \rho \phi_{,k} \quad (1.10.3)$$

where  $\phi$  is a scalar potential, and (1.10.2) shows that such forces do not generate vorticity.

In a Newtonian flow where  $\rho = \rho(t)$ ,  $\mu$  is constant, and  $f_k = \rho \phi_{,k}$ , the vorticity equation becomes

$$\dot{\omega}_i + u_j \omega_{i,j} = \omega_j S_{ij} - \omega_i S_{jj} + \nu \omega_{i,jj}. \quad (1.10.4)$$

This is the form to which we will refer most often in our studies of turbulence; it emphasizes the interaction between strain-rate and vorticity that is so important in turbulence.

One usually sees the vorticity equation with the first term on the right in (1.10.4) replaced using an identity derived from (1.5.1) and (1.9.4),

$$\omega_j S_{ij} = \omega_j u_{i,j}, \quad (1.10.5)$$

We prefer (1.10.4) because it makes the interaction between vorticity and strain-rate very clear.

### 1.11 Vortex lines and tubes

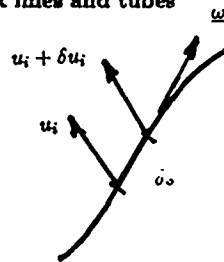


Figure 1.11.1 Velocities along a vortex line

A vortex line is a line everywhere tangent to the  $\underline{\omega}$  vector. Along a vortex line (see Figure 1.11.1)

$$\frac{\delta x_i}{\delta s} = \frac{\omega_i}{|\underline{\omega}|}. \quad (1.11.1)$$

Vortex lines move as the fluid moves. For *inviscid, incompressible flow*, the vortex lines move with the fluid. This fact is extremely helpful in understanding fluid flows in general and turbulence in particular, and forms the basis for an important class of numerical methods for simulating turbulent flow.

We will now prove this important fact about vortex lines. Let  $\underline{\omega}$  be the vorticity at the center of an elemental segment  $\delta s$  of a line marked in the fluid along a vortex line at time  $t$ . The rate of change of the vorticity following the fluid particle attached to the center of this line given by (1.10.4). Neglecting the viscous term, and assuming constant density (so that  $S_{kk} = 0$ ), and using (1.10.5), the rate of change of the vorticity of this fluid particle is

$$\dot{\omega}_i = \omega_j u_{i,j}. \quad (1.11.2)$$

The right hand side of (1.11.2) is evaluated at time  $t$  using (1.11.1) to express  $\delta x_i$  in terms of  $\delta s$ , yielding

$$\dot{\omega}_i = |\underline{\omega}| \frac{\delta u_i}{\delta s}. \quad (1.11.3)$$

Since each end of the line moves with its own velocity,

$$\frac{d(\delta x_i)}{dt} = \delta u_i. \quad (1.11.4)$$

We now examine the changes in  $\delta x_1/\omega_1$ :

$$\frac{d}{dt} \left( \frac{\delta x_1}{\omega_1} \right) = \frac{1}{\omega_1} \frac{d(\delta x_1)}{dt} - \frac{\delta x_1}{\omega_1^2} \frac{d\omega_1}{dt}. \quad (1.11.5)$$

Using (1.11.4) for the first term on the right and (1.11.3) for the second, the right hand side is zero, and hence  $\delta x_1/\omega_1$  is constant in time. The same is true for the other two components. Hence, if the line was originally a vortex line, it will remain a vortex line, as we have claimed. Moreover, since  $\delta x_1 = \tilde{\omega}_1 C$ , it follows that  $|\omega|$  will be proportional to the line length.

We can form a vortex tube from a set of nearby vortex lines. In inviscid, incompressible flow, this tube will move with the fluid, and can be stretched by strain along its length. This strain will intensify the vorticity in the tube. Since the fluid is incompressible, and the tube is imbedded in the fluid, stretching the tube reduces its diameter. The increase in vorticity can be thought of in terms of the increased rotational rate necessary to maintain conserved angular momentum as the tube decreases in diameter. These processes of vortex convection and stretching by the flow are central in turbulence.

It is left as an exercise to show that, in inviscid, compressible flow, lines everywhere tangent to  $\omega/\rho$  move with the fluid. This fact may be useful in simulations of compressible turbulence.

## 2. TURBULENCE EQUATIONS

### 2.1 Averaging concepts

Different kinds of averaging procedures are appropriate for different situations. In situations that are statistically steady, the *time average* is useful. Denoting a random field by  $f(\mathbf{x}, t)$ , its time average is

$$\bar{f}(\mathbf{x}) = \lim_{T \rightarrow \infty} \frac{1}{T} \int_0^T f(\mathbf{x}, t) dt. \quad (2.1.1)$$

The time average can not be used in fields that are statistically developing in time. But if the field is statistically *homogeneous*, i.e. statistically the same at all space points, then a *volume average* can be used,

$$\bar{f}(t) = \lim_{L \rightarrow \infty} \frac{1}{L^3} \int_0^L \int_0^L \int_0^L f(\mathbf{x}, t) d^3\mathbf{x}. \quad (2.1.2)$$

If the field is not statistically steady or homogeneous in space, but is homogeneous on planes or along lines, averages on the planes or lines can be used. But if the field is not statistically the same in time or any space dimension, one has to resort to the concept of *ensemble averaging*, i.e. averaging over a large set of (usually hypothetical) similar experiments:

$$\bar{f}(\mathbf{x}, t) = \lim_{N \rightarrow \infty} \frac{1}{N} \sum_{n=1}^N f_n(\mathbf{x}, t). \quad (2.1.3)$$

One must always be careful to choose an averaging concept appropriate to the situation. It will be assumed that an averaging process has been chosen that commutes with differentiations with respect to both time and space; the ensemble average always has this property.

### 2.2 Turbulence decomposition

Each variable in a random field is represented as the sum of its average and its fluctuation,

$$f = \bar{f} + f'. \quad (2.2.1)$$

The averaging processes defined above are all such that

$$\overline{f'} = 0. \quad (2.2.2)$$

It follows that

$$\overline{\bar{f}h} = \bar{f}\bar{h} \quad (2.2.3)$$

and

$$\overline{f'h'} = 0. \quad (2.2.4)$$

In compressible flows, mass-weighted averaging is often employed. The methods for doing this averaging are simple extensions of those given above.

Most turbulence literature concerns incompressible flows. However, there is a class of compressible flows that can be handled as a very modest extension of incompressible flows, namely flows where  $\rho = \rho(t)$  (*uniform density flows*). Many practical flows fall in this class, including flow in an internal combustion engine cylinder. The equations for uniform density flow are much simpler than those of full compressible flow, and so in the interest of simplicity much of what follows will be limited to uniform density flows with constant viscosity  $\mu$ .

### 2.3 Governing equations

If  $\rho = \rho(t)$ , the continuity equation reduces to

$$\dot{\rho} + \rho u_{i,i} = 0. \quad (2.3.1)$$

We will write the turbulence decomposition with capital letters for mean quantities and lower case letters for the fluctuations,

$$p = P + p' \quad (2.3.2a)$$

$$u_i = U_i + u'_i. \quad (2.3.2b)$$

Inserting these decompositions into the continuity equation (2.3.1), and averaging, we obtain the *mean continuity equation*

$$\dot{\rho} + \rho U_{i,i} = 0. \quad (2.3.3)$$

Subtracting this result from (2.3.1) we obtain the *fluctuating continuity equation*,

$$u'_{i,i} = 0 \quad (2.3.4)$$

Note that, for *uniform density flow*, the *fluctuation velocity field* is divergence-free, as would be the mean velocity field if the flow were incompressible.

For uniform density flow with  $\mu = \text{constant}$  and  $f_k = 0$ , the momentum equation (1.2.2) reduces to

$$\dot{u}_i + u_j u_{i,j} = -\frac{1}{\rho} p_{,i} + \nu u_{i,j,j}. \quad (2.3.5)$$

Introducing the turbulence decomposition, averaging, and making use of (2.3.4), the *mean momentum equation* is found as

$$\dot{U}_i + U_j U_{i,j} = -\frac{1}{\rho} P_{,i} + \nu U_{i,j,j} - R_{i,j,j} \quad (2.3.6)$$

where

$$R_{i,j} = \overline{u'_i u'_j}. \quad (2.3.7)$$

The quantity  $-\rho R_{i,j}$  appears in (2.3.6) like a stress, and so is called the *Reynolds stress* after O. Reynolds, who introduced the basic decomposition.

Equations (2.3.3) and (2.3.6) would permit calculation of the mean density and velocity field if the Reynolds stresses were all known. Since they are not known, we have a closure problem, which can be addressed, but not solved, by further development of the equations for the Reynolds stresses.

An alternative way of thinking about the turbulence "forces" has some physical appeal. From (1.9.1) it follows that

$$\overline{\omega'_i u'_p} = \epsilon_{ijk} \overline{u'_k u'_{j,p}} \quad (2.3.8)$$

Multiplying by  $\epsilon_{qip}$

$$\epsilon_{qip} \overline{\omega'_i u'_p} = \epsilon_{qip} \epsilon_{ijk} \overline{u'_k u'_{j,p}} = (\delta_{pj} \delta_{iq} - \delta_{pq} \delta_{ij}) \overline{u'_k u'_{j,p}} = \overline{u'_{q,p} u'_i} - \overline{u'_{p,i} u'_q}.$$

Using (2.3.4), this produces

$$\epsilon_{qip} \overline{\omega'_i u'_p} = (\overline{u'_q u'_p})_{,p} - \frac{1}{2} (\overline{u'_p u'_p})_{,q}$$

or equivalently

$$(\overline{u'_i u'_j})_{,j} = \frac{1}{2} (\overline{u'_j u'_j})_{,i} + \epsilon_{ijk} \overline{\omega'_j u'_k}. \quad (2.3.9)$$

We define

$$P^* = P + \frac{1}{2} \rho q^2 \quad (2.3.10)$$

where the mean square fluctuation velocity is

$$q^2 = \overline{u_i' u_i'}. \quad (2.3.11)$$

It is convenient to denote the mean-convection substantial derivative by

$$\overline{D}(\cdot) = (\cdot) + U_j(\cdot)_{,j}. \quad (2.3.12)$$

Then, using (2.3.9) in (2.3.6), the mean momentum equation becomes

$$\overline{D}U_i = -\frac{1}{\rho}P_{,i} + \nu U_{i,jj} - \epsilon_{ijk} \overline{\omega_j' u_k'}. \quad (2.3.13)$$

In this alternative representation the turbulence provides a contribution to the normal stress in  $P^*$  and a turbulent body force, but no shear stress. The potential of this alternative view of turbulence forces remains to be investigated.

#### 2.4.1 Mean vorticity equation

The turbulence decomposition of the vorticity is

$$\omega_i = \Omega_i + \omega_i'. \quad (2.4.1)$$

The mean strain rate and rotation rate are denoted by  $S_{ij}$  and  $\Omega_{ij}$ , respectively, and the fluctuation strain rate by  $s'_{ij}$ . By continuity for uniform density flow,  $s'_{ii} = 0$ . Introducing the turbulence decomposition into (1.10.4), and averaging, the mean vorticity equation is found to be

$$\overline{D}\Omega_i = \Omega_j S_{ij} - \Omega_i S_{jj} + \nu \Omega_{i,jj} - \overline{(\omega_i' u_j')_{,j}} + \overline{\omega_j' s'_{ij}}. \quad (2.4.2)$$

Note the appearance of the turbulence body force term  $\overline{\omega_i' u_j'}$  in the equation.

#### 2.5 Turbulent fluctuation equations

The fluctuating continuity equation is (2.3.4). Subtraction of the mean momentum equation (2.3.6) from the full equation (2.3.5) gives the fluctuating momentum equation,

$$\overline{D}u_i' = -u_j' U_{i,j} - (u_i' u_j' - \overline{u_i' u_j'})_{,j} - \frac{1}{\rho} p'_{,i} + \nu u_{i,jj}'. \quad (2.5.1)$$

Subtraction of (2.4.2) from (1.10.4) gives the fluctuating vorticity equation

$$\begin{aligned} \overline{D}\omega_i' &= +\omega_j' S_{ij} - \omega_i' S_{jj} + \Omega_j s'_{ij} \\ &\quad - u_j' \Omega_{i,j} - (u_j' \omega_i' - \overline{u_j' \omega_i'})_{,j} + (\omega_j' s'_{ij} - \overline{\omega_j' s'_{ij}}) + \nu \omega_{i,jj}'. \end{aligned} \quad (2.5.2)$$

By taking (2.5.1)<sub>i</sub>, one obtains an equation for the fluctuating pressure,

$$\frac{1}{\rho} p'_{,ii} = -2u_{i,j}' U_{j,i} - (u_{i,j}' u_{j,i}' - \overline{u_{i,j}' u_{j,i}'}) \quad (2.5.3)$$

These equations are useful for deriving equations relating statistical properties of the turbulence and in the study of the dynamics of turbulent fluctuations.

#### 2.6 Kinetic energy equations

The transport equation for the turbulent kinetic energy

$$\frac{1}{2} q^2 = \frac{1}{2} \overline{u_i' u_i'} \quad (2.6.1)$$

is derived by multiplying (2.5.1)<sub>i</sub> by  $u_i'$  and averaging. After some rearranging, one obtains

$$\overline{D}(\frac{1}{2} q^2) = P - D - J_{ij}. \quad (2.6.2)$$

Here

$$P = -\overline{u_i' u_j' S_{ij}} \quad (2.6.3)$$

is the rate of turbulent energy production,

$$\mathcal{P} = \overline{\nu u'_{i,j} u'_{i,j}} \quad (2.6.4)$$

is the (homogeneous) rate of turbulent energy dissipation, and

$$J_j = \frac{1}{\rho} \overline{p' u'_j} + \frac{1}{2} \overline{u'_j u'_i u'_i} - \nu \left( \frac{1}{2} q^2 \right)_{,j} \quad (2.6.5)$$

is the turbulent kinetic energy flux in the  $j^{\text{th}}$  direction.

Note that  $\mathcal{P}$  involves the product of turbulent stresses and mean strain rates, and that the mean rotation rate does not appear explicitly in the turbulent kinetic energy equation (though it may influence the turbulent kinetic energy by altering terms in the equation).  $\mathcal{P}$  arises from the stretching of the tangle of vortex filaments that make up the turbulence by the mean deformation.  $\mathcal{P}$  is almost always found to be positive, although there are situations in which it is negative.

Since the source of turbulent kinetic energy is the mean flow, the production term should appear with opposite sign in the evolution equation of the mean kinetic energy. Multiplying (2.3.6)<sub>i</sub> by  $U_i$ , and rearranging, the mean kinetic energy equation is

$$\overline{D \left( \frac{1}{2} U_i U_i \right)} = - \left( \frac{1}{\rho} P U_i \right)_{,i} + \frac{1}{\rho} P S_{ii} - 2\nu S_{ij} S_{ij} + 2\nu (U_i S_{ij})_{,i} - \mathcal{P} - (U_i \overline{u'_i u'_j})_{,j} \quad (2.6.6)$$

Indeed,  $-\mathcal{P}$  does appear on the right, indicating a drain from the mean kinetic energy. The two pressure terms represent the power associated with flow work and the power transfer from internal energy due to expansion of the flow. The first viscous term is the rate of dissipation of mean kinetic energy by viscous effects (see 1.8.9), and the second is the reversible viscous power transfer. The last term, which integrates to zero over a large volume of flow bounded by non-turbulent fluid, represents an internally conservative transfer of mean kinetic energy within this volume.

We have been careful to call  $\mathcal{D}$  the homogeneous dissipation, because (as shown in the next chapter) only in homogeneous turbulence does it represent the true rate of energy dissipation. From (1.8.9) the true dissipation rate is

$$\epsilon = \overline{\nu s'_{ij} s'_{ij}} = 2\nu \overline{s'_{ij} s'_{ij}} = \overline{\nu u'_{i,j} (u'_{i,j} + u'_{j,i})}. \quad (2.6.7)$$

The right hand side of the turbulent kinetic energy equation can be modified to replace  $\mathcal{D}$  by  $\epsilon$ , with a concurrent modification in the definition of the flux. This is left as an exercise.

## 2.7 Reynolds stress evolution equation

The evolution equation for  $R_{ij}$  is derived by multiplying the  $i^{\text{th}}$  fluctuation momentum equation by  $u'_j$  and the  $j^{\text{th}}$  equation by  $u'_i$ , adding the resulting equations, and averaging. The result may be written as

$$\overline{D R_{ij}} = P_{ij} + O_{ij} + T_{ij} - D_{ij} - J_{ijk,ik}. \quad (2.7.1)$$

Here the production term

$$P_{ij} = - (R_{ik} S_{kj} + R_{jk} S_{ki}) \quad (2.7.2)$$

is the source of Reynolds stress; note that its trace is

$$P_{ii} = 2\mathcal{P}. \quad (2.7.3)$$

The kinematic rotation term

$$O_{ij} = R_{ik} \Omega_{kj} + R_{jk} \Omega_{ki} \quad (2.7.4)$$

is trace free ( $O_{ii} = 0$ ) and hence this term does not contribute to production of new turbulence energy, but simply rotates the turbulence structure. The pressure strain term

$$T_{ij} = + \frac{1}{\rho} \overline{p' (u'_{i,j} + u'_{j,i})} \quad (2.7.5)$$

is also trace-free and provides intercomponent energy transfer. The dissipation term

$$D_{ij} = 2\nu \overline{u'_{i,k} u'_{j,k}} \quad (2.7.6)$$

has a trace

$$D_{ij} = 2\mathcal{D}. \quad (2.7.7)$$

Finally, the flux of  $R_{ij}$  in the  $k^{th}$  direction is

$$J_{ijk} = \frac{1}{\rho} (\overline{p' u_j' \delta_{ik}} + \overline{p' u_i' \delta_{jk}}) + \overline{u_i' u_j' u_k'} - \nu R_{ijk}. \quad (2.7.8)$$

Again we have used the mean strain-rate and rotation-rate instead of just the mean velocity gradients to bring out the different roles played by strain and rotation. Most previous workers have included the mean rotation term in with the production. But it is trace-free it does not add new energy (it is absent from the turbulent kinetic energy equation), and therefore is different than production. The rotation term provides exactly the changes that would be seen if the  $R_{ij}$  structure were to be rotated as a solid body without change. Only strain, acting on the Reynolds stresses, can act as a new source for additional Reynolds stress.

The  $R_{ij}$  equation is sometimes rewritten so that the trace of the dissipation term is  $2\epsilon$  instead of  $2D$ , with an associated modification in the flux. This is left as an exercise.

The  $R_{ij}$  evolution equation forms the basis for many of the current types of turbulence models. It is very useful in exploring the general nature of the changes that occur in turbulent flows subjected to strain.

### 2.8 Vorticity equation

The mean-square turbulent vorticity, sometimes called the *enstrophy*, is an important quantity in turbulence. Its evolution equation, derived by multiplying (2.5.2)<sub>i</sub> by  $\omega_i'$  and averaging, is useful in studying the small scales of turbulence. Denoting

$$\omega^2 = \overline{\omega_i' \omega_i'} \quad (2.8.1)$$

one finds

$$\begin{aligned} \overline{D\left(\frac{1}{2}\omega^2\right)} &= \overline{\omega_i' \omega_j' S_{ij}} - \omega^2 S_{jj} - \overline{\omega_i' u_j' \Omega_{i,j}} + \overline{\Omega_j S_{ij} \omega_i'} \\ &+ \overline{\omega_i' \omega_j' S_{i,j}} - \nu \overline{\omega_i' \omega_{i,j}} + \left[ -\frac{1}{2} \overline{u_j' \omega_i' \omega_i'} + \nu \left( \frac{1}{2} \omega^2 \right)_{,j,j} \right]. \end{aligned} \quad (2.8.2)$$

## 3. STATISTICAL DESCRIPTIONS OF HOMOGENEOUS TURBULENCE

### 3.1 Introduction

A field in which all statistical properties are independent of position is called *homogeneous*. If the statistical properties are independent of the orientation of the coordinate frame, the field is called *isotropic*. Turbulence may be approximated as homogeneous and/or isotropic, although turbulence is usually homogeneous if it is isotropic. Few practical flows are either homogeneous or isotropic. Nevertheless, regions of practical flows often are essentially homogeneous, and homogeneous flows provide a very important point of departure for models and theories of turbulence. Therefore, development of good understanding of homogeneous turbulence is an important first step in the study of turbulence.

In order for the turbulence to be homogeneous, the terms in the equations for statistical properties of turbulence must be independent of position. Since the production term (2.7.2) involves mean velocity gradients, these must be independent of position if homogeneity is to be achieved. Therefore, a necessary condition for homogeneity is that the mean velocity be a *linear function of the coordinates*. Since there are no Reynolds stress gradients in homogeneous turbulence, the mean momentum equation (2.3.6) shows that the mean velocity field is unaffected by the turbulence.

Since the mean field is decoupled from the turbulence in homogeneous turbulence, almost any mean velocity history can be imposed on homogeneous turbulence. Any mean strain-rate history can be imposed, but the mean rotation history is determined by the imposed strain-rate history. From (1.10.5) it follows that the last term on the right in the mean vorticity equation (2.4.2) is  $(\overline{\omega_j' u_i'})_{,j}$  which vanishes in homogeneous turbulence. Hence, the mean vorticity equation in homogeneous turbulence is

$$\dot{\Omega}_i = \Omega_j S_{ij} - \Omega_i S_{jj}. \quad (3.1.1)$$

Thus, while an initial arbitrary mean rotation can be imposed, any subsequent changes in the mean rotation are governed by (3.1.1). This restriction is important in the analysis and simulation of turbulence distortion by mean strain and rotation.

The statistics of homogeneous turbulence will depend upon time. Experiments on homogeneous turbulence generally involve passing flow through a grid, which generates turbulence, and then through a flow passage of varying cross section. The flow is approximately homogeneous as seen by an observer moving downstream with the mean flow, and the evolution of this turbulence as seen by the observer is interpreted as the time evolution of the turbulence. The behavior of turbulence under imposed mean strain can be studied by changing the cross-sectional geometry of the flow channel. Ingenious experiments permit great flexibility in such experiments (Gence and Mathieu 1980). Homogeneous shear flow, in which the mean

streamwise velocity gradient is uniform across the flow, can be produced using upstream grids of special geometry (Tavoularis and Corrsin 1981).

Grid turbulence is not quite isotropic. However, by placing a contraction in the flow stream downstream of the grid, essentially isotropic turbulence can be obtained (Comte-Bellot and Corrsin 1966) for study in a subsequent constant cross-section duct downstream. One can also study the relaxation of homogeneous turbulence after strain in such a duct.

In the period 1960-1980, a number of basic experiments on homogeneous turbulence provided a sound data base on these flows. Since then numerical simulations of homogeneous turbulence have added considerably to this data base. The insight gleaned from these experiment and simulations now allow us to paint a useful picture of the structure of homogeneous turbulence. The next section presents this picture and discusses the important scales of turbulent motion.

### 3.2 Structure and scales in homogeneous turbulence

One can think of homogeneous turbulence as a complex tangle of vortex filaments, each acting as a "Biot-Savart source" in moving, distorting, and straining all the filaments (Fig.3.2.1). This continual vortex stretching concentrates the vorticity, and so the volume of vortical fluid tends to be a small fraction of the total. Vortex filaments of the same sign tend to collect, and this provides a mechanism for the creation of larger eddies. This is counterbalanced by the three-dimensional straining of filaments, which tend to twist and tangle themselves to produce smaller eddies. The imposition of mean strain distort the tangle of vortex filaments, much as the fibres in a ball of steel-wool are distorted when it is stretched. This alters the structure of the filaments, and hence the structure of the turbulence. Upon removal of the mean strain-rate, interactions between filaments randomize their orientation, bring about a return to isotropy.

This tangle of vorticity produces a very broad range of turbulent motions. The larger scales are more efficient in generating the Reynolds stress required to extract energy from the mean field flow, and new turbulent energy appears initially at large scales. Through the complex non-linear interactions, which are *inviscid* processes, turbulence energy is cascaded successively to smaller and smaller eddies, ultimately to be dissipated by viscous straining in the smallest eddies, where the local strain rates are the greatest.

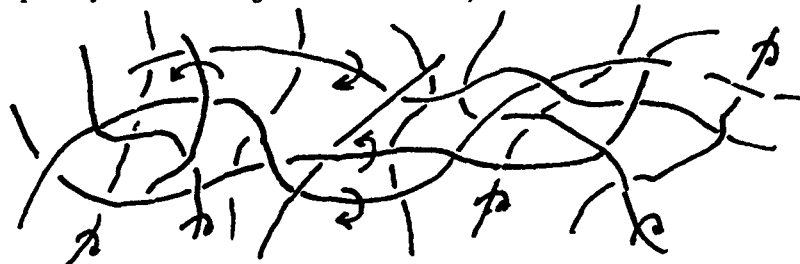


Figure 3.2.1 Homogeneous turbulence as a tangle of vortex filaments

The scale of the largest eddies is set by whatever object produced them. In grid turbulence the grid mesh determines the largest eddies, in wakes the large eddies scale on the diameter of the object, and in pipes they scale on the pipe diameter. The scale of the smallest eddies is set by the rate at which they must dissipate energy, provided to them by the large eddies through the cascade, through viscous stresses. The role of viscosity in turbulence is to set the scale of the smallest eddies.

These ideas suggest that the dissipation rate is determined by the scale of the energetic large-scale turbulence which starts the energy cascade. If we assume that  $q^2$  and  $\epsilon$  characterize these large scales, then by dimensional analysis the length scale of these eddies is

$$\ell = q^3 / \epsilon \quad (3.2.1a)$$

and the time scale is

$$\tau = q^2 / \epsilon. \quad (3.2.1b)$$

The velocity scale is of course just  $q$ . These scales tell us how the statistical properties of large eddies should be non-dimensionalized to collapse data from similar flows at different scales.

The Reynolds number of the turbulence, defined in terms of the velocity and length scales for the large eddies, is

$$R_T = \frac{q \ell}{\nu}. \quad (3.2.2)$$

In practical flows,  $q$  is generally proportional to the velocity difference driving the flow (velocity at the center of a pipe or the velocity defect in a wake), and  $\ell$  is proportional to the object dimension. Thus,  $R_T$  is usually proportional to (but smaller than by a factor of 20-100) the flow Reynolds number.

The scales of the smallest eddies are determined by the  $\epsilon$  and  $\nu$ . By dimensional analysis, the length scale must be

$$\ell_K = (\nu^3/\epsilon)^{1/4} \quad (3.2.3a)$$

and the time scale

$$\tau_K = (\nu/\epsilon)^{1/2}. \quad (3.2.3b)$$

These *Kolmogorov scales* characterize the vortex filaments in turbulence, with the cores of the vortex being of order  $\ell_K$  and rotation time for the core scaling on  $\tau_K$ . The corresponding velocity scale, characterizing the velocity difference developed locally around a vortex filament, is

$$v_K = (\nu\epsilon)^{1/4}. \quad (3.2.3c)$$

Using these scales, the ratio of the largest scales to the smallest scales is

$$\frac{\ell}{\ell_K} = R_T^{3/4} \quad (3.2.4)$$

Thus, the range of turbulence eddies broadens as the Reynolds number increases. This wide range limits direct numerical simulations of turbulence to low Reynolds numbers. *Large eddy simulations* of turbulence, in which turbulence of smaller scale than the computational mesh is modeled and the larger scales are computed, depends heavily on models for the small scales. It is tempting to approximate this sub-grid scale turbulence as homogeneous, and therefore a firm understanding of homogeneous turbulence is important to progress in large eddy simulation.

The remainder of this chapter is devoted to the mathematics used to describe the statistical properties of homogeneous turbulence. Subsequent chapters deal with the dynamic evolution of these statistical properties in response to imposed mean strain.

### 3.3 Correlations and spectra

The statistical properties of homogeneous random fields are most often described in terms of correlations and spectra. For example, if  $f$  and  $g$  are two random field variables, the *two-point correlation* of  $f$  and  $g$  is defined as

$$Q_{fg}(\mathbf{x}, \mathbf{x}', t) = \overline{\langle f(\mathbf{x}, t)g(\mathbf{x}', t) \rangle} \quad (3.3.1a)$$

where the overline denotes a volume average and the brackets denote an ensemble average. Ensemble and volume averages are usually assumed to be the same for homogeneous fields (*ergodic hypothesis*); the dual averaging is therefore redundant but useful in the analysis that follows.

For homogeneous fields  $Q_{fg}$  depends only on the separation of the two points  $\mathbf{r} = (\mathbf{x}' - \mathbf{x})$  and  $t$ ,

$$Q_{fg}(\mathbf{r}, t) = \overline{\langle f(\mathbf{x}, t)g(\mathbf{x} + \mathbf{r}, t) \rangle}. \quad (3.3.1b)$$

Often the time dependence of the correlation is not expressed explicitly, but it must not be forgotten.

There is an infinite set of other correlations of possible interest, for example the two-point correlation with time delay, three-point correlations, etc. A complete statistical description requires knowledge of the *probability density function* for all variables of interest at all space points and time, an impossible goal to achieve. Therefore, statistical descriptions are always limited in what they can provide, and the challenge is to provide what is really essential, with minimum effort and maximum accuracy.

In homogeneous fields, Fourier expansions can be used to represent individual realizations of the fields. Suppose that  $f$  and  $g$  are defined within a box of interest (Fig. 3.3.1). In order to give them Fourier expansions we have to imagine that they are periodic functions, so let

$$\tilde{f}(\mathbf{x}) = \begin{cases} f(\mathbf{x}) & \text{inside the box} \\ \text{periodic repetition outside.} \end{cases}$$

The Fourier representation of  $\tilde{f}$  at any instant of time is

$$\tilde{f}(\mathbf{x}) = \sum_{\mathbf{k}'} \tilde{f}(\mathbf{k}') e^{-i\mathbf{k}' \cdot \mathbf{x}} \quad (3.3.2a)$$

where  $\mathbf{k} = (k_1, k_2, k_3)$  is the three-dimensional *wavenumber vector*, and  $\mathbf{k} \cdot \mathbf{x} = k_n x_n$ . Since the Fourier modes must fit into the box with integer periods,

$$k_i = 2\pi n_i / L. \quad (3.3.2b)$$

The summation is a triple sum over all Fourier modes,



$$\sum_{\mathbf{k}'} = \sum_{k_1}^{\infty} \sum_{k_2}^{\infty} \sum_{k_3}^{\infty}. \quad (3.3.2c)$$

Note that the Fourier coefficients may vary with time; we do not show this explicitly here.

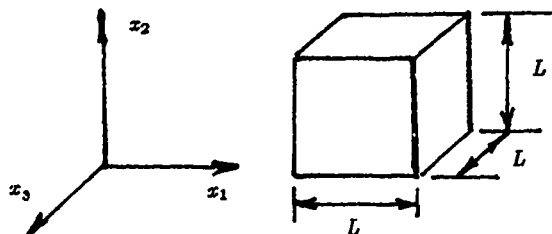


Figure 3.3.1 Box for Fourier representation

There is an important relationship between the Fourier coefficients of positive and negative wavenumbers for a real field. Taking the complex conjugate of (3.3.2a), replacing  $\mathbf{k}'$  by  $\mathbf{k}''$ ,

$$\tilde{f}^*(\mathbf{x}) = \sum_{\mathbf{k}''} \hat{f}^*(\mathbf{k}'') e^{+i\mathbf{k}'' \cdot \mathbf{x}}$$

where the  $*$  denotes a complex conjugate. Letting  $\mathbf{k}'' = -\mathbf{k}'$ ,

$$\tilde{f}^*(\mathbf{x}) = \sum_{\mathbf{k}'} \hat{f}^*(-\mathbf{k}') e^{-i\mathbf{k}' \cdot \mathbf{x}}. \quad (3.3.3)$$

Now, if  $\tilde{f}$  is real it is equal to its complex conjugate. Equating the Fourier coefficients of like exponentials in (3.3.2a) and (3.3.2),

$$\hat{f}(\mathbf{k}') = \hat{f}^*(-\mathbf{k}')$$

or alternatively (for real  $f$ )

$$\hat{f}(-\mathbf{k}) = \hat{f}^*(\mathbf{k}). \quad (3.3.4)$$

The Fourier coefficients are evaluated using the orthogonality property of the Fourier modes, using integrals over the domain. In what follows  $\int()d^3\mathbf{x}$  denotes an integral over the box in Fig. 3.3.1. Then, multiplying (3.3.2a) by  $e^{i\mathbf{k} \cdot \mathbf{x}}$  and integrating over the box,

$$\int e^{i\mathbf{k} \cdot \mathbf{x}} \tilde{f}(\mathbf{x}) d^3\mathbf{x} = \sum_{\mathbf{k}'} \hat{f}(\mathbf{k}') \int e^{i(\mathbf{k}-\mathbf{k}') \cdot \mathbf{x}} d^3\mathbf{x}. \quad (3.3.5)$$

Since each Fourier mode that fits the box contains an integer number of cycles,

$$\int e^{i(\mathbf{k}-\mathbf{k}') \cdot \mathbf{x}} d^3\mathbf{x} = \begin{cases} 0 & \text{if } \mathbf{k} \neq \mathbf{k}' \\ L^3 & \text{if } \mathbf{k} = \mathbf{k}'. \end{cases} \quad (3.3.6)$$

Hence all terms in the summation of (3.3.4) drop out except for the one where  $\mathbf{k}' = \mathbf{k}$ . Thus, the Fourier coefficients can be evaluated as

$$\hat{f}(\mathbf{k}) = \frac{1}{L^3} \int \tilde{f}(\mathbf{x}) e^{i\mathbf{k} \cdot \mathbf{x}} d^3\mathbf{x}. \quad (3.3.7)$$

The two-point correlation of  $f$  and  $g$  can be expressed in terms of the Fourier representations. Consider the correlation of  $f$  and  $g$  within the box of Fig. (3.3.1),

$$\langle \tilde{f}(\mathbf{x}) \tilde{g}(\mathbf{x}') \rangle = \sum_{\mathbf{k}} \sum_{\mathbf{k}'} \langle \hat{f}(\mathbf{k}) \hat{g}(\mathbf{k}') \rangle e^{-i(\mathbf{k} \cdot \mathbf{x} + \mathbf{k}' \cdot \mathbf{x}')}$$

The brackets indicate that the Fourier coefficients are random variables that will differ from from realisation to realisation. Let  $\mathbf{k}'' = -\mathbf{k}'$  and  $\mathbf{r} = \mathbf{x}' - \mathbf{x}$ . Then, using (3.3.4),

$$\langle \tilde{f}(\mathbf{x}) \tilde{g}(\mathbf{x} + \mathbf{r}) \rangle = \sum_{\mathbf{k}} \sum_{\mathbf{k}''} \langle \hat{f}(\mathbf{k}) \hat{g}^*(\mathbf{k}'') \rangle e^{-i\mathbf{x} \cdot (\mathbf{k} - \mathbf{k}'') + i\mathbf{k}'' \cdot \mathbf{r}}. \quad (3.3.8)$$

Now we average by integrating over the box and dividing by  $L^3$ , denoting this average by an overline. Using (3.3.6), all the terms in the sum drop out except the terms where  $\mathbf{k}'' = \mathbf{k}$ . The result is then

$$\tilde{Q}_{fg}(r) = \overline{\tilde{f}(\mathbf{x})\tilde{g}(\mathbf{x}+\mathbf{r})} = \sum_{\mathbf{k}} \langle \tilde{f}(\mathbf{k})\tilde{g}^*(\mathbf{k}) \rangle e^{i\mathbf{k}\cdot\mathbf{r}}. \quad (3.3.9)$$

In computational simulations in which the evolution of the Fourier coefficients is calculated for finite-series approximations to the fields, (3.3.9) is used to calculate the two-point correlation.

Theoretical treatments take the limit as  $L \rightarrow \infty$ , in which case the sums become integrals. To pass to this limit, we note that the difference between consecutive wavenumbers in the summation is  $\Delta k_\alpha = 2\pi/L$  for each direction, so  $\Delta k_i L/2\pi = 1$ . We can multiply each term in the summation by unity three times to obtain

$$\tilde{Q}_{fg}(r) = \sum_{\mathbf{k}} \langle \tilde{f}(\mathbf{k})\tilde{g}^*(\mathbf{k}) \rangle \left(\frac{L}{2\pi}\right)^3 \Delta k_1 \Delta k_2 \Delta k_3 e^{i\mathbf{k}\cdot\mathbf{r}}. \quad (3.3.10)$$

We define the *cospectrum* of  $\tilde{f}$  and  $\tilde{g}$  as

$$\tilde{E}_{fg}(\mathbf{k}) = \left(\frac{L}{2\pi}\right)^3 \langle \tilde{f}(\mathbf{k})\tilde{g}^*(\mathbf{k}) \rangle. \quad (3.3.11)$$

This is the equation used to calculate the cospectrum in discrete spectral simulations of random fields. Then,

$$\tilde{Q}_{fg}(r) = \sum_{\mathbf{k}} \tilde{E}_{fg}(\mathbf{k}) e^{i\mathbf{k}\cdot\mathbf{r}} \Delta k_1 \Delta k_2 \Delta k_3. \quad (3.3.12)$$

Taking the limit as  $L \rightarrow \infty$ , we define the cospectrum of  $f$  and  $g$  by

$$E_{fg}(\mathbf{k}) = \lim_{L \rightarrow \infty} \tilde{E}_{fg}(\mathbf{k}). \quad (3.3.13)$$

$E_{fg}$  does not become infinite as  $L \rightarrow \infty$  because the Fourier coefficients of individual modes become very small as the number of significant modes increases. As  $L \rightarrow \infty$ ,  $\Delta k_1 \Delta k_2 \Delta k_3$  becomes an elemental volume in wavenumber space  $dk_1 dk_2 dk_3 = d^3\mathbf{k}$ . Therefore, in (3.3.12) the two-point correlation

$$Q_{fg}(r) = \lim_{L \rightarrow \infty} \tilde{Q}_{fg}(r) \quad (3.3.14)$$

becomes the *three-dimensional Fourier transform* of the cospectrum,

$$Q_{fg}(r) = \int E_{fg}(\mathbf{k}) e^{i\mathbf{k}\cdot\mathbf{r}} d^3\mathbf{k}. \quad (3.3.15)$$

Here the triple integration is to be carried out over all wavenumbers.

There is an inverse of the transform (3.3.15). Multiplying (3.3.9) by  $e^{-i\mathbf{k}'\cdot\mathbf{r}}$  and integrating over a box of size  $L$  in  $r$  space,

$$\int \tilde{Q}_{fg}(r) e^{-i\mathbf{k}'\cdot\mathbf{r}} d^3\mathbf{r} = \sum_{\mathbf{k}} \int \langle \tilde{f}(\mathbf{k})\tilde{g}^*(\mathbf{k}) \rangle e^{i\mathbf{r}\cdot(\mathbf{k}-\mathbf{k}')} \quad (3.3.16)$$

Each exponential in the summation will execute an integer number of cycles in each direction and hence integrate to zero, except for the term where  $\mathbf{k} = \mathbf{k}'$ . Hence,

$$\int \tilde{Q}_{fg}(r) e^{-i\mathbf{k}'\cdot\mathbf{r}} d^3\mathbf{r} = L^3 \langle \tilde{f}(\mathbf{k})\tilde{g}^*(\mathbf{k}) \rangle = (2\pi)^3 \tilde{E}_{fg}(\mathbf{k}). \quad (3.3.17)$$

In computational simulations based on finite-difference methods, this equation is used to calculate the cospectrum from the two-point correlation. Taking the limit as  $L \rightarrow \infty$ , and replacing  $\mathbf{k}'$  by  $\mathbf{k}$ ,

$$E_{fg}(\mathbf{k}) = \left(\frac{1}{2\pi}\right)^3 \int Q_{fg}(r) e^{-i\mathbf{k}\cdot\mathbf{r}} d^3\mathbf{r}. \quad (3.3.18)$$

Note that  $E_{fg}$  and  $Q_{fg}$  are *Fourier transform pairs*.

We could have obtained the cospectrum simply by Fourier transformation of the two-point correlation. We started with a finite box so that the relationships between the Fourier coefficients and the cospectrum would be made clear, and also to derive results useful to persons engaged in discrete-representation simulations of homogeneous turbulence in finite computational domains. It should be understood that the Fourier transforms of  $f$  and  $g$  defined over an infinite region do not exist. However, because events at distant separations are uncorrelated,  $Q_{fg} \rightarrow 0$  as  $|\mathbf{r}| \rightarrow \infty$ , and hence the Fourier transform of  $Q_{fg}$  does exist.

### 3.4 Velocity correlations and spectra

The velocity field in homogeneous turbulence can be represented in the terms outlined above. Let  $f = u_i$  and  $g = u_j$ . Then, dropping the redundant ensemble average,

$$Q_{ij}(r) = \overline{u'_i(\mathbf{x})u'_j(\mathbf{x} + \mathbf{r})}. \quad (3.4.1)$$

$Q_{ij}$  is the two-point velocity correlation tensor. Note that

$$Q_{ii}(0) = \overline{u'_i(\mathbf{x})u'_i(\mathbf{x})} = q^2. \quad (3.4.2)$$

$Q_{ij}(r)$  expresses the average relationship between two velocity components measured at two locations separated by a distance  $\mathbf{x}$ .  $Q_{\alpha\alpha}$  (repeated Greek indices are not summed) will be largest for zero separation, fall to a fraction of this value for separations comparable with the large eddies in the turbulence, and become zero for infinite separation. If the eddies tend to be long in one direction and short in another, this will be reflected in the different rate at which the correlation falls off with different  $r_\alpha$ . Thus, the two-point correlation tensor can tell one quite a bit about the structure of the turbulence.

Using (3.3.18), the velocity spectrum tensor is

$$E_{ij}(\mathbf{k}) = \left(\frac{1}{2\pi}\right)^3 \int Q_{ij}(\mathbf{r}) e^{-i\mathbf{k}\cdot\mathbf{r}} d^3\mathbf{r} \quad (3.4.3)$$

where the integrations are over all  $\mathbf{r}$ . It is related to the two-point velocity correlation tensor by (3.3.15),

$$Q_{ij}(\mathbf{r}) = \int E_{ij}(\mathbf{k}) e^{i\mathbf{k}\cdot\mathbf{r}} d^3\mathbf{k} \quad (3.4.4)$$

where the integrations are over all  $\mathbf{k}$ .

The Reynolds stresses  $R_{ij} = \overline{u'_i u'_j}$  are given by

$$R_{ij} = Q_{ij}(0) \quad (3.4.5)$$

for which (3.4.4) gives

$$R_{ij} = \int E_{ij}(\mathbf{k}) d^3\mathbf{k}. \quad (3.4.6)$$

Reviewing the developments of the previous section, one sees that  $E_{ij}(\mathbf{k}) d^3\mathbf{k}$  represents the contributions to  $R_{ij}$  coming from an element of  $\mathbf{k}$  space of volume  $d^3\mathbf{k}$  positioned at  $\mathbf{k}$ .

For uniform density flow, the continuity equation (2.3.4) provides important constraints on  $Q_{ij}(\mathbf{r})$ . From (3.4.1)

$$\frac{\partial Q_{ij}}{\partial r_j} = \overline{u'_i(\mathbf{x})u'_j(\mathbf{x} + \mathbf{r})_{,j}} = 0. \quad (3.4.7a)$$

Replacing  $\mathbf{x}$  by  $\mathbf{x}' - \mathbf{r}$  in (3.4.1), then differentiating with respect to  $r_i$ , (2.3.4) also requires that

$$\frac{\partial Q_{ij}}{\partial r_i} = 0. \quad (3.4.7b)$$

The continuity equation (2.3.4) also constrains  $E_{ij}$ . In terms of the Fourier expansion, continuity requires

$$-\sum_{\mathbf{k}} i k_j \hat{u}_j(\mathbf{k}) e^{-i\mathbf{k}\cdot\mathbf{x}} = 0. \quad (3.4.8)$$

This must hold for all  $\mathbf{x}$ , which requires that the coefficient of each and every exponential must vanish. Hence, for each wavenumber vector  $\mathbf{k}$ ,

$$k_j \hat{u}_j(\mathbf{k}) = 0. \quad (3.4.9)$$

Equation (3.4.9) is the continuity equation in Fourier form. It says that, for each  $\mathbf{k}$ , the Fourier coefficient vector  $\hat{\mathbf{u}}$  must be orthogonal to  $\mathbf{k}$  in order for the velocity field to be divergence-free. This condition is used very often in analysis and simulation of homogeneous turbulence. From (3.4.9), it follows (most obviously using the discrete Fourier representations) that

$$k_i E_{ij} = 0 \quad (3.4.10a)$$

and

$$k_j E_{ij} = 0. \quad (3.4.10b)$$

The correlation tensor  $Q_{ij}$  has an important symmetry property. Noting that

$$Q_{ij}(-\mathbf{r}) = \overline{u'_i(\mathbf{x}) u'_{j'}(\mathbf{x} - \mathbf{r})}$$

we let  $\mathbf{x} = \mathbf{x}' + \mathbf{r}$  and rewrite this as

$$Q_{ij}(-\mathbf{r}) = \overline{u'_i(\mathbf{x}' + \mathbf{r}) u'_{j'}(\mathbf{x}')}$$

The right hand side is just  $Q_{ji}(\mathbf{r})$ . Hence

$$Q_{ij}(-\mathbf{r}) = Q_{ji}(\mathbf{r}). \quad (3.4.11)$$

The spectrum tensor  $E_{ij}$  also has a symmetry property. Since the Fourier coefficients for real fields obey (3.3.3), it follows (most obviously from the discrete Fourier representations) that

$$\begin{aligned} \tilde{E}_{ij}(-\mathbf{k}) &= \left( \frac{L}{2\pi} \right)^3 < \hat{u}_i(-\mathbf{k}) \hat{u}_{j'}^*(-\mathbf{k}) > \\ &= \left( \frac{L}{2\pi} \right)^3 < \hat{u}_i^*(\mathbf{k}) \hat{u}_j(\mathbf{k}) > = \tilde{E}_{ji}(\mathbf{k}). \end{aligned} \quad (3.4.12)$$

In the limit  $L \rightarrow \infty$  this becomes

$$E_{ij}(-\mathbf{k}) = E_{ji}(\mathbf{k}). \quad (3.4.13)$$

The turbulence kinetic energy may be expressed as

$$\frac{1}{2} q^2 = \frac{1}{2} Q_{ii}(0) = \frac{1}{2} \int E_{ii}(\mathbf{k}) d^3 \mathbf{k}. \quad (3.4.14)$$

Integral scales of motion may be defined in terms of  $Q_{ij}$ . For example,

$$L_{11} = \frac{\int_0^\infty Q_{11}(r_1, 0, 0) dr_1}{Q_{11}(0, 0, 0)} \quad (3.4.15)$$

is useful as a measure of the  $x_1$  scale of the turbulence. Here the arguments display the three components of the separation vector,

$Q_{ij}$  and  $E_{ij}$  are the classical quantities used to describe homogeneous turbulence. They are less useful for inhomogeneous turbulence because expansion functions other than Fourier modes really should be used in directions of inhomogeneity. They are used for inhomogeneous flows when the turbulence can be approximated as locally homogeneous over regions large compared to the integral scale.

### 3.5 Other statistical quantities

There are many other statistical quantities of interest in turbulence. Those that involve only quadratic forms in the velocity are termed *second-order*. Any second-order statistical property of the velocity field can be derived from the two-point correlation tensor or the velocity spectrum tensor. For example, a tensor of interest is

$$D_{ijpq} = \overline{u'_{i,p} u'_{j,q}}. \quad (3.5.1)$$

From (3.4.1),

$$\frac{\partial Q_{ij}(\mathbf{r})}{\partial r_q} = \overline{u'_i(\mathbf{x}) u'_{j,q}(\mathbf{x} + \mathbf{r})}. \quad (3.5.2)$$

Replacing  $\mathbf{x}$  by  $\mathbf{x}' - \mathbf{r}$  in (3.5.2), then differentiating with respect to  $r_p$ , one has

$$\frac{\partial^2 Q_{ij}(\mathbf{r})}{\partial r_p \partial r_q} = \overline{-u'_{i,p}(\mathbf{x}' - \mathbf{r}) u'_{j,q}(\mathbf{x}')}. \quad (3.5.3)$$

Now letting  $\mathbf{r} = 0$ ,

$$D_{ijpq} = - \left( \frac{\partial^2 Q_{ij}(\mathbf{r})}{\partial r_p \partial r_q} \right)_{|\mathbf{r}|=0}. \quad (3.5.4)$$

The corresponding result in terms of the spectrum tensor can be derived directly by taking the derivatives of the discrete Fourier series for the velocities, and proceeding as in section 3.2 above, or by applying (3.5.4) to (3.4.4). Either approach gives

$$D_{ijpq} = \int k_p k_q E_{ij}(\mathbf{k}) d^3 \mathbf{k}. \quad (3.5.5)$$

Since gradients of all statistical quantities vanish in homogeneous turbulence,

$$\overline{(u_i' u_j')}_{,ij} = 0. \quad (3.5.6)$$

Expanding the differentiation using the continuity equation (2.3.4),

$$D_{ijji} = \overline{u_{i,j} u_{j,i}} = 0. \quad (3.5.7)$$

Note that this is consistent with (3.5.4) and (3.5.5) if the continuity constraints (3.4.7) or (3.4.10) are applied. The dissipation rate  $\epsilon$  may be expressed in general as

$$\epsilon = \nu(D_{iijj} + D_{ijji}). \quad (3.5.8)$$

From (3.5.7), the second term does not contribute, and in homogeneous turbulence the true dissipation rate  $\epsilon$  is the same as the homogeneous dissipation rate  $\mathcal{D}$  defined by (2.6.4).

Using (3.5.8), (3.5.7), and (3.5.5), we find that the dissipation rate is related to the velocity spectrum tensor by

$$\epsilon = \nu \int k^2 E_{ii}(\mathbf{k}) d^3 \mathbf{k}. \quad (3.5.9)$$

The factor  $k^2$  means that the main contributions to the dissipation come from higher wavenumbers (smaller eddies) than those that provide the major contribution to the kinetic energy.

### 3.6 Vorticity

The two-point vorticity correlation tensor is

$$W_{ij}(\mathbf{r}) = \overline{\omega_i'(\mathbf{x}) \omega_j'(\mathbf{x} + \mathbf{r})}. \quad (3.6.1)$$

Note that

$$W_{ii}(0) = \overline{\omega_i' \omega_i'} = \omega^2. \quad (3.6.2)$$

From the definition of vorticity (1.9.1),

$$\omega^2 = D_{iijj} - D_{ijji} \quad (3.6.3)$$

so it follows from (3.5.7) and (3.5.8) that in homogeneous turbulence the dissipation is directly related to the mean-square vorticity,

$$\epsilon = \nu \omega^2. \quad (3.6.4)$$

The enstrophy equation (2.8.1) is therefore sometimes used as a guide in developing model equations for the dissipation.

The vorticity can also be expanded in a Fourier representation; for the box of section 3.2,

$$\tilde{\omega}_i'(\mathbf{x}) = \sum_{\mathbf{k}} \tilde{\omega}_i(\mathbf{k}) e^{-i\mathbf{k} \cdot \mathbf{x}} \quad (3.6.5)$$

Because the vorticity is by definition divergence-free,

$$k_i \tilde{\omega}_i(\mathbf{k}) = 0 \quad (3.6.6)$$

and because the vorticity is real

$$\tilde{\omega}_i(\mathbf{k}) = \tilde{\omega}_i^*(-\mathbf{k}). \quad (3.6.7)$$

The vorticity spectrum tensor  $H_{ij}(\mathbf{k})$  can be developed following the approach above. It is of course the Fourier transform of the two-point vorticity correlation tensor, and can be related to the velocity tensor. Because the vorticity is divergence-free,

$$k_i H_{ij}(\mathbf{k}) = 0 \quad (3.6.8a)$$

and

$$k_j H_{ij}(\mathbf{k}) = 0 \quad (3.6.8b)$$

and because it is real

$$H_{ij}(-\mathbf{k}) = H_{ji}(\mathbf{k}). \quad (3.6.9)$$

The Fourier coefficients of the vorticity are related to those of the velocity. Using (1.9.1),

$$\tilde{\omega}_i(\mathbf{x}) = \sum_{\mathbf{k}} \epsilon_{ipq}(-ik_q) \hat{u}_q(\mathbf{k}) e^{-i\mathbf{k} \cdot \mathbf{x}}. \quad (3.6.10)$$

Equating coefficients of like exponentials, the vorticity coefficients are found to be

$$\hat{\omega}_i(\mathbf{k}) = -ik_p \epsilon_{ipq} \hat{u}_q(\mathbf{k}). \quad (3.6.11)$$

From this it follows that

$$H_{ij}(\mathbf{k}) = \epsilon_{ipq} \epsilon_{jrs} k_p k_r E_{qs}(\mathbf{k}) \quad (3.6.12)$$

One can express  $Q_{ij}$  in terms of the vorticity correlation tensor and  $E_{ij}$  in terms of the vorticity spectrum tensor. This requires the solution of the Poisson equation (1.9.5), which is easily accomplished using the Fourier representations. Alternatively, one can multiply (3.6.10) by  $\epsilon_{rsi} k_s$ . The result is

$$\hat{u}_i(\mathbf{k}) = \epsilon_{ipq} \frac{ik_p}{k^2} \hat{\omega}_q(\mathbf{k}). \quad (3.6.13)$$

where  $k^2 = k_i k_i$ . Substituting in the discrete representation of  $\tilde{E}_{ij}$  and taking the limit, one finds

$$E_{ij}(\mathbf{k}) = \epsilon_{ipq} \epsilon_{jrs} \frac{k_p k_r}{k^4} H_{qs}(\mathbf{k}). \quad (3.6.14)$$

This result finds important use in *rapid distortion theory*, where it is used to estimate the anisotropy in the Reynolds stresses produced by distortion of the vorticity field due to imposed mean strain. It is also useful in constructing models of  $E_{ij}$  for anisotropic turbulence using models for the anisotropic  $H_{ij}$ .

### 3.7 Correlations and spectra in isotropic turbulence

If the statistics are independent of the coordinate system orientation, only two types of correlations completely characterize the velocity correlation tensor (Fig. 3.7.1). The *longitudinal correlation function*

$$f(r) = \frac{3}{q^2} Q_{11}(r_1, 0, 0) \quad (3.7.1)$$

describes the coherence of the velocity fluctuations aligned with the separation of the two points. The *lateral correlation function*

$$g(r) = \frac{3}{q^2} Q_{22}(r_1, 0, 0) \quad (3.7.2)$$

relates to the coherence of fluctuation velocities perpendicular to the separation axis.

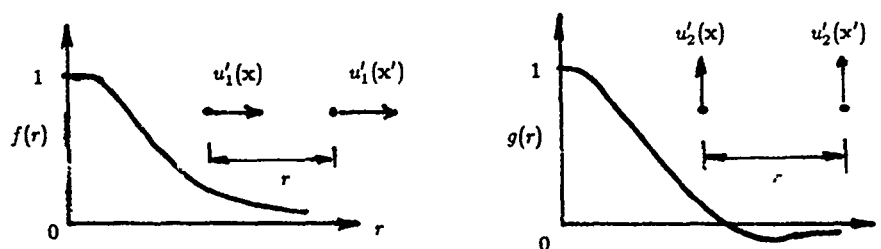


Figure 3.7.1 Longitudinal and lateral correlation functions

The complete tensor  $Q_{ij}(\mathbf{r})$  can be expressed in terms of these two scalar functions. The tensor must be a function of the separation vector  $\mathbf{r}$ . The most general such function is

$$Q_{ij}(\mathbf{r}) = C_1 \delta_{ij} + C_2 r_i r_j \quad (3.7.3)$$

where the coefficients  $C_1$  and  $C_2$  may be functions of the scalar invariant of the vector,  $r = \sqrt{r_i r_i}$ . The coefficients can be identified by expressing the longitudinal and lateral correlations:

$$Q_{22}(r_1, 0, 0) = \frac{q^2}{3} g(r) = C_1 \quad (3.7.4)$$

$$Q_{11}(r_1, 0, 0) = \frac{q^2}{3} f(r) = C_1 + C_2 r^2. \quad (3.7.5)$$

Solving for  $C_1$  and  $C_2$ , one finds

$$Q_{ij}(r) = \frac{q^2}{3} \left[ \frac{f(r) - g(r)}{r^2} r_i r_j + g(r) \delta_{ij} \right]. \quad (3.7.6)$$

Note that  $f$  and  $g$  are scalar functions of the scalar separation magnitude  $r$  (and of time, not shown explicitly). The continuity equation provides a relationship between  $f$  and  $g$ . Since  $r = \sqrt{r_i r_i}$ ,

$$\frac{\partial r}{\partial r_k} = \frac{r_k}{r}. \quad (3.7.6)$$

Differentiating (3.7.6) with respect to  $r_k$ ,

$$Q_{ij,k} = \frac{q^2}{3} \left[ \left( \frac{f-g}{r^2} \right)' r_i r_j \frac{r_k}{r} + \left( \frac{f-g}{r^2} \right) (r_i \delta_{jk} + r_j \delta_{ik}) + g' \frac{r_k}{r} \right] \quad (3.7.8)$$

where the primes denotes differentiation with respect to  $r$ . Setting  $k = j$  and using the continuity condition (3.4.7), one finds

$$f' + \frac{2}{r}(f - g) = 0 \quad (3.7.9)$$

This integrates readily to give

$$f(r) = \frac{2}{r^2} \int_0^r \bar{r} g(\bar{r}) d\bar{r}. \quad (3.7.10)$$

$E_{ij}$  for isotropic turbulence can be obtained by Fourier transform of  $Q_{ij}$  as outlined in section 3.3. Alternatively, we can construct its general form directly since, for isotropic turbulence the  $E_{ij}$  tensor must be a function only the vector  $\mathbf{k}$ . The most general form is

$$E_{ij}(\mathbf{k}) = C_1 \delta_{ij} + C_2 k_i k_j \quad (3.7.11)$$

where the coefficients can depend on the scalar invariant of the vector,  $k = \sqrt{(k_i k_i)}$ . Using the continuity condition (3.4.10),

$$C_1 k_j + C_2 k^2 k_j = 0 \quad (3.7.12)$$

hence

$$C_2 = -C_1/k^2 \quad (3.7.13)$$

Redefining  $C_1$  as  $4\pi k^2 E(k)$ , we have

$$E_{ij}(\mathbf{k}) = \frac{E(k)}{4\pi k^2} \left( \delta_{ij} - \frac{k_i k_j}{k^2} \right). \quad (3.7.14)$$

$E(k)$  is called the *energy spectrum function*. Note that it is a scalar function of the scalar  $k$  (and of time, not shown explicitly).

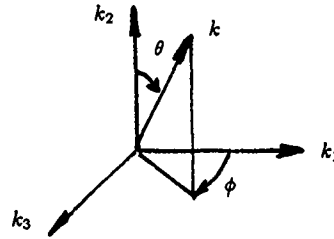


Figure 3.7.2 Coordinate system for  $k$ -space integration

The turbulence energy is, using (3.4.14),

$$\frac{1}{2} q^2 = \int \frac{1}{4\pi k^2} E(k) d^3 \mathbf{k} \quad (3.7.15)$$

The integration of integrals of this type, in which the unknown function depends only on the magnitude of the vector, can best be carried out in spherical coordinates (Fig. 3.7.2). We have

$$\frac{1}{2}q^2 = \frac{1}{4\pi} \int_{k=0}^{\infty} \int_{\theta=0}^{\pi} \int_{\phi=0}^{2\pi} \frac{E(k)}{k^2} k^2 \sin \theta d\theta d\phi dk. \quad (3.7.16)$$

Carrying out the integrations over  $\phi$  and  $\theta$ ,

$$\frac{1}{2}q^2 = \int_0^{\infty} E(k) dk. \quad (3.7.17)$$

We see that  $E(k)dk$  represents the contribution to the kinetic energy per unit mass arising from all the Fourier modes in a spherical shell in  $k$ -space of radius  $k$  and thickness  $dk$ . Once  $E(k)$  is known, the entire velocity spectrum tensor  $E_{ij}$  is known from (3.7.14).

In theory, homogeneous isotropic turbulence evolves in time, and one should measure the spectrum tensor by making measurements at many space points. In reality this is very difficult (but it is what is in fact done in a numerical simulation). Instead, laboratory experiments make use of *Taylor's hypothesis*, which assumes that the velocity pattern measured as a function of time at one point is frozen in the fluid and being swept over the probe. The probe measurement is thereby interpreted as providing  $Q_{11}(r_1, 0, 0)$ . Using (3.7.14) in (3.4.4),

$$Q_{11}(r_1, 0, 0) = \int \frac{E(k)}{4\pi k^2} \left(1 - \frac{k_1^2}{k^2}\right) e^{ik_1 r_1} d^3k \quad (3.7.18)$$

This integration is conveniently carried out in the coordinates of Fig. 3.7.3. We sort the Fourier contributions according to those with the same wavenumber  $|k_1|$ . Terms from both sides of the  $k_1$  axis contribute, with opposite signs in their exponentials; these are combined into a cosine:

$$Q_{11}(r_1, 0, 0) = \int_{k_1=0}^{\infty} \int_{k=k_1}^{\infty} \int_{\phi=0}^{2\pi} \frac{E(k)}{4\pi k^2} \left(1 - \frac{k_1^2}{k^2}\right) 2 \cos(k_1 r_1) k d\phi dk dk_1 \quad (3.7.19)$$

We carrying out the  $\phi$  integration, and define the *one dimensional spectrum function*  $E_1$  by

$$E_1(k_1) = \int_{k=k_1}^{\infty} \frac{E(k)}{k} \left(1 - \frac{k_1^2}{k^2}\right) dk. \quad (3.7.20)$$

Then,

$$Q_{11}(r_1, 0, 0) = \int_{k_1=0}^{\infty} E_1(k) \cos(k_1 r_1) dk_1 \quad (3.7.21)$$

One can taking the Fourier cosine transformation of the measured  $Q_{11}(r_1, 0, 0)$  to get  $E_1(k_1)$ . Then, differentiating (3.7.18) twice (a courageous step with laboratory data!),

$$E(k_1) = \frac{k_1^2}{2} \frac{\partial^2 E_1(k_1)}{\partial k_1^2} - \frac{k_1}{2} \frac{\partial E_1(k_1)}{\partial k_1} \quad (3.7.22)$$

This allows  $E(k)$  to be determined. It also shows that if  $E(k)$  varies as a power of  $k$  in some range then  $E_1(k_1)$  will vary with the same power of  $k_1$ .

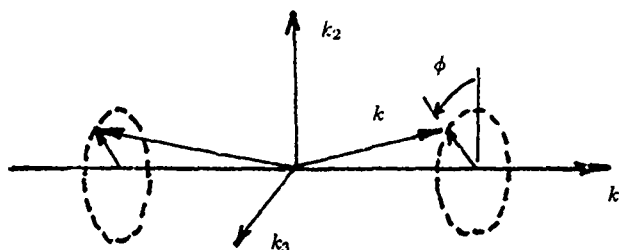


Figure 3.7.3 Coordinates for one-dimensional spectrum integration

Eqn. (3.7.21) in essence defines  $Q_{11}$  as a one-dimensional Fourier cosine transform of  $E_1$ . The inverse transform is

$$E_1(k_1) = \frac{2}{\pi} \int_0^{\infty} Q_{11}(r_1, 0, 0) \cos(k_1 r_1) dr_1. \quad (3.7.23)$$

Noting that  $Q_{11}(0) = q^2/3$  in isotropic turbulence, the integral scale defined by (3.4.15) is given by (3.7.23) as

$$L_{11} = A_f = \frac{3\pi}{2q^2} E_1(0) \quad (3.7.24)$$



$\lambda_f$  is the integral scale derived from the longitudinal correlation function  $f(r)$ , and hence it is called the *longitudinal integral scale*. Since it is non-zero,  $E_1(0) > 0$ , in contrast to  $E(0) = 0$ .

### 3.8 Dissipation in isotropic turbulence

Using the isotropic spectrum (3.7.14) in (3.5.9), carrying out the integrations using polar coordinates as above, the dissipation rate is found as

$$\epsilon = \nu \int_0^\infty k^2 E(k) dk \quad (3.8.1)$$

The factor  $k^2$  means that higher wave numbers (smaller scales) make more contribution to the dissipation (and vorticity) than they do to the energy (compare 3.7.17).

Since the small-scale component of turbulence is generally thought to be very nearly isotropic at high Reynolds numbers, isotropic turbulence theory is used as an aid in estimating  $\epsilon$  from laboratory data. This approach makes use of the tensor  $D_{ijpq}$  defined by (3.5.1). In an isotropic field, the only tensors upon which  $D_{ijpq}$  can depend are the isotropic numerical tensors, hence it must be of the form

$$D_{ijpq} = C_1 \delta_{ij} \delta_{pq} + C_2 \delta_{ip} \delta_{jq} + C_3 \delta_{iq} \delta_{jp} \quad (3.8.2)$$

where the coefficients must be scalars. The coefficients can be evaluated from three known constraints. First, the definition forces symmetry,

$$D_{ijpq} = D_{jipq} \quad (3.8.3a)$$

Second, continuity requires that

$$D_{ijiq} = 0. \quad (3.8.3b)$$

Finally, we know that

$$\epsilon = \nu D_{iipp}. \quad (3.8.3c)$$

Using these conditions, one finds

$$D_{ijpq} = \frac{2\epsilon}{15\nu} \left[ \delta_{ij} \delta_{pq} - \frac{1}{4} (\delta_{ip} \delta_{jq} + \delta_{jp} \delta_{iq}) \right]. \quad (3.8.4)$$

The pertinent quantity most easily measured in an experiment (again using Taylor's hypothesis) is

$$\overline{(u'_{1,1})^2} = \frac{\epsilon}{15\nu}. \quad (3.8.5)$$

This is usually the way that  $\epsilon$  is estimated in laboratory experiments.

Another important turbulence scale defined in terms of the dissipation is the *microscale*. It can be approached through the longitudinal correlation function  $f(r)$ . The symmetry property (3.4.11) indicates that  $f(r)$  must be an even function of  $r$ , so its expansion is

$$f(r) = 1 - \frac{1}{2} ar^2 + O(r^4) \quad (3.8.6)$$

The interception of this osculating parabola (Fig. 3.3.1) with  $f = 0$  defines a scale  $\lambda_f = \sqrt{2/a}$ , called the *longitudinal Taylor microscale*. From (3.5.4), using (3.7.5) and then (3.8.4),

$$a = \frac{3}{q^2} D_{1111} = \frac{\epsilon}{5\nu q^2}$$

so

$$\lambda_f^2 = 10\nu q^2 / \epsilon. \quad (3.8.7)$$

Alternatively, the dissipation rate can be expressed as

$$\epsilon = 10\nu \frac{q^2}{\lambda_f^2}. \quad (3.8.8)$$

This equation is sometimes used to determine  $\epsilon$  from measurements of the longitudinal correlation.

Using (3.2.3) and (3.2.2), the ratio of the Taylor microscale to the Kolmogorov scale is

$$\frac{\lambda_f}{\ell_K} = \sqrt{10} R_T^{1/4} \quad (3.8.9)$$

Using (3.2.1), the ratio of the energy-containing scale to the Taylor scale is

$$\frac{\ell}{\lambda_f} = \frac{1}{\sqrt{10}} R_T^{1/2} \quad (3.8.10)$$

Thus the microscale falls between the smallest and largest scales. Although it is the most commonly reported turbulence scale, it is the least well understood. It has been suggested that it is a measure of the size of the loops in the vortex filaments, but this is not at all certain.

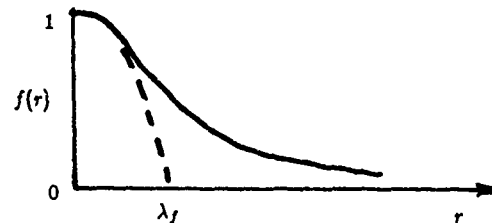


Figure 3.8.1 The osculating parabola defines the Taylor microscale

### 3.9 Scaling of the spectrum in isotropic turbulence

The general form of  $E(k)$  deduced from measurements in isotropic turbulence is shown in Fig. 3.7.1. By (3.7.17), the area under the curve is the turbulent kinetic energy, to which then greatest contributions come from wavenumbers around the peak. The vorticity and dissipation occur predominantly at high wavenumbers.

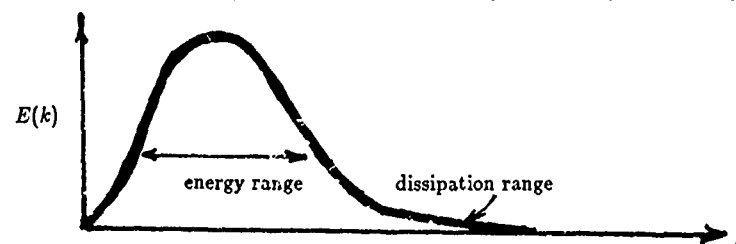


Figure 3.9.1 Form of the spectrum in isotropic turbulence

It is generally thought that the small-scale motions in any turbulent flow become isotropic at high Reynolds numbers, and therefore that the Kolmogorov scales characterize the high wavenumber region of any turbulent flow. Moreover, if one assumes that there is a *universal small-scale spectrum*, then by dimensional analysis it must be of the form

$$\frac{\bar{E}(k)}{\nu^{5/4} \epsilon^{1/4}} = \bar{f}\left(\frac{k\nu^{3/4}}{\epsilon^{1/4}}\right). \quad (3.9.1)$$

The one-dimensional spectrum  $E_1(k_1)$  would have to scale in the same manner. Figure 3.9.2 shows that the data from a wide variety of flows do indeed collapse when plotted in these Kolmogorov variables. The data flatten at low wavenumbers because they are one-dimensional spectra where  $E_1(0)$  is given by (3.7.24).

STREAMWISE ENERGY SPECTRA FOR VARIOUS TURBULENT FLOWS  
(CHAPMAN, 1979)

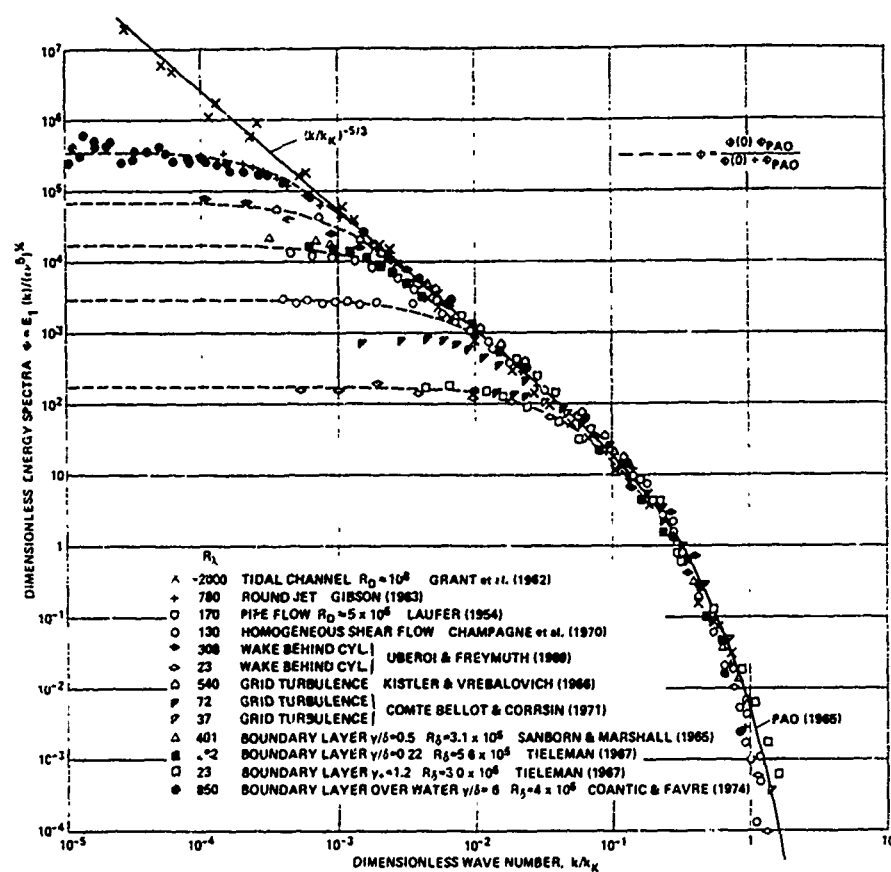


Figure 3.9.2 Spectra in Kolmogorov variables

Kolmogorov suggested that there should be a range of wavenumbers in which the main process is the passing of energy from larger eddies to smaller eddies (the *cascade* of turbulence energy), and that the structure of this region should depend only on the rate of energy cascade. Since this cascade ultimately ends with dissipation at the small scales, the rate of energy cascade must be  $\epsilon$ . If one assumes that  $E(k)$  depends

only on  $\epsilon$  (and of course  $k$ ) in this range, by dimensional analysis

$$E(k)k^{5/3}\epsilon^{-2/3} = \text{constant} = \alpha$$

or

$$E(k) = \alpha\epsilon^{2/3}k^{-5/3}. \quad (3.9.2)$$

This is the *Komogorov spectrum*, a cornerstone of turbulence. Measurements give a *Kolmogorov constant*  $\alpha$  of about 1.5. The data of Figure 3.9.2 show the  $-5/3$  range, with longer runs of  $-5/3$  behavior at larger Reynolds numbers, consistent with the broadening of scales as  $R_T^{3/4}$ .

In the vicinity of the peak in  $E(k)$ , the spectrum should scale on the large-scale variables (see section 3.1), and hence should collapse when plotted as

$$\frac{\epsilon E(k)}{q^6} = G\left(\frac{k\epsilon}{q^3}\right). \quad (3.9.3)$$

Where this form overlaps with the Kolmogorov spectrum the function  $G$  must be such that  $q$  drops out, and this again establishes the  $-5/3$  law for the asymptotic overlap range between low and high wavenumbers.

Figure 3.9.1 indicates that  $E(k) \rightarrow 0$  as  $k \rightarrow 0$ , but there is controversy as to just how. There are good arguments supporting both  $k^2$  (*Saffman*) and  $k^4$  (*Loitskianski*) variation as  $k \rightarrow 0$ . The  $k^4$  behavior is required if  $E_{ij}$  is to be analytic at  $k = 0$ . The  $k^2$  behavior implies some residual preferential directions at zero wavenumbers, which may be more characteristic of physical experiments. Numerical simulations with delta spectra at mid-range fill-out as  $k^4$  as the turbulence develops, but simulations initiated with  $k^2$  behavior at low wavenumbers persist as  $k^2$ . Simple models of turbulence show that the rate of energy decay in isotropic turbulence depends on the low wavenumber portion of the spectrum, and with the experimental decay rates support the  $k^2$ .

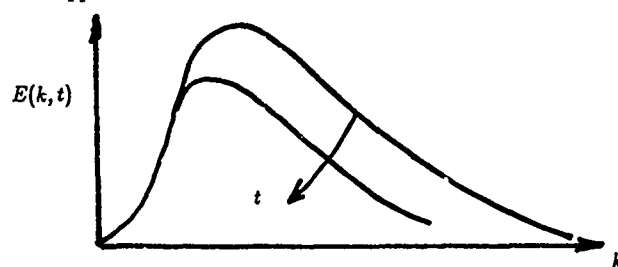


Figure 3.9.3 Evolution of the spectrum in decaying isotropic turbulence

Turbulence not subjected to mean deformation will decay as time passes. The larger eddies take more time to change, and the smallest scales of motion adjust most rapidly. Figure 3.9.3 depicts the nature of the evolution of  $E(k, t)$  (we now include the time variable heretofore suppressed). Note that the peak moves to larger scales (small wavenumbers) because the smaller eddies die out faster. Thus as time progresses the integral scale will grow.

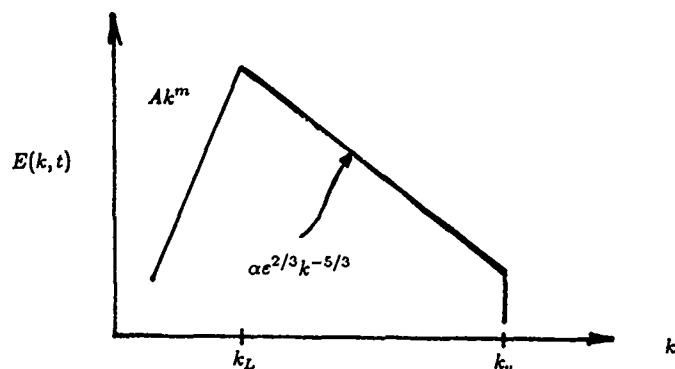


Figure 3.9.4 Model spectrum for isotropic turbulence

A simple model spectrum for isotropic turbulence is shown in Fig. 3.9.4. It assumes a power law behavior at low wavenumbers, a  $-5/3$  inertial range, and a sharp cutoff at the Kolmogorov scale:

$$E(k) = \begin{cases} A k^m & \text{for } k \leq k_L \\ \alpha \epsilon^{2/3} k^{-5/3} & \text{for } k_L \leq k \leq k_v \\ 0 & \text{for } k > k_v \end{cases} \quad (3.9.4)$$

Matching the spectrum at  $k_L$  gives

$$k_L = \left( \frac{\alpha \epsilon^{2/3}}{A} \right)^{3/(3m+5)} \quad (3.9.5)$$

Assuming  $k_v \gg k_L$ ,

$$\frac{1}{2} q^2 = \int_0^\infty E(k) dk = \alpha \left( \frac{1}{m+1} + \frac{3}{2} \right) k_L^{-2/3} \epsilon^{2/3}$$

from which an estimate of the peak wavenumber is obtained,

$$\frac{k_L q^3}{\epsilon} = \left[ 2\alpha \left( \frac{1}{m+1} + \frac{3}{2} \right) \right]^{3/2} \quad (3.9.6)$$

Again assuming  $k_v \gg k_L$ , the viscous cutoff wavenumber is estimated

$$\epsilon = \nu \int_0^\infty k^2 E(k) dk = \nu \frac{3}{4} \alpha \epsilon^{2/3} k_v^{4/3} \quad (3.9.7)$$

from which

$$\frac{k_v \nu^{3/4}}{\epsilon^{1/4}} = \left( \frac{4}{3\alpha} \right)^{3/4} \quad (3.9.8)$$

It is left as an exercise to work out the one-dimensional spectrum  $E_1$  for this model spectrum, and from that to determine the integral scale. For  $m = 2$  and  $\alpha = 1.5$ , one finds

$$\Lambda_f \epsilon / q^3 = 0.11. \quad (3.9.9)$$

This model spectrum exhibits the proper scaling for isotropic turbulence, and gives values of the scales within about a factor of two of those found from actual spectra. It is very useful in constructing simple turbulence models, in setting up initial fields for turbulence simulations, and in addressing other aspects of homogeneous turbulence.

### 3.10 Third-order statistics in isotropic turbulence

Correlations involving products of three quantities are called *third order statistics*. These depend on the relative phases of the Fourier modes, information not contained in the spectrum tensor  $E_{ij}$ . Of particular interest in turbulence modeling are one-point third-order statistics. For isotropic turbulence these tensors can be worked out using the methods used previously. For example,

$$\overline{u_i' u_j' u_k'} = C q^{3/2} \epsilon_{ijk}. \quad (3.10.1)$$

In dealing with the vorticity and dissipation equations, one encounters the tensor

$$\psi_{ijkpqr} = \overline{u_{i,p}' u_{j,q}' u_{k,r}'}. \quad (3.10.2)$$

This is evaluated for isotropic turbulence by first writing the general tensor

$$\begin{aligned} \psi_{ijkpqr} = & \delta_{ip}(C_1 \delta_{jq} \delta_{kr} + C_2 \delta_{jk} \delta_{qr} + C_3 \delta_{jr} \delta_{qk}) + \delta_{ij}(C_4 \delta_{pq} \delta_{kr} + C_5 \delta_{pk} \delta_{qr} + C_6 \delta_{pr} \delta_{qk}) \\ & + \delta_{iq}(C_7 \delta_{pj} \delta_{kr} + C_8 \delta_{pk} \delta_{jr} + C_9 \delta_{pr} \delta_{jk}) + \delta_{ik}(C_{10} \delta_{pj} \delta_{qr} + C_{11} \delta_{pq} \delta_{jr} + C_{12} \delta_{pr} \delta_{jq}) \\ & + \delta_{ir}(C_{13} \delta_{pj} \delta_{qk} + C_{14} \delta_{pq} \delta_{jk} + C_{15} \delta_{pk} \delta_{jq}). \end{aligned} \quad (3.10.3)$$

There are three symmetry constraints,

$$\psi_{ijkpqr} = \psi_{jipqkr} \quad (3.10.4a)$$

$$\psi_{ijkpqr} = \psi_{kji rqp} \quad (3.10.4b)$$

$$\psi_{ijkpqr} = \psi_{ikjprq}. \quad (3.10.4c)$$

Continuity also provides some constraints, but with the symmetries enforced only one is required,

$$\psi_{ijkipq} = 0. \quad (3.10.5)$$

Forming  $(\overline{u_i' u_j' u_k'})_{,ijk}$  and using homogeneity conditions, one can show that

$$\psi_{ijkjki} = 0. \quad (3.10.6)$$

With these constraints, (3.10.3) can be reduced to a form containing only one unknown coefficient. With  $C_6 = A$ , one finds

$$\begin{aligned} \psi_{ijkpqr} = & A[(\delta_{ip} \delta_{jq} \delta_{kr} + \delta_{ij} \delta_{pk} \delta_{qr} + \delta_{ij} \delta_{pr} \delta_{qk} + \delta_{iq} \delta_{pr} \delta_{jk} + \delta_{ik} \delta_{pj} \delta_{qr} + \delta_{ik} \delta_{pq} \delta_{jr} + \delta_{ir} \delta_{pq} \delta_{jk}) \\ & - \frac{4}{3}(\delta_{ip} \delta_{jk} \delta_{qr} + \delta_{ij} \delta_{pq} \delta_{kr} + \delta_{ik} \delta_{pr} \delta_{jq}) - \frac{3}{4}(\delta_{iq} \delta_{pk} \delta_{jr} + \delta_{ir} \delta_{pj} \delta_{qk}) - \frac{1}{6}(\delta_{ip} \delta_{jr} \delta_{kq} + \delta_{iq} \delta_{pj} \delta_{kr} + \delta_{ir} \delta_{pk} \delta_{jq})]. \end{aligned} \quad (3.10.7)$$

For example,

$$\overline{(u_{1,1}')^3} = A \quad (3.10.8)$$

$$\overline{\omega_i' \omega_j' s_{ij}'} = -\frac{35}{2} A. \quad (3.10.9)$$

The derivative skewness  $\gamma$  is related to  $A$ ; using (3.8.5) and (3.10.8),

$$\gamma = \overline{(u_{1,1}')^3} / [\overline{(u_{1,1}')^2}]^{3/2} = A \left( \frac{15\nu}{\epsilon} \right)^{3/2}. \quad (3.10.10)$$

The skewness is measured to be negative, the term given by (3.10.9) is positive. This is the turbulent vortex stretching source term in the equation for mean-square vorticity (2.8.2), by which the turbulence tends to enhance its own mean-square vorticity.

#### 4. RAPID DISTORTION OF HOMOGENEOUS TURBULENCE

##### 4.1 Introduction

The state of homogeneous turbulence changes significantly when it is subjected to mean strain. This occurs in practice whenever turbulence passes through a duct of variable cross-section, such as a nozzle, when turbulence is sheared by the mean flow, or when turbulence is subjected to a mean rotation. The general trends can be understood using vortex stretching concepts. For example, passing turbulence through an axisymmetric nozzle stretches the vortex filaments in the flow direction and tends to align them with the flow direction, *reducing* the turbulent fluctuations in the direction of flow but *increasing* the fluctuations transverse to the flow.

Because of the non-linearity of the governing equations, it is impossible to develop a rigorous theory of these processes. There are two alternative approaches to such a theory. The first is to use some sort of a *closure model* to produce a set of closed equations describing the evolution of statistical properties of the turbulence in response to the mean strain. The second approach is to simplify and then solve the exact equations for special cases. Both approaches are useful. In this chapter we examine *rapid distortion theory* (RDT), in which the exact equations for the fluctuation field are approximated in a way that is valid for very strong imposed mean strain rate, yielding linear equations amenable to exact solution.

It might be thought that the response to large strain rate could be calculated using the Reynolds stress transport equations (2.7.1), neglecting the terms that do not explicitly contain the mean velocity gradients. However, this analysis overpredicts the changes in the Reynolds stresses, because the pressure-strain term  $T_{ij}$  in (2.7.1) produces an immediate effect that reduces the impact of the production term  $P_{ij}$  by a factor of about 50%. The Poisson equation for the fluctuation pressure (2.5.3) shows that a sudden onset of mean velocity gradient *instantly* changes the fluctuation pressure field. The result is a sudden change of  $T_{ij}$  with the onset of applied  $S_{ij}$ , and this must be considered in the analysis. Turbulence modelers refer to the part of  $T_{ij}$  that changes suddenly with a sudden change in the mean deformation rate as the *rapid pressure strain* term. RDT plays a key role in understanding and modeling this term, and this chapter is intended to aid the use of RDT in this work.

The basic idea of RDT is that when  $|S|q^2/\epsilon \gg 1$  the time scale of the turbulence  $q^2/\epsilon$  is long compared to that of the mean deformation, and so the turbulence does not have time to interact with itself. Thus, the non-linear terms in the governing equations (2.5.1)-(2.5.3) involving products of fluctuation quantities are neglected, and so the RDT equations are *linear* in the fluctuation quantities. The viscous terms are linear and can be included in the analysis, but are often neglected and will be here.

These equations contain the mean velocity gradients, which must be independent of position for homogeneous turbulence but may depend on time. The convective operators  $\bar{D}$  contain the mean velocities, which must vary linearly with  $\mathbf{x}$  in homogeneous turbulence. These coefficients prevent representation of the solution as periodic in the coordinates, and this hampers direct solution by Fourier methods. However, when transformed to coordinates marked on the mean flow at the start of the distortion, the variable coefficients are removed and the solution may be obtained by Fourier methods in the transformed system. This transformation is used in the numerical simulations of homogeneous turbulence (Rogallo 1981), where it permits the numerical solution to be *exact* for infinitely rapid distortions! The numerical simulations of the full equations carried out using this program are useful in helping assess the range of applicability of RDT, and it is rather surprising that, for some types of strain, RDT works remarkably well even at relatively low strain-rates (Lee and Reynolds 1985). Thus, RDT is becoming recognized as being very important and useful in turbulence analysis, modeling and simulation (Savill 1987).

##### 4.2 The RDT equations

The most general mean velocity field in which homogeneous turbulence can exist is of the form

$$U_i = A_{ik}(t)x_k \quad (4.2.1a)$$

from which

$$U_{i,k} = A_{ik}(t). \quad (4.2.1b)$$

Note that (3.1.1) restricts the rotational history of the imposed mean deformation, but any mean strain rate history can be imposed.

Substituting (4.2.1) in (2.5.1), the inviscid RDT approximation for homogeneous turbulence is

$$\dot{u}'_i + A_{jk} x_k u'_{i,j} = -u'_j A_{ij} - \frac{1}{\rho} p'_{,i}. \quad (4.2.2)$$

The continuity equation (2.3.4) also applies. We remind the reader that these equations hold if  $\rho = \rho(t)$ , so they can be applied in certain types of compressible flow situations.

Solution by Fourier methods is practical only if the coefficients in the equations are independent of  $\mathbf{x}$ . Therefore, it is necessary to transform the equations to remove the troublesome term on the left-hand side. The transformation is assumed to be

$$\xi_i = B_{ik}(t) x_k \quad \tau = t. \quad (4.2.3)$$

Transforming (4.2.2) to the new coordinates, the left-hand side becomes

$$\frac{\partial u_i}{\partial \tau} + \frac{\partial u_i}{\partial \xi_n} \dot{B}_{nk} x_k + A_{jl} x_k \frac{\partial u_i}{\partial \xi_n} B_{nj}.$$

Setting the coefficient of  $x_k$  to zero to remove the variable coefficient,

$$\dot{B}_{nk} + A_{jk} B_{nj} = 0. \quad (4.2.4)$$

This defines the Rogallo transformation. The  $B_{ij}$  can be found by solving these linear equations, although a closed-form solution is not feasible. The transformation ties the new coordinate systems to the mean motion, with the new grid distorting and rotating as demanded by the mean flow. The Rogallo code for direct simulation of homogeneous turbulence operates in this coordinate system.

With this transformation the RDT momentum equations (4.2.2) become

$$\frac{\partial u'_i}{\partial \tau} = -u'_j A_{ij} - \frac{1}{\rho} \frac{\partial p'}{\partial \xi_k} B_{ki} \quad (4.2.5a)$$

and the continuity equation (2.3.4) becomes

$$\frac{\partial u'_i}{\partial \xi_k} B_{ki} = 0. \quad (4.2.5b)$$

The Poisson equation for the pressure fluctuation is obtained by taking the derivative of (4.2.5a) with respect to  $\xi_k$  and the derivative of (4.2.5b) with respect to  $\tau$  and combining, using (4.2.4). Alternatively, one can simply transform (2.5.3). The result is

$$\frac{1}{\rho} \frac{\partial^2 p'}{\partial \xi_k \partial \xi_n} B_{ki} B_{ni} = -2 B_{ki} A_{ij} \frac{\partial u'_j}{\partial \xi_k}. \quad (4.2.5c)$$

These linear equations can be solved to track the evolution of the Fourier coefficients of the velocity field in the transformed coordinates. The Reynolds stresses are integrals of this spectrum function, and the integrations may be carried out in the transformed coordinates. If the spectrum in the original coordinates is involved, the spectrum must be mapped back to  $\mathbf{x}$  space using the coordinate transformation.

Closed-form solution of the RDT equations for a general problem is not possible. However, exact solutions for special cases can be obtained, in some cases in closed form and in others in terms of integrals. The general solution can be found as a power series in time. Some of these solutions that play useful roles in understanding turbulence and in turbulence modeling will now be discussed.

#### 4.3 Response of turbulence to rapid rotation

RDT can be applied to study the effect of rapid rotation on turbulence in the absence of strain. Taking the rotation as clockwise about the  $x_3$  axis, the mean velocity is

$$U_1 = \Gamma x_2 \quad U_2 = -\Gamma x_1 \quad (4.3.1b)$$



and the coordinate transformation is (Fig. 4.3.1)

$$\xi_1 = x_1 \cos(\Gamma\tau) - x_2 \sin(\Gamma\tau) \quad (4.3.2a)$$

$$\xi_2 = x_2 \cos(\Gamma\tau) + x_1 \sin(\Gamma\tau) \quad (4.3.2b)$$

$$\xi_3 = x_3 \quad (4.3.2c)$$

$$\tau = t. \quad (4.3.2d)$$

Transforming, the RDT equations become

$$\frac{\partial u_1}{\partial \tau} = -\frac{1}{\rho} \left[ \cos(\Gamma\tau) \frac{\partial p}{\partial \xi_1} + \sin(\Gamma\tau) \frac{\partial p}{\partial \xi_2} \right] - u_2 \Gamma \quad (4.3.3a)$$

$$\frac{\partial u_2}{\partial \tau} = -\frac{1}{\rho} \left[ -\sin(\Gamma\tau) \frac{\partial p}{\partial \xi_1} + \cos(\Gamma\tau) \frac{\partial p}{\partial \xi_2} \right] + u_1 \Gamma \quad (4.3.3b)$$

$$\frac{\partial u_3}{\partial \tau} = -\frac{1}{\rho} \frac{\partial p}{\partial \xi_3}. \quad (4.3.3c)$$

The transformed continuity equation is

$$\frac{\partial u'_1}{\partial \xi_1} \cos(\Gamma\tau) + \frac{\partial u'_1}{\partial \xi_2} \sin(\Gamma\tau) - \frac{\partial u'_2}{\partial \xi_1} \sin(\Gamma\tau) + \frac{\partial u'_2}{\partial \xi_2} \cos(\Gamma\tau) + \frac{\partial u'_3}{\partial \xi_3} = 0. \quad (4.3.3d)$$

It is helpful to transform the velocity components to the rotating coordinate system. Denoting these velocities by  $v_i$ ,

$$v_1 = u_1 \cos(\Gamma\tau) - u_2 \sin(\Gamma\tau) \quad (4.3.4a)$$

$$v_2 = u_2 \cos(\Gamma\tau) + u_1 \sin(\Gamma\tau) \quad (4.3.4b)$$

$$v_3 = u_3. \quad (4.3.4c)$$

Forming the equations for the new velocities from the old, one finds

$$\frac{\partial v_1}{\partial \tau} = -\frac{1}{\rho} \frac{\partial p}{\partial \xi_1} - 2v_2 \Gamma \quad (4.3.5a)$$

$$\frac{\partial v_2}{\partial \tau} = -\frac{1}{\rho} \frac{\partial p}{\partial \xi_2} + 2v_1 \Gamma \quad (4.3.5b)$$

$$\frac{\partial v_3}{\partial \tau} = -\frac{1}{\rho} \frac{\partial p}{\partial \xi_3} \quad (4.3.5c)$$

$$\frac{\partial v_i}{\partial \xi_i} = 0. \quad (4.3.5d)$$

The second terms on the right are of course the Coriolis terms.

Now we seek the solution for the evolution of the Fourier modes in the transformed space. Following the developments of section 3.3, we write

$$v'_i = \sum_{\underline{k}} \hat{v}_i(\underline{k}, t) e^{-i\kappa_n \xi_n} \quad (4.3.6a)$$

$$p' = \sum_{\underline{k}} \hat{p}(\underline{k}, t) e^{-i\kappa_n \xi_n} \quad (4.3.6b)$$

where  $\underline{k}$  is the wavenumber in the transformed coordinates. Equating coefficients of like exponentials,

$$\frac{\partial \hat{v}_1}{\partial \tau} = \frac{i\kappa_1}{\rho} \hat{p} - 2\Gamma \hat{v}_2 \quad (4.3.7a)$$

$$\frac{\partial \hat{v}_2}{\partial \tau} = \frac{i\kappa_2}{\rho} \hat{p} + 2\Gamma \hat{v}_1 \quad (4.3.7b)$$

$$\frac{\partial \hat{v}_3}{\partial \tau} = \frac{i\kappa_3}{\rho} \hat{p} \quad (4.3.7c)$$

$$\kappa_i \hat{v}_i = 0. \quad (4.3.7d)$$

Applying the continuity equation (4.3.7d) to (4.3.7a-c),

$$\frac{1}{\rho} \hat{p} = \frac{2\Gamma(\hat{v}_2 \kappa_1 - \hat{v}_1 \kappa_2)}{i\kappa^2} \quad (4.3.8)$$

where  $\kappa^2 = \kappa_1^2 + \kappa_2^2 + \kappa_3^2$ . Substituting (4.3.8) in (4.3.7a-c), and seeking solutions of the form  $\hat{v}_i(\underline{\kappa}, \tau) = a_i \exp(i\beta\tau)$ , one obtains

$$i\beta a_1 - 2\Gamma \frac{\kappa_1}{\kappa^2} (a_2 \kappa_1 - a_1 \kappa_2) + 2\Gamma a_2 = 0 \quad (4.3.9a)$$

$$i\beta a_2 - 2\Gamma \frac{\kappa_2}{\kappa^2} (a_2 \kappa_1 - a_1 \kappa_2) - 2\Gamma a_1 = 0 \quad (4.3.9b)$$

$$i\beta a_3 - 2\Gamma \frac{\kappa_3}{\kappa^2} (a_2 \kappa_1 - a_1 \kappa_2) = 0. \quad (4.3.9c)$$

This linear equation system has non-trivial solutions only if the determinant of the coefficient matrix vanishes. This condition gives

$$\beta^2 = 4\Gamma^2 \left( 1 - \frac{\kappa_1^2 + \kappa_2^2}{\kappa^2} \right) = 4\Gamma^2 \frac{\kappa_3^2}{\kappa^2} > 0. \quad (4.3.10)$$

Hence, except for modes with  $\kappa_3 = 0$ , the solutions are *undamped oscillations* in time at frequency  $\beta(\underline{\kappa})$ .

The  $\kappa_3 = 0$  modes require special attention. They correspond to two-dimensional modes with their vorticity aligned with the rotation axis. The solution for these modes is

$$\hat{v}_1(\underline{\kappa}, \tau) = \hat{v}_1(\underline{\kappa}, 0) - C(\underline{\kappa}) \kappa_2 \tau \quad (4.3.11a)$$

$$\hat{v}_2(\underline{\kappa}, \tau) = \hat{v}_2(\underline{\kappa}, 0) + C(\underline{\kappa}) \kappa_1 \tau \quad (4.3.11b)$$

$$\hat{v}_3(\underline{\kappa}, \tau) = \hat{v}_3(\underline{\kappa}, 0) \quad (4.3.11c)$$

where

$$C = 2\Gamma \left( \frac{\kappa_1 \hat{v}_1(\underline{\kappa}, 0) + \kappa_2 \hat{v}_2(\underline{\kappa}, 0)}{\kappa^2} \right). \quad (4.3.11d)$$

But for  $\kappa_3 = 0$  the numerator of  $C$  is zero by continuity, and hence the Fourier coefficients of these modes do not change under rapid rotation. Thus, these coefficients can also be regarded as undamped oscillations at frequency  $\beta(\underline{\kappa})$ .

The solution for the Fourier coefficients is therefore

$$\hat{v}_i = a_+ e^{i\beta\tau} + a_- e^{-i\beta\tau}. \quad (4.3.12)$$

$a_{1\pm}$  and  $a_{2\pm}$  are related by (4.3.9a) or (4.3.9b),

$$\left( \pm i \frac{\kappa_3}{\kappa} + \frac{\kappa_i \kappa_j}{\kappa^2} \right) a_{1\pm} = \left( \frac{\kappa_1^2}{\kappa^2} - 1 \right) a_{2\pm}. \quad (4.3.13)$$

The coefficients  $a_{i\pm}$  are set by the initial values of the Fourier amplitudes,

$$\hat{v}_{i0} = a_{i+} + a_{i-} \quad (4.3.14)$$

where  $\hat{v}_{i0}$  is the initial value of  $\hat{v}_i(\underline{\kappa})$ . Using (4.3.13) and (4.3.14), one finds

$$a_{1\pm} = \pm i \frac{\kappa}{2\kappa_3} \left[ \left( \mp i \frac{\kappa_3}{\kappa} + \frac{\kappa_1 \kappa_2}{\kappa^2} \right) \hat{v}_{10} + \left( 1 - \frac{\kappa_1^2}{\kappa^2} \right) \hat{v}_{20} \right] \quad (4.3.15)$$

Following section 3.4, the spectrum tensor  $E_{ij}$  (in the rotating coordinate system) is

$$E_{ij}(\underline{\kappa}, \tau) = \left(\frac{L}{2\pi}\right)^3 \langle \hat{v}_i(\underline{\kappa}, \tau) \hat{v}_j^*(\underline{\kappa}, \tau) \rangle. \quad (4.3.16)$$

Using the solution and a bit of algebra, one finds

$$\begin{aligned} E_{11}(\underline{\kappa}, \tau) = & \frac{\kappa^2}{4\kappa_3^2} \left\{ 2 \left( \frac{\kappa_3^2}{\kappa^2} + \frac{\kappa_1^2 \kappa_2^2}{\kappa^4} \right) E_{11}(\underline{\kappa}, 0) + 2 \left( 1 - \frac{\kappa_1^2}{\kappa^2} \right)^2 E_{22}(\underline{\kappa}, 0) + \frac{\kappa_1 \kappa_2}{\kappa^2} \left( 1 - \frac{\kappa_1^2}{\kappa^2} \right) (E_{12}(\underline{\kappa}, 0) + E_{21}(\underline{\kappa}, 0)) \right. \\ & + 2 \left[ \left( \frac{\kappa_3^2}{\kappa^2} - \frac{\kappa_1^2 \kappa_2^2}{\kappa^4} \right) E_{11}(\underline{\kappa}, 0) - \left( 1 - \frac{\kappa_1^2}{\kappa^2} \right)^2 E_{22}(\underline{\kappa}, 0) - \frac{\kappa_1 \kappa_2}{\kappa^2} \left( 1 - \frac{\kappa_1^2}{\kappa^2} \right) (E_{12}(\underline{\kappa}, 0) + E_{21}(\underline{\kappa}, 0)) \right] \cos(2\beta\tau) \\ & \left. - 2 \left[ \frac{\kappa_1 \kappa_2 \kappa_3}{\kappa^3} E_{11}(\underline{\kappa}, 0) + \frac{\kappa_3}{\kappa} \left( 1 - \frac{\kappa_1^2}{\kappa^2} \right) (E_{12}(\underline{\kappa}, 0) + E_{21}(\underline{\kappa}, 0)) \right] \sin(2\beta\tau) \right\}. \end{aligned} \quad (4.3.17)$$

If the initial turbulence is isotropic, the initial spectrum is given by (3.7.14), and one finds that the coefficients of the sin and cos terms vanish; hence there is no change in the spectrum as viewed by an observer in the rotating coordinate system. Since the spectrum is isotropic, the spectrum seen by a stationary observer is also unchanged. Thus, *rotation of itself will not distort the spectrum of isotropic turbulence.*

If the initial spectrum is anisotropic, as for example produced by prior strain and associated rotation, the residual rotation will simply cause the spectrum to oscillate at a frequency  $\omega = 2\beta(\underline{\kappa})$ . The associated Reynolds stress (in the rotating frame), determined by integrating  $E_{11}$  over all  $\underline{\kappa}$ , will oscillate in a complicated manner that depends on the initial spectrum. However, using the symmetry property of the spectrum (3.4.13), the contribution of the  $\sin(2\beta\tau)$  term to the integral is seen to vanish. Hence, relative to a rotating observer, the Reynolds stress oscillations can be expressed as an *even power series* in  $\tau$  arising from the  $\cos(2\beta\tau)$  term. Hence, the Reynolds stresses seen by a stationary observer would, to  $O(t)$ , appear to rotate in the manner described by the kinematic rotation terms, with deviations from this behavior being described by an *even power series* in time.

These are important results for turbulence modeling. Turbulence models, when reduced to the same rapid distortion approximations, should not show any effect of pure rotation (rotation without straining) on isotropic turbulence. Moreover, when applied to the pure rotation of anisotropic turbulence, the models should show the kinematic rotation of the Reynolds stress described by (2.7.4), plus modifications by an *even power series* in time. This condition is very useful in setting coefficients in turbulence models, and we shall use it in Chapter 6.

#### 4.4 Rapid isotropic compression or expansion

Consider next isotropic expansion (or compression) with

$$U_i = \Gamma x_i. \quad (4.4.1)$$

The RDT momentum equations are

$$\dot{u}'_i + \Gamma x u'_{i,j} = -\Gamma u'_i - \frac{1}{\rho(t)} p'_{,i}. \quad (4.4.2)$$

The density is given by the continuity equation,

$$\dot{\rho} = -3\rho\Gamma. \quad (4.4.3)$$

The RDT transformation is

$$\xi_i = x_i e^{-\Gamma t} \quad \tau = t \quad (4.4.4)$$

and the transformed equations are

$$\frac{\partial u'_i}{\partial \tau} = -\Gamma u'_i - \frac{1}{\rho(t)} \frac{\partial p'}{\partial \xi_i} e^{-\Gamma t} \quad (4.4.6)$$

$$\frac{\partial u'_i}{\partial \xi_1} e^{-\Gamma t} = 0. \quad (4.4.7)$$

Multiplying (4.4.6) by  $u'_i$ , the pressure term drops out by continuity (4.4.7). Averaging, we obtain the RDT approximation for the kinetic energy,

$$\frac{1}{2} \frac{dq^2}{d\tau} = -\Gamma q^2. \quad (4.4.8)$$

The solution is

$$q^2 = q_0^2 e^{-2\Gamma t} \quad (4.4.9)$$

where  $q_0^2$  is the initial kinetic energy. Thus, the turbulence kinetic energy will decrease with expansion ( $\Gamma > 0$ ) and increase with compression.

The evolution of the spectrum is obtained by solving the individual component equations. Fourier expansions are used as above. The pressure fluctuations (i.e. the rapid part) are zero by continuity, and all Fourier modes of the velocity vary as  $\exp(-\Gamma t)$ . Thus, the spectrum retains its initial shape in the stretched coordinate system, and simply scales in magnitude with  $q^2$ . As a consequence the integral scale (3.4.15) varies in proportion to the strain,

$$\Lambda_f(t) = \Lambda_f(0) e^{\Gamma t}. \quad (4.4.10)$$

These results are useful in constructing turbulence models for compressible turbulence. Some of the turbulence models currently in use do not predict the proper behavior with compression, some even predicting an increase in length scale as turbulence is compressed!

#### 4.5 Response of turbulence to rapid irrotational strain

RDT analysis for irrotational mean strain is neatly handled using the vorticity equation. Under the RDT approximations, with no mean rotation, (2.5.2) reduces to

$$\overline{D}\omega'_i = \omega'_j S_{ij} - \omega'_i S_{kk}. \quad (4.5.1)$$

We work in principal coordinates of  $S_{ij}$  and take

$$U_\alpha = \Gamma_\alpha(t) x_\alpha. \quad (4.5.2)$$

Recall that Greek indices are not summed. The RDT coordinate transformation is

$$\xi_\alpha = x_\alpha / e_\alpha \quad \tau = t \quad (4.5.3a, b)$$

where

$$e_\alpha = \exp\left(\int_0^t \Gamma_\alpha(t') dt'\right) \quad (4.5.3c)$$

is the total strain in the  $\alpha$  direction. The transformed vorticity equation is

$$\frac{\partial \omega'_\alpha}{\partial \tau} = \tilde{\Gamma}_\alpha \omega'_\alpha \quad (4.5.4a)$$

where

$$\tilde{\Gamma}_\alpha = \Gamma_\alpha - \Gamma_0 \quad (4.5.5a)$$

$$\Gamma_0 = \Gamma_1 + \Gamma_2 + \Gamma_3. \quad (4.5.5b)$$

The solution of (4.5.4) is

$$\omega'_\alpha(\mathbf{x}, \tau) = \omega'_\alpha(\mathbf{x}, 0) \tilde{e}_\alpha \quad (4.5.6)$$

where

$$\tilde{e}_\alpha = \exp\left(\int_0^t \tilde{\Gamma}_\alpha(t') dt'\right) \quad (4.5.7)$$

is a modified total strain in the  $\alpha$  direction. This result clearly shows the essence of RDT; it computes the change in the turbulent state by considering the *rapid vortex stretching* imposed by the mean field. The velocity field can be deduced from the vorticity field. In the transformed coordinates, the Poisson equation (1.9.5) for the velocity gives

$$\tilde{\nabla}^2 u'_1 = \frac{\partial \omega'_2}{\partial \xi_3} \frac{1}{e_3} - \frac{\partial \omega'_3}{\partial \xi_2} \frac{1}{e_2} \quad (4.5.8a)$$

where the transformed Laplace operator is

$$\tilde{\nabla}^2 = \frac{1}{e_1^2} \frac{\partial^2}{\partial \xi_1^2} + \frac{1}{e_2^2} \frac{\partial^2}{\partial \xi_2^2} + \frac{1}{e_3^2} \frac{\partial^2}{\partial \xi_3^2}. \quad (4.5.8b)$$

The equations for  $\omega'_2$  and  $\omega'_3$  can be obtained by permuting the indices. The solution is obtained using Fourier expansions,

$$\omega'_i(\mathbf{x}, \tau) = \sum_{\underline{\kappa}} \hat{\omega}_i(\underline{\kappa}, \tau) e^{-i\kappa_\alpha \xi_\alpha} \quad (4.5.9a)$$

$$u'_i(\mathbf{x}, \tau) = \sum_{\underline{\kappa}} \hat{u}_i(\underline{\kappa}, \tau) e^{-i\kappa_\alpha \xi_\alpha} \quad (4.5.9b)$$

The solution for  $\hat{u}_1$  is

$$\hat{u}_1 = \frac{i(\kappa_3 \hat{\omega}_2 / e_3 - \kappa_2 \hat{\omega}_3 / e_2)}{\frac{\kappa_1^2}{e_1^2} + \frac{\kappa_2^2}{e_2^2} + \frac{\kappa_3^2}{e_3^2}}. \quad (4.5.10)$$

The other components can be found by permutation of the indices.

The velocity spectrum function  $E_{ij}$  is related to the vorticity spectrum function  $H_{ij}$  by

$$E_{11}(\underline{\kappa}, \tau) = \frac{(\frac{\kappa_3}{e_3})^2 H_{22}(\underline{\kappa}, 0) + (\frac{\kappa_2}{e_2})^2 H_{33}(\underline{\kappa}, 0) - 2(\frac{\kappa_2}{e_2})(\frac{\kappa_3}{e_3}) H_{23}(\underline{\kappa}, 0)}{\left[ \left(\frac{\kappa_1}{e_1}\right)^2 + \left(\frac{\kappa_2}{e_2}\right)^2 + \left(\frac{\kappa_3}{e_3}\right)^2 \right]^2}. \quad (4.5.11)$$

From the solution for the vorticity evolution (4.6.6),

$$H_{\alpha\beta}(\underline{\kappa}, \tau) = H_{\alpha\beta}(\underline{\kappa}, 0) \tilde{e}_\alpha \tilde{e}_\beta. \quad (4.5.12)$$

If we assume that the initial turbulence is isotropic, the initial vorticity spectrum is given by (3.7.23), with  $k$  replaced by  $\kappa$ . Using this spectrum and (4.5.12) in (4.5.11),

$$E_{11}(\underline{\kappa}, \tau) = \frac{E(\kappa) \left( \frac{\tilde{e}_2}{e_3} \right)^2 \kappa_3^2 (\kappa^2 - \kappa_2^2) + \left( \frac{\tilde{e}_3}{e_2} \right)^2 \kappa_2^2 (\kappa^2 - \kappa_3^2) + 2 \left( \frac{\tilde{e}_2 \tilde{e}_3}{e_2 e_3} \right) \kappa_2^2 \kappa_3^2}{4\pi\kappa^2 \left[ \left(\frac{\kappa_1}{e_1}\right)^2 + \left(\frac{\kappa_2}{e_2}\right)^2 + \left(\frac{\kappa_3}{e_3}\right)^2 \right]^2}. \quad (4.5.13)$$

The spectra  $E_{22}$  and  $E_{33}$  can be found by permuting the indices.

The Reynolds stresses can now be calculated by integrating  $E_{ij}$  over all wavenumbers (see 3.4.6). The integrations are most easily carried out using spherical coordinates, and can be evaluated in closed form for a few very simple cases, such as isotropic compression. However, the general case of irrotational strain can be handled by power series expansion in the total strains. In (4.5.3c) we expand

$$e_\alpha = \exp(\alpha) = 1 + a_\alpha + \frac{1}{2} a_\alpha^2 + \dots \quad (4.5.14)$$

The integrals are then expressed as power series in the  $a_\alpha$ , and evaluated in spherical coordinates, where the angular integrations can be carried out analytically. The  $\kappa$  integration produces  $q_0^2/3$ , the initial isotropic value of  $R_{11}$ . Using this approach, the Reynolds stress  $R_{ij}$ , dissipation tensor  $D_{ij}$ , and vorticity  $V_{11} = \omega'_1 \omega'_1$

were evaluated by the author and Moon Lee (Reynolds 1983) to  $O(c^2)$ . Subsequently Pionelli used the symbolic manipulation program MACSYMA to extend the Reynolds stress (the most important quantity for turbulence modeling) to  $O(a^5)$  (Lee, Pionelli, and Reynolds 1986). The results are as follows (the other components can be found by permuting the indices):

$$R_{11} = q_0^2 \left[ \frac{1}{3} - \frac{1}{15}(2a_0 + 4a_1) + \frac{1}{105}(10a_0^2 + 12a_1^2 - 32a_2a_3) + \frac{1}{315}(-12a_0^3 + 48a_0a_2a_3 - 8a_1^3 + 48a_1a_2a_3) \right. \\ \left. + \frac{1}{3465}(37a_0^4 + 32a_0^3a_1 - 48a_0^2a_1^2 - 128a_0^2a_2a_3 - 320a_0a_1a_2a_3 + 36a_1^4 - 32a_1^2a_2a_3 + 16a_2^2a_3^2) \right. \\ \left. + \frac{1}{225225}(-244a_0^5 - 1440a_0^4a_1 + 3360a_0^3a_1^2 - 4320a_0^3a_2a_3 - 2488a_1^5 + 1200a_0^3a_2a_3 + 7600a_0^2a_1a_2a_3 + 4320a_0a_1^4 \right. \\ \left. - 3440a_0a_1^2a_2a_3 - 880a_0a_2^2a_3^2 + 5200a_1^3a_2a_3 + 560a_1a_2^2a_3^2) + O(a^6) \right] \quad (4.5.15)$$

$$D_{11} = 2\varepsilon_0 \left[ \frac{1}{3} - \frac{2}{15}a_1 + \frac{1}{15}a_0 + O(a^2) \right] \quad (4.5.16)$$

$$V_{11} = \frac{\omega^2}{3} \left[ 1 + 2a_1 - a_0 + O(a^2) \right] \quad (4.5.17)$$

$$\varepsilon = \varepsilon_0 \left[ 1 - \frac{1}{3}a_0 + O(a^2) \right] \quad (4.5.18)$$

$$b_{11} = -\frac{4}{15}a_1^* - \frac{4}{63}(a_1^{*2} + 2a_2^*a_3^*) + \frac{184}{1575}(a_1^{*3} - a_1^*a_2^*a_3^*) + \frac{124}{3465}(a_1^{*4} + 4a_1^{*2}a_2^*a_3^* - 2a_2^{*2}a_3^{*2}) \\ + \frac{8}{23648625}(196812a_1^{*5} + 25189a_1^*a_2^{*2}a_3^{*2} - 479453a_1^{*3}a_2^*a_3^*) + O(a^{*6}) \quad (4.5.19)$$

where the Reynolds stress anisotropy tensor is

$$b_{ij} = \frac{R_{ij} - q^2 \delta_{ij}/3}{q^2} \quad (4.5.20)$$

and the anisotropic strain components are

$$a_a^* = a_a - \frac{1}{3}a_a. \quad (4.5.21)$$

Note that the anisotropy tensor  $b_{ij}$  depends only on the total anisotropic strain, and is independent of the strain-rate history. These results are useful in turbulence modeling where one seeks to develop models that will be consistent with RDT when the RDT approximations are applied to the model.

#### 4.6 Combinations of strain and rotation

The general RDT problem for homogeneous turbulence involves combinations of strain and rotation, for which a general solution can be developed in symbolic form (Cambon 1981). Using the Fourier expansions (4.5.9) and a similar one for the pressure, (4.2.5c) is first solved to express the Fourier coefficients of the pressure in terms of those of the velocity,

$$\frac{1}{\rho} \hat{p} = -\frac{2i\kappa_k B_{ki} A_{ij}}{\kappa_n \kappa_m B_{mp} B_{np}} \hat{u}_j. \quad (4.6.1)$$

Then, the Fourier expansion of (4.2.5a) gives

$$\frac{\partial \hat{u}_i}{\partial \tau} = -A_{ij} \hat{u}_j + \frac{2\kappa_k B_{ki} \kappa_q B_{qp}}{\kappa_n \kappa_m B_{ms} B_{ns}} A_{pj} \hat{u}_j = H_{ij} \hat{u}_j. \quad (4.6.2)$$

Following Camion, the solution can be expressed using Green's functions,

$$\hat{u}_i(\underline{x}, \tau) = G_{ik}(\underline{x}, \tau) \hat{u}_k(\underline{x}, 0) \quad (4.6.3)$$

where the Green's functions are given by the solution of

$$\frac{\partial G_{ij}(\underline{x}, \tau)}{\partial \tau} = H_{ik}(\underline{x}, \tau) G_{kj}(\underline{x}, \tau) \quad G_{ij}(\underline{x}, 0) = \delta_{ij}. \quad (4.6.4)$$

This allows the spectrum tensor  $E_{ij}$  to be expressed in terms of the initial spectrum,

$$E_{ij}(\underline{x}, \tau) = G_{ip}(\underline{x}, \tau) G_{jq}^*(\underline{x}, \tau) E_{pq}(\underline{x}, 0). \quad (4.6.5)$$

The Reynolds stresses are then simply integrals of the spectrum function over all  $\underline{x}$ .

This method of solution is instructive for looking at the structure of the solution, but the calculations for the Reynolds stresses require approximate evaluation of the integrals, for example by power series expansions. Moreover, when the principal axes of the strain rate vary with time the Green's functions are not easily obtained, except perhaps as power series in time. If one is going to resort to series solution, a direct solution by power series in time is simpler. We will develop this here for future reference.

A superscript summation convention aids the analysis. We denote a series by

$$A = \sum_{n=0}^{\infty} A^{(n)} t^n = A^{(n)} t^n. \quad (4.6.6)$$

Any repeated superscript or power is summed over all possible values. The delimiters on the superscripts establish the range, with ( ) establishing a lowest value of 0 and [ ] establishing a lowest value of unity. Multiplication of two series and sorting out of powers of  $t$  is then very easily accomplished. For example, simply replacing  $n$  by  $r-m$  in the product below collects the coefficient of  $t^r$ ,

$$AB = A^{(n)} t^n B^{(m)} t^m = A^{(r-m)} B^{(m)} t^r. \quad (4.6.7)$$

Here the delimiters correctly establish that the  $m$  summation in the coefficient of  $t^r$  is from 0 to  $r$ . The leading coefficients can also be extracted,

$$A^{(r-m)} B^{(m)} = A^{(r)} B^{(0)} + A^{(0)} B^{(r)} + A^{[r-m]} B^{[m]} \quad (4.6.8)$$

where the  $m$  sum at the end now ranges from 1 to  $r-1$ .

We treat a general case of arbitrary strain and initial rotation as applied to initially isotropic turbulence, and express the velocity gradient tensor  $A_{ik}$  (see 4.2.1) as

$$A_{ik}(t) = S_{ik}(t) + \frac{1}{2} \epsilon_{kij} \Omega_j(t). \quad (4.6.9)$$

The strain-rate history described by  $S_{ik}(t)$  and the initial rotation described by  $\Omega_i(0)$  will be arbitrary, and the rotation history is governed by (3.1.1).

Expanding,

$$\begin{aligned} S_{ik} &= S_{ik}^{(n)} t^n & \Omega_j &= \Omega_j^{(n)} t^n \\ A_{ik} &= A_{ik}^{(n)} t^n & B_{ik} &= B_{ik}^{(n)} t^n \\ \hat{u}_i &= \hat{u}_i^{(n)} t^n & \hat{p} &= \hat{p}^{(n)} t^n. \end{aligned} \quad (4.6.10)$$

The coefficients then are generated recursively. From (3.1.1)

$$(r+1)\Omega_i^{(r+1)} = \Omega_j^{(r)} S_{ij}^{(r-q)} - \Omega_i^{(r)} S_{jj}^{(r-q)}. \quad (4.6.11)$$

From (4.6.11)

$$A_{ik}^{(r)} = S_{ik}^{(r)} + \frac{1}{2} \epsilon_{kij} \Omega_j^{(r)}. \quad (4.6.12)$$

From (4.2.4)

$$(r+1)B_{nk}^{(r+1)} = -A_{jk}^{(r-q)} B_{nj}^{(q)} \quad B_{nk}^{(0)} = \delta_{nk}. \quad (4.6.13a, b)$$

The Fourier representation (in stretched space) of (4.2.5a) gives

$$(r+1)\hat{u}_i^{(r+1)} = -\hat{u}_j^{(r-q)} A_{ij}^{(q)} + \frac{1}{\rho} i \kappa_k \hat{p}^{(r-q)} B_{ki}^{(q)}. \quad (4.6.14)$$

The continuity condition (4.2.5b) gives

$$\kappa_k \hat{u}_i^{(r-q)} B_{ki}^{(q)} = 0. \quad (4.6.15)$$

The Fourier representation of the Poisson equation (4.2.5c) gives

$$-\frac{1}{\rho} \kappa_k \kappa_n \hat{p}^{(q-r)} B_{ki}^{(r-s)} B_{ni}^{(s)} = 2i \kappa_k B_{ki}^{(q-r)} A_{ij}^{(r-s)} \hat{u}_j^{(s)}. \quad (4.6.16)$$

Extracting the leading pressure term given by  $r=0$ , using (4.6.15b),

$$-\frac{1}{\rho} \kappa^2 \hat{p}^{(q)} = \frac{1}{\rho} \kappa_k \kappa_m \hat{p}^{(r-q)} 1^{[r]} B_{ki}^{(q-s)} B_{mi}^{(s)} + 2i \kappa_k B_{ki}^{(q-r)} A_{ij}^{(r-s)} \hat{u}_j^{(s)} \quad (4.6.17)$$

where the notation  $1^{[r]}$  forces  $r > 0$  in the sum.

The procedure is now very simple. At each order  $r$ , one finds the rotation term from (4.6.11), the velocity gradient term from (4.6.12), the transformation term from (4.6.13), the pressure term from (4.6.17), and the velocity terms from (4.6.14). The spectrum tensor is expressed as a similar series expansion, and its terms are generated and integrated in spherical coordinates to calculate the Reynolds stresses, much as in the previous section. This is a natural task for a symbolic manipulator like MACSYMA. The result would enable the determination of all unknown coefficients in the model for the rapid pressure strain term (see Chapter 6); we are attempting to carry out this evaluation.

#### 4.7 Two-dimensional turbulence

RDT of two-dimensional turbulence is useful for testing the range of performance of turbulence models. Stanford student Laura Pauley carried out an RDT analysis of initially axisymmetric two-dimensional turbulence for three-dimensional irrotational strain along the principal axes of  $b_{ij}$ , with  $b_{22} = -1/3$ . Her results are

$$R_{11} = \frac{q_0^2}{2} \left\{ 1 + [a_1 + 2\bar{a}_2 + a_3] + \left[ \frac{1}{2}(a_1^2 + a_3^2) + a_1 a_3 + 2\bar{a}_2(a_1 + \bar{a}_2 + a_3) \right] \right. \\ \left. + \left[ -\frac{11}{24}a_1^3 - \frac{5}{8}a_1^2 a_3 - \frac{11}{8}a_1 a_3^2 - \frac{101}{24}a_3^3 + \bar{a}_2(a_1^2 + a_3^2 + 2a_1 a_3) + 2\bar{a}_2^2 \left( a_1 + \frac{2}{3}\bar{a}_2 + a_3 \right) \right] + O(a^4) \right\} \quad (4.7.1)$$

$$b_{11} = \frac{1}{6} \left[ 1 + \frac{45}{8}(a_1^3 - a_3^3) + \frac{9}{8}(a_1^2 a_3 - a_1 a_3^2) + O(a^4) \right] \quad (4.7.2)$$

where the total strain in the  $i^{\text{th}}$  direction is  $e_i = \exp(a_i)$ ,  $\bar{a}_2 = a_2 - c_0$  and  $c_0 = a_1 + a_2 + a_3$ . Note that strain aligned with the vorticity does not affect the anisotropy, and that changes in anisotropy do not occur until third order. It would be instructive and useful to extend this analysis to more general 2-D cases including rotation. Strain not aligned with the principal axes of  $b_{ij}$ .



## 5. MODELING SCALE EVOLUTION IN HOMOGENEOUS TURBULENCE

### 5.1 Introduction

This chapter and the next are devoted to one-point models of homogeneous turbulence. Here we deal with modeling the evolution of the length and time scales, assuming that whatever must be known about the tensor character of the turbulence can be generated by an anisotropy model. Anisotropy modeling is addressed in the subsequent chapter.

The turbulent kinetic energy equation provides the equation for the turbulence velocity scale  $q^2$ . For homogeneous turbulence (2.6.2) becomes

$$(\dot{q}^2) = 2(P - \epsilon). \quad (5.1.1)$$

If the other model scale variable is  $\epsilon$ , this equation is closed. Alternatively, if one chooses to use a time scale variable  $\tau$  instead, a model relating  $\epsilon$  to  $\tau$  is required. There are many clues that the use of a time scale as the second scale parameter would offer advantages in modeling more general flows. Where it becomes desirable to think along these lines we will use the large-eddy time scale identified in Chapter 3,

$$\tau = \frac{q^2}{\epsilon}. \quad (5.1.2)$$

Following the most popular current trend, we shall start by using a model equation for  $\epsilon$  as our second equation. In homogeneous turbulence (see 3.6.4)  $\epsilon = \nu \omega^2$ , and so the  $q^2$  equation (2.8.12) yields the  $\epsilon$  (care must be taken to account for the density change when introducing  $\nu$ ). For homogeneous turbulence with  $\rho = \rho(t)$  and  $\mu = \text{constant}$  the result is

$$\dot{\epsilon} = 2\nu \overline{\omega_i^t \omega_j^t} S_{ij}^* - \frac{1}{3} \epsilon S_{kk} + 2\nu \overline{s_{ij}^t \omega_i^t} + 2\nu \overline{\omega_i^t s_{ij}^t} - 2\nu^2 \overline{\omega_{i,j}^t \omega_{i,j}^t} \quad (5.1.3)$$

where

$$S_{ij}^* = S_{ij} - \frac{1}{3} S_{kk} \delta_{ij} \quad (5.1.4)$$

is the anisotropic strain rate. The last two terms provide the means by which  $\epsilon$  changes in isotropic turbulence. In addition, we see that incompressible strain, isotropic volume change, and rotation will also modify the evolution of  $\epsilon$ . We shall address these issues separately.

### 5.2 Decay of isotropic turbulence

With no production the energy equation gives

$$\dot{q}^2 = -2\epsilon \quad (5.2.1)$$

Assuming that one can make a model using only  $q^2$  and  $\epsilon$  as variables, the form of the  $\epsilon$  equation for isotropic turbulence can be deduced by dimensional analysis,

$$\dot{\epsilon} = -C_{\epsilon 0} \frac{\epsilon^2}{q^2} \quad (5.2.2)$$

where the coefficient  $C_{\epsilon 0}$  can depend on the turbulence Reynolds number (see 3.2.2)  $R_T = q^4/(\nu \epsilon)$ . This is the form used by all models of this type.

Insight is obtained by recognizing that the right hand side of (5.2.1) comes from the difference of the last two terms in (5.1.3). The first of these is the turbulent vortex stretching term, which is related to the derivative skewness by (3.10.9). The last term can be written as

$$2\nu^2 \overline{\omega_{i,j}^t \omega_{i,j}^t} = 2\nu^2 \int_0^\infty k^4 E(k) dk \quad (5.2.3)$$

which shows that it is dominated by the smallest scales of motion and hence should scale on the Kolmogorov variables. It can be estimated using the model spectrum of Fig 3.9.4. Using the two estimates for isotropic

turbulence, put in terms that resemble the model equation (5.2.1), one finds that both terms scale as  $\sqrt{R_T}$ , and

$$\dot{\epsilon} = \sqrt{R_T} \left[ -\gamma \frac{35}{2} \left( \frac{1}{15} \right)^{3/2} - \frac{3\alpha}{10} \left( \frac{4}{3\alpha} \right)^{5/2} \right] \frac{\epsilon^2}{q^2}. \quad (5.2.4)$$

Experiments clearly indicate that a constant coefficient  $C_{\epsilon 0}$  does a very adequate job at high Reynolds numbers, which means that the *difference* in the two terms within the brackets in (5.2.4) must decrease as  $1/\sqrt{R_T}$ . Both terms are very large and they are nearly in balance (an estimate of the skewness can be made from this balance). It would be unwise to model these two large terms separately when we only need their difference, and for this reason the two are lumped together in (5.2.2).

The value of  $C_{\epsilon 0}$  can be determined by fitting the energy decay rate for isotropic turbulence to that measured experimentally, and this is what most modelers have done. The exact solution of the  $q^2$  and  $\epsilon$  model equations is

$$q^2 = q_0^2 (1 + t/a)^{-n} \quad \epsilon = \epsilon_0 (1 + t/a)^{-(n+1)} \quad (5.2.5a, b)$$

$$a = \frac{q_0^2}{2\epsilon_0} \quad n = \frac{2}{(C_{\epsilon 0} - 2)} \quad (5.2.5c, d)$$

The subscripts 0 denote initial values. The best experiments suggest  $n$  should be in the range 1.1-1.3. At low Reynolds numbers, where the turbulence is in its *final period*,  $n = 5/2$  is found theoretically and confirmed experimentally.

The model spectrum (3.9.4) can be used to find  $n$  (Reynolds 1976) by assuming that the spectrum is permanent below  $k_L$ , i.e. that the low wavenumber spectrum parameter  $A$  is constant. Expressing  $\epsilon$  in terms of  $q^2$  and  $A$  using (3.9.5) and (3.9.6), then using this in (5.2.1) to find the  $q^2$  history, one obtains (5.2.4a) with  $n = (2m+2)/(m+3)$ . This clearly supports the idea that the low wavenumber part of the spectrum affects the energy decay rate. The  $k^4$  spectrum ( $m=4$ ) gives  $n = 10/7$ , which is really too high to fit the best experiments very well. However, the  $k^2$  spectrum, with  $m=2$ , gives  $n = 6/5$ , in quite good agreement with experiments. In a finite Fourier series representation, the assignment of the same energy to each low wavenumber Fourier mode would make  $E_k$  independent of  $k$  and hence  $E(k)$  vary like  $k^2$ , and so  $k^2$  turbulence can be thought of as being *equipartitioned* at low wavenumbers.

With  $n = 6/5$  as suggested by both the experiments and the  $k^2$  spectrum,  $C_{\epsilon 0} = 11/3$ , and this is the value that we prefer. It is very close to the value of 3.84 used by many  $k-\epsilon$  modelers.

### 5.3 Isotropic compression

For isotropic turbulence,  $R_{ij} = q^2 \delta_{ij}/3$ . Denoting  $S_{kk} = 3\Gamma$  (see 4.4.1), and assuming isotropic volume change with  $\rho = \rho(t)$ , the energy equation (2.6.2) reduces to

$$\dot{q}^2 = -2\Gamma q^2 - 2\epsilon. \quad (5.3.1)$$

The  $\epsilon$  must be modified to account for the change in volume. The exact  $\epsilon$  equation (5.1.3) suggests that this modification might be

$$\dot{\epsilon} = -C_{\epsilon 0} \frac{\epsilon^2}{q^2} - \epsilon \Gamma. \quad (5.3.2)$$

For very large  $\Gamma$  the solutions to the above equations are

$$q^2 = q_0^2 e^{-2\Gamma t} \quad (5.3.3a)$$

$$\epsilon = \epsilon_0 e^{-\Gamma t} \quad (5.3.3b)$$

The energy development matches RDT (4.4.9). If we assume that the integral scale is proportional to  $q^3/\epsilon$ , the large-eddy length scale, then according to (5.3.3) the length scale varies as  $\exp(-2\Gamma t)$ . This says that expanding the flow volume will *reduce* the length scale, which should be disturbing to anyone and is not in agreement with RDT. Nevertheless, this modification of the  $\epsilon$  equation was used for some time in i.c. engine modeling before the problem was noted (Reynolds 1980).

The RDT analysis suggests instead that the  $\epsilon$  equation for this problem should be

$$\dot{\epsilon} = -C_{\epsilon 0} \frac{\epsilon^2}{q^2} - \frac{4}{3} \epsilon S_{kk} \quad (5.3.4)$$

For rapid volume change this produces

$$\epsilon = \epsilon_0 e^{-4\Gamma t} \quad (5.3.5)$$

for which the length scale varies in proportion to the strain, i.e. as  $\exp(\Gamma t)$ .

This example points out the pitfalls of using the exact equation for  $\epsilon$  as the basis for its model equation. To paraphrase Saffman, one should model the *Physics* and not the *equations*.

#### 5.4 Rotation

Experiments and numerical simulations show that rotation does not appreciably alter the anisotropy of isotropic turbulence. RDT (section 4.6) showed that rotation does not affect much of the spectrum at all, but does tend to produce a slow growth in the energy of the two-dimensional component of the turbulence aligned with the axis of rotation. The simulations (Bardina et al 1985) reflect this growth as a change in the integral scales, with the scale in the direction of the rotation axis becoming longer than the other two as time passes. Rotation also reduces the dissipation rate, apparently by inhibiting the energy transfer cascade.

Most turbulence models in use today show no effect of pure rotation on  $\epsilon$ , a weakness that has been slow to receive correction. Bardina found that his large-eddy simulations and Wiegand and Nagib's (1978) experimental data could both be predicted extremely well using a simple modification of the  $\epsilon$  equation,

$$\dot{\epsilon} = -\frac{11}{3} \frac{\epsilon^2}{q^2} - C_{\epsilon\Omega} \epsilon \Omega \quad (5.4.1a)$$

where  $\Omega$  is the rms rotation rate

$$\Omega = \sqrt{\Omega_{ij}\Omega_{ij}}. \quad (5.4.1b)$$

Bardina found that  $C_{\epsilon\Omega} = 0.15/\sqrt{2}$  worked well, and we adopt this value.

The imposition of a mean strain-rate provides a source of turbulent kinetic energy through the turbulence production term (2.6.3). We assume that the anisotropy part of the turbulence model will produce  $R_{ij}$  values given  $q^2$  and  $\epsilon$ , hence  $\mathcal{P}$  need not be modeled. Thus, no modeling for the  $q^2$  equation is required for homogeneous turbulence.

The associated changes in the dynamics of  $\epsilon$  must be incorporated in the  $\epsilon$  model equation. To date the most effective means for doing this is to add a term proportional to  $\mathcal{P}$ ,

$$\dot{\epsilon} = -C_{\epsilon 0} \frac{\epsilon^2}{q^2} - C_{\epsilon\Omega} \epsilon \Omega + C_{\epsilon\mathcal{P}} \frac{\mathcal{P}\epsilon}{q^2} \quad (5.4.1)$$

An estimate of  $C_{\epsilon\mathcal{P}}$  can be made using the homogeneous shear flow data of Tavoularis and Corrsin (1981). Homogeneous shear flow apparently reaches an equilibrium structure in which the Reynolds stresses all scale with the turbulent kinetic energy. The energy and dissipation rate both increase with time in a manner that keeps the turbulence time scale very nearly constant at a value set by the mean shearing rate  $\Gamma = dU_1/dx_2$ . The equation for  $\tau$ , derived from (5.1.2) using (5.1.1) and (5.4.1), is

$$\dot{\tau} = (C_{\epsilon 0} - 2) + C_{\epsilon\Omega} \Omega \tau - (C_{\epsilon\mathcal{P}} - 2) \frac{\mathcal{P}}{\epsilon}. \quad (5.4.2)$$

The experiments gave  $\Gamma q^2/\epsilon = 12.7$ , corresponding to  $\Omega \tau = 8.98$ , and  $\mathcal{P}/\epsilon = 1.8$ . Using  $C_{\epsilon 0} = 11/3$  and  $C_{\epsilon\Omega} = 0.15/\sqrt{2}$ , a constant value of  $\tau$  requires  $C_{\epsilon\mathcal{P}} = 3.45$ . This is somewhat higher than the value that Bardina recommended, which was based on his large eddy simulations of strained flows.

Most  $k - \epsilon$  models used today do not include the  $C_{\epsilon\Omega}$  term. For plane shear flows the rotation term and the production terms have the same form, and when these terms are into a single term expressed as in the form of the production term the resulting combined coefficient based on the above coefficients is about 3.0, which is very close to the value of 2.88 used in many  $k - \epsilon$  models.

### 5.5 Proposal for a simple $k - \tau$ model

Compared to the  $\epsilon$  equation (5.4.1), the  $\tau$  equation (5.4.2) is impressive in its simplicity. When one examines models for inhomogeneous turbulence,  $q^2/\epsilon$  frequently appears, suggesting that the time scale might be preferable to  $\epsilon$  as the second model variable. The choice should be based on the ease with which the model extends to new situations. The diffusion terms required for inhomogeneous flows are particularly useful in evaluating various proposals.

For example, consider what happens to the terms in the  $\epsilon$  equation near a solid boundary. The  $\epsilon^2/q^2$  term goes to infinity, but the  $\rho\epsilon/q^2$  term goes to zero. Consequently, a great deal of effort has been spent inventing near-wall patches for these terms. One does not escape these simply by changing variables, unless a slight modification is made. In contrast, Wilcox (1986), who uses a reciprocal time scale in place of  $\epsilon$ , achieves reasonable near-wall solutions, even in the viscous region, with no near-wall modifications of his model equation.

Two-equation models have been criticized because the length scales are anisotropic in anisotropic turbulence but the model assumes isotropy of length scale. The success that two-equation models enjoy would seem remarkable in the light of this objection. But suppose it is really *time scale* information that is carried by  $\epsilon$ , and that the anisotropy of length scales is reflected by anisotropy of  $R_{ij}$ .

Another clue is provided by the case of isotropic volume change, for which the  $\tau$  equation is

$$\dot{\tau} = (C_{\epsilon 0} - 2) - \frac{4}{3} S_{kk} \tau. \quad (5.5.1)$$

Note the appearance of the strain rate term.

It is suggested that it might be better to replace the production term in the  $\tau$  equation by a term proportional to the rms strain rate. Some additional simplicity of form is obtained by using the kinetic energy  $k = q^2/2$  and redefining the time scale and turbulent Reynolds number by

$$\bar{\tau} = k/\epsilon \quad \bar{R}_T = k\bar{\tau}/\nu \quad (5.5.2a, b)$$

The model equation proposed is

$$\dot{\bar{\tau}} = C_{\bar{\tau}0} + C_{\bar{\tau}\Omega} \Omega \bar{\tau} - C_{\bar{\tau}S^*} S^* \bar{\tau} - \frac{4}{3} S_{kk} \bar{\tau}. \quad (5.5.3)$$

Here  $S^*$  is the rms anisotropic strain rate

$$S^* = \sqrt{S_{ij}^* S_{ij}^*} \quad (5.5.4c)$$

determined from the anisotropic strain rate tensor

$$S_{ij}^* = S_{ij} - \frac{1}{3} S_{kk} \delta_{ij}. \quad (5.5.4b)$$

Note that none of these terms is ill-behaved at the wall, and so there is hope that the near-wall modifications can be much simpler. The constants for this model, evaluated in the same manner as those in the  $\epsilon$  equation, are

$$C_{\bar{\tau}0} = 5/6 \quad C_{\bar{\tau}\Omega} = 0.11 \quad C_{\bar{\tau}S^*} = 0.69. \quad (5.5.5a, b, c)$$

Exploration of this idea is encouraged.

## 6. MODELING ANISOTROPY IN HOMOGENEOUS TURBULENCE

### 6.1 Description of anisotropy

The scale equations developed in the previous chapter are closed only for isotropic turbulence. In general, the Reynolds stress tensor must also be determined by the model. The *Reynolds stress anisotropy tensor*

$$b_{ij} = \frac{R_{ij} - \frac{1}{3} q^2 \delta_{ij}}{q^2} \quad (6.1.1)$$

is a very convenient way to describe the deviations from isotropy. This chapter deals with  $b_{ij}$  and its modeling, which must be done with great care if unrealistic predictions are to be avoided.

The anisotropy tensor has some important properties that need to be kept firmly in mind. By definition it is *trace free*,

$$b_{ii} = 0. \quad (6.1.2)$$

It is often convenient to think of  $b_{ij}$  in its principal coordinates, where only diagonal elements are non-zero. By (6.2.1) the sum of these principal values is zero, so only *two* are independent. This means that the anisotropy can be characterized by two independent invariants,

$$II = -b_{ij}b_{ji}/2 \quad III = b_{ij}b_{jk}b_{ki}/3. \quad (6.1.3a, b)$$

If the turbulence is *two-dimensional*, meaning that one (principal-axis) velocity component is always zero, by the definition (recall Greek indices are not summed)

$$b_{\alpha\alpha} = -1/3 \quad \text{if} \quad R_{\alpha\alpha} = 0. \quad (6.1.4)$$

And, if all of the energy becomes concentrated in one component,

$$b_{\alpha\alpha} = 2/3 \quad \text{if} \quad R_{\alpha\alpha} = q^2. \quad (6.1.5)$$

This is called *one-dimensional turbulence*. Note that the one non-zero velocity component could be a function of the other two coordinates, say  $u'_1(x_2, x_3, t)$ , so that the flow would resemble a honeycomb of opposing jets.

Thus, the possible values of the two independent principal  $b_{\alpha\alpha}$ , say  $b_{11}$  and  $b_{22}$ , must lie within the triangle on Fig 6.1.1. The vertices correspond to the three possible states of one-dimensional turbulence, and the sides to states of two-dimensional turbulence. The isotropic state is the origin. The diagonal lines, along which two principal components are the same, are states of *axisymmetric turbulence*.

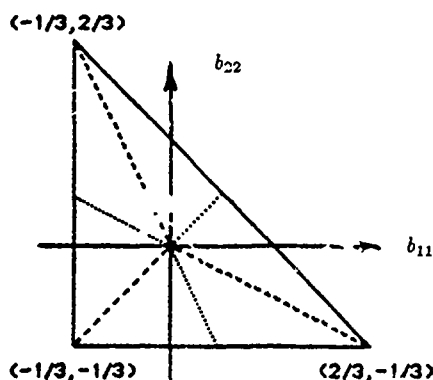


Figure 6.1.1 Range of possible principal values of the anisotropy tensor

Note that one can either move along an axisymmetric line away from isotropy to a two-dimensional state (edge) or to a one-dimensional state (vertex). These limiting cases may seem extreme. However, turbulence near a wall is two-dimensional (the normal component vanishes), and turbulence in a strongly sheared layer moves remarkably far towards one-dimensionality.

In homogeneous turbulence, the move towards a two-dimensional state is made by straining the turbulence in one direction and contracting it equally in the other two. This stretches vortex filaments in the direction of positive strain, aligning these filaments with the flow and thereby reducing the fluctuations in the direction of positive strain. This is what happens to turbulence when it is passed through an *axisymmetric contraction*.

The move towards a one-dimensional state is achieved by straining the flow equally in two orthogonal directions, and contracting it in the third, as one could do in an axisymmetric diffuser (using boundary layer suction to prevent separation). The vortex cores are stretched out to form sheets (pancakes) and the limiting one-dimensional case corresponds to a honeycomb of two-dimensional vorticity. We will call this type of deformation *axisymmetric expansion*.

An equivalent and less specific way to characterize the anisotropy is through the *anisotropy invariant map* introduced by Lumley. For axisymmetric turbulence we write the anisotropy tensor in principal coordinates as

$$b_{ij} = \begin{pmatrix} a & 0 & 0 \\ 0 & a & 0 \\ 0 & 0 & -2a \end{pmatrix}. \quad (6.1.6)$$

Then

$$II = -3a^2 \quad III = -2a^3. \quad (6.1.7)$$

Along lines where  $a < 0$  so that the component along the axis is more energetic than the other two (axisymmetric expansion),

$$III = +2 \left( \frac{-II}{3} \right)^{3/2} \quad (6.1.7a)$$

while if  $a > 0$  so that the axis component is less energetic (axisymmetric contraction)

$$III = -2 \left( \frac{-II}{3} \right)^{3/2}. \quad (6.1.7a, b)$$

The two-dimensional boundaries can be studied in principal coordinates, writing

$$b_{ij} = \begin{pmatrix} -\frac{1}{3} & 0 & 0 \\ 0 & \frac{a+1}{6} & 0 \\ 0 & 0 & \frac{a-1}{6} \end{pmatrix}. \quad (6.1.8)$$

Then

$$II = -\frac{1}{12} \left( 1 + \frac{a^2}{3} \right) \quad III = \frac{a^2 - 1}{108} \quad (6.1.9a, b)$$

so that for two-dimensional turbulence

$$G = \frac{1}{9} + II + 3III = 0. \quad (6.1.10)$$

Using these results, the range of possible turbulence states is shown in the invariant map of Fig. (6.1.2). The origin is the isotropic state, the upper boundary is the locus of two-dimensional states, the two sides are the two types of axisymmetric states, and the upper vertex is the one-dimensional state. The anisotropy invariant map is a very useful way to characterize the state of turbulence in modeling, simulations, and experiments.

Two tensors that can be formed from the anisotropy tensor are its square,

$$b_{ij}^2 = b_{ik} b_{kj} \quad (6.1.11)$$

and its cube,

$$b_{ij}^3 = b_{in} b_{nm} b_{mj}. \quad (6.1.12)$$

The *Cayley-Hamilton theorem* of linear algebra says that a matrix satisfies its own characteristic equation, which in this instance means that

$$b_{ij}^3 + \text{II} b_{ij} - \text{III} \delta_{ij} = 0 \quad (6.1.13a)$$

or alternatively

$$b_{ij}^3 = \frac{1}{2} b_{kk}^2 b_{ij} + \frac{1}{3} b_{kk}^3 \delta_{ij}. \quad (6.1.13b)$$

Hence,  $b_{ij}^3$ , and all higher powers of the tensor, are linearly dependent on the lower powers and hence do not contain new tensorial structure beyond that in  $b_{ij}^2$ ,  $b_{ij}$ , and  $\delta_{ij}$ . As we shall see, this is very important in turbulence modeling. Readers not familiar with this important theorem may find it instructive to verify (6.1.13b) by writing  $b_{ij}$  in its principal coordinates, carrying out the products using the trace-free condition to express one of the principal values in terms of the other two.

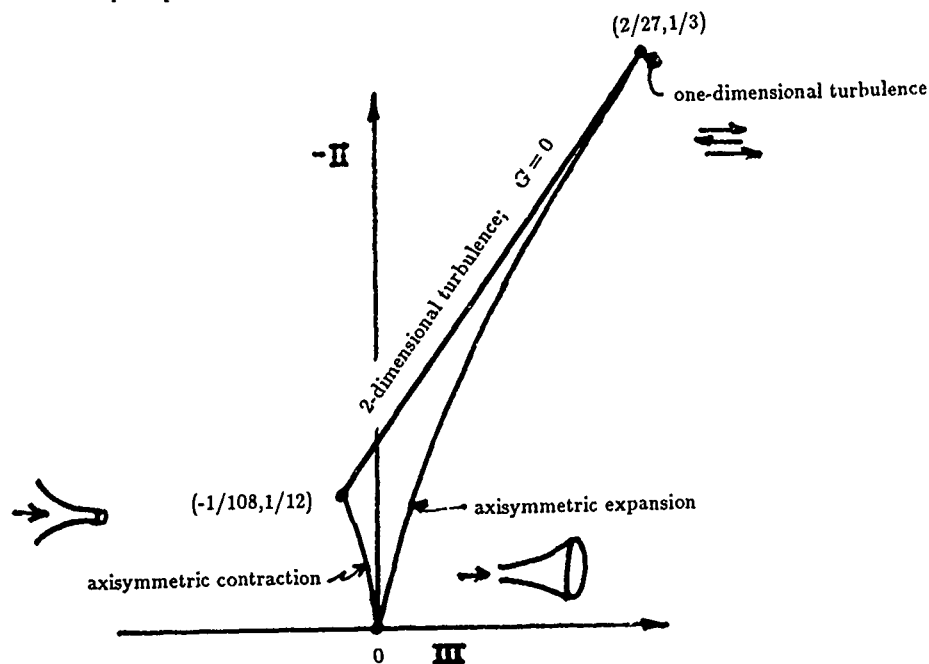


Figure 6.1.2 Anisotropy invariant map

## 6.2 Evolution equation for the anisotropy tensor

Using the evolution equation for  $R_{ij}$  (2.7.1) and the definition of  $b_{ij}$ , the equation for evolution of  $b_{ij}$  in homogeneous turbulence with  $\rho = \rho(t)$  can be written as

$$\begin{aligned} \dot{b}_{ij} = & -\frac{2}{3} S_{ij}^* - (b_{ik} S_{kj}^* + b_{jk} S_{ki}^* - \frac{2}{3} b_{nm} S_{nm}^* \delta_{ij}) + 2 b_{nm} S_{nm}^* b_{ij} \\ & + (b_{ik} \Omega_{kj} + b_{jk} \Omega_{ki}) + \frac{1}{q^2} [T_{ij} - (D_{ij} - \frac{1}{3} D_{kk} \delta_{ij})] + 2 \frac{\epsilon}{q^2} b_{ij} \end{aligned} \quad (6.2.1)$$

Here  $S_{ij}^*$  is the anisotropic strain rate tensor defined by (5.5.4). Note that only anisotropic strain produces Reynolds stress anisotropy, and that the right hand side is properly trace-free. The terms containing the mean rotation tensor  $\Omega_{ij}$  represent a kinematic rotation of the anisotropy tensor. When used in conjunction with  $q^2$  and  $\epsilon$  equations, models for the pressure-strain term  $T_{ij}$  and the anisotropy of the dissipation tensor  $D_{ij}$  must be provided.

There is a class of turbulence models called *algebraic two-equation models* in which it is assumed that the turbulence structure has reached an equilibrium state determined by a balance of the terms on the right hand side of (6.2.1). For example, the standard  $k - \epsilon$  model uses an algebraic equation equivalent to

$$b_{ij} = -\frac{C_\mu q^2}{4\epsilon} S_{ij} \quad (6.2.2)$$

with  $C_\mu = 0.09$ . A problem should be immediately apparent. The sudden imposition of a strong strain could easily produce  $b_{ij}$  states lying outside of the anisotropy invariant map. This is a very serious potential problem when such models are applied in new flows.

Another weakness of this model is that it assumes that the principal axes of stress and strain-rate are aligned. This is not true in the most important engineering flow, namely shear flow. However, the constant  $C_\mu$  has been set to give the right anisotropy of the shearing stress. For example, in the homogeneous shear flow experiment of Tavoularis and Corrsin discussed in section (5.4),  $b_{12} = -0.149$  is predicted by (6.2.2), in excellent agreement with the measurements. However, the model predicts  $b_{11} = 0$ , whereas the experiments show  $b_{11} = 0.196$ , so the normal stresses are badly in error. However, they do not play a significant role in determining the mean velocity field, and so this error usually of little consequence.

Algebraic models assume that the turbulence structure responds instantly to changes in the imposed mean strain. This is reasonable for computing the slow evolution of mean fields, but not satisfactory if the strain rates are large, i.e. if  $S^* q^2 / \epsilon \gg 0$ , where  $S^*$  is the rms anisotropic strain rate. And algebraic models predict instant restoration of isotropy after the removal of an applied mean strain-rate. Hence, if one wants to have realistic predictions of the Reynolds stresses in these cases, a model of the  $b_{ij}$  evolution equation be solved in parallel with the  $q^2$  and  $\epsilon$  equations.

In the balance of this chapter we review the formal methods that have been applied in attempts to develop rational models to close the  $b_{ij}$  evolution equation. Then, at the end we will present a much simpler model that achieves some of the objectives of the more complicated models at much less expense. This new model might be useful for engineering analysis.

### 6.3 Decomposition of the pressure-strain term

The Poisson equation for the fluctuation pressure (2.6.1) has two terms on the right that act as sources for pressure fluctuations. The source involving the mean velocity gradients will change instantly when the gradients change, resulting in an instant change in the fluctuating pressure field and hence an instant change in the pressure-strain term  $T_{ij}$ . The source involving only the turbulence will change only as the turbulence adjusts to its new conditions. This suggests that the pressure fluctuations be split into *rapid* and *slow* parts,

$$p' = p^{(1)} + p^{(2)} \quad (6.3.1a)$$

where the rapid term is the solution of

$$\frac{1}{\rho} p^{(1)}{}_{,ii} = -2u'_{j,i} U_{i,j} \quad (6.3.1b)$$

and the slow term is the solution of

$$\frac{1}{\rho} p^{(2)}{}_{,ii} = -2u'_{j,i} u'_{i,j} + 2\overline{u'_{j,i} u'_{i,j}} \quad (6.3.1c)$$

The resulting contributions to the pressure-strain term (2.7.5) will be denoted by  $T_{ij}^{(1)}$  and  $T_{ij}^{(2)}$ , respectively.

Eqn. (3.6.1b) is linear and has constant coefficients in homogeneous turbulence, and so can be solved by Fourier methods. We follow the approach of Chapter 3, and write



$$p^{(1)} = \sum_{\mathbf{k}} \hat{p}(\mathbf{k}) e^{-i\mathbf{k} \cdot \mathbf{x}} \quad u'_i = \sum_{\mathbf{k}} \hat{u}_i(\mathbf{k}) e^{-i\mathbf{k} \cdot \mathbf{x}}. \quad (6.3.2a, b)$$

The time-dependence of the coefficients is not explicitly expressed because we are solving the Poisson equation at one instant of time. The solution of (6.3.1b) is then

$$\frac{1}{\rho} \hat{p}(\mathbf{k}) = -2U_{p,j} \frac{ik_p}{k^2} \hat{u}_j(\mathbf{k}). \quad (6.3.3)$$

Multiplying the pressure fluctuation series by the the velocity gradient series, using the conjugate symmetry properties of the Fourier modes, averaging over the box of Fig. 3.3.1, then taking the limit as done in section 3.3, one finds

$$\frac{1}{\rho} \overline{p^{(1)} u'_{i,q}} = 2U_{p,j} M_{ijpq} \quad (6.3.4)$$

where

$$M_{ijpq} = \int \frac{k_p k_q}{k^2} E_{ij}(\mathbf{k}) d^3 \mathbf{k}. \quad (6.3.5)$$

The rapid pressure-strain term is the sum of two such terms,

$$T_{iq}^{(1)} = 2U_{p,j} (M_{ijpq} + M_{qjpi}). \quad (6.3.6)$$

Modeling of the rapid pressure strain term therefore becomes a task of modeling  $M_{ijpq}$ , which we address in the next section.

#### 6.4 Modeling the $M_{ijpq}$ tensor

The  $M_{ijpq}$  tensor has been modeled in various ways, all relatively simple, usually with one constant being adjusted to fit data for the predictions of a selection of flows. Here we introduce a very different approach; we argue that the anisotropy model, when applied in circumstances for which rapid distortion theory would apply, should give results consistent with RDT. The RDT form of the *model* equation includes only the rapid pressure strain term, the production term, and the mean rotation term in (6.2.1), exactly the same terms used in RDT theory. The solution above for the rapid pressure field is exactly the same as used in RDT. Therefore, in principle it should be possible to determine all of the coefficients in the rapid pressure strain model (i.e. in  $M_{ijpq}$ ) so as to make the anisotropy predicted by the model equation under RDT approximations *exactly* the same as that predicted by RDT theory, for an *arbitrary* rapid deformation.

Following Shih and Lumley (1985), we begin by writing the general expression for a tensor  $\tilde{M}_{ijpq} = M_{ijpq}/q^2$  that is assumed to be a function of the tensor  $b_{ij}$ , with the symmetries in indices required by the definition. This is

$$\begin{aligned} \tilde{M}_{ijpq} = & C_1 \delta_{ij} \delta_{pq} + C_2 (\delta_{ip} \delta_{jq} + \delta_{iq} \delta_{jp}) + C_3 \delta_{ij} b_{pq} + C_4 \delta_{pq} b_{ij} + C_5 (\delta_{ip} b_{jq} + \delta_{iq} b_{jp} + \delta_{jp} b_{iq} + \delta_{jq} b_{ip}) \\ & + C_6 \delta_{ij} b_{pq}^2 + C_7 \delta_{pq} b_{ij}^2 + C_8 (\delta_{ip} b_{jq}^2 + \delta_{iq} b_{jp}^2 + \delta_{jp} b_{iq}^2 + \delta_{jq} b_{ip}^2) + C_9 b_{ij} b_{pq} + C_{10} (b_{ip} b_{jq} + b_{iq} b_{jp}) \\ & + C_{11} b_{ij} b_{pq}^2 + C_{12} b_{pq} b_{ij}^2 + C_{13} (b_{ip} b_{jq}^2 + b_{iq} b_{jp}^2 + b_{jp} b_{iq}^2 + b_{jq} b_{ip}^2) + C_{14} b_{ij}^2 b_{pq}^2 + C_{15} (b_{ip}^2 b_{jq}^2 + b_{iq}^2 b_{jp}^2). \end{aligned} \quad (6.4.1)$$

Because of the Cayley-Hamilton theorem, higher powers of  $b_{ij}$  are not required. The coefficients  $C_1 - C_{15}$  may be function of the invariants II and III, and of other scalars, such as  $R_T$ .

The continuity (2.3.4) equation requires  $\tilde{M}_{i,jq} = 0$ . When this condition is applied to (6.4.1), an equation containing  $\delta_{jq}$ ,  $b_{jq}$ , and  $b_{jq}^2$  is obtained. Since these are independent tensors, the coefficient of each must vanish. This produces three equations,

$$C_1 + 4C_2 + b_{kk}^2 C_8 + \frac{1}{3} b_{kk}^3 (C_{11} + C_{12} + 2C_{13}) = 0 \quad (6.4.2a)$$

$$C_3 + C_4 + 5C_5 + \frac{1}{2} b_{kk}^2 (C_{11} + C_{12} + 4C_{13}) + \frac{1}{3} b_{kk}^3 (C_{14} + C_{15}) = 0 \quad (6.4.2b)$$

$$C_6 + C_7 + 5C_8 + C_9 + C_{10} + \frac{1}{2}b_{kk}^2(C_{14} + 3C_{15}) = 0. \quad (6.4.2c)$$

From its definition,  $M_{ijpq} = R_{ij}$ , so  $\tilde{M}_{ijpq} = b_{ij} + \delta_{ij}/3$ . In the same way, this condition gives three additional constraints,

$$3C_1 + 2C_2 + b_{kk}^2 C_8 + \frac{4}{3}b_{kk}^3 C_{13} = \frac{1}{3} \quad (6.4.3a)$$

$$3C_4 + 4C_5 + b_{kk}^2(C_{11} + 2C_{13}) + \frac{2}{3}b_{kk}^3 C_{15} = 1 \quad (6.4.3b)$$

$$3C_7 + 4C_8 + 2C_{10} + b_{kk}^2(C_{14} + C_{15}) = 0. \quad (6.4.3c)$$

These six conditions reduce the number of undetermined coefficients to nine, and give

$$C_1 = \frac{2}{15} + b_{kk}^2 \left( \frac{5}{3}C_8 + \frac{2}{5}C_9 + \frac{2}{15}C_{10} \right) + b_{kk}^3 \left( \frac{1}{15}C_{11} + \frac{1}{15}C_{12} - \frac{2}{5}C_{13} \right) + (b_{kk}^2)^2 \left( \frac{1}{15}C_{14} + \frac{7}{5}C_{15} \right) \quad (6.4.4a)$$

$$C_2 = -\frac{1}{30} + b_{kk}^2 \left( -\frac{2}{3}C_8 - \frac{1}{10}C_9 - \frac{1}{30}C_{10} \right) + b_{kk}^3 \left( -\frac{1}{10}C_{11} - \frac{1}{10}C_{12} - \frac{1}{15}C_{13} \right) + (b_{kk}^2)^2 \left( -\frac{1}{60}C_{14} - \frac{7}{20}C_{15} \right) \quad (6.4.4b)$$

$$C_3 = -\frac{1}{3} - \frac{11}{3}C_5 + b_{kk}^2 \left( -\frac{1}{6}C_{11} - \frac{1}{2}C_{12} - \frac{4}{3}C_{13} \right) + b_{kk}^3 \left( -\frac{1}{3}C_{14} - \frac{1}{9}C_{15} \right) \quad (6.4.4c)$$

$$C_4 = \frac{1}{3} - \frac{4}{3}C_5 + b_{kk}^2 \left( -\frac{1}{3}C_{11} - \frac{2}{3}C_{13} \right) + b_{kk}^3 \left( -\frac{2}{3}C_{15} \right) \quad (6.4.4d)$$

$$C_6 = -\frac{11}{3}C_8 - C_9 - \frac{1}{3}C_{10} + b_{kk}^2 \left( -\frac{1}{6}C_{14} - \frac{7}{6}C_{15} \right) \quad (6.4.4e)$$

$$C_7 = -\frac{4}{3}C_8 - \frac{2}{3}C_{10} + b_{kk}^2 \left( -\frac{1}{3}C_{14} - \frac{1}{3}C_{15} \right) \quad (6.4.4f)$$

Once the coefficients are evaluated,  $T_{ij}^{(1)}$  can be determined. The result, written in terms of the anisotropic strain rate tensor (5.5.4) and the rotation tensor, is

$$\begin{aligned} \frac{T_{ij}^{(1)}}{2q^2} = & 2(C_1 + C_2)S_{ij}^* + (C_3 + C_4 + 2C_5) \left( S_{ik}^* b_{kj} + S_{jk}^* b_{ki} - \frac{2}{3}S_{nm}^* b_{mn} \delta_{ij} \right) \\ & + (C_6 + C_7 + 2C_8) \left( S_{ik}^* b_{kj}^2 + S_{jk}^* b_{ki}^2 - \frac{2}{3}S_{nm}^* b_{mn}^2 \delta_{ij} \right) + 2(C_9 + C_{10})S_{pq}^* \left( b_{iq} b_{jp} - \frac{1}{3}b_{pq}^2 \delta_{ij} \right) + 2C_{10}S_{pq}^* b_{qp} b_{ij} \\ & + (C_{11} + C_{12} + 2C_{13})S_{pq}^* \left( b_{iq} b_{pj}^2 + b_{jq} b_{pi}^2 - \frac{2}{3}b_{mn}^3 \delta_{ij} \right) + 2C_{13}S_{pq}^* b_{qi}^2 b_{ij} + 2C_{13}S_{pq}^* b_{qp} \left( b_{ij}^2 - \frac{1}{3}b_{nn}^2 \delta_{ij} \right) \\ & + 2(C_{14} + C_{15})S_{pq}^* \left( b_{ip}^2 b_{jq}^2 - \frac{1}{3}b_{np}^2 b_{nq}^2 \delta_{ij} \right) + 2C_{15}S_{pq}^* b_{pj}^2 \left( b_{ii}^2 - \frac{1}{3}b_{nn}^2 \delta_{ij} \right) \\ & + (C_3 - C_4)(\Omega_{ki} b_{kj} + \Omega_{kj} b_{ki}) + (C_6 - C_7)(\Omega_{ki} b_{kj}^2 + \Omega_{kj} b_{ki}^2) + (C_{11} - C_{12})\Omega_{pq}(b_{iq} b_{pj}^2 + b_{jq} b_{pi}^2). \quad (6.4.5) \end{aligned}$$

*Realisability* has been of much concern in modeling the pressure-strain term and other terms in the  $b_{ij}$  equation. The principal values  $b_{\alpha\alpha}$  can not be less than  $-1/3$ , and any model that would carry a principal value below this amount (i.e. outside the bounds of the invariant map) then produces *unrealizable turbulence* (nonsense). Truncated approximations to the series above have this danger, although the model

just described, with the infinite set of coefficients, would be realizable because RDT solutions are realizable. In order to guarantee realizability one can enforce certain conditions. There are various ways to develop these conditions. Shih and Lumley (1985) get them by requiring that the  $T_{\alpha\alpha}$  terms must not drive  $b_{\alpha\alpha}$  out of bounds. This requires

$$U_{p,j} M_{\alpha j p \alpha} = 0 \quad \text{when } b_{\alpha\alpha} = -1/3 \quad (6.4.6)$$

which produces three additional constraints,

$$C_1 + C_2 - \frac{1}{3}(C_3 + C_4 + 2C_5) + \frac{1}{9}(C_6 + C_7 + 2C_8 + C_9 + C_{10}) - \frac{1}{27}(C_{11} + C_{12} + 2C_{13}) + \frac{1}{81}(C_{14} + C_{15}) = 0 \quad (6.4.7a)$$

$$C_5 - \frac{1}{3}C_{10} + \frac{1}{9}C_{13} = 0 \quad (6.4.7b)$$

$$C_8 - \frac{1}{3}C_{13} + \frac{1}{9}C_{15} = 0. \quad (6.4.7c)$$

We believe it is preferable to impose the realizability conditions directly on the modeled tensor  $M_{jppq}$ . When the velocity component  $u'_\alpha$  is everywhere zero then  $\hat{u}_\alpha = 0$  and consequently  $M_{\alpha j p q} = 0$ . In the principal coordinates of  $b_i$ , this requires

$$M_{1111} = 0 \quad M_{1122} - M_{1133} = 0 \quad M_{1212} = 0 \quad \text{when } b_{11} = -1/3 \quad (6.4.8a, b, c)$$

Using the fact that  $b_{kk}^2 = -1/9 + b_{kk}^2/2$  on the two-dimensional line, (6.4.8a-c) give

$$C_1 + 2C_2 - \frac{1}{3}(C_3 + C_4 + 4C_5) + \frac{1}{9}(C_6 + C_7 + 4C_8 + C_9 + 2C_{10}) - \frac{1}{27}(C_{11} + C_{12} + 4C_{13}) + \frac{1}{81}(C_{14} + 2C_{15}) = 0 \quad (6.4.9a)$$

$$\frac{1}{3}C_3 + \frac{1}{9}(C_6 - C_9) - \frac{1}{27}(C_{11} - C_{12}) + \frac{1}{81}C_{14} = 0 \quad (6.4.9b)$$

$$\frac{1}{6}C_5 + \frac{1}{18}(C_8 - C_{10}) + \frac{1}{162}C_{15} = 0 \quad (6.4.9c)$$

$$C_2 - \frac{1}{6}C_5 + \left(\frac{1}{18} + \frac{1}{2}b_{kk}^2\right)C_8 - \frac{1}{18}C_{10} + \left(\frac{1}{27} - \frac{1}{6}b_{kk}^2\right)C_{13} + \left(-\frac{1}{162} + \frac{1}{18}b_{kk}^2\right)C_{15} = 0. \quad (6.4.9d)$$

When equations (6.4.4) are used to express the lower coefficients, (6.4.9d) is  $-1/2$  (6.4.9a), and so only three independent conditions are obtained,

$$\begin{aligned} & \frac{1}{15} + \frac{1}{3}C_5 + \left(-\frac{1}{9} + \frac{1}{3}b_{kk}^2\right)C_8 + \frac{1}{5}b_{kk}^2C_9 + \left(\frac{1}{9} + \frac{1}{15}b_{kk}^2\right)C_{10} + \left(-\frac{1}{45} + \frac{1}{10}b_{kk}^2\right)(C_{11} + C_{12}) \\ & + \left(-\frac{4}{45} + \frac{2}{5}b_{kk}^2\right)C_{13} + \frac{1}{30}(b_{kk}^2)^2C_{14} + \left(\frac{1}{81} - \frac{1}{9}b_{kk}^2 + \frac{7}{10}(b_{kk}^2)^2\right)C_{15} = 0 \end{aligned} \quad (6.4.10a)$$

$$\begin{aligned} & -\frac{1}{9} - \frac{11}{9}C_5 - \frac{11}{27}C_8 - \frac{2}{9}C_9 - \frac{1}{27}C_{10} - \left(\frac{1}{27} + \frac{1}{18}b_{kk}^2\right)C_{11} + \left(\frac{1}{27} - \frac{1}{6}b_{kk}^2\right)C_{12} \\ & - \frac{4}{9}b_{kk}^2C_{13} + \left(\frac{2}{81} - \frac{2}{27}b_{kk}^2\right)C_{14} + \left(\frac{1}{243} - \frac{4}{27}b_{kk}^2\right)C_{15} = 0 \end{aligned} \quad (6.4.10b)$$

$$\frac{1}{6}C_5 + \frac{1}{18}(C_8 - C_{10}) + \frac{1}{162}C_{15} = 0 \quad (6.4.10c)$$

When these are satisfied, the Shih-Lumley conditions will also be satisfied. It is important to realize that these realizability constraints apply only when the turbulence is two-dimensional, i.e. only on the line  $G = 0$  that forms the top boundary of the invariant map.

The equations above suggest that the coefficients will depend on the invariants and not simply be constants. We might expand each coefficient as a power series in the invariants,

$$C_n = C_n^{(0)} + b_{kk}^2 C_n^{(2)} + b_{kk}^3 C_n^{(3)} + (b_{kk}^2)^2 C_n^{(4)} + b_{kk}^2 b_{kk}^3 C_n^{(5)} + (b_{kk}^3)^2 C_n^{(6)} + \dots \quad (6.4.11)$$

We see that the first approximations to the isotropic coefficients  $C_1$  and  $C_2$  are already known, and the first approximations to the linear coefficients  $C_3$ - $C_5$  are determined by the first approximation to  $C_5$ .

Most turbulence models presently in use include only the terms in  $M_{ijpq}$  through  $C_5$  (the linear terms), employing constant values for the coefficients. But with  $C_6$ - $C_{15} = 0$  no single value of  $C_5$  can satisfy all three realizability conditions (6.4.10), so these linear models do not satisfy realizability.

The simplest set of coefficients satisfying realizability is obtained by truncating  $M_{ijpq}$  to  $O(b^2)$  and assuming all coefficients are constants. The truncation gives

$$C_{11} = C_{12} = C_{13} = C_{14} = C_{15} = 0. \quad (6.4.12a)$$

From (6.4.4a,b), the coefficients  $C_1$  and  $C_2$  will be constants only if  $C_8 = 0$  and  $C_{10} = -3C_9$ . Then, the realizability conditions give

$$\begin{aligned} C_1 &= 2/15 & C_2 &= -1/30 & C_3 &= 1/30 & C_4 &= 7/15 \\ C_5 &= -1/10 & C_7 &= 2/10 & C_9 &= 1/10 & C_{10} &= -3/10 \end{aligned} \quad (6.4.12b)$$

These are the coefficients determined in a slightly different manner by Shih and Lumley (1986). Under the rapid distortion approximations, the time-series solution of the model equations resulting from (6.4.12) match RDT of isotropic turbulence only to  $O(1)$ . The model also predicts that anisotropic turbulence subjected to pure rotation would undergo anisotropy changes, in excess of those caused by the kinematic rotation terms, of  $O(t)$ , whereas RDT indicates that this excess change must be an even power series in  $t$  (see section 4.3) and hence should not appear until  $O(t^2)$ . It would seem desirable to obtain a better match to RDT.

Under rapid pure rotation of anisotropic turbulence, (6.4.5) will produce an  $O(t)$  change in  $b_{ij}$  in excess of that produced by the kinematic rotation terms unless  $(C_3^{(0)} - C_4^{(0)}) = 0$ . This condition gives

$$C_3^{(0)} = -2/7 \quad C_4^{(0)} = C_5^{(0)} = 5/7. \quad (6.4.13)$$

With these values, the RDT-equivalent model predictions also agrees with RDT to  $O(t)$  for all irrotational strains (Reynolds 1983). Le Penven and Gence (1983) carried the analysis to one additional order in  $t$  for the case of irrotational strain at a constant strain rate, and found that the coefficients could indeed be matched to  $O(t^2)$ . Hence, it seems clear that (6.4.13) gives the rational choices for the first approximations to the linear coefficients. However, with  $C_5 = -2/7$  the realizability conditions can not be satisfied by a truncation of  $M_{ijpq}$  to  $O(b^2)$ , and one must include higher-order terms to effect realizability.

It seems clear that continued matching with RDT would determine all of the coefficients, and since RDT predicts realizable turbulence the resulting model would guarantee realizability. The RDT required for a complete matching must be sufficiently general to allow all coefficients to be determined. The arbitrary irrotational strain analysis given in section (4.5) is not sufficient because there the principal axes of  $S_{ij}$  were fixed and hence the principal axes of  $S_{ij}$  and  $b_{ij}$  always remained aligned. An RDT for of isotropic turbulence with arbitrary initial rotation rate and arbitrary strain rate history is required (see section 4.6). It should be possible to select the constants in the coefficient expansions (4.6.10) to match RDT to any arbitrary order in a time-series solution of the RDT-approximate model equations, and then to use the realizability conditions to truncate the expansions, maintaining full realizability. Thus, in principle the rapid pressure strain model should be determined completely by RDT analysis, with no adjustable constants matched to experiments. We are attempting to complete this task.

Another approach that may be fruitful is to use RDT for initially axisymmetric two-dimensional turbulence, in conjunction with the realizability constraints, to develop expressions for the coefficients that must hold along the two-dimensional line  $G = 0$ . The results of section 4.7 should be useful in this regard. These coefficients might then be expanded in power series in  $G$  in order to determine appropriate values for three-dimensional turbulence, perhaps by matching to RDT. Many interesting analyses of this nature remain to be done in turbulence modeling.

### 6.5 Modeling the slow terms

The negative of the slow pressure-strain term and the dissipation anisotropy term are modeled together in (6.2.1) as

$$T_{ij}^{(2)} - (D_{ij} - D_{kk}\delta_{ij}/3) = -\epsilon\phi_{ij}. \quad (6.5.1)$$

Assuming that it is possible to model  $\phi_{ij}$  in terms of  $b_{ij}$ , a premise that is not supported very well by direct numerical simulations, the most general form must be

$$\phi_{ij} = (\alpha + 2)b_{ij} + \beta(b_{ij}^2 + \frac{2}{3}\Pi\delta_{ij}) \quad (6.5.2)$$

where the coefficients  $\alpha$  and  $\beta$  could be functions of the invariants  $\Pi$  and  $\text{III}$  and possibly of other scalars, such as  $R_\tau$ . Under these assumptions, one can in principle evaluate the coefficients by reference to experiments and simulations on the return to isotropy following removal of mean strain rate. In this case (6.2.1) reduces to

$$\dot{b}_{ij} = -\frac{\epsilon}{q^2}(\phi_{ij} - 2b_{ij}) = -\frac{\epsilon}{q^2}[\alpha\dot{b}_{ij} + \beta(b_{ij}^2 - \frac{1}{3}b_{kk}^2\delta_{ij})]. \quad (6.5.3)$$

If the anisotropy is weak,  $\alpha$  controls the return and must be positive if there is to be a return.

Using (6.5.3), the evolution of the state point on the invariant map is described by the two equations

$$\frac{d\Pi}{dt} = -\frac{\epsilon}{q^2}(2\alpha\Pi - 3\beta\text{III}) \quad (6.5.4)$$

$$\frac{d\text{III}}{dt} = -\frac{\epsilon}{q^2}(3\alpha\text{III} + \frac{2}{3}\beta\Pi^2) \quad (6.5.5)$$

so that the trajectory on the map is described by

$$\frac{d\Pi}{d\text{III}} = \frac{2\alpha\Pi - 3\beta\text{III}}{3\alpha\text{III} + \frac{2}{3}\beta\Pi^2}. \quad (6.5.6)$$

Therefore, if the underlying premise of the model is correct, the trajectories must be unique and the ratio  $\gamma(\Pi, \text{III}) = \alpha/\beta$  can be determined by the local trajectory.

There have not been many experiments on the return to isotropy. Those that do exist often show very strange behavior. Direct numerical simulations of Lee and Reynolds (1985) using the Rogallo code in a  $128^3$  mesh attempted to address these questions in the hope of evaluating the parameters. Turbulence that had been strained by axisymmetric contraction relaxed smoothly to isotropy along the axisymmetric line as expected. But turbulence that had been strained by axisymmetric expansion showed very strange behavior, in some cases moving further away from isotropy before starting the return. Turbulence strained by complex combinations that produced states near the middle of the anisotropy map did not show convincingly unique trajectories. A sample of the trajectories following removal of plane strain are shown in Fig. 6.5.1. The points to the left have been strained most rapidly, and the initial states are predicted very well by RDT. The lowermost points are in general agreement with the one experiment on the relaxation from plane strain by Tucker and A. Reynolds (1968). Note that one point begins its "return" by going substantially far in the wrong direction. It seems impossible to incorporate this wierd behavior within the structure of (6.5.2).

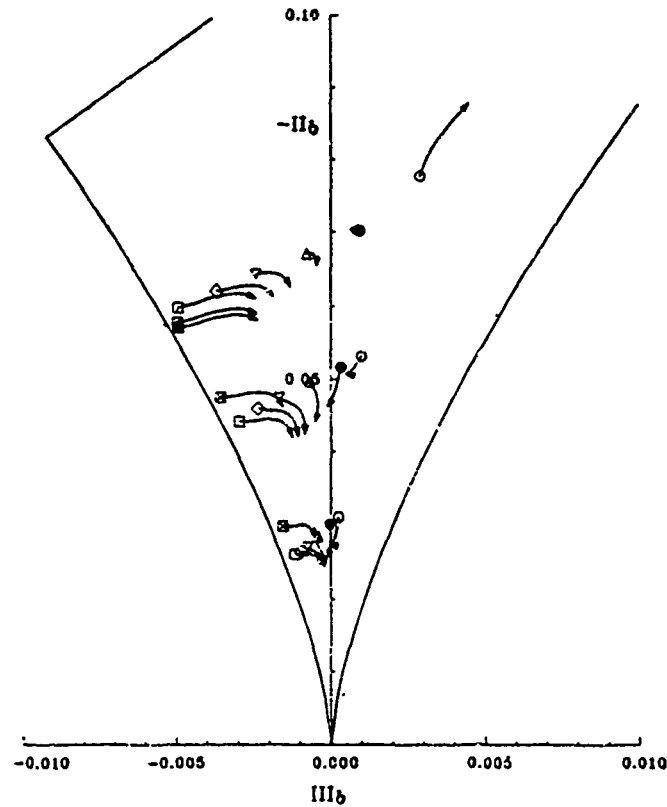


Figure 6.5.1 Trajectories of the return to isotropy from plane strain (simulations)

The simulations cast doubt on the basic idea of modeling these terms using only the  $b_{ij}$  tensor. But the simulations did show that the return of the small-scales to isotropy, as reflected by the anisotropy in the vorticity and dissipation tensors, was quite well behaved and easily modeled. This suggests some directions for future modeling research.

These simulations, as well as those of Rogallo for homogeneous shear flow, suggest very strongly that

$$\phi_{ij} \rightarrow 2b_{ij} \quad \text{as } |b| \rightarrow 0. \quad (6.5.7)$$

This means that there should be no linear return to isotropy. Careful examination of the very nearly isotropic data of Comte-Bellot and Corrsin (1966) seems to support this behavior.

Choi (1983) performed experiments on the return to isotropy from the right side of the invariant map, and did seem to observe more consistent behavior. A fit to his data developed by the Cornell group and reported by Shih and Lumley (1986) is

$$\alpha = 12.44(9G)^2(1 - 9G)^{3/4} \quad \beta \approx 0. \quad (6.5.8)$$

The  $G$  factors provide a sort of realizability, and there is no linear return to isotropy.

A criticism that might be raised about this model is that it does not allow two-dimensional turbulence to remain two-dimensional, relaxing to an axisymmetric state. It is possible to construct a model that does by using the realizability condition. When  $u'_\alpha = 0$  everywhere, then  $D_{\alpha\alpha} = 0$ ,  $T_{\alpha\alpha} = 0$ , and hence  $\epsilon_{\alpha\alpha} = 2b_{\alpha\alpha}$ , which will sustain  $b_{\alpha\alpha} = -1/3$ . Thus, the realizability condition gives

$$\alpha = 3\beta \left( \frac{1}{9} + \frac{2}{3}\Pi \right) \quad \text{when } G = 0. \quad (6.5.9)$$

Since this constraint only need be true for  $G = 0$ , we can add functions of  $G$  without destroying realizability. A linear term suffices, with its coefficient chosen to remove the linear return to isotropy when  $G = 1/9$  and  $\Pi = 0$  and to make  $\beta$  vanish for small anisotropy,

$$\alpha = \left( \frac{1}{3} + 2\Pi - 3G \right) \beta_0 \quad (6.5.10a)$$

$$\beta = \beta_0(1 - 9G). \quad (6.5.10b)$$

The model is then

$$\dot{v}_{ij} = -\frac{\epsilon}{q^2} \left[ \left( \frac{1}{3} + 2\Pi - 3G \right) \beta_0 b_{ij} + \beta_0(1 - 9G) \left( b_{ij}^2 + \frac{2}{3}\Pi \delta_{ij} \right) \right]. \quad (6.5.11)$$

With this model, for nearly isotropic turbulence (6.5.4) becomes

$$\alpha \approx -\beta_0 \Pi \quad (6.5.12)$$

while for small anisotropy (6.5.8) gives

$$\alpha \approx 12.44(-9\Pi)^{3/4}. \quad (6.5.13)$$

Matching at  $-\Pi = 0.05$  suggests  $\beta_0 \approx 10$ . This modified model satisfies realizability, restores axisymmetry in two-dimensional turbulence, displays no linear return to isotropy, and gives return rates of the right order of magnitude.

However, one might suspect that the slightest little three-dimensionality would explode the turbulence into a three-dimensional field, so perhaps it is unreasonable to insist on maintaining two-dimensionality in the model. Undecided issues like this provide fruitful grounds for new research, and we are now exploring questions like these using direct turbulence simulation.

### 6.6 A simple anisotropy model

The gap between the eddy-viscosity models used in the simplest  $k-\epsilon$  models and those discussed above is immense. There is a need for a much simpler model that would protect engineering calculations from the dangers of unrealizable turbulence, provide some indications of the trends in anisotropy for unusual flow situations, and handle dynamic changes on roughly the right time scale, but without such calculational complexity. The beginnings of such an idea are presented here.

We start with the idea that a large positive strain rate in one direction tends to stretch vortex filaments in that direction, aligning them with the flow, thereby intensifying the perpendicular fluctuation components and reducing those along the axis. In the limit of very strong strain rate, the energy in the axial fluctuations axial will approach zero. The anisotropy model must prevent negative values. And, we know that only the anisotropic component of strain produces anisotropy in the turbulence. A simple algebraic model with this character is

$$b_{ij} = \frac{-S_{ij}^* \tau}{A_0 + A_S S^* \tau}. \quad (6.6.1)$$

In order for realizability to be maintained,  $b_{\alpha\alpha}$  should approach  $-1/3$  as  $S_{\alpha\alpha}^* \rightarrow \infty$ , for any combinations of other  $S_{ij}^*$ . This requires that the coefficient  $A_S$  depend on the type of strain.

In the principal coordinates of  $S_{ij}^*$ , we take  $S_{11}^*$  as having a large positive value  $\Gamma$ , and write the strain-rate tensor as

$$S_{ij}^* = \Gamma \begin{pmatrix} 1 & 0 & 0 \\ 0 & -\frac{1+a}{2} & 0 \\ 0 & 0 & -\frac{1-a}{2} \end{pmatrix}. \quad (6.6.2)$$

Note that  $a = 0$  gives axisymmetric contraction,  $a = 1$  gives plane strain, and  $a = 3$  gives axisymmetric expansion. Then

$$S^* = \Gamma \sqrt{1 + \frac{(1+a)^2}{4} + \frac{(1-a)^2}{4}} = \Gamma \sqrt{\frac{3+a^2}{2}} \quad (6.6.3)$$

For large positive  $\Gamma$  our model must yield

$$b_{11} \rightarrow -\frac{1}{3} = -\frac{\Gamma \tau}{A_S S^* \tau} \quad (6.6.4)$$

and this requires that

$$A_S = \sqrt{\frac{18}{3+a^2}}. \quad (6.6.5)$$

We need a way to represent  $a$  for an arbitrary orientation of the coordinates. The structure of  $S_{ij}^*$  is characterized by

$$W = \frac{S_{ij}^* S_{jk}^* S_{ki}^*}{(S^*)^3} \quad (6.6.6)$$

which for (6.6.2) is

$$W = \frac{3(1-a^2)/4}{[(3+a^2)/2]^{3/2}}. \quad (6.6.7)$$

$W$  ranges from  $-1/\sqrt{6}$  for axisymmetric expansion to  $1/\sqrt{6}$  for axisymmetric contraction. Plane strain and shear flow correspond to  $W = 0$ . Using (6.6.5) to express  $a$  in terms of  $A_S$ , and then in turn expressing  $W$  in terms of  $A_S$ , we find

$$W = \frac{A_S^3}{9} - \frac{A_S}{2} \quad (6.6.8)$$

This allows us to determine  $A_S$  from a known  $W$ . The relationship between them is shown in Fig. 6.6.1.



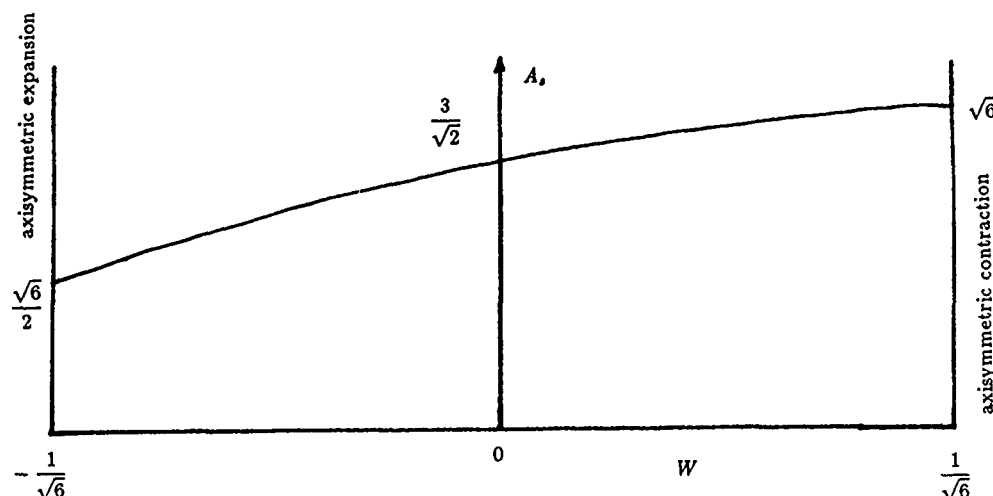


Figure 6.6.1 Variation of the model parameter with strain type

The constant  $A_0$  should be chosen to produce the proper level of shear stress in shear flow, for that is the most important engineering flow. Shear flow can be represented as a combination of rotation and irrotational strain. Denoting  $U_{1,2} = \Gamma$ ,

$$S_{ij} = \begin{pmatrix} 0 & \frac{\Gamma}{2} & 0 \\ \frac{\Gamma}{2} & 0 & 0 \\ 0 & 0 & 0 \end{pmatrix} \quad \Omega_{ij} = \begin{pmatrix} 0 & \frac{\Gamma}{2} & 0 \\ -\frac{\Gamma}{2} & 0 & 0 \\ 0 & 0 & 0 \end{pmatrix}. \quad (6.6.9a, b)$$

Hence, for shear flow  $W = 0$ ,  $A_s = 3/\sqrt{2}$ , and  $S = \Gamma/\sqrt{2}$ . With these values,  $A_0 = 23$  produces  $b_{12} = -0.15$  at  $\Gamma\tau = 12.7$ , corresponding to the homogeneous shear flow experiments of Tavoularis and Corrsin.

We now have an anisotropy model that is always realizable for all types of strain, and has the right general trend of  $b_{ij}$  with  $S_{ij}$ , but assumes that a state of structural equilibrium has been attained. In order to handle transients, we propose an evolution equation for  $b_{ij}$  that would give (6.6.1) as its equilibrium solution,

$$\dot{b}_{ij} = -C_1 [(A_0 + A_s S^* \tau) b_{ij} + S_{ij}^* \tau] / \tau \quad (6.6.10)$$

By choosing  $C_1 = 4/15$ , the model will agree with the initial phase of rapid distortion of isotropic turbulence, and the rate of return to isotropy is of the right general magnitude for linear approximations. Note that the model correctly predicts no change in the anisotropy of isotropic turbulence under pure rotation.

For many engineering problems the main objective of the turbulence model is to reveal important trends. This simple anisotropy model would make the important stresses change in the right general way, without becoming unrealizable, and therefore it should be an attractive alternative for use in simple two-equation turbulence models. Preliminary studies by students in the author's turbulence class support this conjecture.

## 7. NUMERICAL SIMULATIONS OF TURBULENCE

### 7.1 Introduction

Over the past decade, two important types of numerical simulations have become important. The earlier work concentrated on *large eddy simulations* (LES), in which simple models are used for the small-scale turbulence and a realization of the large-scale turbulence is computed. The underlying idea is that the structure of large eddies differ greatly from flow to flow (which is why universal models are elusive), whereas the small eddies are more universal and therefore easier to model. Large eddy simulations have provided important information for turbulence modeling, and there is now great interest in the development of large eddy simulations as a tool for engineering analysis. A prominent program in this direction exists in France at the EDF.

It was argued that, since the ratio of the largest to the smallest scales of turbulence varies as  $R_T^{3/4}$  (see 3.2.4), it would never be practical to do a significant simulation of all the important turbulent scales. However, valid *direct simulations* of turbulent flows at  $R_T$  of the order of 100-300 have become possible. This is the range of *turbulence* Reynolds numbers in turbulent shear flows with Reynolds numbers, based on the layer thickness and the driving mean velocity difference, of about 1000, and a number of direct simulations of channel flows and boundary layer flows at these low Reynolds numbers have now been attained. These direct simulations provide an important new tool for studying turbulence, particularly because they yield essentially any data that one might desire. Already they have contributed important new insight into turbulent structure and have aided advances in turbulence modeling, as well as new understanding of transition physics.

In this chapter we will review the fundamentals and current status of this very fast-moving area of research, drawing primarily from the experience of the large group working in this area at the NASA/Ames Research Center and Stanford University. At present this group involves about ten NASA scientists, three Stanford Professors, a dozen or so graduate students, and some post-doctoral scholars and other visitors, with the work being coordinated by the joint NASA/Stanford Center for Turbulence Research. Some of the exciting new things going on in this group will be outlined, with details being left for the authors to report for themselves.

### 7.2 Fundamentals of large eddy simulation

In LES one needs a way to define the large-scale components of the fields. and filtering is usually used. The *filtered field*  $\bar{f}$  is defined by

$$\bar{f}(\mathbf{x}, t) = \int G(\mathbf{x}, \mathbf{x}'; \Delta) f(\mathbf{x}', t) d^3 \mathbf{x}'. \quad (7.2.1)$$

Here  $G$  is a filter function, which determines exactly what fraction of the motion is defined as being large scale, and  $\Delta$  is a filter parameter that implements this choice. The filter function must be normalized such that

$$\int G(\mathbf{x}, \mathbf{x}'; \Delta) d^3 \mathbf{x}' = 1 \quad (7.2.2)$$

for all  $\mathbf{x}$ . The *residual field*  $f'$  is then what is left over after filtering,

$$f(\mathbf{x}, t) = \bar{f}(\mathbf{x}, t) + f'(\mathbf{x}, t). \quad (7.2.3)$$

The filtered residual field is *not* zero since

$$\bar{f'} \neq \bar{f} \quad \bar{f'} \neq 0. \quad (7.2.4)$$

Filtering (7.2.3),

$$\bar{f} = \bar{\bar{f}} + \bar{f'} \quad (7.2.5a)$$

so the filtered residual field can be expressed in terms of the singly and doubly-filtered resolved fields,

$$\bar{f'} = \bar{\bar{f}} - \bar{f}. \quad (7.2.5b)$$

This proves very useful in modeling the residual turbulence.

In homogeneous turbulence the filter must be of the form  $G(\mathbf{x} - \mathbf{x}'; \Delta)$ . Then

$$\bar{f}(\mathbf{x}, t) = \int G(\mathbf{x} - \mathbf{x}'; \Delta) f(\mathbf{x}', t) d^3 \mathbf{x}'$$

has the Fourier transform

$$\hat{\bar{f}}(\mathbf{k}, t) = \hat{G}(\mathbf{k}; \Delta) \hat{f}(\mathbf{k}, t) \quad (7.2.6)$$

where the  $k$  argument of  $G$  is the magnitude of the  $\mathbf{k}$  vector. Several filters have been explored. The sharp cut-off filter

$$\hat{G} = \begin{cases} C & \text{if } |k_i - k'_i| \leq k_c \\ 0 & \text{otherwise} \end{cases} \quad (7.2.7)$$

make a clean separation of large and small scales in spectral space, but the Gibbs phenomena in the inverse Fourier transform make the physical-space interpretation undesirable. Smoother behavior can be obtained with the Gaussian filter,

$$G(\mathbf{x} - \mathbf{x}'; \Delta) = A e^{-\frac{1}{2}(\mathbf{x} - \mathbf{x}') \cdot (\mathbf{x} - \mathbf{x}') / \Delta^2} \quad (7.2.8)$$

where  $A$  is a constant determined by the normalization and depends on the number of directions in which the filter is applied. The Fourier transform of the Gaussian filter is also Gaussian,

$$\hat{G}(\mathbf{k}; \Delta) = B e^{-k^2 \Delta^2 / 24}. \quad (7.2.9)$$

Filtering is more of a problem for inhomogeneous flows. The most satisfying approach is to use an appropriate set of expansion functions in the inhomogeneous directions and then to define the filtered value as the  $n$ -term approximation. However, most work has instead used finite-difference methods in the inhomogeneous directions with the Gaussian filter in the homogeneous directions, and taken whatever implicit filtering is provided by the difference scheme. This is not very satisfying because it leaves the computed field ill defined, and does not provide a systematic way for estimation of the energy content in the residual field. This is one of the unsatisfying loose ends in LES that needs to be cleaned up by some good research.

The evolution equations for the filtered field are derived by filtering the Navier-Stokes equations, so it is important that the filtering definition commute with differentiations with respect to both time and space. The Gaussian filter has this property, and so homogeneous turbulence really can be done properly with LES using the Gaussian filter. If  $\rho = \rho(t)$  then the filtered continuity equation is

$$\dot{\rho} + \rho \bar{u}_i = 0. \quad (7.2.10)$$

Subtracting this from the full equation,

$$u'_{i,n} = 0 \quad (7.2.11)$$

so the residual field is divergence-free, and if  $\rho = \text{constant}$  the filtered field is divergence-free. Filtering the momentum equations, assuming  $\mu$  is constant and again allowing  $\rho = \rho(t)$ , the equation for the filtered velocity field is

$$\bar{u}_i + (\bar{u}_i \bar{u}_j)_{,j} = -\frac{1}{\rho} \bar{p}_{,i} + \nu \bar{u}_{i,jj}. \quad (7.2.12)$$

Representing the velocity as the sum of filtered and residual components,

$$\bar{u}_i \bar{u}_j = \bar{\bar{u}_i \bar{u}_j} + R_{ij}, \quad (7.2.13)$$

where the residual stress terms are

$$R_{ij} = \bar{u}_i u'_j + u'_i \bar{u}_j + u'_i u'_j. \quad (7.2.14)$$

In LES one needs to model  $R_{ij}$ . Given this model, and a suitable computer, and a few little details like boundary and initial conditions, single realizations of turbulence fields can be generated. In homogeneous turbulence this appears to be sufficient, because volume averages over a single realization seem to provide good representations for ensemble averages.

The term  $\overline{u_i u_j}$  does not need to be modeled because it can be computed directly by filtering the product of the filtered velocities. This is easily done in Fourier space, and we handle this term this way now. Our earlier representation of this in terms of  $\overline{u_i u_j} + L_{ij}$ , where  $L_{ij}$  was the Leonard stress, is now abandoned.

It may be noted that we have not made any mention of numerical methods and have avoided use of the term *sub-grid scale turbulence*. We believe that it is important to cast the LES equations in a way that is independent of the numerical method, and would lend itself to purely theoretical analysis. However, in reality the filter width that is taken is related to the computational grid employed. The results depend upon the ratio of filter width to mesh width, and the best results are obtained when the filter width is twice the mesh width.

### 7.3 Modeling the residual stresses in large eddy simulation

One can not afford a very complex model for the residual stresses in LES. Almost all of the work to date has been done with simple algebraic models, although there have been some explorations with simple one-equation turbulence models.

It is useful to separate  $R_{ij}$  into isotropic and anisotropic parts, as is done with viscous stresses,

$$R_{ij} = \frac{1}{3} R_{kk} \delta_{ij} + T_{ij}. \quad (7.3.1)$$

The isotropic term is absorbed with the filtered pressure by writing

$$P^* = \frac{1}{\rho} \bar{p} + \frac{1}{3} R_{kk} \quad (7.3.2)$$

and then  $P^*$  replaces  $\bar{p}/\rho$  and  $T_{ij}$  replaces  $R_{ij}$  in (7.2.12).

An important element of most LES calculations is the *Smagorinsky* model, which assumes that the residual  $T_{ij}$  is a linear function of the anisotropic strain rate imposed by the filtered field

$$T_{ij} = -2\nu_T \bar{S}_{ij} \quad (7.3.3)$$

where  $\nu_T$  is an eddy viscosity of the residual field. If it is assumed that the length scale of the dominant residual eddies is the filter width, and that the time scale is that set by the strain rate of the filtered field, then

$$\nu_T = (C_S \Delta)^2 \sqrt{\bar{S}_{mn} \bar{S}_{mn}}. \quad (7.3.4)$$

The coefficient in this model can in principle be evaluated by performing direct numerical simulations on a fine mesh (say  $128^3$ ), then filtering this data to a coarse mesh (say  $8^3$ ) to define the filtered and residual fields, and then comparing the model with the residual field from the coarse filtering. Clark et. al. (1979) were the first to employ this technique, which is now known as a *Clark test*. For isotropic turbulence the results are moderately encouraging, and do not show much dependence on Reynolds number, a value of about 0.12 being typical. However, when this test is applied in strained and sheared flows, essentially no correlation is found between the model and the data. The model simply is inadequate under these more interesting circumstances.

An important advance in residual stress modeling was made by Bardina (1985), who first proposed to model

$$R_{ij} = C_B (\overline{u_i u_j} - \overline{u_i} \overline{u_j}). \quad (7.3.5)$$

The basic idea was to characterize the stresses of the residual scales as being similar to that of the smallest resolvable motions, so Bardina called this the *scale similarity model*. By itself it was not adequate either, because it does not dissipate sufficient energy. But it does provide energy transfer from high to low wavenumbers, and effect that is missing in the Smagorinsky model. When used in combination with the Smagorinsky model (the *Bardina mixed model*) remarkably good results are obtained in the Clark tests, with the same values of the constant yielding correlations between predicted and actual stresses of the order of 70% for shear flow, irrotational strain, and unstrained flow!

The value of the constant  $C_B$  can actually be deduced from a simple theoretical argument. If one transform to new coordinates moving linearly with respect to the original ones,

$$x_i^* = x_i - c_i t \quad t^* = t \quad u_i^* = u_i + c_i \quad (7.3.6a, b)$$

the equations of motion of course do not change because they are invariant under such (Galilean) transformations. However, individual terms in the equations do change when transformed. For the filtering operation,

$$\overline{u_i^*} = \overline{u_i} + c_i \quad u_i^{*'} = u_i' \quad (7.3.7a, b, c)$$

so that  $R_{ij}$  transforms to

$$R_{ij} = \overline{u_i^* u_j^{*'}} + \overline{u_i^{*'} u_j^*} + \overline{u_i^{*'} u_j^{*'}} + c_i \overline{u_j^{*'}} + c_j \overline{u_i^{*'}} = R_{ij}^* + c_i \overline{u_j'} + c_j \overline{u_i'}. \quad (7.3.8)$$

The terms modeling  $R_{ij}$  should transform in the same way; the Smagorinsky model is invariant under the transformation, and hence can not possibly represent all of  $R_{ij}$ . The added terms of the Bardina model (7.3.5) transform to

$$R_{ij} = C_B [\overline{u_i^* u_j^*} - \overline{u_i^*} \overline{u_j^*} + c_i (\overline{u_j^*} - \overline{u_j^*}) + c_j (\overline{u_i^*} - \overline{u_i^*})]. \quad (7.3.9)$$

Using (7.2.3) and (7.3.7b), this becomes

$$R_{ij} = R_{ij}^* + C_B (c_i \overline{u_j'} + c_j \overline{u_i'}). \quad (7.3.10)$$

Comparing (7.3.8) and (7.3.10), it is evident that  $C_B = 1$ . Bardina was unaware of this result at the time he did his numerical work, on the basis of which he recommended a value of 1.05!

In recent work yet to be published, Piomelli has been reexamining LES residual modeling using the recent direct simulation of channel flow as the basis for Clark tests, also carrying out LES simulations with various models. This work has shed some new light on LES modeling, which can be summarized as follows. In coarse mesh calculations (say  $16^3$ ) no real difference is observed between using just the Smagorinsky model and the Bardina mixed model, and the results in general reflect the coarseness of the grid. However, at  $64^3$  calculations there are important differences. The calculations are filtering has been in planes parallel to the wall only, because as yet we do not really have any good way to do explicit filtering in directions of inhomogeneity. Piomelli finds that the choice of filter function is important in determining the performance of the residual turbulence model. The filter makes its appearance in the calculations when the term  $\overline{u_i u_j}$  is calculated by filtering the product of the computed filtered components. If the Gaussian filter is used with the Bardina mixed model, *very good* results are obtained. If the Gaussian filter is used with the Smagorinsky model, *very poor* results are obtained. But if the Smagorinsky model is used with the sharp cut-off filter, *fair* results are obtained.

The inference from this work is that the sharp cut-off filter defines a clear length scale for the residual turbulence, whereas the Gaussian filter spreads the residual scales out over a broader range. The Bardina model accounts for the different scales in the residual field generated by the Gaussian filter. On the other hand, only one length scale is carried by the Smagorinsky model, and therefore this model can not account for all the scales filtered by the Gaussian filter.

One might argue that the turbulence time scale in the Smagorinsky viscosity should be a scale appropriate to the residual field. In isotropic turbulence the strain rate of the resolved field sets this scale, but in inhomogeneous flows with strong mean strain rate it may be better to extract the time scale from the high wavenumber end of the resolved field, as in the Bardina model. One possible approach is to use the velocity scale in this range,

$$\nu_T = C \Delta \sqrt{(\overline{u_k} - \overline{\overline{u_k}})(\overline{u_k} - \overline{\overline{u_k}})}. \quad (7.3.11)$$

Another approach would be to use the strain rate,

$$\nu_T = C_1 \Delta^2 \sqrt{(\overline{S_{mn}} - \overline{\overline{S_{mn}}})(\overline{S_{im}} - \overline{\overline{S_{im}}})}. \quad (7.3.12)$$

In LES one probably does not want to attempt to resolve the wall region of boundary layers, and so some appropriate wall conditions are needed. For high Reynolds numbers, it is through this condition that the viscosity will enter the problem. The main thrust of Piomelli's work has been to assess various proposals for these conditions. At this writing about all we can say is that nothing that we or anyone else has suggested shows up very well in Clark tests against the direct simulations of channel flow. However, we are hopeful that a satisfactory working model for the residual wall stress will be found, and this probably will draw upon new knowledge about the structure of the wall region that is currently being extracted from the direct simulations.

#### 7.4 Insights from direct simulations of homogeneous turbulence

Boundary conditions are a problem in turbulence simulations. The problem is avoided in homogeneous turbulence by use of *periodic* boundary conditions. The resulting turbulence is somewhat artificial in that the motion on opposite sides of the computational domain is fully correlated, which of course would not be the case in a real turbulence field. One must select a computational domain large enough that the statistical correlations at separations of *half* the computational domain are small, and when this is done the statistical results up to this separation seem to be quite like those of real turbulence.

A large number of homogeneous turbulence simulations have been carried out by the Ames/Stanford group, almost all using the Rogallo code. This program uses the coordinate transformation (4.2.4), and as a result achieves remarkable robustness in runs with very strong deformation. For a recent description of the code see Lee and Reynolds (1985). Simulations now include homogeneous shear flow at a variety of shear rates, many cases including scalar transport, a variety of irrotational strain flows, return to isotropy following various strains, some rotation cases. Special codes have handled a funny type of homogeneous compressible shear flow and some flow compression cases. Meshes ranging from  $64^3$  to  $256^3$  have been used, although the  $128^3$  cases are now the most abundant.

In a direct simulation one must capture both the energy at large scales and the dissipation at small scales, and this limits the calculations to relatively low Reynolds numbers. One can usually tell when not enough small-scales have been captured by a pile-up of energy at the high wavenumber end of the spectrum. The model spectrum (3.9.4) can be used to estimate the fraction of energy left out of a calculation at any given  $R_T$ . Typical  $128^3$  calculations miss less than 1% of the turbulence energy at  $R_T = 50$ , a typical range for these simulations.

The initial turbulence field must be constructed in a divergence-free manner, and this is easily done with the Fourier representation. The spectrum can be shaped initially and scaled to contain the proper energy for a target  $R_T$ . For details see Lee and Reynolds (1985).

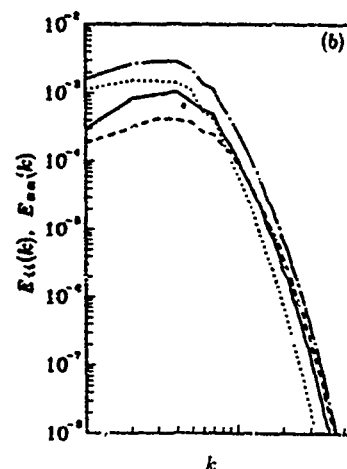


Figure 7.4.1 Spectra for relaxation from plane strain

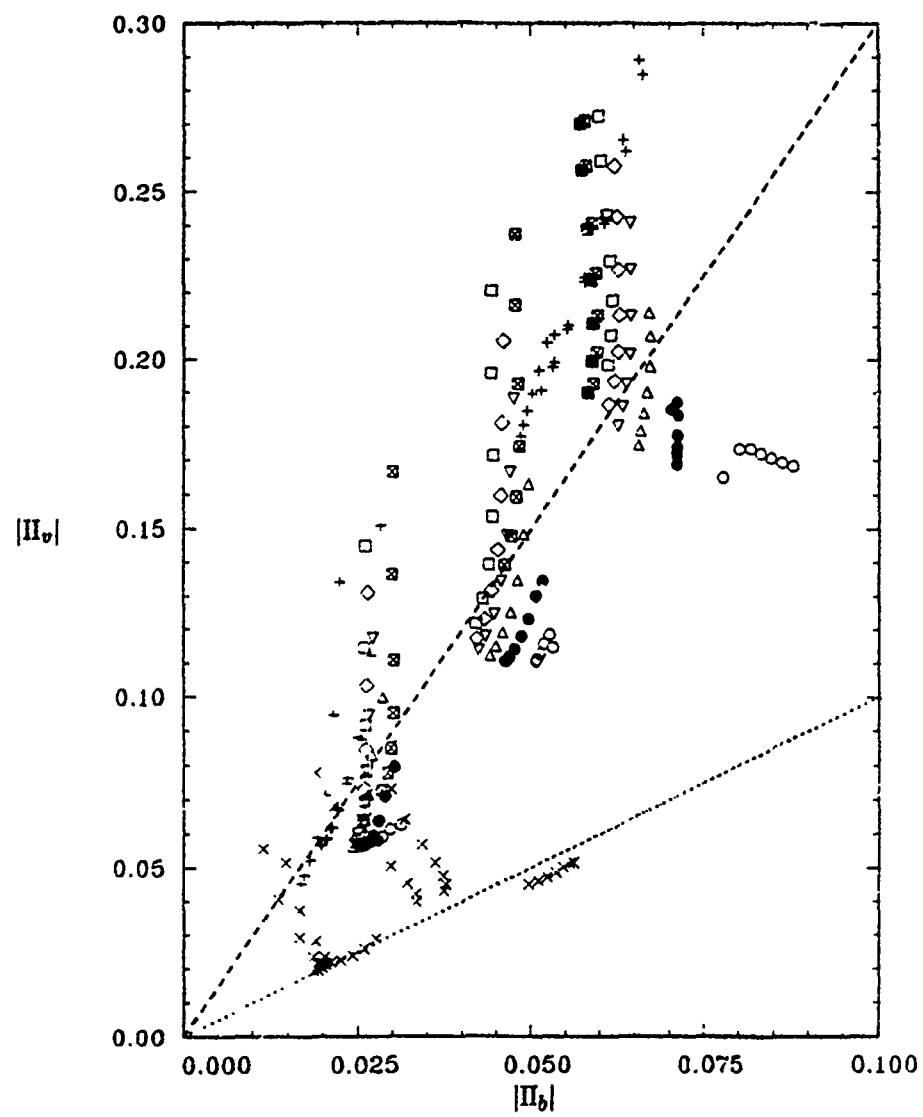


Figure 7.4.2 Anisotropies during relaxation from various strains

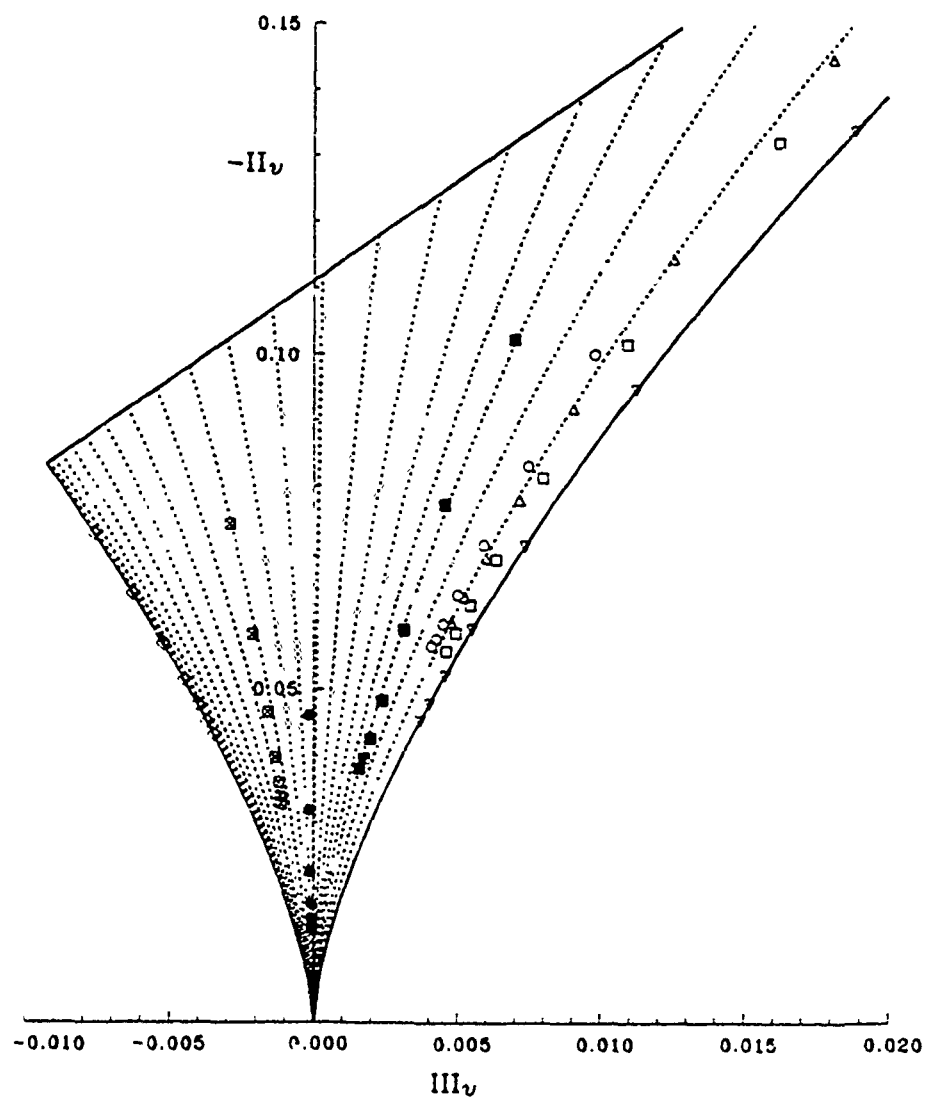


Figure 7.4.3 Vorticity relaxation trajectories



All of these calculations show a remarkable amount of small-scale anisotropy. For example, Fig. 7.4.1 shows one of Lee's spectra during relaxation from plane strain, with the different lines representing different components. Note that the anisotropy persists throughout the  $-5/2$  range of the spectrum. We investigated this issue of small scale anisotropy by extending the measures of anisotropy discussed in Chapter 6 to the vorticity and dissipation fields. The vorticity tensor is defined as

$$V_{ij} = \overline{\omega_i \omega_j} \quad (7.4.1)$$

and the vorticity anisotropy tensor is

$$v_{ij} = \frac{V_{ij} - \omega^2 \delta_{ij}/3}{\omega^2} \quad (7.4.2)$$

The dissipation anisotropy tensor is defined by

$$d_{ij} = \frac{D_{ij} - D_{kk}^2 \delta_{ij}/3}{D_{kk}} \quad (7.4.3)$$

These two anisotropy tensors are characterized by their second and third invariants, defined the same way as those for the Reynolds stress anisotropy tensor  $b_{ij}$  (see 6.1.3). Their anisotropy invariant maps are the same form as those for  $b_{ij}$  explained in section 6.1. The boundary lines are the same for the  $b_{ij}$  and  $d_{ij}$  invariant maps, but on the vorticity invariant map the two axisymmetric side boundaries are reversed, and the uppermost point corresponding to *one-dimensional vorticity* corresponds to the *two-dimensional velocity* field.

Fig. (7.4.2) shows the second invariants of vorticity and velocity during relaxation to isotropy from a variety of different strain types. The trajectories on this diagram are generally down and then to the left. Upon the removal of mean strain rate, the vorticity anisotropy relaxes quickly to a point, and then relaxes slowly, *locked on* to the anisotropy of the Reynolds stress! Moreover, essentially all of the points showed *more* anisotropy of the vorticity than of the Reynolds stress! These are astonishing observations to anyone who has grown up with the idea that the small scales become isotropic quickly, compared to the slow relaxation of the scale anisotropy.

It is also very interesting that the relationship between the two invariants in the lock-on phase returning from axisymmetric expansion is quite different than that when returning from axisymmetric contraction. This suggests that there may be two types of competing structures in turbulence, the noodles formed by axisymmetric contraction and the pancakes formed by axisymmetric expansion, and that perhaps better turbulence models could be made by treating these structures separately.

We have mentioned that the trajectories for return to isotropy on the Reynolds stress invariant map are not well behaved, which casts doubt on the viability of modeling the slow pressure strain and dissipation anisotropy terms in terms of  $b_{ij}$ . However, those on the vorticity map are extremely well behaved. Figure (7.4.3) shows these trajectories, which are well fit by the simple model

$$\dot{v}_{ij} = -\alpha \frac{q^2}{\epsilon} v_{ij} \quad (7.4.4)$$

where  $\alpha$  depends on both the invariants of  $b_{ij}$  and  $v_{ij}$ . The dissipation anisotropy trajectories are quite different, but they too are very well behaved and can be modeled quite neatly. For details see Lee and Reynolds (1985).

Upon reflection, the requirement that the vorticity field be anisotropic is obvious from the Biot-Savart law; if the vorticity spectrum were isotropic, the Reynolds stress spectrum would be isotropic. It may be that explicit consideration of this anisotropy in turbulence modeling could have some advantages. We have been exploring some possibilities.

In another recent study, Rogers (1986) has examined the structure of homogeneous turbulent shear flow. His studies reveal that hairpin vortices of the type found in wall boundary layers are also found in homogeneous turbulence. However, in homogeneous turbulence there are both "up" and "down" hairpins, while in a boundary layer one sees only one kind. He also found evidence of some transverse vortices believed to be associated with the weak orientation of vorticity caused by mean rotation (see section 4.6).

Lee has extended Rogers work to (high) shear rates and Reynolds numbers comparable with the viscous region of turbulent boundary layers. Remarkably, he finds long longitudinal *streaks* that familiar objects in the wall region, with transverse spacings that scale on the turbulent stress and viscosity in exactly the same way as in wall boundary layers. This work suggests that it is the high shear rate, and not the wall, that produces the streaks! This would be good news for modelers, because it would mean that models based on homogeneous turbulence might have far more to do with boundary layer flows than one might think.

Rogers also studied scalar transport in homogeneous shear flow at three different Prandtl numbers. There are three interesting situations corresponding to an (imposed) mean scalar gradient in each direction. He calculated the scalar fields for all three cases at the same time for a set of common hydrodynamic simulations. A surprising result, actually seen in experiments by Tavoularis and Corrsin, is that some cross-gradient scalar fluxes are larger than the flux in the direction of the mean gradient!

Rogers used his insight about the hairpin vortex structures and the transverse vortices to explain the mechanism by which these cross-gradient transports can develop. He then went on to model the scalar flux in two ways, using his simulation data both as a guide in the modeling and as the basis for coefficient evaluation. The models deal with an anisotropic diffusion tensor  $D_{ij}$ , defined by

$$n_i = \overline{u_i \theta'} = -D_{ij} \Theta_{,j} \quad (7.4.5)$$

where  $\theta'$  is the scalar fluctuation and  $\Theta_{,j}$  is a mean scalar gradient. The diffusivity tensor could be calculated from his measurements, and is found to be inherently non-symmetric. However, he did find that it became antisymmetric in a coordinate system that is aligned with the principal axes of the Reynolds stress. This led him to model the diffusion tensor in the form

$$D_{ij} = C_1 \delta_{ij} + C_2 R_{ij} + C_3 \Omega_{ij} \quad (7.4.6a, b)$$

He was able to correlate his coefficients with Reynolds and Prandtl numbers to within about 20%.

Rogers made another model assuming that the scalar flux is aligned with the sum of the mean gradient terms in its own transport equation, and thereby obtained a model of comparable accuracy with only one free coefficient. This model is

$$\frac{1}{\tau} C_D h_i + h_j U_{i,j} + R_{ij} \Theta_{,j} = 0 \quad C_D = 16.1 \left( 1 + \frac{1.17}{Pr} \right)^{0.152} \left( 1 + \frac{131}{\sqrt{R_T}} \right)^{-0.535} \quad (7.4.7a, b)$$

where  $\tau = q^2/\epsilon$  and  $R_T = q^4/(\nu\epsilon)$ . This result should be of immediate use in turbulence modeling for both homogeneous and inhomogeneous flows. Rogers has recently checked this model against direct simulations of turbulent channel flow at  $Pr = 1$  and found that it is remarkably accurate for the flux in the direction of the mean temperature gradient and within about 20% for the flux perpendicular to the mean temperature gradient.

### 7.5 Direct simulations of spatially-developing flows

Some of the most exciting work at present are the boundary layer simulations of Spalart. He is using a clever stretching of the coordinate system that enables him to use periodic inflow-outflow conditions in a growing boundary layer, and has already produced results about the structure of boundary layers in pressure gradients of much interest to experimentalists.

In order to simulate more general turbulent flows, inflow and outflow conditions are needed. The outflow problem is simpler and we have had a reasonable solution for some time. The inflow problem is harder, but we have recently made some excellent progress.

Lowery (1986) simulated the spatially-developing mixing layer, including scalar transport. He found that a soft convective outflow condition,

$$\frac{\partial}{\partial t} + U_c \frac{\partial}{\partial x} = 0 \quad (7.5.1)$$

applied to the velocity components and scalar worked quite well, with minimum upstream influence. The convection velocity  $U_c$  was taken as the average of the two free stream speeds. At the inlet he forced the flow with a combination of fundamental and two subharmonics of a dominant instability of the inlet layer

(tanh profile). because the layer was forced, it responded like a forced layer, with parings occurring cyclicly at frozen locations. And, the layer grows not linearly, as do natural layers, but by leaps and bounds, as do forced mixing layers in the laboratory.

It has been asked if the mixing layer is *absolutely* unstable, in which case if the forcing is stopped after large disturbances have developed downstream the layer should continue to remain. When Lowery terminated forcing, the initial region of the layer relaminarised, suggesting that the instability was *convective*, but midway down the flow the turbulence never went away, and by the exit the flow was quite turbulent. His calculation did not include the splitter plate, which undoubtedly plays a role in promoting absolute instability, so the matter is not really resolved. Lowery also studied the growth of three-dimensional disturbances in the layer, finding that they grew to scales and structures characteristic of the braid region of the mixing layer.

Ongoing extensions of our mixing layer simulation work by Sandham involve the use of random jitter of the forcing to simulate more natural turbulent inflow condition. This produces the linear growth seen in natural experimental layers, at growth rates in excellent agreement with experimnts. The resulting statistical quantities, including the scalar pdf, are much more like those measured for natural layers. It now seems that this will be quite an acceptable method for generating relatively simple yet effective inflow conditons for direct numerical simulations of turbulence.

Current work is concentrating on extensions to compressible mixing layers, the goal being to use these direct simulations as the basis for building better turbulence models for supersonic flows, including combustion, both for use in LES and in simpler turbulence models. There is a growing group at Ames, involving Rogers, Moser and others, beginning to work very seriously on turbulent combustion simulations. It seems safe to forecast that a decade from now the capabilities for know much more about the modeling and simulation of these and flows of technical interest will be considerably advanced, and students who have mastered these notes should be ready to begin the exciting work ahead in this area.

## REFERENCES

- Bardina, J., Ferziger, J.H., and Rogallo, R.S. 1985 Effect of rotation on isotropic turbulence; computation and modelling, *J. Fluid Mechanics*, **154**, p 321.
- Cambon, C. and Jeandel, D. 1981 Approach of non-isotropic turbulence submitted to mean velocity gradients, *Proc. Third Symposium on Turbulent Shear Flows*, Davis, California, p 17.7.
- Choi, K-S 1983 A study of the return to isotropy of homogeneous turbulence, Ph.D. Thesis, Cornell University, Ithaca, New York
- Clark, R.A., Ferziger, J.H. and Reynolds, W.C. 1979 Evaluation of subgrid-scale models using an accurately simulated turbulent flow, *J. Fluid Mech.* **91**, p 1.
- Comte-Bellot, G. and Corrsin, S. 1966 The use of a contraction to improve the isotropy of grid generated turbulence, *J. Fluid Mech* **25**, p81.
- Gence, J.N. and Mathieu, J. 1980 The return to isotropy of turbulence having been submitted to two successive plane strains, *J. Fluid Mech.* **101**, p555.
- Lee, M.J., Piomelli, U., and Reynolds, W.C. 1986 Useful formulas in the rapid distortion theory of homogeneous turbulence, *Phys. Fluids* **29**, p3471.
- Lee, M.J. and Reynolds, W.C. 1985 Numerical experiments on the structure of homogeneous turbulence, Report TF-24, Department of Mechanical Engineering, Stanford University.
- Le Penven, L. and Gence, J.N. 1983 Une méthode de construction systématique de la relation de fermeture liant la partie linéaire de la corrélation pression-déformation au tenseur de Reynolds dans une turbulence homogène soumise à une déformation uniforme, *C.R. Acad. Sc., Paris t. 297, Serie II*, p 309.
- Lowery, F.S. and Reynolds, W.C. 1986 Numerical simulation of a spatially-developing, forced, plane mixing layer, Report TF-26, Department of Mechanical Engineering, Stanford University.
- Reynolds, W.C. 1976 Computations of turbulent flows, *Ann. Rev. Fluid Mech.* **8**, p183.
- Reynolds, W.C. 1983 Physical concepts, analytical foundations, and new directions in turbulence modeling and simulation; in *Turbulence Models and Their Applications*, Publication 56, Editions Eyrolles, Paris, France.
- Reynolds, W.C., and Perkins, H.C. 1977, *Engineering Thermodynamics*, Second Edition, McGraw Hill Book Company, New York.
- Rogers, M.M., Moin, P., and Reynolds, W.C. 1986 The structure and modeling of the hydrodynamic and passive scalar fields in homogeneous turbulent shear flow, Report TF-25, Department of Mechanical Engineering, Stanford University.
- Savill, A.M. 1987 Recent Developments in Rapid Distortion Theory, *Ann. Rev. Fluid Mechanics*, **19**, p531.
- Shih, T-H and Lumley 1985 Modeling of pressure correlation terms in Reynolds stress and scalar flux equations, Report FDA-85-3, Fluid Dynamics and Aerodynamics Program, Cornell University, Ithaca, New York
- Tavoularis, S. and Corrsin, S. 1981 Experiments in nearly homogeneous turbulence with a uniform mean temperature gradient. *J. Fluid Mech.*, **104**, p311 and p349.
- Tucker, H.J. and Reynolds, A.J. 1968 The distortion of turbulence by irrotational plane strain, *J. Fluid Mechanics*, **32**, p657.
- Wiegand, R.A. and Nagib, H.M. 1978 Grid generated turbulence with and without rotation about the streamwise direction, IIT Fluid and Heat Transfer Report R78-1, Illinois Inst. of Technology, Chicago, Ill.
- Wilcox, D.C. 1986 Multiscale model for turbulent flows, AIAA paper 86-0029; see also User's guide to program EDDYBL, DCW Industries.

TURBULENCE MODELLING THROUGH ONE POINT CLOSURES  
- APPLICATIONS - ENLIGHTENING BY LARGE EDDY SIMULATION

D. LAURENCE  
EDF - DER - Laboratoire National d'Hydraulique  
6 Quai Watier, 78400 CHATOU FRANCE

SUMMARY

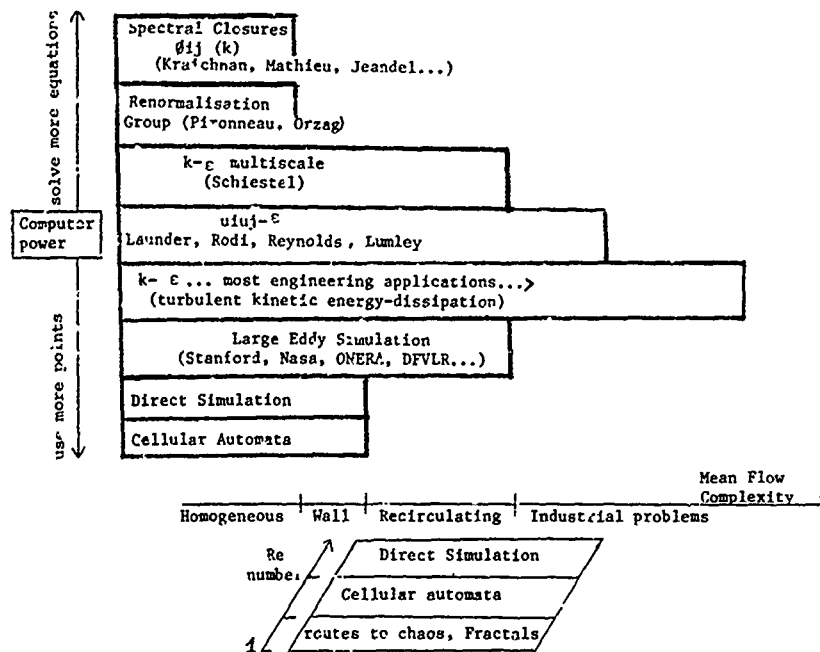
Reynolds stress,  $k-\epsilon$ , and Low Re models for the modelling of inhomogeneous flows are considered. They are shown to provide satisfactory predictions for engineering flows. Near wall and buoyancy effects are also included. Results of Large Eddy Simulations are used as guidance to the standard one point closures, especially for data which cannot be obtained by experiment.

INTRODUCTION

The problem of computing turbulent flows arises from the non-linear term of the Navier-Stokes equations and the simple fact that "the average of a product is not equal to the product of the averaged operands". Hence the Reynolds stresses appearing in the Reynolds averaged Navier Stokes equations :  $R_{ij} = \overline{u'iu'j}$ . The Reynolds Stress transport equations (RST) are also non-linear and contain third order correlations, the evolution of which depend on still extra unknowns etc...

So the system of equations for the statistics of a turbulent flow is infinite. Also if the spacial structure of turbulence is to be studied, 2 point correlations, or equivalently, spectra must be considered. The computational power at our disposal being finite, one has to choose at what level modelling assumptions must be introduced, i.e. this power is shared between the number of variables (turbulence statistics) and the number of points in physical space (inhomogeneity).

This situation can be illustrated by the sketch hereafter :



The top and bottom of this table are illustrated in this course by Dr. Aupoix and Pr. Reynolds while the central part, one point closures, is currently used in engineering problems which we will consider here. Valuable information stems from each type of approach to the problem and in addition to experience, enables improvement of all the other approaches, and in particular the one point closures.

For this reason, when involved in a particular type of turbulence modelling, one must also be aware of the work going on in all the other approaches.

We will consider here industrial applications for incompressible fluids. Many were conducted earlier and have been reported more thoroughly outside of LNH. To keep the reference list short, only mandatory publications are given (in which thorough lists can be found), namely : Mathieu, Jeandel [1] for spectral analysis ; Launder, Reynolds, Rodi [2] for second moment practice, physics, new simulations of turbulence, and applications ; Rodi [3] for engineering practice. Also recommended for an extended introduction : Lumley [4] , Arpacı, Lasen [5] for thermal problems . Favre, Kovasnay et al [6] also consider compressible flows.

### 1. ONE POINT CLOSURES

The oldest proposal is Boussinesq's Eddy Viscosity Model (1877) in which it is assumed that the Reynolds stresses are proportional to the gradients of mean velocity :

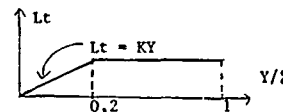
$$-\overline{u_i u_j} = \nu_T \left( \frac{\partial U_i}{\partial x_j} + \frac{\partial U_j}{\partial x_i} \right) - \frac{2}{3} k \delta_{ij} \quad (\text{EVM})$$

$$k = \frac{1}{2} (\overline{u_i u_i})$$

This model provides good predictions provided the velocity and length scales of the turbulence  $U_t$  and  $L_t$  are known, so that  $\nu_T$  can be prescribed :  $\nu_T \sim U_t L_t$ .

This is an easy task only for boundary layers where  $L_t$  (also called "mixing length") can be defined through a ramp function :

$K = 0.4$  (Von Karman constant)  
 $\delta$  = boundary layer thickness  
 $Y$  = distance to wall



Also assuming :  $U_t = L_t \left| \frac{\partial U}{\partial Y} \right|$

Prandtl's mixing length model is obtained :  $\nu_T = L_t^2 \left| \frac{\partial U}{\partial Y} \right|$

This is not a "modern approach" but performs well and more sophisticated models coincide to this one when applied to boundary layers.

Another field where the mixing length is still used is "Large Eddy Simulation" (LES), where the mixing length (size of largest sub-grid scale eddies) is taken proportional to the mesh resolution.

### 1.1. TRANSPORT EQUATIONS

The state of the Reynolds stresses is a consequence of the strains of the mean flow, but turbulence has strong memory effects. Turbulence can be considered as a set of eddies the angular momentum of which can only be changed progressively. Status of the Reynolds stresses thus depend not only on the local mean flow but also on the (Lagrangian) history of the strains which the turbulence has experienced. The rate at which the anisotropy and level of turbulence (statistics of eddy angular momentum) can be changed depends on the ratio of the mean strain,  $S$  ( $du/dy$ ), and the time scale of turbulence  $k/\epsilon$  ( $=$  energy / dissipation).

Hence in modern approaches where it is ambitionned to model complex inhomogeneous mean flows, introduction of transport equations for turbulent statistics, which will account for the Lagrangian history of the turbulence, is necessary.

The most popular of these models for engineering flows is the two equation  $k-\epsilon$  model. However beginners might be confused by the "variations of the constants" often introduced in this model. To see why this is legitimate, it is preferable to begin with the more complex Differential Second Moment Closure (DSM) in which less assumptions are made, and then reduce the DSM to the standard  $k-\epsilon$  model.

### 1.2 DIFFERENTIAL SECOND MOMENT CLOSURE DSM

Let  $U, P, \rho$  be the velocity, pressure and density of the mean flow;  $u, p, \rho'$  the fluctuations;  $\nu$  and  $g$  the molecular viscosity and gravity (density variations only being considered when associate with gravity). The exact equation for the Reynolds stresses can be written as :

$$\begin{aligned} \frac{\partial \overline{u_i u_j}}{\partial t} + \overline{u_k \frac{\partial u_i u_j}{\partial x_k}} &= - \left( \overline{u_i u_k} \frac{\partial U_j}{\partial x_k} + \overline{u_j u_k} \frac{\partial U_i}{\partial x_k} \right) \leftarrow P_{ij} \\ &+ \left( \overline{\frac{\partial^2 u_i}{\partial^2} \frac{\partial^2 u_j}{\partial^2}} + \overline{\frac{\partial^2 u_i}{\partial^2} \frac{\partial^2 u_j}{\partial^2}} \right) \leftarrow G_{ij} \\ &+ \overline{\rho' \left( \frac{\partial u_i}{\partial x_j} + \frac{\partial u_j}{\partial x_i} \right)} \leftarrow \theta_{ij} \\ &- \frac{\partial}{\partial x_k} \left( \overline{u_i u_j u_k} + \frac{\partial u_i}{\partial x_k} \frac{\partial u_j}{\partial x_k} + \frac{\partial u_j}{\partial x_k} \frac{\partial u_i}{\partial x_k} \right) \leftarrow d_{ij} \\ &- \nu \left( \frac{\partial^2 \overline{u_i u_j}}{\partial x_k^2} + \frac{\partial^2 \overline{u_i u_j}}{\partial x_i^2} + \frac{\partial^2 \overline{u_i u_j}}{\partial x_j^2} \right) \leftarrow \epsilon_{ij} \\ &- 2\nu \left( \frac{\partial^2 \overline{u_i}}{\partial x_k^2} \frac{\partial u_j}{\partial x_k} + \frac{\partial^2 \overline{u_j}}{\partial x_k^2} \frac{\partial u_i}{\partial x_k} \right) \leftarrow \end{aligned}$$

The transport by mean flow and production terms  $P_{ij}$  and  $G_{ij}$  are computed exactly.  $d_{ij}$  corresponds to dispersion of turbulence (vanishing for homogeneous turbulence) and  $\epsilon_{ij}$  is the dissipation (transformation of kinetic energy into heat) and is assumed to be isotropic as for fully developed turbulence :  $\epsilon_{ij} = \epsilon \delta_{ij}$

A lot of works have been devoted to the pressure-strain correlations which play an important part in modifying (reducing ?) the anisotropy of the Reynolds stresses. It is shown [2], [6] that  $\theta_{ij}$  can be decomposed into 3 parts

- $\theta_{ij,1}$  - the non linear part depends only on statistics of the fluctuating velocity
- $\theta_{ij,2}$  - the linear part also involves the strains of the mean field
- $\theta_{ij,3}$  - accounts for buoyancy effects.

These quantities are not accessible to measurements, the models have only been tested by their indirect effects. The main assumption is that of a "return to isotropy" and damping or production. Moreover, near wall effects are found to be strong.

This is a problem for which great help is expected from LES and DS and is presently being analysed ("Numerical data" on  $d_{ij}$  or  $c_{ij}$  require non-homogeneous simulations which are only just starting, and DS which are still restricted to very low Re numbers).

The model considered is that of Launder, Reece, Rodi [6] and is quite cumbersome but reduces to 4 equations in 2D flows ( $\overline{u^2}$ ,  $\overline{v^2}$ ,  $\overline{uv}$  and  $\epsilon$ ).

Although it has been proposed for over a decade, progress of computers have made it manageable for engineering computations only recently. It is widely used by the UMIST team (Launder at Al 7, 1986) and is presently developed at LNH. The full model can be written as :

$$\begin{aligned} \frac{D\overline{u_i u_j}}{Dt} &= \frac{\partial}{\partial x_k} \left( \nu + c_s \frac{\overline{u_k u_k}}{k} \frac{\partial \overline{u_i u_j}}{\partial x_k} \right) + P_{ij} + G_{ij} + \phi_{ij} - \frac{2}{3} \delta_{ij} \epsilon \\ &\quad \underbrace{\hspace{10em}}_{D_{ij}} \quad \left\{ \begin{array}{l} \phi_{ij} = \phi_{ij1} + \phi_{ij2} + \phi_{ij3} \\ \phi_{ij1} = -\frac{c_{ij1}}{k} \left( \overline{u_i u_j} - \frac{1}{3} \delta_{ij} \overline{u_k u_k} \right) \\ \phi_{ij2} = -c_{ij2} \left( P_{ij} - \frac{1}{3} \delta_{ij} P_{kk} \right) \quad \phi_{ij3} = -c_{ij3} \left( G_{ij} - \frac{1}{3} \delta_{ij} G_{kk} \right) \end{array} \right. \\ \frac{D\overline{u_i \theta}}{Dt} &= \frac{\partial}{\partial x_k} \left( c_{\theta} \frac{\overline{u_k u_k}}{k} \frac{\partial \overline{u_i \theta}}{\partial x_k} \right) + P_{i\theta_1} + P_{i\theta_2} + G_{i\theta} + \phi_{i\theta} \\ &\quad \underbrace{\hspace{10em}}_{D_{i\theta}} \quad \left\{ \begin{array}{l} \phi_{i\theta} = \phi_{i\theta_1} + \phi_{i\theta_2} + \phi_{i\theta_3} + \phi_{i\theta_4} \\ \phi_{i\theta_1} = -\frac{c_{i\theta_1}}{k} \overline{u_i \theta} \quad \phi_{i\theta_2} = -c_{i\theta_2} P_{i\theta} \quad \phi_{i\theta_3} = -c_{i\theta_3} G_{i\theta} \quad \phi_{i\theta_4} = -c_{i\theta_4} G_{i\theta} \end{array} \right. \\ P_{ij} &\equiv -\left\{ \overline{u_i u_k} \frac{\partial \overline{u_j}}{\partial x_k} + \overline{u_j u_k} \frac{\partial \overline{u_i}}{\partial x_k} \right\} ; \quad G_{ij} \equiv -\frac{\alpha}{\theta} \left\{ \overline{u_j \theta} s_i + \overline{u_i \theta} s_j \right\} \\ P_{i\theta_1} &\equiv -\overline{u_i u_k} \frac{\partial \theta}{\partial x_k} ; \quad P_{i\theta_2} \equiv -\overline{u_k u_k} \frac{\partial \overline{u_i \theta}}{\partial x_k} ; \quad G_{i\theta} \equiv -\frac{\alpha \overline{u_k u_k}}{\theta} s_i \end{aligned}$$

### 1.3 ALGEBRAIC SECOND MOMENT CLOSURE (ASM)

For a three dimensional non isothermal flow the DSM model requires that 15 coupled differential equations be solved. However if only the source and sink terms are considered, the model becomes algebraic. To preserve some generality for inhomogeneous flows, we can assume with RODI [8] proportionality of the differential part of  $\overline{u_i u_j}$  with that of  $k$  :

$$\frac{D\overline{u_i u_j}}{Dt} - \text{Diff}(\overline{u_i u_j}) = \frac{\overline{u_i u_j}}{k} \left[ \frac{Dk}{Dt} - \text{Diff}(k) \right]$$

This is illustrated by Viollet in a appendix A. Applications of the ASM to a stratified shear flow are shown to yield much better results than the standard  $k-\epsilon$  model especially in the unstable situation, where the latter model fails to predict the rapid generation of turbulence by buoyancy. It is only when this effect is more moderate (Froude = 5) that the eddy viscosity assumption yields acceptable predictions.

It is also shown that starting from this model, one can reduce it to the standard  $k-\epsilon$  model but with variable viscosity, diffusivity coefficients and Prandtl numbers,  $C_\mu$ ,  $C_\theta$  and  $\sigma_\theta$  as functions of Richardson number and  $(P+G)/\epsilon$ , ( $P = 1/2 P_{ii}$ ,  $G = 1/2 G_{ii}$ ).

For turbulence driven secondary motions, as in a square duct, the modelling must be at DSM or ASM level. They yield fairly good results as can be seen on Fig I.3.1, where Reece's [21], and Noat and Rodi's [22] computations are compared with measurements of Launder and Ying [23].

The situation is different for a meandering channel where the secondary motion is induced by inertia and pressure forces. In this case, good predictions have been found by reducing the ASM to a  $k-\epsilon$  EVM with variable  $C_\mu$  (Fig I.3.2 ; Demuren Rodi [24])



#### 1.4 THE STANDARD k-ε MODEL

To further reduce the computational effort, one can consider only the transport equations for  $k = \frac{1}{2} \overline{u_i u_i}$  and the dissipation  $\epsilon$ , which still enable to prescribe turbulence scales:

velocity:  $U_t \sim k^{1/2}$ , time:  $t \sim k/\epsilon$ , and length  $L_t \sim k^{1/2}/\epsilon$ . The eddy viscosity is thus written as:  $\nu_T \sim U_t L_t = C_\mu k^2/\epsilon$ .

The k equation, which contains no pressure-strain terms is modeled by:

$$\frac{\partial k}{\partial t} + U_j \frac{\partial k}{\partial x_j} = \frac{\partial}{\partial x_j} \left( \nu_T \frac{\partial k}{\partial x_j} \right) + P + G - \epsilon$$

The ε equation, in which most of the terms are totally unknown is modeled similarly:

$$\frac{\partial \epsilon}{\partial t} + U_j \frac{\partial \epsilon}{\partial x_j} = \frac{\partial}{\partial x_j} \left( \frac{\nu_T}{\sigma_\epsilon} \frac{\partial \epsilon}{\partial x_j} \right) + C_{\epsilon 1} \frac{\epsilon}{k} \left[ P + G \right] - C_{\epsilon 2} \frac{\epsilon^2}{k}$$

For grid turbulence, the equations reduce to

$$\frac{U \partial k}{\partial x} = -\epsilon \quad \text{and} \quad \frac{U \partial \epsilon}{\partial x} = -C_{\epsilon 2} \frac{\epsilon^2}{k}, \quad \text{yielding}$$

$$k \sim x^{-n}, \quad n = \frac{1}{C_{\epsilon 2} - 1}, \quad \text{and experiments give } n \simeq 1.2 \text{ so } C_{\epsilon 2} = 1.92$$

In the final stage of decay of k, n is higher, so  $C_{\epsilon 2}$  must be decreased for low Re flows.

When only shear is relevant in one direction, the production is

$$P = \overline{u v} \cdot \partial U / \partial Y = C_\mu k^2 / \epsilon \quad (\partial U / \partial Y)$$

$$\text{Hence } C_\mu = (\overline{u v} / k)^2 \cdot \epsilon / P$$

The standard value  $C_\mu = 0.09$  is taken after observations of the boundary layer where  $P \sim \epsilon$  and  $\overline{u v} / k = 0.3$ .

However, this formula shows that  $C_\mu$  can be varied in configurations where a better value of the structure parameter  $\overline{u v} / k$  is known (curvature, weak jets). Also  $C_\mu$  can be plotted as a decreasing function of  $P/\epsilon$  (round jet, far wake). See Rcd1 [2] and [3].

Again, for the log region of a boundary layer,  $C_{\epsilon 1}$  can be related to the other constants by:  $C_{\epsilon 1} = C_{\epsilon 2} - \frac{k^2}{\sigma_\epsilon \nu C_\mu}$

The standard, widely used values recommended by Launder and Spalding are

$$C_\mu = 0.09, \quad C_{\epsilon 1} = 1.44, \quad C_{\epsilon 2} = 1.92, \quad \sigma_\epsilon = 1.3$$

The boundary conditions are given by supposing that the first grid point is located in the log region and thus one writes

$$-\nu_T \frac{\partial U}{\partial Y} = \frac{1}{\epsilon} \tau = U_f^2$$

$$k = \frac{U_f^2}{\sqrt{C_\mu}}, \quad \epsilon = \frac{U_f^3}{K Y}$$

$\tau$  is the wall shear stress, and  $U_f$  the friction velocity.

### Applications

When testing the model on "academic" turb flows one can have the impression that the quality of the predictions is only fair, i.e. that constants adjusting is systematically required, (See table II, p.10).

From practice, it seems that for the more complex industrial applications, the standard model is quite satisfactory. This may be because the test cases measure the effect of turbulence solely (which is expected from a good test), whereas in "real life" problems, the main features of a flow result from a balance between turbulence, inertia and pressure forces, these two latter now being well represented by actual numerical schemes. Furthermore, complex geometrics provide strong guidelines for the mean flow, whereas test cases in unbounded space can give rise to large deviations far away from inlet conditions.

### Vehicule aerodynamics

The 3D code of LNH, ESTET, using the standard k- $\epsilon$  model has been applied to vehicle aerodynamics [20]. It is observed that the flow over most of the car can be predicted even with inviscid equations. The friction stresses are not really important for the computation of the flow in the front part, but the nature of the flow in the wake, especially behind blunt obstacles, requires a correct description of the turbulent stresses in the large structures of the wake shown on Fig I.4.1. The rate at which these stresses develop depends in turn on the characteristics of the turbulence in the detaching boundary layer. The correct structure of the wake enables a good comparison of the pressure coefficients with separate computations (Chometon [20]). The overall pressure drag is highly dependant on the values of  $C_p$  found at the back. The slight hump of  $C_p$  in the middle of the rear end is due to the jet formed between the recirculating eddies.

For a slanted back version the pressure gradient between top and bottom associated with lift induces a vertical component of the flow along the side, which in the wake generates a pair of longitudinal vortices ("wing tip vortices") (Fig I.4.2).

### 1.5 NEAR WALL LOW RE MODEL

In many problems, the interest lies in the wall region : heat transfer, wall shear stress, aerodynamics etc... It is now possible to use very fine mesh in this region so that the viscous sublayer can be described. In this case the log law hypothesis can be abandoned and exact boundary conditions can be prescribed :

$$U(\text{wall}) = 0, k(\text{wall}) = 0, T(\text{wall}) = T(\text{solid})$$

The low Re version of the k- $\epsilon$  model must then be used. To see what modifications are requested one can use the following development of the fluctuation, consequence of the continuity equation :

$$\begin{aligned} \text{div } \vec{u} &= 0 \quad \left\{ \begin{array}{l} u = b_1 Y + c_1 Y^2 \dots \\ v = 0 + c_2 Y^2 \dots \\ w = b_3 Y + c_3 Y^2 \dots \end{array} \right. \quad (Y : \text{wall distance}) \end{aligned}$$

Using the non dimensional variables scaled by the friction velocity  $U_f$  :

$$u^+ = u/U_f, Y^+ = Y U_f / \nu,$$

$$\text{We find :} \quad k^+ = A^+ Y^{+2} + B^+ Y^{+3} + \dots, \quad \epsilon^+ = 2A^+ + 4B^+ Y^+, \quad dU^+/dY^+ \sim 1$$

and since the production is  $P^+ \sim Y^{+3}$ , while  $(\nu \Delta k)^+ \sim 2A^+$ , the dissipation at the wall is balanced by the molecular diffusion of  $k$ , which of course must be included in the model. This also means that further away from the wall we must have  $P > \epsilon$ .

Also, since  $\overline{uv}^+ \sim Y^{+3}$  and  $\frac{k^{+2}}{\epsilon^2} \frac{dU^+}{dY^+} \sim Y^{+4}$

We must introduce a variation in the turbulent viscosity :

$\nu T = C_\mu f_\mu \frac{k^2}{\epsilon}$  with the function  $f_\mu = f(Y^+)$  at the wall, so that :  $f_\mu = \left( \frac{\overline{uv}}{k} \right)^{\frac{1}{2}} \frac{\epsilon}{P}$ , (see p.5).

Furthermore, the standard value of  $C_\epsilon/2$  is not suitable for the final stage of decaying turbulence, as mentioned earlier, and  $C_\epsilon/1$  is related to  $C_\epsilon/2$  and  $C_\mu$  so two additional functions  $f_1$  and  $f_2$  are introduced.

Various propositions have been made for  $f_\mu$ ,  $f_1$  and  $f_2$ , and a thorough review can be found in [8]. The models of Launder & Sharma and Lamb & Bremhorst have been tested for pipe flows (Fig I.5.1) and give similar results, although the latter is not applicable for decaying unbounded turbulence since it uses explicitly the wall distance  $Y$ . The results are well compared to experiment and confirms the preceding analysis.

This is a field where experiment can be completed by direct simulation from which pressure strain, turbulence diffusion and dissipation terms can be computed. This type of computation has been conducted by Kim and Moin [9] at NASA Ames and data is now being analysed which should soon greatly improve Low Re modelling (Kim, Moin, Mansour).

#### Near wall buoyant secondary motion

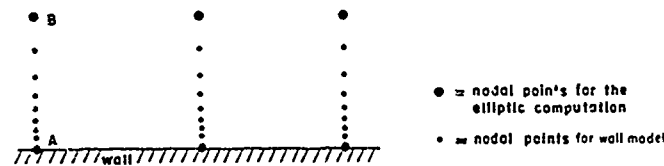
The same model is now applied to an "industrial" problem : in a steam generator, the cold feedwater (7°C) is brought by a horizontal cylinder immersed in hot recirculating water (275°C). The wall temperature inside the cylinder is expected to be ~ 200°C. Density will be reduced by 25% and the Prandtl number will vary by a factor 10. So a very fine mesh is necessary in the boundary layer where a secondary buoyancy motion is expected. A 3D elliptic computation is performed with the ESTET code. The  $k$  and mean velocity profiles are slightly changed and the secondary motion appears right at the entrance (fig I.5.2). The fall of the cold core of the flow is compensated by the buoyant upwards creeping motion of the sublayer and a recirculation at the top of the duct, replacing the cold core by more tepid water coming from downstream. The close up view shows high refinement and distortion of the mesh near the wall (the conjugate gradient method enables convergence although the matrix is very ill-conditioned).

A stratification develops, though not as strong as that actually observed. It is conjectured that the heat transfer is underpredicted since the model does not account for turbulence production increase with buoyancy for a horizontal temperature gradient. This will be analysed by LES in par. II.4.

### Parabolic sub-layer low Re model

The previous computation is very time consuming because of the large number of nodes for all of which advection and pressure are computed. However this is not necessary in the transition sub-layer ( $Y^+ \sim 1$  to 30) when buoyancy is not considered. One can assume that near the wall, advection is negligible and that the main feature is diffusion of momentum in the normal direction with a constant pressure gradient.

The numerical procedure is the following : an elliptic computation is performed on a coarse mesh ( $\Delta Y^+ \sim 50$ ). In the first wall cell a 1D, refined mesh is set between points A and B, on which the parabolic momentum and low Re  $k-\epsilon$  equations are solved.



Definition sketch for the wall treatment

- From the elliptic computation at step  $n$ , values of  $U(\tau)$ ,  $k(B)$ ,  $\epsilon(B)$  are taken as outer boundary conditions for the wall model ;
- From the wall model results, values of  $\partial k / \partial x_n(B)$ ,  $\partial u / \partial x_n(B)$ ,  $\partial \epsilon / \partial x_n(B)$  are taken as boundary conditions for the step  $(n+1)$  of the elliptic computation.
- Study of a simple example : the wall-driven turbulent flow in a rectangular cavity

As an example, the case of the wall-driven turbulent flow in a rectangular cavity is treated : in the experiments from Normandin, a moving belt at the left-hand side of the cavity entrains the fluid motion [26]. A computation with the SBIRE code using wall functions is compared to another one using the above described technique, with the same mesh for the elliptic computation. In the latter, the wall models use an expanding 10 points mesh. Figure I.5.3 shows the computed streamlines for the two computations, while table 1 shows how the higher wall stresses obtained using the local wall models enables better prediction both of the entrained flow rate and of the position of the center of the recirculation. Figure I.5.4 shows the comparison of velocity profiles at 2 locations from the experiment and from the two computations.

Table 1 : Comparison of bulk flow patterns for the wall-driven flow

	Recirculated flow rate	Position of center of recirculation	
		$x_o$ (cm)	$y_o$ (cm)
Experiment	50	23	8
Computation with wall functions	44.5	35.8	8
Computation with local low-Re wall treatment	48.6	32.7	8

#### -- Application to a LMFBR HOT PLENUM

The technique for wall modelling using local one-dimensional wall models, as described above, has been applied to the two-dimensional computation of the hot plenum of the RNR 150J project, at nominal steady-state. This steady-state is non isothermal due to :

- the outlet temperature differences between different parts of the core ;
- the heat transfer with the cold plenum (below).

Figure I.5.4 shows the computed velocity and temperature fields in the whole plenum, while figure I.5.6 shows at two points of the redan the results of the local wall models, in terms of velocity, turbulent kinetic energy and temperature. In this case, the local wall models lead directly to the steel temperature (assuming a given temperature and heat transfer coefficient on the cold plenum side of the redan), without any need of an assumption concerning the heat transfer coefficient in the hot plenum.

#### I.6 COMMENTS ON NUMERICS

##### DSM

The full Differential Stress Model, although proposed since over a decade has not been widely used until recently with both increasing computer capacity and improvement of numerical schemes. Nevertheless it is still a difficult task since with the replacement of the eddy viscosity by source terms in the momentum equation,  $\text{div } \overline{u_i u_j}$ , we lose numerical stability. Indeed, since the modeled turbulent stresses are no longer aligned with the mean strain rate tensor, in some situations this can result in a direct input of energy into the mean flow. The coupling with the mean flow is delicate and often initial data must be given by a standard  $k-\epsilon$  computation. Also, the coupling between components is sensitive and a careful decomposition between explicit and implicit terms is carried out to ensure stability. Indeed, during transients some schemes can lead to negative normal stresses  $\overline{u_i^2}$ .

##### Code maintainance

In order to assert reliability of the code for industrial applications and simultaneously allow modifications for improvement of the scheme or the turbulence models, an ensemble of test cases is maintained on which each version of the codes can be run at any time. The simplest one is the channel flow shown in appendix B. The head loss coefficient  $\lambda$  (Re) is of course correctly predicted, but only at the far end of the channel. This example is shown here to illustrate the strong influence of inlet condition :  $U$ ,  $k$  and  $\epsilon$  are given constant across the width and only after 200 mesh steps, the equilibrium values are found. In applications the values at inlet should be defined as accurately as possible.

For some test cases it is known that the  $k-\epsilon$  model fails to predict the measured values (the backward facing step for instance). On the other hand, it has hapened that discrepencies have been attributed to the model, and in the meantime, improvements of the sole numerics yielded better results. Computations are now compared in IAHR (International Association for Hydraulic Research) work-groups for a set of benchmarks. This defines a " $k-\epsilon$  consensus" solution used as reference for the codes.

The 2 and 3D Finite Element code N3S, developed at LNH now includes the  $k-\epsilon$  model and has passed the "backward facing step" test (Fig I.6). Including such a turbulence model in a FE code nearly doubles the CPU time requirement because the diffusion matrix must now be re-built at each step. Also, introducing the "log law" boundary condition in the diffusion-pressure coupling is not straightfoward ([ 25 ]).

TABLE II - Application examples of  $k - \epsilon$  model

$\Omega$	$k - \epsilon$ Prediction	Improved with
Grid Turbulence	Good	Low Re model for final stage
Channel flow	Good	
Plane Shear	Good	
Round jet	Spread overpredicted (30 %)	$C_\mu = f(P/\epsilon)$
Axisymmetric wake	Good in near field	$C_\mu = f(P/\epsilon)$ for far field ( $x/D > 30$ )
Wall jet	Spread overpredicted (20 %)	ASM, DSM
Adverse pressure gradient	Stress overpredicted	1 eq (mixing length)
Favorable pressure gradient	Good for moderate acceleration	Low Re model for stronger accelerations
Backward facing step	Length of separation bubble underpredicted	None significant
Sudden pipe expansion	Good for main recirculation, second bubble not reproduced	
Curvature/rotation	Fair	$C_\mu$ decreased or rotation in $\epsilon$ eq.
Turbulence driven secondary motion	None	ASM or DSM
Wall driven cavity	Recirculation rate underpredicted	Low Re model, ASM, DSM
Wall heat flux in non homogeneous situation	Badly underpredicted (stagnation point)	Boundary condition accounting for advected free stream turbulence

## II LARGE EDDY SIMULATION

### II.1 Introduction

In the Large Eddy Simulation (L.E.S.) approach the total instantaneous velocity  $\vec{V}(x,t)$  is decomposed in 3 parts :

$$\vec{V}(x,t) = \vec{V}(x) + \vec{\bar{v}}(x,t) + \vec{v}'(x,t)$$

$\vec{V}(x)$  is the mean flow component, while the fluctuating part is decomposed into a resolvable scale part  $\vec{\bar{v}}$  (i.e. : turbulent component of scale larger than the mesh resolution) and subgrid scale (SGS) part  $\vec{v}'$ .

It is assumed that the subgrid scale contribution to the Reynolds stresses,  $\overline{v'_i v'_j}$ , can be more easily modeled by a mixing length model (Smagorinsky) since small scale turbulence is expected to be more isotropic and geometry independent than the total Reynolds stresses.

However, in contrast to the previous closures there is no spectral gap between computed and modelled components. So the strong coupling might not reduce to a simple one-way energy transfer (dissipation of resolvable scale energy). Furthermore, the cross term  $\overline{v'v'} + \overline{v'v'}$  does not cancel if the filter  $\overline{\cdot}$  is not a sharp cut-off filter in Fourier space. It was found that adding the "scale similarity model" of Bardina, Ferziger, Reynolds [10] (B.F.R.), which models the scales just below cut-off using those just above ( $u^c = \overline{u} - \overline{\overline{u}}$ ), significantly improves the predictions; especially the shapes of the energy spectra near cut-off wave number.

For homogeneous flows the mean component is often not included in the computed variables and is accounted for by a source term in the  $\overline{v}$  equation. But this can not hold for more complex flows where  $v$  is also unknown. It has been noticed by several authors (Friedrich, Schumann, Laurence [11]) that the schemes themselves are not Galilean invariant. Better results are obtained by using translational computational frames where the modulus of  $v$  is made as small as possible. The problem addressed here is that of accurate numerical representation of small scale fluctuations undergoing simple transport by the mean flow (without non-linear interaction, and thus theoretically not inducing a CFL condition). This problem will be enhanced as the number of nodes is increased (ie ratio of larger to smaller resolved scales).

Speaking after Dr Reynold's Lecture I can assume this brief introduction will suffice. The previous remarks and numerical code are detailed in appendix C. Results are presented hereafter. The recent computations are from H. PHOUDLI who is preparing his thesis at LNH on LES applied to 1 point closures; this work will finish by the end of 1988.

## II.2 Grid Turbulence

The grid turbulence decay experiment of COMTE-BELLOT and CORRSIN [12] has been used as benchmark for the development of our LES code. The constants of the subgrid scale models were fitted to match experimental results at the second station. The energy spectra at the 3<sup>rd</sup> station is still very well reproduced. We use the implicit filtering of the numerical scheme instead of a Gaussian filter to retain as much information as possible. The high accuracy of the weak formulation (in the sense of the Finite Element approach) for advection enables conservation of energy right up to the maximum resolvable scale. The implicit filtering is thus very sharp. Results (fig II.2.1) are quite satisfactory since the discretisation is performed solely in physical space (the long term goal being LES of highly inhomogeneous flows). When possible, pseudospectral solvers are used to resolve the numerical set of discrete equations, which is done very rapidly using the "Fast Poisson solver" library of Schumann et al [13], extended to our 27 point discretisation of Laplacians and mass matrix.

Since the spectra are correct, the decrease of turbulence intensity is also well compared to experiment on fig II.2.2, where the filtered (computed) value is completed by an evaluation of the subgrid scale intensity using the defiltering procedure proposed by BFR [10].

## II.3 Homogeneous shear

The experiment of Champagne, Harris, Corrsin [14] has been simulated, in which the mean flow reduces to a constant shear:  $dV/dx_3 = S$ ,  $u = 0$ ,  $v_3 = 0$ , where  $S = 12.9 \text{ s}^{-1}$ .

The turbulence intensity shown on fig II.3.1 is well predicted especially when the BFR defiltering procedure is used. Note that both resolvable and SGS energies tend to be constant at the end of the computation, and so does the eddy viscosity,  $\nu_T$ .

Since  $\nu_T$  is constant with respect to time and it is also observed that statistics do not change if  $\nu_T$  is constant in space, one could ask what difference there is with a direct simulation (D.S.) where  $\nu = \nu_T$ . In the LES the high wave number end of the energy spectrum is expected to behave as  $k^{-5/3}$ , which is very different from the behaviour of the spectra in the Kolmogorov range. A direct simulation with  $\nu = \nu_T$  would require a much finer resolution, that is, much more computational power, even for a very moderate Reynolds number. Also, another difference lies in the use of the scale similarity model which cannot be expressed in terms of a viscosity. It actually enhances transfer of energy between computed scales with a zero net drain.

The evolutions of the Reynolds stresses obey the following equations :

$$\begin{aligned} D u_1^2 / Dt &= 2P + \phi_{11} - \epsilon_{11} \\ D u_2^2 / Dt &= \phi_{22} - \epsilon_{22} \\ D u_3^2 / Dt &= \phi_{33} - \epsilon_{33} \\ D u_1 u_3 / Dt &= -u_3^2 S + \phi_{13} - \epsilon_{13} \\ D k / Dt &= P - \epsilon \end{aligned}$$

With the notations of par. 1.2, and  $P = -1/2 \overline{u_1 u_3} S$ . Also, isotropy of the dissipation is commonly assumed :  $\epsilon_{ij} = 2/3 \epsilon \delta_{ij}$ .

This experiment is often referred to as "low shear" since  $S$  is small and the production time scale  $1/S$  is large before the turbulence time scale  $k/\epsilon$ . This means that the equilibrium state is not reached. Indeed in further experiments (Graham, Harris, Corrsin [15]) a higher shear,  $S = 44.5$ , enables to reach higher values of  $S.t$  where it is observed that  $k$  grows linearly and the anisotropy becomes constant.

From the previous equations we can expect that most of the anisotropy will be found in  $u_1^2$  and  $u_1 u_3$  which are directly influenced by the mean flow.

The Reynolds stress anisotropy,  $b_{ij}$ , is compared on Fig II.3.2 :

$$b_{ij} = (\overline{u_i u_j} - 2/3 k \delta_{ij}) / 2k, \quad k = \frac{1}{2} \overline{u_j u_j}$$

The crude LES value  $\langle b_{ij} \rangle$  slightly overpredicts the anisotropy. Very similar results were obtained previously by B.F.R. [10]. This is not surprising since it lacks the contribution of the SGS which are more isotropic. Assuming that they are totally isotropic ( $\overline{u_i u_j}^{SGS} = 2/3 k_{SGS} \delta_{ij}$ ) we can write :  $b_{ij} = \langle b_{ij} \rangle r$ , where  $r = k^{LES} / (k^{LES} + k^{SGS})$ ,  $r \approx 1/1.5$ .

This would reduce too much the anisotropy, which means that the SGS stresses still contain some anisotropy. Note that in the experiment, the initial turbulence seems to be quite anisotropic, hence the intersection of  $b_{22}$  and  $b_{33}$ .

If the anisotropy is to reach a steady state, the pressure strain correlations,  $\phi_{11}$  and  $\phi_{13}$  must be opposed to the production, while  $\phi_{22}$  and  $\phi_{33}$  should redistribute the energy (i.e., be positive) in order to sustain  $\overline{u_1^2}$  and  $\overline{u_3^2}$  despite dissipation. LES prediction for  $\phi_{ij}$  confirms this fact on fig II.3.3.

#### The L.R.R. model

The difference between  $\overline{u_1^2}$  and  $\overline{u_3^2}$  can only be imposed by the pressure-strains (if the dissipation is isotropic). The version of the Launder, Reece, Rodi [16] model presented in 1.2. is a simplified one since  $\phi_{ij,1} = -C_1 \mathcal{L}_{ij}$ .  $\mathcal{L}_{ij}$  can only reduce the anisotropy and  $\phi_{ij,2}$  are equal for the (22) and (33) components. Thus this version makes no distinction between  $\overline{u_1^2}$  and  $\overline{u_3^2}$ .



The initial model presented by L.R.R. [16] was :

$$\phi_{ij2} = -a \{ P_{ij} - 2/3 P \delta_{ij} \} - b \cdot k \cdot \left\{ \frac{\partial U_i}{\partial x_j} + \frac{\partial U_j}{\partial x_i} \right\} - c \cdot \{ D_{ij} - 2/3 P \delta_{ij} \}$$

$$\text{Where } P_{ij} = - \left\{ \overline{u_i u_k} \frac{\partial U_j}{\partial x_k} + \overline{u_j u_k} \frac{\partial U_i}{\partial x_k} \right\}, \quad D_{ij} = - \left\{ \overline{u_i u_k} \frac{\partial U_k}{\partial x_j} + \overline{u_j u_k} \frac{\partial U_k}{\partial x_i} \right\}$$

$$\text{and : } a = (C_2 + 8)/11, \quad b = (30C_2 - 2)/55, \quad c = (8C_2 - 2)/11$$

The only constant  $C_2$  enters by a rather complex manner because the previous equation has been derived from tensorial properties. For this same reason we will not change the expression but only try to fit the constant  $C_2$ . The presence of term  $D_{ij}$  will now distinguish  $\overline{u^2_2}$  and  $\overline{u^2_3}$ .

Considering the present shear flow and assuming steady state for anisotropy,

$$D_{bij}/Dt = 0 \text{ yields :}$$

$$b_{11} = (4/3 P + \phi_{11}) / (P - c)$$

$$b_{22} = (-2/3 P + \phi_{22}) / (P - c)$$

$$b_{33} = (-2/3 P + \phi_{33}) / (P - c)$$

Now replacing  $\phi_{ii}$  by the complete LRR model, we get :

$$b_{11} = (8 + 12 C_2)/33 \cdot P^+, \quad P^+ = P/(P - c + C_1 c)$$

$$b_{22} = (18 C_2 - 10)/33 \cdot P^+$$

$$b_{33} = (2 - 30 C_2)/33 \cdot P^+$$

In L.R.R. [16], the CHC experiment is used to fit  $C_2 \approx 0.4$  after choosing  $C_1 = 1.5$ , but we can fix  $C_2$  independantly of  $C_1$  by considering the ratio  $b_{ii}/b_{jj}$  (this also enables to use LES predictions directly since the previous defiltering factor  $\tau$  vanishes).

Figure II.3.4. shows  $b_{ii}/b_{jj}$  as functions of  $C_2$ . Since we expect  $b_{33} < b_{22}$ , and  $b_{11}$  to be most anisotropic, the possible range for  $C_2$  is  $0.25 < C_2 < 0.55$ .

Thus defining  $C_2$  independantly from  $C_1$ , the CHC low shear experiment with  $b_{22}/b_{11} = -0.4$  and  $b_{33}/b_{11} = -0.6$ , at  $St = 3.5$  would yield  $C_2 = 0.3$ , (and consequently  $C_1 = 1.18$ ), whereas the LES with  $b_{22}/b_{11} = -0.8$  and  $b_{33}/b_{11} = -0.2$ , for  $St = 5$ , gives  $C_2 = 0.411$  (and  $C_1 = 1.306$ ).

If we use the high shear experiment of CHC [15] at  $St = 11$  (published after the LRR paper) we reach very nearly the same conclusions as from the LES. Again we presume that the LES reaches the asymptotic state for  $b_{22}$  and  $b_{33}$  faster than the experiment exhibiting a crossing of  $b_{22}$  and  $b_{33}$  due to anisotropic initial conditions.

Fortunately LRR did not use this procedure with the CHC experiment and the proposed values  $C_1 = 1.5$  and  $C_2 = 0.4$  are close to the present conclusions. Now, if we inject the LES Reynolds stresses into the LRR model for  $\phi_{ij}$  we get the results shown on Fig II.3.5 where  $\phi_{22}$  and  $\phi_{33}$  tend to reduce the difference between  $b_{22}$  and  $b_{33}$ .

To achieve reconciliation, we must abandon the hypothesis of isotropic dissipation. Indeed, the dissipation exhibited by the LES (to be precise : the production term of the SGS Reynolds stresses) is by far not isotropic. The deviator of  $\epsilon_{ij}$  is shown on fig II.3.5. The similarity with  $b_{ij}$  is striking and means that  $\phi_{ij}$  reduces anisotropy (more energy is drained from the stronger components of  $\overline{u_i u_j}$ ). Since  $\epsilon_{33} < \epsilon_{22}$ , the difference between  $\phi_{33}$  and  $\phi_{22}$  must be large to create the anisotropy, and to sustain it, must not vanish in the steady state.

These observations on  $\epsilon_{22}$ ,  $\epsilon_{33}$ ,  $\phi_{22}$ ,  $\phi_{33}$  are in accordance with the BFR [10] simulation (PP 132 - 133, and noticing that the 2 and 3 subscripts must be swapped since  $S = dU_1/dx_2$ ). They furthermore propose improvements of classical models, in particular to account for rotation effects. Of course the LES must overpredict the anisotropy of the dissipation, but direct simulations also show strong influence of dissipation anisotropy, (Moon Joo Lee and Reynolds [17], PP 125 - 126).

To sum-up, since the LRR model performs quite satisfactorily for a variety of test cases, only slight changes should be carefully introduced. But we may consider that the  $\phi_{ij}$  term of the model represents not only the pressure strain term but also dissipation anisotropy. ie :

$$\phi_{ij} \text{ model} = P \left( \overline{\partial u_i / \partial x_j} + \overline{\partial u_j / \partial x_i} \right) - \left( \epsilon_{ij} - 2/3 \epsilon \delta_{ij} \right)$$

as more LES or DS data is made available for a much larger number of nodes in order to simulate very large band width of the spectra, we may expect to model the terms separately

#### II.4 Temperature fluctuations

As illustrated in part I, EDF is concerned by temperature fluctuations in fluid flows. This, in relation with heat discharges, heat transfers or thermal stresses in pipes and vessels induced by stratified flows. LES can help to model these flows since data on temperature fluctuations and their correlation with velocity or pressure is scarce.

##### Passive scalar in grid turbulence

The experiment of Sirkvist and Warhaft [18] is simulated to test the thermal version of the code. It consists of a decaying grid turbulence on which a constant average temperature gradient is superimposed :  $dT/dx_3 = S_T = 3.68 \text{ } ^\circ\text{C/m}$ . This low value enables to neglect buoyancy effects.

The velocity variances shown on fig II.4.1 thus behave as in par II.2. In the experiment, various setups are used to impose  $S_T$ , none of which generate zero initial temperature variances (as done in the LES), therefore only the final stages can be compared hereafter.

The thermal fluxes are shown on fig II.4.2  $\overline{uT}$  and  $\overline{vT}$  should be zero, but  $X/M = 700$  is a long way downstream of the grid (M grid cell size), meaning that only very large structures are left in turbulent field, thus the sample on which statistics are computed is too small, i.e. the number of nodes should be increased.

The previous variables are normalised to give the correlations on fig II.4.3. Initially  $\overline{wT}$  is equal to -1 since the temperature fluctuations are solely produced by the  $w$  fluctuations.

$\overline{wT}$  tends to - .75 while the experiment exhibits a slightly lower value. On fig II.4.4. the velocity-temperature time-scale ratio is satisfactorily compared as well as the  $\overline{T^2}$  dissipation (fig II.4.5). Fig II.4.6 shows that an asymptotic state is reached for the Production-dissipation ratio of  $\overline{T^2}$ , meaning it grows linearly (as  $k$  in the homogeneous shear case).

### Stable - unstable stratification

Now the same computation is re-run considering buoyancy effects in both the stable and unstable case. The velocity variances are shown on fig II.4.7 : in the stable case  $\overline{w^2}$  decreases faster than in the previous computation as well as the other two diagonal components (via pressure-strain) but the anisotropy seems to level at a moderate value, whereas in the unstable case,  $\overline{w^2}$  becomes 10 times larger than  $\overline{u^2}$  and  $\overline{v^2}$ . The thermal flux  $\overline{wT}$  associated with production, after reaching a maximum goes back to zero in the stable case, while it seems to be unlimited in the unstable case.

In the standard k- $\epsilon$  model, the buoyancy production term  $G = -1/2 \overline{wT} S_T$  is directly entered in the k equation while it is multiplied by  $C_{11}(\epsilon/k)(1 - C_{33})$  in the  $\epsilon$  equation (Viollet[19]).  $C_3 = 0$  in the unstable case,  $C_3 = 1$  in the stable case, (see p.5).

Indeed, on fig II.4.8, it is seen that the G, with  $1 - C_3 = 1$  balances the other terms in the equation for the unstable case except in the initial state, while in the stable case all the terms seem to go to zero so the ratio is very scattered. In the unstable case, the buoyancy production term in the  $\epsilon$  equation should have the same weight as in the k equation.

### "Vertical stratification"

In industrial problems, we often have to deal with cases where the temperature gradient is perpendicular (horizontal) to the gravity. This appears in vertical buoyant jets or vertical heated (or cooled) walls (see par. I.5).

In this case, buoyancy production is not usually accounted for in the standard k- $\epsilon$  model whereas the equations show indirect production.

Of course, this effect cannot be separated from shear in experiments because as soon as a horizontal temperature gradient and buoyancy are considered, natural convection and shear in the mean flow appear.

In the LES, however, we can "switch off" gravity in the mean flow while keeping it in the fluctuation. The mean velocity then stays zero while the fluctuations obey the following equations.

$$\begin{aligned} d \overline{u_1^2}/dt &= \emptyset 11 - \epsilon 11 \\ d \overline{u_3^2}/dt &= 2 B \overline{u_3 T} g + \emptyset 33 - \epsilon 33, (B : \text{thermal expansion parameter}) \\ d \overline{u_1 T}/dt &= - \overline{u_1^2} S_T + \emptyset 1T - \epsilon 1T, (S_T = dT/dx1) \\ d \overline{u_3 T}/dt &= - \overline{u_1 u_3} S_T + B T^2 g + \emptyset 3T - \epsilon 3T \\ d \overline{u_1 u_3}/dt &= B \overline{u_1 T} g + \emptyset 13 - \epsilon 13 \end{aligned}$$

Starting from an isotropic state, we will find, with  $S_T > 0$  :

$$\overline{u_1 T} < 0 \Rightarrow \overline{u_1 u_3} < 0 \Rightarrow \overline{u_3 T} > 0 \Rightarrow \overline{u_3^2} \text{ increases.}$$

This qualitative evolution is well reproduced by the LES results shown on fig II.3.6. Note that  $\overline{u_1 T}$  responds immediately due to the production  $\overline{u_1^2} S_T$ .  $\overline{u_3 T}$  and  $\overline{u_3^2}$  respond more slowly since  $\overline{u_1 u_3} T^2$  and  $\overline{u_3 T}$  are initially zero. At a later stage  $\overline{u_2^2}$  and  $\overline{u_1^2}$  follow  $\overline{u_3^2}$  meaning that  $\emptyset 22$  and  $\emptyset 33$  have again strong effects.

Pressure-strain and pressure-temperature correlations will be analysed and compared to models as the case is rerun with a finer resolution.

These are only preliminary results and the runs were performed as feasibility studies since, as mentioned, it is felt that  $32^3$  point computations provide a too small sample especially for long runs during which the turbulence scales undergo large changes. Also, boundary conditions must be carefully reconsidered since the problem is not exactly homogeneous.

Now being satisfied with the SGS model and numerical scheme, we have just ended speeding up the code and are starting  $64^3$  computations, from which more thorough analysis will be conducted. Note that changing from  $32^3$  to  $64^3$  means 8 times more nodes, and if the mesh step is divided by 2, so should be the time step, meaning the overall computational work is multiplied by 16 !

#### CONCLUSION

Computer power and numerical schemes are rapidly improving, allowing the use of more elaborate turbulence models and simulations. As full 3D flows are considered, DSM or ASM will have to replace the EVM since it is often the Reynolds stresses that drive the secondary motions (which in turn modify the principal motion). Near wall low Re modelling will be very useful for aerodynamics and heat transfer computations, and merge the elliptic and boundary layer approaches. We can conjecture that within a few years a consensus will be reached concerning numerical problems and that efforts in fluid mechanics will be devoted to the eternal problem of turbulence modelling. This tendency is illustrated by recent conferences in which authors now say little about numerics and go directly to the physical analysis of their results.

There seems to have been a gap between LES or DS computers, which have been more interested in the physics and analysis of turbulence in terms of structures, and the more engineering area where people have been hoping for enlightenment from LES and DS for one point closure models (as pointed out by Rodi [11]).

It must be remarked that this gap is being bridged but will require time since it means a lot of work for the small teams (solitons ?) performing LES or DS. Indeed it requires :

- elaborate numerics (accuracy and speed)
- processing of huge amounts of data
- analysis of experimental data (+ guessing the uncertain "initial conditions")
- analysis and use of proposed models
- comparison of numerical data, experience and models

This last item requires more work to defilter the LES results (and improve the SGS model). This might be solved by completing the spectra below cut off wave number as proposed by Aupoix [20] or Bertoglio [27], or using a 1 eq model in conjunction with algebraic stress modelling.

"Numerical data" could be used more rapidly if more credit could be given to it from other people than the computer himself, and if it could be widely used in conjunction with experiment by all turbulence modelers. For this, publications are not sufficient and it might be time for LES computers to open "binary data banks".

Finally, we hope that larger computations will tell whether anisotropy of dissipation is due to too low resolution or if it is part of the turbulence characteristics, even at high Re numbers.

# REFERENCES

- [1] J. MATHIEU, D. JEANDEL : "Turbulence models and their application" Collection de la Direction des Etudes et Recherches - EDF - Eyrolles, Paris, 1984 Vol 1
- [2] B.E. LAUNDER, W.C. REYNOLDS, W. RODI : "Turbulence models and their application" Vol 2 DER-EDF, Eyrolles, Paris, 1984
- [3] W. RODI : "Turbulence models and their application in hydraulics". State of the art paper. IAHR. Delft Netherlands (1984)
- [4] H. TENNEKES, J. LUMLEY "A first course in turbulence" MIT Press
- [5] ARFACI, LARCEN "Convection Heat Transfer" Prentice-Hall 1984
- [6] FAVRE, KOVASNAY, DUMAS, GAVOGLIO, COANTIC. "La turbulence en mécanique des fluides". GAUTHIER-VILLARS, PARIS (1976)
- [7] LAUNDER et AL "Computational Fluid Dynamics" Colloquium, UMIST, MANCHESTER, April 1986
- [8] PATEL, RODI, SCHEUERER : "Turbulence Models for Near Wall and Low Reynolds Number Flows : a review" AIAA Journal VOL 23, n°9, 1984
- [9] P. MOIN, J. KIM. "The structure of vorticity in turbulent channel flow". JFM (1985) vol 155, JFM (1986) Vol 162
- [10] J. BARDINA, J.H. FERZIGER, W.C. REYNOLDS : "Improved turbulence models based on LES". Stanford report TF-19 (1983)
- [11] Proc. Euromech 199 : "Direct and Large Eddy Simulation" Vieweg, Braunschweig 1986. U SCHUMANN, R. FRIEDRICH (Eds)
- [12] G. COMTE-BELLOT, S. CORRSIN : "Simple Eulerian time correlation of full and narrow-band velocity signals in grid generated isotropic turbulence. JFM (1971), Vol 48
- [13] H. SCHMIDT, V. SCHUMANN, Hans VOLKERT : "3D Direct and Vectorized Elliptic Solvers for various Boundary Conditions". DFVLR-Mitt 84-15, D-8031 Oberpfaffenhofen
- [14] CHAMPAGNE, HARRIS, CORRSIN : "Experiments on nearly homogeneous turbulent shear flow". JFM (1970), vol 41
- [15] HARRIS, GRAHAM, CORRSIN : "Further experiments in nearly homogeneous turbulent shear flow". JFM (1977), Vol 81
- [16] LAUNDER, REECE, RODI : "Progress in the development of a Reynolds-stress turbulence closure", JFM (1975) Vol 68
- [17] MOON-JOO-LEE, W.C. REYNOLDS : "Numerical Experiments on the structure of homogeneous turbulence". Stanford report, TF-24 (1985)
- [18] A. SIRIWAT, Z. WARHAFT : "The effect of a passive cross-stream temperature gradient on the evolution of temperature variance and heat flux in grid turbulence". JFM (1983) Vol 128

- [19] P.L. VIOLLET : "Turbulent Mixing in a 2 Layer Stratified Shear Flow". Int. Symp. Stratified Flows, Trondheim 1980 ( EDF E44/80.17)
- [20] Von KARMAN Ins. "Vehicle Aerodynamics" Course (1986) (EDF-LNH HE41/86-07 for D. LAURENCE paper)
- [21] REECE, G.J., "A Generalized Reynolds-Stress Model of Turbulence", Ph.D. thesis, University of London, 1977
- [22] NAOT, D. and RODI, W., "Numerical Calculation of Secondary Motions in Channel Flow", ASME J. of the Hydraulics Division, August 1982
- [23] LAUNDER, B.E. and YING, W.M., "Secondary Flows in Ducts of Square Cross-Section", J. Fluid Mech., Vol. 54, pp. 289-295, 1972
- [24] Calculation of flow and pollutant dispersion in meandering channels. A.O. DEMUREN and W. RODI JFM (1986) Vol 172
- [25] CHABARD et AL. "A finite element code for efficient computation of turbulent industrial flows" To appear in 5<sup>th</sup> International Conference on numerical methods in laminar and turbulent flows (also EDF-LNH)
- [26] GARRETON, LACROIX, MAGUET, VIOLLET : "Hot Plenum Computations using local wall models". (EDF HE/44/86.13) (Also 5<sup>th</sup> IAHR Int Meeting, Grenoble, 1986)
- [27] "Macroscopic Modelling of Turbulent Flows" Lecture Notes in Physics 230 - Springer Verlag. (FRISCH, KELLER, PAPANICOLAON, PIRONNEAU Eds)

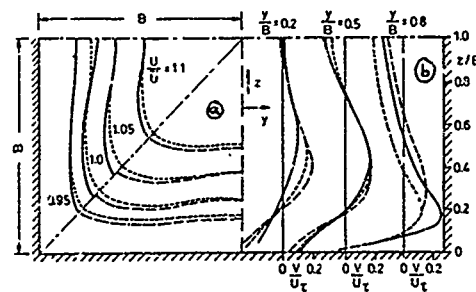


Fig 1.3.1: flow in a square duct (from [2], [23])

a) streamwise velocity  
b) secondary velocity  
ASM [22], --- DSM [21], Exp [23]

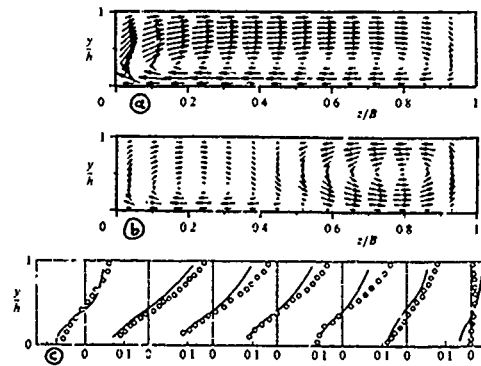
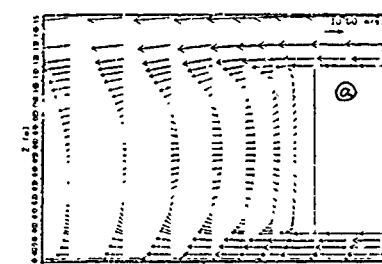
Fig 1.3.2: Secondary velocity in a meandering channel (from [24])  
a) rough bed, b) smooth bed, c) computed, d) Exp.

Fig 1.4.1: 3D computation of the flow around a car (ESTET)

a) wake in the vertical mid-plane (blunt back car)  
b) wake in a horizontal plane (blunt back car)  
c-d-e) views in cross-stream planes (glanted back)  
f-g) pressure coefficients by different codes (from [20])

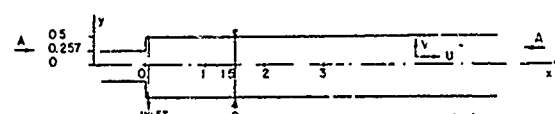
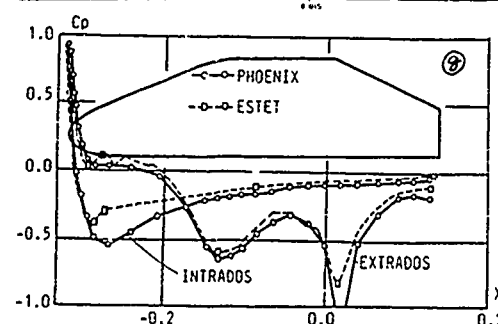
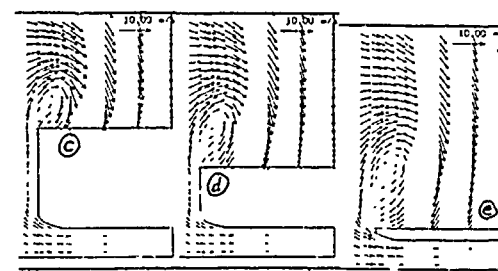
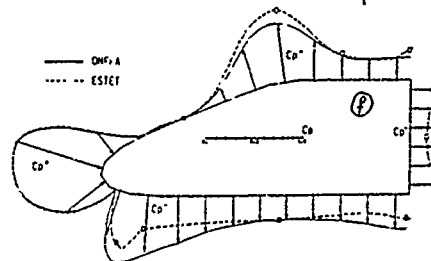
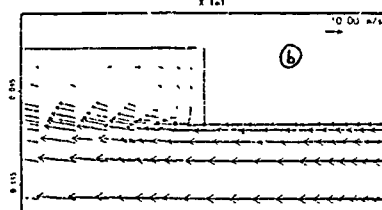
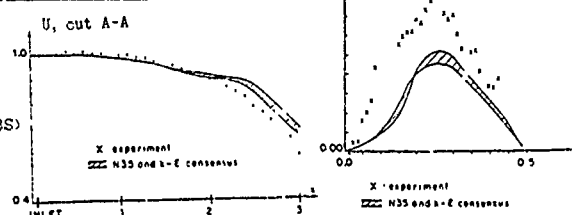


Fig 1.6: Axisymmetric expansion

(a benchmark for the finite element code N3S)  
x: Experiment  
N3S and k-ε consensus



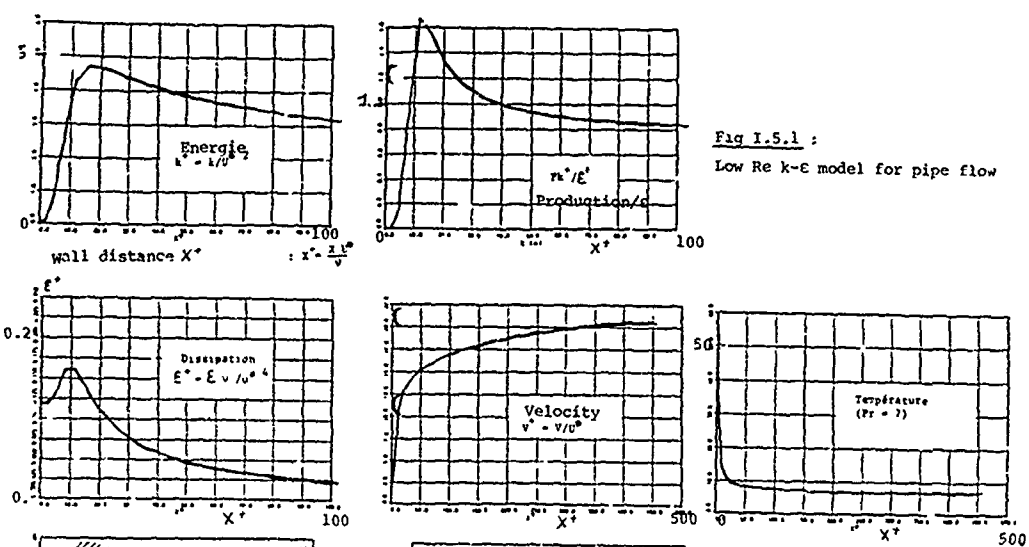
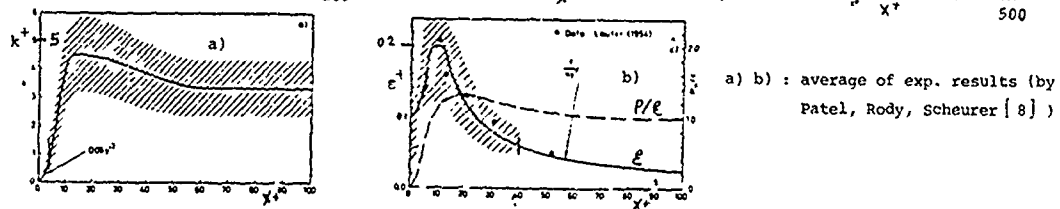


Fig 1.5.1 :  
Low Re  $k-\epsilon$  model for pipe flow



a) b) : average of exp. results (by  
Patel, Rody, Scheurer [8])

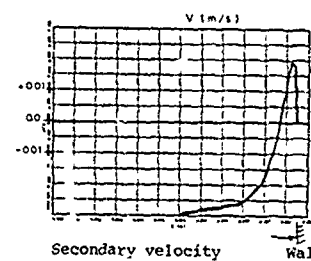
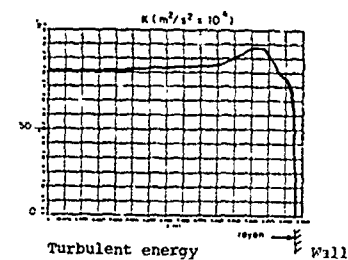
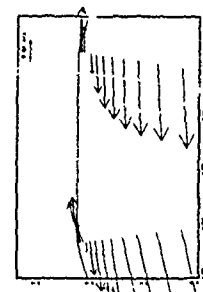


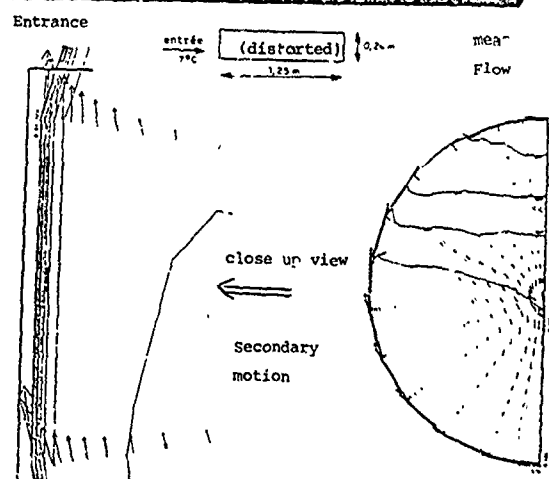
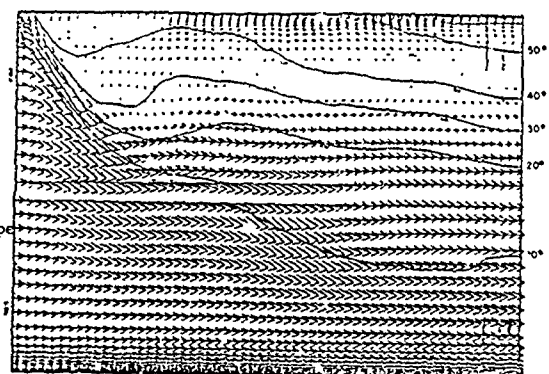
Fig 1.5.2  
buoyancy  
induced  
secondary  
motion in  
horizontal pipe



Turbulent energy



close up view  
near entrance



close up view  
Secondary  
motion



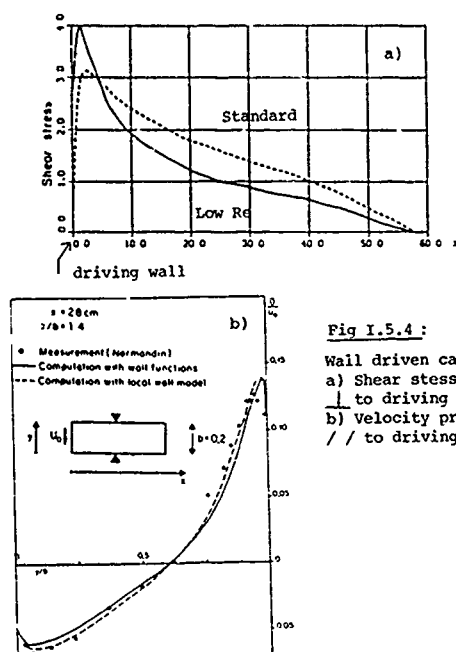


Fig I.5.4:  
Wall driven cavity  
a) Shear stress profile  
/ to driving wall  
b) Velocity profile  
// to driving wall

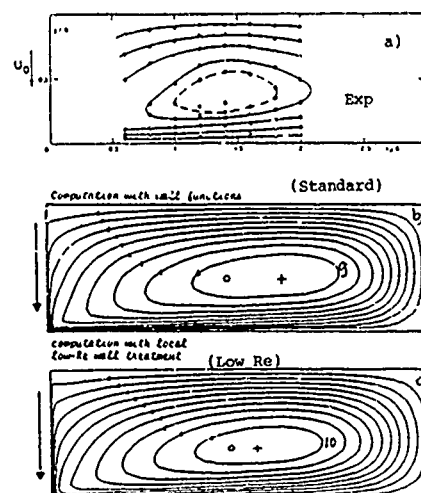


Fig I.5.3 Wall driven cavity  
a) Experiment  
b) Computation with wall functions  
c) Computation with low Re model

#### HOT PLENUM OF RNR 1500

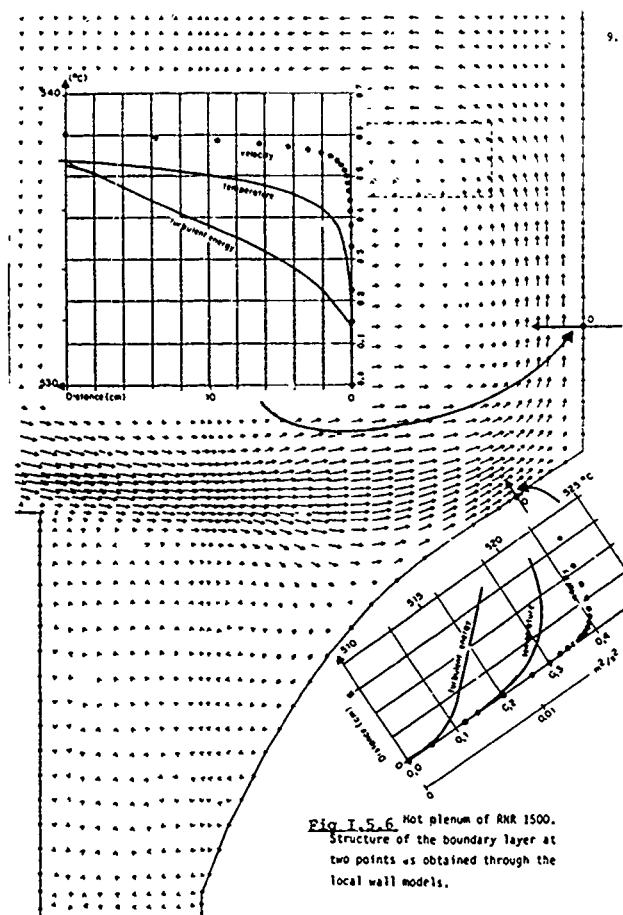


Fig I.5.6 Hot plenum of RNR 1500.  
Structure of the boundary layer at  
two points as obtained through the  
local wall models.

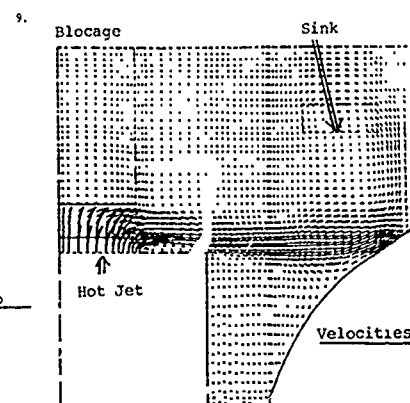
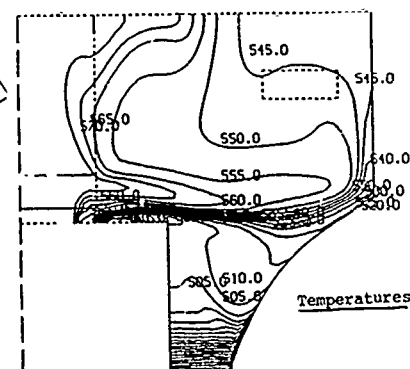


Fig I.5.4 : Velocities and temperatures  
in the hot plenum



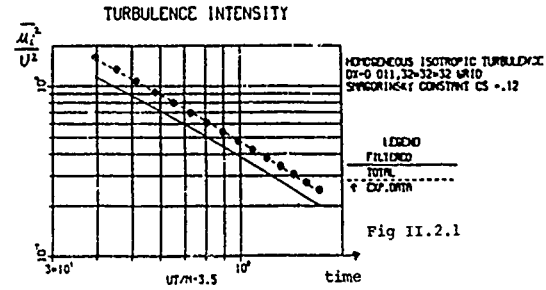
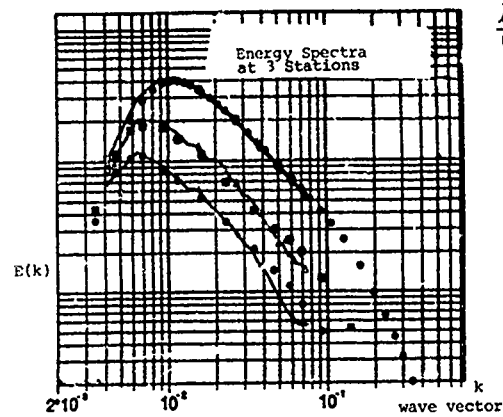


Fig II.2.1 : Grid Turbulence Simulation, CB-C exp [12]  
(solid lines are LES results)

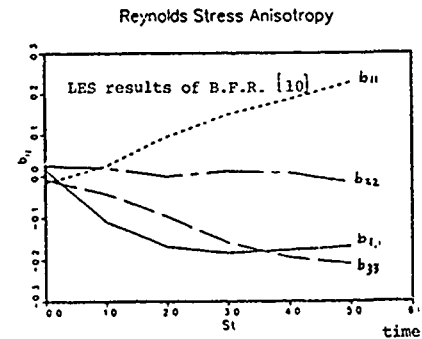
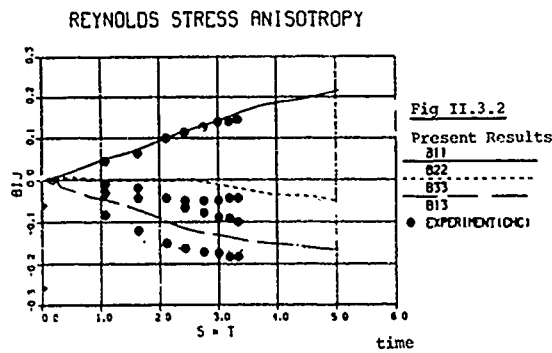
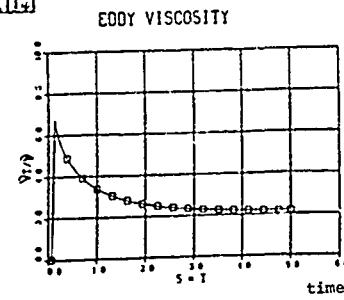
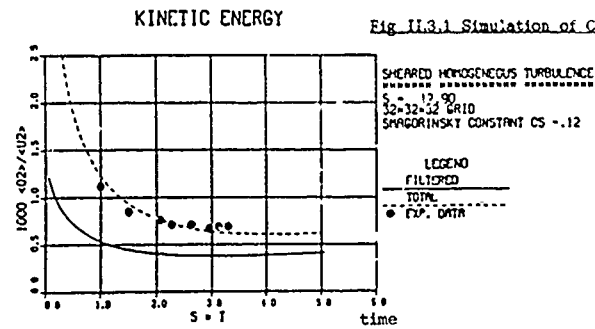


Fig II.3.3 LES results  
DIAGONAL PRESSURE STRAIN CORRELATION

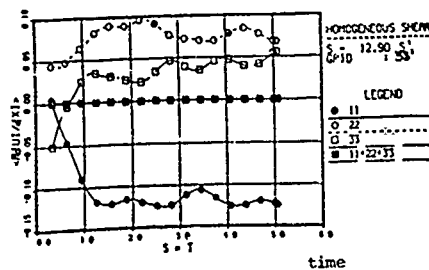
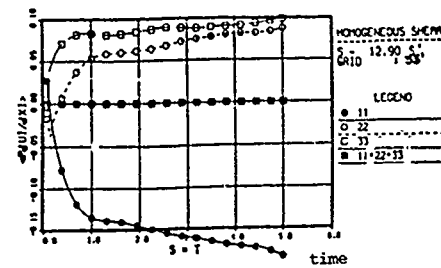
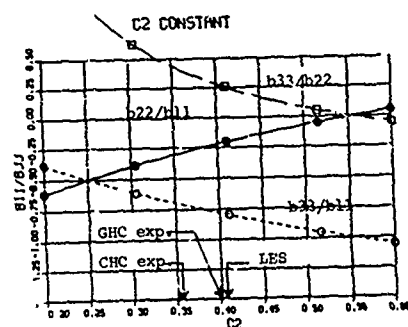


Fig II.3.5 LRR model prediction using LES results  
DIAGONAL PRESSURE STRAIN CORRELATION



Fig II.3.4 Influence of  $C_2$  on anisotropy in LRR model

## DEVIATOR OF THE DISSIPATION TENSOR

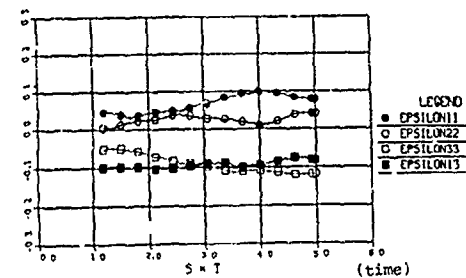


Fig II.3.5

## VELOCITY VARIANCES

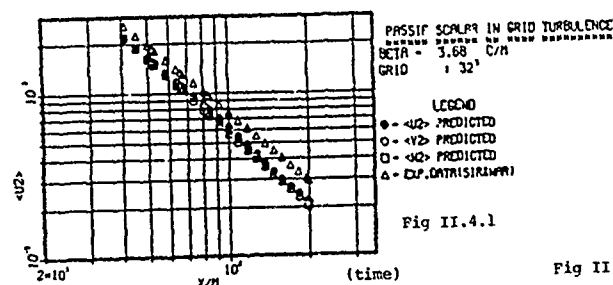


Fig II.4.1

## THERMAL FLUXES

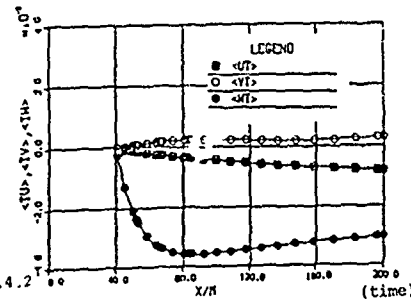


Fig II.4.2

## TEMPERATURE-VELOCITY CORRELATIONS

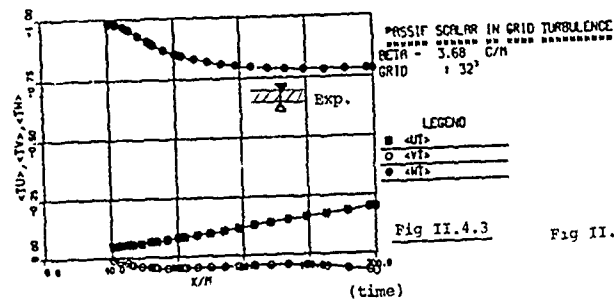


Fig II.4.3

## MECHANICAL/THERMAL TIMESCALE RATIO

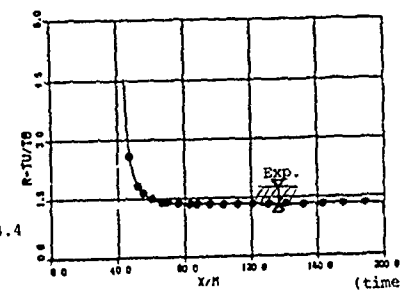


Fig II.4.4

## TEMPERATURE-VARIANCE DISSIPATION RATE

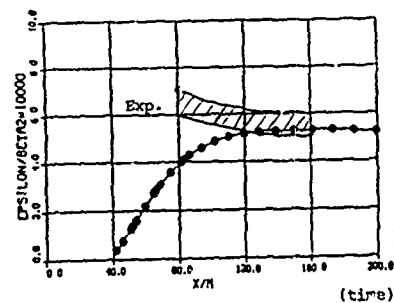


Fig II.4.5

## THERMAL PRODUCTION/DISSIPATION RATIO

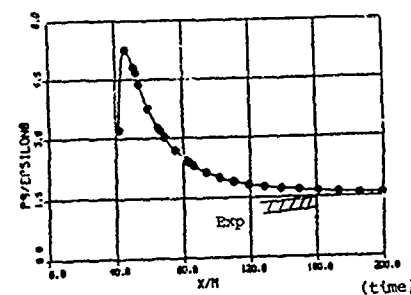
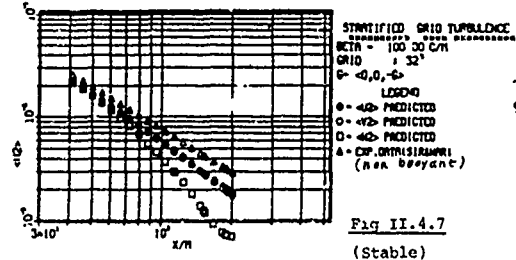
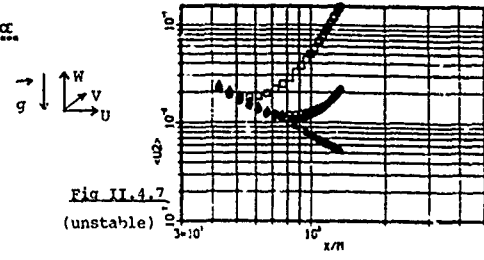


Fig II.4.6

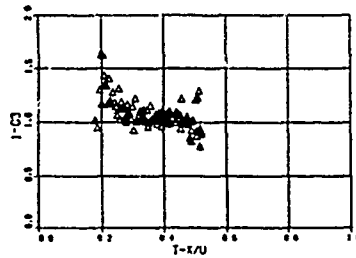
## VELOCITY VARIANCES



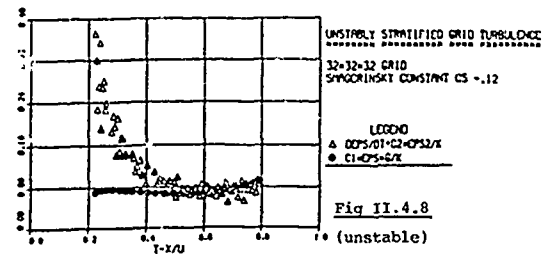
## VELOCITY VARIANCES



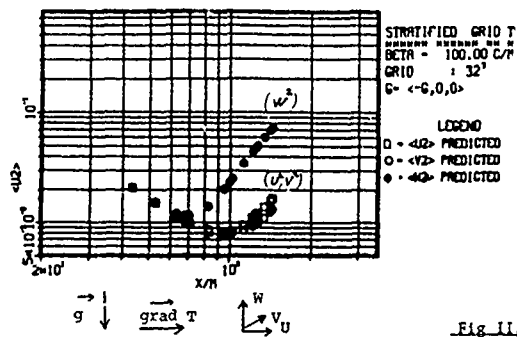
## K-EPSILON C3 CONSTANT



## BALANCE IN EPSILON EQUATION

Weight factor of G in  $\epsilon$  eq. (unstable case)

## VELOCITY VARIANCES



## TEMPERATURE-VELOCITY CORRELATIONS

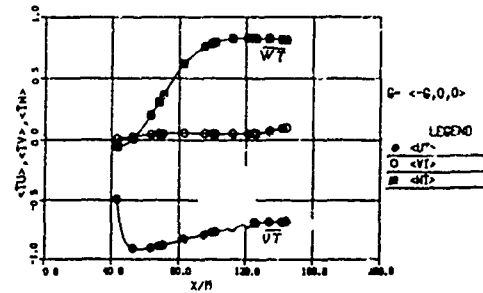


Fig II.4.9 Horizontal temperature gradient (with buoyancy)

APPENDIX A

THE COMPLETE REPORT WAS DISTRIBUTED AT THE VKI COURSE  
AND IS AVAILABLE AT EDF-LNH (ref HE 44.86.21)

VIOLET P.L.

ON THE NUMERICAL MODELLING OF  
STRATIFIED FLOWS

*Conference invitée au Symposium  
« Physical Processes in Estuaries »  
Delft, 9-12 Sept. 1986*

HE 44.86.21

Resume

Ce papier presente une revue des modèles de turbulence applicable aux écoulements stratifiés, et montre comment ces modèles réagissent vis-à-vis d'une situation de stratification stable ou instable. Le cas test d'un écoulement bicouche est présenté en détails.

Abstract :

The paper presents a review of turbulence models for stratified flows and shows how these models react to stable or unstable stratification phenomena. The test-case of a two-layers flow is described in details.

MOTS-CLES :

Mécanique des fluides / Transfert de chaleur / Ecoulement turbulent / Ecoulement stratifié / Mesure / Résolution numérique / Modèle de turbulence / Modèle  $k - \epsilon$ .

**Écoulement turbulent.**

+ Ecoulement laminaire.

Rédacteur : S. SEBAG  
Date : 28/03/1986

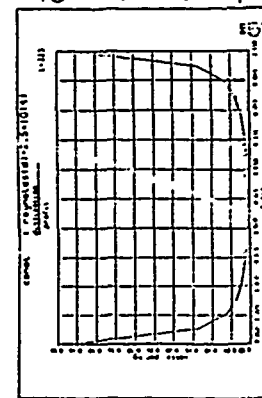
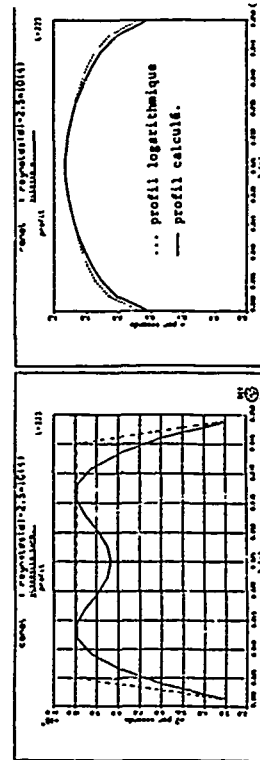
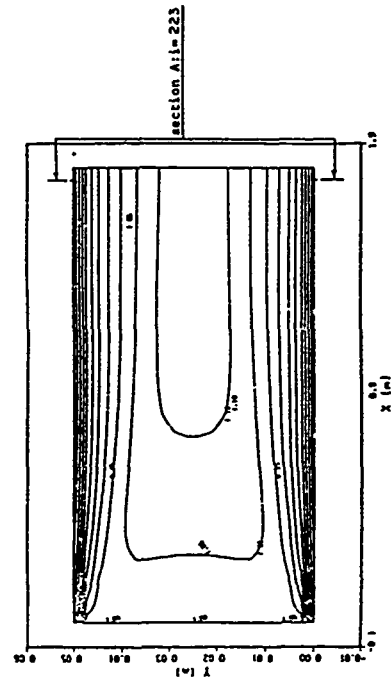
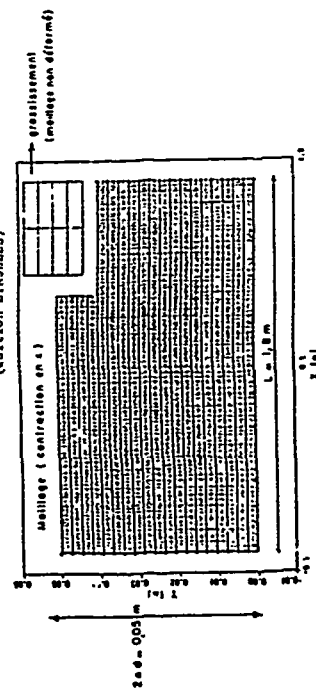
**Date** : 28/03/1986

**Titre :** **Écoulement entre 2 parois.**

Systeme : ULYSSE Version : 19 f4v.A86 (ULYSSE-2)

**Résultats de calcul :**

- **Auteur :** S. SEBAG.
- **Modèle de turbulence :** k- $\epsilon$  option standard (version bidimensionnelle).
- **Conditions aux limites de paroi :** fonctions de paroi (profil logarithmique).
- **Conditions aux limites amont :** vitesse uniforme (profil droit) ;  $k$  défini par la donnée d'une intensité turbulente ( $I$ ) :  $k = I^2 \times$  (vitesse moyenne)<sup>2</sup>
- **Calcul :**  $\epsilon$  calculé pour une extinction en 10 mailles de convection (option standard par défaut).
- **Particularités :** Laplacien compatible pour la pression (volumes finis).
- **Mailles :** Mailles rectangulaires 226 (x)  $\times$  22 (y).
- **References bibliographiques :** "Ecoulement turbulent entre 2 parois"  
G. COMTE-BELLLOT.  
Publications scientifiques et techniques du  
Ministère de l'Air.  
"Les modèles de turbulence K- $\epsilon$  appliqués à  
l'écoulement de Poiseuille plan" Y. COIFFÉ  
ME 04/80.04  
"Mémento des pertes de charge" I.E. IDEL'CIK  
(édition EYNOLLES)



Viscosité turbulente :  $\gamma_T$   
 ---  $\gamma_T = k u^3$  pour  $y \leq 0,1 \text{ m}$   
 (Théorie longueur de mélange)  
 $y$  : distance à la paroi.  
 $k$  : constante de Kármán.  
 ---  $u$  : vitesse de freinage.  
 ---  $\gamma_T$  calculée

3 : nojwa1sq

...  $\xi_{\frac{u^2}{u^2}}$  (modelle analytique)

— 3 calculs

## APPENDIX B

## APPENDIX C

ADVECTIVE FORMULATION OF LARGE EDDY  
SIMULATION FOR ENGINEERING TYPE FLOWS

D. Laurence  
Electricité de France  
Laboratoire National d'Hydraulique  
6 quai Watier - 78400 Chatou, France

## SUMMARY

Having in mind future applications of large eddy simulation to engineering problems, a numerical code operating in physical space only is presented. Results are analysed in Fourier space and quality is shown to be comparable to that of pseudo-spectral codes. An advective formulation of subgrid scale effects is proposed and special care is devoted to the problems arising as a large mean field is present.

## INTRODUCTION

Large Eddy Simulation, today, does not seem to be of such widespread practice as was forecasted a few years ago in connection with the rapid development of computer power. While researchers analysing fundamentals of turbulence make use of increasing computer capabilities to perform direct simulations, LES applications to engineering type flows are still scarce. This is due to the fact that eddy viscosity models are not fully satisfactory outside grid turbulence simulations and because of extra numerical difficulties arising as the homogeneity hypothesis is abandoned. These 2 points are analysed hereafter through a pseudo-Lagrangian approach.

## I TOTAL FIELD DECOMPOSITION

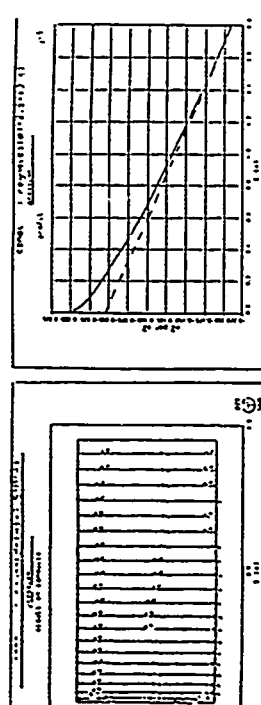
Let  $V(x,t)$  be the total velocity field in a fixed frame with respect to an experimental setup. Prior to performing a LES, this is decomposed as :

$$(1)$$

$$V(x,t) = \bar{V}(x) + \tilde{V}(x,t) + v'(x,t)$$

In addition to the usual grid-scale subgrid-scale decomposition  $v/v'$ , a supporting field  $\tilde{V}$  (i.e. average over an infinite time scale) is always present. It is easily accounted for in homogeneous flows by choice of the computational frame or by a simple function of the space variable  $\tilde{V}$  only. The computed variable is then  $u = \tilde{V}$ .

In engineering applications, with which we are concerned,  $\tilde{V}$  is usually complex and may be even unknown initially, so the computed variable must be  $u = \tilde{V} + \tilde{V}$ . The non-linear term of the u equation,  $u \cdot \nabla u$ , then contains not only pure non-linear turbulent interactions and production effects (with time scales  $\tau_1 \sim \tau_2 \sim \tau_3 \sim (\rho \tilde{V} / \rho \tilde{V})$  respectively), but also transport for which Eulerian numerics introduce an additional time scale  $\tau_{num} \sim h / \max |\tilde{V}|$  (h : mesh step,  $2q$  : kinetic energy,  $\xi$  : dissipation). Thus, if  $\tilde{V}$  is large with small gradients,  $\tau_{num}$  may be smaller than the "more physical" scales  $\tau_1$  and  $\tau_2$ . To obey this CFL criterion may be unnecessarily expensive since transport effects can be taken care of by introducing some Lagrangian approach.



Energie turbulente : K

$$K = \frac{u'^2}{2} \quad C_\mu = 0.09$$

Pression : p

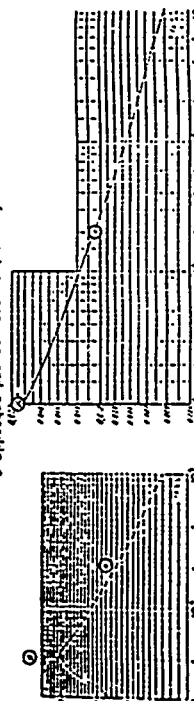
on a représenté  $p/p_{avac} = D \frac{d(\rho/\rho_0)}{dx}$   
... pente donnée par l'abaque de Moody  
(perte de charge)  
— pente calculée

COMPARAISON DES COEFFICIENTS DE PERTE DE CHARGE  
AUX ANNAUX ET A LA THEORIE

Cas laminaire :  $\lambda_{th} = \lambda_{calculé} = 0.24 \quad Re_D = 100$   
 $\lambda_{th} = \lambda_{calculé} = 9.59 \cdot 10^{-2} \quad Re_D = 250$   
(précision :  $10^{-4}$ )

Cas turbulent :  $\kappa$  points de calcul ( $\kappa - \xi$ )

(en toute rigueur, le module  $\kappa - \xi$  ne s'applique pas aux cas  $Re < 5 \cdot 10^4$ )



## II NUMERICAL SCHEME AND FILTERING

The standard scheme [1] uses Smagorinsky's model for the subgrid stresses and the resolution is based on fractional time steps. It's originality lies in the use of a characteristic method for the non linear term (advection of momentum). A 3D particle trajectory  $X_p(t)$  starting from grid point  $X_M$  at time  $t_n$  is computed backwards in time. The advected velocity is then  $u(X_M, t_n) = u(X_p, t_n)$  with  $X_p = X_p(t_n)$ . This is where most of the numerical filtering occurs. In order to retain as much information as possible, this implicit filtering is used instead of the usual Gaussian filter:

$$\bar{v}(x, t) = \int_{\Omega} G(x-y) v(y, t) dy \quad (v = v, \bar{p})$$

or  $\bar{v}(x, t) = G(k, t) v(k, t)$  ;  $G(k, t) = \exp. \left[ -\Delta_0^2 k^2 / 24 \right]$  in Fourier space.

The implicit filtering,  $S_1$ , operates at each time step so the total filtering of a computation performed through  $N$  time steps is  $G_1(k) = (S_1(k))^N$ .  $S_1$  is gaussian-like and thus its width can be estimated by comparison with grid turbulence experiment [14]. (Initial turbulent field matches exactly the spectrum at station  $t^*/M = 42$  and has non-zero skewness, cut-off wave number is well located in the inertial range. Spectra are computed at station  $t^*/M = 98$ , on fig. 1).

This implicit filtering can be checked by performing again the computation, this time adding a (spectral) defiltering after every time step, using the estimated width  $\Delta_0$  (fig. 2). The non dimensional width  $\Delta_0$  ( $\Delta_0 = \delta h$ ) ranges from 1.6 to 3.3 for the total run, depending on the numerical scheme [2]. This "empirical numerical analysis" provides guidance for comparison between alternative schemes.

## III ADVECTIVE FORMULATION OF SGS MODELS

The characteristic scheme brings natural separation between advected ( $U^{ed}$ ) and advecting ( $U^{ing}$ ) velocities. The advection step is:

$$\int_{t_n}^{t_{n+1}} \left[ \frac{\partial u^e}{\partial t} + u_j \frac{\partial}{\partial x_j} u^e \right] dt = 0 \rightarrow \tilde{u}^{n+1}$$

(higher order in time is actually achieved with a non-zero  $\Delta h, S_1$ ).

The standard scheme is  $U^{ing} = U^{ed} = U$ . Subgrid scale eddies can be represented by perturbing the particle trajectory by a random flight model. One sets  $U^{ing} = U + G$ , then if  $G$  is purely random (not correlated with  $U$  ;  $\langle G_i U_j \rangle = 0$ ), and its variance is scaled by  $\langle G^2 \rangle = 2\mu/\Delta t$ , the random flight is equivalent to diffusion and the advection step includes the effect of an eddy viscosity  $\nu_T$ . This results in resetting the sub-grid stresses into an advection form from which they actually originate and shows that modelling through perturbed advection could be a more promising approach since it at least contains the classical eddy viscosity models.

New models the effects of which are not restricted to energy drain can be found by imposing a non-zero  $\langle G_i U_j \rangle$  correlation. The underlying idea is Bardina Pitzinger & Reynolds's scale similarity model [3] : the subgrid scales are modeled using the smallest computed eddies "trapped" between single and double filtering. The force we actually add to the  $U_i$  equation is :

$$F_i = (\bar{v}_i - \bar{v}_i) \cdot \frac{\partial}{\partial x_j} \bar{v}_j \quad (2)$$

which is equivalent to the BFR model :

as it enters the  $U_i$  equation through its divergence :

$$\frac{\partial}{\partial x_j} M_{ij} = \frac{\partial}{\partial x_j} \left[ \bar{v}_i \bar{v}_j - \bar{v}_i \bar{v}_j \right] = \bar{v}_j \frac{\partial}{\partial x_j} \bar{v}_i - \bar{v}_i \frac{\partial}{\partial x_j} \bar{v}_j \quad (3)$$

and after the term responsible for non Galilean invariance is extracted : (see Spziale [4] and [2]) :  $\frac{\partial}{\partial x_j} M_{ij} = \frac{\partial}{\partial x_j} M_{ij} - \bar{v}_j \frac{\partial}{\partial x_j} [\bar{v}_i - \bar{v}_i]$ .

This model, plus the random flight model, in which  $\nu_T$  has the same value as in Smagorinsky's model, give satisfying results for grid turbulence decay (fig. 3), although a very large time step is taken. The effect of the scale similarity model is to enhance transfer of energy between larger and smaller computed scales. Thus improving the shape of the spectra improves in turn the Reynolds stress anisotropy in the homogeneous shear experiment (fig. 7-10). The excessive value of  $b_{ij}$  ( $b_{ij} \approx 2.6$ ) on fig. 9, while experiment shows a final value  $b_{ij} \approx 1.5$  is decreased as well as the discrepancy of  $b_{22}$ . Excess of anisotropy may be related to excess of energy on small wave numbers.

## IV SKETCH OF SCALE SIMILARITY MODELS IN SPECTRAL SPACE

Effects of scale similarity models cannot be investigated on the integral variables. Since they imply a decomposition along the wave number axis, spectral analysis is required. The EDQM approach can be very helpful here (eg : Aupoix, Bertoglio, Chollet, Lesieur, etc ..., present conference) but we will limit ourselves to a rough sketch.

Consider the exact equation of the filtered field ( $\bar{v} = 0$ ) :

$$\frac{\partial \bar{v}_i}{\partial t} + (\bar{v}_i + \bar{v}_i) \frac{\partial}{\partial x_j} (\bar{v}_i + \bar{v}_i) = -\frac{1}{\rho} \frac{\partial}{\partial x_j} \bar{p} + \nu \Delta \bar{v}_i \quad (4)$$

The advection term in spectral space is :

$$\begin{aligned} & (\bar{v}_i + \bar{v}_i) \frac{\partial}{\partial x_j} (\bar{v}_i + \bar{v}_i) \rightarrow (-i) \iint \{ G(\vec{k}) G(\vec{k}') G(\vec{k} - \vec{k}') \\ & + G(\vec{k}) G(\vec{k}') [1 - G(\vec{k} - \vec{k}')] + G(\vec{k}) G(\vec{k} - \vec{k}') [1 - G(\vec{k}')] \} \\ & + G(\vec{k}) [1 - G(\vec{k}')] [1 - G(\vec{k} - \vec{k}')] \} v_i(\vec{k}) v_j(\vec{k} - \vec{k}') d\vec{k}' \end{aligned} \quad (5)$$

I  $\bar{v}_i + \bar{v}_i$  : is the computed term  
II  $\bar{v}_i$  : are the cross terms  
III  $\bar{v}_i$  : is the true subgrid term.



Because of  $K^2 G(K)$ , maximum backscatter is for  $K$  in a ring close to the  $K_m$  circle. Observing powers of  $P$  and  $R$ , triangler leading to a larger contribution to backscatter with respect to true drain should have  $P$  and  $R$  both small (but not too small because of  $\tau_{\text{tr}} [1 - G(P)G(R)]$  term). This kind of triangles can be found in the cross terms, particularly in the sub-regions modelled by the  $(\bar{V}_1 - \bar{V})(\bar{V}_j - \bar{V}_j)$  model.

#### V GALILEAN INVARIANCE

As was pointed out by Spaziale [4] the Leonard term  $L_{ij} = \bar{v}_i \bar{v}_j - \bar{v}_i \bar{v}_j$ , and the cross terms  $U_{ij} = \bar{v}_i \bar{v}_j + \bar{v}_i \bar{v}_j$ , taken separately are not Galilean invariant (G.I.). The same can be said of certain proposed models. This was of little consequence for previous homogeneous turbulence simulations where  $\bar{v}$  (the supporting field) has been excluded. In engineering applications, the problem is more crucial but can be solved by using the near-level decomposition of eq (1) and writing models in terms of  $\bar{v}$  and space derivatives of  $\bar{v}$  only.

However, the numerical schemes themselves are not G.I. as soon as some linearisation has to be introduced.

This is true for the characteristics scheme by which the following equation is solved and where  $U^*$  is a "frozen" velocity field in some reference frame  $\bar{\sigma} \rightarrow [x, t]$ .

$$\int_{\bar{\sigma}}^{(n+1)} \left[ \frac{\partial U}{\partial t} + w_j \frac{\partial U}{\partial x_j} \right] = 0 \quad \text{in } \bar{\sigma}^* \quad (6)$$

Observing this equation from a different reference frame

$$\begin{cases} \bar{x}^* = \bar{x} + W_k t + b \\ \bar{t}^* = \bar{t} + W_k t + b \end{cases} \quad (7)$$

$W$  translational velocity

$$\int_{\bar{\sigma}}^{(n+1)} \left[ \left( \frac{\partial}{\partial t} + W_k \frac{\partial}{\partial x_k} \right) U^* + U^* \frac{\partial U^*}{\partial x_k} \right] = 0 \quad \text{in } \bar{\sigma}^*.$$

Introducing  $U_k^* = U_k^* - W_k$ , cancels the term  $W_k \frac{\partial U^*}{\partial x_k}$  but eq 7 cannot be solved by the standard characteristics scheme because  $(U_k^*)^*$  is not "frozen" in  $\bar{\sigma}^*$ :

$$\frac{\partial (U_k^*)^*}{\partial t} = \frac{\partial U_k^*}{\partial t} - W_j \frac{\partial U_k^*}{\partial x_j} = -W_j \frac{\partial U_k^*}{\partial x_j} \neq 0$$

$(U_k^*)^*$  is in  $\bar{\sigma}^*$  is evolving in time through the translation by  $W$ .

As previously for the non G.I. models, discrepancies are small if the variable  $U$  is  $U = \bar{v}$  only, instead of  $U = \bar{v} + \bar{v}$ , but for channel flow, for instance, influence of the computational frame  $\bar{\sigma}^*$  (equivalently) treatment of mean advection, has been noted (e.g. see [7]). Also, when computing homogeneous shear with Boron's shear-periodic boundary conditions [8] (see also [9]) partial statistics in the  $\bar{x}_1 - \bar{x}_2$  planes are not exactly homogeneous in the  $\bar{x}_3$  direction (turbulent kinetic energy decreases from its value in the centre plane, as  $V_1 = S \bar{x}_3$  increases).

Indeed, if  $\bar{v}$  is large, the approximation:

$$U_k(t) \frac{\partial}{\partial x_k} U(t) \approx U_k^*(t^*) \frac{\partial}{\partial x_k} U(t)$$

The usual procedure here (Kraichnan (76), Leslie and Quarini [5], Bertoglio [6]) is to introduce the Fourier transforms of the 2-point correlations  $\Phi_{ij}(K)$ , integrate over all angles and introduce a closure for the triple correlations. This leads to eq. 6 introduced further on, but masks the local anisotropy of the combined effects of the filters and the "triangler" requirement. Also, some effects of the models might not show directly on  $\Phi_{ij}(K)$  although they can be strong on higher moments (eg: see velocity derivative skewness, B.P.R. [3]). We will thus limit ourselves to the primitive equation (5) and to rough sketch of the regions in which the choice of  $\bar{K}$ , for a given  $\bar{K}$  will not lead to a cancellation through filtering and incompressibility. For instance, term I is illustrated by fig. 19. Action of the filter  $G$  is represented by a disk. Since Gaussian filters are considered, the boundaries are actually not sharp, but decrease rapidly outside the limit circles. Regions having such a line in common actually overlap. "Scale similarity" assumption is that triangler having similar shapes and scales have a similar contribution. Terms II, II' and III are illustrated on figs. 20-21. The  $G(K)$  tends to zero as  $(\bar{K} - \bar{K})$  tends to be aligned with  $\bar{K}$ .

Scale similarity models involve products as  $G(P) [1 - G(P)]$ . This is maximum for  $G(P) = 1/2$ ,  $P = K_m = \sqrt{24 \log 2} / \Delta \sim k/\Delta$ , with  $G(K) = \exp(-\Delta^2 K^2/24)$ .  $K_m$  is close to the maximum resolvable scale  $K_m = 2\pi/\Delta$ , if  $\Delta$  is twice the mesh step. Terms as  $\bar{v}_i - \bar{v}_i$  can thus be represented by a ring near the  $K_m$  circle.

The B.P.R. model (fig. 22) does seem to be a good representation of the terms II and II', and the figures clearly show that III remains to be modelled. This is well done by an eddy viscosity model, due to the larger separation of scales involved in III.

Another model proposed by B.P.R.,  $\partial/\partial x_j [(\bar{v}_i - \bar{v}_i)(\bar{v}_j - \bar{v}_j)]$ , is sketched on fig. 23. It was felt that it did not account for terms II and II', but they still seem to be partly represented especially when incompressibility is considered. Also, this model is G.I.

Finally, our model  $(\bar{v}_i - \bar{v}_i) \frac{\partial}{\partial x_j} \bar{v}_j$  seems to cover the same area (fig. 24).

Effects of scale similarity models on the energy spectra (isotropic case) will depend on the respective positions of  $K_m$  where  $G^2(K) [1 - G^2(K)]$  is maximum and  $K_0$  where the energy transfer rate  $T(K)$  changes sign ( $T(K_0) = 0$ ), fig. 25. The global effect is then extra transfer of energy between computed scales when  $K_m \sim K_0$ . This absence of global drain of the model tends to be related to equilibrium between true drain and backscatter. Using assumptions of [5] for an inertial range spectrum. One can write:

$$\text{true drain} = \int_0^\infty A(K, P, R) \cdot R^{-\frac{2}{3}} \cdot K^{-\frac{2}{3}} \cdot P^{-1} \quad (6)$$

$$\text{backscatter} = \int_0^\infty A(K, P, R) \cdot K^3 \cdot P^{-\frac{2}{3}} \cdot R^{-\frac{2}{3}} \cdot G^2(K).$$

$$(K = |\bar{K}|, P = |\bar{K}|, R = |\bar{K} - \bar{K}|).$$

$$A = A' [1 - G(P) G(R)] \text{ is common to both terms.}$$

Posterior to the Colloquium, results with the 3D version were obtained. The higher accuracy of the present scheme made it necessary to incorporate the Leonard term. Constants of the Smagorinsky and B.F.R. like models were then fitted to match the spectrum at  $t^*/M = 98$ . Then continuing the computation shows that very good agreement is found again further downstream at station  $t^*/M = 172$  (fig. 14).

It must be recalled here that the code operates solely in physical space. Although in spectral space a turbulent viscosity can be written as a function of wave-number,  $\nu_t = f(k)$ , so as to "mold" a spectrum in just about any shape, to obtain a sharp cut-off behaviour in Fourier space of the implicit filtering (as exhibits fig. 14) is not straightforward in physical space. This is a crucial improvement since the total filtering is no longer dependant on the number of time steps (see § II).

#### VII LAGRANGIAN "Λ VORTEX" MODEL FOR WALL TURBULENCE

LES simulations of wall turbulence require high mesh resolution for even moderate Reynolds number and also a very lengthy computation for the establishment of a proper initial field during which maintenance of the turbulent energy level is difficult. This level is self-sustained only once energy producing structures (as shown by Kim and Moin [12]) stand out "by chance" of the random field while on the other hand, the S.G.S. model drains energy right from the first time step.

In an engineering application where wall turbulence might not be the only item of interest, the expensive transitional stage can be avoided and coarseness of the grid near the wall can be compensated through the following steps :

- . prescribe shear velocity  $u^*$  .
- . choose a rough model of energy producing eddy and scale it in wall units (e.g. the  $\Lambda$  vortex of Perry and Chong [13]) .
- . perform a Lagrangian computation of the evolution of the structure (this enables the initially randomly defined eddy to bear some correlation with the Eulerian field : e.g. growth will be associated with bursting events).
- . restore the structure to the filtered field if and when scales are compatible .
- . control the energy input rate (number of  $\Lambda$  vortices) through a balance equation (input proportional to the defect of the observed head loss).

This enables the computation to be almost immediately on an energy producing stage (shear stress  $\langle u'v' \rangle \neq 0$  after 15 time steps) (fig. 15-17). The procedure can be used to rapidly generate an initial field, gives suitable statistics, but will require some theoretical justification in terms of subgrid scale modeling before it can be maintained, after the initial stage, in a LES computation.

as  $t \rightarrow t^{n+1}$  includes large phase errors for high wave numbers. Interaction is forced between uncorrelated eddies since only one is being advected by  $\bar{v}$  while the other is "frozen". Numerical diffusion then results as can be seen on figs. 4-6.

Fortunately, advection is local so an optimal computational frame,  $Op^*$ , can be found for each node point  $x_p$ . The translational velocity is chosen to be the mean velocity of the dependency domain of  $x_p$  (all points involved for integrating the advection step between  $t^n$  and  $t^{n+1}$  :  $\langle u \rangle$ ) is then frozen in this frame  $Gp$  and the usual scheme is applied. Fig. 6 shows that the scheme is no longer sensitive to  $\bar{v}$ .

In this context, Schumann's improved advection scheme, using the three level decomposition (eq. 1) can be considered as the most accurate characteristics scheme for  $\bar{v}$  advection since Fourier interpolation is used (but feasible only because the frame shift  $0 \rightarrow Op^*$  is constant in each  $\bar{v}_1 - \bar{v}_2$  plane).

#### VI WEAK FORMULATION OF THE CHARACTERISTICS SCHEME

The characteristics scheme is used in nearly all codes at L.N.H. because of its unconditional stability and good accuracy in engineering problems [10]. Applied to LES it can lead to a new field of S.G.S. modeling through its interpretation in terms of particle trajectory. But its major drawback lies in the need of interpolation. This is now improved through the weak formulation : the transport equation of a variable  $f$ , in a domain  $\Omega$  bounded by  $\Gamma$  is projected onto time dependent test functions  $\psi$  :

$$\int_{\Omega} \frac{\partial f}{\partial t} \psi \, d\Omega + \int_{\Omega} \bar{v} \cdot \nabla f \, \psi \, d\Omega = 0. \quad (8)$$

After integrating by parts :

$$\int_{\Omega} \frac{\partial f}{\partial t} \psi \, d\Omega - \int_{\Omega} \bar{v} \cdot \nabla f \, \psi \, d\Omega + \int_{\Gamma} f \, \bar{v} \cdot \nabla \psi \, d\Gamma = 0. \quad (9)$$

$$= \int_{\Omega} \frac{\partial f}{\partial t} \psi \, d\Omega + \int_{\Gamma} f \, \bar{v} \cdot \nabla \psi \, d\Gamma.$$

The R.H.S. is zero for solid or periodic boundaries, the last term on the L.H.S. vanishes as the  $\psi$  functions obey :

$$\frac{\partial \psi}{\partial t} + \bar{v} \cdot \nabla \psi = 0. \quad (10)$$

The standard scheme is used for solving (10), and (9) simplifies to :

$$\int_{\Omega} \frac{\partial f}{\partial t} \psi \, d\Omega = \int_{\Omega} \frac{\partial f}{\partial t} \psi \, d\Omega \quad (11)$$

+ (eventually boundary terms).

Proper integration of (11) enables the scheme to be very conservative, even for energy  $\langle f^2 \rangle$  although it is not introduced explicitly. It is now commonly used in 2D [11] and a highly vectorized 3D version is presently tested for LES. The 1D version has been applied to grid turbulence (a low CFL allowing splitting in direct, conv) and has remarkably improved the results (fig. 13).

## REFERENCES

- [1] F. BARON, D. LAURENCE : "Large Eddy Simulation of a Confined Turbulent Jet Flow". Turb. Shear Flow IV (1983).
- [2] J.P. BENOUE, A. HAUGUEL, D. LAURENCE : "Large Eddy Simulation of Turbulence in Physical Space". Macroscopic Mod. of Turb. Flows, Sophia Antipolis (1984), lecture notes in physics, Springer.
- [3] BARDINA, FERZIGER, REYNOLDS : "Improved Turbulence Models based on Large Eddy Simulation". Rep. 77-19, Stanford U. Cal. (1973).
- [4] C.G. SPEZIALE : "Galilean Invariance of Subgrid-Scale Stress models". J. Fluid Mech. Vol. 136 (1985).
- [5] D.C. LESLIE, G.L. QUARINI : "Application of Turbulence Theory to the Formulation of Subgrid Modelling". J. Fluid Mech. Vol. 91 (1979).
- [6] J.P. BERTOGLIO, J. MATHIEU : "Study of Subgrid Models for Sheared Turbulence". Fourth Turb. Shear Flow Symp., Karlsruhe (1983).
- [7] L. SCHMITT, K. RICHTER, R. FRIEDRICH : present conference.
- [8] F. BARON : "Macrosimulation Tridimensionnelle d'Ecoulements Turbulents Ciselés". Thesis and E.D.F. report NE41/62.21 (1982).
- [9] S. ELCHOBASHI, T. GERZ, U. SCHUMANN : Present Conference.
- [10] A. HAUGUEL : "Numerical Modelling of Complex Industrial and Environmental Flows". Int. Symp. on Ref. Flow Modelling, Iowa (1985).
- [11] J.M. HERVOUET : "Application of the Method of Characteristics in their Weak Formulation to Solving Two-dimensional Advection Eq.". (E.D.F. report EA1/85.22).
- [12] J. KIM, P. MOIN : Present Conference.
- [13] A.E. PERRY, M.S. CHONG : "On the Mechanism of Wall Turbulence". J. Fluid Mech. vol. 119 (1982).
- [14] COMTE-BELLOT, CORRSIN : "Simple Eulerian Time Correlation of Full and Narrow-band Velocity Signals in Grid Generated, Isotropic, Turbulence". J. Fluid Mech. (1971), vol. 48.
- [15] CHAMPAGNE, HARRIS, CORRSIN : "Experiments on Nearly Homogeneous Turbulent Shear Flow". J. Fluid Mech. (1970).

## CONCLUSION

Direct simulation is now preferred to LES for fundamental research but should soon regain interest in the engineering field. This is possible because robust physical space codes required for non-homogeneous computations can feature correct behavior of results in spectral space close to that of pseudo spectral codes, even for high wave numbers (yet not competitive with respect to c.p.u. time requirements). This has been achieved by omitting the usual explicit filtering in order to directly measure the implicit numerical filter, and subsequently reducing it by improving the numerical scheme.

Interaction through cut-off wave number is complex and does not reduce to pure dissipation effects. Use of additional S.O.S. models significantly improve results. Still, fundamental analysis (in spectral space) is still required for these new models. A profitable approach here is to first write whatever models can be introduced in physical space and subsequently analyze them in spectral space (instead of the reverse).

Special care must be devoted to pure transport effects of turbulence which arise as a large mean flow results from the non-homogeneity. Galilean invariance of models and numerical schemes is essential here. In this non-homogeneous context, transport effects on the SGS level will probably have to be included through "Schumann-like" models.

LES for high Reynolds channel flows can be attempted on a coarse grid by introduction of more empirical data and downgrading techniques. Structural "ad hoc" models can be introduced through discrete vortex methods, at least in the initial stage, in order to trigger energy producing mechanisms. The author is thankful to Dr. BERTOGLIO and BARON for helpful discussions, and to an unknown reviewer for his remarks in turning the manuscript into an acceptable paper.

DECREASING GRID TURBULENCE [14]  
Computed Energy Spectra at station  $tu^*/H=98$  (Initial:  $tu^*/H=62$ )

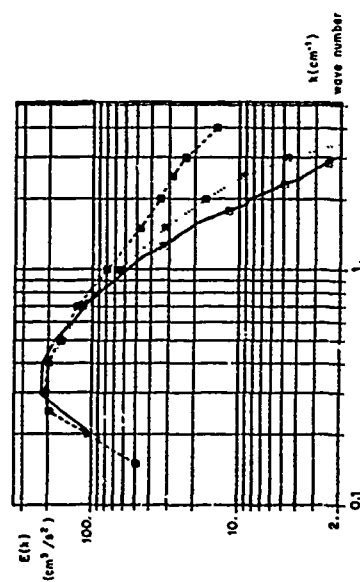


Fig. 1 : Standard scheme,  $CFL_{max} = 0.5$  ( $CFL_{max} = 2.5$ ).  
Solid lines are LES results, dashed lines are experimental results,  
dotted lines are filtered exp. results (Gaussian,  $\Delta = 2$  h for comparison).

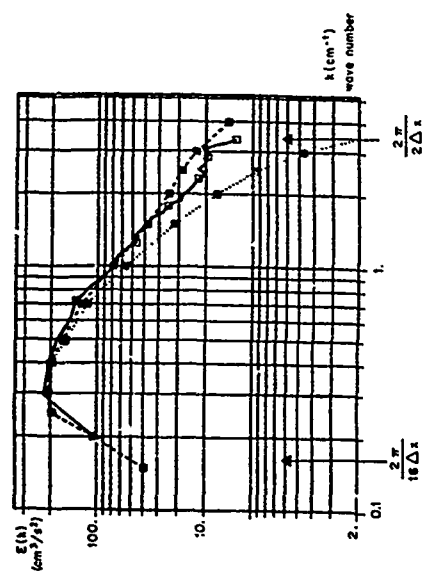


Fig. 2 : same as fig. 1, spectral defiltering at each time step.

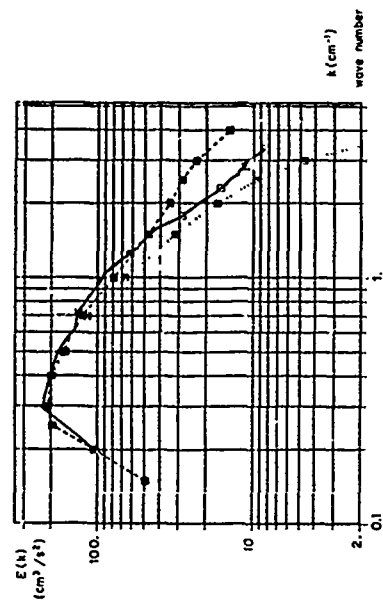


Fig. 3 : same as fig. 1, with random flight + scale similarity model.

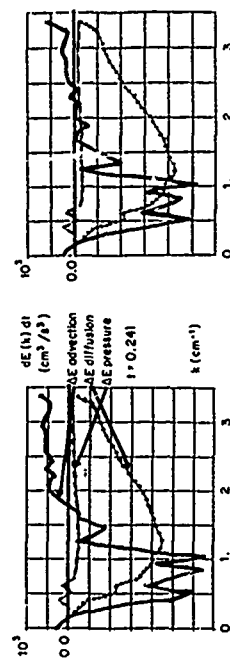


Fig. 4



Fig. 5

Fig. 6 : same as fig. 4, with code computed optimum local frame.

Fig. 4 : Standard run,  $\gamma = 0$   
Fig. 5 : same as 4, with  $\gamma/60$   
Fig. 6 : same as 5, with code computed optimum local frame.

# HOMOGENEOUS 'SLOWLY' SHEARED TURBULENCE [15]

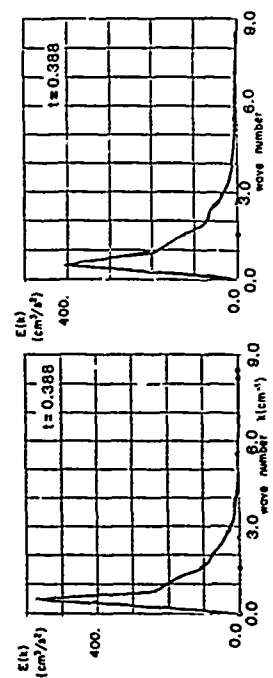


Fig. 7 : Final energy spectrum, standard scheme.  
Fig. 8 : same as 7, +scale similarity model.

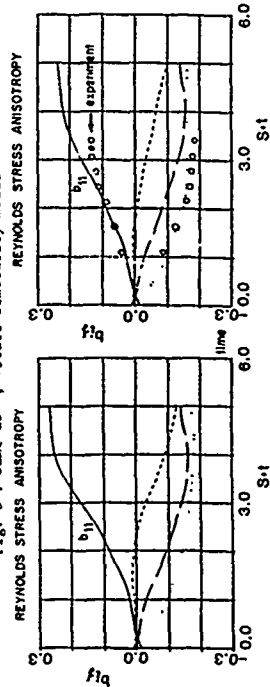


Fig. 9 : standard scheme.  
Fig. 10 : same as 8, +scale similarity model.

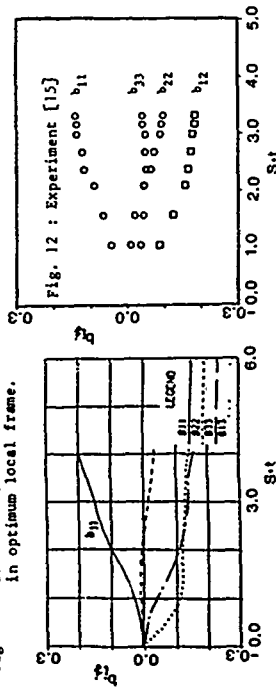


Fig. 12 : Experiment [15]

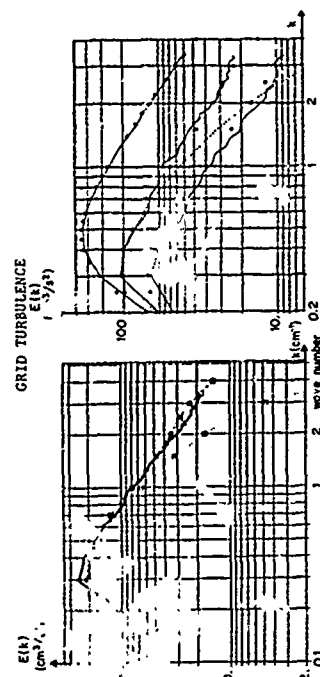


Fig. 13 : W-v formulation  
- advection,  $\epsilon_{PLMS} \approx 1$   
(see Fig. 1).  
Fig. 14 : Results of the final code  
(3D weak formulation, Smagorinsky,  
B.F.R. and Leonard terms), comparison  
at the 3 exp. stations.

## TURBULENT CHANNEL FLOW

(LES results after 15 time steps only, turbulence is initially zero and is generated by  $\Lambda$  vortices).

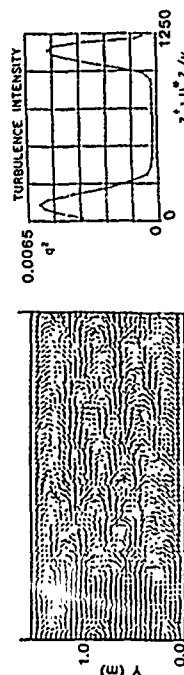


Fig. 15

Fig. 15 : Velocity field in horizontal plane (parallel to walls,  $z^+ = 50$ ).

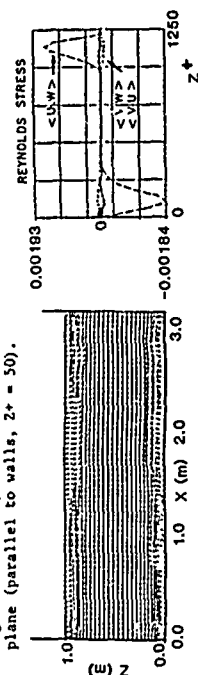


Fig. 17

Fig. 18 : Reynolds stress

$$G(K) \cdot G(K') \cdot G(K-K')$$

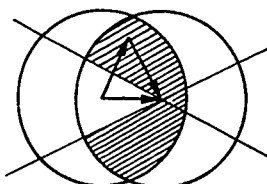


Fig. 19 : Term I of eq. 5

$$G(K) \cdot G(K') \cdot (1-G(K-K'))$$

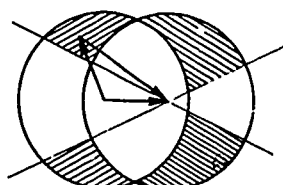


Fig. 20 : Terms II and II'

$$G(K) \cdot (1-G(K')) \cdot (1-G(K-K'))$$

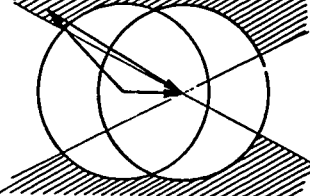


Fig. 21 : Term III

$$G(K') \cdot G(K-K') \cdot (1-G(K')) \cdot G(K-K')$$

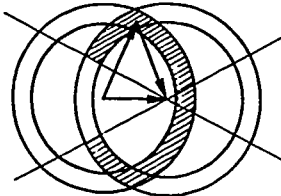


Fig. 22 :

$$G(K') \cdot (1-G(K')) \cdot G(K-K') \cdot (1-G(K-K'))$$

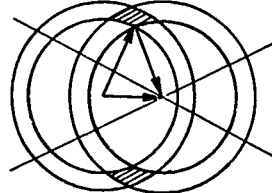


Fig. 23 :

$$G(K) \cdot G(K-K') \cdot (1-G(K-K'))$$

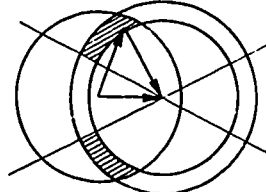


Fig. 24 :

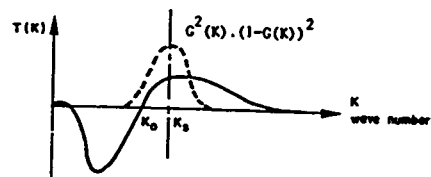


Fig. 25 : Energy transfer rate and scale similarity model filter.

HOMOGENEOUS TURBULENCE  
TWO-POINT CLOSURES AND APPLICATIONS TO ONE-POINT CLOSURES

B. AUPOIX

ONERA/CERT

Department of Aerothermodynamics  
 2 avenue E. Belin - 31055 TOULOUSE Cedex (FRANCE)

SUMMARY

This paper deals with homogeneous, i.e. translation invariant, turbulence. Homogeneous turbulence is an ideal situation in which the mean field is unaffected by the turbulent motion, so that the turbulent motion can be studied solely with a prescribed mean field. Such a flow can nearly be achieved in very simple experimental set-ups.

FOURIER transforms are convenient to study the turbulent motion. The momentum equation shows that the evolution of the turbulent motion is due, on the one hand, to the action of turbulence upon itself (non linear effects) and, on the other hand, to the action of the mean field upon turbulence (linear effects). The linear problem can be solved with the help of a GREEN function. Some important solutions are then studied. The non linear problem is open and requires modelling. Various approaches are described, in the simple case of homogeneous isotropic turbulence.

The resolution of the transport equation for the REYNOLDS stresses requires the closure of the pressure strain terms and of the dissipation equation. Application of two-point closures to the modelling of these terms is studied in the last part.

Part I - HOMOGENEOUS TURBULENCE - INTRODUCTION TO TWO-POINT CLOSURES

1 - HOMOGENEOUS TURBULENCE

1.1. Introduction

We shall restrict our study to incompressible flows, without buoyancy effects, passive scalar ... The flow is then governed by the continuity and momentum equations which read, in a cartesian reference frame :

$$\frac{\partial \tilde{u}_i}{\partial x_i} = 0$$

$$\frac{\partial \tilde{u}_i}{\partial t} + \tilde{u}_j \frac{\partial \tilde{u}_i}{\partial x_j} = -\frac{1}{\rho} \frac{\partial \tilde{p}}{\partial x_i} + \nu \frac{\partial^2 \tilde{u}_i}{\partial x_j^2}$$

The instantaneous velocity field  $\tilde{U}$  can be decomposed in various ways to study the turbulent motion. The standard decomposition proposed by REYNOLDS is very suitable for engineering purpose. The flow variables (velocity, pressure) are split into a mean part defined as an ensemble average and a fluctuation as :

$$\begin{aligned} \tilde{U} &= U + u' & U &= \langle \tilde{u} \rangle \\ \tilde{P} &= P + p' & P &= \langle \tilde{P} \rangle \end{aligned}$$

Equations for the mean and the fluctuating motions can be derived from the above continuity and momentum equations. They read :

$$\frac{\partial U_i}{\partial x_i} = 0$$

$$\frac{\partial U_i}{\partial t} + U_j \frac{\partial U_i}{\partial x_j} = -\frac{1}{\rho} \frac{\partial P}{\partial x_i} + \nu \frac{\partial^2 U_i}{\partial x_j^2} - \frac{\partial}{\partial x_j} \langle u'_j u'_i \rangle$$

$$\frac{\partial u'_i}{\partial x_i} = 0$$

$$\frac{\partial u'_i}{\partial t} + U_j \frac{\partial u'_i}{\partial x_j} = -\frac{1}{\rho} \frac{\partial p'}{\partial x_i} + \nu \frac{\partial^2 u'_i}{\partial x_j^2} - u'_j \frac{\partial U_i}{\partial x_j} - \frac{\partial}{\partial x_j} (u'_j u'_i - \langle u'_j u'_i \rangle)$$

The non linear advection term couples the evolutions of the mean and fluctuating motions. In the mean field momentum equation, the turbulent motion appears through the REYNOLDS stress  $\langle u'_j u'_i \rangle$  while the mean field appears in the fluctuating field momentum equation. The two fields are interconnected and must be studied together.

The mean field equations can be unaffected by the turbulent motion if the REYNOLDS stresses and, more generally, all the statistical variables, are independent of the point, i.e. if the flow is translation invariant.

The interesting feature of homogeneous turbulence is that the mean field is decoupled from the turbulent motion. The mean field can then be prescribed to study solely the evolution of the turbulent motion.

### 1.2. Constraints on the mean field

A translation invariant turbulent field can only be obtained with special mean fields. The constraints on the mean field have been pointed out by CRAVA /1/.

The first constraint is that the mean flow must satisfy the continuity equation :  $\frac{\partial U_i}{\partial x_i} = 0$ .

The second constraint can be derived by writing that any correlation is translation invariant. For the sake of clarity, we just impose to the REYNOLDS stress to be translation invariant. The demonstration for a higher level, multi-point correlation, will be analogous.

The transport equation for the REYNOLDS stress  $\langle u_i' u_j' \rangle$  is constructed by multiplying the momentum equation for  $u_i'$  by  $u_j'$ , the momentum equation for  $u_j'$  by  $u_i'$ , adding and averaging. After some algebra, it reads :

$$\begin{aligned} \frac{\partial}{\partial t} \langle u_i' u_j' \rangle + u_k \frac{\partial}{\partial x_k} \langle u_i' u_j' \rangle = & - \langle u_i' u_k' \rangle \frac{\partial U_j}{\partial x_k} - \langle u_j' u_k' \rangle \frac{\partial U_i}{\partial x_k} \\ & + \langle \frac{p'}{\rho} \left( \frac{\partial u_i'}{\partial x_j} + \frac{\partial u_j'}{\partial x_i} \right) \rangle - 2\nu \langle \frac{\partial u_i'}{\partial x_k} \frac{\partial u_j'}{\partial x_k} \rangle \\ & - \frac{\partial}{\partial x_k} \left( \langle u_i' u_j' u_k' \rangle - \nu \frac{\partial}{\partial x_k} \langle u_i' u_j' \rangle \right) \\ & + \langle \frac{p'}{\rho} (u_i' \delta_{jk} + u_j' \delta_{ik}) \rangle \end{aligned}$$

where  $\delta_{ij}$  is the KRONECKER tensor.

The REYNOLDS stress must be translation invariant, i.e.  $\frac{\partial}{\partial x_m} \langle u_i' u_j' \rangle = 0$ . By taking the derivative of the above transport equation and using the translation invariance of all correlations, the above equation reduces to :

$$0 = - \langle u_i' u_k' \rangle \frac{\partial^2 U_j}{\partial x_k \partial x_m} - \langle u_j' u_k' \rangle \frac{\partial^2 U_i}{\partial x_k \partial x_m} \quad (\forall i, j, m)$$

Homogeneous turbulence can exist only when the mean field has constant velocity gradients.

The third constraint can be derived from the HELMHOLTZ equation. As the mean flow is unaffected by the turbulent motion, the momentum equation for the mean flow reads :

$$\frac{\partial \underline{U}}{\partial t} + \underline{U} \cdot \nabla \underline{U} = - \frac{1}{\rho} \nabla p + \nu \nabla^2 \underline{U}$$

So, taking the curl of the momentum equation and taking into account the fact that the velocity gradient is constant over space lead to the equation :

$$\frac{\partial}{\partial t} \text{curl } \underline{U} + \text{curl } \underline{U} \cdot \nabla \underline{U} = 0$$

For steady mean flows, to which we shall restrict our study, this relation imposes to the mean field to be either a pure strain ( $\text{curl } \underline{U} = 0$ ) :

$$\left( \frac{\partial \underline{U}}{\partial x} \right) = \begin{pmatrix} d & 0 & 0 \\ 0 & md & 0 \\ 0 & 0 & -(m+1)d \end{pmatrix}$$

or a plane strain plus a rotation, the rotation axis being normal to the plane of the strain, i.e. :

$$\left( \frac{\partial \underline{U}}{\partial x} \right) = \begin{pmatrix} 0 & 0 & 0 \\ 0 & d & \omega \\ 0 & -\omega & -d \end{pmatrix} \quad \begin{matrix} d \text{ strain} \\ \omega \text{ rotation} \end{matrix}$$

An important case corresponds to the equality of the strain and rotation rates. In a reference frame rotated by 45 degrees, the velocity gradient reduces to :

$$\left( \frac{\partial \underline{U}}{\partial x} \right) = \begin{pmatrix} 0 & 0 & 0 \\ 0 & 0 & 0 \\ 0 & -(d+\omega) & 0 \end{pmatrix}$$

i.e. a plane shear flow. The study of sheared flow is important as shear appears in a lot of inhomogeneous situations of practical interest such as boundary layers, wakes ...



### 1.3. Nearly homogeneous turbulence

Homogeneous turbulence, as described above, does not exist. The flow is always bounded, so there is only a restricted domain upon which the turbulent flow is translation invariant. The turbulent motion is thus homogeneous only for a restricted range of length scales. However, if the domain is large enough, compared with the turbulence length scales, it exists a core where the turbulent motion is hardly affected by the boundaries and in which the flow can be assumed to be homogeneous.

In most experiments, turbulence is generated by a grid in a wind tunnel. As the flow moves downstream, the turbulent field evolves continuously. Turbulence statistics are not translation invariant. However, if the evolution length scale of the turbulence statistics is large when compared with the turbulence length scales, the turbulent flow can be assumed to be locally translation invariant. So nearly homogeneous turbulence can be obtained experimentally.

### 1.4. Some nearly homogeneous flow experiments

The various turbulent flow fields can be classified by looking at the REYNOLDS stress transport equation, which reads, for homogeneous flows :

$$\frac{\partial}{\partial t} \langle u'_i u'_j \rangle + U_k \frac{\partial}{\partial x_k} \langle u'_i u'_j \rangle = - \langle u'_i u'_k \rangle \frac{\partial U_j}{\partial x_k} - \langle u'_j u'_k \rangle \frac{\partial U_i}{\partial x_k} + \langle \frac{p'}{\rho} \left( \frac{\partial u'_i}{\partial x_j} + \frac{\partial u'_j}{\partial x_i} \right) \rangle - 2\nu \left\langle \frac{\partial u'_i}{\partial x_k} \frac{\partial u'_j}{\partial x_k} \right\rangle$$

#### 1.4.1. Flows without mean velocity gradients

The simplest cases correspond to the absence of mean velocity gradient. The turbulent field then decays and turbulence is converted into heat by the viscous effects.

The first case is the decay of isotropic turbulence. Turbulence is isotropic when all the turbulence statistics are independent of the direction, i.e. rotation invariant. Therefore,  $\langle u'_i u'_j \rangle = (\delta_{ij}/3) q^2$  where  $q^2 = \langle u'_i u'_i \rangle$  is twice the turbulent kinetic energy. The REYNOLDS stress equation then reduces to a transport equation for the turbulent kinetic energy :

$$\frac{\partial}{\partial t} \frac{1}{2} q^2 + U_k \frac{\partial}{\partial x_k} \frac{1}{2} q^2 = - \nu \left\langle \frac{\partial u'_i}{\partial x_k} \frac{\partial u'_i}{\partial x_k} \right\rangle$$

Isotropic turbulence is difficult to obtain experimentally. A mean flow without any velocity gradient can be obtained in a constant area duct (or, more precisely, slightly diverging to account for wall boundary layer displacement effect). The standard experimental set-up used by most experimentalists consists in a turbulence producing grid placed ahead of the test section. However grids produce anisotropic turbulence.

COMTE-BELLOT and CORRSIN /2, 3/ proposed to improve the isotropy of grid-generated turbulence with the help of a small contraction downstream of the grid and before the test section (figure 1). Besides the extensive study of COMTE-BELLOT and CORRSIN, we can mention the works of STEWART and TOWNSEND /4/, VAN ATTA et al /5, 6, 7, 8/ who studied energy transfer and multi-point time correlations. GAD-EL-HAK and CORRSIN /9/ used a jet grid to improve the flow homogeneity. At last, we must mention the works by TSUJI /10, 11/ and KELLOG and CORRSIN /12/ who used two successive grids to produce turbulence with perturbed energy spectra.

The second case of homogeneous flow without mean velocity gradient is the return to isotropy of anisotropic turbulence. The turbulence anisotropy can be due to the grid but is often enlarged through a distorting duct. At the end of the distorting duct, a constant area duct in which there is no mean velocity gradient is placed (figure 2). Experiments show that the turbulence decays in absence of mean velocity gradient. The REYNOLDS stresses are then governed by the equation :

$$\frac{\partial}{\partial t} \langle u'_i u'_j \rangle + U_k \frac{\partial}{\partial x_k} \langle u'_i u'_j \rangle = \left\langle \frac{p'}{\rho} \left( \frac{\partial u'_i}{\partial x_j} + \frac{\partial u'_j}{\partial x_i} \right) \right\rangle - 2\nu \left\langle \frac{\partial u'_i}{\partial x_k} \frac{\partial u'_j}{\partial x_k} \right\rangle$$

and the rôle of both the viscous term and the pressure-strain correlations is to decrease the flow anisotropy during decay. Such experiments have been conducted by UBEROI /13/, TUCKER and REYNOLDS /14/, GENGE and MATHIEU /15/, CHOI /16/ or LE PENVEN et al /17/.

#### 1.4.2. Solid body rotation

In the presence of mean velocity gradients, the transport equation for the turbulent kinetic energy reads :

$$\frac{\partial}{\partial t} \frac{1}{2} q^2 + U_k \frac{\partial}{\partial x_k} \frac{1}{2} q^2 = - \langle u'_i u'_j \rangle \frac{\partial U_i}{\partial x_j} - \nu \left\langle \frac{\partial u'_i}{\partial x_k} \frac{\partial u'_i}{\partial x_k} \right\rangle$$

The first term of the RHS represents the production of turbulent kinetic energy by action of the mean velocity gradient on the REYNOLDS stresses. As the REYNOLDS stress tensor is symmetric, only the symmetric part of the mean velocity gradient acts to produce turbulent kinetic energy, i.e. strain produces turbulent kinetic energy while rotation does not. So turbulence submitted to solid body rotation can only decay. Turbulence submitted to solid body rotation is an interesting flow for two reasons : on the one hand, rotation exists in a large variety of flows such as geophysical flows or turbomachinery and, on the second hand, it is a very simple homogeneous flow with mean velocity gradient.

Experiments were first conducted by TRAUGOTT /18/ in the flow between two concentric cylinders. Flow is set into rotation by an impeller at the entrance of the rotating annulus test section. IBBETSON and TRITTON /19/ moved two perforated plates into a rotating water tank to generate the turbulent motion and then studied the time decay of the turbulence. Unfortunately, homogeneity conditions do not seem to be fulfilled in their experiment. HOPFINGER et al /20, 21/ have done an extensive study in a rotating water tank. Turbulence is produced by a vibrating grid at the bottom of the tank and distance from the grid is identified with time of evolution of the turbulence. The most extensive experiments have been conducted by WIGELAND and NAGIB. The air flow is set into rotation by passing through a rotating honeycomb and, downstream in the rotating test section, turbulence is generated by a grid (figure 3). Despite important boundary layers, there remains a central core in which homogeneity is satisfied in all the test section. Tests have been done for various grids, streamwise velocity and rotation rates. A similar experiment, with a larger and longer test section, has been performed at ONERA by L. JACQUIN /112/.

#### 1.4.3. Plane strain

The next class of homogeneous flows is strained flows. Such a flow is energy producing, so that no term can now be suppressed in the transport equations for the turbulent REYNOLDS stresses and the turbulent kinetic energy. Energy can be decaying or increasing according to the balance between production due to the mean strain and dissipation by viscous effects, i.e. grossly to the ratio between the strain and turbulence time scales.

The simplest strained flow is the plane strain in which turbulence is compressed in one direction while expanded in the other. Plane strain can be obtained with constant area duct of evolving plan form (figure 2). The form of the duct to produce a constant strain was studied by TOWNSEND /23/ who performed one of the first experiments. Further experiments have been performed by TUCKER and REYNOLDS /14, 24/, MARECHAL /25/ and GENCE and MATHIEU /26/. An interesting feature of this last experiment is to impose successively two plane strains of different principal axis (figure 4).

#### 1.4.4. Three-dimensional strain

Plane strain is just a peculiar case. More generally, strained flows can be expanding in one (resp. two) direction(s) while compressing in the other two (resp. one) directions. The form of duct which produces such mean velocity gradients has been studied by REYNOLDS and TUCKER /24/ who performed several three-dimensional strain experiments. Other experiments, for axisymmetric strain, i.e. having two equal compressions, have been performed by UBEROI et al /13, 27/, RANJEE et al /28, 29/ or TAN ATICHAH /30/.

#### 1.4.5. Shear

As shown previously, homogeneous flow can be obtained for any combination of a plane strain and a rotation, the axis of which is normal to the plane of strain. A peculiar case occurs when the strain and the rotation are equal, purely sheared flow is then obtained. Shear plays an important rôle as it occurs in a lot of practical, inhomogeneous flows such as boundary layers, wakes ..., so it has been widely studied. Various devices have been used to generate a sheared flow. ROSE /31/ first used a grid of varying solidity to produce such a flow. Later, he used a honeycomb with cell axes parallel to the flow direction and variable cell length as a shear generator (figure 5) /32/. CHAMPAGNE et al /33/ used an array of parallel, equal width channels with adjustable internal resistances made of screens (figure 6). This apparatus was later used by HARRIS et al /34/, TAVOULARIS et al /35, 36/ while MULHEARN and LUSTON /37/ used a varying solidity grid.

In the first experiments of ROSE, MULHEARN or CHAMPAGNE, the shear was weak, the energy production did not balance the viscous dissipation and the turbulence decayed. In the experiments of HARRIS or TAVOULARIS, strong shear is obtained and the turbulent kinetic energy increases.

#### 1.4.6. Strain + rotation

Shear is just a peculiar case of the combination of a plane strain and a rotation. However, the combination of a plane strain and a rotation of different strengths has been hardly studied. SREENIVASAN /38/ added a distorting duct to a sheared flow experiment to study the influence of extra rate of strain on sheared turbulence. Another experiment with various strain/rotation ratios is under development at ONERA.

Readers interested in homogeneous turbulence experiments may also look at the review papers by FERZIGER /39/ and GENCE /40/.

### 1.5. Reduction to a time problem

The continuity and momentum equations in a moving reference frame read :

$$\frac{\partial \tilde{u}_i}{\partial x_i} = 0$$

$$\frac{\partial \tilde{u}_i}{\partial t} + \tilde{u}_k \frac{\partial \tilde{u}_i}{\partial x_k} + 2 \epsilon_{ipq} \omega_p \tilde{u}_q - \frac{\omega^2}{2} \frac{\partial^2 \tilde{u}_i}{\partial x_1^2} + \Gamma_{ei} = -\frac{1}{\rho} \frac{\partial \tilde{p}}{\partial x_i} + \nu \frac{\partial^2 \tilde{u}_i}{\partial x_k \partial x_k}$$

where  $\omega_p$  are the components of the rotation of the moving reference frame ;  $\omega$ , its modulus ;  $r$ , the distance between the considered point and the rotation axis ;  $\epsilon_{ijk}$ , the alternating RICCI tensor and  $\Gamma_{ei}$ , the entrainment acceleration term due to the translation of the reference frame along the  $x_i$  axis.

If the REYNOLDS decomposition is applied in this moving reference frame, the equations for the fluctuation read :

$$\frac{\partial u'_1}{\partial x_1} = 0$$

$$\frac{\partial u'_1}{\partial t} + u'_l \frac{\partial u'_1}{\partial x_l} = -\frac{1}{\rho} \frac{\partial p'}{\partial x_1} + \nu \frac{\partial^2 u'_1}{\partial x_l^2 \partial x_l} - u'_l \left( \frac{\partial U_l}{\partial x_l} + 2 \omega_{ll} \right) - \frac{\partial}{\partial x_l} (u'_1 u'_l - \langle u'_1 u'_l \rangle)$$

The equations for the fluctuation are thus the same in a fixed reference frame and in a moving reference frame if the rotation of the reference frame is added to the mean velocity gradient, in order to recover the mean velocity gradient which exists in the fixed reference frame.

Therefore, the evolution of homogeneous turbulence can be studied as well in a fixed reference frame as in a moving reference frame.

For a mean flow without velocity gradient, a reference frame moving with the flow, as suggested by G.I. TAYLOR, is a convenient reference frame to study the evolution of the turbulent motion. The space evolution problem is then reduced to a time evolution problem.

When there exist velocity gradients, a reference frame moving with the mean flow along a selected streamline is still a good candidate. The mean velocity field can be written as :

$$U_l = U_l^0 + \frac{\partial U_l}{\partial x_m} x_m$$

where  $U^0$  is the velocity of the origin which is assumed to be conveyed by the mean flow along a streamline. For the sake of simplicity, the reference frame is translated and not rotated. The momentum equation then becomes, for homogeneous turbulence :

$$\frac{\partial u'_1}{\partial t} + U_l^0 \frac{\partial u'_1}{\partial x_l} = -\frac{1}{\rho} \frac{\partial p'}{\partial x_1} + \nu \frac{\partial^2 u'_1}{\partial x_l^2 \partial x_l} - u'_l \frac{\partial U_l}{\partial x_l} - \frac{\partial u'_1 u'_l}{\partial x_l} - x_m \frac{\partial U_l}{\partial x_m} \frac{\partial u'_1}{\partial x_l}$$

where the LHS is the time derivative in the moving reference frame, i.e. :

$$\frac{du'_1}{dt} = -\frac{1}{\rho} \frac{\partial p'}{\partial x_1} + \nu \frac{\partial^2 u'_1}{\partial x_l^2 \partial x_l} - u'_l \frac{\partial U_l}{\partial x_l} - \frac{\partial u'_1 u'_l}{\partial x_l} - x_m \frac{\partial U_l}{\partial x_m} \frac{\partial u'_1}{\partial x_l}$$

The problem is so reduced to a time evolution problem in a reference frame linked to the flow.

## 2 - SPECTRAL APPROACH OF TURBULENCE

### 2.1. Introduction

Standard models of turbulence only deal with one-point statistics such as the REYNOLDS stresses or the turbulent kinetic energy. One-point statistics cannot give direct information about the characteristic turbulent length scales. To get information about these length scales and to know how eddies of different sizes contribute to the turbulent motion, one has to look at multi-point statistics. Dealing with high order, multi-point correlations rapidly become cumbersome and even inextricable. Two-point correlations are sufficient to get information.

As pointed out by BATCHELOR /41/, FOURIER analysis is a suitable tool to bring into evidence the rôle of the different length scales in a turbulent motion. CRAYA /1/ derived the equation for two-point correlations and then transformed it in FOURIER space. We shall prefer to immediately FOURIER transform the NAVIER equations to derive more easily the governing equation for any statistics in FOURIER space.

### 2.2. FOURIER transform

The FOURIER transform of a function  $f(\underline{x})$  is defined as :

$$\hat{f}(\underline{k}) = \frac{1}{(2\pi)^3} \int f(\underline{x}) e^{-i\underline{k} \cdot \underline{x}} d^3 \underline{x}$$

where  $\underline{x}$  is the position vector in physical space and  $\underline{k}$  the wave vector. Reciprocally, the function  $f(\underline{x})$  can be obtained from its FOURIER transform as :

$$f(\underline{x}) = \int \hat{f}(\underline{k}) e^{i\underline{k} \cdot \underline{x}} d^3 \underline{k}$$

From the definition of FOURIER transform, it is obvious that, if  $\alpha$  is a constant :

$$\widehat{\alpha f(\underline{x})} = \alpha \hat{f}(\underline{k})$$

Moreover, if  $f$  is real :

$$\hat{f}(-\underline{k}) = \hat{f}^*(\underline{k})$$

where the asterisk denotes the complex conjugate.

Two other important properties of FOURIER transform can be found by looking at derivatives. From the definition of derivatives, it can be easily demonstrated that :

$$\begin{aligned} \widehat{\frac{\partial f(\underline{x})}{\partial x_m}} &= i k_m \hat{f}(\underline{k}) \\ \widehat{\frac{\partial \hat{f}(\underline{k})}{\partial k_m}} &= -i x_m \widehat{f(\underline{x})} \end{aligned}$$

At last, the FOURIER transformation changes product in one space into convolution in the other space. The FOURIER transform of a product then reads :

$$\widehat{f g}(\underline{k}) = \widehat{f} \otimes \widehat{g} = \iint \widehat{f}(\underline{p}) \widehat{g}(\underline{q}) \delta(\underline{k} - \underline{p} - \underline{q}) d^3 p d^3 q$$

where  $\delta$  is the DIRAC distribution  $\delta(\underline{k}) = \frac{1}{(2\pi)^3} \int e^{-i\underline{k}\underline{x}} d^3 x$  which is zero when its argument is non zero and infinite when its argument is zero in such a way as to make :

$$\int \delta(\underline{k}) d^3 k = 1$$

We shall use the incorrect, compacted notation :

$$\widehat{f g}(\underline{k}) = \int \widehat{f}(\underline{p}) \widehat{g}(\underline{k} - \underline{p}) d^3 p$$

For the sake of simplicity, we shall now omit  $\widehat{\phantom{x}}$  to indicate FOURIER transform. The presence of space coordinates  $\underline{x}$  or of wave vectors  $\underline{k}$  is assumed to be enough to know whether the equation is written in physical or FOURIER space.

### 2.3. FOURIER transform of the equations for the turbulent motion

The turbulent motion is ruled by the continuity and momentum equations. The continuity equation :

$$\frac{\partial u'_i}{\partial x_i} = 0$$

is easily FOURIER transformed as :

$$i k_i u'_i = 0 \quad \text{or} \quad k_i u'_i = 0$$

This means that, in FOURIER space, the continuity equation imposes to the velocity field  $\underline{u}(\underline{k})$  to be in a plane normal to the wave vector  $\underline{k}$ . This property is often used to simplify calculations.

We have expressed the momentum equation for the turbulent motion as :

$$\frac{du'_i}{dt} = -\frac{1}{\rho} \frac{\partial p'}{\partial x_i} + \nu \frac{\partial^2 u'_i}{\partial x_j \partial x_j} - u'_j \frac{\partial u'_i}{\partial x_j} - \frac{\partial u'_j u'_i}{\partial x_j} - x_m \frac{\partial u'_j}{\partial x_m} \frac{\partial u'_i}{\partial x_j}$$

With the above mentioned properties of the FOURIER transformation, this equation can be written in FOURIER space as :

$$\frac{du'_i}{dt} = -i k_i \frac{p'}{\rho} - \nu k^2 u'_i - \frac{\partial u'_j}{\partial x_j} u'_i - i k_j \int u'_j(\underline{k} - \underline{p}) u'_i(\underline{p}) d^3 p + \frac{\partial u'_j}{\partial x_m} \frac{\partial}{\partial k_m} (k_j u'_i)$$

The last term of the RHS can be developed as :

$$\frac{\partial u'_j}{\partial x_m} \frac{\partial}{\partial k_m} (k_j u'_i) = \frac{\partial u'_j}{\partial x_m} k_j \frac{\partial u'_i}{\partial k_m} + \frac{\partial u'_j}{\partial x_m} \delta_{jm} u'_i = \frac{\partial u'_j}{\partial x_m} k_j \frac{\partial u'_i}{\partial k_m}$$

as the mean velocity gradient satisfies the continuity equation.

A POISSON equation for the pressure can be obtained by taking the divergence of the momentum equation (i.e. multiplying by  $i k_i$ ). With the help of the continuity equation, the POISSON equation reads :

$$0 = k^2 \frac{p'}{\rho} - 2i k_i \frac{\partial u'_j}{\partial x_j} u'_i + k_i k_j \int u'_j(\underline{k} - \underline{p}) u'_i(\underline{p}) d^3 p$$

In physical space, the pressure at a given point  $\underline{x}$  can be obtained, with the help of the POISSON equation, as an integral of the velocity field over the whole space. In FOURIER space, on the other hand, the pressure at wave vector  $\underline{k}$  can be expressed in terms of the velocity fields  $\underline{u}$  and  $\underline{u} \otimes \underline{u}$  at wave vector  $\underline{k}$ . The pressure can therefore be said local in FOURIER space.

The rôle of the pressure term can be enlightened by looking at the momentum equation written in compact form :

$$A_i + i k_i \frac{p'}{\rho} = 0$$

where  $A_i$  stands for all the other terms. The POISSON equation now reads :

$$k_i A_i + i k^2 \frac{p'}{\rho} = 0$$

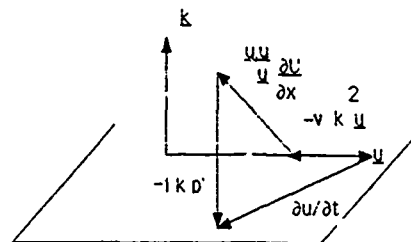
If the pressure is eliminated, the momentum equation can be rewritten as :

$$A_i - \frac{k_i}{k^2} k_j A_j = \left( \delta_{ij} - \frac{k_i k_j}{k^2} \right) A_j = \Delta_{ij}(\underline{k}) A_j = 0$$

The tensor  $\Delta_{ij}(\underline{k})$  corresponds to the projection on the plane normal to the wave vector  $\underline{k}$  as

$\Delta_{ij}(\underline{k}) k_j = \Delta_{ij}(\underline{k}) k_i = 0$ . The continuity equation imposes to the velocity vector  $\underline{u}(\underline{k})$  to be normal to the wave vector  $\underline{k}$ . The terms  $\frac{\partial u'_j}{\partial x_j}$  and  $\nu k^2 u'_i$  satisfy the continuity constraint while the other terms  $\frac{\partial u'_j}{\partial x_m} \frac{\partial}{\partial k_m} (k_j u'_i)$ ,  $\frac{\partial u'_j}{\partial x_m} \frac{\partial k u'_i}{\partial k}$  and  $\underline{u} \otimes \underline{u}$  do not.

The pressure term projects all these terms on the plane normal to the wave vector  $\underline{k}$ ; the rôle of the pressure is to ensure continuity.



The momentum equation can be rewritten by eliminating the pressure term. This can be done either by taking the pressure term from the POISSON equation and replacing it in the momentum equation or directly by multiplying the momentum equation by  $\Delta(\underline{k})$ . The final form of the momentum equation reads :

$$\frac{du_i}{dt} + v k^2 u_i = -u_j \frac{\partial u_i}{\partial x_j} + 2 \frac{k_i k_j}{k^2} \frac{\partial u_i}{\partial x_j} u_j + \frac{\partial u_j}{\partial x_i} \frac{\partial k_j u_i}{\partial k_m} - i k_j \Delta_{ij}(\underline{k}) \int u_j(\underline{k} - \underline{p}) u_i(\underline{p}) d^3 p$$

The advantage of this form for the momentum equation, with pressure term removed, is that the velocity field is now the only unknown. The pressure field, if needed, can be derived from the velocity field with the help of the POISSON equation.

The momentum equation can be written, in symbolic form, as :

$$\left( \frac{d}{dt} + v k^2 \right) u_i = \Delta_{ij}(\underline{k}) \left( -u_j \frac{\partial u_i}{\partial x_j} + \frac{\partial u_j}{\partial x_i} \frac{\partial k_j u_i}{\partial k_m} - i k_j u \otimes u \right)$$

By taking the divergence and using the relation  $k_i \Delta_{ij} = 0$ , we obtain :

$$\left( \frac{d}{dt} + v k^2 \right) k_i u_i = 0$$

If the flow field initially satisfies the continuity constraint, the solution of the momentum equation with pressure term removed will satisfy the continuity constraint at all times. The above form of the momentum equation is thus the only equation to consider as it includes the continuity condition.

#### 2.4. Linear and non linear effects

The terms involved in the momentum equation can be separated into two distinct classes. If the last term is removed, the truncated momentum equation reads :

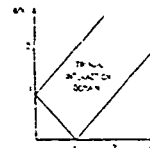
$$\frac{\partial}{\partial t} u_i(\underline{k}) + v k^2 u_i(\underline{k}) = \frac{\partial u_j}{\partial x_i} k_j \frac{\partial u_i(\underline{k})}{\partial k_m} - \frac{\partial u_i}{\partial x_j} u_j(\underline{k}) + 2 \frac{k_i k_j}{k^2} \frac{\partial u_i}{\partial x_j} u_j(\underline{k})$$

In this truncated equation, only the velocity field at wave vector  $\underline{k}$  appears and all operators are linear operators. The influence of the viscosity and of the mean velocity gradient can therefore be called linear effects. These effects only involve the velocity field at the given wave vector.

The convolution term  $-i k_j \Delta_{ij}(\underline{k}) \int u_j(\underline{k} - \underline{p}) u_i(\underline{p}) d^3 p$  represents the action of the turbulent motion upon itself. According to the product under the integral, it will be called non linear effect. An important property of this convolution integral is that it links the evolution of various modes. The flow field at wave vector  $\underline{k}$  interacts with all wave vectors  $\underline{p}$  and  $\underline{q}$  such as  $\underline{k} = \underline{p} + \underline{q}$ . These interactions are called triadic interactions. The set of wave vectors  $\underline{p}$  and  $\underline{q}$  which can form a triangle with wave vector  $\underline{k}$  is a restricted set. According to triangle relations, their modulus, i.e. the wave numbers, must satisfy the inequalities :

$$p + q \geq k \geq |p - q|$$

where the equalities are satisfied when the triangle degenerates into a line segment. The wave vectors which can contribute to triadic interactions with a given wave vector must therefore lie into a semi-infinite rectangle limited by the lines  $k = p + q$ ,  $k = p - q$ ,  $k = q - p$ .



It must be noticed that, according to the POISSON equation, the pressure term involves linear and non linear effects.

The momentum equation has been split into three terms, the viscous and mean velocity gradient terms which correspond to linear effects and the non linear turbulence-turbulence interaction. The characteristic time scales are  $(\nu k^2)^{-1}$  for the viscous effect and  $\left( \frac{\partial u}{\partial x} \right)^{-1}$  for the mean velocity gradient action. As concerns the turbulence/turbulence interaction, a characteristic time scale can be formed with the energy spectrum  $E(k)$  we shall define later and the wave number which are the basic parameters. Dimensional analysis gives a time scale of the form  $(k^3 E(k))^{-1/2}$ . With these time scales, the respective rôle of the three effects can be compared.

In the absence of mean velocity gradient, only the viscous and non linear effects are to be compared. The time scale ratio reads  $\sqrt{\frac{k}{E}}$ . The viscous effect is the leading effect when  $\sqrt{\frac{k}{E}}$  is small compared to the fluid viscosity, i.e. when the turbulent REYNOLDS number is small. This can occur at the end of the decay process when the turbulent kinetic energy is decreasing towards zero. As the turbulence level is low,  $E$  is small and the non linear effect is negligible when compared with the viscous effect. Another possibility is to look at very large wave numbers. As the wave number  $k$  increases, the ratio  $E/k$  decreases, otherwise the turbulent kinetic energy will be infinite. Therefore, at a given wavenumber, viscous effects and non linear effects balance. Above this wave number, the flow is governed by viscous effects. Besides these two cases, i.e. low energy or high wave numbers, the non linear turbulence/turbulence interaction is the leading term.

In presence of mean velocity gradient, we will only compare the mean velocity gradient time scale  $(\frac{\partial U}{\partial x})^{-1}$  and the non linear time scale  $(k^3 E(k))^{-1/2}$ . For a given turbulent field, i.e. for a given energy spectrum, the balance will depend upon the strength of the mean velocity gradient. If the velocity gradient is weak, the linear effect only dominates for small wave numbers while, if the velocity gradient is strong, the linear effect has a leading rôle over a broad part of the turbulent scales. The second case is known as rapid distortion; the mean velocity gradient time scale is smaller than the turbulence time scale and the turbulent motion evolves only under the influence of the mean velocity gradient. This kind of behaviour is however restricted to a short time period as the turbulence tends to adjust its time scale to the mean velocity gradient time scales so that, in fine, linear and non linear effects will balance. However, the study of the rapid distortion plays an important rôle in turbulence theories.

### 2.5. Moments

We shall now turn our attention to statistical properties of turbulence. From the REYNOLDS decomposition of the flow into an average value and a fluctuation, it is obvious that  $\langle u_i(\underline{k}) \rangle = 0$ .

The first interesting statistical variable is the second order moment  $\langle u_i'(\underline{k}) u_j'(\underline{p}) \rangle$ . According to the FOURIER transform definition, it can be expressed as :

$$\langle u_i'(\underline{k}) u_j'(\underline{p}) \rangle = \frac{1}{(2\pi)^6} \int \langle u_i'(\underline{x}) e^{-i\underline{k} \cdot \underline{x}} \int u_j'(\underline{y}) e^{-i\underline{p} \cdot \underline{y}} d^3 \underline{y} \rangle d^3 \underline{x}$$

where  $\underline{x}$  and  $\underline{y}$  are independent variables, so :

$$\langle u_i'(\underline{k}) u_j'(\underline{p}) \rangle = \frac{1}{(2\pi)^6} \iint \langle u_i'(\underline{x}) u_j'(\underline{y}) \rangle e^{-i(\underline{k} \cdot \underline{x} + \underline{p} \cdot \underline{y})} d^3 \underline{x} d^3 \underline{y}$$

The two variables  $\underline{x}$  and  $\underline{y}$  can be replaced by  $\underline{x}$  and  $\underline{x} + \underline{r}$ . As the flow is homogeneous, the two point correlation under the integral only depends upon the separation vector  $\underline{r}$ , so :

$$\langle u_i'(\underline{k}) u_j'(\underline{p}) \rangle = \frac{1}{(2\pi)^6} \int \langle u_i' u_j'(\underline{r}) \rangle e^{-i\underline{p} \cdot \underline{r}} d^3 \underline{r} \int e^{-i(\underline{k} + \underline{p}) \cdot \underline{x}} d^3 \underline{x} = \delta(\underline{k} + \underline{p}) \frac{1}{(2\pi)^3} \int \langle u_i' u_j'(\underline{r}) \rangle e^{-i\underline{p} \cdot \underline{r}} d^3 \underline{r}$$

The homogeneity condition thus allows only a restricted set of non zero second order moments.

For the sake of simplicity, we shall note then :

$$\phi_{ij}(\underline{k}) = \langle u_i'(\underline{p}) u_j'(\underline{k}) \rangle \delta(\underline{k} + \underline{p})$$

The tensor  $\phi_{ij}(\underline{k})$  can be interpreted as the FOURIER transform of the two-point correlation  $\langle u_i'(\underline{x}) u_j'(\underline{x} + \underline{r}) \rangle$ .

The continuity equation imposes :  $k_i \phi_{ij}(\underline{k}) = k_j \phi_{ij}(\underline{k}) = 0$

The two-point correlation only depends upon the separation vector. Moreover,  $\langle u_i'(\underline{x}) u_j'(\underline{x} + \underline{r}) \rangle = \langle u_j'(\underline{x}) u_i'(\underline{x} - \underline{r}) \rangle$  and consequently :

$$\phi_{ij}(\underline{k}) = \phi_{ji}(-\underline{k})$$

At last, the velocity field or the two-point correlation are real function, so :

$$\phi_{ij}(-\underline{k}) = \phi_{ij}^*(\underline{k})$$

These properties can be used to construct a simpler description of the second order moment tensor. Following CRAYA's ideas [1], we introduce a reference frame linked to the wave vector  $\underline{k}$  to take advantage of the continuity equation. We shall use a tri-orthogonal reference frame with basis vectors  $\underline{\alpha}$ ,  $\underline{\beta}$  and  $\underline{\gamma}$ ;  $\underline{\alpha}$  is parallel to the wave vector  $\underline{k}$ . The two-point correlation can be expressed in this reference frame as :

$$\phi_{ij} = P_j \alpha_i + Q_j \beta_i + R_j \gamma_i$$

The continuity constraint imposes  $P_j = 0$ .  $\alpha_j Q_j = \alpha_j R_j = 0$  so that  $Q_j$  and  $R_j$  can be expressed as :

$$Q_j = N_1 \beta_j + S \gamma_j$$

$$R_j = S' \beta_j + N_2 \gamma_j$$

The symmetry and reality constraints impose :

$$\begin{aligned} N_1(-\underline{k}) &= N_1(\underline{k}) = N_1^*(\underline{k}) \\ N_2(-\underline{k}) &= N_2(\underline{k}) = N_2^*(\underline{k}) \\ S(-\underline{k}) &= -S^*(\underline{k}) = -S^*(\underline{k}) \\ S'(-\underline{k}) &= -S(\underline{k}) = -S^*(\underline{k}) \end{aligned}$$

so that the second order moment can be expressed as :

$$\phi_{ij}(\underline{k}) = N_1 \beta_i \beta_j + S \beta_i \gamma_j + S^* \gamma_i \beta_j + N_2 \gamma_i \gamma_j$$

where  $N_1$  and  $N_2$  are real and even with respect to  $\underline{k}$  while  $S(-\underline{k}) = -S^*(\underline{k})$ .  $S$  can be real and, therefore,  $\phi$  can be real only if  $\langle u_i' u_j'(\underline{x}) \rangle = \langle u_i' u_j'(-\underline{x}) \rangle$ . This condition is fairly satisfied by grid turbulence. Thus,  $\phi_{ij}(\underline{k}) = \phi_{ij}(-\underline{k}) = \phi_{ji}(\underline{k}) = \phi_{ji}^*(\underline{k})$ , so  $\phi_{ij}(\underline{k})$  is real and symmetric.

The second order moment, which has a priori nine different components, has been reduced to three independent variables with the use of a suitably chosen reference frame. CRAYA /1/ has proposed the use of a reference frame linked to the wave vector and has derived all the algebra needed to easily use this reference frame. This reference frame is given in Appendix A.

The interpretation of second order moment as the FOURIER transform of two-point correlations enlightens the physical meaning of the wave vector. In homogeneous turbulence, statistics depend only upon the separation vectors and not upon the location. Wave vectors are the reciprocal of separation vectors, i.e. they are related to the size and the direction of the turbulent structure which contribute to the turbulent motion. The study in FOURIER space is thus an analysis of the contribution of turbulent structures according to their sizes and orientations.

A similar analysis can be conducted for the third order moment  $\langle u_i'(\underline{k}) u_j'(\underline{p}) u_l'(\underline{q}) \rangle$  /1/. Here again the homogeneity imposes  $\underline{k} + \underline{p} + \underline{q} = 0$  and this moment can be interpreted as the FOURIER transform of three-point correlation with respect to two separation vectors. Similarly, the third order tensor can be reduced to a restricted set of constants. We shall use the notation :

$$i \langle u_i'(\underline{k}) u_j'(\underline{p}) u_l'(\underline{q}) \rangle = \phi_{ijl}(\underline{p}, \underline{q}) \delta(\underline{k} + \underline{p} + \underline{q})$$

The continuity equation thus imposes :

$$(p_i + q_i) \phi_{ijl}(\underline{p}, \underline{q}) = p_j \phi_{ijl}(\underline{p}, \underline{q}) = q_l \phi_{ijl}(\underline{p}, \underline{q}) = 0$$

## 2.6. Evolution equation for the second order moment

BURGERS and MITCHER /42/ and CRAYA /1/ have derived transport equations for the second and third order moments. They first obtained equations for the two- and three-point correlations and then FOURIER transformed these equations. A more convenient way, as proposed by CAMBON et al /43/, is to derive these equations from the FOURIER transformed momentum equation. The transport equation for the second order moment is obtained by multiplying the momentum equation for  $u_i'(\underline{k})$  by  $u_j'(-\underline{k})$ , multiplying the momentum equation for  $u_j'(-\underline{k})$  by  $u_i'(\underline{k})$ , adding and taking averages. It reads :

$$\begin{aligned} \frac{d}{dt} \phi_{ij}(\underline{k}) + 2\nu k^2 \phi_{ij}(\underline{k}) &= -\phi_{il}(\underline{k}) \frac{\partial u_j}{\partial x_l} - \phi_{lj}(\underline{k}) \frac{\partial u_i}{\partial x_l} + 2 \frac{\partial u_m}{\partial x_l} \frac{k_m}{k^2} (k_i \phi_{lj}(\underline{k}) + k_j \phi_{il}(\underline{k})) \\ &+ \frac{\partial u_m}{\partial x_l} \frac{\partial}{\partial k_l} (k_m \phi_{ij}(\underline{k})) + \Delta_{il}(\underline{k}) k_m \int \phi_{lmj}(\underline{p}, \underline{k}) d^3 p \\ &+ \Delta_{lj}(\underline{k}) k_m \int \phi_{lmi}(\underline{p}, \underline{k}) d^3 p \end{aligned}$$

The transport equation for the third order moment can be obtained similarly. As we shall not use it in the general case, we refer the reader to reference /1/.

## 2.7. Connections with one-point closures

The use of FOURIER space enables us to get information on the contributions of eddies of different scales to the turbulent motion. On the other hand, it leads to an increasing number of unknowns so that it would require enormous computational time in complex flows.

One-point closures, dealing only with one-point statistics in physical space, are more suitable to study complex flows. It is important to know what moment to study in FOURIER space to obtain information on the unknowns in one-point closures.

One-point closures are aimed at computing the REYNOLDS stress  $\langle u_i' u_j' \rangle$ . From the reciprocal FOURIER transform, two-point correlations are obtained as :

$$\langle u_i' u_j'(\underline{x}) \rangle = \int \phi_{ij}(\underline{k}) e^{-i \underline{k} \cdot \underline{x}} d^3 k$$

and so the REYNOLDS stresses can be derived, for zero separation, as :

$$\langle u_i' u_j' \rangle = \int \phi_{ij}(\underline{k}) d^3 \underline{k}$$

The second order moment contains the information about the contribution of each wave vector to the REYNOLDS stresses. The second order moments can be interpreted as the "spectrum" of the REYNOLDS stresses. Their knowledge is a priori sufficient to derive useful information for one-point closures.

A variable used in most one-point closure model is the turbulent kinetic energy  $\frac{1}{2} q^2 = \frac{1}{2} \langle u_i' u_i' \rangle$ . It is obvious that  $\frac{1}{2} q^2 = \int \frac{1}{2} \phi_{ii}(\underline{k}) d^3 \underline{k}$ . However, it is customary not to look at the contribution of each wave vector to the kinetic energy but to consider the contribution of each wave number. The energy spectrum is then defined as an integral over the sphere of radius  $k$  :

$$E(k) = \frac{1}{2} \int_{||\underline{k}||=k} \phi_{ii} dA(k)$$

and the turbulent kinetic energy is thus obtained as :

$$\frac{1}{2} q^2 = \int E(k) dk$$

As the second order moments can be interpreted as the spectrum of the REYNOLDS stresses, it is interesting to compare the transport equation for both quantities. With the homogeneity assumption, the transport equation for the REYNOLDS stresses reads :

$$\frac{d}{dt} \langle u_i' u_j' \rangle = - \langle u_i' u_k' \rangle \frac{\partial u_j}{\partial x_k} - \langle u_j' u_k' \rangle \frac{\partial u_i}{\partial x_k} + \langle p' \left( \frac{\partial u_i}{\partial x_j} + \frac{\partial u_j}{\partial x_i} \right) \rangle - 2\nu \langle \frac{\partial u_i}{\partial x_k} \frac{\partial u_j}{\partial x_k} \rangle$$

From the relation between the REYNOLDS stresses and the second order moments, the time derivative terms can be connected as :

$$\frac{d}{dt} \langle u_i' u_j' \rangle = \int \frac{d}{dt} \phi_{ij}(\underline{k}) d^3 \underline{k}$$

and also :

$$- \langle u_i' u_k' \rangle \frac{\partial u_j}{\partial x_k} - \langle u_j' u_k' \rangle \frac{\partial u_i}{\partial x_k} = \int \left( - \phi_{ik}(\underline{k}) \frac{\partial u_j}{\partial x_k} - \phi_{kj}(\underline{k}) \frac{\partial u_i}{\partial x_k} \right) d^3 \underline{k}$$

which represents the production of turbulence by action of the velocity gradient upon the REYNOLDS stresses, i.e. a kinetic energy exchange between the mean flow and the turbulent motion.

The connection between the viscous terms is obvious as :

$$- 2\nu \langle \frac{\partial u_i}{\partial x_k} \frac{\partial u_j}{\partial x_k} \rangle = - \int 2\nu k^2 \phi_{ij}(\underline{k}) d^3 \underline{k}$$

The contribution to the pressure strain correlation at wave number  $\underline{k}$  can be obtained by deriving the pressure from the POISSON equation as :

$$\frac{p'(\underline{k})}{\rho} = - 2i \frac{k_i}{k^2} \frac{\partial u_i}{\partial x_j} u_j' + \frac{k_i k_j}{k^2} \int u_i'(\underline{k} - \underline{p}) u_j'(\underline{p}) d^3 \underline{p}$$

The pressure strain correlation can thus be obtained as :

$$\langle p' \frac{\partial u_i}{\partial x_j} \rangle = 2 \frac{\partial u_j}{\partial x_m} \int \frac{k_i k_m}{k^2} \phi_{im}(\underline{k}) d^3 \underline{k} - \iint \frac{k_i k_m k_n}{k^2} \phi_{imn}(\underline{p}, \underline{k}) d^3 \underline{p} d^3 \underline{k}$$

Each term in the above equation is trace-free ; they redistribute the energy among the components of the turbulent kinetic energy. As the rôle of the pressure is to ensure the continuity constraint at the wave vector level or, in other words, as the pressure is local in FOURIER space, the pressure strain terms redistribute energy at the wave vector level. At last, it must be noticed that the contribution of the pressure is twofold ; the first term is a linear term due to the action of the mean velocity gradient while the second term is a non linear term due to turbulence/turbulence triadic interactions.

## 2.8. Transfers

The connection between the second order moment equation and the REYNOLDS stress transport equation has brought into evidence the rôle of various terms in the moment equation. However, the terms

$\frac{\partial u_m}{\partial x_l} \frac{\partial}{\partial k_l} (k_m \phi_{ij}(\underline{k}))$  and  $\delta_{il} k_m \int \phi_{lmj}(\underline{p}, \underline{k}) d^3 \underline{p} + \delta_{jl} k_m \int \phi_{ilm}^*(\underline{p}, \underline{k}) d^3 \underline{p}$  have not been concerned. As the REYNOLDS stress transport equation can be derived from the second order moment equation by integration over the FOURIER space, the integrals of these terms are zero. It is easily verified that :

$$\int \frac{\partial}{\partial k_l} (k_m \phi_{ij}(\underline{k})) d^3 \underline{k} = 0$$

as  $k^n \phi_{ij}(\underline{k})$  tends towards zero when  $k$  becomes infinite, otherwise correlation of high order derivatives should be infinite in physical space. The physical meaning of this term will be detailed in the next chapter.



The study of the other integral is more cumbersome and instructive. Let us start with the basic term, i.e. :

$$\delta_{il} k_m u_l'(q) u_m'(p) u_j'(k) \quad \delta(k + p + q)$$

In this term, the wave vectors  $p$  and  $q$  play the same rôle, so this term can be written in a symmetric form as :

$$\frac{1}{2} \delta(k + p + q) (k_m u_l'(q) u_m'(p) u_j'(k) + k_m u_l'(p) u_m'(q) u_j'(k))$$

If we now sum the three terms obtained by circular permutation of the three wave vectors, we get :

$$\begin{aligned} & k_m u_l'(q) u_m'(p) u_j'(k) + k_m u_l'(p) u_m'(q) u_j'(k) \\ & p_m u_l'(k) u_m'(q) u_j'(p) + p_m u_l'(q) u_m'(k) u_j'(p) \\ & q_m u_l'(p) u_m'(k) u_j'(q) + q_m u_l'(k) u_m'(p) u_j'(q) \end{aligned}$$

The terms are now grouped according to the  $u_m'$  term ; one of the three groups reads :

$$u_m'(p) (k_m u_l'(q) u_j'(k) + q_m u_l'(k) u_j'(q))$$

and a symmetric group can be formed by permuting the indices  $i$  and  $j$ . Thus, from the continuity equation, the sum :

$$u_m'(p) (k_m u_l'(q) u_j'(k) + q_m u_l'(q) u_j'(k))$$

is null as  $k + p + q = 0$ . Consequently, if we note :

$$T_{ij}^1(k, p, q) = \delta_{il} k_m \int \phi_{lmj}^*(p, k) d^3p + \delta_{jl} k_m \int \phi_{lmj}^*(p, k) d^3p$$

and

$$T_{ij}^1(k, p, q) = T_{ij}^1(k, p, q) + T_{ji}^1(k, p, q)$$

we have :

$$T_{ij}^1(k, p, q) + T_{ij}^1(p, q, k) + T_{ij}^1(q, k, p) = 0.$$

Thus,  $\iiint T_{ij}^1(k, p, q) \delta(k + p + q) d^3p d^3k = 0$ , as supposed previously.

This part of the triadic interaction does not delete or create REYNOLDS stresses ; it is just an exchange of contribution to the REYNOLDS stresses between wave vectors which form a triangle. We shall use the term of detailed conservation to emphasize the fact that the conservation holds for any arbitrary triad of wave vectors.

The two terms we have first studied have zero integrals over the FOURIER space and do not directly contribute to the REYNOLDS stress budget. These terms correspond to transfer of the REYNOLDS stress spectrum between wave vectors, without creation or destruction of the REYNOLDS stress. They are called transfer terms. The first term is due to the action of the mean velocity gradient and is a linear effect. As will be shown below, this term represents the drift of eddies in the FOURIER space as they are distorted by the mean velocity gradient. The transfer due to linear effects deals with neighbouring wave vectors. By contrast, the non linear transfer concerns all wave vectors which can form a triad, i.e. as shown previously, a band in FOURIER space.

## 2.9. Conclusion

The study of the momentum equation has led us to introduce the notions of linear and non linear effects to characterize the action of the mean velocity gradient upon turbulence and the triadic interactions between turbulent modes.

The analysis of the transport equation for the second order moment has brought into evidence the different ways this moment is altered. Production terms due to the mean velocity gradient create second order moments. Pressure terms redistribute them among the components of the energy spectrum at a given wave vector while transfer terms cause exchanges between wave vectors. Both pressure and transfer terms have linear and non linear parts. At last, viscosity destroys the second order moments and converts the turbulent motion into heat.

The most striking difference lies between linear and non linear terms. Linear terms only involve second order moments at a given wave vector. Non linear terms, due to the triadic interaction, introduce the third order moment in the second order moment equation. An equation can be derived for the third order moment, but the non linear term will now introduce fourth order moments and so on, ad infinitum. An infinite hierarchy of equations can be constructed without closing the problem. Linear terms lead to a closed problem, the solution of which can be obtained analytically while non linear terms require modelling. Therefore, we shall study these two problems separately.

## 3 - THE LINER PROBLEM

## 3.1. Introduction

We have already seen that, if the mean velocity gradient is strong enough, the non linear effects are negligible with respect to the mean velocity gradient effect. The second order moment equation can then be reduced to :

$$\frac{d}{dt} \phi_{ij} + 2 \nu k^2 \phi_{ij} = - \phi_{il} \frac{\partial U_l}{\partial x_j} - \phi_{lj} \frac{\partial U_l}{\partial x_i} + 2 \frac{\partial U_m}{\partial x_l} \frac{k_m}{k^2} (k_l \phi_{lj} + k_j \phi_{il}) + \frac{\partial U_m}{\partial x_l} \frac{\partial}{\partial k_l} (k_m \phi_{ij})$$

This simplified equation is known as rapid distortion model. It must be kept in mind that it is valid over all the wave number range for only a short period of time as the turbulent field will respond in such a way that the turbulence time scale will become of the same order of magnitude as the mean velocity gradient time scale and non linear effects will no longer be negligible.

Rapid distortion has already been studied by various groups. TOWNSEND /44/ and CAMBON /45/ proposed to study the effect of the mean velocity gradient directly on the fluctuating motion. BATCHELOR /46/ gave the solution of the second order moment equation with viscosity term neglected for strained turbulence. DEISSLER /47/ conducted numerical studies of sheared turbulence. COURSEAU and LOISEAU /48/ gave analytical solution for turbulence submitted to plane shear or strain and tried to extend the method for third order moments. LEE et al /49/ gave an original solution for arbitrary strain. A recent review on rapid distortion theory for inhomogeneous flows has been given by SAVILL /111/.

## 3.2. Solution of the linear problem

For specified initial data, the above linear equation can be integrated by numerical means. Analytical solutions are however much more convenient for further theoretical studies.

We shall adopt the methodology proposed by CAMBON et al /45/ as it is more powerful. We shall just bring into evidence the key ideas of this method. The reader is referred to the original papers /45, 50, 51/ for further details on the calculations.

The first point is to solve the linear problem not for a moment equation but directly for the fluctuation equation. The fluctuating field at a given time is expressed as a function of the fluctuating field at the initial time. All moments can thus be constructed and developed in terms of moments at the initial time. This method is more powerful than the classical method which solves the linear problem only for a given moment equation. The equation to be solved is the momentum equation for the fluctuating motion with non linear terms discarded, i.e. :

$$\frac{\partial u_i'}{\partial t} + \nu k^2 u_i' = - u_l' \frac{\partial U_l}{\partial x_i} + 2 \frac{k_l k_i}{k^2} \frac{\partial U_l}{\partial x_j} u_l' + \frac{\partial U_l}{\partial x_m} \frac{\partial}{\partial k_m} (k_l u_i')$$

The second point is the analysis of the term  $\frac{\partial u_i'}{\partial t} - \frac{\partial U_l}{\partial x_m} \frac{\partial}{\partial k_m} (k_l u_i')$ . They are the FOURIER transform of the advection term  $\frac{\partial u_i}{\partial t} + x_m \frac{\partial u_i}{\partial x_m} \frac{\partial}{\partial x_l}$  in physical space. In physical space, these terms represent the time derivative in a lagrangian reference plane, i.e. following a mean flow streamline. Similarly, in FOURIER space, this term corresponds to a time derivative following trajectories in FOURIER space as eddies are stretched and rotated by the mean velocity gradient. The advection process can be described by the deformation matrix which links the coordinates of a particule at time  $t$  to their values at the time origine :

$$x_i(t) = F_{ij}(t) x_j(t=0)$$

or, reciprocally, from the FOURIER transform definition :

$$k_i(t) = F_{ji}^{-1}(t) k_j(t=0)$$

The deformation matrix is easily obtained as :

$$F_{ij}(t=0) = \delta_{ij}$$

$$\frac{dF_{ij}}{dt} = \frac{\partial U_l}{\partial x_j} F_{li}(t)$$

This deformation matrix is often used in direct simulations of turbulence to transform the eulerian reference frame into a lagrangian reference frame (see e.g. ref. /49/ and /52/). In the lagrangian reference frame, the momentum equation reduces to :

$$\frac{du_i'}{dt} + \nu k^2 u_i' = \left( 2 \frac{k_l k_i}{k^2} \frac{\partial U_l}{\partial x_j} - \frac{\partial U_l}{\partial x_l} \right) u_l'$$

with

$$u'(t) = u^T F^{-1} k(t=0) \quad k = F^{-1} k(t=0)$$

The resolution of the above equation proceeds in two steps. The first step is the removal of the viscosity term. In the simple case without velocity gradient, the wave vector does not depend upon time and the LHS can be rewritten as :

$$\frac{du_i'}{dt} + \nu k^2 u_i' = e^{-\nu k^2 t} \frac{d}{dt} (e^{\nu k^2 t} u_i')$$

In the general case, the time dependence of the wave vector  $k$  leads to a more complicated form. The second step is the use of a GREEN's function to solve the equation. The final solution reads :

$$u_i(k, t) = \exp(-\nu \int_0^t V_{ln}(t) k_l k_n) G_{ij}(k, t) u_j(k(t=0), 0)$$

where  $V_{ln}$  is defined as a time integral of a function of the deformation motion  $F$  while the GREEN's function  $G$  is the solution of :

$$\frac{dG_{ij}}{dt} = \left( 2 \frac{k_i k_m}{k^2} \frac{\partial u_m}{\partial x_l} - \frac{\partial u_i}{\partial x_l} \right) G_{lj}$$

with the initial condition  $G_{ij}(t=0) = \Delta_{ij}$  to satisfy the continuity equation. The use of the CRAYA's reference frame simplifies the computation of the GREEN's function.

As the linear problem is solved for the fluctuating motion, all moments can be constructed. For example, the second order moment reads :

$$\phi_{ij}(k) = \exp(-2\nu \int_0^t V_{ln}(t) k_l k_n) G_{ip}(-k, t) G_{jq}(k, t) \phi_{pq}(k(t=0))$$

The solution algorithm developed by CAMBON is very powerful as it can treat any mean velocity gradient, any initial condition, and give information about any moment. Of course, solutions previously found in simple cases are verified by this method.

Let us finally mention some published solutions which can be directly used to test closures. COURSEAU and LOISEAU /48/ gave the evolution of second order moments for an initially isotropic turbulence submitted to strain or shear. Recently, LEE et al /49/ gave the evolution of the REYNOLDS stresses and vorticity correlations for isotropic turbulence submitted to strain in terms of time series.

### 3.3. Examples of applications

Rapid distortion theory has been used by BOSCHIERO et al /53/ to study the effects of two successive plane strains on turbulence in order to design the experiments conducted by GEKCE and MATHIEU /26/. They focused their attention on quantities which can easily be measured in an experiment, mainly the REYNOLDS stresses  $\langle u_i u_j \rangle$ . The REYNOLDS stresses can be represented by forming invariants, i.e. reference frame independent scalars. The first invariant is the turbulent kinetic energy which is half the trace :

$$\frac{1}{2} q^2 = \frac{1}{2} (\langle u^2 \rangle + \langle v^2 \rangle + \langle w^2 \rangle)$$

The departure from isotropy of the REYNOLDS stresses can be characterized by the anisotropy tensor defined as :

$$b_{ij} = \frac{\langle u_i u_j \rangle}{q^2} - \frac{\delta_{ij}}{3}$$

which is a symmetric, second order, traceless tensor. Due to the CAYLEY-HAMILTON theorem, only two invariants can be formed with such a tensor, i.e. :

$$II = \text{tr } b^2 \quad III = \text{tr } b^3$$

where  $\text{tr}$  indicates the trace.

Rapid distortion theory does not account for non linear effects, so energy transfer and dissipation are not included in the model. When viscous terms are omitted, energy is conserved ; when viscous terms are included, the energy decay is poorly predicted at high REYNOLDS numbers as energy transfers are not accounted for. Consequently, the evolution of the turbulent kinetic energy is badly predicted by the rapid distortion theory, as shown on figure 7. However, the influence of the relative angle between two successive plane strains is brought into evidence by the calculation. Moreover, the evolution of the anisotropy, which is less affected by the transfer, is qualitatively well reproduced by the rapid distortion theory. It must be kept in mind that, in this experiment, the strain and turbulence time scales are of the same order of magnitude so that rapid distortion hypothesis is not valid.

Another example deals with the study of turbulence submitted to a plane shear. In such a flow, we are mainly interested in the non diagonal REYNOLDS stress  $\langle u'v' \rangle$  due to the shear  $\partial U/\partial y$ . Here again, the rapid distortion theory is unable to predict the REYNOLDS stress level but gives a good estimate of the time evolution of the anisotropy, when compared with experiment, as shown on figure 9.

## 4 - THE NON LINEAR PROBLEM

### 4.1. Introduction

As already mentioned, the equation for the  $n^{\text{th}}$  order moment exhibits the  $(n+1)^{\text{th}}$  order moment because of the non linear terms. An infinite set of equations can so be derived but the problem cannot be solved by analytical means ; modelling is required.

For the sake of simplicity, we shall restrict our presentation to isotropic turbulence without mean velocity gradients. The influence of mean velocity gradients on non linear terms has been recently studied by CAMBON /45/, /50/ and BERTOGLIO /55/.

In this chapter, we shall just try to bring into evidence the various ideas used to tackle the problem. Readers interested in the closure of the non linear problem may refer to the books of LESLIE /56/ and LESIEUR /108/, the lectures of ORSZAG /57/ and the papers of KRAICHNAN and ORSZAG.

#### 4.2. Isotropic turbulence spectrum

Isotropic turbulence is rotation-invariant turbulence. All statistical properties depend only upon the modulus of the separation vector, not upon its direction. As concerns the REYNOLDS stresses, the isotropy hypothesis leads to :

$$\langle u_i' u_j' \rangle = \frac{\delta_{ij} q^2}{3}$$

As concerns the second order moment, the isotropy hypothesis and the continuity constraint give :

$$\phi_{ij}(\underline{k}) = \frac{1}{2} \Delta_{ij}(\underline{k}) U(|\underline{k}|)$$

where  $U(|\underline{k}|)$  is the energy density on the sphere of radius  $k$ . The factor  $\frac{1}{2}$  is used to have :

$$\phi_{ii}(\underline{k}) = U(|\underline{k}|)$$

and consequently :

$$E(k) = 2\pi k^2 U(k)$$

The isotropy hypothesis highly simplifies the problem as the knowledge of second order moments is reduced to the knowledge of energy spectrum which depends only upon the wave number.

Isotropic turbulence can exist only in the absence of mean velocity gradients. Strain elongates eddies in one direction, compresses them in another so that the isotropy hypothesis is no longer valid. Similarly, rotation introduces a preferred direction, the rotation axis and isotropy is broken.

Momentum equation, without mean velocity gradient, reduces to :

$$\frac{\partial u_i'}{\partial t} + v k^2 u_i' = -ik_l \Delta_{lj}(\underline{k}) \int u_j'(\underline{k} - \underline{p}) u_l'(\underline{p}) d^3 p$$

It is customary, and convenient too, to symmetrize the RHS ; the momentum equation can then be written as :

$$\frac{\partial u_i'}{\partial t} + v k^2 u_i' = -\frac{i}{2} \Delta_{ijl}(\underline{k}) \int u_j'(\underline{k} - \underline{p}) u_l'(\underline{p}) d^3 p$$

with

$$\Delta_{ijl}(\underline{k}) = k_l \Delta_{ij}(\underline{k}) + k_j \Delta_{il}(\underline{k})$$

This symmetrized form has already been used to study the detailed conservation property of the non linear transfer term.

#### 4.3. Energy spectrum

The energy spectrum can be interpreted as the integral, over spheres of constant wave number, of half the trace of the second order moment. The evolution equation for the energy spectrum can be directly derived from the second order moment equation. With the above symmetrized momentum equation, this equation reads :

$$\frac{\partial}{\partial t} E(k) + 2vk^2 E(k) = T(k) = \iiint_{\underline{k} = \underline{p} + \underline{q}} T(\underline{k}, \underline{p}, \underline{q}) d^3 p d\Lambda(k)$$

where  $T(k)$  is the transfer at wave number  $k$  due to the interactions with all wave vectors which form a triangle. It must be noticed that the isotropy assumption implies that the detailed transfer  $T(\underline{k}, \underline{p}, \underline{q})$  depends only upon the magnitude of the three wave vectors  $\underline{k}$ ,  $\underline{p}$  and  $\underline{q}$ , not upon their direction. The integral extends upon all wave vectors  $\underline{p}$  and  $\underline{q}$  and over the sphere of radius  $k$ , i.e. over all possible directions for the wave vector  $\underline{k}$ . At last, the detailed transfer can be expressed as :

$$T(\underline{k}, \underline{p}, \underline{q}) = \frac{1}{2} I_m(\Delta_{ijl}(\underline{k}) \phi_{jl}(-\underline{k}, \underline{p})) \quad (\text{with } \underline{k} = \underline{p} + \underline{q})$$

where  $I_m$  stands for imaginary part of the complex variable. It must be kept in mind that this detailed transfer conserves energy, i.e. :

$$T(\underline{k}, \underline{p}, \underline{q}) + T(\underline{q}, \underline{k}, \underline{p}) + T(\underline{p}, \underline{q}, \underline{k}) = 0$$

If viscosity is turned off, the energy spectrum evolves only under the influence of the transfer term. The transfer term does not create or delete energy so that the kinetic energy is conserved. If the energy is initially concentrated in a narrow band, triadic interactions will immediately redistribute this energy to all wave vectors which can make triadic interactions with an energy containing mode, i.e. triadic interactions will redistribute this energy over all the space of wave vectors.

We shall now imagine that there exists a maximum value for the wave number, i.e. a minimum value for the size of the turbulent motion. This kind of situation seems to be difficult to realize experimentally but is easily treated by numerical or analytical means. The rôle of the transfer is then to share energy among all possible modes. After a sufficient time, a steady state is reached in which energy is uniformly distributed over all modes. The energy density  $U(k)$  is then constant and the energy spectrum  $E(k) = 2\pi k^2 U(k)$  behaves as  $k^2$ . The density can be found from the knowledge of the kinetic energy :

$$\frac{1}{2} q^2 = \int_0^{k_{\max}} E(k) dk = \frac{2\pi}{3} k_{\max}^3 U$$

When the fluid is viscous, which is the real case, the evolution of the energy spectrum results from the balance between transfer and viscous effects. The rôle of viscosity is to dissipate turbulent kinetic energy into heat while the rôle of the transfer term is to redistribute energy among all the modes. The analysis of the orders of magnitude of both terms has shown that, for large enough wave numbers, viscosity plays the dominant rôle. The order of magnitude of the wave number where viscous effects are important, can be obtained from the dissipation rate  $\epsilon$  and the viscosity  $\nu$ . Dimensional analysis shows that this wave number, known as the KOLMOGOROV wave number, must be  $k_D \sim \left(\frac{\epsilon}{\nu^3}\right)^{1/4}$ .

Let us now suppose that energy is injected, at a constant rate  $\epsilon$ , in an hypothetical isotropic manner, at a wave number small compared to the KOLMOGOROV wave number. Energy is distributed among the wave numbers by the non linear transfer and dissipated by viscosity, mainly at higher wave numbers. After some times, an equilibrium energy spectrum is found; energy injected at low wave number is dissipated into heat at high wave numbers. Between the wave numbers where energy is injected and the range of wave numbers where it is dissipated, there may exist a range of wave numbers where viscosity plays little rôle and where the rôle of the transfer is to "convey" the energy from lower to higher wave numbers. The spectrum in this region depends upon the wave number and the energy injection rate. Dimensional analysis shows that the energy spectrum reads :

$$E(k) = K_0 \epsilon^{2/3} k^{-5/3}$$

This spectrum law is known as KOLMOGOROV spectrum or inertial range spectrum. This law has been derived for a stationary solution, in a region where viscous effects are negligible. The equation for the energy spectrum then reduces to  $T(k) = 0$ , i.e. in this wave number range, the non linear energy transfer does not input or output energy; the energy injected at a given wave number by some triadic interactions is extracted by others. As energy transfers are mainly efficient between structures of similar sizes, i.e. close wave numbers, energy cascades down the inertial range from the low wave number range in which it is injected to the range where it is dissipated by viscous effects. The existence of a  $k^{-5/3}$  inertial range is difficult to bring into evidence in usual homogeneous turbulence experiments because the turbulent REYNOLDS number is low and this range, when it exists, is small. However, in geophysical turbulent flows where REYNOLDS numbers are very large, the inertial range can extend over decades of wave numbers. Experiments performed by GRANT et al /58/ in a tidal channel have brought clear evidence of the existence of such spectrum. Such experiments can be used to evaluate the constant  $K_0 \sim 1.4$ .

The KOLMOGOROV law cannot be valid over all the wave number range, otherwise the integrals :

$$\frac{1}{2} q^2 = \int_0^\infty E(k) dk$$

$$\epsilon = 2\nu \int_0^\infty k^2 E(k) dk$$

which give the turbulent kinetic energy and its dissipation range both diverge. Viscous effects dissipate energy and damp the energy spectrum at high wave numbers. It can be noticed that, as fluctuation derivatives correlation read :

$$\left\langle \frac{\partial^2 u}{\partial x^2} \frac{\partial^2 u}{\partial x^2} \right\rangle = \int_0^\infty k^2 E(k) dk$$

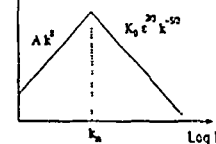
the energy spectrum must be steeper than any  $k^{-m}$  as  $k$  tends towards infinity, so that these correlations should be finite. The divergence of the energy integral is due to the behaviour of KOLMOGOROV law when the wave number tends towards zero. In the vicinity of zero, the energy spectrum can be expressed in TAYLOR series as  $E(k) = Ak^s + O(k^{s+1})$ . The convergence of the energy integral imposes  $s > -1$ . The study of turbulence decay imposes  $-1 \leq s \leq 4/59$ .

The complete figure of the energy spectrum now emerges, with a growing  $k^s$  spectrum, at low wave number, a maximum corresponding to energy-containing eddies, an inertial range along which energy cascades to be dissipated in a viscous range where the spectrum falls rapidly. Experimental measurements, such as the ones performed by COMTE-BELLOT and CORRSIN /3, 4/ or VAN ATTA and YEH /7, 8/ confirm the image (figure 11). The energy transfer can also be measured. The figure 12 shows the rôle of the energy transfer which removes energy from the energy-containing range to the dissipative range. It must be noticed that, in this experiment, the REYNOLDS number is too low, no inertial range exists and the energy transfer is null only for one wave number.

The existence of an inertial range only at sufficiently high REYNOLDS number can be easily explained by considering a simplified energy spectrum made with two power laws :  $\log E$

$$k < k_m \quad E(k) = A k^s$$

$$k > k_m \quad E(k) = K_0 \epsilon^{2/3} k^{-5/3}$$



which mimics real energy spectra. The turbulent kinetic energy reads :

$$\frac{1}{2} q^2 = \int_0^\infty E(k) dk = \int_0^{k_m} A k^s dk + \int_{k_m}^\infty K_0 \epsilon^{2/3} k^{-5/3} dk = \frac{1}{s+1} A k_m^{s+1} + \frac{3}{2} K_0 \epsilon^{2/3} k_m^{-2/3}$$

$$= \left( \frac{1}{s+1} + \frac{3}{2} \right) K_0 \epsilon^{2/3} k_m^{-2/3}$$

so that

$$k_m = \left( \frac{3s+5}{2(s+1)} K_0 \right)^{3/2} \frac{\epsilon}{(\frac{1}{2} q^2)^{3/2}}$$

On the other hand, the KOLMOGOROV wave number, which is characteristic of the dissipation range reads :  $k_D = \left( \frac{\epsilon}{\nu^3} \right)^{1/4}$  so that the ratio :

$$\frac{k_D}{k_m} = \left( \frac{3s+5}{2(s+1)} K_0 \right)^{-3/2} \frac{(\frac{1}{2} q^2)^{3/2}}{(\epsilon \nu)^{3/4}} = R_e^{3/4}$$

where  $R_e = \frac{(q^2)^2}{9\nu\epsilon}$  is the turbulent REYNOLDS number. For low Reynolds numbers, the energy-containing range and the dissipation range overlap and, as the REYNOLDS number increases, these two ranges separate and leave room for an inertial range in between.

#### 4.4. Simple non linear models

The first models proposed to estimate the non linear effects tried to model directly the energy transfer  $T(k)$ . KOVASZNAVY /60/ proposed to express the energy transfer at wave number  $k$  directly in terms of the energy spectrum at wave number  $k$ . He considered the energy flux at wave number  $k$ , i.e. :

$$W = \int_0^k -T(k) dk$$

and expressed it as :

$$W = C_K k^{5/2} E^{3/2}$$

which is such that the energy flux is constant and equal to  $\epsilon$  in an inertial range provided that  $C_K = K_0^{-3/2}$ . KOVASZNAVY mentioned that this coefficient  $C_K$  could be REYNOLDS number dependent. Such a model is clearly too simple to account for the dynamics of triadic interactions. For example, the influence of a local disturbance in the energy spectrum /10, 11, 12/ cannot be accounted for.

Let us now consider the case of a spectrum with a scale separation such as the one depicted on figure 13. The small eddies have little energy and small scales when compared with the large eddies. They can be viewed as a Brownian motion superimposed on the large eddies. Such a Brownian motion extracts energy from the large scales through an effective viscosity. By analogy with the viscous effects, this energy exchange reads :

$$\int_{k_0}^{k_1} -T(k) dk = \int_{k_0}^{k_1} 2\nu_e k^2 E(k) dk$$

HEISENBERG /61/ proposed to extend this formula to continuous energy spectra. He assumed the effective viscosity to be wave number independent and expressed it in terms of the energy spectrum of the small scales. The final model, dictated by dimensional analysis, reads :

$$W(k) = \int_0^k -T(k) dk = C_H \int_0^k 2k^2 E(k) dk \int_k^\infty \frac{E}{k^3} dk$$

with  $C_H = \frac{1}{2} K_0^{-3/2}$ .

Such a model links the energy transfer at a given wave number to the energy spectrum over all the wave number range. The HEISENBERG model can give fairly good predictions of isotropic decaying turbulence. However, it is unable to give information about the detailed energy transfer  $T(k, p, q)$  and it is difficult to extend to anisotropic flows.

Some other simple models have been proposed using similar approaches. Recently, CROCCO /62/ revisited KOVASZNAVY and HEISENBERG models to improve them by comparison with experimental data.

#### 4.5. The direct interaction approximation

The best way to introduce the DIA may be to cite ORSZAG /57/ : "The direct interaction approximation, developed by KRAICHNAN, is the only fully self consistent analytical turbulence theory yet discovered. While its predictions do not accord with experiment at very high REYNOLDS numbers, the insights that it has given into the nature of turbulence are many and important. It is the only theory to account for non linear scrambling and stochastic relaxation in a fundamental way."

The DIA was proposed by KRAICHNAN /63, 64/. However, we shall adopt here the presentation proposed by LESLIE /56/ and extended by MATHIEU and JEANDEL /65/. Let us consider isotropic turbulence submitted to a stirring force  $f$ . The momentum equation reads :

$$\frac{du_i^j(k)}{dt} + \nu k^2 u_i^j(k) = -\frac{1}{2} \Delta_{ijl}(k) \int u_j^l(k-p) u_l^j(p) d^3p + f_i^j(k, t)$$

The first idea is to introduce the infinitesimal unit response tensor  $G$  which links the variations of the velocity field to variations of the driving force :

$$\delta u_i^j(k, t) = \int_{-\infty}^t G_{in}(k, t, t') \delta f_n^j(k, t') dt'$$

The equation for this tensor can easily be derived from the NAVIER equation as :

$$\frac{d}{dt} G_{in}(k, t, t') + \nu k^2 G_{in}(k, t, t') = -i \Delta_{ijl}(k) \int u_j(k-p) G_{ln}(p) d^3p + \delta_{in} \delta(t-t')$$

The problem is now to solve both momentum and response tensor equations. For this, the velocity field and the response tensor are developed as TAYLOR series :

$$u = u^0 + \lambda u^1 + \dots$$

$$G = G^0 + \lambda G^1 + \dots$$

where  $\lambda$  is a small parameter associated to non linear effects. The momentum and response tensor are thus similarly modified as :

$$\left(\frac{d}{dt} + \alpha\right) u = \lambda u u + f$$

$$\left(\frac{d}{dt} + \alpha\right) G = \lambda G \cdot + \delta(t-t')$$

where symbolic notation is used now for the sake of simplicity. The equations for the first two orders read :

$$\left(\frac{d}{dt} + \alpha\right) u^0 = f^0$$

$$\left(\frac{d}{dt} + \alpha\right) G^0 = \delta(t-t')$$

$$\left(\frac{d}{dt} + \alpha\right) u^1 = 2 u^0 u^0$$

$$\left(\frac{d}{dt} + \alpha\right) G^1 = G^0 u^0$$

The first equation gives the velocity field  $u^0$  only due to the driving force and the viscosity. The second equation gives the response tensor  $G^0$  which does not depend upon the flow field realization and is statistically sharp. This response tensor  $G^0$  can be used to solve the two following equations :

$$u^1 = 2 G^0 u^0 u^0$$

$$G^1 = G^0 G^0 u^0$$

so that the first two orders are completely determined.

Statistical variables can also be obtained for the first two orders expansion. For that, the velocity field  $u^0$  is assumed to have a Gaussian distribution. The third order moment reads :

$$\langle u u u \rangle = \langle u^0 u^0 u^0 \rangle + \lambda \Sigma \langle u^1 u^0 u^0 \rangle = 2 \lambda \Sigma G^0 \langle u^0 u^0 \rangle \langle u^0 u^0 \rangle$$

as, for a Gaussian distribution, third order moments are zero and fourth order moments decompose as products of second order moments. Moreover, as  $G^0$  is statistically sharp :

$$\langle G u \rangle = \langle G^0 u^0 \rangle + \lambda \langle G^1 u^0 \rangle + \lambda \langle G^0 u^1 \rangle = \lambda G^0 G^0 \langle u^0 u^0 \rangle$$

The final step is to restrict the TAYLOR development to order one, to put  $\lambda$  equal to one and to identify the zeroth order terms  $u^0$  and  $G^0$  with the velocity field and the response tensor. The DIA equations are so obtained ; they read :

$$\left(\frac{d}{dt} + \alpha\right) \langle u u \rangle = \Sigma G \langle u u \rangle \langle u u \rangle$$

$$\left(\frac{d}{dt} + \alpha\right) \langle G \rangle = \langle G \rangle \langle G \rangle \langle u u \rangle + \delta$$

or, in a more complete form :

$$\left(\frac{d}{dt} + k^2\right) U(k, t-t') = 2\pi \iint k p q b(k, p, q) dp dq \left[ \int_{-\infty}^{t'} G(k, t'-t'') U(p, t-t'') U(q, t-t'') dt'' - \int_{-\infty}^t G(p, t-t'') U(q, t-t'') U(k, t'-t'') dt'' \right]$$

$$\left(\frac{d}{dt} + \nu k^2\right) G(k, t-t') = -2\pi \iint k p q b(k, p, q) dp dq \int_{t'}^t G(p, t-t'') U(q, t-t'') G(k, t''-t') dt'' + \delta(t-t')$$

where  $b(k, p, q)$  is a coefficient which depends upon the geometry of the triad.

The last statements in the derivation of the DIA, while standard in theoretical physics, may seem quite crude. We shall try to justify them later.

The first important information given by this model is that the third order moment can be expressed as :

$$\langle u u u \rangle = 2 \Sigma G \langle u u \rangle \langle u u \rangle$$

i.e. third order moments can be expressed in terms of second order moments and of a response tensor  $G$  which measures the time coherence of the turbulent field. This property will be used later.

With the above expression for the third order moments, the contribution of each triad to the energy transfer can be analyzed. If the geometrical coefficient  $b$  is assumed positive, which is true for the major parts of the triads (ORSZAG /57/), the above energy equation shows that the action of wave numbers  $p$  and  $q$  is to inject energy at wave number  $k$  while the action of wave numbers  $k$  and  $q$  is to extract energy at wave number  $k$ . The final picture of triadic interaction is that two wave vectors give energy to the third one in such a way that the detailed energy conservation is satisfied.

It must be stressed that the DIA equations are not only dealing with the energy density  $U(k, t)$  at a given time but with the two-time energy density  $U(k, t - t')$  obtained from second order moments at two different times. Therefore they are quite heavy to use as they lead to a large amount of variables.

At last, one of the most interesting features of the DIA equations is that they include no adjustable coefficient.

The DIA equations can be justified by considering dynamical systems. NAVIER equations can be approximated by the following system :

$$\frac{d}{dt} Y_i + v_i Y_i = \sum A_{ijk} Y_j Y_k$$

where the  $A_{ijk}$  must satisfy the constraint :

continuity	$A_{ijj} = 0$
symmetry	$A_{ijk} = A_{ikj}$
detailed energy conservation	$A_{ijk} + A_{jki} + A_{kij} = 0$

KRAICHNAN (1966) introduces the Random Coupling Model in which the sign of  $A_{ijk}$  is taken randomly from triads to triads while satisfying the above constraints. He showed that the DIA equations are exact solutions of the Random Coupling Model as concerns the correlations  $\langle YY \rangle$ . The justification of DIA equations is discussed at length by LESLIE /56/.

The above presentation has made the name Direct Interaction Approximation a little strange. It must be kept in mind that the model is obtained from a small parameter expression of the non linear term. A given wave vector  $k$  interacts with wave vectors  $p$  and  $q$  such as  $k = p + q$ . These wave vectors  $p$  and  $q$  interact with other wave vectors which form a triangle, these wave vectors interact ... and so on ad infinitum. The truncation of the non linear term expression only accounts for "direct" interactions and neglect "indirect" influence via multiple triadic interactions.

The main consequence of this direct interaction approximation is that the rôle of the larger eddies is badly represented. The rôle of larger eddies is twofold : on the one hand, they exchange energy via triadic interactions while, on the other hand, they advect smaller eddies. As this advection rôle is not well captured by the DIA, the DIA equations are not Galilean invariant. One of the most striking consequences of this failure is that the DIA equations lead to a  $k^{-3/2}$  inertial range. KRAICHNAN /67/ proposed to cure this defect by using a Lagrangian reference frame to automatically account for advection effects. The formalism becomes heavier, but the model is able to predict  $k^{-5/3}$  inertial range and to give a value of the KOLMOGOROV constant of 1.43 very close to the experimental value 1.40 measured by GRANT et al /58/.

#### 4.6. The Test-field Model

To keep the advantage of the Eulerian reference frame, KRAICHNAN proposes to analyze the evolution of a fluid blob in an Eulerian reference frame. A fluid blob is distorted by advection effects but this is a "false" distortion as it makes no sense in a Lagrangian reference frame. On the contrary, KRAICHNAN considers that pressure effects cause a "real" distortion of fluid blobs.

To restore the Galilean invariance in an Eulerian framework, one has to account for the pressure effects only and to eliminate the effect of advection. We have previously seen that the rôle of the pressure is to improve the continuity constraint by suppressing the compressible part of the velocity field, i.e. to impose to the velocity field to be in the plane normal to the wave vector. The idea is then to use an hypothetical field with a compressible part, i.e. a component parallel to the wave vector, to measure the rôle of the pressure. This test field is advected by the incompressible field and pressure terms are discarded in the test field transport equations to obtain a compressible velocity field. This test field is used to obtain the response tensor  $G$ . The test field model is simplified by getting rid of all time memory effects by a Markovianisation. This procedure highly simplifies the model but introduces a model constant to adjust to partly restore the turbulence memory.

The test field model was first developed by KRAICHNAN /68/ with the help of a dynamical system and extended to anisotropic turbulence /69/. Connection with other closures is studied in /70/. Validation of the test field model by comparison with direct resolution of the NAVIER equations at low REYNOLDS numbers is shown in /57/ and /77/.

#### 4.7. Gaussian approximations

The fact that velocity fluctuations are close to a Gaussian distribution and the peculiar properties of moments of Gaussian variables have already been used in the formulation of the DIA. Here we shall adopt a somewhat heuristic approach to derive a closure.



The NAVIER equation can be written, in symbolic form, as :

$$\frac{\partial u}{\partial t} + \nu k^2 u = uu$$

So that, due to the non linear term, an infinite hierarchy of moment equations can be obtained :

$$\frac{\partial}{\partial t} \langle uu \rangle + 2\nu k^2 \langle uu \rangle = \langle uuu \rangle$$

$$\frac{\partial}{\partial t} \langle uuu \rangle + \nu(k^2 + p^2 + q^2) \langle uuu \rangle = \langle uuuu \rangle$$

...

If the velocity fluctuations were exactly Gaussian (or normal), the third order moments should be zero and the fourth order moment should decompose as products of second order moments. As third order moments are responsible for the non linear energy transfer, the energy spectrum would then decrease only under the influence of viscosity.

MILLIONSHTCHIKOV /83/ and PROUDMAN and REID /71/ proposed the quasi normal hypothesis in which fourth order moments are still assumed to decompose as product of second order moments but third order moments are no longer null to allow energy transfer. The equations now become :

$$\frac{\partial}{\partial t} \langle uu \rangle + 2\nu k^2 \langle uu \rangle = \langle uuu \rangle$$

$$\frac{\partial}{\partial t} \langle uuu \rangle + \nu(k^2 + p^2 + q^2) \langle uuu \rangle = \langle uu \rangle \langle uu \rangle$$

OGURA /72/ performed numerical integration of the above equations and showed that they rapidly lead to negative values in the energy spectrum, which is unphysical. The reason, as pointed out by ORSZAG /73/, is that there is no damping in the third order moment equation, so that the third order moment can increase indefinitely without reaching an equilibrium state. ORSZAG proposed to add a damping term in the third order moment equation :

$$\frac{\partial}{\partial t} \langle uuu \rangle + \nu(k^2 + p^2 + q^2) \langle uuu \rangle = \langle uu \rangle \langle uu \rangle - (\eta_k + \eta_p + \eta_q) \langle uuu \rangle$$

in order to limit the third order moment and hence the energy transfer and to avoid negative regions in the energy spectrum. The solution of the above equation reads :

$$\langle uuu \rangle = \int_0^t \langle uu \rangle \langle uu \rangle e^{-(\mu_k + \mu_p + \mu_q)t} dt$$

with  $\mu_k = \eta_k + \nu k^2$

where time 0 corresponds to an initial state when the turbulence is assumed to be Gaussian. To get rid of the time integral, a Markovianisation process is proposed in which the damping exponential function is supposed to vary much more rapidly with time than the second order moments so that :

$$\langle uuu \rangle = \langle uu \rangle \langle uu \rangle \int_0^t e^{-(\mu_k + \mu_p + \mu_q)t} dt = \frac{1 - e^{-(\mu_k + \mu_p + \mu_q)t}}{\mu_k + \mu_p + \mu_q} \langle uu \rangle \langle uu \rangle$$

$$\sim \frac{1}{\mu_k + \mu_p + \mu_q} \langle uu \rangle \langle uu \rangle \text{ for large } t$$

Another interest of this Markovianisation is that it ensures realisability, i.e. negative energy spectra can no longer be obtained. After some algebra, the equation for the energy transfer can be obtained as :

$$\frac{\partial}{\partial t} E(k) + 2\nu k^2 E(k) = \int \theta_{kpq} \frac{xy + z^3}{q} (k^2 E(p)E(q) - p^2 E(k)E(q)) dp$$

where the integral holds over all triangle interactions  $k = p + q$ . The geometrical coefficient, while expressed in a different way, is of course the same as in the DIA equations,  $x$ ,  $y$  and  $z$  are the cosines of the angles respectively opposite to the wave vectors  $k$ ,  $p$  and  $q$ . The damping coefficient  $\theta_{kpq}$  is the one we have already obtained, i.e.

$\theta_{kpq} = \frac{1}{\mu_k + \mu_p + \mu_q}$  for large  $t$ . ORSZAG /57/ first proposed

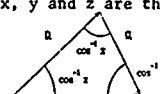
an expression for the damping coefficient  $\eta_k$  based upon local properties of the energy spectrum, i.e.  $\eta_k \sim k^{3/2} E^{1/2}$ . The final form for the damping term proposed by ANDRE and LESIEUR /70, 74/ is :

$$\eta(k) = \lambda \left( \int_0^k p^2 E(p) dp \right)^{1/2}$$

where  $\lambda$  is a constant connected to the KOLMOGOROV constant.

This model, based on a quasi normal approximation with an additional eddy damping and finally a Markovianisation, is called Eddy Damped Quasi Normal Markovian or EDQNM closure.

The above presentation of the EDQNM model leads to a phenomenological model obtained as an improvement of the quasi normal approach based on physical ground. This EDQNM model can also be derived from a dynamical system as proposed by LEITH /76/. A third way to analyse the EDQNM Model is to interpret it as a Markovian version of the DIA in which the damping of the third order moments is no longer computed as in the DIA or the TFM but simply prescribed. Connections between the EDQNM model and the DIA or the TFM have been analysed by ORSZAG /73/, SULEM et al /70/ or HERRING et al /109/.



The EDQNM model is simpler to use than the DIA or TFM model and gives good predictions of the turbulence decay as shown on figure 14 and in reference /75/.

Finally it must be mentioned that numerical methods to solve these equations have been proposed by LEITH /76/ and improved by LESIEUR and SCHERTZER /59/ and later CROCCO and ORLANDI /78/.

### 5 - CONCLUSION

The homogeneous turbulence assumption provides a framework in which the turbulence field can be studied solely in presence of constant mean velocity gradients.

The study of the NAVIER equation in FOURIER space has brought into evidence the distinction between the linear action of viscosity and of the mean velocity gradients on the turbulent motion and the non linear action of turbulence upon itself.

The linear problem only involves contribution at a given wave vector and can be solved by analytical means.

On the contrary, the non linear problem is open and modelling is required. Although some simple models can give good approximations for the energy transfer, analytical theories are needed to construct models for the detailed energy transfer. The DIA was first proposed but this model needs a Lagrangian treatment to be Galilean invariant. However, it is the only model to give information on time correlations. TFM and EDQNM are Markovian models which only give information about one-time moments; they are therefore easier to use. The response function is computed in the TFM with the help of the compressible test field and prescribed in the EDQNM; the EDQNM closure is thus simpler. All these models can be derived from dynamical system and are interrelated; so no empirical constant has to be introduced in the models.

As the linear problem is analytical while the non linear problem needs no constant tuning, the second order moment equations in FOURIER space can be solved without tuning any constant with respect to experiment.

## Part 2 - APPLICATIONS OF TWO-POINT CLOSURES TO THE DEVELOPMENT OF ONE-POINT CLOSURES

### 1 - INTRODUCTION

In quite all engineering problems, one-point closures are used to reduce the amount of turbulent unknowns to an acceptable level. The problem is then to evaluate the REYNOLDS stresses. The transport equation for the REYNOLDS stresses can be derived from the NAVIER equation as :

$$\frac{\partial}{\partial t} \langle u_i' u_j' \rangle + u_k \frac{\partial}{\partial x_k} \langle u_i' u_j' \rangle = - \langle u_i' u_k' \rangle \frac{\partial u_j}{\partial x_k} - \langle u_j' u_k' \rangle \frac{\partial u_i}{\partial x_k} + \langle \frac{p'}{\rho} \left( \frac{\partial u_i}{\partial x_j} + \frac{\partial u_j}{\partial x_i} \right) \rangle - 2\nu \langle \frac{\partial u_i'}{\partial x_k} \frac{\partial u_j'}{\partial x_k} \rangle + \frac{\partial}{\partial x_k} \left( \langle u_i' u_j' u_k' \rangle - \nu \frac{\partial}{\partial x_k} \langle u_i' u_j' \rangle + \langle \frac{p'}{\rho} (u_i' \delta_{jk} + u_j' \delta_{ik}) \rangle \right)$$

where the LHS represents the total derivative of the REYNOLDS stress and the RHS the production by action of the mean velocity gradient, the redistribution by pressure effect, the destruction by viscosity and the diffusion. Often, only the transport equation for the kinetic energy is retained. This equation is deduced from the REYNOLDS stress transport equation as :

$$\frac{\partial}{\partial t} \frac{1}{2} q^2 + u_k \frac{\partial}{\partial x_k} \frac{1}{2} q^2 = P - \epsilon + \frac{\partial}{\partial x_k} \left( \frac{1}{2} \langle u_i' u_j' u_k' \rangle - \nu \frac{\partial}{\partial x_k} \frac{1}{2} q^2 + \langle \frac{p' u_k'}{\rho} \rangle \right)$$

where  $P = - \langle u_i' u_j' \rangle \frac{\partial u_i}{\partial x_j}$  is the turbulent kinetic energy production and  $\epsilon = \nu \langle \frac{\partial u_i'}{\partial x_j} \frac{\partial u_i'}{\partial x_j} \rangle$  its dissipation rate by viscous effects. To solve the kinetic energy transport equation, the dissipation rate has to be evaluated. A transport equation for the dissipation rate can be deduced from the NAVIER equation. It reads :

$$\frac{\partial \epsilon}{\partial t} + u_k \frac{\partial \epsilon}{\partial x_k} = - 2\nu \frac{\partial u_i}{\partial x_k} \left( \langle \frac{\partial u_k'}{\partial x_j} \frac{\partial u_i'}{\partial x_j} \rangle + \langle \frac{\partial u_k'}{\partial x_k} \frac{\partial u_i'}{\partial x_i} \rangle \right) - 2\nu \langle \frac{\partial u_k'}{\partial x_k} \frac{\partial u_i'}{\partial x_k} \frac{\partial u_i'}{\partial x_k} \rangle - 2\nu^2 \langle \frac{\partial^2 u_i'}{\partial x_k \partial x_k} \frac{\partial^2 u_i'}{\partial x_k \partial x_k} \rangle - 2\nu \frac{\partial^2 u_i}{\partial x_k \partial x_k} \langle u_k' \frac{\partial u_i'}{\partial x_k} \rangle + \nu \frac{\partial}{\partial x_k} \left( - \langle u_k' \frac{\partial u_i'}{\partial x_k} \frac{\partial u_i'}{\partial x_k} \rangle - \frac{2}{\rho} \langle \frac{\partial p'}{\partial x_k} \frac{\partial u_i'}{\partial x_k} \rangle + \frac{\partial \epsilon}{\partial x_k} \right)$$

The REYNOLDS stress, kinetic energy and dissipation rate transport equations are the transport equations commonly used in one-point closure models. All these transport equations are open and terms which include new variables require modelling. In the REYNOLDS stress transport equation, only the production term does not introduce new variables, the pressure strain term, the viscous dissipation term and the diffusion term require modelling. In the kinetic energy transport equation, only the diffusion term requires modelling while in the dissipation rate transport equation, all terms are unknown.

In the framework of homogeneous turbulence, the diffusion terms disappear due to the translation invariance of the turbulent flow. The use of two-point closures for homogeneous turbulence can only provide information about the pressure strain correlation and the dissipation term in the REYNOLDS stress transport equation and the first three terms of the RHS of the dissipation equation. Two-point closures require no turning of empirical constant and can be viewed as "exact" solutions. Of course, as modelling is needed for the non linear terms, they are not as exact as numerical simulations of the NAVIER equations. However, they directly give information about statistical averages and can be used at any REYNOLDS number.

## 2 - APPLICATION OF TWO-POINT CLOSURES TO THE MODELLING OF THE REYNOLDS STRESS TRANSPORT EQUATION

## 2.1. Introduction

The two unknown terms in the REYNOLDS stress transport equation are the pressure-strain term and the dissipation term.

Following CHOU's idea /79/, the pressure can also, in physical space, be decomposed to bring into evidence linear and non linear effects. The POISSON equation is obtained by taking the divergence of the momentum equation as :

$$-\frac{1}{\rho} \frac{\partial^2 p}{\partial x_i \partial x_i} = \frac{\partial u_j}{\partial x_i} \frac{\partial u_i}{\partial x_j}$$

and, with the help of the REYNOLDS decomposition, the pressure fluctuation is given by :

$$-\frac{1}{\rho} \frac{\partial^2 p'}{\partial x_i \partial x_i} = 2 \frac{\partial u_j}{\partial x_i} \frac{\partial u_i'}{\partial x_j} + \frac{\partial^2 u_i' u_j' - \langle u_i' u_j' \rangle}{\partial x_i \partial x_j}$$

The pressure fluctuation is then deduced from the GREEN formula, which reads, far from boundaries :

$$\frac{p'(\underline{x})}{\rho} = \frac{1}{4\pi} \int \left( 2 \frac{\partial u_j}{\partial x_i} \frac{\partial u_i'}{\partial x_j} + \frac{\partial^2 u_i' u_j' - \langle u_i' u_j' \rangle}{\partial x_i \partial x_j} \right) \underline{x}' \frac{d^3 \underline{x}'}{\|\underline{x} - \underline{x}'\|}$$

Finally, the pressure strain term can be decomposed as :

$$\left\langle \frac{p'}{\rho} \frac{\partial u_i'}{\partial x_j} \right\rangle = \phi_{ij,1} + \phi_{ij,2}$$

where

$$\phi_{ij,1} = \frac{1}{4\pi} \int \left\langle \left( \frac{\partial u_i'}{\partial x_j} \right) \underline{x} \left( \frac{\partial^2 u_i' u_j' - \langle u_i' u_j' \rangle}{\partial x_i \partial x_j} \right) \underline{x}' \right\rangle \frac{d^3 \underline{x}'}{\|\underline{x} - \underline{x}'\|}$$

is the contribution of the non linear effects while :

$$\phi_{ij,2} = \frac{1}{2\pi} \frac{\partial u_j}{\partial x_m} \int \left\langle \left( \frac{\partial u_i'}{\partial x_m} \right) \underline{x}' \left( \frac{\partial u_i'}{\partial x_j} \right) \underline{x} \right\rangle \frac{d^3 \underline{x}'}{\|\underline{x} - \underline{x}'\|}$$

is the linear part where the mean velocity gradient has been extracted from the integral under the assumption of homogeneous flow. As these two terms correspond to different phenomena, they are usually modelled separately

## 2.2. Return to isotropy

The study of the decay of anisotropic turbulence in the absence of mean velocity gradient provides a good test case to study the non linear effects. Experiments have shown that the rôle of the non linear pressure-strain term and of the viscous dissipation is to reduce the turbulence anisotropy as the turbulence decays. The REYNOLDS stress transport equation then reduces to, in a reference frame conveyed by the mean flow :

$$\begin{aligned} \frac{d}{dt} \langle u_i' u_j' \rangle &= \phi_{ij,1} + \phi_{ij,2} - \epsilon_{ij} \\ \epsilon_{ij} &= 2\nu \left\langle \frac{\partial u_i'}{\partial x_k} \frac{\partial u_j'}{\partial x_k} \right\rangle \end{aligned}$$

As the viscous dissipation is mainly due to the smaller eddies which are supposed to be nearly isotropic, it is customary to assume  $\epsilon_{ij} = 2/3 \delta_{ij} \epsilon$ . LUMLEY and NEWMAN have proposed to model together the non linear pressure-strain term and the anisotropic contribution of the dissipation as :

$$\frac{d}{dt} \langle u_i' u_j' \rangle = -\epsilon \phi_{ij} - \frac{2}{3} \delta_{ij} \epsilon$$

where

$$\phi_{ij} = \frac{1}{\epsilon} (\phi_{ij,1} + \phi_{ij,2}) - \frac{\epsilon_{ij}}{\epsilon} + \frac{2}{3} \delta_{ij} = \phi_{ij}(\langle u_i' u_j' \rangle, \epsilon, \nu)$$

They have shown that the function  $\phi_{ij}$  can be reduced to :

$$\phi_{ij} = \beta b_{ij} + \gamma (b_{ij}^2 - \frac{1}{3} \delta_{ij} II)$$

with

$$\beta = \beta(II, III, R_\lambda) \quad \gamma = \gamma(II, III, R_\lambda)$$

$$II = b_{ij} b_{ij} \quad III = b_{ij} b_{jk} b_{ki} \quad b_{ij}^2 = b_{ik} b_{kj}$$

where  $b_{ij} = \frac{\langle u_i' u_j' \rangle}{q^2} - \frac{\delta_{ij}}{3}$  is the anisotropy tensor and  $R_\lambda = \frac{(q^2)^2}{9\nu\epsilon}$  the turbulent REYNOLDS number.

The problem is to determine the functions  $\beta$  and  $\gamma$ . The most popular model is due to ROTTA /81/ who assumed a linear return to isotropy ( $\beta \sim 1$ ,  $\gamma = 0$ ). Recently, CHOI /16/ performed a large investigation to "measure" the  $\beta$  and  $\gamma$  functions over a wide range of anisotropy and REYNOLDS numbers.

Direct numerical simulations of turbulence can be used to easily study different values of the anisotropy invariants II and III but they are restricted to low REYNOLDS numbers (e.g. /52/, /82/). Figure 15 shows the prediction of two simple EDQNM closures developed by BERTOGLIO /84/ and CAMBON /43/ which both compare favourably with experiments.

Two-point closures could be an interesting complement to direct simulations and experiments, in order to study the return to isotropy process in situation that cannot be easily achieved by these two methods as e.g. large REYNOLDS number or to study, at low cost, the influence of one parameter (REYNOLDS number, total strain imposed before the return to isotropy phase, strain/turbulence time scale ratio, ...). Such a study could easily confirm or infirm the LUMLEY and NEWMAN approach over a wide range of situations.

### 2.3. Linear part of the pressure-strain correlation

Rapid distortion theory holds when the turbulence is submitted to a strong velocity gradient, when compared with the turbulence time scale. The non linear effects are then negligible and the REYNOLDS stress evolution is governed by the production term and the linear part of the pressure-strain correlation.

LE PENVEN and GENGE /85/ used rapid distortion theory to model the pressure-strain correlation. They considered initially isotropic, strained flow. Using the approach of the linear problem developed by CAMBON /43/, they showed that the anisotropy tensor can be expanded in time series as :

where  $D_{km}$  is the deformation tensor  $\frac{1}{2} \left( \frac{\partial u_k}{\partial x_m} + \frac{\partial u_m}{\partial x_k} \right)$  and that the pressure-strain correlation can also be expanded as :

$$b_{km}(t) = -\frac{4}{15} D_{km} t - \frac{4}{21} \left( D_{km}^2 - \frac{D_{II}}{3} \delta_{km} \right) t^2 + O(\|Dt\|^3)$$

$$(\phi_{ij,2} + \phi_{ji,2})(t) = 2D_{km} \bar{q}^2 \left[ \frac{1}{10} (\delta_{ik} \delta_{jm} + \delta_{im} \delta_{jk} - \frac{2}{3} \delta_{ij} \delta_{km}) \right. \\ + \frac{1}{105} \left[ 16(D_{ij} \delta_{km} + D_{km} \delta_{ij}) - 12(D_{im} \delta_{jk} + D_{jm} \delta_{ik} + D_{ik} \delta_{jm} + D_{jk} \delta_{im}) \right] t \\ + \frac{1}{1575} (98 \delta_{ij} \delta_{km} - 17(\delta_{ik} \delta_{jm} + \delta_{im} \delta_{jk})) D_{II} t^2 \\ + \frac{1}{315} \left[ -76 D_{ij} D_{km} + 50(D_{im} D_{jk} + D_{ik} D_{jm}) - 52(D_{ij}^2 \delta_{km} + D_{km}^2 \delta_{ij}) \right. \\ \left. + 14(D_{ik}^2 \delta_{jm} + D_{jk}^2 \delta_{im} + D_{im}^2 \delta_{jk} + D_{jm}^2 \delta_{ik}) \right] t^2 + O(\|Dt\|^3) \Big]$$

with  $D_{km}^2 = D_{kl} D_{lm}$  ;  $D_{II} = D_{kl} D_{kl}$ .

The time can then be eliminated between the two expressions to obtain the proposed expression for the pressure-strain correlation :

$$\phi_{ij,2} + \phi_{ji,2} = 2D_{km} \bar{q}^2 \left[ \frac{1}{10} (\delta_{ik} \delta_{jm} + \delta_{im} \delta_{jk} - \frac{2}{3} \delta_{ij} \delta_{km}) - \frac{4}{7} (b_{ij} \delta_{km} + b_{km} \delta_{ij}) \right. \\ + \frac{3}{7} (b_{im} \delta_{jk} + b_{jm} \delta_{ik} + b_{ik} \delta_{jm} + b_{jk} \delta_{im}) + \frac{743}{392} II \delta_{ij} \delta_{km} - \frac{719}{784} II (\delta_{ik} \delta_{jm} + \delta_{im} \delta_{jk}) \\ - \frac{95}{28} b_{ij} b_{km} + \frac{125}{56} (b_{ik} b_{jm} + b_{im} b_{jk}) - \frac{755}{196} (b_{ij}^2 \delta_{km} + b_{km}^2 \delta_{ij}) \\ \left. + \frac{695}{392} (b_{ik}^2 \delta_{jm} + b_{jk}^2 \delta_{im} + b_{im}^2 \delta_{jk} + b_{jm}^2 \delta_{ik}) \right]$$

All coefficients in the model are constants as the time series have been truncated to second order. If the time series were truncated to higher orders, these coefficients will be functions of the anisotropy invariants II and III (GENGE, private communication).

REYNOLDS /110/ also used rapid distortion solutions for initially isotropic turbulence submitted to strain to improve the pressure-strain term model. Instead of looking directly at the pressure-strain term, he studied the fourth order tensor  $a_{ijkl}^{(4)}$  which appears naturally as :

$$\phi_{ij,2} = a_{ij}^{(4)} \frac{\partial u_k}{\partial x_m}$$

and can easily be expressed in terms of second order moments. Properties of this tensor and realisability constraints are advocated to reduce the number of independent coefficients. He first studied the standard model (REYNOLDS /87/, LAUNDER et al /107/) in which this fourth order tensor is expressed as a linear function of the anisotropy tensor  $b$  and computed the only adjustable constant to be consistent with rapid distortion theory. As the so obtained model violates realisability constraints for two-dimensional turbulence, he extended the model for the fourth order tensor to include quadratic terms and obtained the same model as LE PENVEN and GENGE.

LECOINTE et al /86/ used CAMBON's analytical solutions to extend the above procedure to temperature variance and also sheared flows.

At last, LEE et al /49/ solved the linear problem for initially isotropic strained flow in an original way and deduced time series which can be used to calibrate pressure-strain correlation models.

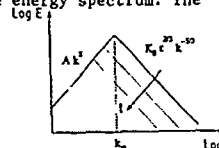
It must be kept in mind that rapid distortion is valid only for large strains but for very short times compared to turbulence time scales. As time increases, non linear effects become important and the expressions for both the anisotropy tensor and the pressure-strain correlation diverge from the rapid distortion solution. However rapid distortion theory can provide analytical solutions which must be satisfied by the pressure-strain correlation model for short time. This approach, restricted for now to isotropic turbulence, could be extended to any initial condition.

### 3 - DISSIPATION EQUATION : PURE DECAY

The rôle of the various terms on the RHS of the dissipation equation is difficult to analyse. We will prefer to try to model them together in various situations. The first use of spectral space to model the dissipation equation is due to COMTE-BELLOT and CORRSIN /2/, in the case of purely decaying turbulence. The argument has been extended later by REYNOLDS /87/.

The basic idea is to use a simple shape to mimic the real shape of the energy spectrum. The energy spectrum is defined by two simple power laws :

$$\begin{aligned} k \leq k_m & \quad E(k) = Ak^s \\ k \geq k_m & \quad E(k) = K_0 \epsilon^{2/3} k^{-5/3} \end{aligned}$$



This simple law of course does not account for the exact form of the energy spectrum in the energy containing range and in the dissipation range. The turbulent kinetic energy can be evaluated as :

$$\begin{aligned} \frac{1}{2} q^2 &= \int_0^\infty E(k) dk = \int_0^{k_m} Ak^s dk + \int_{k_m}^\infty K_0 \epsilon^{2/3} k^{-5/3} dk \\ &= \frac{3s+5}{2(s+1)} \frac{K_0^{3s+5}}{k_0^{3s+5}} \frac{1}{\epsilon^{3s+5}} \end{aligned}$$

During the decay, experiments have shown that the energy spectrum evolves in a self similar way (e.g. cf /88/, vol. II, p. 204), i.e. the energy spectrum decays with a given shape  $E(k,L)$  in the large scales,  $L$  being a characteristic length scale of the large eddies and a shape  $E(k/k_D)$  in the small scales, both laws overlapping over the inertial range. The coefficients  $A$  and  $s$  are therefore time independent.

Moreover, the turbulent kinetic energy reduces to :

$$\frac{d}{dt} \frac{1}{2} q^2 = -\epsilon$$

Assuming that the flux  $\epsilon$  cascading along the inertial range and the dissipation rate  $\epsilon$  are equal, which is a standard one-scale assumption, the two above equations can be combined to obtain the dissipation transport equation :

$$\frac{d\epsilon}{dt} = -C_{\epsilon 2} \frac{\epsilon^2}{\frac{1}{2} q^2} \quad C_{\epsilon 2} = \frac{3s+5}{2(s+1)}$$

The above equation has already been proposed on dimensional analysis grounds and the coefficient  $C_{\epsilon 2}$  calibrated by reference to experiment. The main interest of the above argument is to validate simply this form at high REYNOLDS number and to show that there is no universal value for the coefficient  $C_{\epsilon 2}$  as the exponent  $s$  lies between 1 and 4. LESIEUR and SCHERTZER /59/ have shown however that tricky non linear effects invalidate the argument when  $s$  is equal to 4.

### 4 - DISSIPATION EQUATION : SOLID BODY ROTATION

#### 4.1. Introduction

Experiments (/18/, /22/) or numerical simulations (/89/, /90/) have shown that the rôle of rotation is to reduce energy transfer and hence the decay rate of turbulent and to lead to axisymmetric turbulence, the departure from isotropy being small in all experiments.

This double rôle of rotation can be simply explained by looking at the momentum equation in FOURIER space. It reads, in symbolic form :

$$\frac{d}{dt} u + \nu k^2 u = uu + \omega \wedge u$$

It must be kept in mind that the rôle of the pressure term is to satisfy continuity i.e. to project the velocity field on the plane normal to the wave vector. The rotation action is thus partially inhibited by the pressure; for wave vectors parallel to the rotation axis, there are no pressure effects while for wave vectors normal to the rotation axis, the CORIOLIS term is completely compensated by the pressure action. All wave vectors do not rotate at the same rate and thus, the energy exchange between wave vectors which form a triad is decreased as the coherence between these modes is damaged. The energy transfer is then reduced. Moreover, the pressure effects introduce a preferred direction; the rotation axis and the turbulence tends to evolve towards an axisymmetric state, the symmetry axis of which is the rotation axis.

#### 4.2. CAMBON's EDQNM models

CAMBON (/45/, /91/, /92/) has developed a complete model, in the framework of the EDQNM closures, which accounts for the rôle of rotation on third order moments and is able to predict the selected reduction of energy transfer and anisotropisation of the turbulent structures according to the relative angle between the wave vector and the rotation axis. This model is however intricate and time consuming.

A simpler model has been proposed by CAMBON /93/ on more heuristic grounds. The idea is that the damping time in the EDQNM model :

$$\eta(k) = \left( \int_0^k p^2 E(p) dp \right)^{1/2}$$

as proposed by ANDRE and LESIEUR can be interpreted as twice the square of the rotation imposed at wave number  $k$  by all the larger eddies. CAMBON's idea is to add the contribution of wave number zero, i.e. the solid body rotation as :

$$\eta(k) = \left( \int_0^k p^2 E(p) dp + 2 \omega^2 \right)^{1/2}$$

This modification increases the damping of the third order moments and, as third order moments are responsible for energy transfer, reduces the energy transfer and then the rate of decay of turbulence. However such a model is isotropic and does not account for the anisotropisation of turbulence submitted to solid body rotation. This model is thus only valid to compute energy spectra of fairly isotropic turbulence. This limitation is not drastic as experiments and numerical simulations have shown that anisotropy develops very slowly.

#### 4.3. Validation of the EDQNM model

The simplified EDQNM model has been validated by comparison with results of the complete EDQNM model (CAMBON, private communication), by comparison with the experiments of WIGELAND and NAGIB /93/ and by comparisons with numerical simulations /90/.

Direct simulations, i.e. resolutions of the NAVIER equations, were first performed at very low REYNOLDS number ( $R_\lambda \sim 35$ ;  $R_\epsilon \sim 80$ ) with an initial spectrum similar to the one used by ORSZAG and PATTERSON /77/, i.e. of the form  $k^4 \exp(-k^2)$ . Energy spectra after seven eddy turnover times obtained with the direct simulation and the EDQNM closures compared favourably whatever the rotation rates (figure 16a).

Direct simulations could not be performed at higher REYNOLDS numbers, so large eddy simulations, in which only the largest eddies are computed while the smaller eddies are modelled, were used. Two subgrid scale models were used to represent the effect of the smaller eddies, both models being derived from the modified EDQNM model. The first model, labelled SGS 1, represents the smaller eddies with the help of a wave number independent eddy viscosity which depends upon the small scales turbulent kinetic energy, the rotation rate, the REYNOLDS number and an assumed shape for the energy spectrum of the small scales /94/, /95/, /96/. The second model, labelled SGS 2, is more elaborate and couples the evolution of the large scales with an EDQNM computation of the energy spectrum of the small scales /96/. Both models were used to simulate a fictitious experiment where the initial energy spectrum of the COMTE-BELLOT and CORRSIN's experiment ( $R_\lambda \sim 75$ ;  $R_\epsilon \sim 15$ ) is submitted to solid body rotation over the experimental time, i.e. thirteen eddy turnover time. Large eddy simulations with both subgrid scale models compare favourably with EDQNM computation at all rotation rates (figure 16b, /96/).

#### 4.4. Exploitation of the EDQNM model

Direct and large eddy simulations have been very useful to validate the modified EDQNM model. However these methods are restricted to low REYNOLDS number and are much more expensive to use than an isotropic EDQNM model. The idea is then to use the EDQNM model to study the effect of rotation upon turbulence over a wide range of REYNOLDS numbers, rotation rates, energy spectrum shapes (mainly the exponent of the large eddies). EDQNM computations give the time evolution of the turbulent kinetic energy and of the dissipation rate which are the variables used in one-point closures.

The problem is to reduce the data obtained from EDQNM simulations to extract a new decay law for the dissipation rate as the turbulent kinetic energy is the same for pure decay and for solid body rotation, i.e. :

$$\frac{d}{dt} \frac{1}{2} q^2 = -\epsilon$$

The dissipation rate decay can be reduced to a dimensionless form as  $\frac{1}{2} \frac{q^2}{\epsilon^2} \frac{d\epsilon}{dt}$  which is constant ( $C_{\epsilon 2}$ ) in the pure decay case. The evolution of this quantity has shown to vary during decay in presence of solid body rotation; the rotation rate is thus not a good parameter. A plausible parameter is the ratio of the rotation time scale and the turbulence time scale  $\omega^* = \frac{\omega 1/2 q^2}{\epsilon}$  which is the inverse of a ROSSBY number.

The evolution of the decay constant  $\frac{1}{2} \frac{q^2}{\epsilon} \frac{d\epsilon}{dt}$  as function of this parameter  $\omega^*$  is the same, for a given large eddies exponent  $s$ , for various REYNOLDS numbers and rotation rates. At last, the results obtained for various large eddies exponent  $s$  can be reduced to a single law as :

$$\frac{1}{2} \frac{q^2}{\epsilon} \frac{d\epsilon}{dt} = C_{\epsilon 2}(s) + C_{\epsilon}^*(\omega^*)$$

The function  $C_{\epsilon}^*$  is plotted on figure 17. The points indicate the extreme values obtained in the EDQNM simulations when the equilibrium regime has been reached. Two curves, labelled B and HL, indicate previous models respectively proposed by BARDINA et al /89/ from large eddy simulations and WIGELAND and NAGIB experiments and HANJALIC and LAUNDER /97/ to improve jet flows predictions. These models can be expressed as :

BARDINA et al	$C_{\epsilon}^* = 0.15 \omega^*$
HANJALIC and LAUNDER	$C_{\epsilon}^* = 0.27 \omega^{*2}$

#### 4.5. Realisability constraints

Before proposing a new law to represent the data obtained from EDQNM simulations, let us examine the realisability constraints this model must satisfy. Both turbulent kinetic energy and dissipation rate are positive variables and must not become negative. Without rotation, the equations :

$$\frac{d}{dt} \frac{1}{2} q^2 = -\epsilon$$

$$\frac{d}{dt} \epsilon = -C_{\epsilon 2} \frac{1}{2} \frac{\epsilon^2}{q^2}$$

prevent both the turbulent kinetic energy and the dissipation rate to become negative if they tend towards zero.

In the presence of rotation, when the turbulent kinetic energy tends towards zero, the inverse ROSSBY number  $\omega^*$  tends towards zero so that rotation effects are negligible. As it seems natural that  $C_{\epsilon}^*(0) = 0$ , the problem is then the same as in the no rotation case and realisability is ensured.

When the dissipation rate tends towards zero, the inverse ROSSBY number tends towards infinity. The function  $C_{\epsilon}^*$  can then be reduced to its higher order, i.e.  $C_{\epsilon}^* \sim \alpha \omega^{*n}$  so that the dissipation equation becomes :

$$\frac{d\epsilon}{dt} = - (C_{\epsilon 2} + C_{\epsilon}^*) \frac{1}{2} \frac{\epsilon^2}{q^2} = - C_{\epsilon 2} \frac{1}{2} \frac{\epsilon^2}{q^2} - \alpha \left( \frac{\omega}{2} \frac{1}{q^2} \right)^n \frac{1}{2} \frac{\epsilon^2}{q^2}$$

which tends towards zero when  $n < 2$ . This constraint is not satisfied by the HANJALIC and LAUNDER's model.

We have already supposed  $C_{\epsilon}^*(0) = 0$  as it is natural. This relation can of course be easily deduced from the EDQNM model. Moreover, it can be shown, with the EDQNM model that :

$$\frac{\partial C_{\epsilon}^*}{\partial \omega^*} (\omega^* = 0) = 0$$

The EDQNM simulation results on figure 17 have been approximated by the following law :

$$C_{\epsilon}^* = \frac{0.2236 \omega^{*2} + 0.0303 \omega^*}{0.2540 \omega^{*2} + 0.1567 \omega^* + 1}$$

This law satisfies the realisability constraint but not the property  $\frac{\partial C_{\epsilon}^*}{\partial \omega^*} (\omega^* = 0) = 0$ . However, when the inverse ROSSBY number  $\omega^*$  is small, the decay is ruled by the  $C_{\epsilon 2}$  coefficient so that it is insensitive to the exact form of the  $C_{\epsilon}^*$  law in the vicinity of zero.

#### 4.5. Application to solid body rotation experiments

The experiments of WIGELAND and NAGIB /22/ have been used to compare the various models as they are the most documented and fulfil the homogeneity conditions. Computations have been performed for various grids, upstream velocities and rotation rates /90/. Figures 18 and 19 give examples for the lowest upstream velocity and the highest rotation rates, i.e. when the flow field undergoes the maximum rotation in the test section. For each grid and each velocity, the  $C_{\epsilon 2}$  coefficient has been tuned for the no rotation case and, as all homogeneous flow computation is an initial value problem, special care was taken in the determination of the initial dissipation rates. The curve labelled O corresponds to the case without rotation, the curves A, B and HL to ours, BARDINA et al and HANJALIC and LAUNDER models. These figures bring into evidence the reduction of the dissipation rate due to the blockage of the energy cascade by the rotation. As the inverse ROSSBY number  $\omega^*$  remains moderate ( $\omega^* < 7$ ), both BARDINA et al and our model give good predictions in every case. HANJALIC and LAUNDER model leads to negative dissipation rates and increasing turbulent kinetic energy, which is unphysical and is due to the violation of the realisability constraint.

#### 4.6. Extension to flows with energy production

Homogeneous turbulence is restricted to a certain class of mean velocity gradients. Rotation can only be combined with a plane strain, the axis of rotation being normal to the plane of the strain. When rotation and strain rates are equal, shear is obtained. Shear is an important case as it occurs in most of practical flows such as boundary layers, wakes, ...

For flows with energy production, the dissipation rate transport equation is usually modelled as /98/ :

$$\frac{\partial \epsilon}{\partial t} + U_j \frac{\partial \epsilon}{\partial x_j} = C_{\epsilon 1} \frac{P \epsilon}{\frac{1}{2} q^2} - C_{\epsilon 2} \frac{\epsilon^2}{\frac{1}{2} q^2} + \text{diffusion terms}$$

where  $P = - \langle u_i' u_j' \rangle \frac{\partial U_i}{\partial x_j}$  in the turbulent kinetic energy production. The coefficient  $C_{\epsilon 2}$  has been previously modified to account for rotation effects. Is it necessary to modify also the coefficient  $C_{\epsilon 1}$  ?

A comparison of the different possible solutions showed that the solution was to add the same  $C_{\epsilon}^*$  term to both  $C_{\epsilon 1}$  and  $C_{\epsilon 2}$  (AUPOIX, Ph. D. dissertation). A first argument was proposed by AUPOIX et al /90/, but the best argument to add  $C_{\epsilon}^*(\omega^*)$  to both coefficients will be given later with the MIS approach.

Shear flow experiments have been computed by solving the REYNOLDS stress transport equations with the LRR model /107/ with different dissipation equations (figures 20 to 22). The curve labelled 0 is obtained with the standard equation while the curves labelled A and B correspond to the addition to both  $C_{\epsilon 1}$  and  $C_{\epsilon 2}$  of the  $C_{\epsilon}^*$  functions respectively proposed by AUPOIX et al and BARDINA et al. The use of this modification improves the prediction of both weakly and strongly sheared turbulence. With respect to the standard model, the turbulent kinetic energy is increased for weakly sheared flows and decreased for strongly sheared flows. The differences between AUPOIX and BARDINA models can only be observed for strongly sheared flows where relatively large inverse ROSSBY numbers  $\omega^*$  are encountered. Our model seems to give better predictions but the difference remains small.

#### 4.7. Conclusion

This study of rotation effects shows how two-point closures can be used to improve the dissipation equation. A complete EDQNM model could be used but it was too time-consuming (and still in development at that time). A simpler EDQNM closure has been preferred. Direct simulations of turbulence were first used to validate the EDQNM model at low REYNOLDS numbers. Subgrid scale models were then derived from the EDQNM model and large eddy simulations were used to validate the EDQNM model at higher REYNOLDS numbers. The EDQNM model was then used to perform, at low cost, a large amount of simulations and derive the new dissipation rate equation, the form of which cannot be obtained by simple a priori modelling.

It must be emphasized that no empirical tuning of coefficient with respect to experiments has been done in this study. The  $C_{\epsilon}^*(\omega^*)$  was directly obtained and afterwards checked in computations of rotating and sheared turbulence.

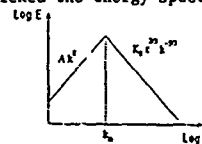
### 5 - THE MIS APPROACH

#### 5.1. The spectrum shape family

MIS are the initials, in French, for Integral Spectral Method. It is an integral method similar to the familiar boundary layer integral methods where a shape family is assumed, not for the velocity profile here but for the energy spectrum.

The basic idea is to try to generalize the argument introduced by COMTE-BELLOT and CORRSIN /2/ and REYNOLDS /87/ for self similar decay of isotropic turbulence. They mimicked the energy spectrum shape by two simple power laws :

$$\begin{aligned} k \leq k_m & \quad E(k) = A k^s \\ k \geq k_m & \quad E(k) = K_0 \epsilon^{2/3} k^{-5/3} \end{aligned}$$



and the turbulent kinetic energy then reads :

$$\frac{1}{2} q^2 = \int_0^\infty E(k) dk = \frac{3s+5}{2(s+1)} K_0 \frac{3(s+1)}{3s+5} A \frac{2}{3s+5} \epsilon \frac{2(s+1)}{3s+5}$$

This family of spectrum shape is too rough and does not describe finely the spectrum shape in the energy containing range. More elaborate transitions between the two power laws could be used but, as far as the spectrum shape in the energy containing range is just a fixed for, it will only change the factor

$\frac{3s+5}{2(s+1)} K_0 \frac{3(s+1)}{3s+5}$  to another constant. Our proposal is to introduce an unknown but variable spectrum shape in the energy containing range and to express the turbulent kinetic energy as :

$$\frac{1}{2} q^2 = F A \frac{2}{3s+5} \epsilon \frac{2(s+1)}{3s+5}$$

where  $F$  is unknown, time-dependent and reflects the shape of the energy spectrum in the energy containing range.



### 5.2. Basic assumptions

As in the COMTE-BELLOT and CORRSIN /2/ or REYNOLDS /87/ argument, extra hypotheses are needed to describe the spectrum shape evolution.

The one-scale hypothesis still holds. The energy flux  $\epsilon$  which cascades down the inertial range is supposed to be equal to the turbulent kinetic energy dissipation rate.

The second assumption concerns the evolution of the large scales. The non linear time scale  $(k^3 E(k))^{-1/2}$  and the viscous time scale  $(\nu k^2)^{-1}$  are very large for small wave numbers. Thus non linear and viscous effects are negligible and the evolution of the large eddies is ruled only by an inviscid rapid distortion theory.

It must be noticed that this argument is strictly valid only for wave numbers close to zero. The existence of a power law  $E = Ak^s$  at higher wave numbers must be due to both linear and non linear effects. As the spectrum shape  $E = Ak^s$  has been prescribed over the large eddies, it is easier to study its evolution for very small wave numbers where only linear terms are important than at higher wave numbers.

The first consequence of the use of rapid distortion theory to study the evolution of the large eddies is that the exponent  $s$  remains constant.

### 5.3. Dissipation rate transport equation

The transport equation for the turbulence kinetic energy reads, for homogeneous turbulence :

$$\frac{d}{dt} \frac{1}{2} q^2 = P - \epsilon$$

where  $P = - \langle u_i' u_j' \rangle \frac{\partial u_i}{\partial x_j}$  is the turbulent kinetic energy production. This equation is exact and no modelling is required, provided that the REYNOLDS stresses and the dissipation rate be known.

On the other hand, the turbulent kinetic energy reads, with the above hypothesis :

$$\frac{1}{2} q^2 = F A^{\frac{2}{3s+5}} \epsilon^{\frac{2(s+1)}{3s+5}}$$

The dissipation equation can then be derived from these two equations as :

$$\frac{1}{\epsilon} \frac{d\epsilon}{dt} = - \frac{1}{s+1} \frac{1}{A} \frac{dA}{dt} + C_{\epsilon 2} \left( \frac{P-\epsilon}{\frac{1}{2} q^2} - \frac{1}{F} \frac{dF}{dt} \right)$$

with  $C_{\epsilon 2} = \frac{3s+5}{2(s+1)}$ .

This form brings into evidence new time scales. While the standard equation introduces  $\frac{1}{2} \frac{q^2}{P}$  and  $\frac{1}{2} \frac{q^2}{\epsilon}$  which can only be interpreted respectively as the mean strain and the turbulence time scale, this model directly connects the dissipation rate evolution time scale to the evolution time scales of the large eddies, of the energy containing range shape and of the turbulent kinetic energy. The degrees of freedom initially introduced in the definition of the spectrum shape family reappear ; modelling is required to determine these new time scales. Comparison with simple flows will be used for that.

### 5.4. Pure decay

This first simple flow was the only case considered originally by COMTE-BELLOT and CORRSIN /2/ and REYNOLDS /87/. The rapid distortion theory shows that, in the absence of mean velocity gradient, the large eddies energy spectrum remains invariant, i.e.  $dA/dt = 0$ . Moreover, the hypothesis of self similar decay previously advocated means that the shape of the energy spectrum in the energy containing range remains constant, i.e.  $dF/dt = 0$ . The dissipation rate equation then reduces to the classic form :

$$\frac{1}{\epsilon} \frac{d\epsilon}{dt} = - C_{\epsilon 2} \frac{\epsilon}{\frac{1}{2} q^2}$$

as there is no energy production.

### 5.5. Solid body rotation

In the case of turbulence submitted to a solid body rotation, the rapid distortion theory still shows that the energy spectrum of the large eddies remains constant, i.e.  $dA/dt = 0$ . The dissipation rate equation then reduces to :

$$\frac{1}{\epsilon} \frac{d\epsilon}{dt} = - C_{\epsilon 2} \left( \frac{\epsilon}{\frac{1}{2} q^2} + \frac{1}{F} \frac{dF}{dt} \right)$$

as the energy production is still null.

On the other hand, we have already modelled the dissipation equation as :

$$\frac{1}{\epsilon} \frac{d\epsilon}{dt} = - (C_{\epsilon 2} + C_{\epsilon}^*(\omega^*)) \frac{\epsilon}{\frac{1}{2} q^2} \quad \omega^* = \frac{\omega \frac{1}{2} q^2}{\epsilon}$$

so that the two formulae can be identified to prescribe the evolution law for the energy containing range spectrum shape factor  $F$  as :

$$C_{\epsilon 2} \frac{1}{F} \frac{dF}{dt} = C_{\epsilon}^*(\omega^*) \frac{\epsilon}{\frac{1}{2} q^2}$$

This relation is valid only in the case of solid body rotation, i.e. without energy production. In the presence of production, two different time scales need to be considered :

\*  $\frac{1}{2} \frac{q^2}{\epsilon}$  is the characteristic time scale of the turbulent flow ; it can be interpreted as a time scale of non linear effects in the energy containing range. As the action of rotation is to reduce energy transfer, it seems natural to keep this time scale in the definition of the inverse ROSSBY number

$$\omega^* = \frac{\omega \frac{1}{2} q^2}{\epsilon}$$

\*  $\frac{1}{P - \epsilon}$  is the evolution time scale of the turbulent kinetic energy. As the evolution of the spectrum shape in the energy containing range is a balance between energy production and energy transfer, it seems natural to relate the spectrum shape time scale to the time scale.

The proposed law for the spectrum shape factor evolution then reads :

$$\frac{1}{F} \frac{dF}{dt} = - \frac{C_{\epsilon}^*}{C_{\epsilon 2}} \frac{P - \epsilon}{\frac{1}{2} q^2}$$

so that the dissipation rate transport equation becomes :

$$\frac{1}{\epsilon} \frac{d\epsilon}{dt} = - \frac{1}{s+1} \frac{1}{A} \frac{dA}{dt} + (C_{\epsilon 2}(s) + C_{\epsilon}^*(\omega^*)) \frac{P - \epsilon}{\frac{1}{2} q^2}$$

with

$$C_{\epsilon 2} = \frac{3s+5}{2(s+1)} \quad \omega^* = \frac{\omega \frac{1}{2} q^2}{\epsilon}$$

#### 5.6. Linear model

The study of the solid body rotation and the analysis of the various time scales has enabled us to link the variation of the spectrum shape in the energy containing range to the trapping of energy due to the reduction of energy transfer by rotation.

The only problem is now to express the variation of the large eddies with the help of rapid distortion theory. The use of a complete rapid distortion calculation would be too cumbersome and time-consuming so that an approximate, simple linear model is needed.

A solution is the use of the tensorial volumes of turbulence introduced by LIN and WOLFSHTEIN /100/. These volumes are defined as space integrals of two-point correlations as :

$$\frac{1}{2} q^2 v_{ij}(\underline{x}) = \int \langle u_i'(\underline{x}) u_j'(\underline{x} + \underline{r}) \rangle d^3 \underline{r}$$

They can be related to second order moments as :

$$\phi_{ij}(\underline{k}) = \frac{1}{(2\pi)^3} \int \langle u_i'(\underline{x}) u_j'(\underline{x} + \underline{r}) \rangle e^{-i \underline{k} \cdot \underline{r}} d^3 \underline{r}$$

thus

$$\frac{1}{2} q^2 v_{ij}(\underline{x}) \sim \lim_{k \rightarrow 0} \left( \frac{\int \phi_{ij}(\underline{k}) dA(\underline{k})}{4\pi k^2} \right)$$

These volumes of turbulence make sense only when all the second order moments behave like  $k^2$  in the vicinity of zero. The spherically averaged second order moments can thus be identified with the tensorial volumes of turbulence as :

$$\phi_{ij}(\underline{k}) = \int \phi_{ij}(\underline{k}) dA(\underline{k}) = A_{ij} k^2$$

$$A_{ij} \sim 4\pi q^2 v_{ij} \quad \frac{1}{2} A_{ii} = A$$

LIN and WOLFSHTEIN derived from the NAVIER equation a transport equation for the tensorial volumes of turbulence which reads, for homogeneous turbulence :

$$\frac{dA_{ij}}{dt} = - A_{ik} \frac{\partial u_j}{\partial x_k} - A_{jk} \frac{\partial u_i}{\partial x_k}$$

CAMBON (private communication) noticed that the derivation of the above equation is somewhat spurious as pressure-velocity correlations are assumed to vanish when the separation tends towards infinity while one is dealing with the properties of turbulence near wave number zero, i.e. for infinite wave length.

We prefer to consider this model as a very simple model with pressure effects omitted. Such a simple model has to be validated by comparison with exact rapid distortion theory solutions.

Figure 23 shows the predictions of the large eddies evolution time scale  $\frac{1}{s+1} \frac{1}{A} \frac{dA}{dt}$  for various values of the exponent  $s$ , for isotropic turbulence submitted to a plane strain. The LIN and WOLFSHTEIN model gives the same prediction as the complete rapid distortion theory, when the exponent  $s$  is equal to two, i.e. when tensorial volumes make sense. However, as pressure terms are omitted, the evolution of all  $A_{ij}$  coefficients is not absolutely correct. The reasons for the correct prediction of  $A$  and the incorrect predictions of  $A_{ij}$  have been studied by CAMBON et al /45/. It must be noticed that the exponent  $s$  influences the asymptotic value of the large eddies time scale for high total strain; however, these values are never achieved in experiments (TOWNSEND /14/,  $Dt_{max} \sim 1.75$ ; MARECHAL /25/,  $Dt_{max} \sim 2.6$ ). The same conclusions can be drawn for three-dimensional strains.

Figure 24 shows the predictions of the large eddies evolution time scale for various values of the exponent  $s$  for isotropic turbulence submitted to shear. The influence of the exponent  $s$  is small but the LIN and WOLFSHTEIN model does not exactly fit with the exact solution. The agreement is however acceptable. The inference of asymptotic behaviour between the strained and sheared flows must be noticed. While for strained flows, the time scale  $\frac{1}{s+1} \frac{1}{A} \frac{dA}{dt}$  tends towards an asymptotic value, it tends towards zero for large total strains  $S.t.$

The linear model without pressure effects is not correct for sheared flows as the linear pressure effects are mainly due to mean flow rotation. For turbulence submitted to strain plus rotation with a rotation rate larger than the strain rate, the linear pressure effects are large and the simple linear model fails (CAMBON, private communication).

Better linear models, taking into account pressure effects to give the correct evolution of the  $A_{ij}$  for strained flows, a better prediction for sheared flows and strain plus rotation flows, and even valid for various values of the exponent  $s$ , have been looked for unsuccessfully (AUPOIX, Ph. D. dissertation). The LIN and WOLFSHTEIN model will be used as it is simple and gives fairly good predictions of the large eddies time scale.

A special attention has to be paid to the initial values of the large eddies coefficients  $A_{ij}$  as they reflect the past history of turbulence. Figures 23 and 24 show that the large eddies time scale depends drastically upon the total strain of shear encountered.

For strained flow experiments, it always exists a decay relation between the turbulence generating grid and the distorting duct. At the entrance of the distorting duct, the REYNOLDS stress anisotropy is small. One can imagine that the same anisotropy could be produced by applying a large strain to isotropic turbulence during a very short time. Rapid distortion theory connects the anisotropy to the applied strain as :

$$b_{ij} = \frac{\langle u_i' u_j' \rangle}{q^2} - \frac{\delta_{ij}}{3} = -\frac{2}{15} \left( \frac{\partial u_i}{\partial x_j} + \frac{\partial u_j}{\partial x_i} \right) t + O(t^2)$$

On the other hand, the LIN and WOLFSHTEIN model gives the evolution of the coefficients  $A_{ij}$  for initially isotropic strained flows as :

$$A_{ij} = \frac{2}{3} A_0 e^{2 \left( \frac{\partial u_i}{\partial x_j} + \frac{\partial u_j}{\partial x_i} \right) t}$$

so that, by eliminating  $\left( \frac{\partial u_i}{\partial x_j} + \frac{\partial u_j}{\partial x_i} \right) t$ , the coefficients  $A_{ij}$  can be connected to the anisotropy. The initial coefficient  $A_0$  plays no rôle as one is only interested in the time scale  $\frac{1}{A} \frac{dA}{dt}$ .

For sheared flows, experimental values are taken downstream of the shear generator. The solution of the LIN and WOLFSHTEIN model for initially isotropic, sheared turbulence, reads :

$$\begin{aligned} A_{11} &= \frac{2}{3} A_0 (1 + (St)^2) \\ A_{12} &= -\frac{2}{3} A_0 St \quad S = \frac{\partial u_1}{\partial x_2} \\ A_{22} &= A_{33} = \frac{2}{3} A_0 \end{aligned}$$

The initial values of the  $A_{ij}$  are thus set according to the travel time of the flow from the shear generator to the first station.

### 5.7. Low REYNOLDS number effects

The above proposed energy spectrum shape is only valid at high REYNOLDS numbers. At low REYNOLDS numbers, the  $k^{-5/3}$  inertial range is reduced or even does not exist. The presence of the dissipation range must then be accounted for. Various laws have been proposed to represent the energy spectrum in the dissipation range. The most popular are the one proposed by PAO /101/ :

$$E(k) = K_0 \epsilon^{2/3} k^{-5/3} \exp \left\{ - \frac{3K_0}{2} \left( \frac{k}{k_D} \right)^{4/3} \right\} \quad k_D = \left( \frac{\epsilon}{\nu^3} \right)^{1/4}$$

and SAFFMAN /102/ :

$$E(k) = K_0 \epsilon^{2/3} k^{-5/3} \exp \left\{ - 2 \left( \frac{k}{k_D} \right)^2 \right\}$$

EDQNM computations lead to the more complex formula /103/ :

$$E(k) = K_0 \epsilon^{2/3} k^{-5/3} \exp \left\{ - 3.5 \eta^2 (1 - \exp(6\eta + 1.2 - (196\eta^2 - 33.6\eta + 1.4532)^{1/2})) \right\} \quad \eta = \frac{k}{k_D}$$

which has the advantage to exhibit a bump at the beginning of the dissipative range as observed experimentally /104/.

These above laws could be introduced in the computation of the turbulent kinetic energy to derive a new dissipation equation. A simpler solution is to define a truncation wave number  $\alpha k_D$  such as :

$$\int_0^\infty \epsilon^{2/3} k^{-5/3} f\left(\frac{k}{k_D}\right) dk = \int_0^{\alpha k_D} K_0 \epsilon^{2/3} k^{-5/3} dk$$

and to proceed with inertial ranges truncated at  $\alpha k_D$ . The constant  $\alpha$  is close to unity whatever the dissipative spectrum used. The dissipation equation can then be derived in a way similar to the high REYNOLDS number case. It reads :

$$\left( 1 + (2 - C_{\epsilon 2}) \frac{\beta}{3\sqrt{R_e}} \right) \frac{1}{\epsilon} \frac{d\epsilon}{dt} = - \frac{1}{s+1} \left( 1 + \frac{2\beta}{3\sqrt{R_e}} \right) \frac{1}{A} \frac{dA}{dt} + C_{\epsilon 2} \left( \frac{P - \epsilon}{\frac{1}{2} q^2} - \left( 1 + \frac{2\beta}{3\sqrt{R_e}} \right) \frac{1}{F} \frac{dF}{dt} \right)$$

where  $R_e = \frac{(q^2)^2}{9\nu\epsilon}$  is the turbulent REYNOLDS number and  $\beta$  a constant related to  $\alpha$ . For the different spectrum shapes, the following values have been obtained :

PAO	$\beta = 2.065$
SAFFMAN	$\beta = 2.047$
EDQNM	$\beta = 2.079$

An average value  $\beta = 2.06$  has been used.

As the REYNOLDS number decreases, the inertial range diminishes, disappears and then the energy containing range shape variations should be modified at low REYNOLDS number but no tool is available to simply predict the influence of low REYNOLDS numbers on this time scale  $(1/F)(dF/dt)$ . Assuming that this time scale is unaffected by low REYNOLDS number effects, the decay law can be expressed as :

$$- \frac{1}{\epsilon} \frac{d\epsilon}{dt} = \frac{C_{\epsilon 2}}{1 + (2 - C_{\epsilon 2}) \frac{\beta}{3\sqrt{R_e}}} \quad C_{\epsilon 2} = \frac{3s+5}{2(s+1)} = \frac{11}{6} \quad (s=2)$$

This decay law has been compared with predictions of EDQNM simulations. As shown on figure 25, the agreement is pretty good. This simply deduced model is better than any low REYNOLDS number model compiled by PATEL et al /105/.

### 5.8. Comparison with experiments

The MIS approach has been checked by comparison with experiments for various strained and sheared flows, as shown on figures 26 to 31. The continuous line corresponds to the standard dissipation equation improved by adding the rotation correction presented above. The dotted line corresponds to the simple MIS model without rotation and low REYNOLDS number effects. The largely dotted line corresponds to the MIS model with rotation effects (i.e.  $F$  variations) included and the chain-dotted line to the MIS model with both rotation and low REYNOLDS number effects included.

The only tunable parameter in the MIS model is the exponent  $s$  which has been set equal to two to be consistent with the LIN and WOLFSHTEIN model.

For strained flows, the agreement with the MIS model is as good as with the standard dissipation equation, the coefficients of which have been tuned for this kind of flow (figures 26-27). No rotation effect occurs and low REYNOLDS number effects are weak.

For weakly sheared flows (figures 28-29), the MIS prediction are as good even a little better as with the improved standard model. Rotation effects and low REYNOLDS number effects improve the prediction of CHAMPAGNE flow.

The most striking improvement is obtained for highly sheared flows (figures 30-31). Low REYNOLDS number effects are small but the agreement with the bare MIS model is as good as with the improved standard equation. This brings into evidence the important rôle of the large eddies time scale in the MIS equation ; this term is large for strained or weakly sheared turbulence and tends towards zero for highly sheared turbulence. For highly sheared flows, the MIS equation is equivalent to the standard dissipation equation provided that the coefficient  $C_{\epsilon 1}$  tends towards  $C_{\epsilon 2}$ , which is not the case in the standard equation. Moreover, the rotation effects correction highly improves the prediction.

### 5.9. Conclusion

The MIS approach, based upon simple physical arguments concerning the energy spectrum evolution introduces new time scales in the dissipation equation. Low REYNOLDS number effects can be naturally accounted for by reasoning on the spectrum shape.

Although a too simple linear model has been used, the introduction of the large eddies time scale and of rotation effects highly improves the prediction of highly sheared flows.

Moreover, without any tuned coefficient, the prediction of strained and weakly sheared flow is as good as with standard, tuned, dissipation equation.

### 6 - CONCLUSIONS

Two-point closures are a very convenient tool to solve purely linear problem as the problem is analytical in FOURIER space. Rapid distortion theory can thus give constraints to improve pressure-strain correlation models.

Two-point closures are a suitable tool to perform high REYNOLDS number simulations. As no adjustable coefficient is introduced in the model, they can be viewed as "exact". The return to isotropy problem can be studied over a wide range of REYNOLDS numbers and initial conditions with a two-point closure in order to improve one-point closures.

The study of the influence of rotation on the dissipation equation has brought into evidence the rôle of simulations in the derivation of closures. The modified EDQNM model can be obtained as a simplification of the exact, anisotropic model but was first validated by comparison with direct and large eddy simulations. The extensive use of this model has led to a correction function  $C_\epsilon^*$  which cannot be obtained by a priori modelling and constant tuning.

At last, the use of simplified energy spectra, either in the simple decay study or in the MIS approach, have shown to be a powerful tool to study the dissipation equation. This is due to the fact that, with the one-scale hypothesis of standard one-point closures, the dissipation equation is equivalent to a turbulent length scale equation while, on the other hand, the use of these simplified spectra gives information about the contribution of each length scale to the turbulent kinetic energy. The main advantage of the MIS approach is to introduce new time scales which were not used in standard models and improve the prediction.

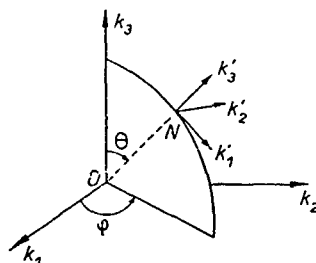
The author would like to acknowledge Dr. COUSTEIX for his critical review of the paper.

### APPENDIX A CRAYA'S REFERENCE FRAME

The description of second order moments can be simplified by the use of a suitable reference frame linked to the wave vector to take advantage of the continuity equation. CRAYA /1/ has proposed to build such a reference frame as follows :

- The FOURIER space reference frame consists of the three basis wave vectors  $\underline{k}_1$ ,  $\underline{k}_2$  and  $\underline{k}_3$ .

- For a given wave vector  $\underline{k}$ , the local CRAYA's reference frame  $\underline{k}'_1$ ,  $\underline{k}'_2$ ,  $\underline{k}'_3$  is such that  $\underline{k}'_3$  is parallel to  $\underline{k}$ ,  $\underline{k}'_1$  is tangent to the circle drawn on the plane containing  $\underline{k}_3$ , and  $\underline{k}'_2$  such as  $\underline{k}'_1$ ,  $\underline{k}'_2$ ,  $\underline{k}'_3$  be direct.



from /1/

In this reference frame, the second order moment reduces to  $\phi_{11}' = N_1$ ,  $\phi_{12}' = S$ ,  $\phi_{21}' = S^*$ ,  $\phi_{22}' = N_2$ .

The relations between components in the initial reference frame and in the CRAVA's reference frame are obtained with the knowledge of the matrix  $\omega$ :

$$(\omega) = \begin{pmatrix} \cos\theta \cos\varphi & \cos\theta \sin\varphi & -\sin\theta \\ -\sin\varphi & \cos\varphi & 0 \\ \sin\theta \cos\varphi & \sin\theta \sin\varphi & \cos\theta \end{pmatrix}$$

where the angles  $\theta$  and  $\varphi$  can be expressed from the components  $\alpha_1$ ,  $\alpha_2$  and  $\alpha_3$  of a unit vector parallel to  $\underline{ON}$  (i.e. parallel to  $\underline{k}$  or  $\underline{k}'_3$ ) in the initial reference frame :

$$(\omega) = \begin{pmatrix} \frac{\alpha_1 \alpha_3}{\sqrt{1-\alpha_3^2}} & \frac{\alpha_2 \alpha_3}{\sqrt{1-\alpha_3^2}} & -\sqrt{1-\alpha_3^2} \\ \frac{-\alpha_2}{\sqrt{1-\alpha_3^2}} & \frac{\alpha_1}{\sqrt{1-\alpha_3^2}} & 0 \\ \alpha_1 & \alpha_2 & \alpha_3 \end{pmatrix},$$

The connection between components in the CRAVA's reference frame, denoted by a prime, and in the initial reference frame, are then :

$$\begin{aligned} X'_1 &= \omega_{1l} X_l & X_l &= \omega_{li} X'_i \\ \frac{\partial}{\partial k'_1} &= \omega_{1l} \frac{\partial}{\partial k_l} & \frac{\partial}{\partial k_l} &= \omega_{li} \frac{\partial}{\partial k'_i} \\ \phi'_{ij} &= \omega_{il} \omega_{jm} \phi_{lm} & \phi_{ij} &= \omega_{li} \omega_{mj} \phi'_{lm} \end{aligned}$$

Consequently :

$$\begin{aligned} \phi_{11} &= \frac{1}{1-\alpha_3^2} (\alpha_1^2 \alpha_3^2 N_1 + \alpha_2^2 N_2 - \alpha_1 \alpha_2 \alpha_3 (S + S^*)) \\ \phi_{22} &= \frac{1}{1-\alpha_3^2} (\alpha_2^2 \alpha_3^2 N_1 + \alpha_1^2 N_2 + \alpha_1 \alpha_2 \alpha_3 (S + S^*)) \\ \phi_{33} &= (1 - \alpha_3^2) N_1 \\ \phi_{12} &= \frac{1}{1-\alpha_3^2} (\alpha_1 \alpha_2 \alpha_3^2 N_1 - \alpha_1 \alpha_2 N_2 + \alpha_1^2 \alpha_3 S - \alpha_2^2 \alpha_3 S^*) \\ \phi_{23} &= -\alpha_2 \alpha_3 N_1 - \alpha_1 S^* \\ \phi_{31} &= -\alpha_1 \alpha_3 N_1 + \alpha_2 S \end{aligned}$$

and the trace, i.e. the contribution to the kinetic energy, is the same in both reference frames :

$$\phi_{11} + \phi_{22} + \phi_{33} = N_1 + N_2$$

Derivation rules in CRAVA's reference frame are detailed in reference /1/.

## REFERENCES

- /1/ A. CRAYA - "Contribution à l'analyse de la turbulence associée à des vitesses moyennes" - Publications scientifiques et techniques du Ministère de l'Air (1958)
- /2/ G. COMTE-BELLOT, S. CORRSIN - "The use of a contraction to improve the isotropy of grid generated turbulence" - JFM Vol. 25 Part 4, pp. 657-682 (1966)
- /3/ G. COMTE-BELLOT, S. CORRSIN - "Simple Eulerian time correlation of full- and narrow-band velocity signals in grid generated, "isotropic" turbulence" - JFM Vol. 48 Part 2, pp. 273-337 (1971)
- /4/ R.W. STEWART, A.A. TOWNSEND - "Similarity and self-preservation in isotropic turbulence" - Phil. Trans. A 283, pp. 359-386 (1951)
- /5/ C.W. VAN ATTA, W.Y. CHEN - "Correlation measurements in grid turbulence using digital harmonic analysis" - JFM Vol. 34 Part 3, pp. 497-515 (1968)
- /6/ C.W. VAN ATTA, W.Y. CHEN - "Measurements of spectral energy transfer in grid turbulence" - JFM Vol. 38 Part 4, pp. 743-763 (1969)
- /7/ C.W. VAN ATTA, T.T. YEH - "Some measurements of multi-point time correlations in grid turbulence" - JFM Vol. 41 Part 1, pp. 169-178 (1970)
- /8/ T.T. YEH, C.W. VAN ATTA - "Spectral transfer of scalar and velocity fields in heated-grid turbulence" - JFM Vol. 58 Part 2, pp. 233-261 (1973)
- /9/ M. GAD-EL-HAK, S. CORRSIN - "Measurements of the nearly isotropic turbulence behind a uniform jet grid" - JFM Vol. 62 Part 1, pp. 115-143 (1974)
- /10/ H. TSUJI - "Experimental studies of the characteristics of isotropic turbulence behind two grids" - Journal of the Physical Society of JAPAN Vol. 10 N° 7, pp. 578-586 (1955)
- /11/ H. TSUJI - "Experimental studies on the spectrum of isotropic turbulence behind two grids" - Journal of the Physical Society of JAPAN Vol. 11 N° 10, pp. 1096-1104 (1956)
- /12/ R.M. KELLOG, S. CORRSIN - "Evolution of a spectrally local disturbance in grid-generated, nearly isotropic turbulence" - JFM Vol. 96 Part 4, pp. 641-669 (1980)
- /13/ M.S. UBEROI - "Effect of wind tunnel contraction on free stream turbulence" - Journal of the Aeronautical Sciences Vol. 23, pp. 754-764 (1956)
- /14/ H.J. TUCKER, A.J. REYNOLDS - "The distortion of turbulence by irrotational plane strain" - JFM Vol. 32 Part 4, pp. 657-673 (1968)
- /15/ J.N. GENCE, J. MATHIEU - "The return to isotropy of an homogeneous turbulence having been submitted to two successive plane strains" - JFM Vol. 101 Part 3, pp. 555-566 (1980)
- /16/ K.S. CHOI - "A study of the return to isotropy of homogeneous turbulence" - CORNELL University, Ph. D. (1983)
- /17/ L. LE PENVEN, J.N. GENCE, G. COMTE-BELLOT - "On the approach to isotropy of homogeneous turbulence : effect of the partition of kinetic energy among the velocity components" - Fundamentals of Fluid Mechanics, Northwestern University (1984) - Published by Springer Verlag
- /18/ S.C. TRAUGOTT - "Influence of solid-body rotation on screen-produced turbulence" - NACA TN 4135 (1958)
- /19/ A. IBBETSON, D.J. TRITTON - "Experiments on turbulence in a rotating fluid" - JFM Vol. 68 Part 4, pp. 639-672 (1975)
- /20/ E.J. HOPFINGER, J.A. TOLLY - "Spatially decaying turbulence and its relation to mixing across density surfaces" - JFM Vol. 78 Part 1, pp. 155-175 (1976)
- /21/ E.J. HOPFINGER, R.W. GRIFFITHS, M. MORY - "The structure of turbulence in homogeneous and stratified rotating fluids" - Journal de Mécanique Théorique et Appliquée, Numéro Spécial 1983, pp. 21-24 (1983)
- /22/ R.A. WIGELAND, H.M. NAGIB - "Grid generated turbulence with and without rotation about the streamwise direction" - IIT Fluids & Heat Transfer Report R78-1, ILLINOIS Institute of Technology (1978)
- /23/ A.A. TOWNSEND - "The uniform distortion of homogeneous turbulence" - Quarterly Journal of Mechanics and Applied Mathematics Vol. VII Part 1, pp. 104-127 (1954)
- /24/ A.J. REYNOLDS, H.J. TUCKER - "The distortion of turbulence by general uniform irrotational strain" - JFM Vol. 68 Part 4, pp. 673-693 (1975)
- /25/ J. MARECHAL - "Etude expérimentale de la déformation plane d'une turbulence homogène" - Journal de Mécanique Vol. 11 N° 2, pp. 263-294 (1972)
- /26/ J.N. GENCE, J. MATHIEU - "On the application of successive plane strains to grid generated turbulence" - JFM Vol. 93 Part 3, pp. 501-513 (1979)

- /27/ M.S. UBEROI, S. WALLIS - "Small axisymmetric contraction of grid turbulence" - JFM Vol. 24 Part 3, pp. 539-543 (1966)
- /28/ V. RAMJEE, A.K.M.F. HUSSAIN - "Influence of the axisymmetric contraction ratio on free-stream turbulence" - Journal of Fluids Engineering - Transaction of the ASME, pp. 506-515 (Sept. 1976)
- /29/ E.G. TULARPURIKARA, V. RAMJEE - "Effect of contraction on screen generated turbulence" - The Aeronautical Journal of the Royal Aeronautical Society, pp. 290-295 (Sept. 1980)
- /30/ J. TAN ATICHA - "Effects of axisymmetric contractions on turbulence of various scales" - NASA CR 165136 ILLINOIS Institute of Technology (1980)
- /31/ W.G. ROSE - "Results of an attempt to generate a homogeneous turbulent shear flow" - JFM Vol. 25 Part 1, pp. 97-120 (1966)
- /32/ W.G. ROSE - "Interaction of grid turbulence with a uniform mean shear" - JFM Vol. 44 Part 4, pp. 767-779 (1970)
- /33/ F.H. CHAMPAGNE, V.G. HARRIS, S. CORRSIN - "Experiments on nearly homogeneous turbulent shear flow" - JFM Vol. 41 Part 1, pp. 81-139 (1970)
- /34/ V.G. HARRIS, J.A.H. GRAHAM, S. CORRSIN - "Further experiments in nearly homogeneous turbulent shear flow" - JFM Vol. 81 Part 4, pp. 657-687 (1977)
- /35/ S. TAVOULARIS, S. CORRSIN - "Experiments in nearly homogeneous turbulent shear flow with a uniform mean temperature gradient" - JFM Vol. 104, pp. 311-347 and 349-367 (1981)
- /36/ U. KARNIK, S. TAVOULARIS - "The asymptotic development of nearly homogeneous turbulent shear flow" - Fourth Symposium on Turbulent Shear Flow - KARLSRUHE (1983)
- /37/ P.J. MULHEARN, R.E. LUXTON - "The development of turbulence structure in a uniform shear flow" - JFM Vol. 68 Part 3, pp. 577-590 (1975)
- /38/ K.R. SREENIVASAN - "The effect of contraction on a homogeneous turbulent shear flow" - JFM Vol. 154, pp. 187-215 (1985)
- /39/ J.H. FERZIGER - "Homogeneous turbulent flows" - The 1980-81 AFOSR-HITM-STANFORD Conference on Complex Turbulent Flows : Comparison of Computation and Experiments - Vol. I, pp. 405-433 (1981)
- /40/ J.N. GENCE - "Homogeneous turbulence" - Annual Review of Fluid Mechanics, pp. 201-222 (1983)
- /41/ G.K. BATCHELOR - "The theory of homogeneous turbulence" - CAMBRIDGE University Press (1953)
- /42/ J.M. BURGERS, M. MITCHNER - "On homogeneous non isotropic turbulence connected with a mean motion having a constant velocity gradient" - Proc. Kon. Ned. Akad. v. Met. B Vol. 56, pp. 228-235 and 343-354 (1953)
- /43/ C. CAMBON, D. JEANDEL, J. MATHIEU - "Spectral modelling of homogeneous non isotropic turbulence" - JFM Vol. 104, pp. 247-262 (1981)
- /44/ A.A. TOWNSEND - "The response of sheared turbulence to additional distortion" - JFM Vol. 98 Part 1, pp. 171-191 (1980)
- /45/ C. CAMBON, C. TEISSEDE, D. JEANDEL - "Etude d'effets couplés de déformation et de rotation sur une turbulence homogène" - Journal de Mécanique Théorique et Appliquée - Vol. 4 N° 5, pp. 629-657 (1985)
- /46/ G.K. BATCHELOR, J. PROUDMAN - "The effect of rapid distortion of a fluid in turbulent motion" - Quarterly Journal of Mechanics and Applied Mathematics - Vol. 7 Part 1 (1954)
- /47/ R.G. DEISSLER - "Effect of initial conditions on weak homogeneous turbulence with uniform shear" - Physics of Fluids Vol. 13, pp. 1868-1869 (1970)
- /48/ P.A. COURSEAU, M. LOISEAU - "Contribution à l'analyse de la turbulence homogène isotrope" - Journal de Mécanique Vol. 17 N° 2, pp. 245-297 (1978)
- /49/ M.J. LEE, U. PIOMELLI, W.C. REYNOLDS - "Useful formulas in the rapid distortion theory of homogeneous turbulence" - Physics of Fluids Vol. 29 Part 10, pp. 3471-3474 (1986)
- /50/ C. CAY - "Etude spectrale d'un champ turbulent incompressible soumis à des effets couplés de déformation et de rotation, imposés extérieurement" - Thèse d'Etat, Université Claude Bernard, LYON 1 (1982)
- /51/ C. CAMBON, D. JEANDEL - "Approach of non isotropic homogeneous turbulence submitted to mean velocity gradients" - Third Symposium on Turbulent Shear Flow - DAVIS (1981)
- /52/ R.S. ROGALLO - "Numerical experiments in homogeneous turbulence" - NASA TN 81315 (1981)
- /53/ M. BOSCHIARO, J.N. GENCE, J. MATHIEU - "Réponse d'une turbulence homogène à un changement brusque de position des axes principaux du tenseur de déformation" - Comptes rendus de l'Académie des Sciences de PARIS - B 285, p. 89 (1977)



- /54/ D. JEANDEL, J.F. BRISON, J. MATHIEU - "Modelling methods in physical and spectral space" - Physics of Fluids Vol. 21-2, pp. 169-182 (1978)
- /55/ J.P. BERTOGLIO - "Etude d'une turbulence anisotrope : modélisation de sous-maille et approche statistique" - Université Claude Bernard, LYON 1 (1986)
- /56/ D.C. LESLIE - "Developments in the theory of turbulence" - Clarendon Press OXFORD (1973)
- /57/ S.A. ORSZAG - "Lectures on the statistical theory of turbulence" - Fluid Dynamics Les Houches (1973) - GORDON and BREACH Science Publishers (1977)
- /58/ H.L. GRANT, R.W. STEWART, A. MOILLIET - "Turbulence spectra in a tidal channel" - JFM Vol. 12, pp. 241-268 (1962)
- /59/ M. LESIEUR, D. SCHERTZER - "Amortissement auto-similaire d'une turbulence à grand nombre de REYNOLDS" - Journal de Mécanique Vol. 17 N° 4, pp. 609-646 (1978)
- /60/ L.S.G. KOVASZNYI - "Spectrum of locally isotropic turbulence" - Journal of Aeronautical Sciences Vol. 15 p. 745 (1948)
- /61/ W. HEISENBERG - "Zur statistischen Theorie der Turbulenz" - Zeitschrift der Physik 124, p. 628 (1948)
- /62/ L. CROCCO - "On certain models in isotropic turbulence" - ONERA Publication 1981-2
- /63/ R.H. KRAICHNAN - "Irreversible statistical mechanics of incompressible hydromagnetic turbulence" - Physical Review N° 109, pp. 1407-1422 (1958)
- /64/ R.H. KRAICHNAN - "The structure of isotropic turbulence at very high REYNOLDS numbers" - JFM Vol. 5, pp. 497-543 (1959)
- /65/ J. MATHIEU, D. JEANDEL - "Turbulence models and their applications - Volume one : Turbulence et approche spectrale - Eyrolles (1984)
- /66/ R.H. KRAICHNAN - "Dynamics of non linear stochastic systems" - Journal of Mathematical Physics Vol. 2, pp. 124-148 (1961) + Erratum Vol. 3 p. 205 (1962)
- /67/ R.H. KRAICHNAN - "Lagrangian history closure approximation for turbulence" - Physics of Fluids, Vol. 8, p. 575 (1965)
- /68/ R.H. KRAICHNAN - "An almost Markovian Galilean invariant turbulence model" - JFM Vol. 47 Part 3, pp. 513-524 (1971)
- /69/ R.H. KRAICHNAN - "Test field model for inhomogeneous turbulence" - JFM Vol. 56 Part 2, pp. 287-304 (1972)
- /70/ P.L. SULEM, M. LESIEUR, U. FRISCH - "Le 'Test Field Model' interprété comme méthode de fermeture des équations de la turbulence" - Annales de Géophysique Tome 31 Fascicule 4, pp. 487-495 (1975)
- /71/ I. PROUDMAN, W.H. REID - "On the decay of a normally distributed and homogeneous turbulent velocity field" - Phil. Trans. A Vol. 247, p. 163 (1954)
- /72/ Y. OGURA - "A consequence of the zero-fourth-cumulant approximation in the decay of isotropic turbulence" - JFM Vol. 16, pp. 33-40 (1962)
- /73/ S.A. ORSZAG - "Analytical theories of turbulence" - JFM Vol. 41 Part 2, pp. 363-386 (1970)
- /74/ J.C. ANDRE, M. LESIEUR - "Influence of helicity on the evolution of isotropic turbulence at high REYNOLDS number" - JFM Vol. 81 Part 4, pp. 187-207 (1979)
- /75/ J.M. VIGNON, C. CAMBON, M. LESIEUR, D. JEANDEL - "Confrontation aux expériences de turbulence thermique homogène et isotrope de calculs spectraux basés sur la théorie EDQNM" - CRAS Tome 288 Série B, pp. 335-339 (1979)
- /76/ C.E. LEITH - "Atmospheric predictability and two-dimensional turbulence" - Journal of Atmospheric Sciences Vol. 28 N° 2, pp. 145-161 (1971)
- /77/ S. ORSZAG, G.R. PATTERSON - "Numerical simulation of turbulence" - Lecture Notes in Physics Vol. 12, pp. 127-147 (1971)
- /78/ L. CROCCO, P. ORLANDI - "A transformation for the energy transfer term in isotropic turbulence" - JFM Vol. 156, pp. 405-424 (1985)
- /79/ P.Y. CHOU - "On velocity correlations and the solutions of the equations of turbulent fluctuations" - Quarterly Applied Mathematics Vol. 3, p. 38 (1945)
- /80/ J.L. LUMLEY, G.R. NEWMAN - "The return to isotropy of homogeneous turbulence" - JFM Vol. 82 Part 1, pp. 161-178 (1977)
- /81/ J.C. ROTTA - "Statistische Theorie nichthomogenes Turbulenz" - Zeitschrift für Physik, Bd 129, pp. 547-572 Bd 131, pp. 51-77 (1951)

- /82/ K. DANG - "Direct numerical simulation of homogeneous strained turbulence" - VKI Lecture Series - ONERA TP N° 1986-17
- /83/ M. MILLIONSHTCHIKOV - "On the theory of homogeneous isotropic turbulence" - Compte rendu de l'Académie des Sciences d'URSS N° 32, p. 615 (1941)
- /84/ J.P. BERTOGLIO - "A model of three-dimensional transfer in non isotropic homogeneous turbulence" - Third Symposium on Turbulent Shear Flow, DAVIS (1981)
- /85/ L. LE PENVEN, J.N. GENCE - "Une méthode de construction systématique de la fermeture liant la partie linéaire de la corrélation pression-déformation au tenseur de REYNOLDS dans une turbulence homogène soumise à une déformation uniforme" - CRAS Tome 297 Série II, pp. 309-312 (1983)
- /86/ Y. LECOINTE, J. PIQUET, M. VISONNEAU - "Rapid term modelling of REYNOLDS stress closures with the help of rapid distortion theory" - Fifth Symposium on Turbulent Shear Flows, CORNELL (1985)
- /87/ W.C. REYNOLDS - "Computation of turbulent flows" - AIAA Paper 74-556
- /88/ A.S. MONIN, A.M. YAGLOM - "Statistical fluid mechanics" - The MIT Press (1979)
- /89/ J. BARDINA, J.H. FERZIGER, R.S. ROGALLO - "Effect of rotation on isotropic turbulence : computation and modelling" - JFM Vol. 154, pp. 321-336 (1985)
- /90/ B. AUPOIX, J. COUSTEIX, J. LIANDRAT - "Effect of rotation on isotropic turbulence" - Fourth Symposium on Turbulent Shear Flow, KARLSRUHE (1983)
- /91/ C. CAMBON, L. JACQUIN - "Non isotropic aspects in homogeneous turbulence subjected to rotation" - 7th Annual Meteorology Society Symposium on Turbulence and Diffusion, BOULDER (1985)
- /92/ C. CAMBON, L. JACQUIN - "Analyse spectrale des effets de la rotation sur la turbulence homogène" - European Turbulence Conference, LYON (1986)
- /93/ C. CAMBON, J.P. BERTOGLIO, D. JEANDEL - "Spectral closure for homogeneous turbulence" - The 1980-81 AFOSR-HTTM-STANFORD Conference on Complex Turbulent Flows Vol. III, pp. 1307-1311
- /94/ B. AUPOIX, J. COUSTEIX - "Modèles simples de tension de sous-maille en turbulence homogène isotrope" - La Recherche Aérospatiale N° 1982-4, pp. 273-283 - Available in English
- /95/ B. AUPOIX, J. COUSTEIX - "Subgrid scale model for isotropic turbulence" - Refined Modelling of Flows, PARIS (1982)
- /96/ B. AUPOIX - "Eddy viscosity subgrid scale models for homogeneous turbulence" - Lecture Notes in Physics N° 230, pp. 45-64 (1984)
- /97/ K. HANJALIC, B.E. LAUNDER - "Sensitizing the dissipation equation to irrotational strains" - Journal of Fluid Engineering - Transactions of the ASME Vol. 102, pp. 34-40 (1980)
- /98/ K. HANJALIC, B.E. LAUNDER - "A REYNOLDS stress model of turbulence and its applications to thin shear flows" - JFM Vol. 52 Part 4, pp. 609-638 (1972)
- /99/ B. AUPOIX, J. COUSTEIX, J. LIANDRAT - "MIS : an alternative for the dissipation equation" - European Turbulence Conference, LYON (1986)
- /100/ A. LIN, M. WOLFSHTEIN - "Tensorial volume of turbulence" - Physics of Fluids Vol. 23 N° 3, pp. 644-646 (1980)
- /101/ Y.M. PAO - "Structure of turbulent velocity and scalar fields at large wave numbers" - Physics of Fluids Vol. 8, p. 1063 (1965)
- /102/ P.G. SAFFMAN - "On the fine-scale structure of vector fields convected by a turbulent field" - JFM Vol. 16, p. 545 (1963)
- /103/ B. AUPOIX - "Subgrid scale models for homogeneous anisotropic turbulence" - Notes on Numerical Fluid Mechanics - Volume 15 "Direct and Large Eddy Simulation of Turbulence", pp. 37-66 (1986)
- /104/ P. MESTAYER, J.P. CHOLLET, M. LESIEUR - "Inertial subrange of velocity and scalar variance spectra in high REYNOLDS number three-dimensional turbulence" - Proceedings of Turbulence and Chaotic Phenomena in Fluids - T. TATSUMI Editor - Elsevier Science Publisher, pp. 285-288 (1984)
- /105/ V.C. PATEL, W. RODI, G. SCHEUERER - "Evaluation of turbulence models for near wall and low REYNOLDS number flow" - Third Symposium on Turbulent Shear Flow, DAVIS (1981) or AIAA Journal Vol. 23 N° 9, pp. 1308-1318 (1985)
- /106/ M. HAMADICHE - "Analyse spectrale des mécanismes linéaires des écoulements turbulents inhomogènes" - Thèse d'Etat, LYON (1985)
- /107/ B.E. LAUNDER, G.J. REECE, W. RODI - "Progress in the development of a REYNOLDS stress turbulence closure" - JFM Vol. 68 Part 3, pp. 537-566 (1975)

- /108/ M. LESIEUR - "Turbulence in fluids - Stochastic and numerical modelling" - Martinus Nijhoff Publishers (1987)
- /109/ J.R. HERRING, D. SCHERTZER, M. LESIEUR, G.R. NEWMAN, J.P. CHOLLET, M. LARCHEVEQUE - "A comparative assessment of spectral closures as applied to passive scalar diffusion" - JFM Vol. 124, pp. 411-437 (1982)
- /110/ W.C. REYNOLDS - "Turbulence models and their applications : physical and analytical foundations, concepts and new directions in turbulence modelling and simulation" - Eyrolles (1984)
- /111/ A.M. SAVILL - "Recent developments in rapid distortion theory" - Annual Review of Fluid Mechanics Vol. 19, pp. 531-575 (1987)
- /112/ L. JACQUIN, O. LEUCHTER, P. EFFROY - "Experimental study of homogeneous turbulence in the presence of rotation" - To be presented at the Sixth Symposium on Turbulent Shear Flow, TOULOUSE (Sept. 1987)

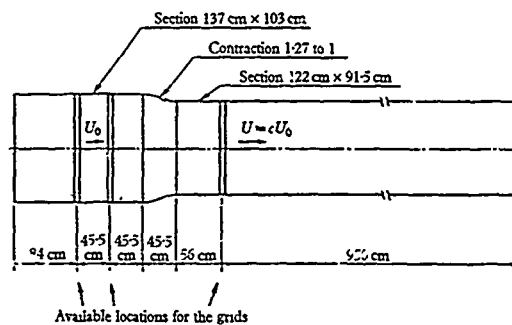


Figure 1

Sketch of the wind tunnel test section used by COHIE-BELLOT and CCRSIN to produce isotropic turbulence (from /2/)

Figure 2

Sketch of the wind tunnel test section used by TUCKER and REYNOLDS to produce plane strain and study the return to isotropy (from /14/)

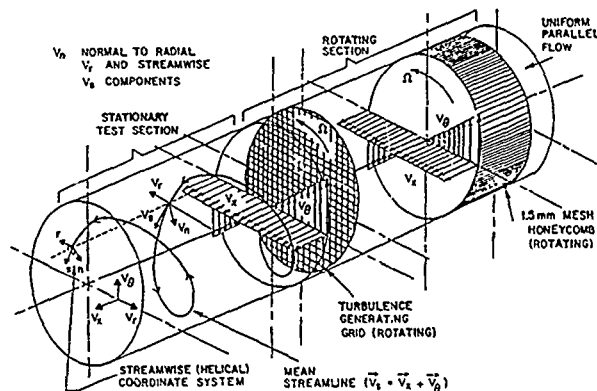
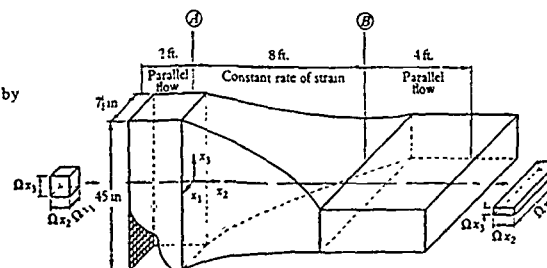


Figure 3

Sketch of the wind tunnel test section used by WIGELAND and NAGIB to study turbulence submitted to solid body rotation (from /21/)

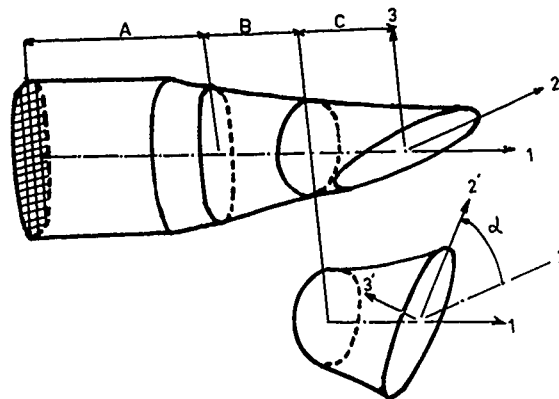


Figure 4

GENCE and MATHIEU experimental set-up. The second straining can be rotated to impose different strain axes (from /26/)

Figure 5

Experimental set-up used by ROSE to study sheared turbulence (from /32/)

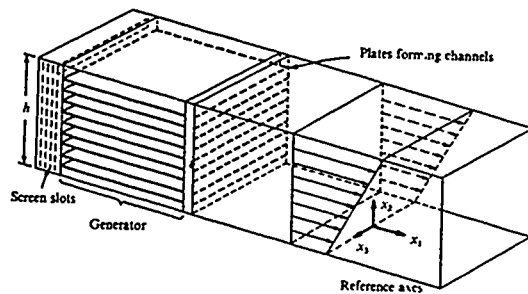
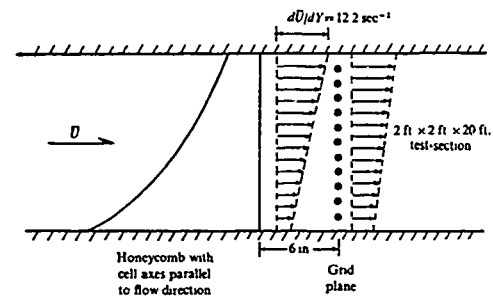


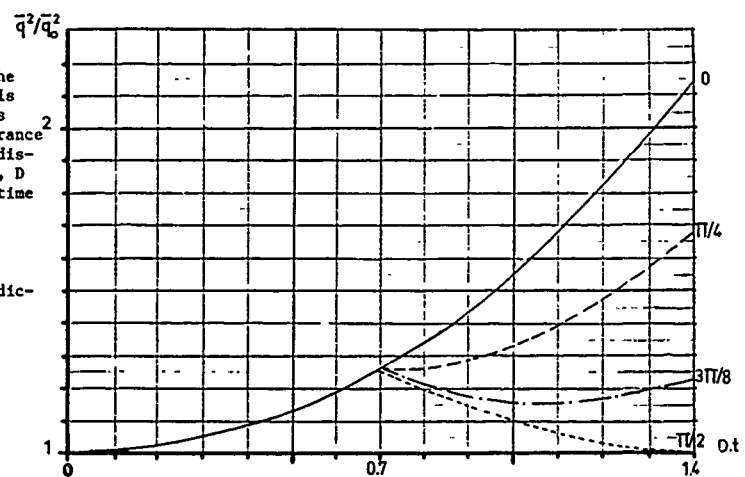
Figure 6

Experimental set-up used by CHAMPAGNE et al to study sheared turbulence (from /33/)

Figure 7

GENCE and MATHIEU experiment. Evolution of the ratio  $\bar{q}^2/\bar{q}_0^2$  versus  $X_1/L$  or  $Dt$  for different values of the angle  $\alpha$  between the two successive strain axes ( $\bar{q}^2$  is the trace of the REYNOLDS stress tensor,  $\bar{q}_0^2$  its value at the entrance of the distorting duct,  $X_1$  the distance,  $L$  the length of the duct,  $D$  the strain and  $t$  the residence time in the duct)

7a) Rapid distortion theory predictions (from /54/)



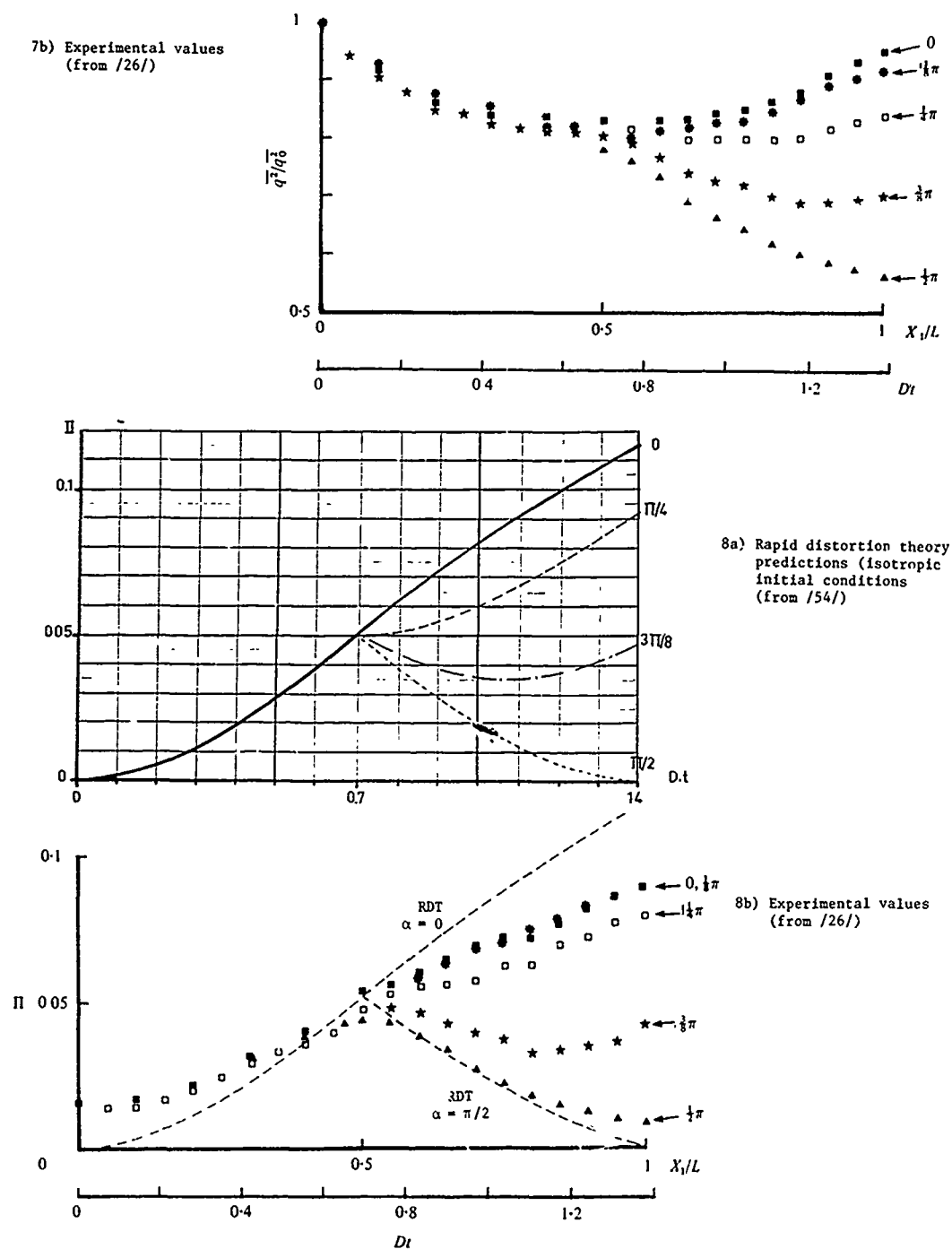


Figure 8 - GENGE and MATHIEU experiment. Evolution of the second anisotropy tensor invariant versus  $X_1/L$  or  $Dt$  for different values of the angle  $\alpha$  between the two successive strain axes

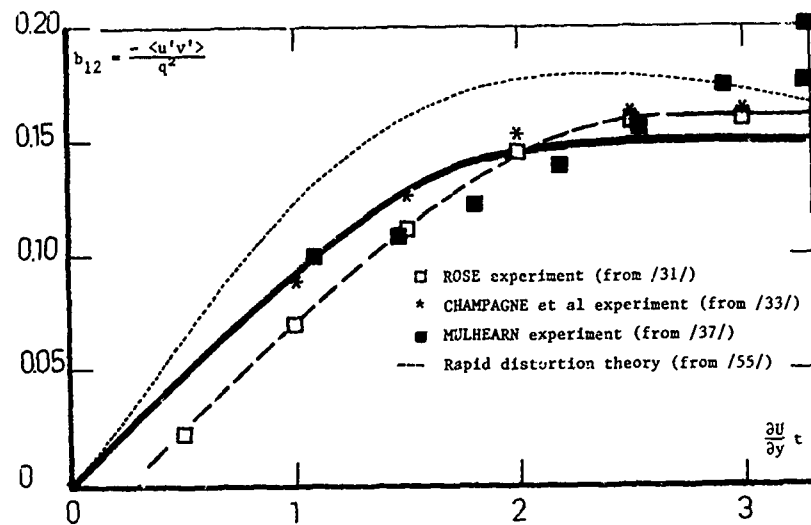


Figure 9 - Evolution of the shear stress anisotropy in sheared flow

Figure 10

Energy spectrum versus wave number in a tidal channel (from /58/)

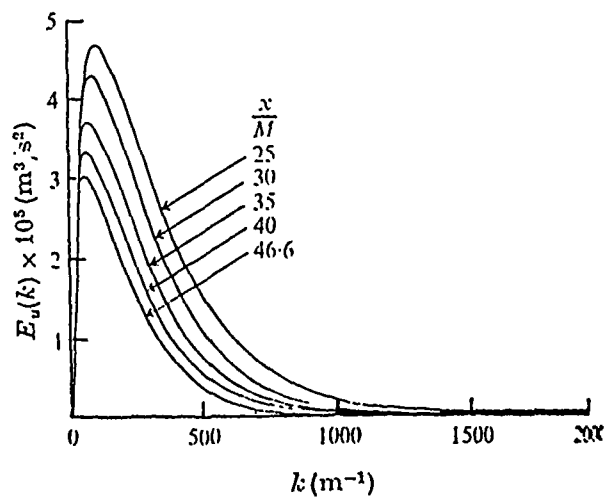
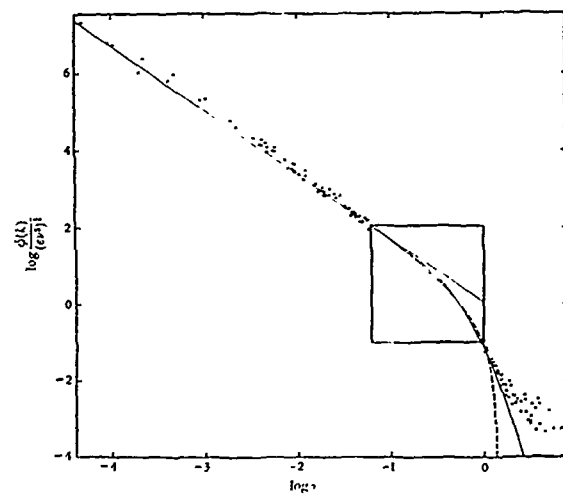


Figure 11

Energy spectra of wind tunnel isotropic turbulence (from /8/)

Figure 12

Energy transfer spectrum of wind tunnel, isotropic turbulence

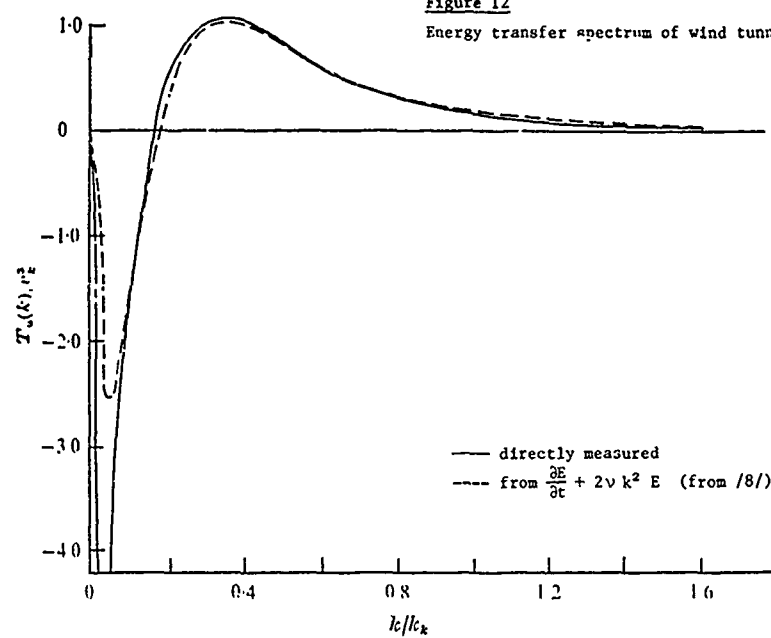


Figure 13

Energy spectrum with scale separation

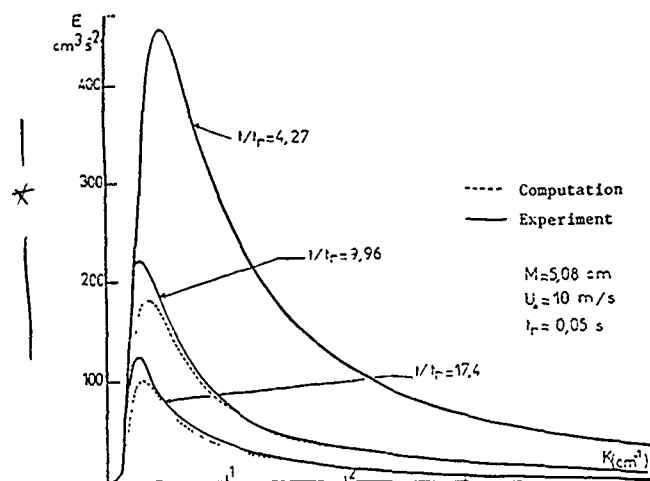
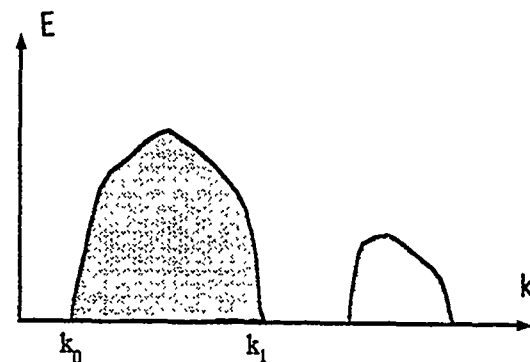


Figure 14

Comparison between experiment and EDQM computation for the COMTE-BELLOT and CORRISIN experiment (from /75/)

$M=5.08 \text{ cm}$   
 $U_0=10 \text{ m/s}$   
 $t_r=0.05 \text{ s}$

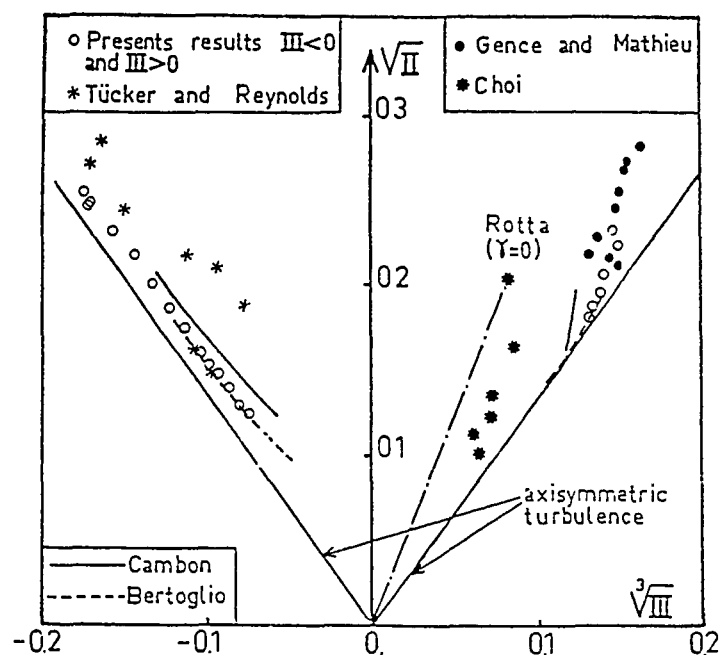


Figure 15  
Return to isotropy trajectories  
(from /17/)

Figure 16a  
Comparison between direct simulations  
and EDQNM computations for initially  
isotropic turbulence submitted to  
solid body rotation

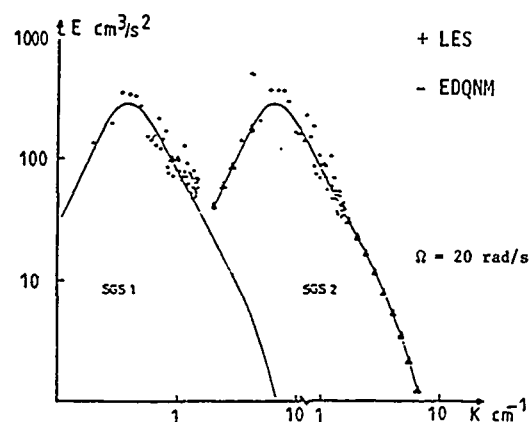
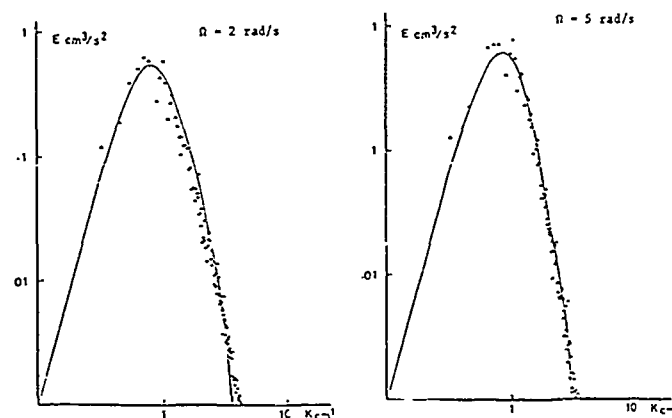


Figure 16b  
Comparison between large eddy simulations  
and EDQNM computations for initially iso-  
tropic turbulence submitted to solid body  
rotation



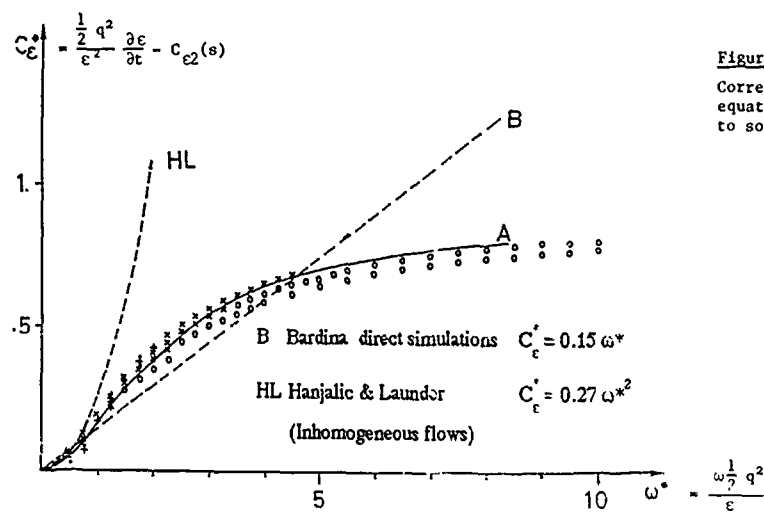


Figure 17

Correction to the dissipation equation for turbulence submitted to solid body rotation

Figure 18

Comparison of predictions with various rotation correction for the WIGELAND and NAGIB experiment (Screen 5 -  $U_\infty = 6$  m/s  $\Omega = 80$  rad/s)

x experiment  
o no rotation effect  
A AUPOIX et al model  
B BARDINA et al model  
HL HANJALIC and LAUNDER model

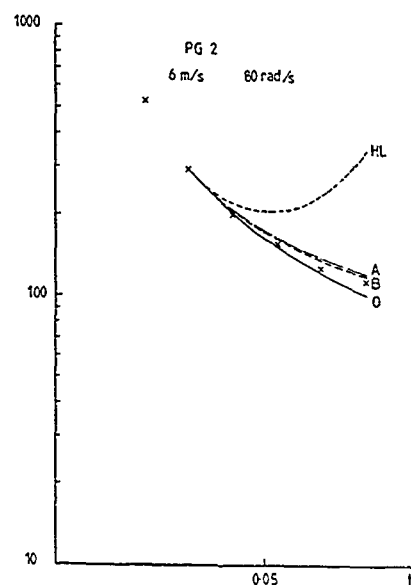
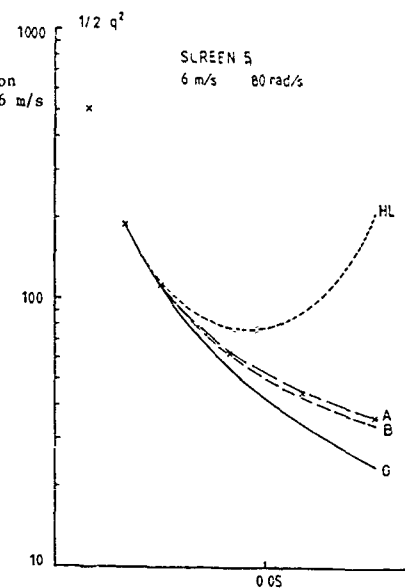


Figure 19

Comparison of predictions with various rotation correction for the WIGELAND and NAGIB experiment (Screen PG2 -  $U_\infty = 6$  m/s  $\Omega = 80$  rad/s)

x experiment  
o no rotation effect  
A AUPOIX et al model  
B BARDINA et al model  
HL HANJALIC and LAUNDER model

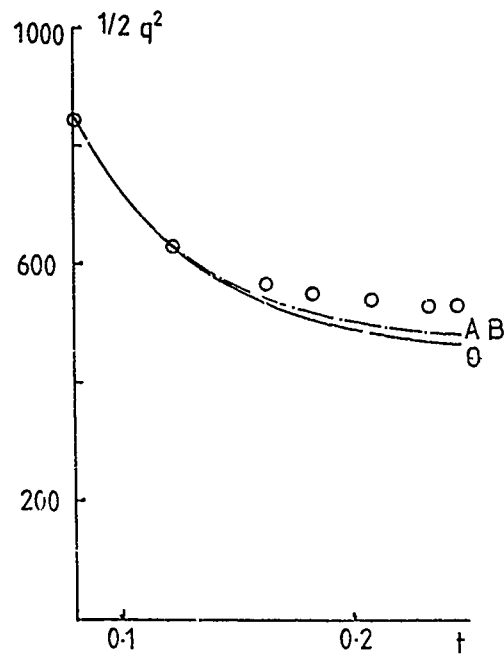


Figure 20

Influence of the rotation terms in the dissipation equation for sheared flow predictions - Weak shear - CHAMPAGNE et al experiment

- o experiment
- 0 no rotation effect
- A AUPOIX et al model
- B BARDINA et al model

Figure 21

Influence of the rotation terms in the dissipation equation for sheared flow predictions - Strong shear - HARRIS et al experiment

- o experiment
- 0 no rotation effect
- A AUPOIX et al model
- B BARDINA et al model

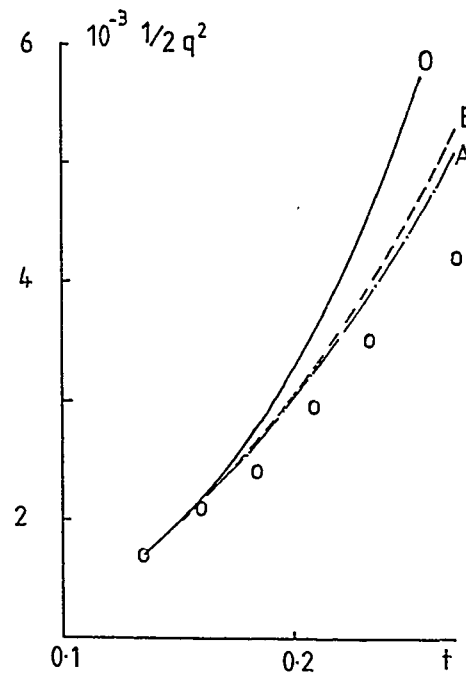
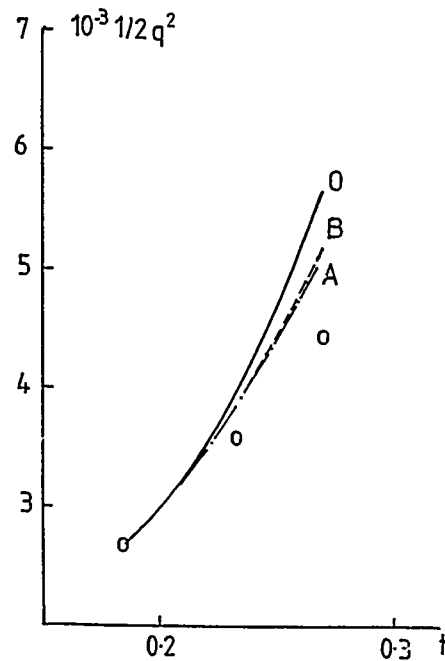


Figure 22

Influence of the rotation terms in the dissipation equation for sheared flow predictions - Strong shear - TAVOULARIS et al experiment

- o experiment
- 0 no rotation effect
- A AUPOIX et al model
- B BARDINA et al model

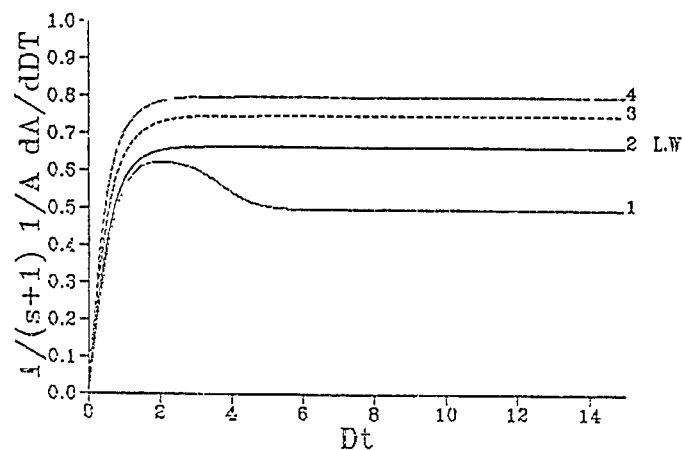


Figure 23 - Comparison of very large eddies evolution time scale given by the rapid distortion theory for various values of the exponent  $s$  ( $s = 1, 2, 3, 4$ ) with the LIN and WOLFSHTEIN model (LW) for strained turbulence versus total strain

Figure 24

Comparison of very large eddies evolution time scale given by the rapid distortion theory for various values of the exponent  $s$  ( $s = 1, 2, 3, 4$ ) with the LIN and WOLFSHTEIN model (LW) for sheared turbulence versus total shear

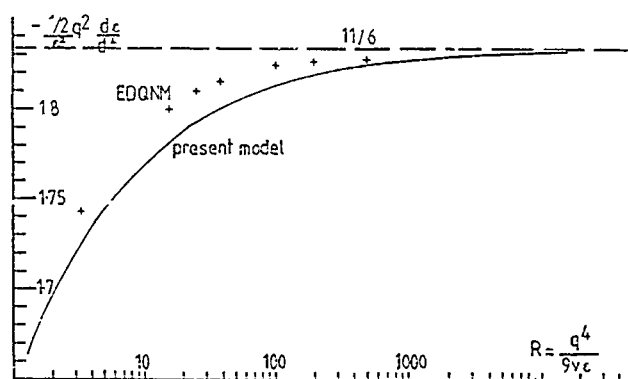
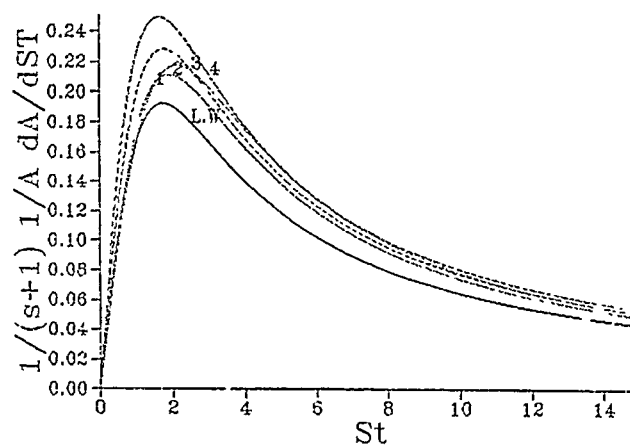


Figure 25

Decay of isotropic turbulence at low REYNOLDS number - Comparison between EDQNM simulations and the proposed model

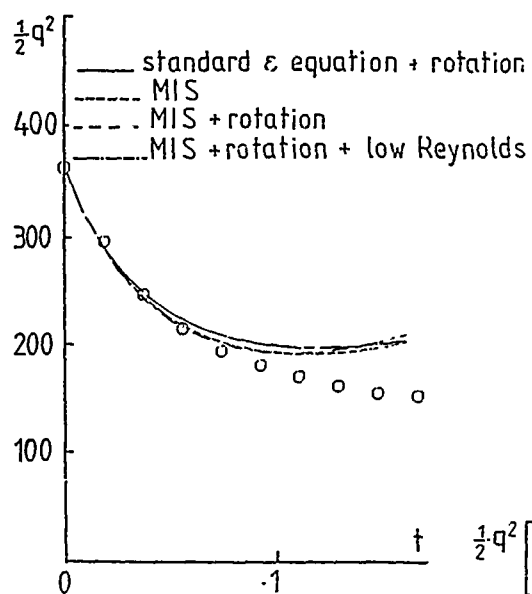


Figure 26

Comparison of predictions obtained with the standard dissipation equation including rotation effects and with MIS models including various effects - Strained flow : TOWNSEND experiment

Figure 27

Comparison of predictions obtained with the standard dissipation equation including rotation effects and with MIS models including various effects - Strained flow : GENCE and MATHIEU experiment

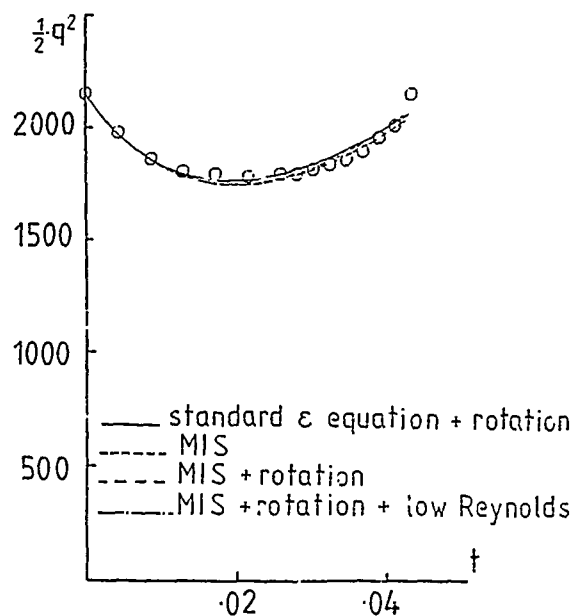
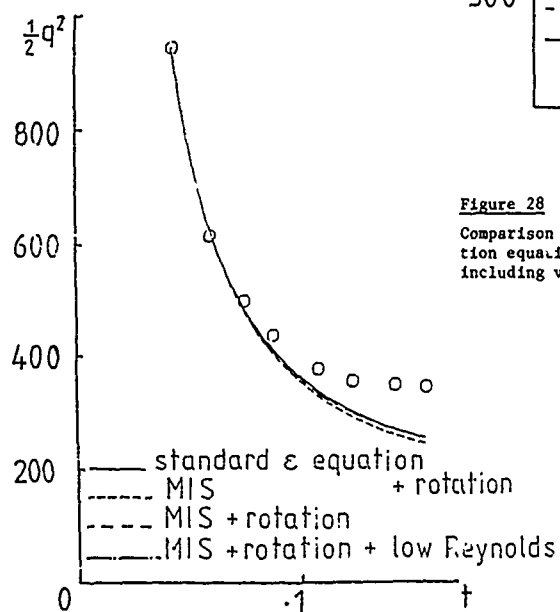


Figure 28

Comparison of predictions obtained with the standard dissipation equation including rotation effects and with MIS models including various effects - Weakly sheared flow : ROSE experiment



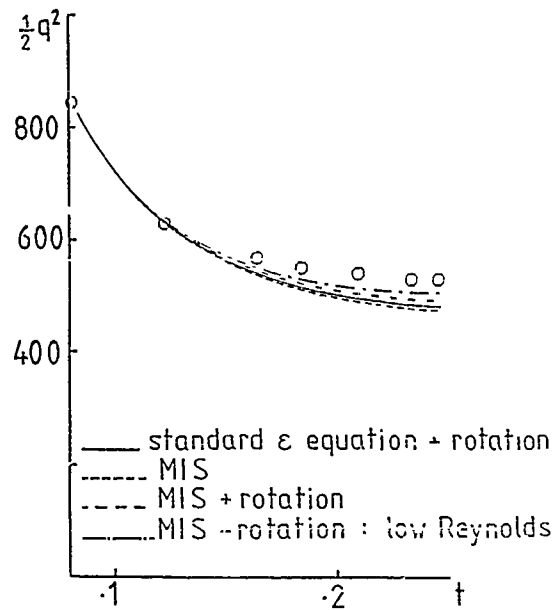


Figure 29

Comparison of predictions obtained with the standard dissipation equation including rotation effects and with MIS models including various effects - Weakly sheared flow : CHAMPAGNE et al experiment

Figure 30

Comparison of predictions obtained with the standard dissipation equation including rotation effects and with MIS models including various effects - Strongly sheared flow : HARRIS et al experiment

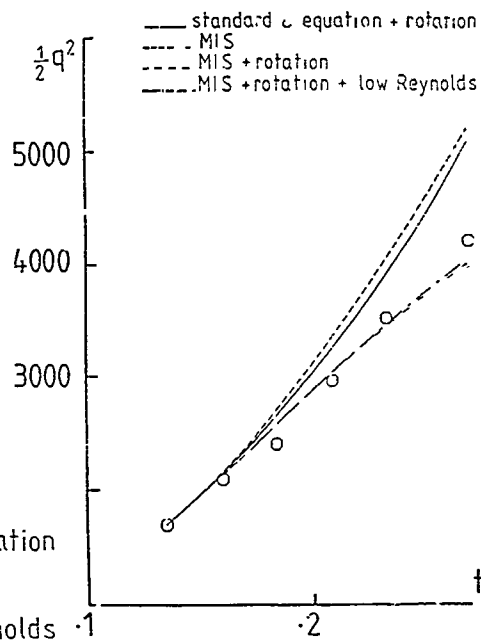
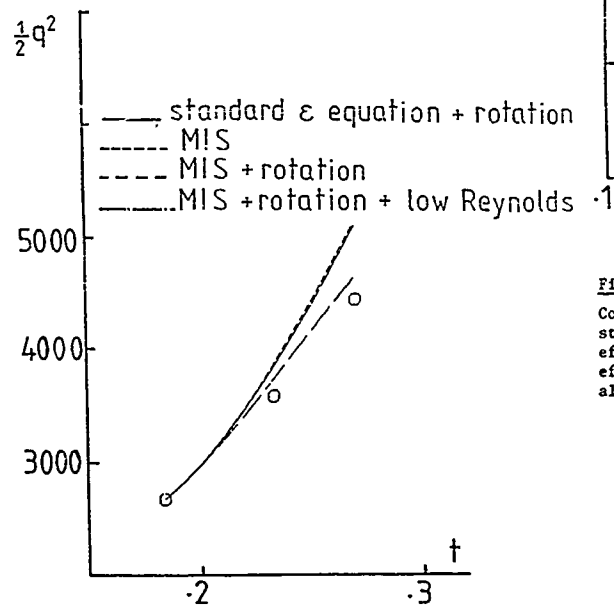


Figure 31

Comparison of predictions obtained with the standard dissipation equation including rotation effects and with MIS models including various effects - Strongly sheared flow : TAVOULARIS et al experiment

## DYNAMICS AND ROUTES TO CHAOS FROM QUASIPERIODICITY

by

M. Dubois  
 Service de Physique du Solide et de Résonance Magnétique  
 CEA-Saclay  
 91191 Gif-sur-Yvette Cedex, France

## PLAN

- I - Quasiperiodicity in Rayleigh-Bénard convection
  - The experiment: structures and dynamics
  - The measurements. Reconstruction of the phase space trajectories
  - Forced convection
- II - Quasiperiodic models
  - Forced pendulum
  - The Arnold model: the phase locked tongues and the critical line
  - Experimental results on the properties of the critical line
- III - Dynamical properties near the critical line
  - Phase intermittecies
    - a) Models
    - b) Experimental convective results
  - Direct route from quasiperiodicity to chaos
    - a) Models and theory
    - b) Experimental convective results
  - Two oscillators evolution in a free Rayleigh-Bénard experiment
- IV - Dynamics inside the phase locked tongues.

-----

One of the routes leading to deterministic chaos is the route through the quasiperiodicity; the simplest one involves the presence of two oscillators, whose the dynamics may become chaotic by the increase of the amount of the non-linearities between them. Though this dynamics is generally related to non-linear dynamical systems, it may be found in hydrodynamical flows, as soon as the increase of a control parameter (Reynolds number, Rayleigh number, etc...) initiates the appearance of periodic behaviours. So, in the following, the physical examples will be taken from Rayleigh-Bénard experiments, which provide good illustrations of quasiperiodic behaviours in dissipative systems.

I - QUASIPERIODICITY IN RAYLEIGH-BÉNARD CONVECTIONOscillators and spatial structures

In a fluid submitted to the Rayleigh-Bénard instability [1], the increase of the Rayleigh number  $Ra$  (i.e. of the temperature difference between the top and the bottom plates confining the fluid - see the lecture of P. Bergé) favours the appearance of new instabilities which may be time dependent. It is the case of the oscillatory instability [2] when we are working with low Prandtl number fluids ( $Pr = \nu/D_t$  with  $\nu$ , the cinematic viscosity and  $D_t$ , the thermal diffusivity). When convection is achieved with high  $Pr$  fluids, these instabilities take place in the thermal boundary layers, by first the formation and then the advection of thermal heterogeneities [3][4]. These phenomena may

be time-periodic, if the rolls arrangement is fixed, i.e. there is no spatial phase turbulence. So it is necessary to work with confined geometries, for which the horizontal extents of the cell confining the fluid are of the same order of magnitude as the depth  $d$  (typically in rectangular cells,  $L_x \approx 2d$  and  $L_y \approx 1$  to  $1.5d$ ) (figure 1). Nevertheless, when  $Ra$  is varied, many different structures are available, though each one can be stable in a relatively great range of  $Ra$  numbers. The point is that, unfortunately, the choice of the spatial arrangement is not made by the experimentalist, but by the convection itself, among the different stable solutions which have the same probability to be formed.

Nevertheless, for a fixed and given structure, the evolution of the dynamical behaviour with  $Ra$  is well determined and reproducible. This may be understood by the fact that specific thermal oscillators and the evolution of the coupling between them, are related, in an unique way, to the spatial arrangement of the convective motion.

#### Experimental phase-space trajectories

The convective state is generally pointed out by the measurement of a local variable. The velocity measurements are not really adequate to evidence low chaotic regimes, for they induce intrinsically a small amount of noise in the signal. So, temperature measurements are preferred. A local probe may be put at the top or the bottom plate (to minimize the perturbations in the fluid motion) as it has been done in helium [5] or mercury convection experiments. But we can take advantage of the presence of temperature gradients in the fluid to use optical device. This is particularly easy to perform with high  $Pr$  fluid convection, near room temperature. The local temperature gradients in the fluid deviate the rays of a parallel light beam crossing the cell, giving then a vertical or horizontal image, related to these gradients. Generally, with small cells, a vertical image is formed in a plane  $XZ$ , with integration along the  $Y$  direction (parallel to the smaller side of the cell). The image may be direct "shadowgraphy", or treated by the knife-edge technique (Foucault or Schlieren image).

As the oscillators are localised in the boundary layers, (with high  $Pr$  fluids), the study of these images is very powerful because we can follow the appearance and the evolution of the oscillators in all the fluid; and by putting a photodiode in any place of the image, we get informations about their time dependence, by the measurement of the variations of the local light intensity.

When two oscillators are present, two photodiodes can be set judiciously to have mainly the behaviour of the one and the other oscillator. An example is shown in figure 2: the signal of one photodiode,  $I_1(t)$ , is mainly sensitive to the lower frequency oscillator, meanwhile the other one,  $I_2(t)$ , reflects more the behaviour of the higher frequency oscillator. This combined measurement is of great interest in the reconstruction of the trajectories in the phase space; if this reconstructed space is three dimensional, the three variables may be  $I_1(t)$ ,  $I_2(t)$  and the time derivative of one of them,  $\dot{I}_1(t)$  for example. Then Poincaré sections will be drawn by taking the points  $I_1(t) = f(I_2(t))$  when  $I_2(t)$  reaches a defined value  $I_2^*(t)$  [8].

In the figure, two examples are given; one corresponds to a normal bi-periodic regime, for which we obtain the section of a torus. The other one is a strange attractor, drawn in the same manner as the first one, and obtained from the preceding bi-periodic regime by changing the Rayleigh number.

#### Forced convection

In experiments on free convection, the only parameter we can vary is the Rayleigh number, which acts together on the amount of the non-linearities and on the frequencies of the actual oscillators. More, these frequencies are imposed by the convection, then their ratio. But, as we will see further, the two parameters which are involved in the dynamical behaviours undergone by a system consisting of two oscillators, are the frequency ratio and the coupling or the amount of the non-linearities. So to understand experimental dynamics, it is very important to control independently the two parameters. Different experimental devices have been set up where a natural convective oscillator is forced by an external periodic oscillation. In the case of mercury convection, a vertical alternative sheet of current associated with a small dc magnetic field has been applied [6]. With higher  $Pr$  fluids, a local periodic heating in the lateral boundaries

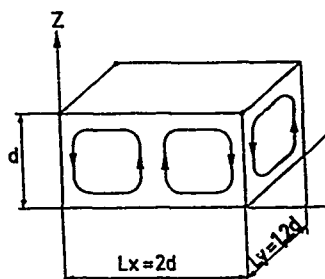


Figure 1: Scheme of a small box (confined geometry), as used for Rayleigh-Bénard convection experiments to the study of the routes leading to chaos. In this picture, the convective structure is organized with 2X-rolls and 1Y-roll.

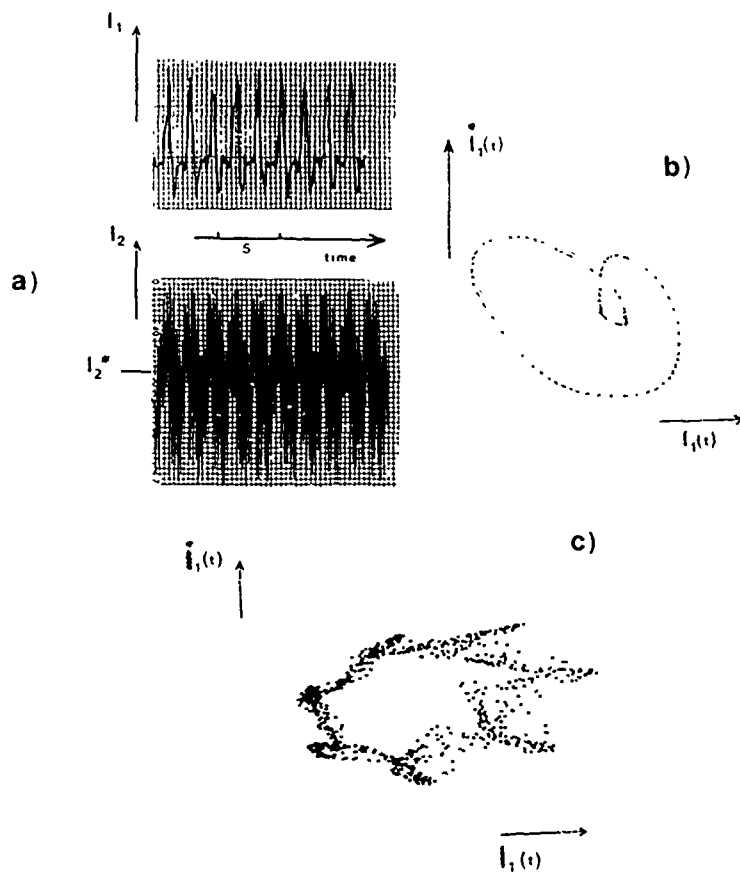


Figure 2: a) Time dependences  $I_1(t)$  and  $I_2(t)$  of the light intensity, measured simultaneously in two places of the Foucault image in the case of a normal biperiodic regime ( $f_2/f_1 \approx 7.2$ ,  $Ra/Rac \approx 324$ ). The Poincaré section, obtained with these two signals is shown in b); the dots have been marked each time  $I_2(t) = I_2^*$ , with a given sign for  $I_1(t)$ ; c) Poincaré section, drawn in the same manner as for b), but with a chaotic regime obtained from the preceding one by a variation of the Rayleigh number ( $f_2/f_1 = 6.63$ ;  $Ra/Rac \approx 318$ ).



[7], or in the bottom plate can provide a good oscillator, coupled to the natural one. The electrical power is driven in amplitude,  $A_{ex}$ , and frequency  $f_{ex}$ , by a synthesizer, allowing, in principle, to explore the whole plane of the parameters  $(A_{ex}, f_{ex})$ .

In this manner, fundamental results have been obtained. A part of them will be discussed further. Here we want just to demonstrate the appearance of chaos under the influence of an external oscillator: the experiment is conducted with Si-Oil ( $Pr \approx 38$ ) confined in a small box, as usual. At  $Ra/Rac = 310$ , a natural monoperiodic regime is present, with an oscillator (hot droplet) whose frequency  $f_0$  is  $29.5 \cdot 10^{-3}$  Hz. This oscillator is forced by a local periodic electrical heating - in a thin conductor in the bottom plate - just underneath the place where the droplet is growing. Depending on the values of  $A_{ex}$  and  $f_{ex}$ , different regimes may be observed, including chaotic regimes as shown in Figure 3: the dynamical regime, periodic at first, becomes progressively chaotic when the amplitude  $A_{ex}$  of the external oscillator is increased, whereas the frequency ratio  $\rho = f_{ex}/f_0$  is kept constant ( $\rho = 0.97$ ). The Poincaré section of the attractor corresponding to the strongest forcing displays the typical features of strange attractors despite the complexity of the distribution of the points (figure 4).

So we have seen that chaotic behaviours, issued from biperiodic regimes may be observed experimentally. But to understand why these regimes are chaotic and what are the evolutions leading to them, we have to look first at theoretical models. They will show to us how two coupled oscillators can exhibit a great (somewhat fascinating) richness of dynamical behaviours.

## II - QUASIPERIODIC MODELS

### The forced pendulum

The simplest quasiperiodic system may be schematized by the forced pendulum. The pendulum, sustained or not, is one of the oscillator; it is influenced by the second one, given by an external periodic force which remains stable. The dynamics is then described by the following equation:

$$m \frac{d^2 \theta}{dt^2} + \alpha \frac{d\theta}{dt} + mg \sin \theta = A \cos \omega t \quad (1)$$

$\theta$  being the variable of the system (the angle with the vertical direction in this case);  $g$  is the gravitational field,  $m$  the mass and  $\alpha$  is an expression which depends on the fact that the pendulum is sustained or not.  $A \cos(\omega t)$  gives the external periodic forcing at the frequency  $\omega$ , which together with the amplitude  $A$ , is a parameter of this dynamics.

Different expressions may be derived from the relation (1). We want here just to mention two of them which have been particularly studied:

#### 1) The Van der Pol equation:

$$\frac{d^2 \theta}{dt^2} - \epsilon (1 - \theta^2) \frac{d\theta}{dt} + \theta = B \cos \omega t \quad (2)$$

which describes a sustained forced pendulum. When  $B = 0$ , the asymptotic behaviour of the pendulum is periodic (after the transients).

#### 2) The Duffing equation

$$\frac{d^2 \theta}{dt^2} + a \frac{d\theta}{dt} + \theta^3 = B \cos \omega t + B_0 \quad (3)$$

where  $a$  is a damping coefficient. The asymptotic behaviour is the rest (a fixed point in the phase space), when  $B = B_0 = 0$ .

All these relations can be replaced by a set of three ordinary differential equations, which are for the case of the equation (1):

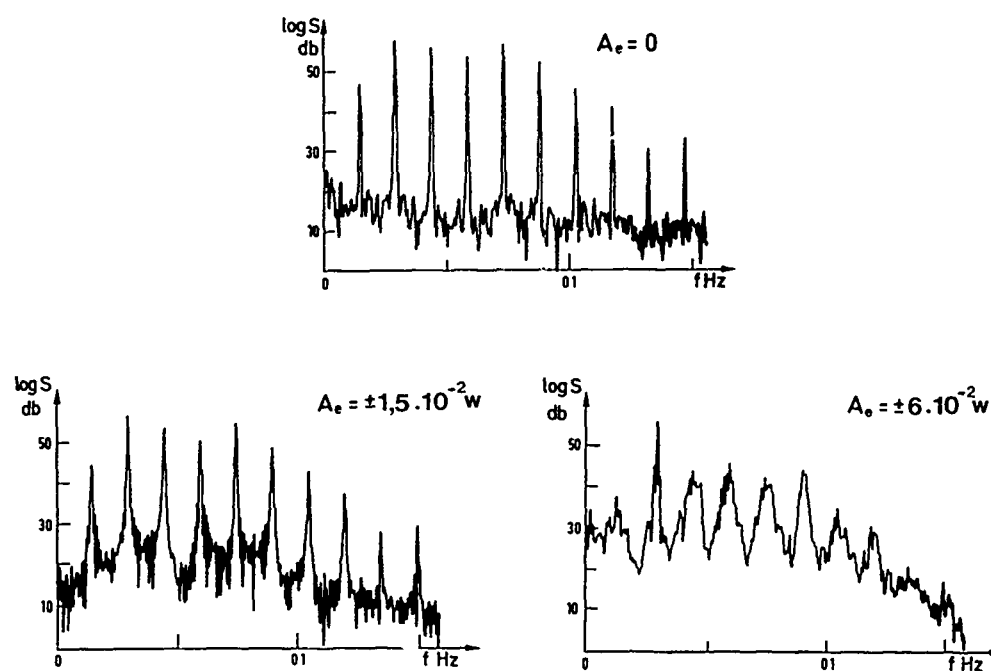


Figure 3: Fourier spectra of a convective signal for different values of the forcing cad of the modulation amplitude  $A_e$  of the external oscillator,  $f_{ext}/f_0 = 0.97$  with  $f_0 = 29.5 \cdot 10^{-3} \text{ Hz}$ ,  $Ra/Rac = 310$ .

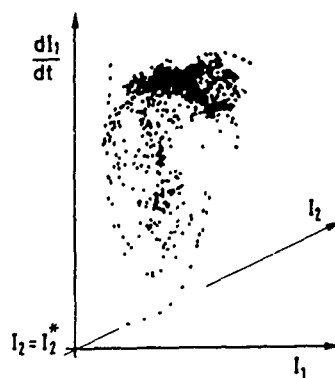


Figure 4: Poincaré section of the 3d attractor corresponding to the forcing  $A_e \approx 6 \cdot 10^{-2} \text{ W}$ , ( $Ra/Rac = 310$ ,  $f_{ext}/f_0 = 0.97$ ).

$$\begin{aligned}\frac{dx}{dt} &= -ax - b \sin y + A \cos z \\ \frac{dy}{dt} &= x \\ \frac{dz}{dt} &= \omega\end{aligned}\quad (4)$$

with  $x = d\theta/dt$  and  $y = \theta$ .

This set expresses the fact that three variables are necessary to describe the dynamics of the forced pendulum in the phase space. (Note that this corresponds to the minimum condition - 3d phase space - to get chaotic trajectories due to S.C.I. properties).

As the trajectories are not easy to be visualised, in particular when they will be chaotic, it is more convenient to draw Poincaré sections, or stroboscopic sections at the frequency of the forcing. So  $x$  and  $y$  values are taken, each time the phase of the forcing has rotated  $2\pi$ , and the set of equations (4) becomes an iterated transformation in the plane of the  $x, y$  variables

$$\begin{aligned}x_{n+1} &= f(x_n, y_n) \\ y_{n+1} &= g(x_n, y_n)\end{aligned}\quad (5)$$

or

$$\begin{aligned}\varphi_{n+1} &= f'(\varphi_n, r_n) \\ r_{n+1} &= g'(\varphi_n, r_n)\end{aligned}\quad (5')$$

in polar coordinates, where  $\varphi_n$  gives, in a certain sense, the phase of the forced oscillator relative to that of the forcing oscillator.

#### The Arnold model

Different models are expressed with the form (5'). The simplest and the most extensively studied up to day is the Arnold model [9] [10] [11], which takes only into account the variation of the relative phase  $\varphi$ , with the relation  $\varphi_{n+1} = f'(\varphi_n)$  such as

$$\varphi_{n+1} = \varphi_n + \Omega - \frac{K}{2\pi} \sin(2\pi\varphi_n) \bmod 1 \quad (6)$$

(Note that here the phase is normalized to 1).

The parameter  $K$  gives the amount of the non-linearities. When  $K = 0$ ,  $\varphi_{n+1} = \varphi_n + \Omega$ , and  $\Omega$  plays the role of a frequency ratio, since it could be the variation of the phase of the studied oscillator (with frequency  $f_0$ ) when an external one (with frequency  $f_{ext}$ ) has rotated  $2\pi$  ( $\Omega = f_0/f_{ext}$ ).

What we learn by studying this model in the plane of the two parameters  $[K, \Omega]$ ? A first picture of the evolution of the different dynamical regimes with  $K$  and  $\Omega$  is shown in figure 5. When  $K = 0$ , all the regimes for  $0 < \Omega < 1$  are quasiperiodic i.e.  $\varphi_n$  takes all the values between 0 and 1, except for the exact rational values of  $\Omega$ . But as soon as  $K$  is increased, the effective frequency ratio is no longer equal to  $\Omega$ , but becomes the rotation number, defined as

$$\rho = \lim_{n \rightarrow \infty} \left[ \frac{f'^n(\varphi) - \varphi_0}{n} \right]$$

The non-linearities favour in particular phase-lockings, i.e. for a given interval of  $\Omega$  values,  $\varphi_n$  takes only a definite number of values. This means that  $\rho$  has become a rational ( $\rho = p/q$  with  $p$  and  $q$  integer) near the initial  $\Omega$  value. When  $K$  is increased, the phase-locked tongues broaden (the smaller the  $q$  is, the broader they are) and there is appearance of the tongues with higher  $p$  and  $q$  values. The tongues are generated by Farey sums i.e. between two tongues with  $\rho_1 = p_1/q_1$  and  $\rho_2 = p_2/q_2$ , there is the tongue  $\rho_s = (p_1 + p_2)/(q_1 + q_2)$  and so on, from the widest tongue to the thinnest one.

On a line  $K = \text{cte}$ , we find successively, by  $\Omega$  variation, plateaus of locking states separated by biperiodic states; for  $K = 1/2$ , the probability of observing rational and

irrational rotation numbers are almost equal, but at  $K = 1$ , the probability of finding a rational rotation number is close to 1, as shown in figure 6. We have a complete devil staircase. This object is fractal and its dimension, calculated on numerical models is  $D \approx 0.87$ , number which seems to be universal. It represents a local property of the map and is defined in any point of the line  $K = 1$ ; then it expresses the self-similarity of the locking states on this line.

By a further increase of  $K$  ( $K \geq 1$ ), an overlap of the tongues takes place leading to a competition between different dynamical regimes, competition which can lead to chaos. Indeed, the line  $K = 1$  is called the critical line, as this line corresponds also to the loss of invertibility in the maps  $\varphi_{n+1} = f_n(\varphi_n)$  (this means that the relation  $\varphi_{n+1} = \varphi_n$  is not unique).

The critical line has also been calculated for 2d mappings, [10] in particular for the standard mapping

$$\begin{aligned}\varphi_{n+1} &= \varphi_n + \Omega - \frac{K}{2\pi} \sin(2\pi \varphi_n) + b r_n \\ r_{n+1} &= r_n - \frac{K}{2\pi} \sin(2\pi \varphi_n)\end{aligned}$$

It is no longer the line  $K = 1$ , but a smooth curve resembling a parabola, with discontinuities near the major phase-locked tongues. Along this curve, the fractal dimension corresponding to the locked portions is the same universal number  $D_0 \rightarrow 0.87$  as found for the circle maps, like the Arnold mapping.

#### Experimental results on the properties of the critical line

Details of an experimental study can be found in [6]. We want just to note here that this study has been conducted on forced convection with mercury, in a small box. The Rayleigh number is increased until a monophasic regime is reached ( $Ra/Rac \approx 4$ ). Then, this one is forced periodically as indicated section I. The properties of the local plateaus of phase lockings have been studied around two rotation numbers: the golden mean  $\Omega_g = (\sqrt{5}-1)/2$  and the silver mean  $\Omega_s = \sqrt{2}-1$  which have only "ones"  $\{1,1,1,\dots\}$  and twos  $\{2,2,2,\dots\}$  respectively in their continued fraction representation.

The local fractal dimension  $D_0$  has been calculated by using the relation

$$(S_1/S)^{D_0} + (S_2/S)^{D_0} \approx 1$$

where  $S$  is the length of the frequency ratio interval between two phase locked tongues  $p_1/q_1$  and  $p_2/q_2$ ;  $S_1$  and  $S_2$  are the distances of the intermediate tongue, generated by the Farey sum  $(p_1+p_2)/(q_1+q_2)$  respectively to its two "parent" tongues  $p_1/q_1$  and  $p_2/q_2$ .

The results are in good agreement with numerical studies

$$D_0(\rho = \Omega_g) = 0.86 \pm 0.03 \quad ; \quad D_0(\rho = \Omega_s) = 0.85 \pm 0.03$$

### III - DYNAMICAL PROPERTIES NEAR THE CRITICAL LINE

The study of the global properties, in the plane of the parameters  $[K, \Omega]$  (Arnold model) has pointed out the fundamental aspect of the phase locking phenomenon which dominates all the dynamical behaviours, when the non-linearities are sufficiently high. We will discuss now some points, with more details, leading to the understanding of the mechanisms involved near the critical line and leading to chaos.

#### Phase intermittencies

They correspond to a specific behaviour, which is generic of the approach of phase-locking. It can be understood first by studying iterated models, as these described previously, but also with the 2d Curry-Yorke model [12] [13]. In a major phase-locked tongue, with  $\rho = 1/q$ , the phase  $\varphi_n$  takes repeatedly the same values  $\varphi_1, \varphi_2, \dots, \varphi_q, \varphi_1, \varphi_2, \dots$  etc. versus  $n$ . But very near the tongue (in B in the figure 7a), the phase shows a very interesting behaviour: for a certain number of iterations (which

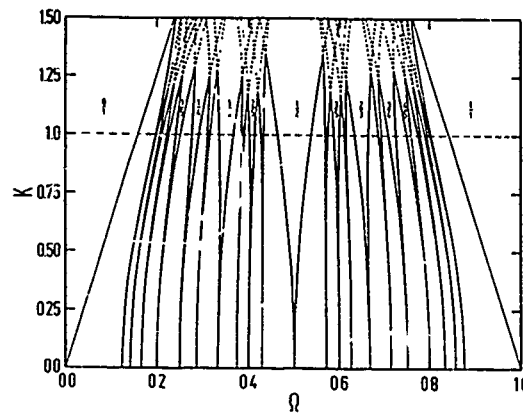


Figure 5: Phase diagram for the sine circle map (Arnold model).

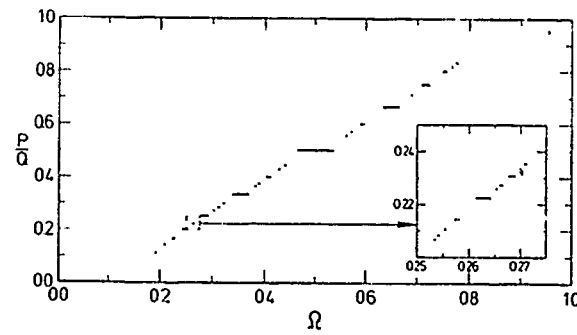


Figure 6: Rotation number  $\rho$  versus  $\Omega$  for the circle map at  $K = 1$ . The enlarged picture shows the self-similar nature of the staircase (from [10]).

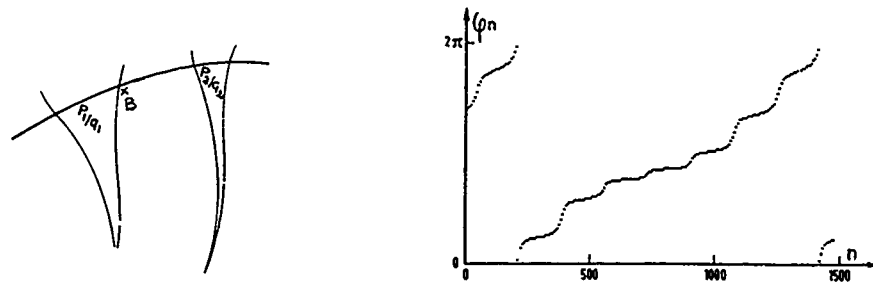


Figure 7: a) Schematic situation of the phase intermittencies near a major phase-locked tongue; b)  $\phi_n$  variation versus  $n$  for 2d model calculated for a point like B. Every seventh point has only been drawn (B is near the phase-locked tongue  $1/7$ ).

corresponds to a time duration in experiments), the sequence of  $\varphi_n$  values is very similar to this observed in the tongue, but from "time" to "time", the plateaus of quasi phase-locking are interrupted by fast rotations of the phase, to recover the actual rotation number  $\rho \approx 1/q$ . When the system is below the critical line, the fast rotations of the phase are periodic (figure 7); this leads to specific properties:

- In the Fourier spectrum of  $\varphi(n)$  (which may be seen as  $\varphi(t)$ ), there is appearance of a low frequency  $\delta f$ , which is the frequency of the fast phase rotations; this one is given by the distance of the actual rotation number to the locking state; many of its harmonics are also present.

- In the Poincaré section, the density of the points is non uniform, with a higher density in the regions corresponding to the quasi phase-locking.

- The return maps  $\varphi_{n+1} = \varphi_n$  looks like those obtained from amplitude intermittencies.

When the non-linearities are increased, beyond the critical line, the behaviour remains very similar but the intervals between the fast rotations of the phase has become chaotic, leading to a broadening of the peaks in the Fourier spectrum, to a Poincaré section with wrinkles and a non-invertible return map.

Note that these phase intermittencies may be seen as dynamical phasons.

#### The experimental results

As said before, the results concern Rayleigh-Bénard convection in a small cell, ( $L_x = 2d$ ,  $L_y = 1.2d$ ) filled with Si-Oil ( $Pr = 38$ ) for the example described in the following. In a certain domain of Rayleigh numbers, and for a given spatial arrangement, two oscillators are present in the convecting fluid, with a rotation number  $\rho = f_1/f_2$  around  $1/7$  [14]. The phase-locking  $\rho = 1/7$  ( $f_1 \approx 9.5 \cdot 10^{-2} Hz$ ,  $f_2 \approx 66 \cdot 10^{-2} Hz$ ) is observed for the interval  $320 < Ra/Rac < 322$ . At the exit of the locking state, by varying the Rayleigh number, ( $Ra/Rac \approx 319.5$ ), there is evolution of the dynamical behaviour, so that the Fourier spectrum of a convective signal becomes typical of phase intermittencies (see figure 8); indeed we can notice the presence of the peak at the low frequency  $\delta f = 7f_1 - f_2$  and of its harmonics.

From the Poincaré section (figure 9), drawn as described in section I, we can get the variation of the relative phase  $\varphi$  with time. As expected,  $\varphi$  does not vary linearly with time, as it would be the case in a normal quasiperiodic regime, but with tendency to phase-locking, interrupted by fast rotations of the phase. The longer are these periods, the nearer  $1/7$  is the rotation number.

From the successive  $\varphi_n$  values, we can draw the return map  $\varphi_{n+1} = f(\varphi_n)$ . Clearly, this map indicates the intermittent nature of the dynamics by the presence of points on (or very near) the bissectrix. More, in the case shown figure 9c, we can affirm that the regime is very near the experimental critical line for near the point P, an inflexion point seems to be present. So the corresponding dynamical behaviour may be chaotic, though very weakly. This weakly chaotic behaviour, given by phase intermittencies before falling in a phase-locking is a general feature observed in Rayleigh-Bénard convection, since by varying the Rayleigh number, not only the amount of the non-linearities are varied, but also the frequency ratio: so this observed evolution is in agreement with the behaviour given by the models, if we consider the related variation in the two parameters.

#### Direct route from quasiperiodicity to chaos

##### The models

We have seen, that on "the critical line", we go from one phase-locked tongue to another one when the frequency ratio is varied. Nevertheless, it remains some "points" (of zero measure) which correspond to quasiperiodic orbits i.e. those for which the rotation number has remained irrational when increasing the non-linearities. The most famous irrational number is the golden mean,  $\Omega_g = (\sqrt{5}-1)/2$  whose representation as a continuous fraction contains only ones

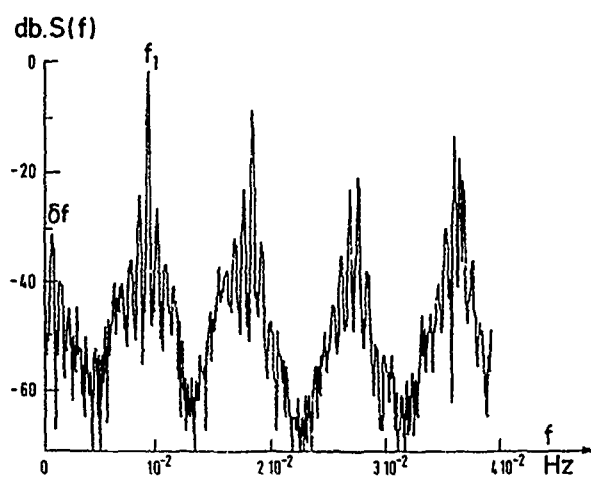


Figure 8: Fourier spectrum of the convection signal  $I_1(t)$  ( $Ra/Rac \approx 319.5$ ;  $f_2/f_1 \approx 6.91$ ). The  $f$ -scale does not permit to see  $f_2$ .

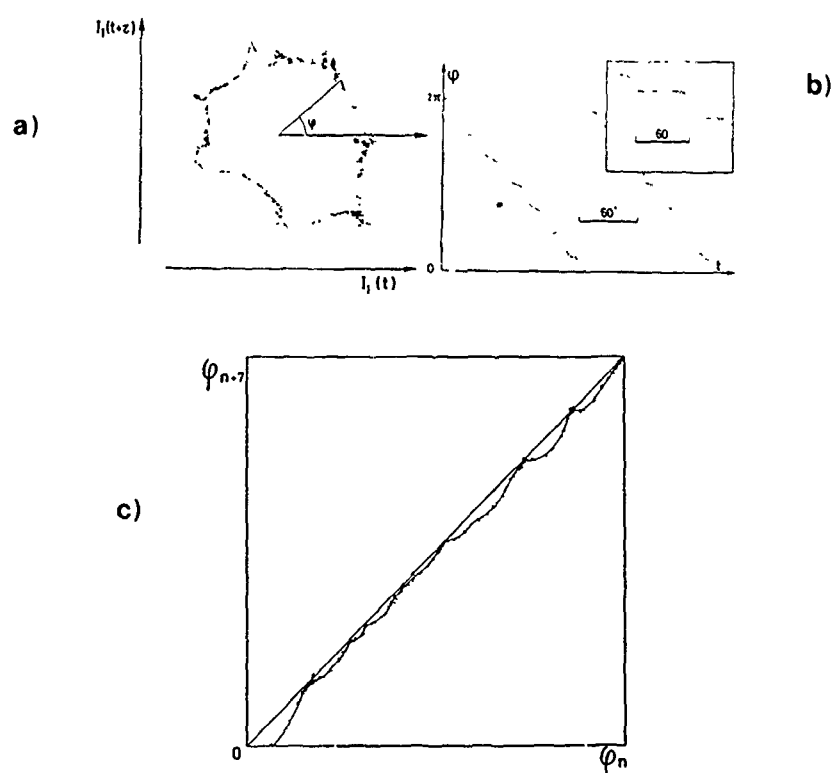


Figure 9: a) Poincaré section corresponding to the regime  $f_2/f_1 = 6.91$ ; b) Evolution of the phase  $\varphi$  versus time. The phase has been measured in the Poincaré section as indicated, every seventh point has been drawn. (Same evolution in the frame for  $f_2/f_1 = 6.99$ ); c) Experimental return map  $\varphi_{n+7} = f(\varphi_n)$ .

$$\Omega_c = \frac{1}{1 + \frac{1}{1 + \frac{1}{1 + \dots}}}$$

and has, therefore, the slowest possible convergence in a rational approximation  $\frac{p_i}{q_i}$  (successively,  $p_i/q_i = 1/2, 2/3, 3/5, 5/8, 8/13$ , the numbers 1, 1, 2, 3, 5, 8, 13, ... being the Fibonacci sequence).

Theoretical and numerical studies [15] have shown that if the irrational number is preserved when increasing the non-linearities, the successive combinations  $p_i f_{ext} - q_i f_0$  appear in the Fourier spectrum. The higher are the  $q_i$  and  $p_i$  values, the nearer we approach the critical line. In the particular case of  $\rho = \Omega_c$ , we have to observe then a very large increase of the number of peaks with frequency lower than  $f_0$  (see figure 10). These peaks may be regarded as due to the generalisation of the mechanism giving the peak  $\delta f_0$  (related to phase intermittencies) near strong phase-locked tongue as discussed before. With this picture, all the peaks  $\delta f_i = p_i f_{ext} - q_i f_0$ , corresponding to the distances of the actual rotation number to its successive fraction representation could be explained by the superposition of different phase intermittencies, relative to the different neighbouring phase-locked tongues.

At the critical line, as we know, there is overlap of the tongues but this overlap is not simultaneous for all the tongues. At first, the nearest and (thinnest) ones overlap, and the peaks, given by the highest order combinations in the spectrum broaden, followed then by the others, peak by peak.

#### Experiments

This evolution to chaos has been well studied by A. Fein, M. Heutmaker and J.P. Gollub [7] and by J. Stavens, F. Heslot, A. Libchaber [6] on experiments with forced Rayleigh-Bénard convection. In the first case, a convective water layer in a small cell was brought to a monoperiodic regime by increasing the Rayleigh number ( $f_0 \approx 0.186$  Hz). Then a periodic forcing was imposed by modulating heat sources in the short sidewalls, at constant Ra ( $Ra/R_c \approx 57$ ).

The experimental conditions of the second reference have been reported above, in section II. In the two cases, the rotation number was kept equal to  $\Omega_c$  (up to 0.03%), by adjusting  $f_{ext}$  ( $\rho = f_{ext}/f_0 < 1$ ) at each value of the amplitude of the external forcing. The observations are very similar to the results obtained theoretically and numerically; in particular all the peaks  $p_i f_0 - q_i f_{ext}$  have been measured, until  $55f_0 - 89f_{ext}$  and combinations of them. The self similarity of the spectrum has been pointed out at the onset of chaos, for the golden mean and the silver mean [6]; indeed this self similarity is due to the particular periodic representation as a continued fraction of these two numbers.

This direct route to chaos from quasiperiodicity is not reserved to the "noble" irrational numbers as  $\Omega_c$  and  $\Omega_s$  but it is expected for any irrational number. The probability of finding this kind of number is very low in a natural convective experiment; nevertheless one of them with high Pr fluid, has provided a dynamical behaviour related to this route.

The conditions of the experiments [16] are the same as these which have been reported for the observation of phase intermittencies, but for a slightly different value of the Rayleigh number ( $Ra/R_c \approx 317$ ). For this situation, the rotation number is  $\rho = f_1/f_2$  ( $f_1$  and  $f_2$  = natural frequencies of the convection) with  $\rho = 1/6.59$ . The different rationals  $p_i/q_i$  which approximate this number are  $1/6, 1/7, 2/13, 5/33, \dots$ . All the peaks  $q_i f_1 - p_i f_2$  are present in the Fourier spectrum of the convective signal (figure 11). Nevertheless, we have to remark that the lowest frequency which would correspond to  $A_1 = 33f_1 - 5f_2$  is broadened. This is in agreement with the fact that the studied regime is slightly chaotic and probably just beyond the critical line.

#### Two oscillators evolution in a free Rayleigh-Bénard experiment

As we have already said, in a free Rayleigh-Bénard experiment, only the Rayleigh



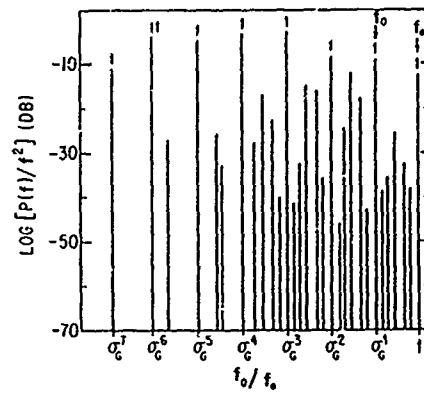


Figure 10: Schematic Fourier spectrum near the onset of chaos with  $\rho = \Omega_c$ .

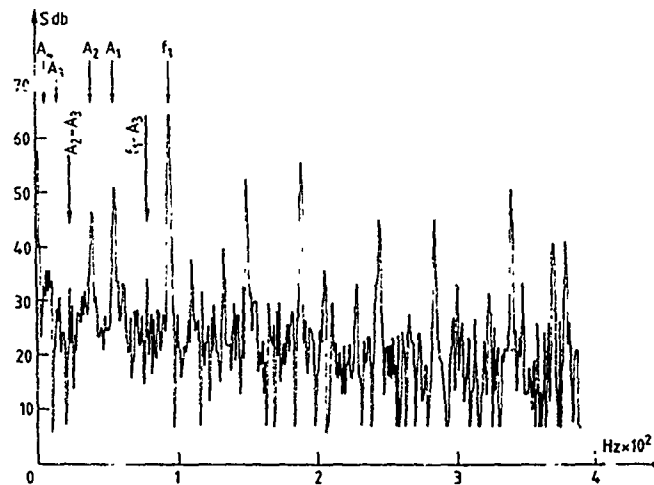


Figure 11: Fourier spectrum of the signal  $I(t)$  for  $Ra/Rac = 317$  and  $f_2/f_1 = 0.59$ . The peak  $A_3$  is poorly distinguishable because of its low level; its existence is better evidenced through higher frequency combinations like  $A_2-A_3$ ,  $f_1-A_3$ ,  $f_1+A_3$ , etc...

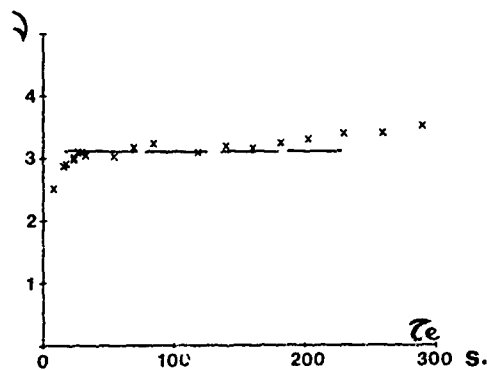


Figure 12: Calculated fractal dimension  $D$  versus the embedding time  $\tau_e = (D-1)P\Delta t$  for the most chaotic attractor ( $f_2/f_1 \approx 6.62$ ), shown in the right part of the figure.

number can be varied and its variation acts on both the coupling intensity and the frequency ratio of the oscillators. Nevertheless some interesting results have been obtained recently on the behaviour of two natural oscillators near the critical line. In this case indeed, the oscillators are both free to react on their mutual influence and the relevant phase space is four dimensional. (Note once more that all the study corresponds to a well defined and stable spatial configuration of the convective rolls).

The exact evolution of the observed dynamical regimes is as follows:

- At  $Ra/Rac = 317$ , the regime is the one, described just above i.e. a low chaotic behaviour obtained directly from biperiodicity ( $\rho = 1/6.59$ ).
- $317 < Ra/Rac < 319.5$ , different chaotic regimes take place ( $1/6.59 < \rho < 1/6.9$ ).
- At  $Ra/Rac \approx 319.5$  the regime is unambiguously related to phase intermittencies. It has been discussed at the beginning of the section III.
- Then a locking state is observed for  $320 < Ra/Rac < 322$ , with  $\rho = 1/7$ ; it is followed by a normal biperiodic regime when increasing further the Rayleigh number.

We are interested here in the understanding of the different chaotic regimes which has been observed in the range  $317 < Ra/Rac < 320$ , knowing that the observations at the extremities of the range correspond to dynamical regimes very near the onset of chaos, then near the experimental critical line. (When phase intermittencies with  $\rho = 1/6.91$ , we have seen that the return map is just at the limit of invertibility). In these cases, the study of Fourier spectra and the treatment of the attractor's Poincaré sections have provided fundamental informations about the dynamics. When the regimes become more chaotic, it is necessary to rely on other methods to get quantitative characterization

Fortunately, since some years, theoreticians have searched for and found algorithms, allowing to calculate typical features of chaotic states from experimental data, namely the fractal dimension of the attractor [17], [18] the metric entropy of the chaotic state [19], [20] and then, more recently [21], [22], [23] the positive Lyapunov exponents. For all these methods, the attractor is at first reconstructed by the time delay method, as discussed in the lecture of Bergé.

We used some of these algorithms to study the different observed chaotic regimes.

In a first step, the fractal dimension, or more exactly the correlation dimension was calculated, using the algorithm proposed by P. Grassberger and I. Procaccia [17], and which is discussed in details in the lecture of Bergé. The signal, from which time series of 15.000 points were obtained, was measured in the same place on Foucault image of the convective fluid for each  $Ra/Rac$  value (the digitalisation was made with around 16 points per fast period  $\tau_2 = 1/f_2$ ). Then these time series were processed in the same way. As expected, the slope  $\nu$  of the characteristics  $\log[C(R)] = f(\log(R))$  with  $R$  the distance in the phase space increases with  $D$ , the dimension of the reconstructed phase space, until it reaches a nearly constant value (figure 12); this value gives a fractal dimension of the chaotic attractor and then a lower bound of the effective dimension of the relevant phase space. But it can give also a quantitative estimate of the evolution of the chaotic state, with the hypothesis that the dissipation remains constant along the different measurements.

To confirm this assumption, the metric entropy has also been calculated, with an algorithm given by P. Grassberger and I. Procaccia and discussed in details in [19]. Just we recall here that the method allows to get a value of the entropy,  $K_2$ , which is a lower bound of the Kolmogorov entropy  $K_1$ .

$$K_2 \leq K$$

with

$$K_2 = \frac{1}{\tau} \ln \left( \frac{C_D(R)}{C_{D+1}(R)} \right) \quad (9)$$

$\tau$  is the time delay taken to construct each component of the points in the phase space (namely  $X(t_1)$ ,  $X(t_1 + \tau)$ ,  $X(t_1 + 2\tau)$ , ...,  $X(t_1 + (D-1)\tau)$ ) in a  $D$  dimensional phase space if  $X(t_1)$  is the time series). The  $K_2$  calculation as we can see from the relation (9) takes advantage of the calculation of the fractal dimension, since  $K_2$  is obtained from the shift of the successive curves  $\log C(R) = f(R)$ , with increasing  $D$ . In figure 13, the results are given for two attractors for which respectively  $\nu = 2.4$  and  $\nu = 3.1$ .

Some remarks have to be made:

1) As it was already pointed out for the calculation of the correlation dimension  $\nu$  [24], the good parameter seems to be, not the dimension  $D$  but rather the embedding time  $\tau_e = (D-1)\tau$  i.e. the length of the time sequence taken to define a point in the reconstructed phase space.

2) In the case of the discussed experimental data, the  $K_2$  values vary as the correlation dimension

$$K_2 \approx 2 \cdot 10^{-3} \text{ s}^{-1} \quad \text{for the attractor with } \nu = 2.4$$

$$K_2 \approx 5 \cdot 10^{-3} \text{ s}^{-1} \quad \text{for the attractor with } \nu = 3.1$$

this confirms the first idea that the correlation dimension varies in the experimental sequence as the amount of chaos. (Note that  $\nu = 2$  corresponds to a torus in the phase space, i.e. a biperiodic regime without chaos).

3) The entropy may be regarded as the inverse of a characteristic time of the divergence of the trajectories. In the case of the two considered attractors, if  $K_2$  is normalized to the longest period  $\tau_1$  of the regime, we find  $K_2 \tau_1 \approx 0.21$  for the first attractor and 0.53 for the most chaotic one. In this latter case, the characteristic time of the divergence in the phase space is around two times the longest period of the dynamics.

Now let us return to the evolution of all the chaotic states under study ( $317 \leq Ra/Rac \leq 320$ ). From the  $\nu$  values (and  $K_2$  values in some cases), we remark that the variation of the amount of chaos is non monotonous as shown in figure 14. How we can explain this result? As mentioned previously, the variation of the Rayleigh number induces the variation of the frequency ratio  $\rho$  of the two oscillators. In the considered experimental situation, it turns out that an important variation of  $\rho$  occurs within a very small range of  $Ra/Rac$ ; so in a first approximation, we can consider that the dynamical properties are then essentially due to the frequency ratio variation, as pointed out by the two end cases ( $\rho = 1/6.59$ ,  $\nu \approx 2.4$ ;  $\rho = 1/5.91$ ,  $\nu \approx 2.1$ ). It follows that the  $\nu$  variation versus  $\rho$  is related to the local properties of the critical line.

Direct comparison with theoretical and numerical models is difficult since the results obtained here correspond to a four dimensional phase space [30] but nevertheless they are in qualitative agreement with theoretical predictions.

Note, to finish this discussion, that the calculation of the positive Lyapunov exponents  $\lambda_i$  has confirmed the presence of two positive  $\lambda_i$  [25]; this calculation was performed on the most chaotic signal (attractor in the figure 12b) with the algorithm developed by J.P. Eckmann and D. Ruelle, after testing this method on numerical models [26].

#### IV - DYNAMICS INSIDE THE PHASE-LOCKED TONGUES

We have seen how a biperiodic regime can become chaotic, together on numerical models and in physical situations but the examples we have discussed, were all related to the direct onset of chaos from biperiodicity. What happens when the rotation number is rational and that the non-linearities are increased, i.e. when the regime remains inside a phase-locked tongue? Without entering in the details which may be found in particular in [11], it is important to note that the route to chaos is different from those studied before. The study of the circle map has shown that inside the tongues, the approach of chaos is achieved by period doubling [29] i.e. in the tongue  $p/q$ , appears progressively the periodic orbits with rotation number  $(p \cdot 2^n)/(q \cdot 2^n)$ . Note that the value of the

Figure 13: Calculated  $K_2$  values versus the embedding time  $\tau_e$ .

(O) = attractor with  $\nu = 2.4$   $\rho = 1/6.59$ ;

(X) = attractor with  $\nu = 3.1$   $\rho = 1/6.62$ .

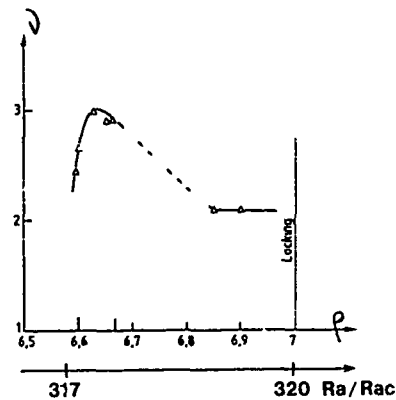
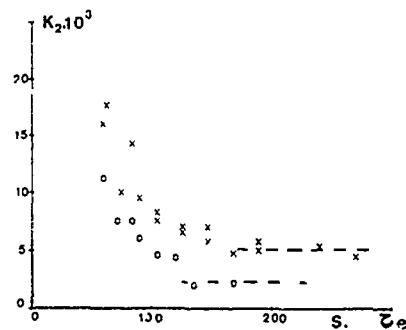


Figure 14: Variation of the calculated fractal dimension  $\nu$  with the measured frequency ratio in the range of Rayleigh numbers corresponding to all the chaotic states.

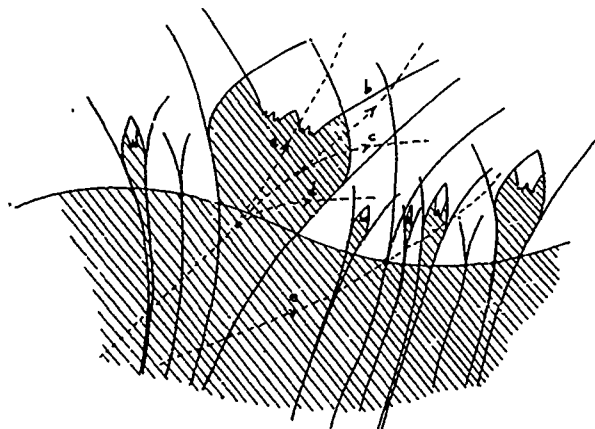


Figure 15: Schematic representation of phase-locked tongues for the circle map (from [11]). The dashed area corresponds to non-chaotic regimes and the wavy line is the critical line. The dotted curves represent different paths which may be followed in an experimental situation.

rotation number is preserved, but corresponds to different values of the actual frequencies. The sequence of period doubling ( $n \rightarrow \infty$ ) may be not complete when chaos appears and the line in the plane of the parameters  $\{K, \Omega\}$ , which gives the onset of chaos is not simple, as shown in figure 15 (taken from [11]). A great interest of this figure is to show, beyond its esthetic aspect a scheme of the possible imbrication of the different regimes (biperiodism phase-locking, biperiodic chaos, period doubling and so on), when an experimental path is followed.

In fact the experimental situations are often much more complicated than those which are deduced from the circle maps. Some parts of the experimental results may agree with the predictions, others disagree but could be explained probably from 2d models. In particular, in an experiment of forced convection with mercury [28], the detailed study of the approach of chaos inside the tongue  $8/13$  has been performed. A complicated structuration of different dynamical regimes has been observed inside the tongue, when the amplitude of the forcing was increased. In some regions, the influence of the neighbouring tongues was found.

So if a conclusion has to be made, we could say that the dynamics of two coupled oscillators, and only two, is fascinating by its great richness. This kind of behaviour is not a "privilege" of theoretical models, but it can be found in many systems. We have seen some examples in convection, but the different dynamical regimes, related to the interaction of two oscillators and leading to chaos, can also be responsible of behaviours observed in mechanical systems, biology, climatology, etc...

## BIBLIOGRAPHY

- [1] P. Bergé, M. Dubois, Contemporary Physics 26, 535 (1984).
- [2] F.H. Busse, Rep. Prog. Phys. 41, 1929 (1978);  
F.H. Busse, J. Fluid Mech. 91, 319 (1979).
- [3] P. Bergé, M. Dubois, J. Phys. Lettres 40, L505 (1979).
- [4] M. Dubois, P. Bergé, Physics Letters 76A, 53 (1980).
- [5] A. Libchaber, J. Maurer, J. Phys. Lettres 39, L369 (1978).
- [6] J. Stavens, F. Heslot, A. Libchaber, Phys. Rev. Letters 55, 596 (1985).
- [7] A. Fein, M.S. Heutmaker, J.P. Gollub, Physica Scripta T9, 79 (1985).
- [8] M. Dubois, P. Bergé, V. Croquette, J. de Physique Lettres 43, L29 (1982).
- [9] V.I. Arnold, Trans. Am. Math. Soc. 2e Ser. 46, 213 (1965).
- [10] M.H. Jensen, P. Back, T. Bohr, Phys. Rev. A30, 1960 (1984).
- [11] R.S. MacKay, C. Tresser, Physica 19D, 206 (1986).
- [12] J. Curry, J.A. Yorke, "The structure of attractors in dynamical systems", Springer Notes in Mathematics. 668, 48 (1977).
- [13] M. Dubois, P. Bergé, Traitement numérique des attracteurs étranges, Grenoble, fév. 1985, ed. by M. Cosnard and C. Mira, CNRS.
- [14] P. Bergé, M. Dubois, J. de Phys. Lettres 46, L431 (1985).
- [15] S.J. Shenker, Physica 5D, 405 (1982);  
M.J. Feigenbaum, L.P. Kadanoff and S.J. Shenker, Physica 5D, 370 (1982);  
S. Ostlund, D. Rand, J. Sethna, E. Siggia, Physica 8D, 303 (1983).

- [16] M. Dubois, P. Bergé, *Physica Scripta* 33, 159 (1986).
- [17] P. Grassberger, I. Procaccia, *Phys. Rev. Letters* 150, 346 (1983); *Physica* 9D, 189 (1983).
- [18] J.D. Farmer, E. Ott, J. Yorke, *Physica* 7D, 153 (1983).
- [19] P. Grassberger, I. Procaccia, *Phys. Rev.* A28, 2591 (1983).
- [20] Y. Termonia, *Phys. Rev.* A29, 1612 (1984).
- [21] J.P. Eckmann, D. Ruelle, *Rev. Mod. Physics* 57, 617 (1985).
- [22] A. Wolf, J. Swift, H. Swinney, J. Vastano, *Physica* 16D, 285 (1985).
- [23] J.P. Eckmann, S.O. Kamphorst, D. Ruelle, S. Ciliberto, *Phys. Rev.* A34, 4971 (1986).
- [24] P. Atten, J.P. Caputo, B. Malraison, Y. Gagne, J. de Mécanique, Volume spécial 1984 "Bifurcations et comportements chaotiques".
- [25] R. Conte, M. Dubois, to be published.
- [26] R. Conte, private communication.
- [27] V. Croquette, *Pour la Science* 62, 62 (1982).
- [28] J.A. Glazier, M.H. Jensen, A. Libchaber, J. Stavens, *Phys. Rev.* A34, 1621 (1986).
- [29] M.J. Feigenbaum, *J. of Stat. Physics* 19, 25 (1978);  
C. Tresser, P. Coullet, *C.R. Acad. Sciences Paris* A287, 577 (1978).
- [30] M. Sano, Y. Sawada, *Phys. Letters* 97A, 73 (1983).

A DETERMINISTIC APPROACH TO TURBULENCE :  
CHAOS IN RAYLEIGH-BENARD CONVECTION

P. BERGE  
Service de Physique du Solide et de Résonance Magnétique  
CEA Saclay  
91191 Gif-sur-Yvette Cedex, France

TABLE

I - RAYLEIGH BENARD CONVECTION
I.1. Physical meaning of the Prandtl number
I.2. Mechanism of the instability
I.3. Spatial organization
I.4. Towards confined geometries
II - BASIC CONCEPTS ABOUT DISSIPATIVE DYNAMICAL SYSTEMS
II.1. Definitions and examples
II.2. The simplest attractors, their Poincaré section and comparison with mappings
II.3. Iteration of a one-dimensional map
III - TOWARDS DETERMINISTIC TURBULENCE OR CHAOS
III.1. A definition of chaos
III.2. The key of chaos: the strange attractor
III.3. Brief introduction to bifurcations
III.4. Ways in which chaos appears, main routes to chaos
IV - SOME EXPERIMENTAL ILLUSTRATIONS
IV.1. The method
IV.2. Reconstruction of the phase space
IV.3. Measuring of the dimension of the attractors
IV.4. Type I intermitencies
IV.5. Type II intermitencies
IV.6. The subharmonic cascade
IV.7. The quasiperiodicity
REFERENCES

I - RAYLEIGH BENARD CONVECTION

Convection is a very common phenomenon in nature and its study and understanding have fundamental importance in meteorology, oceanography, geophysics etc... and in many transport processes involved in practical applications (material science, power engineering, combustion etc...). The term "convection" seems to have been applied first to denote the transportation of heat through fluid motion. Generally speaking, convection arises when a thermal inhomogeneity exists in a fluid. The competition between the destabilizing effects like buoyancy and stabilizing ones like viscosity leads to an instability. Such instabilities are characterized by the existence of a threshold beyond which there is organization of fluid motions into a relatively ordered pattern sometimes called "dissipative structures".

Rayleigh-Benard convection is one of the simplest instabilities [1]. It is related to the case of a horizontal layer of a thermally expansive fluid which is confined above and below by rigid plates of good thermal conductivity, submitted to purely vertical adverse thermal gradient (adverse means "heated from below").

I.1. Physical meaning of the Prandtl number

Let us first consider the layer of fluid and suppose the existence of a localized thermal gradient. The propagation of this localized gradient through the whole

fluid layer is governed by a heat diffusion equation. The diffusion coefficient of the temperature is

$$D_T = \frac{\lambda_T}{\rho_0 C_p}$$

where  $\lambda_T$  is the thermal conductivity of the fluid,  $C_p$  the specific heat at constant pressure and  $\rho_0$  the density. On the other hand, the diffusion coefficient of a velocity gradient (more generally of the vorticity) is simply the kinematic viscosity  $\nu = \eta/\rho_0$ .

These two diffusion coefficients allow us to calculate the order of magnitude of the characteristic relaxation times  $\tau$  of the gradients in a layer of depth  $d$ . For the temperature:

$$\tau_{t,b} \approx d^2/D_T.$$

and for the velocity:

$$\tau_\nu \approx d^2/\nu.$$

The ratio of these times is the Prandtl number which controls the temporal behaviour in a fluid layer submitted to the two kinds of gradient. Then in convective motion,

$$Pr = \frac{\tau_{t,b}}{\tau_\nu} = \frac{\nu}{D_T}$$

We may have two opposite situations:

- (a) High Prandtl number fluids: the vorticity diffuses (then the velocity relaxes) faster than the temperature. Then the velocity perturbations follow the temperature perturbations without delay; one says that the viscous effects are dominant.
- (b) Low Prandtl number fluids: the temperature relaxes faster than the vorticity: a velocity perturbation may persist even after the thermal cause has disappeared: the inertial effects are dominant.

From these two opposite situations, one can point out the qualitative analogy between the Prandtl number and the reciprocal of the Reynolds number  $Re$ , because, in a flowing liquid,  $Re$  measures the balance between inertial terms and viscous terms.

### 1.2. Mechanism of the instability

The origin of the instability can be seen as follows. If fluid elements are displaced along the paths  $HH'$  and  $BB'$  (see Figure 1) a torque which would amplify the displacement is created. After the displacements  $HH'$  and  $BB'$  have occurred, the temperature difference between the two fluid elements diminishes, due to the thermal diffusivity  $D_T$ , with a characteristic time on the order of:

$$\tau_{t,b} \sim \frac{d^2}{D_T}.$$

where  $d$  is the depth of the layer. The characteristic time of the displacement  $HH' - BB'$  depends on the forces acting on the fluid - that is, the buoyant force due to the density difference and the viscous frictional force. This characteristic time  $\tau_\mu$  behaves like:

$$\tau_\mu \sim \frac{\eta}{\rho_0 g \alpha d \Delta T}$$

$\eta$  : dynamic viscosity  
 $\alpha$  : expansion coefficient  
 $\rho_0$  : mean density  
 $g$  : gravitational acceleration.

} of the fluid

The condition for the onset of sustained motion is that the time  $\tau_{t,b}$  (lifetime of the cause) be greater than  $\tau_\mu$  (time for appearance of the effect). Hence the condition for sustained convection is:



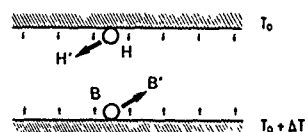


**Fig.1** - Diagram of the generation of motion in the fluid. We consider two fluid elements  $H$  and  $B$  displaced to  $H'$  and  $B'$  respectively. This motion is damped or maintained, according to the value of  $\Delta T$ .

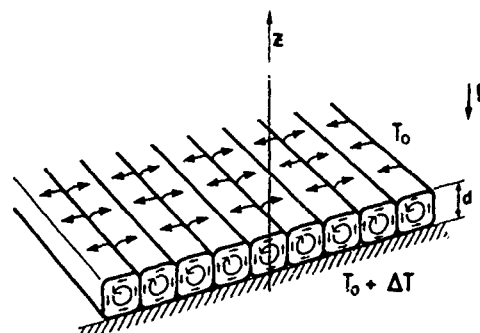


**Fig.2** - Convective arrangement of straight rolls (ideal case, near onset).



**Fig.2a** - Shadowgraphy of disordered convective structures in cylindrical and rectangular containers.

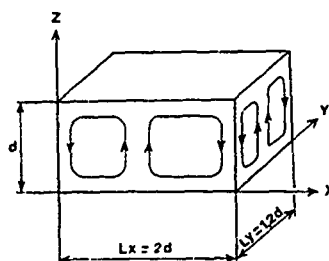


**Fig.2b** - Geometry of a "small box" : an example of convective arrangement.

$$\frac{\rho_0 g \alpha d^3}{\eta D_r} \Delta T \gg \text{constant.}$$

The left hand side, called the Rayleigh num.  $Ra$ , is a nondimensional measure of the temperature difference  $\Delta T$ . The inequality above states that there exists a critical Rayleigh number  $Ra_c$  (or equivalently, a critical temperature difference  $\Delta T_c$ ) above which the state of rest ceases to be stable and convection begins. Convective instabilities were first clearly observed experimentally by Bénard in 1900 and first interpreted by Lord Rayleigh in 1916; it is for this reason that the two names are associated to the phenomenon.

Fluid	Air	Water	Si oil $\nu \approx 1$ stokes
$\Delta T_c$ ( $d=1$ cm)	17°	0.1°	2.2°
$Pr$	0.7	7	900

Table - Some critical temperature differences corresponding to  $Ra_c$  for some fluids near room temperature.

### 1.3. Spatial organization

We have seen that when the temperature difference applied to a horizontal fluid layer is increased beyond a given value (or  $Ra > Ra_c$ ), the fluid begins to move. How does it do this?

To study the convective structure, it is necessary to look at the fluid from above. This is the reason why, in experiments which deal with this problem, the upper plate is often made of transparent sapphire whose thermal conductivity is large compared to that of the usual fluids (in some cases, when the (expensive) sapphire is not available, one can work with glass plates but the results can be slightly different).

The spatial organization takes the form of ascending and descending motions which carry along the fluid, in rolls turning clockwise and counter clockwise successively in space. These almost periodic motions obviously introduce in the fluid a succession of "warm" and "cold" currents. One can make these currents visible (without perturbing the fluid) through the temperature gradients which induce refractive index gradients able to refract light beams so that the fluid acts as many local lenses. Then, a parallel light beam which crosses the fluid is focused where the refractive index is largest (cold streams) and diverges where the refractive index is lowest (warm streams): the light intensity modulation of the beam after crossing the convective cell reveals the structure of the motion with bright lines corresponding to downwards motions.

If the horizontal extent of the layer is large compared to the depth  $d$ , we generally obtain (after a transient period which may be very long) a stationary (time-independent) roll pattern which has the following properties (near onset):

- (a) the axes of the rolls tend to be perpendicular to the lateral walls.
- (b) In the core of the pattern, relatively far from the boundaries, the axes of the rolls tend to be equidistant and, so, locally parallel.

Except for some particular cases, these two conditions cannot be simultaneously fulfilled, creating a topological frustration. This frustration gives rise to defects such as dislocations, bending of the rolls, grain boundaries. So, very generally, in large containers the natural structures are disordered see figure 2a) [2].

By increasing the  $Ra$  number, the convection leaves the steady state and becomes directly turbulent. In the case of high Prandtl number fluid the onset of turbulence is larger than  $10 Ra_c$ , but depends on the particular conditions. For low Prandtl number fluid, the onset of turbulence may be very near  $Ra_c$ . But the common and important feature is the following: in both cases, this turbulence is due to the erratic motion of

the rolls themselves. In other words, the phase of the rolls is continuously changing; this is the reason why this kind of turbulence had been called "phase turbulence". This phase turbulence is characterized by a continuous change of the convective pattern with complex motion of all kind of structural defects. This phase turbulence is not well understood. Note, however, that in the case of low Prandtl number fluid, some physical mechanisms have been recently elucidated [3] but many progress as well experimental as theoretical remain to be done.

#### I.4. Towards confined geometries

How can the order of the convective pattern be preserved, the phase of the rolls fixed and, then, manifestation of phase turbulence prevented? It suffices to drastically reduce the number of possible configurations which are compatible with the imposed constraints. A natural idea is to place the fluid in a cell whose horizontal dimensions  $L_x, L_y$  are on the same scale as the height. The *aspect ratio*, defined as  $\Gamma = L/d$ , is small in such a cell and the number of rolls necessarily limited. For example the presence of lateral boundaries separated by a distance of only twice the depth stabilizes the convective structure and reduces the number of rolls to two, at least for moderate values of  $Ra$ . Note that in the direction perpendicular, the distance  $L_y$  between the boundaries is even smaller. Experiments show that with this type of cell, spatial order is indeed preserved over a very large range of  $Ra$  (typically hundreds time  $Ra_c$ ). This kind of experimental cell corresponding to a confined geometry is sometimes called "small box" (see figure 2b). Under that conditions, the first instability encountered (after the onset of steady convection) is that of the thermal boundary layers. In these boundary layers, thermal oscillators develop which can have different forms. The important fact is that, by increasing  $Ra$ , one obtains, first, only one oscillator whose pulsations are easily visualized through simple optical means. The corresponding regime is periodic (i.e. the temperature and velocity of the convective fluid vary periodically with time), with a frequency well determined and stable [4].

By increasing the control parameter  $Ra$ , the regime becomes more complicated and, finally, a turbulent state is reached. But, this turbulence is not related to the interaction of many complicated spatial modes like in the case of the large aspect ratio cells (phase turbulence). On the contrary, in such a small box, the turbulence is related to the interaction of a very small number of modes or degrees of freedom. To distinguish these last turbulence from the phase (or developed) turbulence it is named "deterministic turbulence" or "chaos", or even, "temporal chaos" to well stress the fact that spatial effects are not involved. As a matter of fact, Rayleigh-Benard convection in confined geometry can be considered as a dissipative dynamical system.

## II - BASIC CONCEPTS ABOUT DISSIPATIVE DYNAMICAL SYSTEMS

### II.1. Definitions and examples

A consequence of what we have discussed in the case of a confined geometry is that we can expect to be able to interpret the corresponding turbulence in the frame of the theory of non-linear dynamical systems with a small number of degrees of freedom [5]. Let us rapidly address the question: what is a dissipative dynamical system? An example of dynamical system is for example, a forced (and sustained) pendulum. The dissipative character is due to the presence of unavoidable friction and the existence of permanent oscillations is allowed by a convenient *sustaining*. In a general manner, the time evolution of a dynamical system can be described through a set of ordinary differential equations. In all that follows, we will consider that these equations are *non linear*, these non linearities giving all the richness in the behaviour.

For example, we will consider a system of 3 equations:

$$\begin{cases} dX/dt = f(X, Y, Z) \\ dY/dt = g(X, Y, Z) \\ dZ/dt = h(X, Y, Z) \end{cases} \quad (II.1)$$

where  $X, Y, Z$  are the variables of the system or *degrees of freedom*. The corresponding dynamics is represented by the solutions of (II.1):

$$X = F(t) \quad Y = G(t) \quad Z = H(t)$$

which give the time evolution of the various variables allowing to determine the state of our system.

In an alternative description of the dynamics, one considers the trajectory of the point whose coordinates are  $X, Y, Z$ ; doing so, we define the so called *phase space*, the coordinates of which are the variables of the system. The prime importance of this particular space will appear all along this lecture.

As an illustration, let us look at a simple example: that of the sustained pendulum as modeled by Van der Pol whose second order non-linear differential equation is:

$$d^2 X/dt^2 - (\epsilon - X^2) dX/dt + X = 0 \quad (II.2)$$

Equivalently, we can describe the system by a system of 2 first order-equations:

$$\begin{cases} dX/dt = Y \\ dY/dt = (\epsilon - X^2) Y - X \end{cases}$$

in which the two degrees of freedom, i.e. the position  $X$  and velocity  $Y$  of the pendulum, clearly appear. The motion of the point of coordinate  $X, Y$  in the phase space tends to the asymptotic trajectory which is a closed loop, named the "limit cycle". Note that this limit cycle is only reached after a long time during which the trajectory is progressively attracted towards the limit cycle, and named, for this reason, *attractor* (see figure 3).

The existence of an attractor arises from the dissipation of the system represented here by the second term of equation (II.2). In the same manner, dissipation produces area (or volume) contraction in phase space and, as such, the dimension of the attractor is lower than that of the phase space. In the example quoted above the attractor has a dimension 1 in a two dimensional phase space.

## II.2. The simplest attractors, their Poincaré section and comparison with mappings

The simplest attractors are the *fixed point* corresponding to the state of rest, the *limit cycle* to the periodic regime, and the *tori* which correspond to the multiperiodic regimes. Furthermore, instead of considering the full trajectories, one can consider its intersection with a plane (or hyperplane). This representation obtained this way, the *Poincaré section*, has a dimension lowered by 1 in comparison with the original representation. In particular, this procedure allows one to draw on a sheet of paper the Poincaré section of an attractor immersed in a three-dimensional phase space. This procedure is particularly useful in the case of experimental attractors. As one can see on figure 4a, the Poincaré section of the trajectories of an attractor embedded in a three-dimensional phase space consists in an ensemble of points  $P_1, P_2, P_3, \dots$ . Instead of considering the full trajectory, one can focus our attention on the properties of this ensemble  $P_i$ . A very rich and simple way to do so is to compare this ensemble with models called "iterated map". In a two-dimensional case, if  $X_k, Y_k$  are the coordinates of a point  $P'_k$ , the general form of such a mapping reads:

$$\begin{cases} X_{k+1} = F(X_k, Y_k) \\ Y_{k+1} = G(X_k, Y_k) \end{cases}$$

meaning that a point  $P'_{k+1}$  is defined as a function of the previous one  $P'_k$ . An ensemble of points is thus generated, when the "discrete time"  $n$  runs (see figure 4b). The topological properties of this set can be usefully compared with that of an experimental Poincaré section. This method presents great advantages: comparison between full trajectory of an experimental attractor with that of a continuous three-dimensional flow (i.e. a theoretical model) would require a numerical integration of this flow, a delicate and time-consuming matter compared with the iteration of a two-dimensional mapping.

Still more simple and nevertheless very useful is the one-dimensional map. Only one variable is used in such a mapping which can be written:

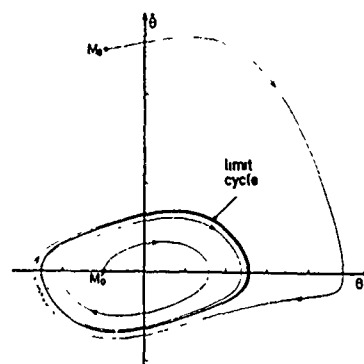


**Fig. 3** - Phase diagram of the Van der Pol equation ( $\epsilon = 0.4$ ). The asymptotic solution to this equation is represented in the  $(\theta, \dot{\theta})$  phase plane by a closed curve, the limit cycle towards which all trajectories converge.

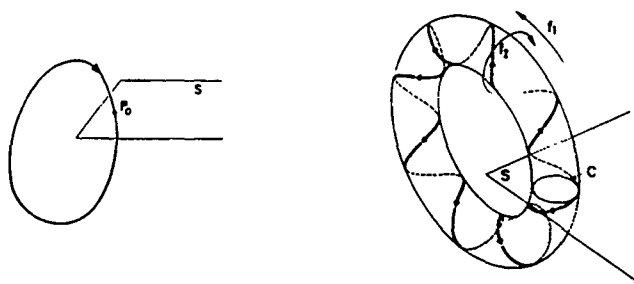


**Fig. 4a** - Simple attractors and their Poincaré section. On the left the limit cycle whose Poincaré section by the plane  $S$  is a point  $P_0$ . On the right, the torus, whose Poincaré is the closed loop  $C$ .

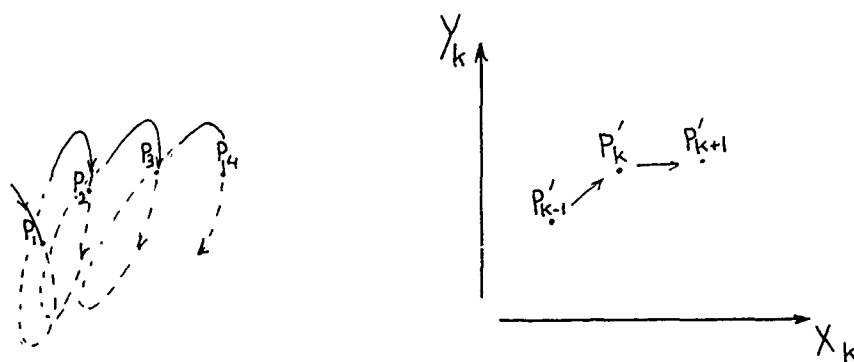


**Fig. 4b** - Comparison between a Poincaré section and a two dimensional mapping.

$$x_{k+1} = H(x_k)$$

This allows useful comparison with the experimental "return maps". Consider a variable  $x$  of an experimental dynamical system, suppose that this variable undergoes successive maxima ...  $x_k, x_{k+1}, x_{k+2}$  etc...

The diagram  $x_{k+1} = f(x_k)$  is the "first return map" when the one obtained by plotting  $x_{k+2} = f(x_{k+1})$  is named "second return map".

### II.3. Iteration of a one-dimensional map

Classically, the tools used to study a one-dimensional map are the graphs in the  $(x_k, x_{k+1})$  plane of the function  $f: x_{k+1} = f(x_k)$  and of the identity map:  $x_{k+1} = x_k$ . To illustrate the method, we will take as an example the nonlinear mapping:

$$x_{k+1} = 4\mu x_k(1-x_k), \quad x \in [0, 1].$$

The graph of the function  $f(x) = 4\mu x(1-x)$  for a given value of  $\mu$  between 0.25 and 0.75 is zero at  $x = 0$  and  $x = 1$ , and has a maximum equal to  $\mu$  at  $x = 0.5$ . With the help of this graph, let us now study the iteration defined above, starting from an initial condition  $x_0$  ( $\mu = 0.7$ ). The first iterate  $x_1$  is at the intersection of the graph  $f$  with the vertical line with abscissa  $x_0$  (see figure 5). Similarly, the second iterate  $x_2 = f(x_1)$  is located at the intersection of  $f$  with the vertical line with abscissa  $x_1$ , and so on. A simple and efficient method of constructing the successive iterates consists of using the identity map, or diagonal,  $x_{k+1} = x_k$ . Indeed the horizontal line  $x_{k+1} = x_k$  intersects the diagonal  $x_{k+1} = x_k$  at a point with  $x_k = x_k$ . It then suffices to draw a vertical from this point without referring to the abscissa axis.

By repeating the sequence of operations:

- draw a vertical from the diagonal till its intersection with the graph of  $f$ ,
- from the point obtained, draw a horizontal until its intersection with the diagonal,

we obtain the successive iterates of the mapping. We ascertain from Figure 5 that the iteration converges to the point with abscissa  $x^*$ , the intersection of the diagonal with the graph of  $f$ . One can easily verify that any initial condition  $x_0$  chosen converges to  $x^*$  under iteration of  $f$  with the exception of the endpoints 0 and 1 of the interval. It is clear that any point of intersection of  $f(x)$  with the identity map is its own iterate; it is a fixed point of  $f$ . This is the case for the origin: taking  $x_0 = 0$ , we find  $x_1 = 0, x_2 = 0$ , etc. However, "or a value of  $x_0$  that is arbitrarily close but not equal to 0, the iteration converges to  $x^*$ . A point at a small distance from the origin moves further away from this fixed point, which is therefore called unstable. In contrast, the fixed point  $x^*$  towards which the iteration converges for any initial condition in  $]0, 1[$  is a stable fixed point.

There is a criterion for determining whether a fixed point is stable or unstable which does not require tedious calculation. The graphical construction shows that if the slope of  $f(x)$  at the fixed point is of absolute value greater than one, then the fixed point is unstable; this is the case for the origin. On the other hand, if the slope of  $f$  is less than one in absolute value, then the iteration converges towards the fixed point: this is the case for  $x^*$ .

### III - TOWARDS DETERMINISTIC TURBULENCE OR CHAOS

#### III.1. A definition of chaos

We will say that a dynamical regime is chaotic if the power spectrum of a variable of the system (amplitude of a pendulum, velocity of the fluid in a convection experiment... etc) contains a continuous part - a broad band - regardless of the possible presence of peaks. Or else we may use the criterion that the autocorrelation function of the time signal has finite support, i.e. that it goes to zero in a finite time. In either case, the same concept is involved: the loss of memory (or similarity) of the signal with respect to itself. Consequently, knowledge of the state of the system for an arbitrarily long time does not enable us to predict its later evolution.

Fig. 5 - Graph of  $f(x) = x_{n+1} = 4\mu x_n(1-x_n)$  for  $\mu = 0.7$ . The fixed points of the map are the intersections of the graph with the diagonal. There is a stable fixed point  $x^*$  towards which the iterates of all initial conditions in the interval  $]0, 1[$  converge. The origin is an unstable fixed point. The stability of a fixed point can be determined from the slope of the tangent of the curve at that point: if the absolute value of the slope is less than one, the fixed point is stable ( $x^*$ ), and otherwise it is unstable (0).

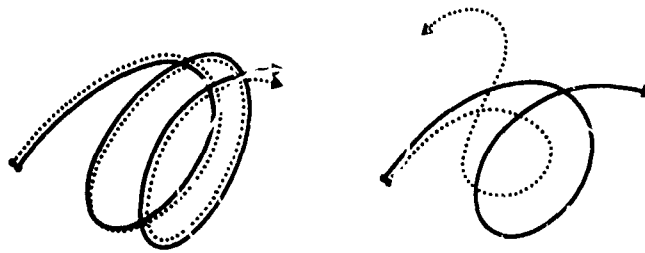
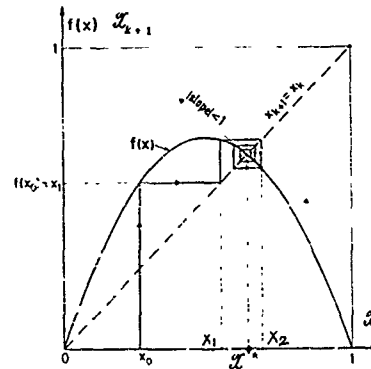


Fig. 6 - Behaviour of neighbouring trajectories in phase space. On the left, the two trajectories remain neighbour and similar when time runs (non chaotic regime) but they diverge rapidly becoming completely dissimilar in a chaotic regime.

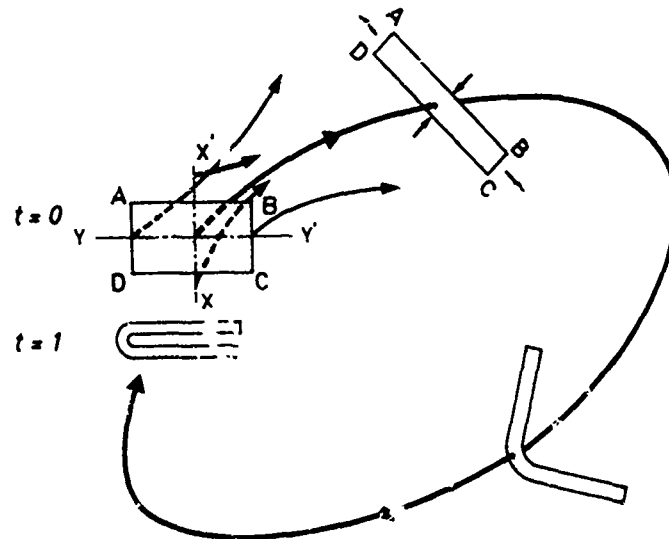


Fig. 7 - The first step of the construction of a chaotic (or strange) attractor. The ensemble of the initial conditions lie in the rectangle ABCD which is contracted along  $XX'$  (attraction) and stretched along  $YY'$  (S.I.C.), the "mean" trajectory being drawn as a continuous loop.

Essentially, this means that we are making unpredictability the quality which defines chaos. As a matter of fact, prediction is based on the possibility to extrapolate the past towards the future. This works very well in the case of periodic signals because of the repetition of a pattern (permanence of the self-similarity). The loss of self-similarity does not allow this extrapolation to be done, except for very short time intervals. In the phase space, the question of permanence (periodic) or loss (chaotic) of the self-similarity has a particular and important consequence. In the case of a periodic (or multi periodic) signal, two neighbouring trajectories will remain  $\epsilon_0$  when the time runs (conservation of similitude). On the contrary, they will diverge in the case of a chaotic signal (loss of similarity) see figure 6. This very important property of the trajectories of a chaotic regime is called Sensitivity on Initial Conditions or S.I.C. Once more, the consequence of S.I.C. is the following: even a very small (infinitesimal) difference on the knowledge of the exact condition of the system will be (exponentially) amplified and, as such, has dramatic consequence in the subsequent behavior, producing unpredictability. Then, it suffices that a system presents the property of S.I.C. to be chaotic, whatever the number of its degrees of freedom may be. Indeed, we have arrived at a highly nontrivial result: the impossibility of predicting the behavior of certain deterministic flows with only a few number of degrees of freedom [5][6] !

### III.2. The key of chaos: the strange attractor

Returning to figure 3, we have yet seen that all the points corresponding to different initial conditions are folded back to the limit cycle, the attractor of the periodic regime. Let us see, by comparison, how it is possible to construct the attractor of a chaotic regime. We take the simple case of a three-dimensional phase space; see figure 7. Let us start with initial conditions ( $t=0$ ) lying the rectangle ABCD. When the time runs, we have two opposite effects; in one direction, let us say  $X X'$  we have contraction towards the attractor, but in the other  $Y Y'$  we have divergence (S.I.C.). So, the rectangle is at the same time, contracted (area contraction due to dissipation) and stretched (S.I.C.). Then, the rectangle becomes narrow and elongated; but in order to remain in a bounded region of the phase space it has to fold. So, after one turn ( $t=1$ ), we are back to the starting plane which we can choose as the Poincaré plane (in the following, we will not consider the full attractor but only its Poincaré section). Due to the combined effects of contraction, stretching and folding, the initial rectangle has been transformed into some kind of horseshoe. With time evolution, contraction stretching and folding continue to act on this horseshoe, giving some kind of double hairpin after two turns ( $t=2$ ) see figure 8. When many turns will be made, one obtains, in the Poincaré plane, a complicated structure with an infinite number of sheets. One can see on figure 8 that the transverse structure of the Poincaré section is formed according to the same manner than a Cantor fractal ensemble. So, a chaotic attractor is a fractal object with a non integer dimension  $D$  (here  $2 < D < 3$ ). Because of the very particular and complex topology of these chaotic attractors, they were named "strange attractors".

Among the conclusions of this geometrical reasoning, one can point out the fact that a strange attractor (i.e. an attractor with S.I.C.) can exist in a low dimensional phase space (minimum 3 dimensions). That means that chaos may appear in a system with only 3 variables (or, in this context, 3 degrees of freedom). In other words, the system of 3 differential equations (II.1) may have chaotic solutions in spite of its deterministic character. This is the reason why this kind of chaos has been named "deterministic chaos" (or deterministic turbulence if we deal with an hydrodynamical system).

### III.3. Brief introduction to bifurcations

When discussing about Rayleigh-Benard convection, we have seen that for values of  $Ra < Ra_c$  the fluid remains at rest when, for  $Ra > Ra_c$ , convective velocity is present. We observe a complete change in behavior upon crossing the boundary between stable and unstable solutions. One says that at  $Ra = Ra_c$ , the system undergoes a bifurcation. More generally, whenever the solution to an equation or system of equations changes qualitatively at a fixed value - called a critical value - of a parameter, this is called a bifurcation. From a bifurcation point emerge several (two or more) solution branches, either stable or unstable [5].



Fig. 8 - First steps of the construction of a chaotic attractor in the Poincaré plane with the corresponding transverse structures.

$t=0$  initial rectangle  
 $t=1$  horse shoe  
 $t=2$  double hairpin  
 Compare the transverse structures with that of a Cantor set (fig.12a).

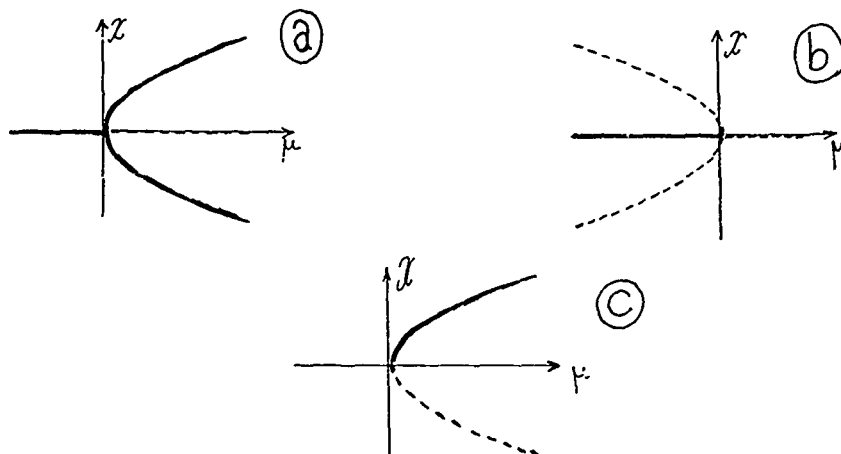
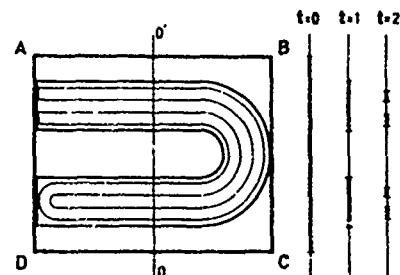


Fig. 9 - Diagrams of simple bifurcations

a) pitchfork (or normal or supercritical) bifurcation  
 b) subcritical (or inverse) bifurcation  
 c) saddle-node bifurcation.

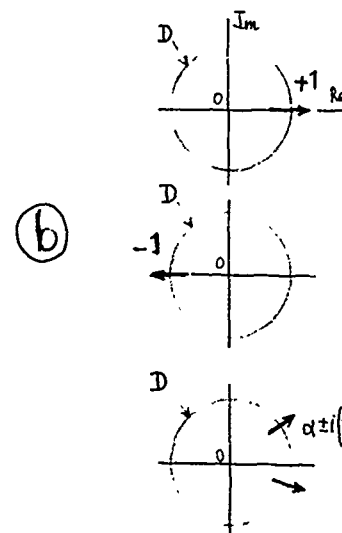
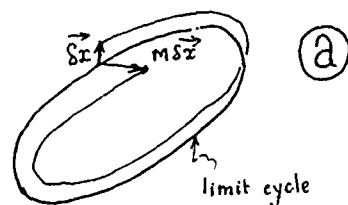
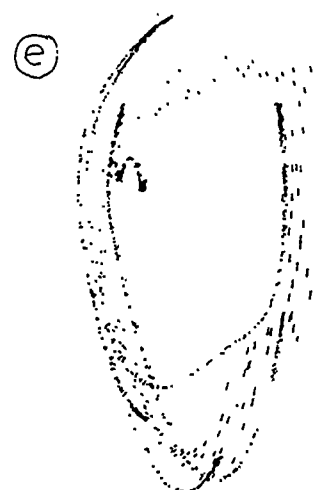
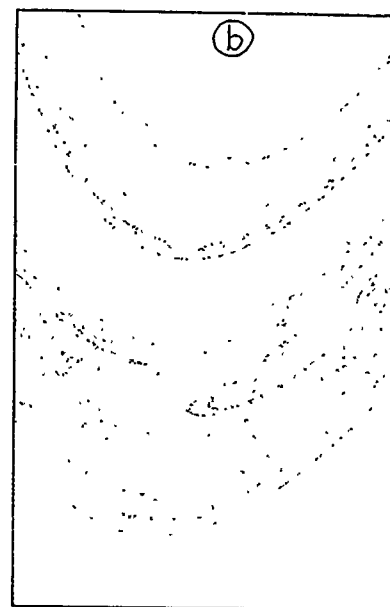
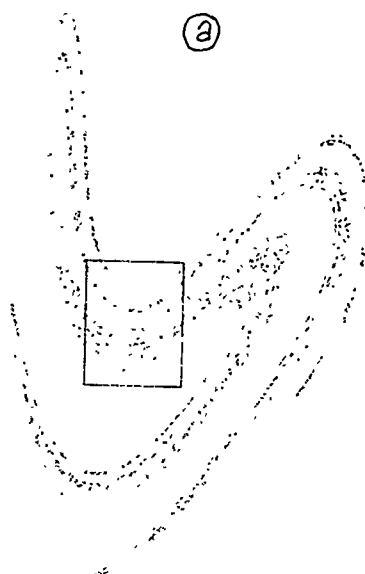


Fig. 10 - a) Instability of a limit cycle. A departure  $\delta x$  is transformed, after a turn into  $M\delta x$  where  $M$  is the Floquet matrix.

b) The 3 generic crossing of the unit circle.



SOME POINCARÉ SECTIONS OF STRANGE ATTRACTORS

a, b) forced pendulum (angular velocity, angle)  
(numerical model)

c, d, e) turbulent R.B. convection

Let us illustrate some different bifurcations through their bifurcation diagrams,  $x$  being a (real) variable characteristic of the bifurcation (for example the velocity in the R.B. case) and  $\mu$  the bifurcation parameter (for example the Rayleigh number). In figure 9a one can see a pitchfork (or normal or supercritical) bifurcation the corresponding equation is

$$\frac{dx}{dt} = \mu x - x^3$$

for  $\mu < 0$  the only stable solution is  $x = 0$ ; for  $\mu > 0$  this solution becomes unstable and the two stable branches are  $x = \pm \sqrt{\mu}$ . Note that the nonlinear term  $-x^3$  limits the exponential growing due to the linear term.

One can see on figure 9b the subcritical bifurcation (or inverse bifurcation). The equation is

$$\frac{dx}{dt} = \mu x + x^3$$

Contrary to the case of the normal bifurcation the nonlinear term  $+x^3$  has also a destabilizing effect on the solution.

The figure 9c represents a saddle-node bifurcation whose equation is  $\frac{dx}{dt} = \mu - x^2$ ; for  $\mu > 0$  there exists 2 branches, one stable and one unstable. For  $\mu < 0$  there exists no solution, stable or unstable.

#### III.4. Ways in which chaos appears, main routes to chaos

What are the routes that lead a dynamical system from regular behavior to chaos? To answer this question, we must list the different possible transitions between attractors, a task as indispensable as identifying the attractors [7].

First, we must say that, very generally, the first step after the steady regime consists in a periodic behavior. For example, in a small box, the increase of Ra number produces a transition from the steady regime to a periodic one. A natural step towards addressing the question posed above is to examine the conditions under which a periodic regime loses its stability.

Consider a flow in an  $m$ -dimensional phase space which has a periodic solution of period  $T$   $\vec{X}(t+T) = \vec{X}(t)$ .

To find out if this solution is stable or not, it suffices to look at what happens to a small initial displacement  $\delta\vec{X}$  away from the solution. Linearizing the flow about the periodic trajectory, we find that an initial condition  $\vec{X}_0 + \delta\vec{X}$  ( $\delta\vec{X}$  infinitesimal) is mapped at the end of the period  $T$  into  $\vec{X}_0 + M\delta\vec{X}$ , where  $M$  is an  $m \times m$  matrix called the Floquet matrix.

The problem of the linear stability of a periodic solution has been reduced in this way to the study of the eigenvalues of  $M$ . We first note that this matrix always has an eigenvalue equal to one; this corresponds to a displacement  $\delta\vec{X}$  along the trajectory. We must study what happens in the directions perpendicular to the trajectory, as shown in the diagram of figure 10a. We see intuitively that, while the eigenvalues of  $M$  depend on the form of the limit cycle, they are independent of the reference point  $\vec{X}_0$  chosen along it. Since over one period  $\vec{X}_0 + \delta\vec{X}$  is mapped into  $\vec{X}_0 + M\delta\vec{X}$ , the solution is linearly stable if all of the eigenvalues of  $M$  are located inside the unit circle  $D$  of the complex plane. Then, all the components of the vector  $\delta\vec{X}$  which are perpendicular to the limit cycle are reduced with each period. On the other hand, if (at least) one of the eigenvalues of  $M$  is outside of  $D$ ,  $\delta\vec{X}$  grows continually in at least one direction: the trajectory moves further and further away from the limit cycle, which is therefore unstable.

By continuous variation of a parameter  $\mu$ , the periodic solution gradually changes; the same is true of the matrix  $M$  and of its eigenvalues. Each of the

eigenvalues can be represented in the complex plane by a curve parametrized by  $\mu$ . Loss of stability of the periodic solution, accompanied by a bifurcation, occurs when one of these curves exits from the unit circle as  $\mu$  is varied. There exist three generic ways in which to cross the unit circle  $D$ , as indicated on figure 10b: at  $(+1)$ , at  $(-1)$  and at two complex conjugate eigenvalues ( $\alpha \pm i\beta$ ). Aside from the loss of stability, each of these crossing types has different consequences on the later behavior of the system, which depend on the nonlinearities and are closely related to the bifurcations involved.

When  $(+1)$  is crossed, a saddle-node bifurcation occurs. The periodic solution does not merely become unstable: it disappears entirely. In a parameter region slightly above the bifurcation threshold, the system enters a regime called Type I intermittency. It is characterized by phases of regular, almost periodic behavior (laminar phases), interrupted from time to time by phases of apparently anarchical behavior (turbulent bursts).

If the circle is traversed at  $(-1)$ , the bifurcation is called subharmonic, and may be either supercritical (normal) or subcritical (inverse). In the case of a supercritical subharmonic bifurcation, a new stable periodic solution, whose period is twice as long, replaces the solution which has become unstable. Period-doubling is repeated for each of the periodic solutions obtained, resulting in an infinite sequence of bifurcations called a subharmonic cascade and ending in chaos. A subcritical bifurcation, on the other hand, leads to Type II intermittency, which qualitatively resembles Type I intermittency: long phases of almost periodic behavior are interrupted from time to time by chaotic bursts. However, Type II is characterized by progressive increase of the amplitude of the subharmonic during the almost periodic phase, the reason being that, here, nonlinear effects amplify the subharmonic instability of the limit cycle. The amplitude increases with each successive oscillation: when it exceeds a critical value, the laminar phase is interrupted.

Finally, a third mode of instability takes place when two complex conjugate eigenvalues ( $\alpha \pm i\beta$ ) simultaneously cross the unit circle: this is called a Hopf bifurcation. If the Hopf bifurcation is supercritical, it leads to a stable attractor, close to the limit cycle which is now unstable (but which still exists). This attractor is a torus  $T^2$  on the surface of which is inscribed the new solution corresponding to a quasiperiodic regime. A second instability can then generate a transition from this quasiperiodic regime to chaos. If the bifurcation is subcritical, we can encounter another phenomenon, called Type II intermittency.

Some of this routes to chaos will be illustrated later in more details.

#### IV - SOME EXPERIMENTAL ILLUSTRATIONS

##### IV.1. The method

In the case of Rayleigh-Benard convection at room temperature and with high Prandtl number fluid (silicone oil) many optical methods can be used. The advantage is their non-perturbative character; furthermore, they are local or semi-local with large facility to change the measurement point. Finally, one can easily visualize the convective arrangement and, then, have a permanent overlook on the structure. Note that, here, we are only concerned with the "small box": a rectangular plexiglass frame (vertical boundaries) is inserted between two massive copper plates, the temperature of which is regulated. Horizontal or nearly horizontal light beams can be sent through the layer. In such an arrangement, laser Doppler anemometry seems to be the best technique for determining a fundamental variable of the convection, namely the velocity. Though used whenever possible, this type of measurement is necessarily contaminated by instrumental noise; this noise represents a serious drawback as far as the dynamical properties are concerned. On the contrary, one can use another optical method with a much higher signal-to-noise ratio. The method uses the fact that a temperature gradient in the fluid causes a gradient in the index of refraction. One then measures deflection of a light ray due to the nonuniformity of the refraction index [5][8]. This easily implemented technique provides a signal corresponding to the mean temperature gradient traversed by the light ray over its entire path through the fluid. It is therefore only a semi-local measure, not related in a simple way to the variable  $\theta$ , but is nonetheless used successfully. Use of the light deflection technique is limited to transparent fluids of sufficiently high density, since it is only in such fluids that appreciable

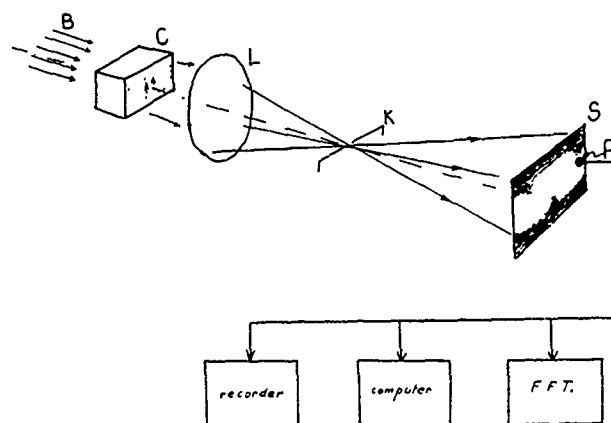


Fig. 11 - Scheme of the experimental arrangement.

B incoming parallel beam  
 C Rayleigh-Benard cell (small box)  
 L converging lens  
 K knife edge (in the focal plane of L)  
 S screen (real image of C by L)  
 P photodiode

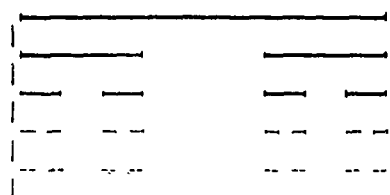


Fig. 12a) - First steps in the construction of the Cantor set.

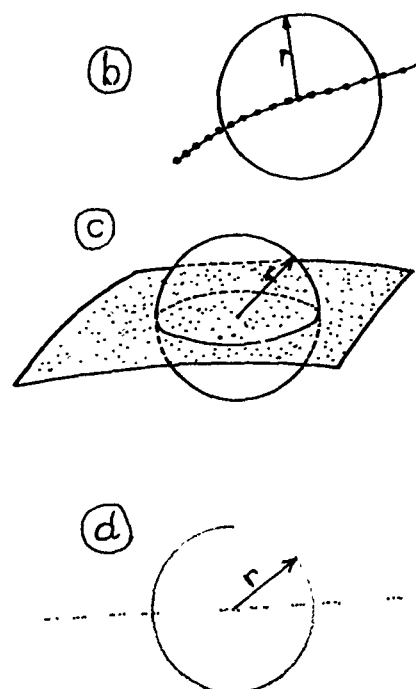


Fig. 12 - Principle of the determination of the correlation dimension.

b) one-dimensional object  
 c) surface  
 d) fractal object

gradients of temperature, and thus of the index of refraction, can exist.

In practice, one makes a Foucault (or Schlieren) image of the convecting cell (knife-edge method). The intensity on this image is roughly proportional to the horizontal or vertical thermal gradient, depending on the orientation of the knife edge. By setting a photodiode on a suitable location of the image, one obtains a photocurrent roughly proportional to the thermal gradient (see figure 11). From the time dependence of this photocurrent, one gets relevant informations about the dynamical regime of the convection such as Fourier spectra, a powerful method of data analysis of any dynamical regime.

#### IV.2. Reconstruction of the phase space

Contrary to the case of theoretical dynamical systems for which we know the variables, we do not know the variables in a convection experiment (as in any real system). Most often one measures the variation of only one (or two) property, related in a simple or complicated way to one or several of the independent variables of the system. In such conditions how it is possible to have access to the attractors of the system i.e. how it is possible to reconstruct a relevant phase space?

In the case of a periodic regime, if  $X(t)$  is the periodic signal from the photodiode, one can obviously construct the limit cycle - the attractor of this regime - just by plotting  $\frac{dX(t)}{dt}$  as a function of  $X(t)$  (i.e. the analog of plotting the velocity  $\frac{dX}{dt}$  as a function of the position  $X$  in the case of a pendulum). Equivalently, one can consider that two variables of the system in a periodic regime are  $X(t)$  and  $X(t+\tau)$ ,  $\tau$  being a suitable delay. F. Takens has shown that this last procedure can be generalized to phase spaces of higher dimension. Starting from observations of only the signal  $X(t)$ , it should be possible to reconstruct the topology of the attractor, by taking as the phase space  $X(t)$ ,  $X(t+\tau)$ ,  $X(t+2\tau)$ , ... In other words, we can consider the signal  $X(t)$  to be independent of the same signal at a later time  $X(t+\tau)$  where  $\tau$  is an arbitrary constant called the delay. This does not mean that the attractor obtained in the new space is identical to that in the original phase space, but merely that the new representation of the attractor retains the same topological properties, which may suffice for studying its essential characteristics.

#### IV.3. Measuring of the dimension of the attractors

Let us recall that a limit cycle being a curve has a dimension 1, a torus  $T^2$ , a surface, has a dimension 2; on the other hand, strange attractors are fractals with a non integer dimension.

Without entering into the details, let us describe a practical method which allows a measurement of a fractal dimension (called "correlation dimension") of a set of points [9].

First, to illustrate simply this method, let us define a simple fractal set the Cantor set (Remember that we have met this kind of set in the transverse structure of a strange attractor). This set is obtained by an iterative process from the unit segment. First, the central third of this segment is removed. Then, the central third of each of the two remaining segments is removed. The operation is repeated indefinitely, as illustrated in Figure 12a. In this way we obtain an infinite set of disconnected points whose dimension is, then, between 0 and 1 (a single point has a dimension zero and a segment has a dimension 1). One can calculate easily the fractal (Hausdorff) dimension:  $D = 0.63...$

Returning to the correlation dimension, let us illustrate this approach with examples from plane geometry. Consider a set of points on the plane and let  $N(r)$  be the number of points of the set located inside a circle of radius  $r$ . The correlation dimension  $\nu$  is determined from the variation of  $N(r)$  with  $r$ . For a discrete set of points uniformly distributed on a curve (dimension one), we have, for  $r$  sufficiently small:

$$N(r) \sim r$$

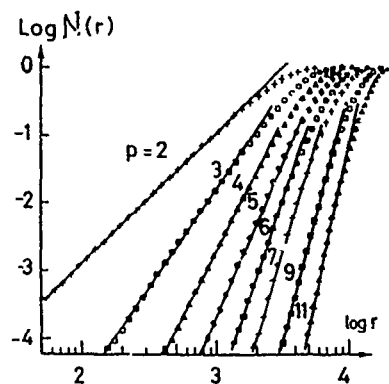


Fig. 13 - Log-log plot of  $N(r)$  for white noise. Note that the slope (which measures the exponent  $\nu$ ) continues to grow as the dimension  $p$  of the representation space is increased.

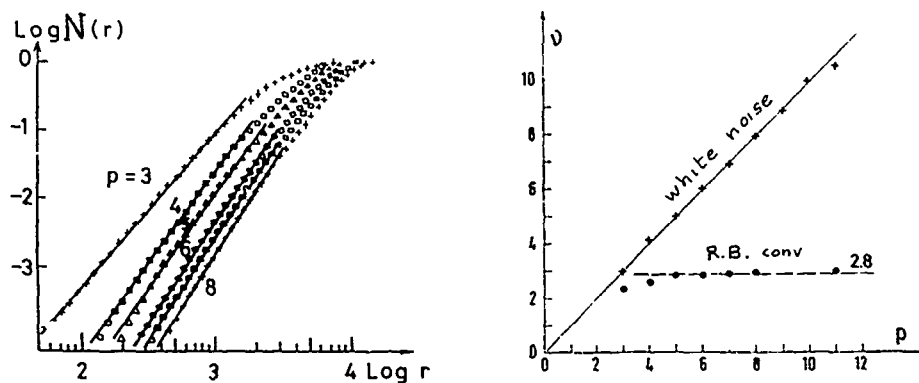


Fig. 14 - Measurement of the dimension  $\nu$  in the case of a deterministic turbulence in R.B. convection

a) characteristics  $\log N(r)$ ,  $\log r$   
 b) variation of the exponent  $\nu$  as a function of the dimension  $p$ . We deduce  $\nu$  from the slopes of the characteristics presented in Figures 13 and 14a. For white noise,  $\nu$  increases linearly with  $p$ . In contrast we see a distinct saturation of  $\nu$  when the data is taken from turbulent R.B. convection.

that is,  $N(r) \sim r^\nu$  with  $\nu = 1$  (see figure 12b). If, on the other hand, the points are uniformly distributed on a surface (dimension two; see figure 12c):

$$N(r) \sim r^2, \quad \nu = 2.$$

We can now consider general objects of arbitrary dimension, such as the Cantor set described above (see figure 12d). The number of points  $N(r)$  located inside a circle will grow, on the average, more slowly than the radius  $r$ . Setting  $N(r) \sim r^\nu$ , it can be calculated that  $\nu \approx 0.63$ , which is equal the Hausdorff dimension mentioned previously.

The method is generalized to  $p$ -dimensional spaces by defining  $N(r)$  to be the number of points contained in a  $p$ -dimensional hypersphere of radius  $r$ . From this method one can calculate the dimension on an attractor. Starting from a time series  $X(t)$ , through the method of time delays we can reconstruct a trajectory in a  $p$ -dimensional phase space by taking as coordinates  $X(t)$ ,  $X(t+\tau)$ ,  $X(t+2\tau)$ ... $X(t+(p-1)\tau)$  where  $\tau$  is an appropriate delay time. In practice the time  $t$  is discretized, so that we obtain a series of  $p$ -dimensional vectors representing the phase portrait of the dynamical system. Then, the method described above is applied counting up the points in hyperspheres centered on many (eventually on every) points of the attractor. If a law such as  $N(r) \sim r^\nu$  do exist, then  $\nu$  is the dimension of the attractor.

Starting from the discrete values  $X(t_i)$  obtained experimentally, we reconstruct the trajectory in a  $p$ -dimensional space, as described above, for increasing integer values of  $p$ :

$$p = 2, 3, 4, 5, \dots$$

For each value of  $p$ , we calculate  $N(r)$  and determine the slope of the function  $f$  defined by  $\log N(r) = f(\log r)$ , arriving at an exponent  $\nu$ . For a periodic regime, whose phase portrait is a limit cycle, the dependence of  $N(r)$  on  $r$  is strictly linear (up to size effects). Contrast this with the case of white noise. The signal can be considered to be a superposition of an infinite number of independent oscillatory modes (or system with a very large number of degrees of freedom). Such a regime can therefore be described by an attractor  $T^n$ , with  $n$  very large. The trajectories will densely cover any phase space of dimension:

$$p \leq n.$$

Indeed, Figure 13 shows that the characteristic functions  $N(r)$  obtained from a white noise have slopes on a log-log plot which continue to increase with  $p$ : we find  $\nu \sim p$ . This result can be extended: as long as the calculated value of  $\nu$  is equal to  $p$  (or continues to grow with  $p$ ), we know that the dimension of the space used for the calculation is smaller than (or comparable to) that of the corresponding attractor. If, on the other hand, the dimension  $\nu$  calculated for a chaotic regime becomes independent of  $p$ , then the chaos is deterministic and the corresponding attractor strange.

As an illustration, one can consider the results obtained from an experimental time series corresponding to a chaotic regime in Rayleigh-Benard convection in confined geometry [10]. Figure 14a shows that the slopes of the functions  $N(r)$  on a log-log plot are reasonably well-defined and independent of the dimension  $p$  of the phase space as soon as  $p$  exceeds 3. The saturation of  $\nu$  as  $p$  is increased is better illustrated by Figure 14b, and contrasted with the linear dependence of  $\nu$  on  $p$  for white noise (or random signal). This type of data analysis demonstrates the deterministic nature of the chaotic behavior in this regime and, in addition, determines a lower bound on the number of degrees of freedom excited [11]. For many other illustrations about experimental strange attractors obtained in the same experiment and their fractal dimension, see the Lecture of M. Dubois. See also the lecture of S. Ciliberto.

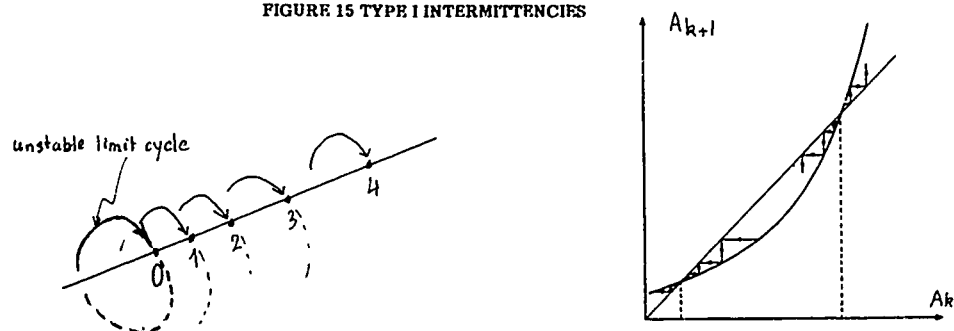
#### IV.4. Type I intermittencies

We have seen in section III.4 that type I intermittencies correspond to a destabilization of a limit cycle when the unit circle is traversed at +1. In the simplest case, we can illustrate his destabilization in the Poincaré plane (see figure 15a). If the limit cycle is represented by its Poincaré section 0, a small departure from this cycle will be multiplied, at each period, by a real number slightly larger than 1, and the successive intersections will be 1, 2, 3 etc...

As mentioned previously, many dynamical systems can be described by the

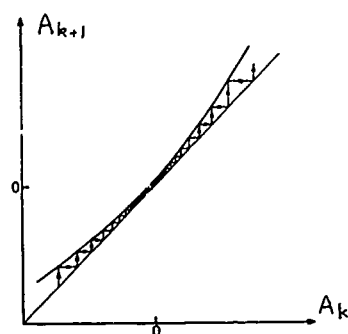


FIGURE 15 TYPE I INTERMITTENCIES

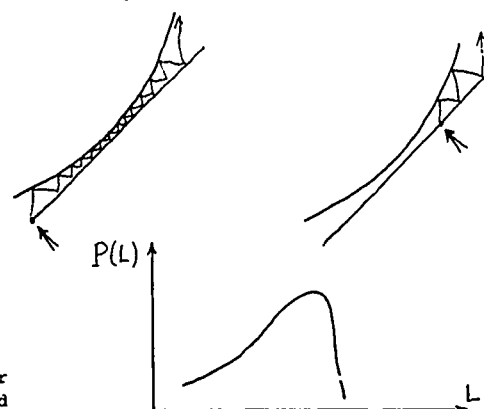


15a) successive intersections in the Poincaré plane; 0 corresponds to the (unstable) limit cycle.

15b) Mapping  $A_{k+1} = A_k + \epsilon + a A_k^2$  for  $\epsilon < 0$ . There exists one stable fixed point and one unstable fixed point.



15c) Mapping  $A_{k+1} = A_k + \epsilon + a A_k^2$  for  $\epsilon > 0$ . The fixed points have disappeared and a channel is now open. After the crossing of the channel, the point wanders in the phase space and is reinjected somewhere in the channel.



15d) long and short laminar phase with a scheme of the distribution of the lengths of laminar phases.

$$Ra = 270 Ra_c$$



$$Ra = 300 Ra_c$$



t

15e) Behavior of the velocity near the threshold of type I intermittency in R.B. convection.

(a) Periodic regime for  $Ra < Ra_c$ , where  $Ra_c = 295 Ra_c$  is the threshold for onset of intermittency.

(b) Intermittent regime for  $Ra > Ra_c$ . Notice the long sequences (of unequal length) of barely perturbed oscillations (passage through the channel) interrupted by sudden brief events.

iteration, of a one-dimensional mapping.

The simplest iteration describing type I intermittencies is

$$A_{k+1} = A_k + \epsilon + a A_k^2$$

where  $\epsilon$  is the control parameter measuring the departure from the threshold of intermittencies. As one can see on figure 15b, for  $\epsilon < 0$  there exist two fixed points\*, one stable, the other one unstable. For  $\epsilon = 0$  they merge into one another: as seen previously, this corresponds to a saddle-node bifurcation. Both fixed points disappear for  $\epsilon > 0$ . One can notice that for  $\epsilon$  positive but small, a narrow channel is open between the parabola and the bissector. Under that condition, the representative point travels through the channel very slowly: this corresponds to a dynamics which slowly evolves. In particular, the representative point spends a long time in the vicinity of the "ghost" of the fixed point. Translated in the full phase space, this means that the trajectory remains a certain time near the (disappeared) limit cycle. In other words, for a while the behavior is nearly periodic: one says that the system is in a laminar sequence. After that, the representative point escapes out of the mapping and wanders in the phase space: this corresponds to a "burst" of turbulence. Then, there is a reinjection somewhere in the channel and a new crossing begins. The reinjection being made at random, the iterations can start anywhere in the channel; then the duration of the laminar phase are distributed at random. The distribution of the length of the laminar phases can be calculated. One can see in figure 15d that the general shape of this distribution is qualitatively characterized by a value of the most represented  $T$ , not too far from the maximum duration. On the other hand,  $T$  is expected to vary like  $\sqrt{\epsilon}$  [12].

This kind of intermittencies has been observed in Rayleigh-Benard convection in confined geometry. The convective structure consisted of 2 rolls in the longer size ( $L_x = 2d$ ) and 1 roll in the other one ( $L_y = 1.2d$ ) (Prandtl number of the oil = 130) [13]. The dynamics of the regime was studied through velocity measurements (laser doppler velocimetry). At  $Ra = 250 Ra_c$ , the regime is monopерiodic; the thermal oscillator responsible for this regime is a thermal droplet. At  $Ra = 290 Ra_c$  a qualitatively different regime sets in: the oscillations are still present, but, from time to time, they are interrupted by a short burst (see figure 15e). As expected, near the threshold of intermittencies the length of the laminar sequences is long and the bursts are rare; they become more and more frequent when  $Ra$  is increased. The distribution of the duration of the laminar sequences was found in qualitative agreement with what theoretically expected.

#### IV.5. Type III intermittencies

We know from section III.4 that this kind of intermittencies is associated with the destabilization of a limit cycle when the unit circle is traversed at -1 through a subcritical (or inverse) bifurcation.

A departure from the limit cycle is thus multiplied at each period by a negative real number, the absolute value of which is slightly larger than one. In the Poincaré plane, this means that the representative point leaves the ancient fixed point 0, oscillating, on the axis, from positive to negative values: the system returns in (almost) the same state each two periods (see figure 16a). This is the phenomenon of "period doubling": basically, this kind of instability produces a subharmonic of increasing amplitude (in a subcritical bifurcation the non linear term does not saturates the exponential growth). This loss of stability of a limit cycle through the growing of the subharmonic mode is the basic mechanism of type III intermittencies [5].

\* Note that the term "fixed point" has to be understood in the context of a Poincaré section: in the full phase space it corresponds to a limit cycle.

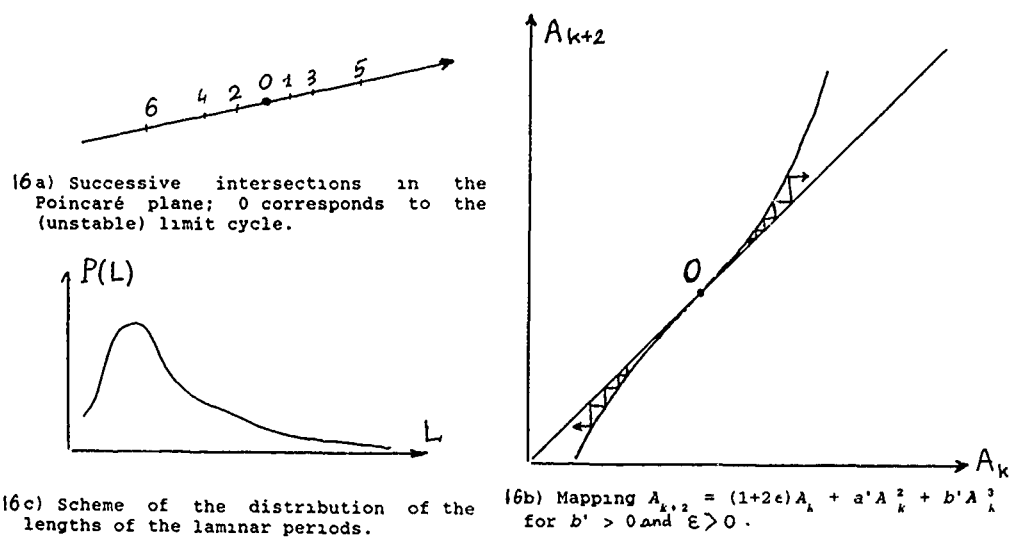


FIGURE 16; TYPE III INTERMITTENCIES

The mapping (or iterated map) which describes type III intermittencies is

$$A_{k+1} = -A_k(1+\epsilon) + a A_k^2 + b A_k^3 + \dots$$

It is natural, from what we have seen above to consider the second iterate  $A_{k+2}$  as a function of  $A_k$ .

Neglecting the higher order terms:

$$A_{k+2} = (1+2\epsilon) A_k + a' A_k^2 + b' A_k^3 + \dots$$

with  $b' = 2(a^2 + b)$  and  $a' \ll b'$ .  $b' < 0$  would correspond to a normal bifurcation, a case not considered in this section. On the contrary,  $b' > 0$  describes the subcritical case which gives rise to type III intermittencies. Let us consider in figure 16b, the graph of  $A_{k+2} = f(A_k)$ . For  $\epsilon > 0$ , the unique fixed point  $(0,0)$  is unstable (remember that it represents the unstable limit cycle). From the  $(0,0)$  point, the upper branch of this cubic curve corresponds to the growth of the subharmonic and the lower branch represents the correlative decrease of the fundamental. When the amplitude of the subharmonic attains a certain value, a burst appears shattering the signal's regularity. Immediately afterwards, regular behavior reappears due to a reinjection somewhere in the channel. As in the case of type I intermittencies, this reinjection is made anywhere in the channel with equal probability. Then, the amplitude for the subharmonic at the beginning of a new laminar sequence is at random. This initial amplitude determines the length of the laminar phase until the next turbulent burst. One can calculate the distribution of the lengths of the laminar phase. By contrast with the case of type I intermittencies, this distribution is characterized by a long tail towards long durations (figure 16c). This important difference can be understood from the graphs of the two kinds of intermittencies. In type I intermittencies a reinjection at the beginning of the channel corresponds to the maximum of the duration of the laminar phase. In type III intermittencies, the smaller the initial amplitude of the subharmonic, the longer the laminar phase lasts. Then, by opposition with the case of type I intermittencies, there is not a strict limit for the maximum of the length of a laminar phase: in principle, a reinjection exactly at the point  $(0,0)$  would produce a laminar period of infinite length.

Type III intermittencies have been observed in Rayleigh-Benard convection in the same experimental cell as for type I intermittencies. The differences consisted in the Prandtl number of the oil, (36 instead of 130) and the kind of convective structure (3 rolls instead of 2 rolls). Under that conditions the following regimes were observed:

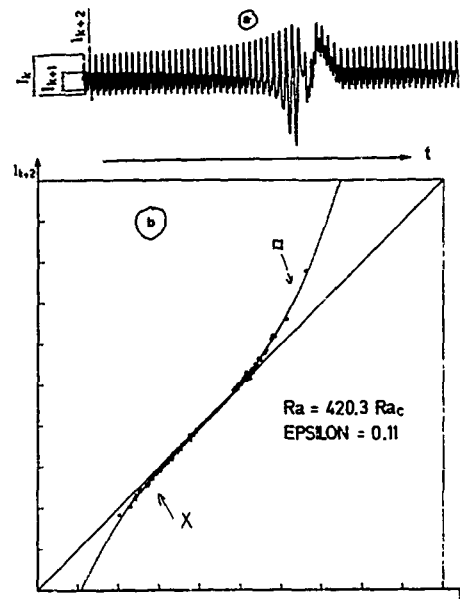
$$\begin{aligned} 333 < \frac{Ra}{Ra_c} < 377 & \quad \text{steady regime} \\ 377 < \frac{Ra}{Ra_c} < 416.7 & \quad \text{monoperiodic regime} \\ \frac{Ra}{Ra_c} > 416.7 & \quad \text{growing of} \end{aligned}$$

the subharmonic mode with appearance of bursts. This last behavior is well illustrated in figure 16d which represents the variation of semi local thermal gradients (detected through optical techniques). One can note the growing of the subharmonic, the decrease of the fundamental and, at a certain level of subharmonic, the appearance of a short burst, followed by a relaminarization etc... One can clearly check that, as expected, the smaller the initial amplitude of the subharmonic, the longer the laminar phase lasts.

Figure 16e shows in more details how one can construct, from experimental data, a return map - here, a second return map  $I_{k+2} = f(I_k)$  - in order to compare with the mapping described above; one can remark a very good agreement between theory and experiment.

Finally, figure 16f shows a distribution of the lengths of the laminar phases; as expected, there is a broad distribution of times with a pronounced tail towards long durations.

FIGURE 16: TYPE III INTERMITTENCIES (CONTINUED)

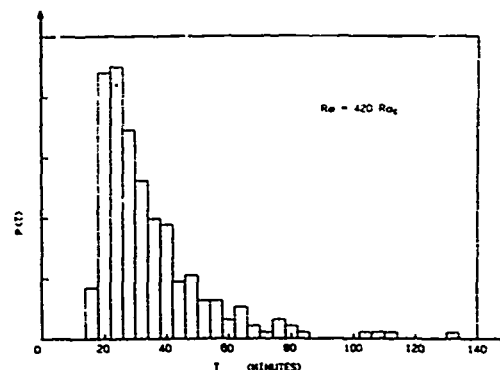


16e) a) Sample of a time signal from the same regime as Figure 16d. Expanding the time scale provides a better illustration of the growth of the subharmonic and the correlated decay of the fundamental. To the left are defined the quantities  $I_k$  used in graphing the second return map.

b) Graph of the second return map  $I_{k+2} = f(I_k)$ . Two different symbols are used to construct this graph from the experimental results: one of them (o) corresponds to the subharmonic (increasing amplitudes) and the other (x) to the fundamental (decreasing amplitudes). The continuous curve is the graph of the function:

$$f(I) = (1 + 2\epsilon)I + aI^2 + bI^3$$

( $a$  and  $b$  constants with  $a \ll b$ ) predicted by theory to be the functional form of the second return map near the intermittency threshold. We note the excellent agreement with experimental results obtained by adjusting the value of the parameter  $\epsilon$  ( $\epsilon = 0.11$ ).



16f) Histogram of the lengths of laminar phases. The lengths observed vary from eighteen minutes to more than two hours. The most significant feature is the long tail for  $T$  large, characteristic of type III intermittency.

## IV.6. The subharmonic cascade [15][16][17]

We have studied in section II.3 the iteration of a quadratic mapping of the interval  $f(X)$

$$X_{k+1} = 4\mu X_k (1 - X_k)$$

For  $\mu = 0.7$ , we pointed out the existence of a stable fixed point at  $X^*$  (see fig.5). (Remember, once again, that a stable fixed point in a mapping corresponds to a stable limit cycle in the real phase space). However, this situation for which we find a single stable fixed point is far to be the unique possibility. Indeed, the results depend on the value of  $\mu$  which plays the role of a control parameter. For example, let us consider the situation corresponding to  $\mu = 0.8$ , see fig.17.

Now the fixed point  $X^*$  is unstable, for the slope of the tangent at this point is greater than one in absolute value. The graphical construction shows that the mapping has two special points  $X_1^*$  and  $X_2^*$  such that:

$$X_2^* = f(X_1^*) \quad \text{and} \quad X_1^* = f(X_2^*)$$

In other words, the iteration alternates between one point and the other; starting from one of these points, we must iterate twice to return to it. The two points constitute an attractor of period two, also called a 2-cycle. Given that:

$$X_2^* = f(X_1^*) = f(f(X_2^*))$$

$$X_1^* = f(X_2^*) = f(f(X_1^*))$$

these two points - which are not fixed points of  $f$  - are fixed points of the function:

$$g(X) = f(f(X)) = f^2(X)$$

as can be verified on Figure 18. More detailed study shows that we pass continuously from the situation of a stable fixed point to that of an attractor of period two by increasing the value of  $\mu$ . Transition occurs at the threshold value  $\mu_1 = 0.75$ . At this value, the stable fixed point of  $f$  becomes unstable, and, correspondingly, there appear two stable fixed points of  $f^2$ . An attractor of period two takes the place of the attractor of period one: the period has doubled. This is exactly the situation expected when the unit circle is traversed at  $-1$  and when the associated bifurcation is normal. Let us return to the iteration of section IV.5

$$A_{k+2} = (1+2\epsilon) A_k + a' A_k^2 + b' A_k^3$$

but, now, with  $b' < 0$  (normal bifurcation). One can see in figure 19 the graph of this iteration for  $\epsilon > 0$ . Clearly, the point 0 is unstable and there are two stable fixed points corresponding to the attractor of period two.

Let us now return to the quadratic map. What happens when we continue to increase  $\mu$ ? The graphs of  $f$  and  $f^2$  gradually change, in such a way that the fixed points of  $f^2$  also end up losing their stability. Another simple graphical construction, helps to foretell and to explain the sequence of events. Consider the square around the fixed point  $X_2^*$  in Figure 18. Inside the square, we observe a locally parabolic curve containing a stable fixed point - i.e. a situation just like that of Figure 5. Therefore when the fixed point becomes unstable by deformation of the curve, we can expect the same phenomenon as before: the fixed point of  $g$  will be replaced by two points which will be the fixed points of the function:

$$h(X) = g(g(X)) = f^4(X).$$

This conclusion applies equally to the fixed points  $X_1^*$  and  $X_2^*$ : both become unstable for a value  $\mu_2 = 0.862...$

For  $\mu > \mu_2$   $g$  has no more stable fixed point but,  $h$ , has now four fixed points. Starting from any one of these points, four iterations are required to return to it: we now have a 4-cycle. Again, the period has doubled via a subharmonic bifurcation.

By continuing to increase  $\mu$ , the same phenomenon will be repeated *ad infinitum*. We will see a cascade of bifurcation, each accompanied by the period doubling associated

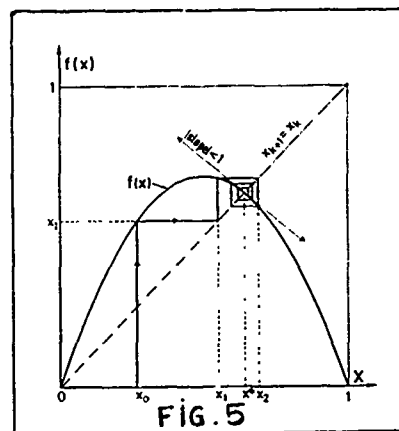


FIG. 5

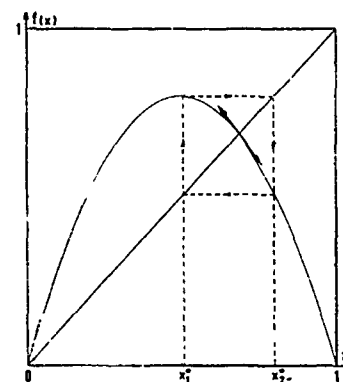


Fig. 17 - Graph of  $f(x) = 4\mu x(1-x)$  for  $\mu = 0.8$ . Both fixed points of  $f$  are unstable at this value of  $\mu$ . Any initial condition in  $]0, 1[$  has as its asymptotic limit the pair of points  $x_1^*$  and  $x_2^*$  visited in turn.

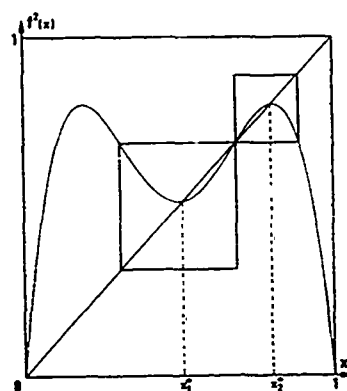


Fig. 18 - Graph of the mapping  $g(x) = f(f(x))$  for  $\mu = 0.8$ . This mapping has four fixed points, of which two,  $x_1^*$  and  $x_2^*$ , are stable.  $f$  maps each one onto the other. The two squares drawn around the fixed points serve to emphasize the structural similarity with the graph of  $f(x)$  in Figure 5.

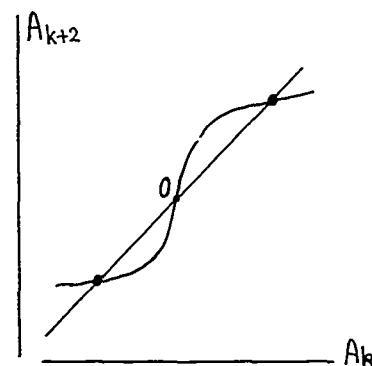


Fig. 19 - Mapping  $A_{k+2} = (1+2\epsilon)A_k + a'A_k^2 + b'A_k^3$  for  $b' < 0$ .

with a subharmonic instability. As  $\mu$  is increased we observe a succession of attractors of period  $2^l$ , or  $2^l$ -cycles,  $l$  an integer varying between 0 (for  $\mu \leq 0.75$ ) up till infinity. The values of  $\mu$  at which the bifurcation in the cascade occur have a remarkable property: they form an increasing series converging rapidly towards an accumulation point  $\mu_\infty$ , whose value can only be obtained numerically:

$$\mu_\infty = 0.892486418...$$

The following table gives the values of  $\mu$  corresponding to the first few bifurcations of the subharmonic cascade.

Periodicity of the attractor	$\mu$ value at the bifurcation point
$1.2^0 = 1$	
$1.2^1 = 2$	$\mu_1 = 0.75$
$1.2^2 = 4$	$\mu_2 = 0.86237...$
$1.2^3 = 8$	$\mu_3 = 0.88602...$
$1.2^4 = 16$	$\mu_4 = 0.89218...$
.....	.....
$1.2^\infty = \infty$	$\mu_\infty = 0.892486418...$

Examination of the values of  $\mu$  collected above reveals that the convergence towards the accumulation point obeys a simple and rigorous law: the difference between values of  $\mu$  associated with two consecutive bifurcations is reduced each time by an almost constant factor:

$$\lim_{i \rightarrow \infty} \frac{\mu_i - \mu_{i-1}}{\mu_{i+1} - \mu_i} = \delta.$$

An essential result, which cannot be overemphasized, is that the scale reduction factor  $\delta$  is a universal constant, independent of the details of the function  $f$  considered:

$$\delta = 4.6692016091029909...$$

More precisely, in iterating any mapping which has a *quadratic extremum* we always find the same period-doubling cascade, with the same scaling laws as above. The theory is indeed extremely general, which justifies in retrospect the attention we have devoted to this particular function  $f$ . What is remarkable is that quantitative predictions can be made provided that a simple qualitative condition is satisfied.

A graph of the  $\mathcal{X}$  values of the points on each attractor, as a function of  $\mu$ , aids in visualizing the subharmonic cascade just described (see Figure 20). The first bifurcations, each doubling the number of points of the attractor, appear very clearly. But the bifurcations rapidly become so close to one another that they can no longer be distinguished if  $\mu$  is represented on a linear scale. On Figure 20, the attractor of period eight is the last that can be discerned without difficulty. What happens beyond the accumulation point?

Numerical simulations show that traversal of the value  $\mu_\infty$  marks the beginning of a very complex domain. On the graph of Figure 20 different zones appear, some lighter and others more shaded. Detailed analysis reveals that in this region, periodic attractors alternate with chaos.

In the latter case, iteration of  $f$  yields a sequence of values of  $\mathcal{X}$  that:

- never repeat themselves
- depend on the initial condition  $\mathcal{X}_0$ .

In particular, two arbitrarily close initial conditions give to two sequences of iterates - or trajectories - that always eventually diverge from one another (S.I.C.). Take in mind that  $\mu_\infty$  is the threshold for chaos in the period doubling scenario.



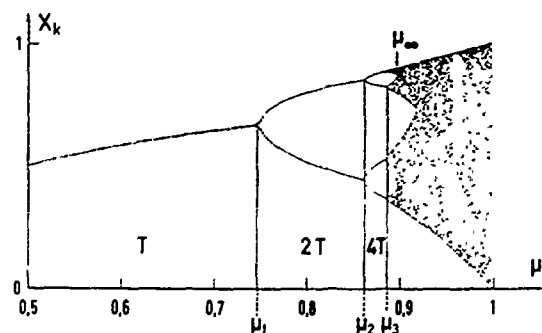


Fig. 20 - Asymptotic iterates of the mapping  $f(x)$  for  $\mu \in [0.5, 1]$ . As a function of the parameter  $\mu$ , we have plotted the value or values of  $x_k$  obtained by iteration of  $f(x)$  as  $k$  tends to infinity. From left to right we see:

- a sequence of periodic attractors, separated by subharmonic bifurcations each of which doubles the number of points on the attractor, as well as its period.
- beyond  $\mu_{\infty}$ , a region where aperiodic and periodic attractors alternate.

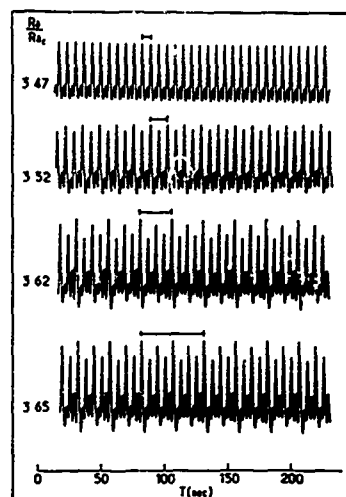


Fig. 21 - Cascade of period doubling in R.B. convection in mercury. The changing shape of the signal (temperature of the fluid at one point as a function of time) clearly shows the period-doubling process that takes place as the control parameter  $Ra/Ra_c$  is increased. The line segments indicate the length of one period, defined by a basic pattern which is repeated indefinitely.  
From A. Libchaber, S. Fauve, C. Laroche.

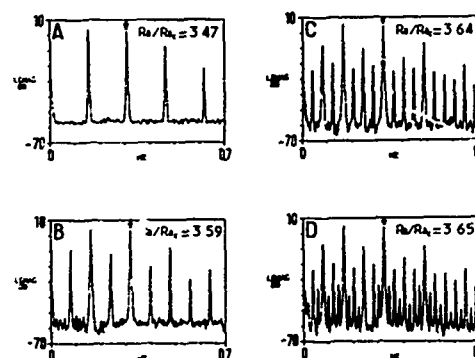


Fig. 22 - Fourier spectra corresponding to data of figure 21. Starting from  $f_1/2$  (in A) we see appear the subharmonics  $f_1/4$  (in B),  $f_1/8$  (in C) and  $f_1/16$  (in D), as well as their odd harmonics.  
From A. Libchaber, S. Fauve, C. Laroche.

The route to turbulence via subharmonic cascade (or cascade of period doubling) has been very well illustrated in Rayleigh-Benard convection. The most precise experiments have been done with liquid mercury stabilized against some parasitic instabilities with a magnetic field [18][19]. Needless to say that the experimental techniques are completely different from that described previously.

Larger aspect ratios than for the case of oil are used ( $L_x = 4d$  or  $6d$ ) and two purposes are served in placing a magnetic field. First, given the high electrical conductivity of mercury, the convection rolls have a strong tendency to align themselves in the direction parallel to the magnetic field. This fixes the spatial order and prevents the creation of defects as  $Ra$  is increased. In addition, the magnetic field damps certain modes causing oscillation of the rolls; it intensifies dissipation, which favours dynamical behaviors understandable in terms of one dimensional mappings.

The mercury is placed between two thick copper plates. The convective motions are measured using bolometers, since optical methods cannot be used in an opaque medium. In a first phase of the experiment, one fixes the magnetic field strength at zero and increase the temperature difference until the onset of convection at a value  $Ra_c$  of the Rayleigh number. Continuing to increase  $Ra$ , one notices at a value close to  $2Ra_c$ , the onset of a new instability. The signal recorded by the bolometer begins to oscillate in time with a frequency  $f_1$ . This oscillary instability can be attributed to a wave propagating along the roll axes. As  $Ra$  is further increased, the periodic regime in turn becomes unstable, and there appears in the power spectrum of the signal a second frequency  $f_2$  close to, but nonetheless distinct from  $f_1/2$ . For a slightly larger value of  $Ra$ , the frequencies of the two oscillators lock when the condition of subharmonic resonance  $f_2 = f_1/2$  is satisfied.

This frequency locking marks the beginning of the second phase of the experiment. A constant and uniform magnetic field is applied, whose intensity is such that the amplitudes of the two oscillators become comparable. By gradually increasing the Rayleigh number, one notices a succession of well-defined values of  $Ra$  at which one periodic regime bifurcates to another of twice the period. Figure 21 shows recordings from several consecutive periodic regimes. The emergence in the Fourier spectrum of the subharmonics  $f_1/4$ , then  $f_1/8$ ,  $f_1/16$ , the signature of period doubling (see fig.22). From these results, we can attempt to evaluate the convergence ratio of the successive bifurcations. We find a value of 4.4, extremely close to the universal asymptotic limit 4.669... predicted by theory. Chaos (or turbulence) appears for  $Ra$  number immediately above that corresponding to the emergence of  $f_1/16$ .

This Rayleigh-Benard convection experiment confirms the existence of the route to turbulence via the subharmonic cascade. Let us also mention that thermoconvection in other fluids (liquid helium, water, oil) also gives rise to a period-doubling cascade, as well as other dynamical systems [20].

#### IV.7. The quasiperiodicity

The route to chaos via quasiperiodicity is developed in many details in the lectures given by M.Dubois. Let us just describe in a few words the loss of stability of the limit cycle giving rise to quasiperiodicity by comparison with what happens in the case of intermittencies or period doubling cascade. In these last two cases, the unit circle is traversed either at  $+1$  or at  $-1$ . This means that the eigenvalues whose modulus becomes larger than 1 is real in both cases. Then, in the Poincaré plane, (see figure 23), the successive vectors representing the increasing departure from the point 0 - section of the limit cycle - are on a straight line. On the contrary, when the unit circle is traversed at two complex conjugate value ( $\alpha \pm i\beta$ ) the eigenvalue whose modulus becomes larger than 1 is complex. Then, the successive vectors are amplified and rotate in the Poincaré plane. If this loss of stability is associated with a normal bifurcation, the non linear terms saturate the growth of the modulus and, after a short transient the points of the Poincaré section rotate on a circle (see figure 23). That is to say, the corresponding attractor is now a Torus  $T^2$  whose Poincaré section is a circle (see figure 4). Returning to the dynamics itself, the periodic regime has been replaced by a quasiperiodic regime. The corresponding transition is called a Hopf bifurcation. Different kind of instabilities may then occur giving rise to chaos via what is called, generically, "the route (or scenario) to chaos via quasiperiodicity".

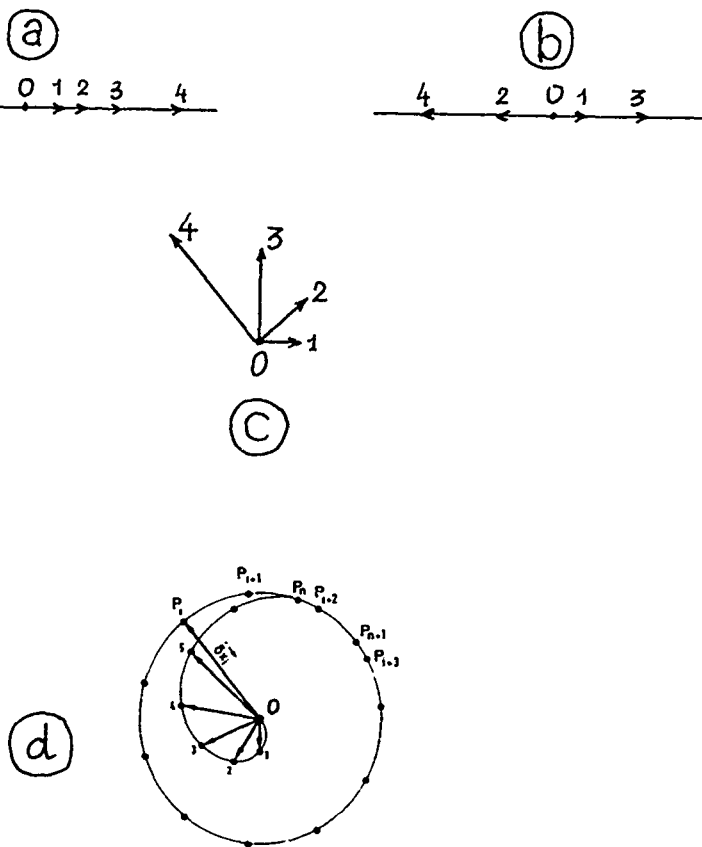


**Fig.23** - Successive intersections in the Poincaré plane when the unit circle is traversed:

- a) at  $+1$   
b) at  $-1$   
c) at  $\alpha \pm i\beta$   
d) Hopf bifurcation; the point 0 is the Poincaré section of the (unstable) limit cycle and the points  $P_i$  belong to the Poincaré section of the Torus  $T^2$ .

Acknowledgements

I wish to thank more particularly M.Dubois for constant collaboration in the experimental work described above, V.Croquette, M.Labouise, P.Le Gal, B.Ozenda, C.Poitou, A.Pocheau for discussions and helpful assistance and D.Bunel for a patient and careful typing of the manuscript.

## REFERENCES

- [1] P.Bergé, M.Dubois, Contemp.Phys. 25, 535 (1984);  
M.Dubois, P.Bergé, J.Fluid Mechanics, 85, 641 (1978).
- [2] P.Bergé, "Chaos and Order in Nature", Elmau 1981, ed. by H.Haken,  
(Springer-Verlag) p.14.
- [3] A.Pocheau, Thèse d'Etat Paris VIII, mars 1987.
- [4] M.Dubois, P.Bergé, Phys.Lett. 76A, 53 (1980).  
M.Dubois, P.Bergé, J.de Physique 42, 167 (1981).
- [5] P.Bergé, Y.Pomeau, Ch.Vidal, L'ordre dans le Chaos, Hermann (1984).  
English translation; Order within Chaos, Wiley-Hermann (1986).
- [6] M.Dubois, P.Bergé, P.Atten, La Recherche, p.190, Février 1987.
- [7] J.P.Eckmann, Rev.Mod.Phys. 53, 643 (1981).  
E.Ott, Rev.Mod.Phys. 53, 655 (1981).
- [8] P.Bergé, M.Dubois, in "Scattering techniques applied to supramolecular and  
nonequilibrium systems", edited by S.H.Chen, B.Chu, R.Nossal, Plenum Publishing  
Corporation, p.493 (1981).
- [9] P.Grassberger, I.Procaccia, Phys.Rev.Lett. 50, 346 (1983).  
P.Grassberger, I.Procaccia, Physica 9D, 189 (1983).
- [10] B.Malraison, P.Atten, P.Bergé, M.Dubois, C.R.Acad. Sci. Paris, C297, 209 (1983).
- [11] P.Atten, J.G.Caputo, B.Malraison, Y.Gagne, J.de Mécanique, vol.special 1984,  
"Bifurcations et comportements chaotiques".
- [12] Y.Pomeau, P.Manneville, Comm.Math.Phys. 74, 189 (1980)
- [13] P.Bergé, M.Dubois, P.Manneville, Y.Pomeau, J.de Phys.Lettres 41, L341 (1980).
- [14] M.Dubois, M.A.Rubio, P.Bergé, Phys.Rev.Lett. 51, 1446 (1983).
- [15] M.J.Feigenbaum, J.Stat.Phys. 19, 25 (1979).
- [16] C.Tresser, P.Coullet, C.R.Acad.Sci.Paris A287, 577 (1978).
- [17] P.Collet, J.P.Eckmann, "Iterated maps on the interval as dynamical systems",  
Birkhäuser, Boston (1980).
- [18] A.Libchaber, C.Laroche and S.Fauve, J.Phys.Lettres 43, L211 (1982).
- [19] A.Libchaber, S.Fauve and C.Laroche, Physica 7D, 73 (1983).
- [20] V.Croquette, C.Poitou, C.R.Acad.Sci.Paris C292, 1353 (1981).

# Transition to turbulence via spatio-temporal intermittency

Paul Manneville

Service de Physique du Solide et de Résonance Magnétique  
CEA Saclay  
91191 Gif sur Yvette Cedex, France

## 1 General setting

As discussed in the lectures given by P. Bergé and M. Dubois, our understanding of the process of transition to turbulence has made a great advance thanks to the irruption of deep mathematical concepts from dissipative dynamical systems theory.

However it should be stressed immediately that, while this approach is fully adapted to confined systems where the spatial structure remains frozen, the situation of weakly confined systems is much less settled. Indeed, in continuous media where instabilities can develop, the number of interacting modes is linked first of all to the physical processes involved but, more importantly, to confinement effects measured by *aspect ratios*. In confined systems (small aspect ratio limit), eigenmodes associated with instability mechanisms have markedly different critical values and spatial structures; one can easily restrict the number of effective excited modes to a small value. On the other hand when the geometry allows a large number of equivalent configurations (large aspect ratio limit), except in a vanishingly small vicinity of the threshold, one cannot avoid that chaos then gains an irreducible spatial component linked to the specific position/orientation degeneracy. In this lecture, we shall be interested mainly in some original features of the transition to turbulence at the limit of very large aspect ratios.

A conceptually simple way to increase the number of degrees of freedom consists in coupling identical dynamical systems and giving a spatial meaning to this coupling. This can be done for example by assuming interactions between systems sitting at near-neighboring nodes of a regular lattice. The simplest possible such coupled systems seem to be the so called *cellular automata* which are discrete-time discrete-space systems with a finite number of accessible states per site. In spite of their apparent simplicity they can display a particularly rich manifold of behaviors, some simple, others quite complicated (see [23]). A step beyond the discrete local phase space of cellular automata is performed in allowing a continuous local phase space. This leads to the level of *coupled map lattices*; a typical governing equation reads:

$$X_i^{t+1} = F(X_i^t) + D (X_{i+1}^t - 2X_i^t + X_{i-1}^t)$$

where the  $X_i$ 's are the local degrees of freedom,  $i$  being the (discrete) space variable,  $t$  the (discrete) time,  $F(X)$  the local evolution law, and  $D$  the coupling constant. The interaction is chosen so as to look like a discrete approximation to the Laplacian characteristic of a diffusive process.

In principle, there is no difficulty (except practical) to pass from discrete time to continuous time by performing a *suspension* of a given  $n$ -dimensional invertible map to get a flow in a  $(n+1)$ -dimensional phase space, i.e. the reverse of a Poincaré section. In order to go from coupled lattice maps to partial differential equations which are the actual concern of turbulence theory we have thus to perform nested suspensions, the first one to recover continuous time, and the second one for continuous space. Needless to say that the theoretical status of this procedure is yet unclear, especially because the reverse of the *reduction to a center manifold* [7] or more generally to some *inertial manifold* (for an introduction with references to recent work, see [16]) leads not to a discretized physical space but to an abstract low dimensional phase space.

Avoiding a thorough discussion of this delicate topic, we shall assume that the information gained in the study of coupled map lattices will be meaningful also for flows in enclosures (i.e. not necessarily for *open flows* also of great interest) with spatial modulations playing the major role in the process of transition to turbulence (this will be justified by hand-waving arguments later).

The conventional approach to the problem of modulated structures involves so called *envelope equations* accounting for long wavelength, slow modulations of cellular structures either steady or propagating. These envelope equations themselves can be viewed as belonging to the more general class of *reaction-diffusion* systems of the form:

$$\partial_t X = G(X) + D \nabla^2 X$$

where the second term on the right hand side accounts for the diffusion of chemical species reacting according to some scheme  $G$ . In turn reaction-diffusion equations are a special case of even more general hydrodynamic equations for reacting fluid systems, which close the circle sketched in fig. 1.

Let us come back to the evaluation of the number of degrees of freedom. Confinement effects are illustrated in fig.2 in the standard case of a convection-like instability. The marginal stability

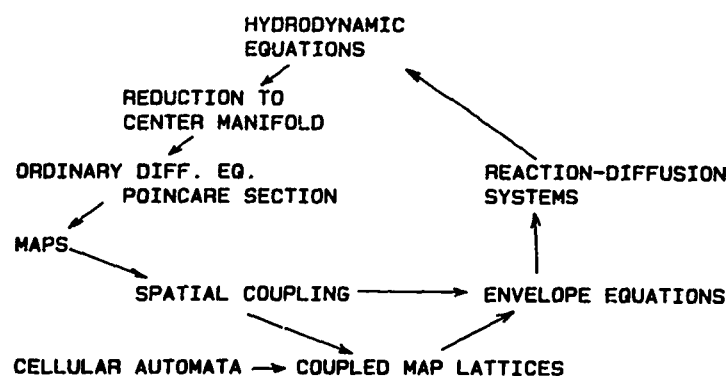


Figure 1: From hydrodynamic equations to hydrodynamic equations: reduction to center manifold dynamics, Poincaré sections and maps, coupled map lattices, and envelope equations.

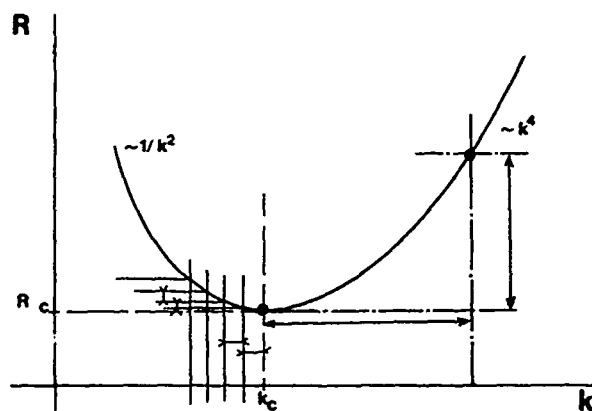


Figure 2: Effects of confinement on eigen-modes of a convection-like instability; on the left of the minimum: large aspect ratio limit; on the right: small aspect ratio limit.

curve then looks parabolic in the vicinity of its minimum  $(k_c, R_c)$ :

$$\frac{R - R_c}{R_c} = \epsilon = \xi_0^2 (|k| - k_c)^2$$

where  $\xi_0$  is the (naked) coherence length of the structure (it may be convenient to choose a length unit such that  $k_c = 1$ ). Using periodic boundary conditions at a distance  $L$  in one space dimension leads to possible wavevectors which are integer multiple of  $2\pi/L$ . When  $L$  increases, the distance between neighboring allowed wavevectors gets smaller as  $1/L$ , the reciprocal of the aspect ratio. At the same time, the number of easily excited modes in the vicinity of the threshold scales as  $\Delta n = (L/2\pi)\sqrt{\epsilon}$ . At threshold the coherence of the unstable mode is complete; slightly above the threshold, modulations are allowed since more modes can participate. The width of the wavepacket varies as  $\sqrt{\epsilon}$ , the corresponding coherence length being  $\xi_0/\sqrt{\epsilon}$ . Further from the threshold, the coherence is restricted to a length of the order of  $\xi_0$ , which makes the nucleation of structural defects much easier; a large manifold of imperfect structures or *textures* can then survive in a metastable way.

Usually, the study of the transition to turbulence involves the control of an applied stress, here measured by  $\epsilon$ , while keeping the aspect ratio constant (and small). In order to understand the specific role of confinement in experiments at large aspect ratio, it may be useful to consider a situation where stress variations are irrelevant while the aspect ratio is the actual control parameter. Let us have a look at the bifurcation diagram —fig.3— of the Kuramoto-Sivashinsky equation:

$$\partial_t \theta + \partial_{xx} \theta + \partial_{xxxx} \theta + \frac{1}{2} (\partial_x \theta)^2 = 0$$

with periodic boundary conditions for  $L$  small to moderate [8]. Stable steady cellular structures (corresponding to rolls in a convection experiment) with an increasing number of cells are observed in narrow  $L$ -windows. The transition between solutions with different numbers of cells can be quite complicated with very long turbulent transients displaying weakly unstable anomalous cellular structures with defects, etc. up to the large  $L$  limit where sustained turbulence prevails. A quite analogous scenario has been observed in convection at high Prandtl numbers [1].

From what we have just said, it seems that as long as we remain with only one parameter at our disposal, either  $\epsilon$  or  $L$ , we do not get excitingly new things that do not closely fit the framework of dynamical systems theory (this conclusion would not be changed by the presence of several physically different unstable modes in competition controlled by a whole set of parameters

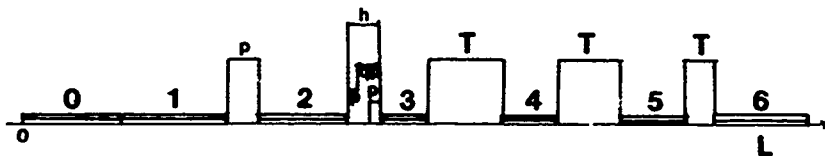


Figure 3: Bifurcation diagram of the Kuramoto-Sivashinsky equation for  $L$  moderate; stable cellular solutions are labelled by their number of cells and windows of persistent turbulence by the letter "T"; stable steady states for  $L$  large are reached only after very long transients.

$\epsilon_1, \epsilon_2, \dots$ , —multiple codimension problem— plus the aspect ratio  $L$ ). In fact, as soon as the aspect ratio is sufficiently large, the number of effective degrees of freedom is also large. This is attested by estimates of the dimensions of attractors [15,1] and of course by the existence of long transients exploring regions of phase space of increasing complexity. Assuming from the start that the aspect ratio is large thus leads to accept the idea that even if we are observing a laminar state, this state can be stable with respect to infinitesimal fluctuations but not globally stable (i.e. with respect to perturbations of any kind, which can be proven only close to thermodynamic equilibrium) and that the global structure of the phase space can be sufficiently complicated to afford several attractors, among which some can be turbulent and possibly also turbulent quasi-attractors (finite life-time attractors [6]) explaining the presence of long-lived transients.

Considering from a general point of view the cases where the process of transition to turbulence is well understood in low dimensional dynamical systems we arrive at the conclusion that this is mainly because everything can be made local both in parameter space and in phase space. The two best known examples are the sub-harmonic route and the Ruelle-Takens scenario. When these two conditions are not fulfilled, we have to face more or less important difficulties, the signature of which turns out to be *intermittency*, often associated with *crises*. The three types of intermittency arising from subcritical bifurcations of a limit cycle have been presented in P. Bergé's lecture; for a recent illustration of intermittency occurring in a crisis context see [2]. In such cases, the main problem comes from the fact that one already needs a detailed knowledge of properties of regions in phase space which are not close to the attractor which loses its stability (turbulent burst) and more generally of the global structure of phase space (relaminarization problem).

What is implied in the previous two paragraphs is that, in order to get something which has a chance of going beyond the standard approach in terms of dynamical systems, we must consider subcritically unstable laminar regimes. If we remember that sufficiently far from the threshold the coherence length is short enough, we can thus consider the total system as an assembly of weakly interacting units of individual size  $O(\xi_0)$ . Then we can assume that the system can be locally in one or another of the states that can exist at the global scale as attractors or quasi-attractors. This determines a partition of the physical space into domains that can fluctuate in size and shape. This kind of weak turbulence is called *spatio-temporal intermittency*.

The transition to turbulence via spatio-temporal intermittency presents itself as a scenario specific to large aspect ratio systems. As a natural frame for this type of transition in which a laminar regime is progressively contaminated by spatially localized turbulent bursts above some threshold while bursts recede below it, Y. Pomeau [19] has proposed a process introduced in statistical physics under the name of *directed percolation*. In the following we shall present (§2) numerical results obtained on a one-dimensional convection model displaying a transition to turbulence via spatio-temporal intermittency. Then we shall shift to an analysis of the same phenomenon in coupled lattice maps (§3) and introduce measuring tools from the field of directed percolation (§4) in order to characterize the critical behavior observed. Concluding remarks and perspectives will be gathered in §5.

## 2 A case study: Model-(b)

Here we consider a variant of the Swift-Hohenberg model of convection

$$\partial_t w = (\epsilon - (\nabla^2 + k_c^2)^2) w - g(w)$$

The field  $w$  accounts for perturbations to the pure conduction regime " $w \equiv 0$ " and can be understood as either the temperature modulation or the vertical velocity component evaluated in the horizontal plane at mid-height in the cell. The linear term can be shown to derive from the Boussinesq equations close to the convection threshold. It works as a "roll-mill": the growth rate  $\sigma$  of infinitesimal fluctuations with wave-vector  $k$  is given by

$$\sigma = \epsilon - (k^2 - k_c^2)^2$$



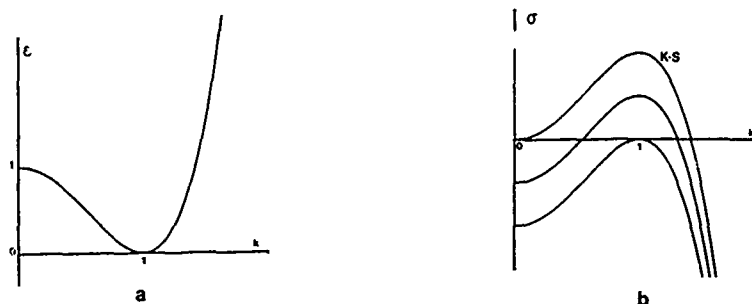


Figure 4: Marginal stability curve (a) and growth rate of infinitesimal perturbations (b) for the Swift-Hohenberg model

with a maximum for  $k = k_c$ , positive when  $\epsilon > 0$  (fig.4). In the following we shall choose a length unit such that  $k_c = 1$  which makes a critical wavelength  $\lambda_c = 2\pi$ . At  $\epsilon = 0$  modes with  $|k| = 1$  become unstable and for  $\epsilon$  slightly larger, a ring of width  $O(\sqrt{\epsilon})$  with radius 1 is destabilized. Nonlinear interactions described by  $g(w)$  should then insure the saturation of the unstable modes. In the original model,  $g$  was taken as  $g(w) = w^3$ ; in that case, the bifurcation is supercritical and one can show that the global dynamics derives from a potential. Though this property does not forbid the existence of metastable complicated textures in 2-dimensions, the asymptotic temporal behavior must remain trivial, which is reasonable only for fluids with a large Prandtl number (Pr). Extensions required to get a more realistic behavior at intermediate or small Pr include both non-potential contributions to  $g(w)$  and the coupling to large scale secondary flows induced by curvature effects. Numerical simulations in the 2-dimensional case remain out of our present reach for aspect ratios of real interest. On the other hand in 1-dimension one can handle systems with hundreds of rolls either by spectral methods (fast Fourier transform) or by efficient finite difference methods.

In the following we shall consider a model with  $g(w) = w\partial_x w$ , i.e. a nonlinear coupling through the classical advection term of Navier-Stokes equations (the Burgers equation in 1-dimension). This new model, called Model-(b) [17], no longer derives from a potential and, as such, can display a nontrivial time dependence. The control parameter  $\epsilon$  is not allowed to become larger than 1 for, above this limiting value, the  $(k = 0)$ -mode is no longer damped from both linear and nonlinear point of views. At  $\epsilon = 1$ , one can cast Model-(b) under the form of a Kuramoto-Sivashinsky equation for the space derivative of  $\theta$ :  $\phi = \partial_x \theta$ . For  $\epsilon < 1$ , Model-(b) is equivalent to a Kuramoto-Sivashinsky equation with damping introduced earlier by LaQuey *et al.* in the context of plasma instabilities [14]:

$$\partial_t \phi + \phi \partial_x \phi = -\eta \phi - \partial_{xx} \phi - \partial_{xxxx} \phi$$

In order to allow the comparison with results quoted in fig.3 for the Kuramoto-Sivashinsky equation we give here the explicit correspondance:  $x \rightarrow x/\sqrt{2}$ ,  $t \rightarrow t/4$ ,  $w \rightarrow 2\sqrt{2} \phi$  with  $\eta = (1 - \epsilon)/4 > 0$ . Obviously, the term  $(\epsilon - 1)w$  in Model-(b) breaks the Galilean invariance displayed by the equivalent Kuramoto-Sivashinsky equation. In order to break also the translational invariance, we shall supplement the partial differential equation by so called rigid boundary conditions:

$$w = \partial_x w = 0$$

at the two ends of an interval of length  $L$ .

As discussed in the introduction we have now two control parameters at our disposal and we can examine the qualitative changes of the bifurcation diagram when  $L$  increases. Numerical simulation have been performed using a finite difference code, second order in space and second order in time (Crank-Nicolson scheme for the linear part, Adams-Bashford scheme for the nonlinear term). The algorithm was designed to take advantage of vectorization capabilities of the Cray-1S. The spatio-temporal resolution has been varied in order to check the reliability of the phenomena observed (up to 70 points per  $\lambda_c$  and a time step adapted to the asymptotic dynamics of the solution, steady, periodic, ...).

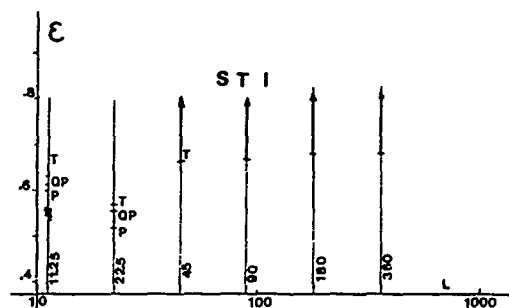


Figure 5: Qualitative aspect of the bifurcation diagram of Model-(b):  $\epsilon = 1$  corresponds to the Kuramoto-Sivashinsky limit; the length  $L$  is given in units of  $\lambda_c$  (logarithmic scale).

The complete bifurcation diagram has not been studied as thoroughly as that of the Kuramoto-Sivashinsky equation with periodic boundary conditions sketched in fig.3. Only the most important qualitative features have been recognized. From a numerical point of view it is easier to keep  $L$  constant and to vary  $\epsilon$ . As expected one can distinguish mainly three domains in  $L$  (fig.5).

In the small  $L$  domain, with  $L$  up to about  $4 - 5\lambda_c$ , Model-(b) is typically a confined system, subjected to crises and bifurcating according to the classical scenarios. The envelope equation formalism is hardly applicable. We shall discard this domain and concentrate our interest on the range  $L \geq 10$ . All the results to be presented from now on have been obtained in collaboration with H. Chaté (SPSRM, Saclay) and make a part of his PhD Thesis, some have already been published [3,4], others not.

For  $L$  in the range  $10 - 50\lambda_c$ , typical solutions to the Kuramoto-Sivashinsky ( $\epsilon = 1$ ) are turbulent. On the other hand, the theoretical approach to Model-(b) close to the threshold ( $\epsilon = 0$ ) is easier since it begins to make sense to try to approximate the solution by modulating a perfect roll solution. Wavelength selection by nonlinear end-effects turns out to be non-trivial [5,18]. Fig.6 displays steady solutions obtained numerically with  $L = 11.25$  for  $\epsilon = 0.04$  close to the threshold (the coherence length  $\xi_0/\sqrt{\epsilon}$  is large and for  $\epsilon = 0.44$  slightly below the threshold of time dependence. These steady solutions, odd with respect to the middle point, turn out to be unstable to oscillatory perturbations which involve the  $1/2$ -subharmonic of the basic wavevector selected by boundary effects, and their harmonics ( $3/2$  and  $2$  principally). The bifurcation is subcritical, with a linear threshold at about  $\epsilon = 0.544$  and hysteresis down to  $\epsilon = 0.537$  as sketched in fig.7. Next, a supercritical bifurcation towards a quasi-periodic state takes place, with a second frequency related to the propagation of a phase perturbation well synchronized over the width of the system. The transition to turbulence then takes place through a loss of spatial coherence of these propagating waves. The main process at the origin of this behavior seems to be a strong local instability of the oscillatory state immediately followed by a reinforcement of coherence of that segment of the solution that becomes messy, i.e. the birth of a *coherent structures* in which waves come and die. In fact, a whole manifold asymptotic states can be observed at the same value of  $\epsilon$ . Typical samples for  $L = 11.25$  and  $L = 22.50$  given in fig.8 and fig.9 respectively (time flows downwards, visualization of the solutions by the position of maxima and minima).

When  $L$  becomes much larger than  $50$ , confinement effects, now quite weak, do not seem to play a direct role in controlling the appearance of time dependence and the transition process looks much like a bulk phenomenon. A severe compression of the data is needed in order to visualize the dynamical regime reached by the system in this large  $L$ , long time limit. What seems important is the occurrence of coherent structures and it turns out that in these regions the peak to peak amplitude is larger than in turbulent regions. As illustrated in fig.10, choosing some cut-off and setting to black regions where the peak to peak amplitude is larger than the cut-off allows us to clearly discriminate domains remaining laminar from turbulent patches.

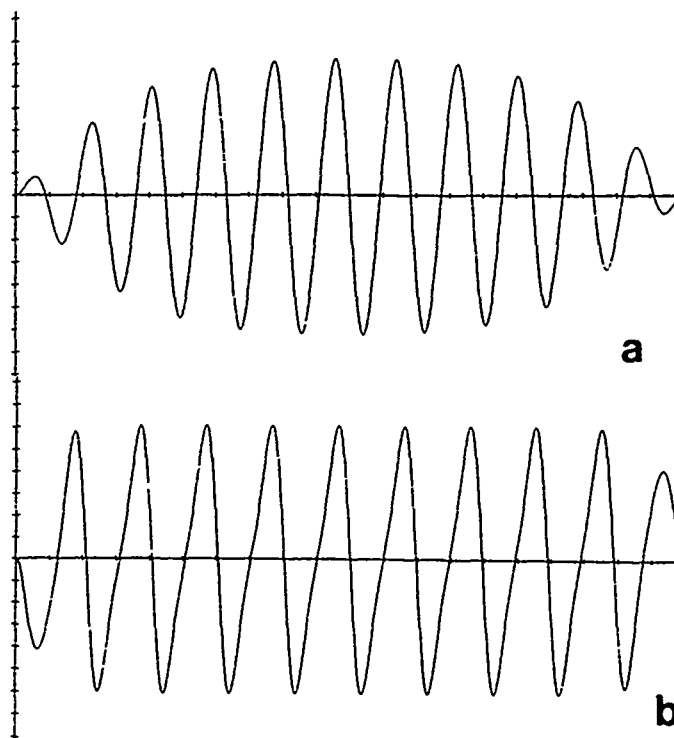


Figure 6: Two steady solutions of Model-(b): a)  $\epsilon = 0.04$  and b)  $\epsilon = 0.44$ .

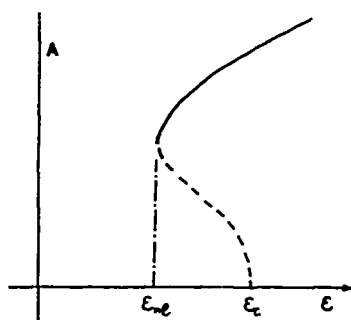


Figure 7: Qualitative sketch of a subcritical bifurcation

Fig.11 displays the solution for  $L = 180$  (about 350 rolls involved) and  $\epsilon = 0.692$ . It can be viewed as made of a mixture of small islands of laminar domains of various size scattered amidst a large ocean of turbulence. Such a dynamical regime is called *spatio-temporal intermittency*. The main problem is to understand its birth and to predict its statistical characteristics as a function of the control parameter. Increasing  $\epsilon$  one observes that the size of the largest laminar domains decreases rapidly (see fig.12 for  $\epsilon = 0.84$ ). On the other hand, when  $\epsilon$  decreases the largest laminar domains reach sizes of the order of magnitude of  $L$  itself. Then, they can merge and completely invade the system (see fig.13 for  $\epsilon = 0.68$ ).

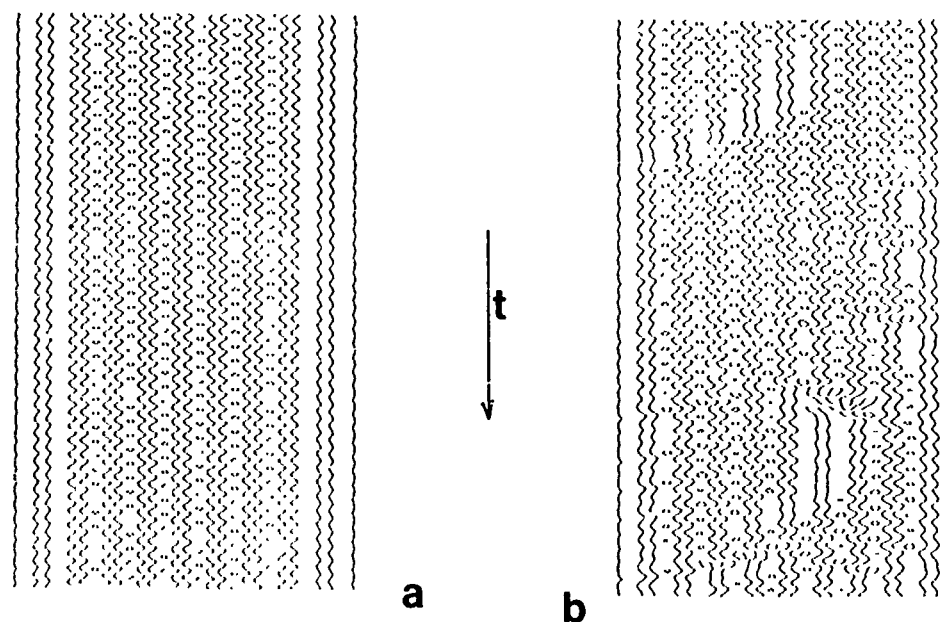


Figure 8: For  $L = 11.25$ , solutions contain about 20 rolls as expected; a) periodic regime at  $\epsilon = 0.600$ ; b) weakly chaotic regime displaying the birth of a coherent structure at  $\epsilon = 0.632$ .

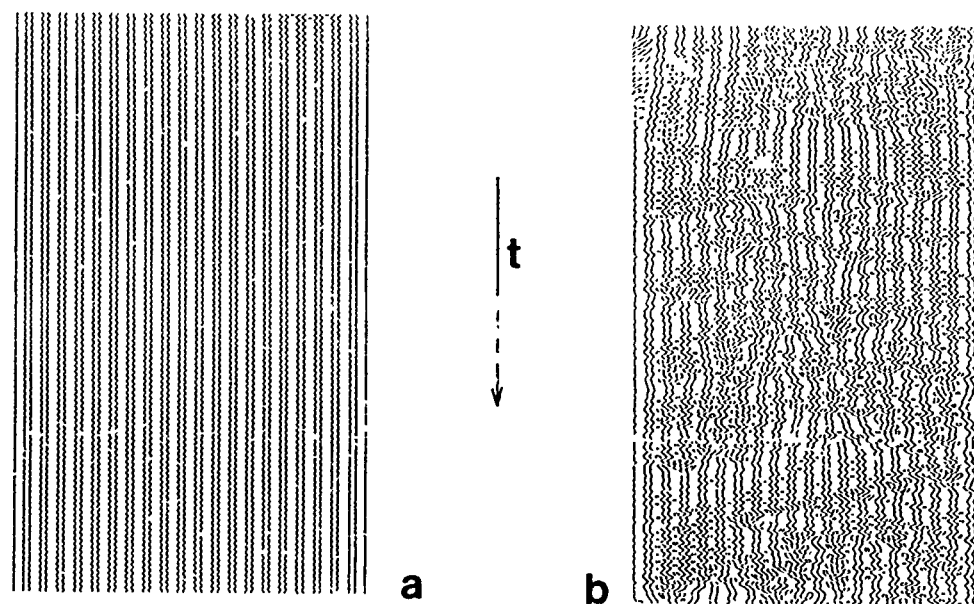


Figure 9: For  $L = 22.5$  one gets about 40 rolls; a) and b) two drastically different asymptotic states at  $\epsilon = 0.640$  one extremely weakly quasi-periodic, the other chaotic.

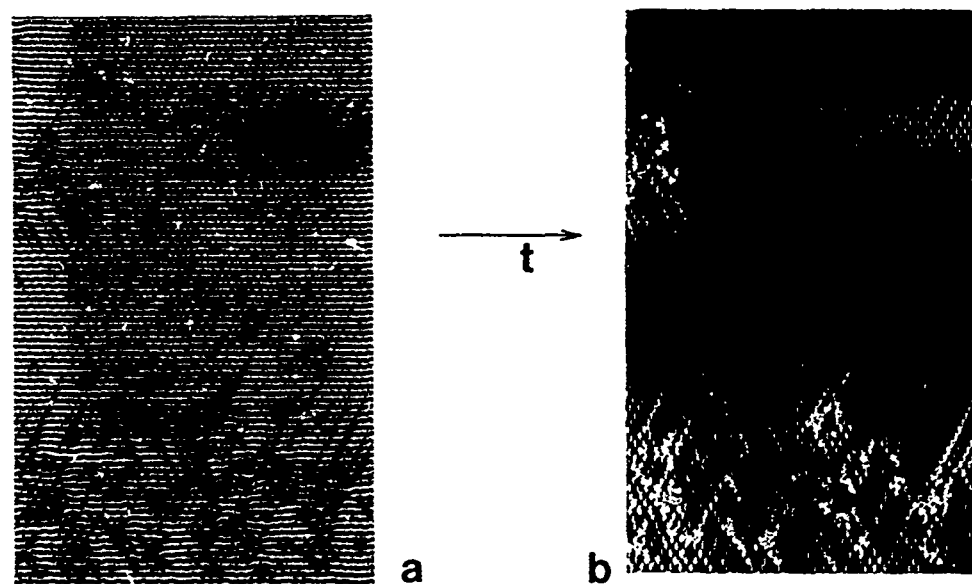


Figure 10: Visualisation of laminar domains ( $L = 90$ ,  $\epsilon = 0.68$ , time running from the left to the right): a) evolution of the solution from the position of extrema as before; b) same evolution using the reduction process described in the text.

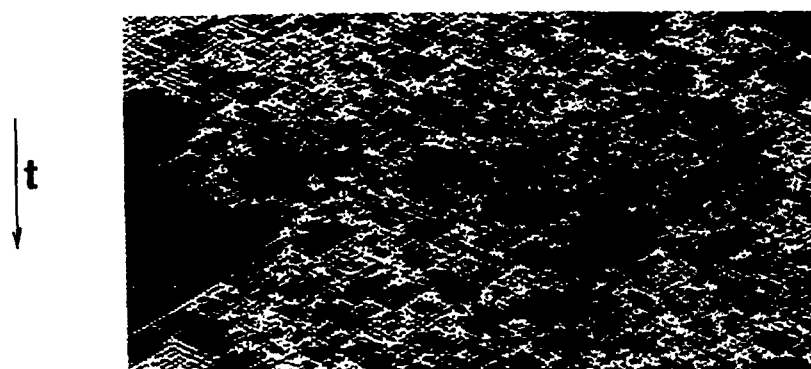


Figure 11: Spatio-temporal intermittency for  $L = 180$  and  $\epsilon = 0.692$ .

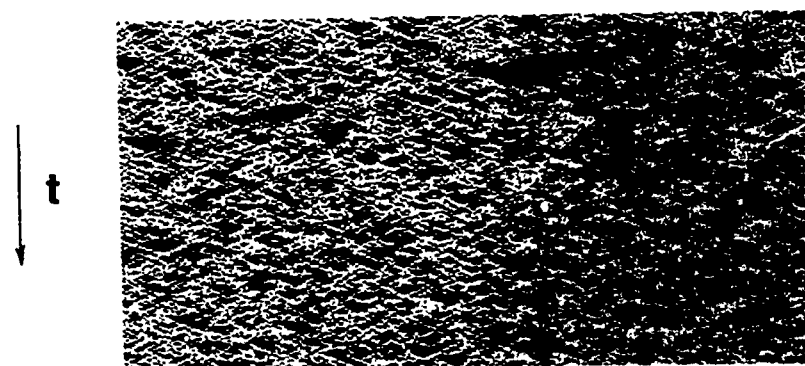


Figure 12: At  $\epsilon = 0.84$  the coherent structures are much smaller.

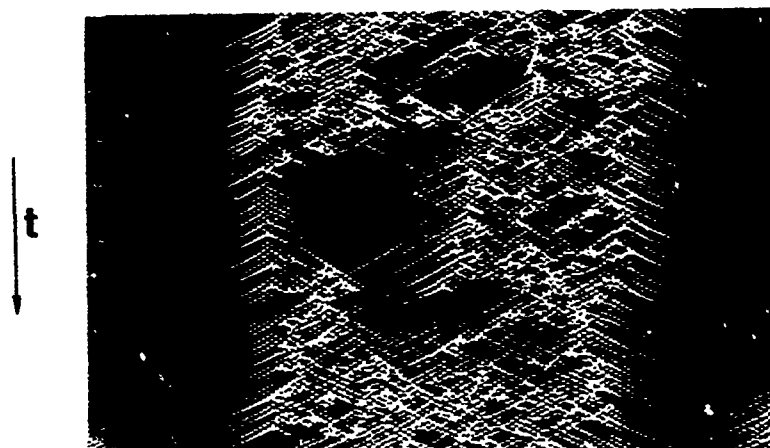


Figure 13: Below  $\epsilon = 0.68$ , spatio-temporal intermittency recedes more or less regularly, leaving a quiescent state; around this value the situation is confused, with neither a marked recession nor a steady invasion; this defines the threshold.

Numerical experiments suggest the existence of a well defined threshold above which the system is intermittent, while it remains laminar below. As shown in fig.5, this threshold does not seem to vary with  $L$  in the large  $L$  limit, hence the bulk character of the phenomenon. We shall come back to the statistical signature of this transition later, after having examined the simpler case of coupled map lattices.

### 3 Spatio-temporal intermittency in coupled map lattices

In view of applications, rather than the form chosen in the introduction, it is more convenient to consider a coupled map evolution rule given by [9]:

$$X_i^{n+1} = \sum_{j=-p}^p W_j F(X_{i+j}^n)$$

where the  $W_j$  are well chosen weights such that  $W_j \leq 0$  and  $\sum_j W_j = 1$  (this has the advantage of avoiding spurious instabilities of the type found in numerical simulation of partial differential evolution equations using explicit schemes). Spatio-temporal properties of such systems have been studied mostly because of their ability to mimic certain aspects of nonlinear pattern formation with a great economy of numerical resources (for a review see chapter 7 of [10]). Taking  $F$  as the so called logistic map:  $F(X) = RX(1 - X)$  or equivalently  $F(X) = 1 - AX^2$  one can observe spatial structures that develop for  $P$  or  $A$  in the direct cascade, or at the beginning of the inverse cascade (see P. Bergé's lecture). Consider for example step  $k$  of the period doubling cascade at the limit of zero coupling. Time translational invariance is broken and one out of  $2^k$  equivalent possible phases is chosen by each site independently. Switching the coupling on, one obliges the sites to take the phase of their neighbors into account. The result is a splitting of the system in domains of identical phase, separated by walls. In practice, it is quite difficult to detect more than a few period doublings. In the inverse cascade one gets a similar situation except that the dynamics is chaotic instead of regular inside the domains. Of greater interest to us here is the occurrence of temporal intermittency close to the lower end of the Period-3 window [11]. Well inside the Period-3 window, when the coupling is weak one gets the same regime as above, with domains and walls. But closer to the intermittency threshold, when the coupling is increased, the walls are seen to "explode" and spatio-temporal intermittency sets in (fig.14).

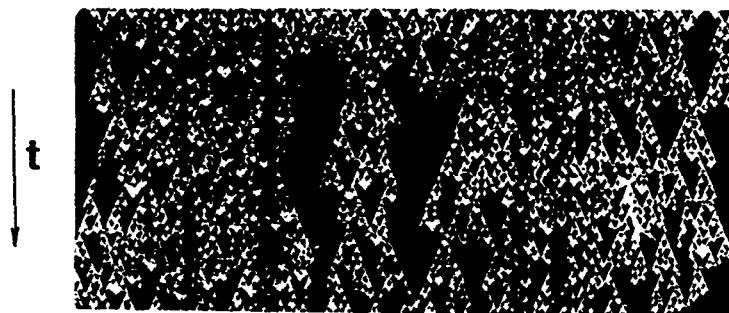


Figure 14: Sample of spatio-temporal intermittency at threshold for the logistic map close to the Period-3 onset

The connection between spatio-temporal intermittency observed in coupled maps and that in Model-(b) seems relatively obvious, but should be proven rigorously. As discussed earlier, one can consider the whole system of length  $L$  as made of weakly coupled sub-units with lengths of the order of the coherence length of the oscillations that were seen to decay as they penetrated into the coherent structures. This "renormalization" of lengths would allow to define more precisely the coupled local systems. Note that the status of the invariance properties of the continuous model becomes unclear since one arrives at a lattice, which breaks translation invariance; however one can reasonably think that their "macroscopic" consequences —on distances of the order of  $L$  and on a corresponding phase diffusion time scale— can be averaged out by the small scale fluctuations which could take them into account as a dynamical source among others ("renormalisation" of mechanisms).

The discrete model we are supposed to derive from first principles should read:

$$X_i^{t+1} = F(X_i^t) + \frac{1}{2} (F(X_{i+1}^t) - 2F(X_i^t) + F(X_{i-1}^t))$$

In order to describe in a realistic way the spatio-temporally intermittent state we must ask the local iterations to split the local phase space in 2 different regions: a) the vicinity of a stable fixed point where the dynamics is reduced to a relaxation towards the fixed point and b) a chaotic region "far" from the fixed point. This two regions should be connected most probably intrinsically by the iteration itself but an extrinsic connection through the coupling force is also conceivable. The demonstration will be performed here using a local model of type I intermittency (fig.15 [11]) but the vicinity of a crisis phenomenon could have been used. Take:

$$F(X) = -a + X + X^2 \quad \text{for} \quad X \leq c$$

$$F(X) = -3(X - c) + 1 - a \quad \text{for} \quad X > c$$

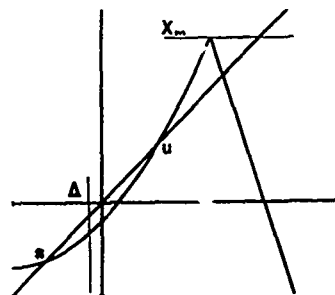


Figure 15: Local form of the iteration used for the coupled map lattice:  $\Delta$  is the cut-off value which discriminate between laminar and turbulent states

with  $c = (\sqrt{5} - 1)/2$ . Parameter  $a$  which controls the distance to the intermittency threshold will be kept constant:  $a = 0.01$ , the coupling constant  $\epsilon$  will control the transition.

Sites  $i$  for which  $X_i$  will be close enough to the stable fixed point  $X_s = -\sqrt{a} = -0.1$  will be considered as laminar, otherwise they will be turbulent:

$$X_i \leq X_s + \Delta \quad \rightarrow \quad L$$

$$X_i > X_s + \Delta \quad \rightarrow \quad T$$

A starting state which is laminar everywhere stays laminar since no infinitesimal perturbation can bring a site outside the attraction basin of the stable fixed point. On the other hand a finite amplitude localized perturbation that bring a single site  $X_j$  outside the attraction basin of  $X_s$ , i.e.  $X_j + \delta > X_u = +\sqrt{a} = +0.1$  can grow and even destabilize its neighbors if the coupling is large enough. As illustrated in fig.16, the expected change of behavior takes place at  $\epsilon = 0.0618$  with finite duration turbulent transients below and sustained spatio-temporal intermittency above.

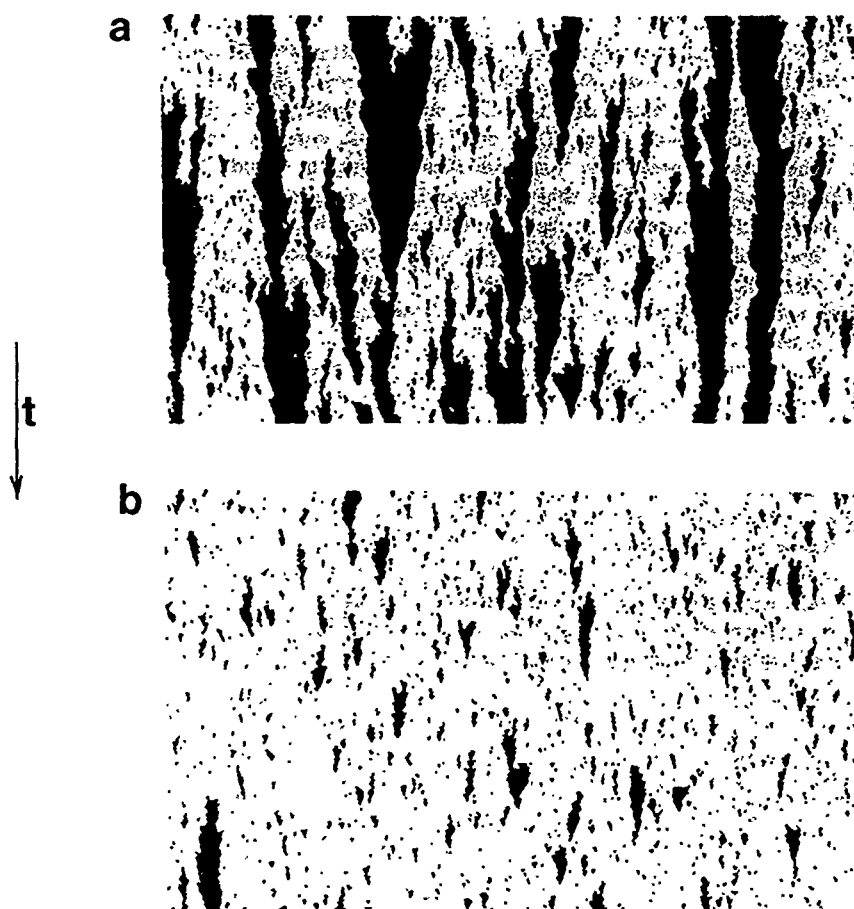


Figure 16: Spatio-temporal intermittency in coupled map lattice: a) close to the threshold ( $\epsilon = 0.0618$ ); b) slightly above the threshold ( $\epsilon = 0.0630$ )



#### 4 The directed percolation approach

Let us now consider a fully stochastic approach in terms of probabilistic cellular automata. Such systems are defined by transition probabilities which control the transfer of some information through the system. To be specific consider a chain of sites labelled by an index  $i$ . At each site the local state  $X_i$  can be either  $A$  or  $B$ , 0 or 1 and the future state at site  $i$  depends on the states at  $2n+1$  sites  $j$ ,  $-(i+n) \leq j \leq +(i+n)$  with most often  $n=1$ , i.e. three consecutive sites (fig.17a). The most general process depends on  $2^{2n+1}$  free parameters but this number can be reduced by symmetry considerations or other requirements (totalistic rules that depend only on the number of sites in a given state among the interacting neighbors).

A simpler process can be defined with a coupling between only two sites. Take a square lattice and look at it diagonally (fig.17b) then assume transition probabilities of the form:  $p(01|1) = p(10|1) = p_b$ ,  $p(11|1) = 1 - (1 - p_b)^2$ . In addition one takes  $p(00|1) = 0$  so that no spontaneous creation of information can occur. This defines a process which can be understood as the transfer in a well defined direction of the information  $X = 1$  through a lattice from which some bonds (hence the index  $b$ ) have been removed at random. This can model for example the infiltration of a liquid in a porous medium with sites at the end of pores that can be randomly open or occluded, the sites being either wet (1) or dry (0); a site being connected to two dry sites cannot be wet, hence the last condition. It is said that we have an *absorbing state*, from which no escape is possible.

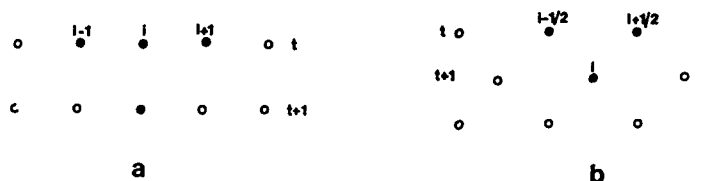


Figure 17: One-dimensional probabilistic cellular automata: a) with 3 neighbors; b) with 2 neighbors

Assuming that the information is introduced at some place in the lattice (the root of the process, level 0) one has to determine the probability of transfer to some level  $k$  as a function of  $p_b$ . This is equivalent to say that the percolation cluster to which the root belongs can reach sites at level  $k$  (directed bond percolation). It is known that when  $p_b > 0.6445$  the information is transferred to infinity with probability  $> 0$ . A slightly more general process allows for additional loss of information at each site according to some site probability  $p_s$ . Transition probabilities are then given by  $p(01|1) = p(10|1) = p_s p_b$ ,  $p(11|1) = p_s (1 - (1 - p_b)^2)$ , still forbidding spontaneous creation of information ( $p(00|1) = 0$ ). Even more general processes can be defined (see [12,13] for a review).

In the present context the correspondence is fixed by the condition that the laminar state "L" should be absorbing. Moreover the definition of the deterministic process suggest rather a probabilistic automaton with 3 sites coupled. In addition to  $p(LLL|T) = 0$  which account for the local stability of the laminar state we can impose a priori left-right symmetry:  $p(LLT|T) = p(TLL|T)$  and  $p(TTL|T) = p(LTT|T)$ . This leaves 5 free parameters which can be determined empirically from simulation on the initial model.

At the intermittency threshold for model the studied here,  $\epsilon = 0.0618$ , we have found  $p(LLL|T) = 0$  as expected,  $p(TTL|T) = 0.9903$  close to  $p(LTT|T) = 0.9906$ , and  $p(TLL|T) = 0.0115$  close to  $p(LLT|T) = 0.0116$ . However  $p(TLT|T) = 0.0522$  and  $p(LTL|T) = 0.6036$  are different from the two previous sets of values so that the equivalent probabilistic automaton is certainly not governed by totalistic rules. At a qualitative level, simulations on the original coupled map lattice and the probabilistic system with empirically found probabilities are practically undistinguishable (fig.18).

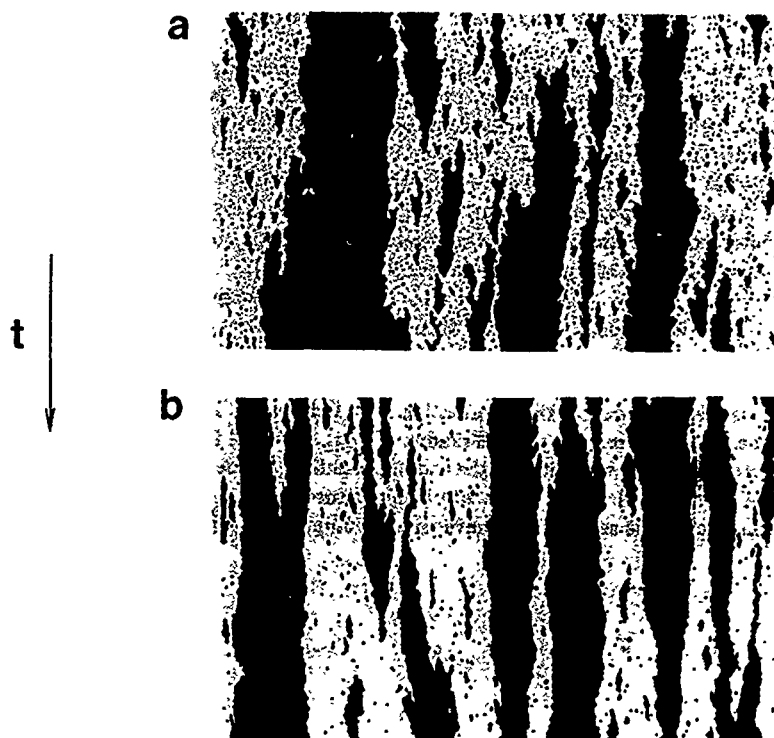


Figure 18: Qualitative comparison between simulation results from the coupled map lattice (a) and the probabilistic cellular automaton (b) is quite conclusive

Let us sketch the beginning of a theory connecting coupled map lattices and probabilistic cellular automata. For simplicity, we shall consider the case of the transition  $(LLT|T)$  which correspond in general to the growth of a turbulent patch. Assume the laminar sites at  $i = -1, 0$  and the turbulent site at  $i = 1$ . The future state at  $i = 0$  is given by:

$$X_0^1 = X_0^0 + \delta = (1 - \epsilon) F(X_0^0) + \frac{\epsilon}{2} (F(X_{+1}^0) + F(X_{-1}^0))$$

In order to simplify the problem we shall assume that laminar sites at  $t = 0$  sit exactly at the fixed point. Using the fact that  $F(X_s) = X_s$ , we get:

$$\delta = \frac{\epsilon}{2} (F(X_{+1}^0) - X_s)$$

The site  $i = 0$  will be turbulent at time  $t = 1$  if  $\delta > \Delta$ , that is to say if  $F(X_{+1})$  belongs to the interval  $(X_\Delta; X_m)$  where  $X_\Delta = X_s + 2\Delta/\epsilon$  and  $X_m$  is the upper bound of the interval invariant by  $F$  ( $X_m = 1 + a$ ), see fig.15. Assuming further that the probability of the turbulent state is uniformly distributed on the interval  $(X_s + \Delta, X_m)$  so that the probability of having  $F(X_{+1})$  in the interval  $(X_\Delta, X_m)$  is simply proportional to the length of the interval, one gets:

$$p(LLT|T) \sim \left( X_m - X_s - \frac{2\Delta}{\epsilon} \right)$$

The variation of this probability is in reasonable agreement with experimental data. Other cases where the central site is laminar can be handled in the same way. The cases where the central site is turbulent are more delicate since one has to take into account the fact that it has already a nontrivial dynamics for its own (turbulent transient subjected to noise from neighbors)

The main interest of pointing out an analogy between the transition to turbulence via spatio-temporal intermittency and directed percolation is that one can borrow tools and concepts of statistical theory, especially the notion of *critical behavior* and *critical exponents*. Their use has not yet been extensively developed in the present problem since the practical implementation requires a huge amount of computation to get reliable results. Up to now only the statistics of the lengths of coherent structures have been examined both for the coupled map lattices and for Model-(b). The comparison between statistics for the coupled maps and the probabilistic automaton shows that the analogy goes beyond the qualitative level (fig.19) while calculations for Model-(b) exemplify the distinction between the vicinity of the threshold where the distribution of lengths of coherent structures decays as a power law, as opposed to the exponential decay observed far from the threshold, thus supporting the idea of a critical domain in the sense of critical phenomena (fig.20).

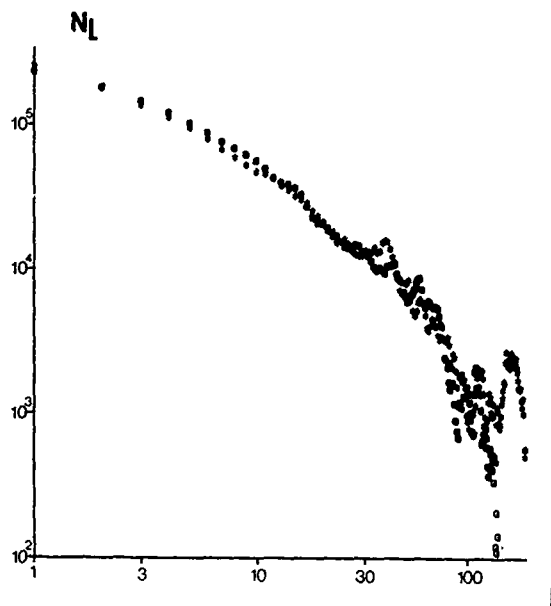


Figure 19: Statistics of the lengths of coherent structures for the coupled map lattice (o) and the probabilistic cellular automaton (\*) are practically identical up to lengths of the order of 80 above which end effects are sizable (simulation on 500 sites)

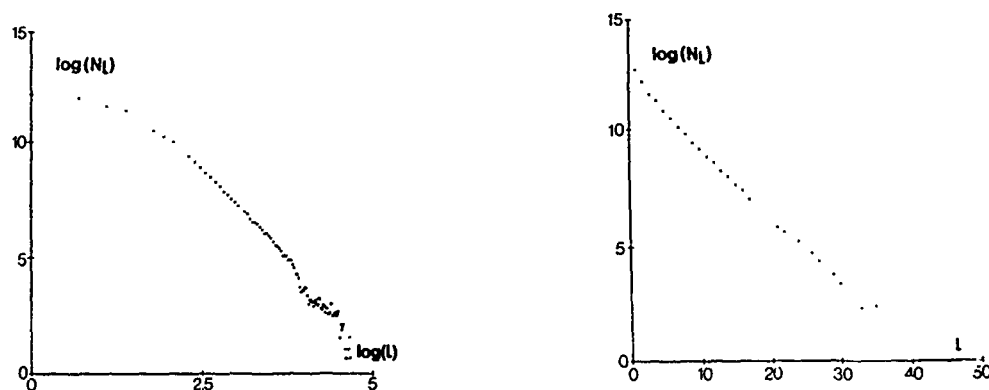


Figure 20: Distribution of the lengths of coherent structures in the intermittent phase for Model-(b): a) log-log plot at threshold  $\epsilon = 0.688$ : algebraic decay; b) lin-log plot above threshold,  $\epsilon = 0.84$ : exponential decay.

## 5 Summary, conclusion, and perspectives

In this lecture we have presented a scenario of transition to turbulence specific to large aspect ratio systems. Starting with simulations on a model chosen for its relevance to the field of convective instabilities we have characterized the spatio-temporal intermittent "phase". Then we have examined the transition process having recourse to simpler systems: coupled maps lattices. This process appeared to involve the propagation of an information, laminar/turbulent which seemed stochastic though it was generated by a deterministic dynamics. Concepts first introduced in the statistical physics of critical phenomena applied to directed percolation allowed to account for most features of spatio-temporal intermittency, and especially the change of behavior at what turned out to be a true threshold.

The implications of this approach are important because in large aspect ratio systems we have to face the possibility that what we think is turbulence may be simply a finite life-time but very long turbulent transient. If the percolation analogy is valid, then a threshold exists above which the turbulent state percolates through the system and turbulence as virtually no chance to decay. At a more conceptual level one can say that the described process can help us reconcile local, short-term determinism with turbulence for weakly confined systems in much the same way as strange attractors allow to reconcile determinism and temporal chaos for systems with a small number of degrees of freedom.

Now, a question: is this scenario only a nice theoretical view which works in model systems built on purpose? The answer seems to be: No! In a recent experiment briefly sketched in fig.21, P. Bergé and M. Dubois [1] have observed a transition to turbulence which may follow the theoretical scenario. Indeed, as indicated in fig.22, the loss of spatial coherence involves the alternation of coherent structure a few rolls long, and messy regions with the possible breakdown of a messy patch into a coherent structure.

Intermittency has a spatio-temporal meaning in many other contexts of fluid dynamics (see [21] for a general review). First, one can think of small scale active structures in the dissipation range of fully developed turbulence, though the connection could be only visual (fig.12). Second, the present approach could help understand the growth/decay of turbulent plugs in pipe flows. Finally, one could also try to introduce analogous percolation concepts for the description of the intermittent structure of the frontier of turbulent boundary layers like that in fig.23.

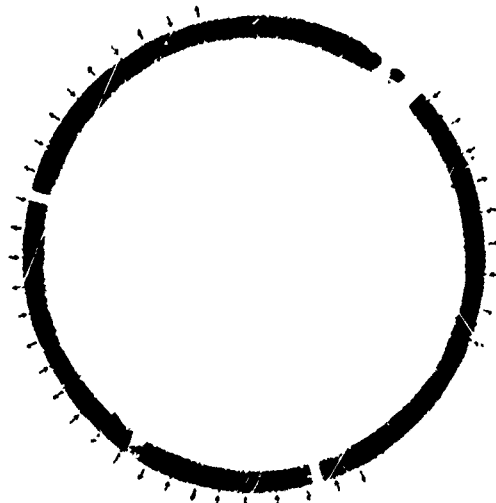


Figure 21: Annular cell used by P. Bergé and M. Dubois: coherent domains are separated by messy regions; the whole evolves chaotically in the long term.

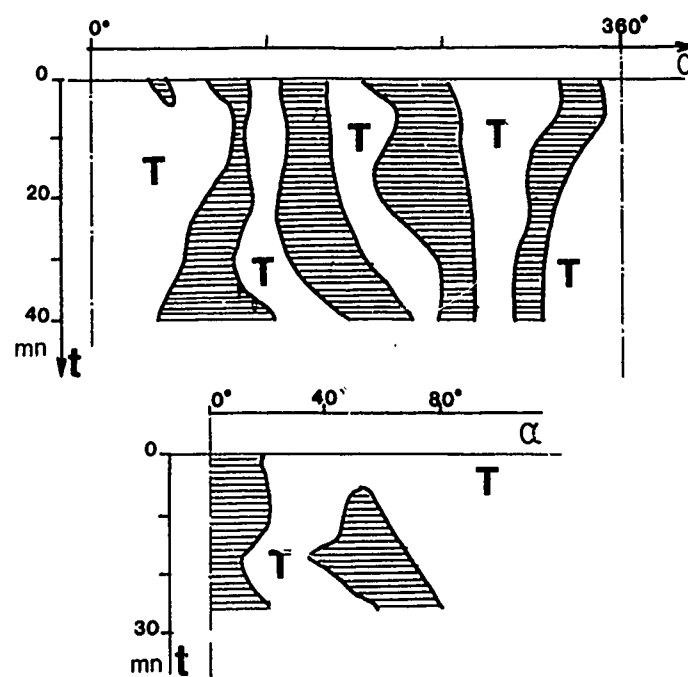


Figure 22: Example of spatio-temporally intermittent signal with the birth of a laminar domain comparable to coherent structures appearing in the model; time is running downwards, the hatched region is laminar.

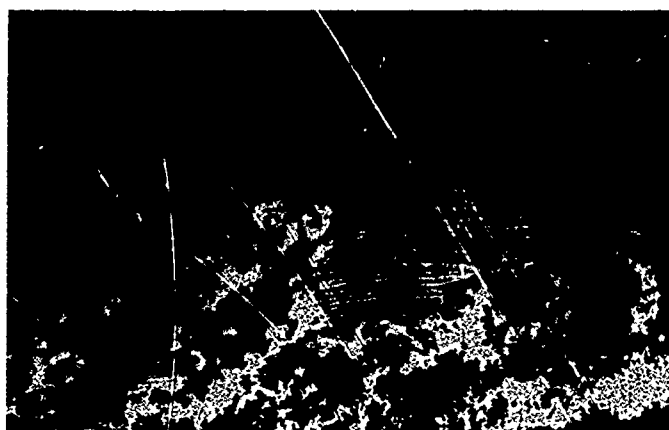


Figure 23: Illustration of the intermittent nature of the outer part of a turbulent boundary layer from ref.22 plate 157

## References

- [1] P. Bergé, Proceedings of *Chaos'87*, Monterey (1987).
- [2] H. Chaté, P. Manneville, Phys.Rev. **A32** (1985) 3065.
- [3] H. Chaté, P. Manneville, Phys.Rev.Lett. **58** (1987) 112.
- [4] H. Chaté, P. Manneville, C.R.Acad.Sc.(Paris) in press.
- [5] M.C. Cross, P.G. Daniels, P.C. Hohenberg, E.D. Siggia, J.Fluid Mech **127** (1983) 155.
- [6] J.P. Eckmann, D. Ruelle, Rev.Mod.Phys. **57** (1985) 617.
- [7] J. Guckenhiemer, P. Holmes, *Nonlinear Oscillations, Dynamical Systems, and Bifurcation of Vector Fields* (Springer-Verlag, New-York, 1983).
- [8] J.M. Hyman, B. Nicolaenko, S. Zaleski, Physica **D23** (1986) 265.
- [9] J.D. Keeler, J.D. Farmer, Physica **D23** (1986) 413.
- [10] K. Kaneko, *Collapse of Tori and Genesis of Chaos in Dissipative Systems* (World Scientific, Singapour, 1986).
- [11] K. Kaneko, Prog.Theor.Phys. **74** (1985) 1033.
- [12] W. Kinzel, in *Percolation structures and processes* Annals of the Israel Phys.Soc. **5** (1983) 425.
- [13] W. Kinzel, Z.Phys. **B58** (1985) 229.
- [14] R.E. LaQuey, S.M. Majhajan, P.H. Rutherford, W.M. Tang, Phys.Rev.Lett. **34** (1975) 391.
- [15] P. Manneville, in *Macroscopic Modelling of Turbulent Flows* Lect.Notes in Physics **230** (Springer-Verlag, Berlin, 1985).
- [16] B. Nicolaenko, Physica **D20** (1986) 109.
- [17] Y. Pomeau, P. Manneville, Physics Lett. **75A** (1980) 296.
- [18] Y. Pomeau, S. Zaleski, J.Physique **42** (1981) 515.
- [19] Y. Pomeau, Physica **D23** (1986) 3.
- [20] J. Swift, P.C. Hohenberg, Phys.Rev. **A15** (1977) 319.
- [21] D.J. Tritton *Physical Fluid Dynamics* (Van Nostrand Reinhold, New-York, 1977).
- [22] M. Van Dyke, *An Album of Fluid Motion* (Parabolic Press, Stanford, 1982)
- [23] S. Wolfram Ed., *Theory and Applications of Cellular Automata* (World Scientific, Singapour, 1986).

# DETERMINATION OF FRACTAL DIMENSION, CONNECTION OF SPACE AND TEMPORAL CHAOS AND APPLICATION TO EXPERIMENTAL RESULTS

by  
S. Ciliberto  
Istituto Nazionale di Ottica  
Largo E. Fermi 6  
50125 Firenze (Italy)

## I - INTRODUCTION

In the last decade many experiments have demonstrated that the transition to chaos is a low dimensional phenomenon even in hydrodynamic instabilities governed by an infinite number of degrees of freedom /1/.

However in fluid systems the physical origin of the chaotic regimes is not very well understood. Mathematical models that incorporate the correct dynamics and allow a prediction of the behavior as a function of the control parameter are not generally available. Very often experimental observations can be just correlated with the behavior of simple maps, as in the case, for example, of the Feigenbaum cascade /2/, and quasi periodicity /3/.

Besides an other problem remains open: is low dimensional chaos a precursor of fully developed turbulence, where the fluid flow exhibits chaotic states both in space and time? To give new insight into this problem there is nowadays a growing interest in the study of the relationship between spatial order and temporal chaos.

For example it has been observed in numerical studies of certain partial differential equations (P.D.E.) /4,5/, and of coupled maps /6/ that coherent spatial structures coexist with temporal chaos. From an experimental point of view spatial patterns have been quantitatively analysed in time dependent chaotic regimes only in few experiments /7-10/. We describe here two of these experiments, where the chaotic states have been also quantitatively characterized in terms of fractal dimension, metric entropy and Lyapunov exponents. The method to compute these quantities are briefly summarized in the appendix.

In Section II we report experiments on surface waves instabilities /9/, where the competition between two spatial patterns produces time dependent behavior and chaos. The results of this experiment are in good agreement with a low dimensional model obtained from Navier-Stokes equations /11/.

In Section III we describe experiments on time dependent behavior /10/ of a horizontal fluid layer, heated from below, that is Rayleigh-Benard convection (R-B). We show that time dependent regimes are characterized by the presence of either traveling waves or localized oscillations. These spatio temporal regimes turn out to be similar to those observed in numerical simulations /4/ of Kuramoto-Shivanshisky (K-S) /12/ and Kuramoto-Velarde (K-V) /13/ partial differential equations. At the end of section III we report experimental evidence that the properties of the chaotic regimes depend on space coordinates.

## II - SURFACE WAVES INSTABILITIES

The system of interest is a cylindrical fluid layer in a container that is subjected to a small vertical oscillation of amplitude  $A$  and frequency  $f_0$ . It is well known that, if the driving amplitude exceeds a critical value  $A_c(f_0)$ , which is a function of frequency, the free surface develops a pattern of standing waves. The surface deformation  $S(r, \theta, t)$  can then be written as a superposition of normal modes:

$$S(r, \theta, t) = \sum_{\ell, m} a_{\ell m}(t) J_{\ell}(k_{\ell m} r) \cos \ell \theta,$$

where  $J_{\ell}$  are Bessel functions of order  $\ell$  and the allowed wave numbers  $k_{\ell m}$  are determined by the boundary condition that the derivative  $J'_{\ell}(k_{\ell m} R) = 0$ , where  $R$  is the radius of the cylinder. The modes may be labeled by the indices  $\ell$  (giving the number of angular maxima) and  $m$  (related to the number of nodal circles). The mode amplitude  $a(t)$  develops an instability when the corresponding eigenfrequency (given by the dispersion law for capillary gravity waves) is approximately in resonance with half the driving frequency  $f_0$  and  $A$  exceeds  $A_c(f_0)$ .

This parametric instability leads to standing waves in which the mode amplitude oscillates at  $f_0/2$ . To take into account the possibility of a further slow modulation of the mode amplitudes, which, in fact, occurs due to mode competition, we write each amplitude in terms of fast oscillations at  $f/2$  and slow envelopes  $C_{\ell}(t)$  and  $B_{\ell}(t)$ :

$$a_{\ell}(t) = C_{\ell}(t) \cos(\pi f_{\ell} t) + B_{\ell}(t) \sin(\pi f_{\ell} t).$$

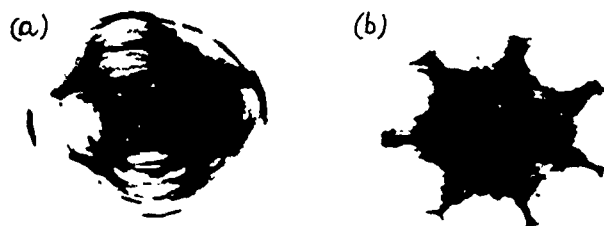


FIGURE 1

Optical intensity patterns for the (4,3) and (7,2) modes. The first index gives the number of angular maxima.

We omit the second subscript because, in practice, only a single value of  $m$  is significant for a given value of  $\ell$ . In our experiment the working fluid was water of depth of 1 cm, and the radius of the tank was 6.35 cm. Examples of stable patterns involving a single mode (and possibly harmonics) are shown in Fig. 1 for the (7,2) and (4,3) modes. The index  $\ell$  is obvious from the symmetry while  $m$  was determined by matching the frequency to known dispersion law. The white areas correspond to surface depressions (typically 0.5 mm) and the black ones to surface elevations. The driving amplitude  $A$  was about 1.1.  $A$  and the frequency was at the minimum of the stability curve in each case. The two figures have been obtained with a focalisation technique.

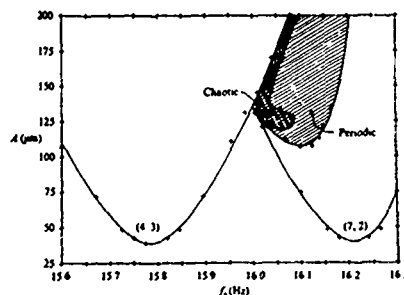


FIGURE 2

Phase diagram as a function of driving amplitude  $A$  and frequency  $f_0$ . The crosses are experimentally determined points on the stability boundaries. Stable patterns occur in the regions labeled (4,3) and (7,2). Slow periodic and chaotic oscillations involving competition between these modes occur in the shaded regions.

The behavior of the system as a function of  $A$  and  $f_0$  is shown in Fig. 2, where a small part of the phase diagram is reported. Below the parabolic stability boundaries, the surface is essentially flat. Above the stability boundaries, the fluid surface oscillates at half the driving frequency in a single stable mode,  $C_\ell$  and  $B_\ell$  are constant as function of times. The shaded areas are regions of mode competition, in which the surface can be described as a superposition of the (4,3) and (7,2) modes with amplitudes having a slowly varying envelope in addition to the fast oscillation at  $f_0/2$ . They oscillate periodically or chaotically at a mean frequency that is two order of magnitude smaller than  $f_0$ .

Our experimental apparatus, described in Ref. 9, allows us to study a fixed linear combination of the slow coefficients  $C_\ell(t)$  and  $B_\ell(t)$ , which we denote by  $a^\circ(t)$ . In Fig. 3 is shown the time dependence of  $a_4^\circ$  and  $a_7^\circ$ .

The slow oscillation resulting from mode competition is periodic in this case and  $a_7^\circ$  leads  $a_4^\circ$  by about  $90^\circ$ . This phase relationship is significant it implies that the mode (7,2) pump (4,3). The dynamic of the slow oscillation was explored by varying  $A$  and  $f$  separately inside of the interaction region. In Fig. 4 time series and corresponding power spectra of the slow oscillation are shown for three different driving amplitudes but fixed driving frequency of 16.05 Hz.

As the driving amplitude is increased, a chaotic state with a broad power spectrum is obtained. We characterize the chaotic behavior quantitatively by computing from the experimental data the correlation dimension  $\gamma$  of the attractor and a lower bound  $K_2$ ,



for the Kolmogorov entropy  $K$ . When the oscillation is periodic ( $A=121 \mu\text{m}$ ), we find  $\gamma=1.0 \pm 0.04$  and  $K_2=(0.01 \pm 0.01) \text{ sec}^{-1}$ . On the other hand when the slow oscillation is chaotic ( $A=190 \mu\text{m}$ ),  $\gamma=2.22 \pm 0.04$  and  $K_2=(0.1 \pm 0.01) \text{ s}^{-1}$ . These measurements clearly demonstrate that the attractor has a low (and fractional) dimension and that there is at least one positive Lyapunov exponent.

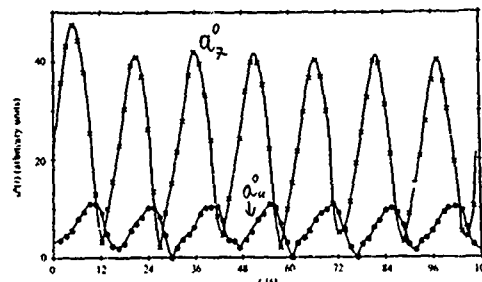


FIGURE 3  
The slowly varying amplitudes  $a_4^0$  and  $a_2^0$  oscillate periodically.

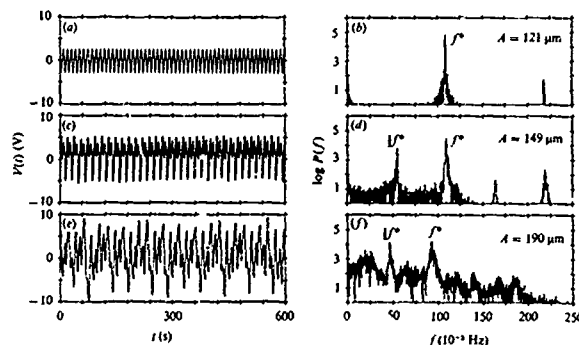


FIGURE 4  
The transition from periodic to chaotic oscillation. Time series and corresponding power spectra of the slow oscillation are shown for  $f_0=16.05 \text{ Hz}$  and three different driving amplitudes. Broad-band noise is associated with the appearance of a subharmonic  $f_0/2$  of the dominant oscillator.

This result can seem in contrast with the fact that time resolved spatial Fourier spectra show the presence of many other modes with  $\bar{Q}_z=3,8,11,14$  besides the mode (7,2) and (4,3). However this has been explained by a theory of E. Meron, I. Procaccia [11]. They start from Navier-Stokes equations with suitable boundary conditions. They can prove rigorously, using center-manifold and normal form theories that the dynamics is governed by the modes (7,2) and (4,3) and all the other modes are enslaved by these two. Finally they obtained a system of four coupled ordinary differential equations for the amplitude of the mode (7,2) and (4,3). The phase diagram of this system is in very good agreement with the experimental one. Time dependent behaviors either chaotic or periodic are indeed reproduced at the intersection of the stability curves of the two modes.

This experiment and the associated theory have shown how the incredible reduction from a large to a very small number of degrees of freedom occurs in practice. They have also shown that temporal chaotic behavior is produced by the interaction of spatial modes and that spatial order can be preserved in time dependent aperiodic regimes. This result was made possible by a time resolved analysis of the spatial patterns which allows a more direct comparison with the theory.

In other instabilities, such as (R-B convection) a time resolved analysis of spatial patterns in temporal chaotic regimes has been carried out only in few experiments and we will show in the next paragraph that also in this case the study of

spatial patterns is very useful to compare the observed behavior with that of a realistic model.

### III - RAYLEIGH-BENARD CONVECTION

#### IIIa Experimental apparatus.

We remind very briefly the properties of thermal convection in a fluid layer heated from below, that is Rayleigh-Benard instability [1]. When the temperature difference  $\Delta T$  between the two horizontal plates, confining the fluid exceeds a critical value  $\Delta T_c$ , convection begins and the fluid motion forms a periodic structure, a set of parallel rolls, with a wave number  $q \approx \pi/d$ , where  $d$  is the depth of the layer. The most relevant parameters are the Rayleigh number  $R = \alpha g \Delta T d^3 / \nu \kappa$  and the Prandtl number  $P = \nu / \kappa$ . Here  $\alpha, g, \nu, \kappa$  are respectively the volumetric expansion coefficient, the acceleration of gravity, the kinematic viscosity and the heat diffusion constant. It has been computed that for an infinitely extended horizontal layer the critical Rayleigh number at which convection sets in is  $R_c = 1708$ .

Increasing  $R$  above  $R_c$  another threshold  $R_+$  is reached where the fluid motion becomes time dependent. The value of  $R_+$  and the behavior of the fluid strongly depend on  $P$  and on the aspect ratio  $\Gamma$ , that is the ratio between the horizontal length and depth of the layer.

Rayleigh-Benard convection has been widely used to study the transition from a regular to a chaotic motion. Nevertheless spatial patterns in R-B have been studied just near the threshold of the instability in large aspect ratio cells and a good agreement with theories has been found [14]. On the contrary convective patterns in time dependent states has been investigated just in a few experiments [7-8] leaving open many question on the role that the spatial degrees of freedom play in the transition into these regimes.

Thus to have a better insight into the mechanisms leading to chaos in thermal convection and to allow a more direct comparison with numerical models we have experimentally [10] studied the evolution of the temperature field in time dependent regimes of R-B convection.

In our set up the fluid layer has horizontal size  $l_x = 4$  cm,  $l_y = 1$  cm and height  $d = 1$  cm. The  $x$  and  $y$  axis of the coordinate reference frame are respectively perpendicular and parallel to the rolls axis, (Fig. 5). The  $z$  axis is the vertical one.

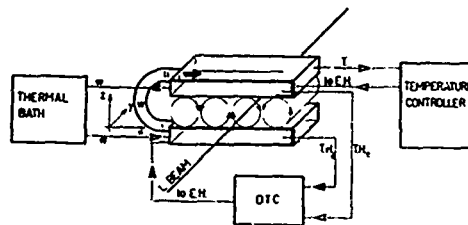


FIGURE 5

Schematic diagram of the cell:  $T, T_1, T_2$  thermistors,  $W$  water circulation, DTC temperature difference controller,  $E_d$  electric heater.

The fluid is silicon oil with Prandtl number  $= 30$ . The bottom and top plates are made of copper and the long term stability of the temperature difference is better than  $4$  m°C. This stability has been obtained with three independent temperature regulators. The first one is a water bath with a stability of about  $0.05^\circ\text{C}$ . The water circulates in the bottom and top plates where an electrical resistor is inserted in each of them. The two heating resistors are connected with other two stages of regulation. One stabilizes the temperature of the upper plate, the other controls temperature difference between the two plates. The last regulator is connected to a micro-computer that allows a complete automatization of the measurement.

The lateral walls of the cell are made of glass to allow for optical inspection. The detection system consists of a laser beam that crosses the silicon oil perpendicular to the  $(x, z)$ -plane and is deflected by the thermal gradients inside the fluid. The laser beam sweeps the  $(x, z)$ -plane and we can measure the temperature gradient averaged along  $y$  in 1024 points of the  $(x, z)$ -plane by a method described elsewhere [15]. The 1024 points are in an array with 16 rows of 64 points each. Precisely, for each position of the impinging beam, the unpercurbed zero gradient is measured by a position-sensitive

detector and recorded in a computer. Later upon application of temperature gradients we can measure the horizontal and vertical shift components, respectively proportional to the horizontal and vertical refractive index gradients  $\partial n / \partial x$  and  $\partial n / \partial z$  averaged along the y-axis, that is along the optical path of the laser beam. From these gradients one infers the temperature through the relation  $\partial T / \partial x = (\partial n / \partial T) (\partial T / \partial x)$  and similar for z. The temperature field is then easily recovered by numerical integration of the two recorded gradients. The sweeping time is fast compared to the time scales of the phenomena under study. Therefore, by this method we can study the time evolution of the temperature field.

We perform the experiment in the following way. We start from zero temperature difference between the two plates and then we increase the temperature of the bottom plate till the maximum allowed in our apparatus corresponding to about  $R=400 R_c$ . The steps in which the temperature has been increased are separated by sufficient amount of time to allow the system to relax to a stable state. This type of run has been repeated several times to check the dependence of the found regimes on the way in which the control parameter has been varied.

#### IIIb Spatial Patterns.

Analysing the fluid behavior as a function of  $r=R/R_c$  we find a stable four rolls structures at  $r=80$ . Above this threshold the regimes of the system are outlined in table I

TABLE I

Interval	r	regime	Spatial structure
I1	80-90	TD	R4 + LO
I2	90-95	S	R4
I3	95-130	TD	R4 + LO+TW
I4	130-150	S	R4
I5	150-182	TD	R4 + LO
I6	182-186	SHO	R4 + TW
I7	186-200	**	**
I8	200-300	TD	R4 + LO+TW

TW = Traveling waves

TD = Time dependent

S = Stationary

LO = Localized oscillations

SHO = Shilnikov type homoclinic orbit

R4 = 4 rolls

\* The interval I1 is not observed in all of the runs

\*\* the interval I7 presents a stationary regime in some runs and localized oscillations of very small amplitude in others.

From a run to another the interval initial positions are reproducible within 10%, whereas the length of the interval does not change sensitively. Instead the behavior of the system in the time dependent regimes can be different from a run to another. For example, in the interval I5 we can find other subintervals of periodic, hiperiodic and chaotic behavior, but their existence is related on the speed with which the temperature gradient is increased and on the previous story of the system.

So we focus just on the general features that we always observe. In particular we see in Table I that the time dependent regimes are associated with two different spatial patterns one characterized by localized oscillations the other by traveling waves.

After verifying that the dynamics does not depend sensitively on the z coordinate, except for the amplitude of T, we focus our attention just on the evolution of the horizontal component of the gradient  $u(x,t) = \partial n / \partial x$  measured at a fixed z. The horizontal gradient is in fact a direct result of the measurement and furthermore it does not contain the amplitude of the stationary gradient imposed between the two plates.

In what follows  $w(x,t) = u(x,t) - \bar{u}(x)$  and  $\bar{u}(x)$  is the time average of  $u(x,t)$ . The "energy"  $E(t)$  is the spatial average of  $w^2(x,t)$ .

Besides the study of u just in one direction allows, a more direct comparison with numerical simulations done in unidimensional partial differential equations (P.D.E.).

As an example we show in Figure 6 the evolution of w as a function of x and time t. We see here that the oscillations are localized in space both in the periodic regime Fig. 6a at  $r=83$  and in the chaotic one Fig. 6b) at  $r=87.5$ . The localization can be also quantitatively measured by making the Fourier spectrum  $S(f,x)$  of time series  $w(x,t)$  recorded in different position of the cell. The spectrum  $S(f,x)$ , with  $x=1.5$  cm is shown in Fig. 7a) at  $r=86.5$  biperiodic regime and Fig. 7b) chaotic regime at  $r=87.5$ . The amplitude of  $S(f,x)$  at  $f_1, f_2$  as a function of x at  $r=86.5$  and at  $r=87.5$  is shown in

Figure 8a-b) respectively.

The amplitude of  $S(f, x)$  changes of about 3 order of magnitude by moving the measuring point of only 4 mm. We see the high degree of localization of the oscillations. We also observe in Fig. 8b) that the maximum amplitude of the two frequencies tends to become equal at the onset of chaos.

This spatio temporal regime with localized oscillations is not the only one that we observe. Increasing  $R$  we find other windows of time dependent regimes that were characterized by the presence of traveling waves. As an example we report in Fig. 9b) the evolution of  $w(x, t)$  at  $r=230$  where a biperiodic regime was present. We see that there are waves starting in the center of the cell that propagate toward the sides of the cell. This traveling structure is more evident in Fig. 9c) where the spatio temporal correlation function  $C(\Delta, \tilde{\omega}) = \int \int w(x+\Delta, t+\tilde{\omega})w(x, t)dx dt$  is reported. We see that the extrema (Fig. 9d) of  $C$  propagates with a velocity of about 0.06 cm/sec. This velocity is consistent with the velocity scale constructed with  $\dot{w}/d=0.03\text{cm/sec}$  for our fluid.  $w(x, t)$  the time evolution of the maxima of  $C(\Delta, \tilde{\omega})$  measured in the chaotic regimes at  $r=268$  are reported in Fig. 10. We see that the spatial behavior does not change sensitively when the system is driven from a periodic to a chaotic time dependent regime.

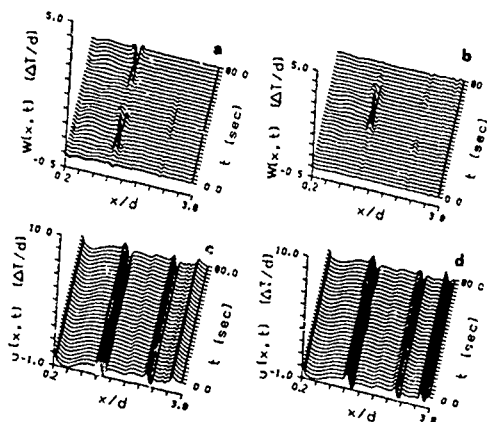


FIGURE 6

Evolution of the time dependent component of the horizontal temperature gradient  $w(x, t)$  recorded at  $r = 83.5$  a) and  $r = 87.5$  b). The corresponding horizontal gradients  $u(x, t)$  are instead reported in c) and d) respectively.

The transition between localized oscillations and traveling waves occurs at  $r \simeq 180$  with a regime that has an evolution like that shown in Fig. 11a). This evolution is characterized by the presence of quasi laminar oscillations that are interrupted by very large bursts. This regime is produced by a sort of competition between two spatial structures, one associated with the laminar period, the other with the fast transient. This is shown in Figure 11b) where the temporal evolution of  $u(x, t)$ , averaged over 4 periods of the fast oscillation of Figure 11a, is reported. We see that during the fast transient of Figure 11a, the time averaged structure of the convective motion shifts in an appreciable way the position of the rolls boundaries (points where

This change corresponds to a switch of energy (the energy in a mode is the amplitude of the spatial Fourier spectrum) between the odd and even modes of the spatial Fourier transform of  $w(x, t)$ . The period of time  $T$  between two bursts diverges with the following law  $T_b = 850(r - r_0)^{-0.1}$  sec when the bifurcation point for this regime  $r_0 = 182.5$  is approached.

It is important to note that the presence of two different time dependent spatial patterns, one characterized by localized states and the other by traveling waves are also observed in numerical simulations of some partial differential equations [4] and in particular in the Spiegel model [4b] written just to describe buoyancy driven convection in astrophysics context.

The transition between localized oscillation and traveling in this equation takes places via a Shilnikov type homoclinic bifurcation. This bifurcation is characterized by a time evolution like that shown in Fig. 11a and is related with big changes of the spatial structure during the burst as indeed happens in our experiment.

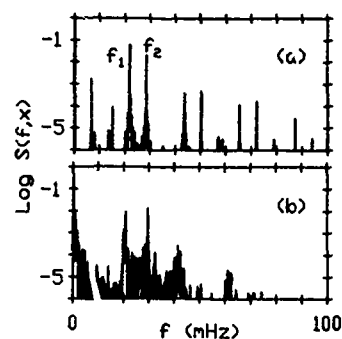


FIGURE 7  
Fourier Spectrum  $S(f, x)$  of the time series of  $u(x, t)$  recorded in the point  $x=1.5$  at  $r=86.49$  biperiodic regime a) and at  $r = 87.49$  b) chaotic regime.

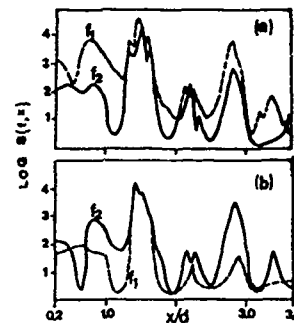


FIGURE 8  
Amplitude  $S(f, x)$  at frequency  $f$ ,  $f$  as a function of the  $x$  coordinate in the biperiodic regime a) and in the chaotic regimes  $r = 87.5$  b).

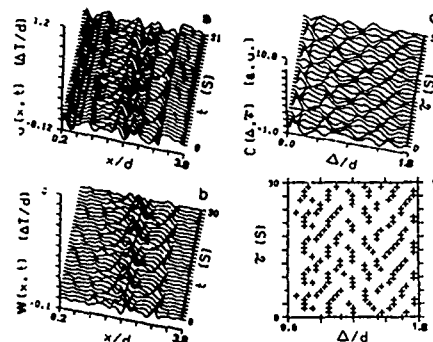


FIGURE 9  
Traveling waves. Time evolution of  $u(x, t)$  a) and  $w(x, t)$  b) recorded at  $r=230$ .  $C(\Delta, \tau)$  is reported in c). In d) the time evolution of the position of the maxima of  $C$  (crosses) is shown.

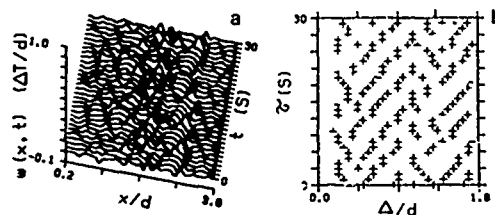


FIGURE 10  
Traveling waves. a) time evolution at  $w(x, t)$  recorded at  $r=268$ , b) time evolution of the maxima positions of the spatio-temporal correlation functions  $C(\Delta, \tau)$ .

### IIIc Fractal dimension and metric entropy

Several methods have been proposed [16] to compute fractal dimension  $D$  and metric entropy (M.E.) from experimental time series. These two quantities are indeed very useful to characterize the chaotic dynamics. To compute  $D$  and M.E. the dynamics of the system in phase space has to be reconstructed from experimental time series.

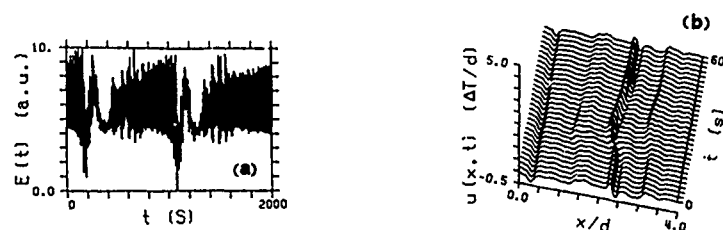


FIGURE 11

Transition between localized oscillations and traveling waves.

a) temporal evolution of the energy.

b) temporal evolution of the spatial structure  $u(x,t)$  averaged over 4 periods of the fast oscillation.

In many experiments only a single scalar signal  $V(t)$  is monitored. In this case the attractor can be reconstructed invoking the embedding theorem /1/ (see Appendix). However in extended systems the use of a single scalar signal cannot always describe the global behavior of the system. In several experiments done in fluid systems /17/ the scalar signal  $V(t)$ , used to reconstruct the attractor and to compute F.D., is often obtained by the local measurement of a variable (e.g. horizontal temperature gradient, vertical component of the velocity). On the basis of the results described in the previous section some questions arise naturally. Does F.D. depend on the point where the measurement has been taken? Do we get different results using a spatially averaged measurement instead of a local one? Furthermore with our experimental apparatus there are other ways of constructing the phase space. Suitable  $m$ -dimensional phase spaces can be generated by using as coordinates either the mode amplitudes of the spatial Fourier transform of  $u(x,t)$  or simply the  $u(x_i,t)$  measured in  $m$  different points  $x_i = i \Delta$ . In what is following the first one will be called Fourier space (F.S.) and the second one space shifted coordinate phase space (S.C.S.).

To estimate  $D$  the correlation dimension  $\mathcal{D}/16a/$  (see appendix) is computed with a number of data points  $N$  ranging from 4000 to 8000.

The correlation dimension obtained using the embedding technique, the F.S. and S.C.S. will be indicated respectively with  $\mathcal{D}$ ,  $\mathcal{D}_F$ ,  $\mathcal{D}_S$ . Using the method proposed in Ref. 18 we have also computed the quantity  $K_2$ , (see appendix) that is a lower bound for the metric entropy. We checked the dependence of  $\mathcal{D}$  and  $K_2$  on the point of the cell where the time series have been recorded. The results are reported in Figs. 12a and 12b respectively at  $r=267$  and  $r=270$ . In Figs. 12c and 12d the corresponding  $K_2$  is shown. We see that  $\mathcal{D}$  and  $K_2$  slightly depend on the point of measurement in both cases.

We point out that this result is not correlated with the local signal-to-noise ratio whose reduction normally produces an increasing in the estimation of  $\mathcal{D}/19/$ .

For a constant instrumental noise, the above ratio is proportional to the local time dependent amplitude whose rms value is shown in Figs. 12e and 12f. (The maximum in the vertical scale corresponds to a signal to noise ratio of about  $10^4$ .) Comparing Figs. 12c and 12b respectively with Figs. 12e and 12f, we see that an increasing of fractal dimension does not necessarily correspond to a decreasing of the signal amplitude. More specifically there are points where  $\mathcal{D}$  is large and the amplitude of the signal is large. This fact clearly demonstrates that the spatial dependence of  $\mathcal{D}$  is intrinsic of the fluid behavior. Indeed it is related to neither to signal to noise ratio nor to the delay time used to reconstruct the attractor.

The values of  $\mathcal{D}$  have been compared with  $\mathcal{D}_F$  and  $\mathcal{D}_S$ . We find that  $\mathcal{D}_F$  is very close to the value obtained by averaging the  $\mathcal{D}$  computed in different positions of the cell.  $\mathcal{D}_S$  is equal, within error bars, to  $\mathcal{D}$ .

The results of  $\mathcal{D}$ ,  $\mathcal{D}_F$  and  $K_2$  at different  $r$  are summarised in Table 2. The results of  $\mathcal{D}$  reported are those obtained from the time series  $u(x,t)$  measured in  $x=2$  cm. In the periodic and quasiperiodic case  $\mathcal{D}$  does not change as a function of the position within error bars.

TABLE 2

$R/R_c$	$\mathcal{D}$	$\mathcal{D}_F$	$K_2$
220	$1.02 \pm 0.001$	$1.04 \pm 0.02$	$0.03 \pm 0.01$
252	$2.14 \pm 0.01$	$2.31 \pm 0.06$	$0.06 \pm 0.01$
268	$2.45 \pm 0.05$	$2.61 \pm 0.06$	$0.08 \pm 0.01$
270	$3.68 \pm 0.08$	$4.14 \pm 0.05$	$0.15 \pm 0.01$
271	$3.89 \pm 0.1$	$4.20 \pm 0.1$	$0.18 \pm 0.01$

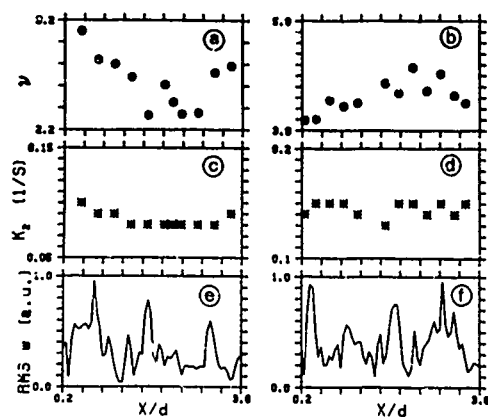


FIGURE 12

The spatial dependence of the correlation dimension (a)  $K_2(c)$  and the signal amplitude of  $w(x,t)$  measured at  $r=267$ . The same quantities measured at  $r=270$  are respectively shown in b), d), f). The errors of  $y$  are about 3% and those of  $K_2$  about 5%.

#### IV - CONCLUSION

The main result of this investigation is that the study of the spatial feature of temporal chaotic regime is very important to understand the physical mechanism leading to chaos.

Besides, the results described in section IIIc on the calculation of fractal dimension and metric entropy open some interrogatives on the reason why  $y$  depends on the position and  $\overline{y}, \overline{y}$  are equal to the averaged value of  $y$ .

Much more theoretical and experimental work will be necessary to better understand this problem and the role of spatial pattern in time dependent regimes. We believe that our approach can be very useful in the study of the transition from low dimensional chaos to turbulence where the system exhibit a chaotic behavior both in space and time.

## APPENDIX

Many phenomena exhibit chaotic states that can be described by a low dimensional strange attractor in phase space /1/. Such an object is characterized by fractal dimension and metric entropy and several methods have been proposed to compute them from experimental time series /16/. The former roughly estimates the number of independent variables involved in the process. The latter measures the average rate of information loss per unit time. Fractal dimension and metric entropy can be advantageously used to discriminate in an experiment between a purely stochastic phenomenon and low dimensional chaos /19/. Also the direct measure of the Lyapunov exponents is useful to characterize the chaotic motion. They measure the average divergences of the trajectory in phase space. These three quantities are indeed related. The metric entropy is the sum of the Lyapunov exponents and fractal dimension is related to the Lyapunov exponents by the Kaplan-York formula.

## A1 Phase Space

In many systems only a single variable  $V(t)$  is monitored the phase space of the system has to be reconstructed invoking the embedding theorem,  $V(t)$  that is constructing a vector  $x(t)$  of coordinates  $\{V(t), V(t+\tau), \dots, V(t+(m-1)\tau)\}$ , where  $m$  is the dimension of the space and  $\tau$  an arbitrary delay. (In practice  $\tau$  can be varied only within a certain range to have a reliable estimation of fractal dimension /20/. In Ref. 21 a method to find the optimum value of  $\tau$  has been recently proposed).

Examples of the projection of the phase space on the plane  $(V(t), V(t+\tau))$  for the experiment described in section I are shown in Fig. 4. The delay  $\tau$  is 3 sec.

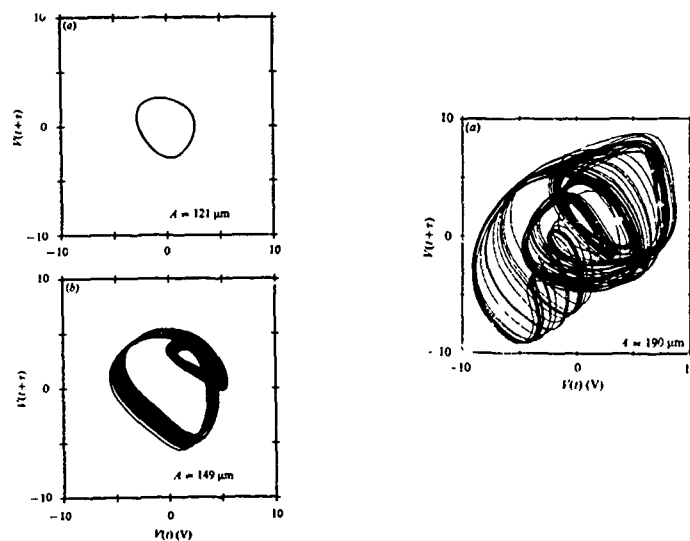


Figure A1

Phase portrait for the data of Figure 4. Divergence of nearby orbits can be seen quantitatively in the phase portrait.

## A2 Fractal dimension

A strange attractor is in general an object of fractional dimension. This means that the number of cells of size  $\epsilon$  needed to cover the attractor scales as  $\epsilon^{-D}$ , where  $D$  is the fractal dimension. The calculation of  $D$  is a useful way to characterize the degree of chaos but it needs a very big memory and it consumes a lot of computer time. However several other definitions of dimension lead to more practical algorithms.

To estimate fractal dimension  $D$  we use the correlation dimension  $\nu$  that is smaller than  $D$ . However in practical cases the difference  $D-\nu$  turns out to be very small. The correlation dimension is defined in terms of  $C(\epsilon)$ , number of data points whose separation in phase space is less than  $\epsilon$  (divided by  $N^2$ ). For  $N \rightarrow \infty$  this quantity scales as  $\epsilon^\nu$ , therefore:

$$\nu = \lim_{\epsilon \rightarrow 0} \frac{\log C(\epsilon)}{\log \epsilon}$$



An example of  $C(\varepsilon)$  for the chaotic attractor of Fig. 4c is shown in Fig. A2 for different embedding dimensions. The local derivative of  $C(\varepsilon)$  is shown in Fig. A3a. The slope can be seen to reach a limit value in the scaling region  $-1.5 < \varepsilon < 0$  and does not increase once  $m$  is larger than about 4.

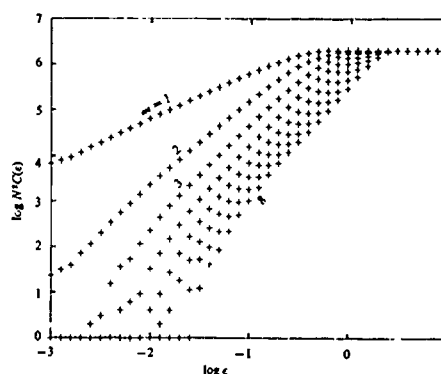


Figure A2

The correlation function  $C(\varepsilon)$  for various values of the embedding dimension  $m$ . The limiting slope for large  $m$  is the correlation dimension  $\nu$  of the attractor.

The height of the plateau is  $2.20 \pm 0.04$  that is the correlation dimension of the attractor at  $A = 190 \mu\text{m}$ .

For values of  $\varepsilon$  smaller than those in the scaling region that is comparable with the noise level the slope has about the same value of the embedding dimension  $/19/$ .

#### A3 Kolmogorov Entropy

The Kolmogorov entropy measures the average rate of information lost per unit time and it is the sum of the positive Lyapunov exponents. From the measurement of  $C(\varepsilon)$  it is also possible to determine  $K_2$  that is a lower bound of the Kolmogorov entropy. It is defined as

$$K_2 = \lim_{\varepsilon \rightarrow 0} \lim_{m \rightarrow \infty} \frac{\ln C_m(\varepsilon) - \ln C_{m+1}(\varepsilon)}{\varepsilon}$$

Here  $C_m(\varepsilon)$  indicates the correlation function  $C(\varepsilon)$  computed for the embedding dimension  $m$ . An example is shown in Fig. A4 for the chaotic data at  $A = 190 \mu\text{m}$  reported in fig. 1 of section 1. We see that  $K_{2,m}$  reaches a limiting value of  $(0.1 \pm 0.01) \text{sec}^{-1}$ . this means that at least 1 Lyapunov exponents is positive.

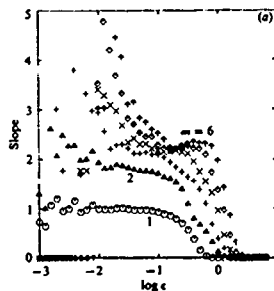


Figure A3

Measurements of correlation dimension  $\nu$ . The derivative (local slope) of the function  $\log C(\varepsilon)$  with respect  $\log \varepsilon$  reaches a limiting value in the scaling range of  $d = 2.20 \pm 0.04$  for  $m > 4$ .

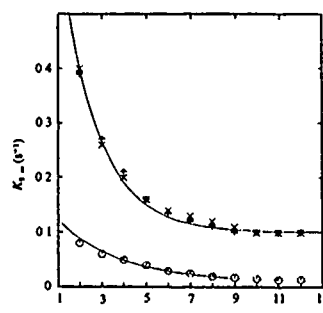


Figure A4

Dependence on embedding dimension of the function  $K_{2,m}$  (defined in (5.3)), which is less than or equal to the sum of the positive Lyapunov exponents. The curves are fits to the data for the chaotic state (upper points) and periodic state (lower points), for  $\log = -1$ . The positive limit of the upper curve for large  $m$  demonstrates that at least one Lyapunov exponent must be positive, so that the trajectories exhibit exponential divergence.

#### A4 Lyapunov exponents

We analyze now the algorithm proposed in Ref. 1b for computing Lyapunov exponents from an experimental time series. We first describe the method and then we apply it to an experiment of Rayleigh-Benard convection /22/.

The discussion below deals with scalar signal but the method can be easily extended to multidimensional signal.

Conceptually, the algorithm to be discussed involves the following steps:

- reconstructing the dynamics in a finite dimensional space,
- obtaining the tangent maps to this reconstructed dynamics by a least squares fit,
- deducing the Lyapunov exponents from the tangent maps.

We now consider these different steps in detail.

(a) In general the variable experimental  $V(t)$  is sampled at fixed time interval so we define  $x_i = V(i\Delta t)$  for  $i = 1, \dots, N$  where  $N$  and  $\Delta t$  are respectively the number of data points and  $\Delta t$  the sampling time. We choose an embedding dimension  $d_E$  and construct a  $d_E$ -dimensional orbit representing the time evolution of the system by the time-delay method. This means that we define

$$x_i = (x_i, x_{i+1}, \dots, x_{i+d-1}), \quad (1)$$

for  $i = 1, \dots, N-d+1$ .

(b) Having embedded our dynamical system in  $d_E$  dimension, we want to determine the  $d_E \times d_E$  matrix  $T_i$  which describes how the time evolution sends small vectors around  $x_i$  to small vectors around  $x_{i+1}$ . The matrix  $T_i$  is obtained by looking for neighbors  $x_j$  of  $x_i$  and imposing

$$T_i(x_j - x_i) \simeq x_{j+1} - x_{i+1}. \quad (2)$$

the matrix  $T_i$  is determined by a least square fit with the condition  $|x_j - x_i| < \epsilon$ . Note that, in view of (1), (2), the matrix  $T_i$  has the form

$$T_i = \begin{bmatrix} 0 & 1 & 0 & \dots & 0 \\ 0 & 0 & 1 & \dots & 0 \\ \vdots & \vdots & \vdots & \ddots & \vdots \\ 0 & 0 & 0 & \dots & 1 \\ a_1 & a_2 & a_3 & \dots & a_{d_E} \end{bmatrix}$$

(c) Step (b) gives a sequence of matrices  $T_1, T_{i+1}, T_{i+2}, \dots$ . One determines successively orthogonal matrices  $Q_{(j)}$  and upper triangular matrices  $R_{(j)}$  with positive diagonal elements such that  $Q_{(0)} =$  unit matrix and

$$\begin{aligned}
 T_1 Q(0) &= Q(1) R(1) \\
 T_2 Q(1) &= Q(2) R(2) \\
 &\vdots \\
 T_{1+j} Q(j) &= Q(j+1) R(j+1) \\
 &\vdots
 \end{aligned}$$

Then the Lyapunov exponents  $\lambda_n$  are given by 
$$\lambda_n = \frac{1}{K \Delta t} \sum_{j=0}^{K-1} \ln R(j)_{nn}$$

where  $K \leq (N-d_E-1)$  is the available number of matrices. As an example we present in Fig. A5 the Lyapunov exponents for the Lorenz model as a function of  $d_E$ . The horizontal dashed lines represent the correct values. To reduce the dimension of the matrix  $T$ , without spoiling the calculation of the first positive Lyapunov exponents, that can be useful when  $d_E$  becomes very large, we define a  $d_M$  such that

$$d_E = (d_M - 1) m + 1$$

and the associate vector is

$$x_1 = (x_1, x_{1+m}, \dots, x_{1+(d_M-1)m})$$

To maintain the same form of  $T_1$ , providing of changing  $d_E$  with  $d_M$  the (2) is replaced by the condition

$$T_1(x_i - x_j) \leq x_{i+m} - x_{j+m}$$

However this does not means that the number of used points are reduced by a factor  $m$  but all the data points are used to find the nearest neighbours.

We have applied the method to the R-B experiment described in section 3. Specifically we have studied the chaotic regime in the interval  $170 < R/R_c < 185$  where the system exhibited a transition to chaos via intermittency. The main frequency was about 75 mHz. To have a sufficient number of neighbours in the calculation of  $T_1$ , 40000 points with a sampling frequency of 5 Hz, have been recorded for each measurement. This way, the time evolution of the system is followed for about 600 periods of the main oscillation. Many tests have been done to verify how Lyapunov exponents depend on  $d_E$  and  $d_M$ . It has been found that the value of  $\lambda$  is sufficiently stable in the interval  $20 < d_E < 25$  and  $5 < d_M < 8$ . The results are reported in Figure A6, where the values of the positive Lyapunov exponents are shown as a function of  $R$  for different  $d_E$  and  $d_M$ . We see that the quantitative behavior of the curves is similar and the difference between them is about 10%. The measurements were done for  $R/R_c = 171.41, 174.08, 176.75, 182.10, 183.44, 184.79$ . Figs. A7 show details for  $R/R_c = 182.10$ . By moving the detection point inside the cell of about 1cm and keeping  $R$  at the last value shown in figure A7 we find that the Lyapunov exponents change by less than 5%. As a conclusion, the positive Lyapunov exponents in the chaotic regime of a R-B convection experiment have been determined using the method proposed in Ref. 1b. Even though the error of the measurement is not small (about 10%) it is still possible to follow how the number of the Lyapunov exponents and their values change as a function either of the control parameter  $R$  or of the position where the measurement has been recorded inside the fluid.

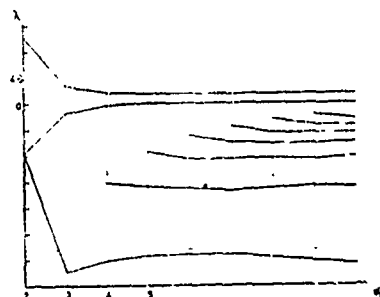


Figure A5  
Lyapunov exponents for the Lorenz model as a function of  $d_M$ .

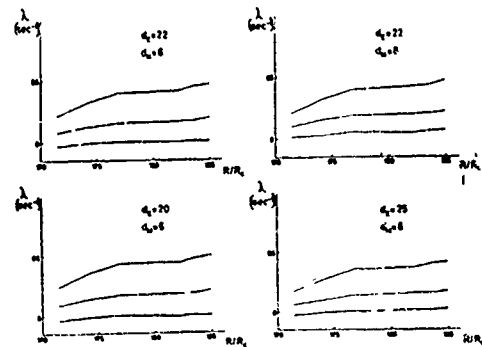


Figure A6

The three largest Lyapunov exponents as a function of the Rayleigh number for different  $d_M$  and  $d_E$ .

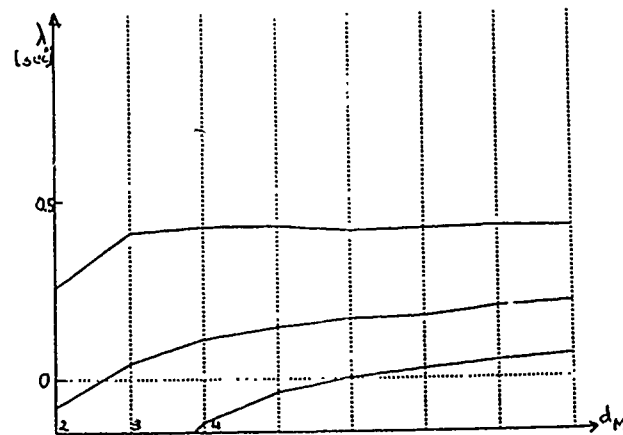


Figure A7

The largest 3 Lyapunov exponents as a function of  $d_E$  at  $R/R_c = 182.5$ , for different values of  $d_M$ .

## REFERENCES

- 1a) P. Bergé, Y. Pomeau, C. Vidal, *L'ordre dans le chaos*, Herman (Paris).
- b) J.P. Eckmann, D. Ruelle, *Rev. Mod. Phys.* 57 (1985) 617.
- 2) M. Giglio, S. Musazzi, E. Perini, *Phys. Rev. Lett.* 52 (1984) 240.
- 3) M.H. Jensen, L.P. Kadanoff, A. Libchaber, I. Procaccia, J. Stavans, *Phys. Rev. Lett.* 55 (1985) 2798.
- 4a) J.M. Hyman, B. Nicolaenko, Los Alamos Report UR-86-1388. J.M. Hyman, B. Nicolaenko, *Physica* 180 (1986) 13.
- b) B. Nicolaenko, *Proceeding of the Conference Chaos* 87.
- 5) A.R. Bishop, K. Fessler, F.S. Lamdhal, W.C. Kerr, M.B. Williams, S.E. Trullinger, *Phys. Rev. Lett.* 50 (1983) 1095.
- H. Chaté, P. Manneville to be published in *Phys. Rev. Lett.*
- 6) G.L. Oppo, R. Kapral, *Phys. Rev.* A33 (1986) 4.19.
- 7) J. P. Gollub, S.V. Benson, *J. Fluid Mech.* 100 (1985) 2927.
- 8) M. Dubois, P. Bergé, *Phys. Lett.* 73 (1983) 1095.
- 9) S. Ciliberto, J.P. Gollub, *J. Fluid Mech.* 158 (1985) 381.
- 10) S. Ciliberto, F. Simonelli, *Europhysics Lett.* 2 (1986) 285.
- S. Ciliberto, M.A. Rubio, to be published in *Physica Scripta*.
- 11) E. Meron, I. Procaccia, *Phys. Rev. Lett.* 93 (1986) 1323.
- 12) Y. Kuramoto, Y. tsuzuky, *Progr. Theor. Phys.* 55 (1976) 356.

- 13) P.L. Garcia-Ybarra, M.G. , M.G. Velarde, Submitted to Physics of Fluids.
- 14) A. Pocheau, V. Croquette, P. Le Gal, Phys. Rev. Lett. 55 (1985) 1094.  
M.S. Heutmaker, P.N. Fraenkel, J.P. Gollub, Phys. Rev. Lett. 54 (1985) 1369.  
G. Ahlers, D.S. Cannell, V. Steinberg, Phys. Rev. Lett. 54 (1985) 1373.
- 15) S. Ciliberto, F. Francini, F. Simonelli, Opt. Comm. 54 (1985) 251.
- 16a) P. Grassberger, I. Procaccia, Phys. Rev. Lett. 50 (1983) 346.  
b) J.D. Farmer, E. Ott, J.A. Yorke, Physica 7D (1983) 153.  
R. Badii, A. Politi, Journal of stat. Phys. 40 (1985) 725.
- 17) B. Malraison, P. Atten, P. Bergé, M. Dubois, J. Phys. Lett. 44 (1983) 897.  
M. Giglio, M. Musazzi, P. Perini, Phys. Rev. Lett. 53 (1984) 240.
- 18) P. Grassberger, I. Procaccia, Phys. Rev. A28 (1983) 259.
- 19) A. Ben Mizracni, I. Procaccia, P. Grassberger, Phys. Rev. A29 (1984) 975.
- 20) J.P. Caputo, B. Malraison, P. Atten, Dimension and entropy in chaotic systems, G. Mayer-Kress ed., Springer Verlag (1986).
- 21) A.M. Fraser, H.L. Swinney, Phys. Rev. A3 (1986) 1134.
- 22) J.F. Eckmann, S. Oliffson Kamphorst, D. Ruelle, S. Ciliberto, Phys. Rev. A34 (1985) 4971.

## LATTICE GAS HYDRODYNAMICS

Jean Pierre BOON and Alain NOULLEZ

Faculté des Sciences, C.P. 231

Université Libre de Bruxelles

B-1050 Bruxelles, Belgium

## 1. MULTI-SCALE FLUID DYNAMICS

A fluid is a multi-scale system whose dynamics cannot be described uniquely. At the microscopic level such a description involves the virtually infinite complexity of the many-body problem, which can be bypassed by statistical mechanical methods. At large scale - that is for wavelengths large compared to the molecular size - the fluid can be treated as a continuous medium and is therefore adequately described by classical hydrodynamics. Now, complexity is also reflected at large scale by the non-linearities in the hydrodynamical equations, which, except for particular (usually oversimplified) cases, cannot be solved explicitly. The connection between microscopic level - the domain of molecular dynamics - and macroscopic level - the domain of hydrodynamics - is established by Liouville-Boltzmann kinetic theory /1/. Correspondingly, three computational approaches have been developed for the numerical study of fluid dynamics.

(i) The approach via continuous medium description is to solve numerically the Navier-Stokes equations /2/, which raises the usual difficulties associated with the numerical treatment of partial differential equations. In practice, feasibility is achieved by finite elements methods and finite difference equations; these methods, which use quite involved numerical techniques, have produced spectacular results. However, they require considerable computational power and so turn out to be very expensive.

(ii) The molecular dynamics approach starts from a microscopic modeling of the fluid, simulating a real system of interacting particles. This method has been used extensively for studying thermodynamic and transport properties as well as small scale dynamical behavior of fluid systems /1,3/. Recently it has been extended to investigate systems subject to external constraints /4/. The major difficulty here arises from the ratio of time scales and spatial scales, i.e. the ratio of the characteristic hydrodynamic time versus the molecular interaction time, and the ratio of hydrodynamic wavelength versus intermolecular potential range. Both quantities assume large values; as a result molecular dynamics simulations require long computation times and large systems (i.e. large number of particles), and consequently costly computational means.

(iii) Quite recently, the development of a "poor man version" of the molecular dynamics approach has been stimulated by progress and perspectives in parallel computers. Similarly as for molecular dynamics simulations, the prediction of flows in fluids will follow from a microscopic description of interacting particles, but here the particles are confined to points moving along the links of a regular lattice, and interactions reduce to simple mathematical rules. The motivation for using a lattice gas (in fact, a well known model system in Statistical Physics) to simulate hydrodynamics stems from the idea that the details of the microscopic properties should be

unimportant to the macroscopic behavior of the fluid. So whether the fictitious microworld one uses is a caricature of a real fluid does not matter as long as it produces correct hydrodynamics. To what extent does lattice gas hydrodynamics meet this goal? In order to answer this question, we shall first build up the constitutive elements to construct a lattice gas; then we shall put a model system to work and present the results of hydrodynamic simulations; finally the computational aspects of present and future realizations will be reviewed.

## 2. THE LATTICE GAS

In a sense, the lattice gas approach to hydrodynamics simulation appears as intermediate between the two other numerical methods ((i) and (ii) in section 1) in the way kinetic theory establishes the connection between molecular dynamics and hydrodynamics. Indeed the hydrodynamic equations can be obtained from kinetic theory by multi-scale expansion, i.e. with the expansion parameters:  $\lambda/L$  ( $\lambda$ =mean free path;  $L$ =hydrodynamic length) and  $\tau_c/\tau_H$  ( $\tau_c$ =molecular interaction time;  $\tau_H$ =hydrodynamic time). At low (and up to moderate) densities, the Boltzmann approximation combined with the Chapman-Enskog method yields the hydrodynamic equations and the transport coefficients /5/. At high densities, there is no natural scale separation, and smallness parameter expansion breaks down; one then uses the Green-Kubo-Zwanzig autocorrelation formalism to obtain the dynamical properties /1/. However, these methods are unable to treat non-linear hydrodynamics. So, the question arises as to how a kinetic model can be constructed to simulate hydrodynamics? Such a program will require to define (i) proper mathematical objects (e.g. in classical hydrodynamics, density, momentum, and energy), and (ii) appropriate rules governing them (e.g. the hydrodynamic equations).

In constructing the lattice gas model, one introduces a primary simplification (of considerable computational convenience) by discretizing space (point particles on a lattice), time, and velocity. Each node on the lattice will behave as a Boolean processor updated at each time step according to the rules "connecting" neighboring nodes (via the lattice links), which rules must satisfy conservation laws (mass, i.e. particle number; momentum; and energy). Such a system appears as a Cellular Automaton /6/ with interactions restricted to first neighbors according to a set of collision rules to be specified.

## 3. THE HPP MODEL

A 2-D square lattice model was first proposed by Hardy, de Pazzis, and Pomeau /7/ in the mid-seventies to investigate the ergodic problem and was reactivated about ten years later for attempting to simulate hydrodynamics /8/. Consider a plane square lattice where each node has its state defined by a 4-bit word to represent the presence (or the absence) of particles with discrete velocities (1= particle with unit velocity; 0=no particle) on each of the four links connecting to the four neighboring nodes (see Fig.1). So each node has  $2^4$  possible input configurations and as many possible output configurations, which yields  $16^{16}$  possible rules, only a limited number of them being acceptable according to conservation laws. The collision rules are shown in Fig.2; note that the convention of outgoing arrows is usually adopted to indicate to which node particles are associated. The model is referred to as HPP.

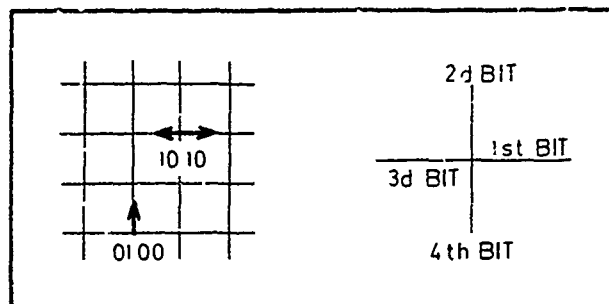


Fig.1. b-bit word representation of node state (here  $b=4$ )

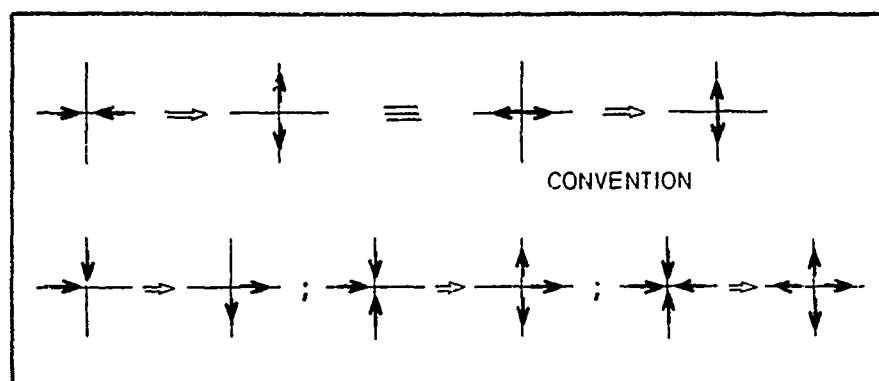


Fig.2. Collisions for HPP model. Note that only collisions of the first type are efficient (i.e. produce momentum transfer).

An exclusion principle is introduced in that no two particles with same velocity  $\vec{c}_i$  can occupy simultaneously the same link (or site  $i=0,1,2,3$ ). Obviously, collision rules must be constructed so as to satisfy conservation laws, i.e. number of particles and momentum. Note that energy conservation is degenerate here ( $C^2=1$ ), which is unimportant for incompressible or isothermal flows. (Such a lattice gas is a model fluid with equal specific heats,  $C_p=C_v$ , and equal compressibilities,  $\kappa_s=\kappa_T$ ).



## 4. THE MICRODYNAMICAL EQUATIONS

One defines the state of a node at time  $t_*$  and position  $\vec{r}_*$  on the lattice by the Boolean field :  $n_i(t_*) = \{n_i(t_*, \vec{r}_*); \vec{r}_* \in \mathcal{L}\}$ , where  $i$  denotes the site bit (direction, defined mod.4) and  $*$  indicates discrete variables. The updating rule for the cellular automaton follows from a 2-step process : collision, followed by propagation.

(1) Collision : the state of site  $i$  after collision is given by its state before collision minus the depopulating contribution plus the populating contribution, i.e.

$$n'_i = n_i - n_i n_{i+2} (1 - n_{i+1}) (1 - n_{i+3}) + n_{i+1} n_{i+3} (1 - n_i) (1 - n_{i+2}) \quad (1)$$

(2) Propagation : after collision, particles are shifted one unit lattice length over one unit time step, so that the complete evolution equation reads

$$n_i(t_*+1, \vec{r}_* + \vec{c}_i) = n_i(t_*, \vec{r}_*) + \Delta_i \quad (2)$$

$$\Delta_i = n_{i+1} n_{i+3} \bar{n}_i \bar{n}_{i+2} - n_i n_{i+2} \bar{n}_{i+1} \bar{n}_{i+3} \quad (3)$$

evaluated at  $t_*$  and  $\vec{r}_*$ , and where  $\bar{n}_i = 1 - n_i$ . An explicit example is shown in Fig.3 and a global example of updating is given in Fig.4. Note that this lattice gas model is deterministic (a given configuration at time  $t_*$  yields the  $(t_*+1)$  configuration uniquely).

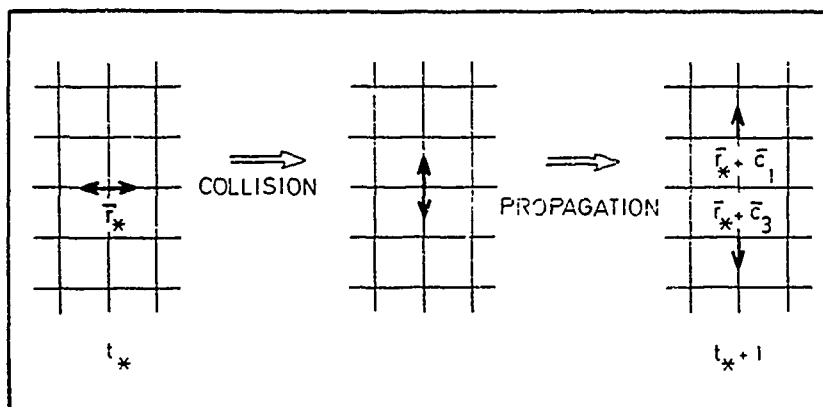


Fig. 3. Example of updating rule according to Eq.(2) :

$$n_i(t_*+1, \vec{r}_* + \vec{c}_i; i=1,3) = 0+1-0 = 1$$

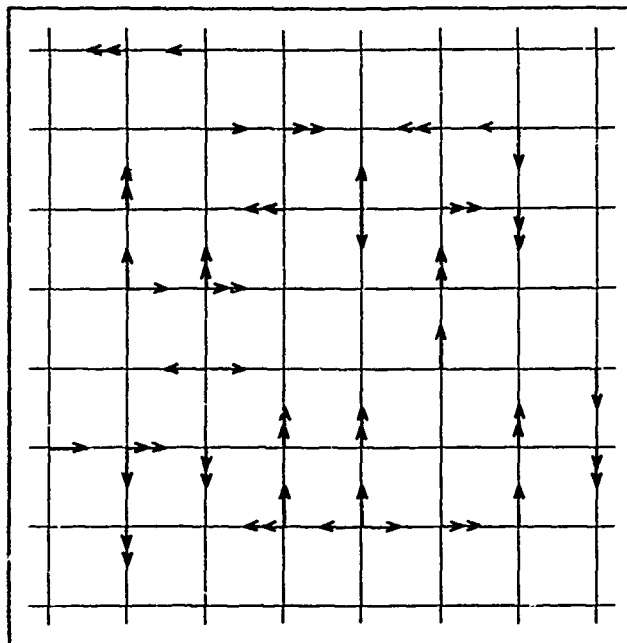


Fig. 4. Global example of evolution of cellular automaton from time  $t_*$  (single arrows) to time  $t_*+1$  (double arrows).

#### 5. THE MACRODYNAMICAL EQUATIONS

The average population is defined as the occupancy probability of site  $i$  at node  $\bar{r}_*$  at time  $t_*$ , that is [9]

$$N_i(t_*, \bar{r}_*) = \langle n_i(t_*, \bar{r}_*) \rangle \quad (4)$$

where the brackets denote an ensemble average over initial configurations (see section 8). It then follows from conservation, i.e.  $\sum_i \Delta_i = 0$  and  $\sum_i \bar{c}_i \Delta_i = 0$ , that

$$\sum_i [N_i(t_*+1, \bar{r}_* + \bar{c}_i) - N_i(t_*, \bar{r}_*)] = 0 \quad (5)$$

$$\sum_i \bar{c}_i [N_i(t_*+1, \bar{r}_* + \bar{c}_i) - N_i(t_*, \bar{r}_*)] = 0 \quad (6)$$

Next one defines the density and the mass current respectively by

$$\rho(\bar{r}_*, t_*) = \sum_i N_i(t_*, \bar{r}_*) \quad ; \quad \underline{j}(\bar{r}_*, t_*) = \sum_i \bar{c}_i N_i(t_*, \bar{r}_*) \quad (7)$$

or equivalently the density per site :  $d = \rho/b$ , and the mean velocity  $\underline{u} = \underline{j}/\rho$ , where we have introduced the generalization to a set of  $b$  vectors  $\underline{c}_i (i=0, \dots, b-1)$  with components  $C_{i\alpha} (\alpha=1, \dots, D)$  and modulus  $C$ , for a  $b$ -nearest-neighbor  $D$ -dimensional lattice. (For the HPP model,  $b=4$ ,  $D=2$ , and  $C=1$ ).

Most important is that  $\rho$  and  $\underline{j}$  (or  $d$  and  $\underline{u}$ ) are slow variables, that is they vary over a spatial range and on a time scale which are large compared to the microscopic space and time scales. Now the dynamical behavior of the system involves characteristic times related to (i) relaxation to local equilibrium ( $\tau_0$ ); (ii) sound propagation ( $\tau_s$ ), and (iii) dissipation ( $\tau_D$ ), with  $\tau_0 \ll \tau_s \ll \tau_D$ . Considering the spatial scale expansion parameter  $\varepsilon$ ,  $\tau_s$  and  $\tau_D$  will scale as  $\varepsilon^{-1}$  and  $\varepsilon^{-2}$  respectively, whereas local equilibrium relaxation is independent of scaling (i.e.  $\tau_0 \sim \varepsilon^0$ ). So a multi-scaling follows with time variables  $t_*$ ,  $t_1 = \varepsilon t_*$ ,  $t_2 = \varepsilon^2 t_*$  and space variables  $\underline{F}_*$ ,  $\underline{F}_1 = \varepsilon \underline{F}_*$ . Consequently, not too far from equilibrium the population distribution function  $N_i$  may be expanded as

$$N_i = N_i^{(0)}(t, \underline{F}) + \varepsilon N_i^{(1)}(t, \underline{F}) + O(\varepsilon^2)$$

with  $N_i^{(0)}$ , the equilibrium distribution function /10/

$$N_i^{(0)} = [1 + \exp(h + \underline{q} \cdot \underline{c}_i)]^{-1} \quad (8)$$

where the Lagrange multipliers  $h$  and  $\underline{q}$  can be expressed in terms of  $\rho$  and  $\underline{j}$ . Considering the physical nature of the lattice gas model, it is quite logical that a system with built-in exclusion principle has a Fermi-Dirac equilibrium distribution function (8). Now for low velocities,  $u = |\underline{u}| \ll C$ , expansion of (8) up to second order in  $u$  yields /10/

$$N_i^{(0)}(d, u) = d [1 + (D/C^2) C_{i\alpha} u_\alpha + G(d) Q_{i\alpha\beta} u_\alpha u_\beta + O(u^3)] \quad (9)$$

$$G(d) = (D/C^2)^2 (\frac{1}{2} - d)/(1-d), \quad Q_{i\alpha\beta} = C_{i\alpha} C_{i\beta} - (C^2/D) \delta_{\alpha\beta}$$

Note that at zero velocity,  $N_i^{(0)}(d, 0) = d = \rho/b$  is independent of  $i$ . Starting from the conservation equations (5) and (6), one performs a multi-scale expansion,  $\partial_t \rightarrow \varepsilon \partial_{t_1} + \varepsilon^2 \partial_{t_2}$ ,  $\partial_{\underline{F}} \rightarrow \varepsilon \partial_{\underline{F}_1}$ ,  $N_i = N_i^{(0)} + \varepsilon N_i^{(1)}$ . To first significant order,  $O(\varepsilon)$ , one obtains /9/

$$\partial_{t_1} \sum_i N_i^{(0)} + \partial_{1\beta} \sum_i C_{i\beta} N_i^{(0)} = 0 \quad (10)$$

$$\partial_{t_1} \sum_i C_{i\alpha} N_i^{(0)} + \partial_{1\beta} \sum_i C_{i\alpha} C_{i\beta} N_i^{(0)} = 0 \quad (11)$$

with the notation  $\partial_1 = \partial_{\underline{F}_1} = \{\partial_{1\alpha}\}$ . Substitution of the equilibrium distribution (8) into (10) and (11) yields the macrodynamical Euler Equations

$$\partial_{t_1} \rho + \nabla_1 \cdot (\rho \underline{u}) = 0 \quad (12)$$

$$\partial_{t_1} (\rho u_\alpha) + \nabla_{\alpha} \cdot \underline{P} = 0 \quad (13)$$

where the leading order contribution to the momentum-flux tensor is given by

$$P_{\alpha\beta} = (c^2/D) \rho \delta_{\alpha\beta} + \rho G(\rho) T_{\alpha\beta\gamma\delta} u_\gamma u_\delta + O(u^4) \quad (14)$$

with  $G(\rho) = G(d)/b$  and  $T_{\alpha\beta\gamma\delta} = \sum_i c_{i\alpha} c_{i\beta} Q_{i\gamma\delta}$ . One thus finds that the hydrostatic pressure is  $p = \rho (c^2/D)$ , and as a result the sound velocity is given by

$$c_s = (\partial p / \partial \rho)^{1/2} = c/D^{1/2} \quad (c_s = 2^{-1/2} \text{ for the HPP Model}) \quad (15)$$

To next order,  $O(\epsilon^2)$ , the first equation obtained is  $\partial_{t_2} \rho = 0$ , which means that a single species model yields no mass diffusion, and the second equation  $\partial_{t_2} (\rho u) + \dots = 0$  describes momentum diffusion over long range  $O(\epsilon^{-2})$ . Contracting the  $O(\epsilon)$  and  $O(\epsilon^2)$  equations, one obtains the macrodynamical equations (for details see /10/)

$$\partial_t \rho + \nabla \cdot (\rho u) = 0, \quad \text{continuity equation} \quad (16)$$

$$\partial_t (\rho u) + \nabla \cdot \underline{P} = \nabla \cdot \underline{S} + \text{h.o.t.}, \quad \text{momentum equation} \quad (17)$$

where  $S_{\alpha\beta\gamma\delta} \propto T_{\alpha\beta\gamma\delta} \partial_\gamma (\rho u_\delta)$  and h.o.t. denotes higher order terms  $O(\epsilon u^3), O(\epsilon^2 u^2), O(\epsilon u^4)$ . This result is important because Eq.(17) now bears striking resemblance to the Navier-Stokes equation.

## 6. ISOTROPY CONSIDERATIONS

The question now arises as to whether, the HPP lattice gas constitutes a model fluid that produces correct hydrodynamic behavior; put as a straightforward question, are the macrodynamical equations for the HPP model Navier-Stokes?

Consider the stress tensor for an isotropic medium in classical hydrodynamics. Isotropy implies rotational invariance, as a consequence of which the momentum flux tensor (less the hydrostatic contribution) has the form /11/

$$\eta_1 (\partial_\alpha u_\gamma + \partial_\beta u_\delta) + \eta_2 (\partial_\gamma u_\gamma) \delta_{\alpha\beta} \quad (18)$$

The square lattice HPP model has  $\pi/2$  rotational invariance, which is a subgroup of the continuous rotational invariance group; as a result,  $P_{\alpha\beta}$  is not isotropic for the square lattice gas /10/. So the HPP model produces correct sound propagation /8/,

but viscous dissipation is anisotropic.

Besides the square lattice, the only basic regular two-dimensional tiling geometries are the triangular lattice and the hexagonal lattice (which, in fact, are reciprocal to each other). Frisch, Hasslacher, and Pomeau /9/ proposed to use a triangular lattice with hexagonal symmetry which has  $\pi/3$  rotational invariance; in this geometry,  $T_{\alpha\beta\gamma\delta}$  has the form /10/

$$\frac{1}{2} \phi (\delta_{\alpha\gamma} \delta_{\beta\delta} + \delta_{\alpha\delta} \delta_{\beta\gamma}) + \frac{3}{2} \chi (\delta_{\alpha\beta} \delta_{\gamma\delta}) \quad (19)$$

which is isotropic, and so ensures isotropy in the momentum equation. This model will be referred to hereafter as the FHP model (see section 7).

Extension to 3-D systems faces the problem that the tensors  $\underline{T}$  and  $\underline{S}$ , Eq.(17), may not be isotropic, i.e. invariant under arbitrary rotations. Indeed none of the fourteen 3-D Bravais lattices has sufficient symmetry to produce the required isotropy of fourth order pairwise symmetric tensors. Solutions to bypass this difficulty, have been proposed by d'Humières, Lallemant, and Frisch /12/. The first solution is a multispeed model on a cubic lattice, where particles can have three different velocities: 0, 1,  $\sqrt{2}$ ; zero for particles at rest, one for particles moving along lattice links to nearest neighbor, and  $\sqrt{2}$  for particles moving along the diagonal to next-nearest neighbor. As represented in Fig.5a, the state at one node is then given by a 19-bit word. This model is shown /12/ to yield, under appropriate conditions, the proper form for the tensor  $\underline{T}$  (whereas a slight anisotropy persists in  $\underline{S}$ ) and so produces correct inviscid isotropic hydrodynamics.

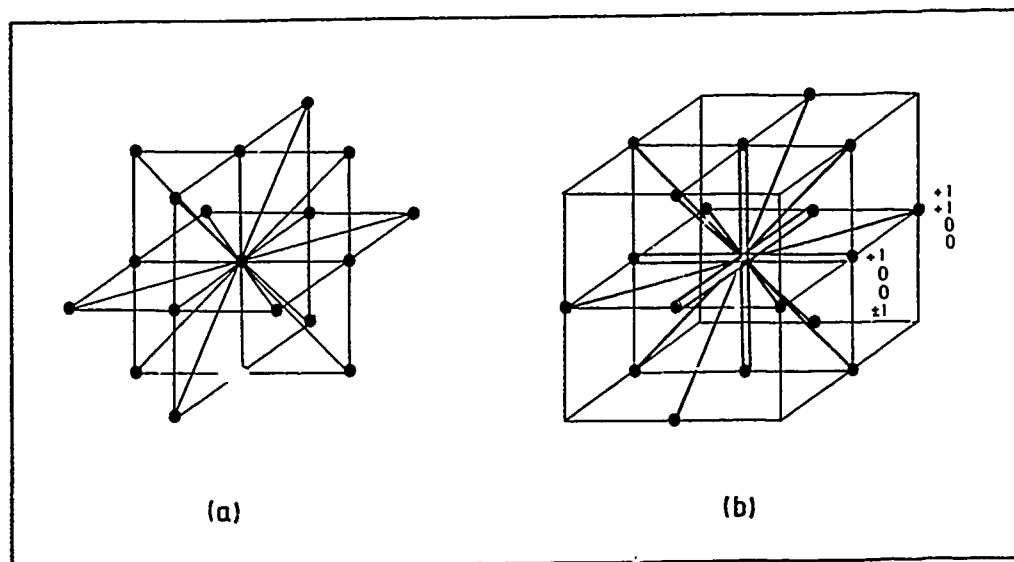


Fig. 5. 3-D models for lattice gas hydrodynamics. (a) multispeed model on cubic lattice; (b) 3-D projection of 4-D FCHC.

A second model, proposed by the same authors /12/, is based on the observation that in 4-D, there exists a regular Bravais lattice with all the required symmetries. Indeed the 24-hedron, with 24 vertices represented by the Schläfli symbol  $\{3,4,3\}$  can be used to tile regularly the 4-D space with a 4-D face-centered-hypercubic lattice (FCHC). A 3-D projection of the 4-D FCHC (i.e. one lattice site wide in the 4th dimension) produces a 3-D lattice with the required symmetries. A representation of the 3-D projected FCHC is given in Fig.5b. This is a single-speed model, with all lattice nodes connected via links with unit length  $c = 2$ .

The state at each node is given by a 24-(or 25- if particles at rest are included) bit word. Note that an additional momentum equation follows from the existence of a 4th momentum component; this component however is a passive scalar because its governing equation decouples from the others (at least in the low Mach number limit) and is therefore unimportant. This model, referred to as FCHC, has been put to work very recently by Rivet to produce the first three-dimensional cellular automaton simulation of hydrodynamic flow /13/.

An alternative possible realization of 3-D cellular automata for hydrodynamic simulation should be mentioned. It was indeed suggested by Hasslacher that 3-D isotropy could be achieved on a quasi-lattice with icosahedral symmetry by projection of an "oblique" slice out of a 6-D cubic lattice /14/.

#### 7. THE FHP MODEL

Consider a triangular lattice with hexagonal symmetry (see Fig.6); each node has regular hexagonal neighborhood (i.e. 6 links and 6 first neighbors). So the state of a node will be given by a 6-(or 7-, if one allows for rest particles at the node) bit word, and the number of configurations associated to one node is  $2^6$ , which yields  $64^{64}$  possible rules. Restriction to a limited number follows from conservation laws; in addition the exclusion principle and efficiency of collisions are to be taken into account. The collision rules are illustrated in Fig.7.

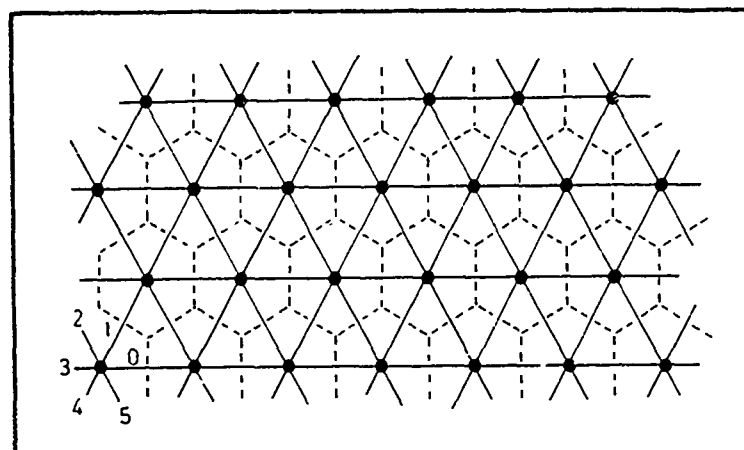


Fig.6. Triangular lattice with hexagonal symmetry for FHP model. The unit area around each node is  $\sqrt{3}/2$  (for link length=1).

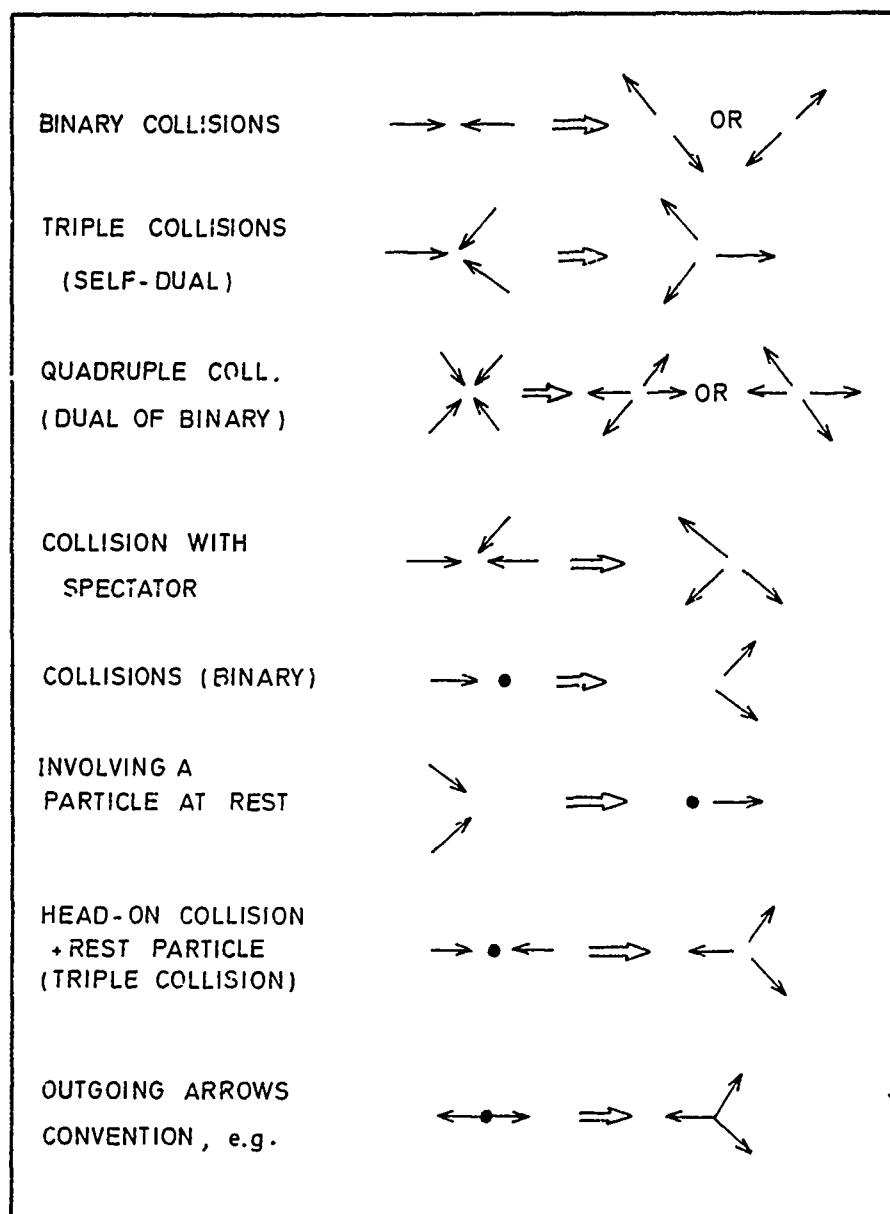


Fig.7. Collision rules for FHP model

Although the probability of actual triple collisions in a real gas is quite small compared to the probability of binary collision, triple collisions are very important here. Indeed head-on collisional processes conserve particle number and momentum, but also difference in particle number in opposite directions, which yields a total of 4 conservation laws in a 2-D system! Therefore triple collisions are crucial in that they remove the spurious invariant. On the other hand, head-on colli-

sions exhibit an interesting feature because they have two possible output channels (see Fig.7). So by making a random choice of output configuration, mirror-symmetry is preserved, and furthermore the model is non-deterministic.

Microdynamical equations. For simplicity we consider the case with binary and triple collisions (without particles at rest; the generalization is straightforward). As described in section 4, updating the cellular automaton proceeds in a two-step sequence (with collisions followed by propagation) which is expressed by the operation

$$n_i(t_{*+1}, \bar{r}_{*+1}, \bar{c}_i) = n_i(t_*, \bar{r}_*) + \Delta_i \quad (20)$$

where  $i=0, \dots, 5$  denotes the site number (or link direction) as shown in Fig.6. Here  $\Delta_i$  is the sum of the positive (populating) contributions and of the negative (depopulating) contributions from binary and triple collisions, i.e.

$$\begin{aligned} \Delta_i = & \xi_{F_*} n_{i+1} n_{i+4} \bar{n}_i \bar{n}_{i+2} \bar{n}_{i+3} \bar{n}_{i+5} + \bar{\xi}_{F_*} n_{i+2} n_{i+5} \bar{n}_i \bar{n}_{i+1} \bar{n}_{i+3} \bar{n}_{i+4} \\ & - n_i n_{i+3} \bar{n}_{i+1} \bar{n}_{i+2} \bar{n}_{i+4} \bar{n}_{i+5} \\ & + n_{i+1} n_{i+3} \bar{n}_{i+5} \bar{n}_i \bar{n}_{i+2} \bar{n}_{i+4} - n_i n_{i+2} n_{i+4} \bar{n}_{i+1} \bar{n}_{i+3} \bar{n}_{i+5} \end{aligned} \quad (21)$$

all quantities being evaluated at  $t_*$ ,  $\bar{r}_*$ , and where  $\langle \xi \rangle$  and  $\langle \bar{\xi} \rangle = 1 - \langle \xi \rangle$  denote the probabilities for output channel selection in head-on collisions (corresponding to  $\pi/3$  rotation in configuration); usually  $\langle \xi \rangle = 1 - \langle \bar{\xi} \rangle = 1/2$ . An example of evolution after one time step is shown in Fig.8.

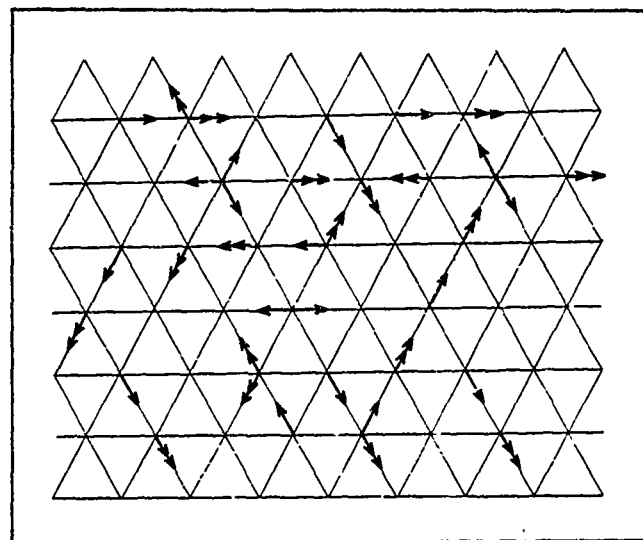


Fig.8. Example of evolution from time  $t_*$  (single arrow) to time  $t_{*+1}$  (double arrow) on the hexagonal lattice gas.  
(Note the convention of outgoing arrows in the collision representation)



## 8. MACRODYNAMICS FOR NON-DETERMINISTIC MODELS

As usual in Statistical Mechanics, we now switch to a probabilistic description /10/, and define the phase space  $\Gamma$  as the set of all possible assignments  $S(\cdot) = \{S_i(\vec{r}_*)\}$  ( $i = 0, \dots, b-1$ ) of the Boolean field  $n_1(\vec{r}_*)$ . Then  $P(t_*, S(\cdot))$  is the probability, at time  $t_*$ , for assignment  $s(\cdot)$  (which can also be called a configuration) with  $\sum P(t_*, S(\cdot)) = 1$ , ( $S(\cdot) \in \Gamma$ ). Starting from an ensemble of initial conditions, each configuration evolves according to the updating rules of the automaton. This is formally expressed by the "Liouville equation"

$$P(t_* + 1, \mathcal{E} S(\cdot)) = P(t_*, S(\cdot)) \quad (22)$$

with  $\mathcal{E}$ , the evolution operator, which can be written as  $\mathcal{E} = \mathcal{J} \circ \mathcal{C}$ , where  $\mathcal{J}$  is the streaming operator and  $\mathcal{C}$ , the collision operator. In order to indicate explicitly the two-step sequence of the automaton evolution, one can rewrite Eq.(22) as

$$P(t_* + 1, \mathcal{J} S(\cdot)) = P(t_*, \mathcal{C}^{-1} S(\cdot)) \quad (23)$$

Now, for non-deterministic systems, the description must be generalized so as to include all possible choices of the Boolean variables  $\xi_{ss'}$ , giving the transition selection from state  $s$  to state  $s'$ . Each transition being assigned a probability  $A(s \rightarrow s')$ , one has  $\langle \xi_{ss'} \rangle = A(s \rightarrow s')$ ,  $\forall s, s'$ , in accordance with the "semi-detailed balance" assumption

$$\sum_s A(s \rightarrow s') = 1, \quad \forall s' \quad (24)$$

which expresses that, if all states have equal probabilities before collision, they also have equal probabilities after collision. Given that the  $\xi$ 's take values independent of each other at each time, defining in this way a Markov process, and given that the  $\xi$  values may be assumed to be independently chosen at each node, Eq.(23) becomes

$$P(t_* + 1, \mathcal{J} S(\cdot)) = \sum_{S(\cdot)} \prod_{\vec{r}_*} A(S(\vec{r}_*) \rightarrow S'(\vec{r}_*)) P(t_*, S(\cdot)) \quad (25)$$

This Master Equation describes the evolution of a probabilistic cellular automaton by expressing the probability for a (propagated) configuration  $s'(\cdot)$  in terms of all possible initial configurations  $s(\cdot)$  weighted by the transition probabilities. Note that in the deterministic case,  $A(s \rightarrow s')$  reduces to  $\mathcal{C}^{-1} s'(\cdot)$ , and Eq.(25) becomes simply the Liouville equation (23).

Lattice properties being translation - invariant, equilibrium solutions should be the same at each node; so steady-state solutions to Eq.(25) should be of the form

$$P(S(\cdot)) = \prod_{\vec{r}_*} p(S(\vec{r}_*))$$

where the probabilities  $p(s)$  of a given state are node independent, and can therefore be factorized over all cells, i.e.

$$p(s) = \prod_i (s_i N_i + (1-s_i)(1-N_i))$$

By substitution of the above expressions into (25), one obtains a Master Equation expressed in terms of the  $N_i$ 's, and it can be shown /10/ that its steady state solutions are given by the Fermi-Dirac distribution introduced in section 5.

Macro-dynamics describes the evolution of the observables. An observable  $X$  is defined by the mean value

$$X(t_*) \equiv \langle x(n, (t_*)) \rangle = \sum_{s(\cdot)} x(s(\cdot)) P(t_*, s(\cdot)) \quad (26)$$

which yields the explicit definition, for non-deterministic systems, of the quantities introduced in section 5. Following the scheme outlined in that section (for details see ref./10/), one obtains the macrodynamical equations, (16) and (17), which now, provided isotropy is satisfied, can be cast into a form stressing their analogy with the equations of classical hydrodynamics

$$\partial_t \rho + \partial_\beta (\rho u_\beta) = 0 \quad (27)$$

$$\partial_t (\rho u_\alpha) + \partial_\beta P_{\alpha\beta} = \partial_\beta S_{\alpha\beta} + \text{h.o.t.} \quad (28)$$

with

$$\frac{1}{\rho} P_{\alpha\beta} = c_s^2 (1 - g(d) u^2/c^2) \delta_{\alpha\beta} + g(d) u_\alpha u_\beta \quad (29)$$

$$S_{\alpha\beta} = \nu(\rho) [\partial_\alpha (\rho u_\beta) + \partial_\beta (\rho u_\alpha) - (2/D) \partial_\gamma (\rho u_\gamma) \delta_{\alpha\beta}] \quad (30)$$

where

$$g(d) = \frac{2D}{D+2} \frac{\frac{1}{2} - d}{1 - d} \quad (31)$$

The factor  $g(d)$  is specific of the lattice gas description and is related to particle - hole duality. In particular it vanishes when the particle density and the hole density are equal ( $d=1/2$ ). At any rate, since the coefficient  $g(d)$  weights quadratic terms, it should be of minor importance at low speeds. However it raises a more serious problem that will be discussed later.

In (29),  $c_s = C/\sqrt{D}$  is the sound velocity (ignoring corrections  $\propto u^2/C^2 \ll 1$ ), and in (30),  $\nu(\rho)$  is the kinematic viscosity which contains a positive contribution,  $\nu_c$ , the collisional viscosity, and a negative contribution,  $\nu_p$ , the propagation viscosity (with  $|\nu_p| < \nu_c$ , so that  $\nu(\rho) > 0$ ). The existence of the latter is a consequence of the discrete nature of the system: there is a collisionless step in the dynamics (propagation) during which fluctuations do not regress /15/.

Linearized hydrodynamics : To first order in the perturbations,  $\underline{u}$ , and  $\rho' = \rho - \rho_0$  (where  $\rho_0$  is the mean equilibrium density), the linearized hydrodynamic equations read

$$\partial_t \rho' + \rho_0 \nabla \cdot \underline{u} = 0 \quad (32)$$

$$\partial_t \underline{u} + \frac{c_s^2}{\rho_0} \nabla \rho' = \nu(\rho_0) (\nabla^2 \underline{u} + (1 - \frac{2}{D}) \nabla \nabla \cdot \underline{u}) \quad (33)$$

Measurements of sound propagation and damping /16/ were performed on a FHP lattice gas by applying an initial perturbation to the velocity field :  $(\underline{u}_{\parallel} + \underline{u}_{\perp}) \cos \underline{k} \cdot \underline{r}$ , where  $\underline{k}$  is the wave vector of the perturbation;  $\underline{u}_{\parallel} = \hat{\underline{k}} \cdot \underline{u}$  corresponds to the longitudinal current, and  $\underline{u}_{\perp} = |\hat{\underline{k}} \times \underline{u}|$  to the transverse current. The results of the lattice gas experiment /16/ are shown in Fig.9.

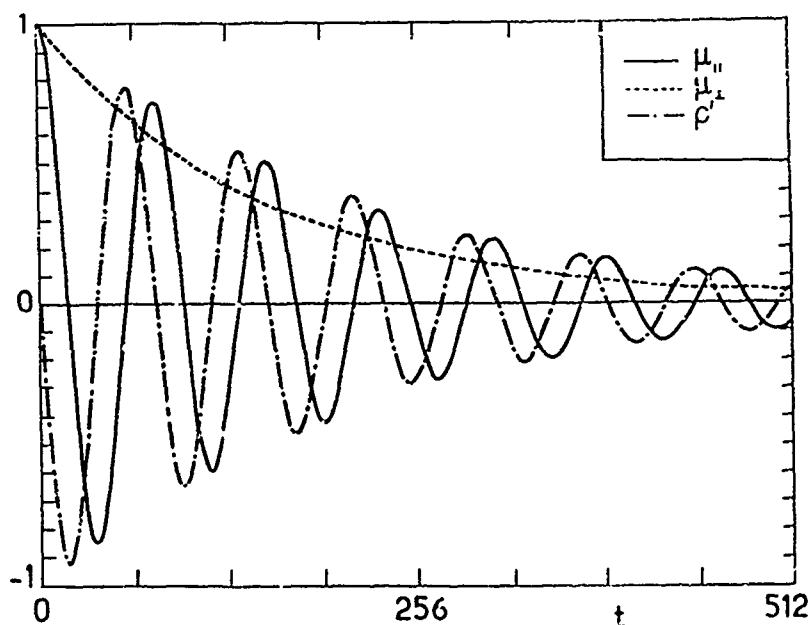


Fig.9. Sound propagation and damping in FHP lattice gas ( $10^6$  nodes). Time evolution (unit time is time step) of normalized density fluctuations and velocity fields (d'Humières, Lallemand, and Shimokura; 1985).

Viscosities : we rewrite the hydrodynamic equations for the hexagonal lattice gas as

$$\partial_t \rho + \sum_{\alpha} \partial_{\alpha} (\rho u_{\alpha}) = 0 \quad (34)$$

$$\begin{aligned} \partial_t (\rho u_{\alpha}) + \sum_{\beta} \partial_{\beta} (\rho g(\alpha) u_{\alpha} u_{\beta} + \mathcal{O}(u^4)) = \\ -\frac{1}{2} \partial_{\alpha} \rho + \eta_s(\rho) \nabla^2 u_{\alpha} + \eta_B(\rho) \partial_{\alpha} \nabla \cdot \underline{u} \end{aligned} \quad (35)$$

with  $g(d) = (\frac{1}{2} - d)/(1 - d)$ . Here  $\eta_s$  and  $\eta_B$  are the coefficients of shear and bulk viscosity respectively, for which explicit expressions have been obtained by Rivet and Frisch, either from the Boltzmann approximation /17/ or from the Green-Kubo autocorrelation formalism /18/. A comparison of theoretical results with lattice gas simulation data /19/ is given in Fig.10. The basic model is the FHP lattice with binary and triple collisions (five collision rules, see Fig.7); this model is noted I in Fig.10. The model noted II includes collisions with particles at rest (see Fig.7; twenty-two collision rules). In the model noted III, all possible collisions satisfying conservation laws have been used (seventy-six collision rules). It should be noted that the agreement between theory and experiment is improved (in particular, negative values are eliminated) when model III is restricted to sixty-four collision rules /20/. Most important is the observation that viscosities decrease when more collision rules are used, a fact of considerable interest for achievable Reynolds number values, as discussed below.

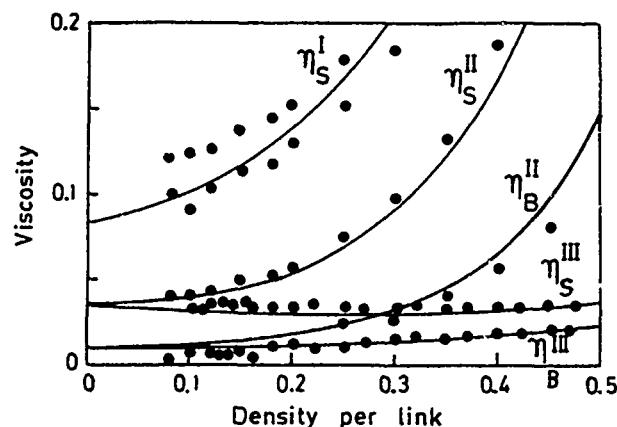


Fig.10. Shear and bulk viscosities for FHP lattice gas. Curves are for theoretical results, dots for cellular automata simulations ( $256^2$  nodes). I,II,III refer to the models described in text. (d'Humières and Lallemand, 1986)

Incompressible Fluid: The incompressible hydrodynamics limit is obtained by setting  $\rho = \rho_0$  ("frozen density") except in the pressure term of the momentum equation, i.e.

$$\partial_t \underline{u} + g_0 \underline{u} \cdot \nabla \underline{u} = - \frac{c_s^2}{\rho_0} \nabla \rho' + \nu_s (\rho_0 \nabla^2 \underline{u}) ; \quad \nabla \cdot \underline{u} = 0 \quad (36)$$

where  $g_0 = g(\rho_0/\ell)$ . This set of equations differs from the classical incompressible fluid equations (obtained by a low Mach number,  $u/c_s$ , expansion of the hydrodynamic equations) by the presence of the factor  $g_0$ . However appropriate scaling

$$\tau = g_0 t ; \quad \nu = \nu_s(\rho_0)/g_0 ; \quad p' = (c_s^2/\rho_0) \rho'/g_0 \quad (37)$$

yields the correct form of the hydrodynamic equations in the incompressible fluid limit (except for the particular value  $d=1/2$ , which is a peculiarity of the lattice gas duality invariance). Note that the factor  $g(c)$  raises a difficulty in the compressible case, since time scaling is different for the momentum equation and for the continuity equation, and therefore mass propagation would not occur on correct time scale.

Reynolds Number : An important consequence of the scaling is felt through the Reynolds number which now reads

$$Re = l_0 u / \nu \quad (38)$$

Here  $l_0$  is the characteristic length (measured in lattice length unit),  $u$  is the characteristic velocity (with velocity unit  $C$ ), and  $\nu$  is the rescaled kinematic viscosity, (37). Obviously, higher Reynolds number simulations will be more easily performed with systems with lower viscosity. An illustration is given in Fig.11 for the models FHP I,II,III for which the viscosities are shown in Fig.10. So the optimization of the Reynolds number should be viewed not only in terms of large systems and high speeds, but also of those factors that minimize the kinematic viscosity, i.e. via an optimization of the collision rules. For instance, the highest achievable Reynolds number with FHP III is six times the value obtained with FHP I, (see Fig. 11); and the gain factor should be at least sixteen for the pseudo 4-D FHC model (see section 6) /10/.

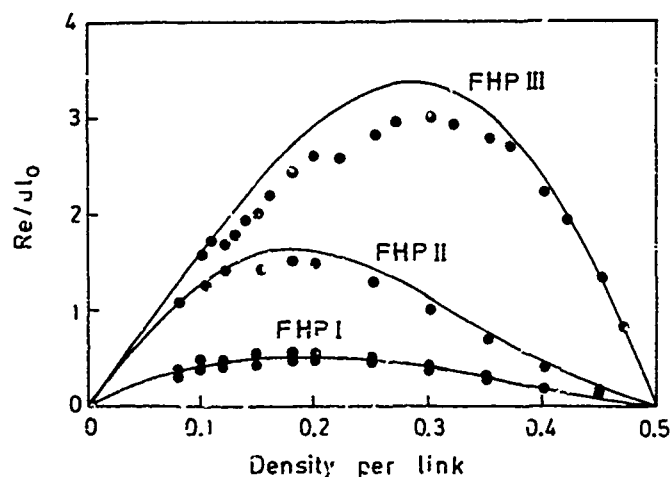


Fig.11. Reynolds number optimization for models FHP I,II,III, as a function of density per link,  $d$ . (d'Humières and Lallemand; 1986)

#### 9. CELLULAR AUTOMATA SIMULATIONS

Most of the hydrodynamics simulations performed to date have been realized on 2-D hexagonal lattices, i.e. with the FHP model, using collision rules including centers (particles at rest). The state of the system at time  $t_*$  is given by a

$L_1 \times L_2$  matrix (size of the CA universe) of 6-(or 7-) bit words assigned to each node. The bit value 1 or 0 reflects the presence or the absence of a particle at site  $i$  ( $i=0, \dots, 5$  or  $6$ ) with velocity  $C_i$ . Updating the universe is performed by "solving" the microdynamical equations (collisions + propagation) by a sequence of logical operations (Computational aspects are presented in Appendix). Boundary conditions and initial conditions are set according to the problem studied. For instance, in the sound propagation experiment illustrated in Fig.9, a uniformly random distribution of particles and velocities is realized as initial condition, and periodic boundary conditions are imposed, which confine the system on a torus (particles escaping the universe at one boundary are reinjected symmetrically at the opposite boundary). On the other hand, a directed flow simulation experiment requires an initially biased velocity distribution along a given direction, with boundary conditions ensuring steady incoming flow of particles at the input side and "sink" condition at the output boundary. In experiments such as channel flow and flow behind obstacles, their shape is designed according to the lattice geometry by specific collision rules, with reflection conditions corresponding to free-slip boundaries (specular reflection; Fig.12a), no-slip boundaries (bounce-back reflection, Fig.12b), or rough surfaces (combination of specular and bounce-back reflections with equal probabilities, Fig.12c). The obstacle size  $l_0$  must be small compared to the size  $L$  of the CA Universe in order to avoid artefacts. In turn large  $L$  implies large numbers of particles, i.e. large lattices.

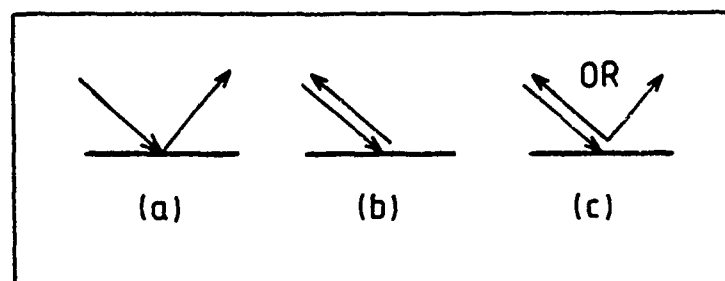


Fig.12. Boundary reflections : (a) free-slip; (b) no-slip; (c) combination of (a) and (b).

Presently typical 2-D lattices are of the order of  $3 \times 10^6$  nodes (e.g.  $1024 \times 3072$ ) populated with  $6 \times 10^5$  particles, i.e. with a density  $d \sim 0.2$  ( $\rho \sim 1.4$ ). Streamline maps are obtained by representing the velocity field vectors associated to the fluid elements, i.e. by averaging the particle velocities over a number of nodes (e.g.  $8 \times 8$ ,  $32 \times 32$ , ... depending on the problem under investigation). Technical restrictions as to the universe size, the minimal kinematic viscosity, and the velocity  $u$  (which must be small compared to the upper limit  $C$ ) are determinant; within these limits presently achievable flows are for Reynolds numbers not exceeding  $10^3$ . It is to be expected that fastly progressing developments will overcome these limitations in the near future.

Poiseuille flow in a channel. Flow at the inlet of a 2-D duct was simulated by d'Humières and Lallemant /21/ on a  $512 \times 3072$  LHP II lattice gas with  $d=.22$  and average velocity  $u=.30$ . Velocity profiles so obtained are presented in Fig.13 for the region close to the input boundary (Fig.13a) and for a region located about ten times further downstream (Fig.13b) where a characteristic Poiseuille profile has developed. Fig.13 shows good agreement between the CA simulation and the profiles computed by the Slichting method. This is the first example of quantitative comparison between lattice gas flow and classical fluid mechanics for a hydrodynamic system involving both viscous dissipation and non-linear behavior.

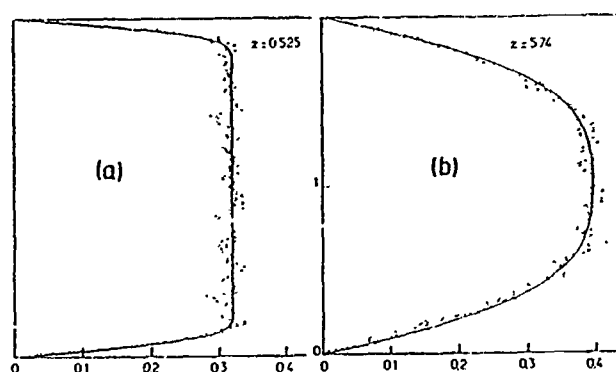


Fig.13. Velocity component profile in a channel (a) close to the inlet, and (b) further downstream (relative distances from inlet are  $\sim .5$  (a) and  $\sim 6$ . (b)) (d'Humières and Lallemant; 1986).

von Karman streets. The first hydrodynamic flow "experiments" on a lattice gas were performed in 1985 by d'Humières, Lallemant, Shimomura, and Pomeau /16,22/, then by Salem and Wolfram /23/, to simulate wakes behind a plate. More accurate results for this and related problems are now available /19,24/. An example of von Karman street developing behind a flat plate at  $Re=300$  is given in Fig.14, where two successive velocity maps are shown, indicating the unsteady nature of the flow. Similar experiments have also been performed to simulate flow around a stationary cylinder /24,25/.

Flow around a wing profile. The example in Fig.15 showing streamlines around an airplane wing profile at various inclinations with respect to the mean flow direction /26/ illustrates the ability of the method to conveniently realize more complex obstacle shapes and modify their orientation without computational difficulty.

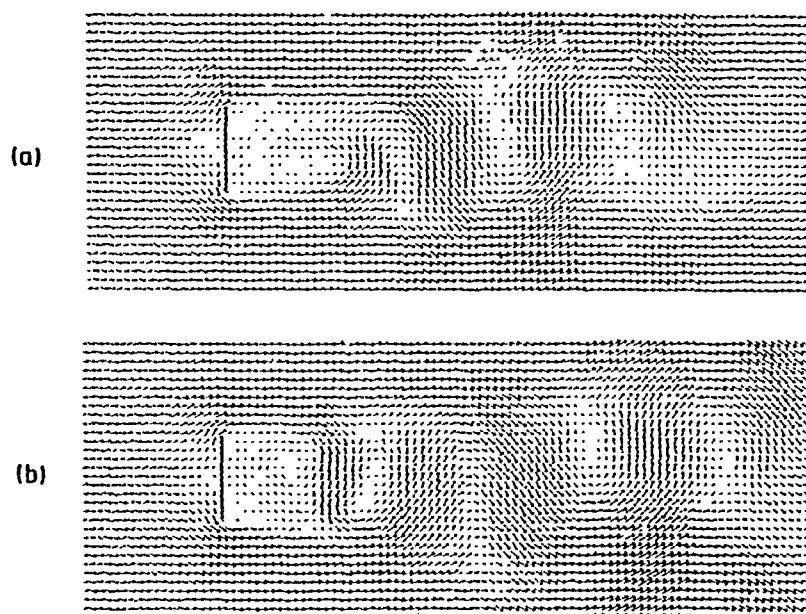


Fig.14. von Karman street formation behind a "bounce-back" (see fig.12) flat plate in 512x1024 CA wind tunnel experiment at  $Re=70$ ; time (b) = time (a)+1500 time steps. (d'Humières and Lallemand; 1986)

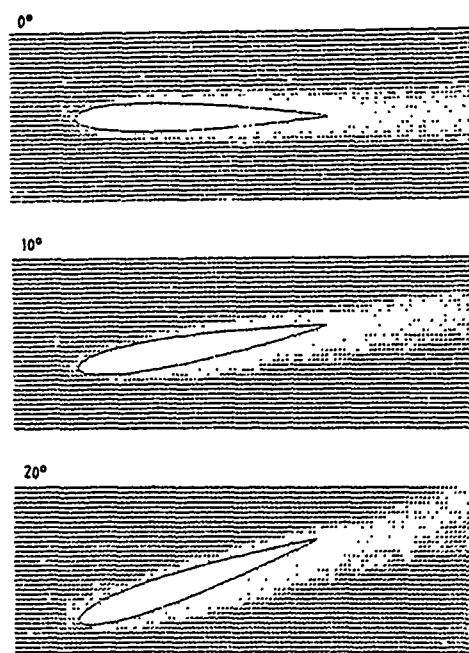


Fig.15. Flow around an airplane wing at various inclinations with respect to the direction of average input flow. (Lallemand and d'Humières; 1986)



Channel flow in expanded geometry. This phenomenon was studied by simulating flow in a channel with sudden expansion (Fig.16) where recirculation (back flow) takes place behind the step profile /26/. Isomach curves map the velocity field at Reynolds numbers  $Re=50$  (Fig.16a) and  $Re=150$  (Fig.16b); the latter is also shown on an expanded scale (Fig.16c) along with the corresponding isodensity curves (Fig.16d). The arrow in Fig.16b indicates the location of the reattachment point as evaluated from Navier-Stokes finite elements-finite differences computations; as seen, good agreement is obtained.

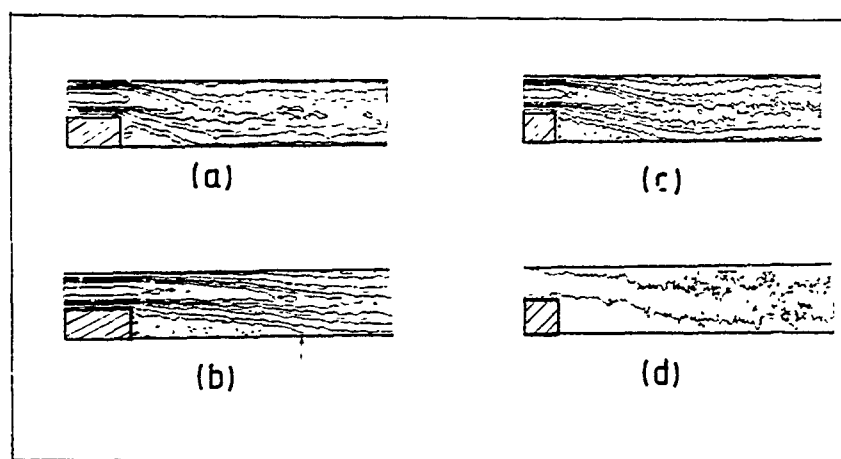
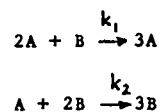


Fig.16. Channel flow with sudden expansion. Isomach curves for velocity component along the average input flow direction at  $Re=50$  (a) and  $Re=150$  (b,c);  $\Delta u = 10\%$ . Isodensity curves (at  $\rho = 0.95 \rho_{max}$ ) at  $Re=150$  (d). (Note 2x expanded spatial scale in c and d). Arrow (in b) indicates reattachment point (Noullez, Lallemand, and d'Humières, 1986)

#### 10. FURTHER DEVELOPMENTS

Important progress has been realized recently in CA simulations of hydrodynamic flows to study problems like jets in periodic channels, flame fronts, and the Kelvin-Helmoltz and Rayleigh-Taylor instabilities /27/. Such problems involve the introduction of two-species particles. In this respect, current research activity on lattice gas hydrodynamics has led to interesting variations of the FHP model. One of the most promising versions is a two-species model where a "color" bit is added to the particles. The automaton is then a 14-bit model which uses the FHP collision rules between identical particles, but additional rules for color exchange between colliding particles of different species /27/. If "color" is to be conserved during collisions, the model is for mutual diffusion of two equivalent non-reacting gases. As the two species are then perfectly miscible, the system reaches homogeneous state in short time. On the other hand, interfaces can form between different species if

reactive collisions change the relative number of particles of each type. A simple chemical reaction is described by the majority rule for autocatalytic transformation:



Such a transformation rule induces a phase separation between A-dominant and B-dominant regions. These regions are separated by interfaces whose stationary length is proportional to  $(D/k_i)^{1/2}$ , with  $D$ , the mutual diffusion coefficient, and  $k_i$  the reaction rate. Different collision rules can be used to model other types of chemical reactions, like e.g. combustion /27/.

Body-forces can be introduced by including collision rules that do not conserve momentum. These collisions flip bits in the required direction with the correct probability to simulate external forces (e.g. gravity effects). With different probabilities for different particle species, gravitational instabilities can be simulated. As an example, Fig.17 shows the 2-D simulation of the Rayleigh-Taylor instability, which develops when a heavy fluid penetrates a lighter fluid layer /27/. Another illustration is the Kelvin-Helmoltz instability where two fluid layers moving in opposite directions with respect to each other, develop, by shear constraint, a roll up at the interface, as shown in Fig.18.

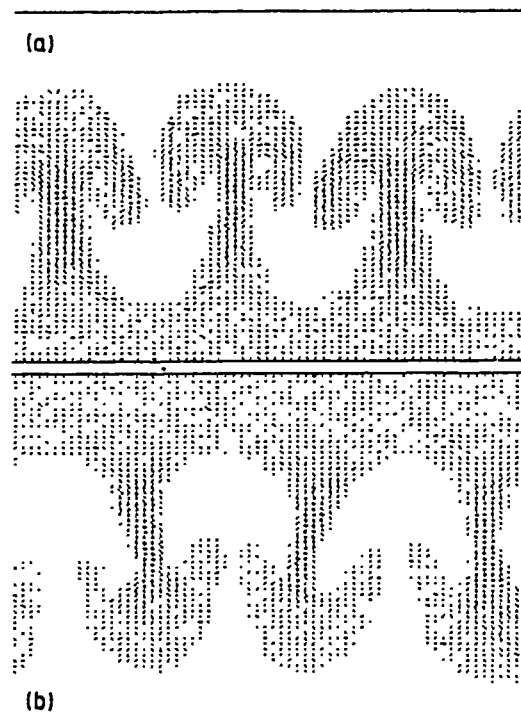


Fig.17 : 2-D lattice gas simulation of the Rayleigh-Taylor instability. Maps of A-particle flux (a) and of B-particle flux (b) after  $t=1600$ . (Clavin, d'Humières, Lallemand, and Pomeau; 1986)



Fig.18 : 2-D lattice gas simulation of the Kelvin-Helmoltz instability. Average velocities are  $+u$  (left to right) and  $-u$  (right to left) in lower half and in upper half of channel respectively. Map shows flux of particles of one species (d'Humières, Lallemand, and Searby; 1987)

Among the numerous problems encountered in the realization of lattice gas simulations, one of the most acute is contained in the  $g(d)$  factor appearing in the pseudo-Navier-Stokes equations (29); this factor should be equal to one for mass and momentum propagation speeds to be the same (this is crucial when mass diffusion is important, e.g. in chemistry experiments) /27/. It would also be interesting to decrease the value of the sound speed and of the kinematic viscosity, particularly in 2-D systems, in order to investigate supersonic and turbulent flows. So far, only athermal model systems have been treated; temperature can be introduced via many-speed models, yielding a velocity distribution and thus an additional collision invariant. Major progress will be realized when 3-D models become tractable; the first results in that direction have been obtained very recently /13/. They concern 3-D simulations of Taylor-Green vortices performed with the FCHC model (see section 6) and are illustrated in Fig.19.

Lattice gas models exhibit attractive properties of simplicity, both conceptually and operationally. Considering the fast development of this field of research over the past two years, and the considerable interest raised by its perspectives, further progress is to be expected in the theory, in the experimental methods, and in the computational techniques, in the near future.

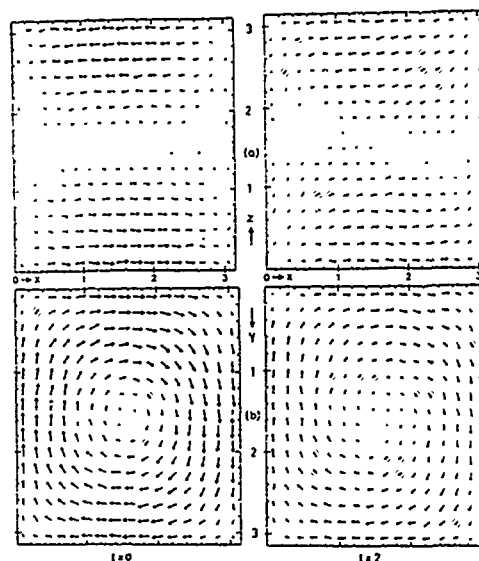


Fig.19 : 3-D hydrodynamics simulation of Taylor-Green vortex on  $128 \times 128 \times 128$  FCHC lattice at time  $t=0$  and time  $t=2$  (256 automaton time steps). Velocity fields are shown for the vertical "wall" plane (a) and for the horizontal "floor" plane (b) (Rivet, 1987).

#### ACKNOWLEDGEMENTS

We thank Dominique d'Humières, Uriel Frisch, Pierre Lallemand, and Jean-Pierre Rivet for stimulating discussions. One of us (AN) has benefited from a grant by the "Institut pour l'Encouragement à la Recherche Scientifique dans l'Industrie et l'Agriculture" (IRSIA, Belgium). JPB acknowledges support from the "Fonds National de la Recherche Scientifique" (FNRS, Belgium). This work was supported by European Community Grant ST2J-0190-2-B.

#### APPENDIX : COMPUTATIONAL ASPECTS

Most of the lattice gas hydrodynamics experiments performed to date have been simulated on conventional computers, the initial objective being to validate the method and to improve the model(s) before designing a dedicated lattice gas machine. The state of the lattice gas is kept in a general computer as a large array of 6- (or 7-, if rest centers are included) bit words per node : each bit specifies, if true, the presence of a particle leaving that node in one of the six directions. The evolution of the system is obtained by a sequence of two-step processes : propagation and collisions. The propagation operation reduces simply to moving each bit to the adjacent memory location in the direction specified by its speed index. Collisions can be dealt with in two ways.

(i) The "brute-force" approach is to construct a look-up table giving, for each possible input configuration, the output configuration according to the collision rules. For the 2-D FHP model, there are 64 possible input states; so the table will be 64 6-bit words long. However this procedure becomes untractable for many-bit models when the size of the table overflows the available memory (for instance, the 4-D FCHC model would require a 16.77...million 24-bit words table, which is clearly unrealistic).

(ii) The second method for generating collisional processes is to evaluate the new state as a function of the previous state using logical operations which can be performed very fast on a binary computer. The arithmetic version of such operations is given in section 3 (see e.g. Eqs (3) and (21)); in logical form, they can be optimized to obtain maximum efficiency. As an example, the logical version of the HPP collision rule (Eq. (3)) is cast as

$$n'_i = n_i \vee s \quad ; \quad i = 0, 1, 2, 3$$

$$s = (n_0 \vee n_1) \wedge (n_1 \vee n_2) \wedge (n_2 \vee n_3) \quad (\text{A.1})$$

which takes 9 logical operations per site ( $\vee$ =exclusive OR;  $\wedge$  = AND). Similarly, the FHP collision operator (see Eq. (21)) can be expressed in a form involving about 60 logical operations (130 if rest particles are included). Writing the collision operator in terms of logical operations presents the advantage that many collisions can be realized in parallel by operations between whole computer words instead of single bits; for instance, an FPS-164 vector processor can compute simultaneously the evolution of 64 nodes (note that although there are more operations per site than a single look-up table access, this method is nevertheless four times faster than the table method on a 64-bit machine). When the logical operation method is implemented on the FPS-164 computer, it takes 0.6  $\mu$ s to update a node (collisions + propagation), which implies that, for maximum efficiency, the whole lattice should be stored in main memory. Consequently, the number of nodes is limited to a few millions on conventional computers, i.e. lattice sizes a few thousand nodes square.

The lattice is initialized by computing a random initial state whose macroscopic properties correspond to the desired density and velocity fields. The average link populations are given by /16/

$$\langle n_i \rangle(\bar{r}) = d(\bar{r}) \left[ 1 + \frac{\rho}{3d} \underline{u}(\bar{r}) \cdot \bar{C}_i + O(u^2) \right] \quad (\text{A.2})$$

$$= d(\bar{r}) \left[ 1 + 2 \underline{u}(\bar{r}) \cdot \bar{C}_i \right], \quad \text{for FHP I}$$

Given the local density and velocities, the link populations are generated randomly by Monte-Carlo method to obtain the required averages (A.2). Boundaries are implemented by special "tagged" nodes with different collision rules. These collision rules can be specified so as to specularly reflect the particles to simulate free-slip boundaries or to have the particles bounce back to obtain no-slip boundaries (see Fig.12). Different types of boundary nodes are needed depending on the excluded links determined by the boundary geometry around these nodes. Obstacles of any desired shape are set by dividing their boundaries along the lattice links and imposing proper reflection conditions. Pressure on an obstacle is measured by averaging the momentum transfers between particles and boundary. Macroscopic quantities are obtained by averaging the corresponding microscopic quantities on small rectangu-

lar regions. The size and shape of these regions can be adapted to suit the problem considered (e.g.  $32 \times 32$  nodes for channel flow, Fig.16;  $1 \times 256$  nodes for 1-dimensional boundary layer experiment, Fig.18). The macroscopic quantities need only be calculated at times separated by many microscopic times because characteristic hydrodynamic times are large compared to molecular times. Generally, microscopic equilibrium is attained in a few tens of time steps and stationary solutions (when such solutions do exist) are reached after a number of time steps corresponding to a few times the characteristic lattice length (note indeed that perturbations travel at the sound speed which is  $O(1)$  for the lattice gas model).

Once started, the evolution of the model is completely deterministic; this means that it can never run into unphysical regimes and is free of numerical instabilities such as those encountered in finite elements methods. The maximum Reynolds number value that can be reached by the lattice gas method is limited by the memory size. Indeed, the rescaled shear viscosity (37) has a minimum value at a given density (see Fig.10) and the flow velocity should remain small compared to  $c_s$  (in order to preserve incompressibility). So the Reynolds number is at best proportional to the obstacle characteristic length, which itself is a fraction of the lattice length. Consequently, the size of the lattice should increase like the square of the desired Reynolds number value. As the calculation time per node is roughly constant, the time for a single lattice update grows as  $Re^2$  and the complete calculation time scales as  $Re^3$ . On the other hand, since  $Re$  is inversely proportional to  $\nu$ , a decrease in kinematic viscosity by a factor  $\alpha$  will induce a gain factor  $O(\alpha^3)$  in computation time. This can be achieved by improving the collision rules and/or the lattice geometry (note that a factor of 6 on the viscosity has been gained in the current best implementations of the FHP model as compared to its original version).

Alternately, higher speeds can be obtained by dedicated hardware for which lattice gases are particularly well suited; indeed, the lattice gas state is specified by a small number of bits at each node and the evolution rule is strictly local and deterministic and can be written with logical operations only. The number of logical operations necessary for the FHP model is however too large to render a completely parallel machine competitive: most of the silicon would have to be dedicated to the gates computing the evolution rather than to registers keeping the node states. Also, parallel modules would require a large number of wired connections between modules if the whole lattice does not fit in a single module. So only serial machines have been constructed to date. In these machines, delay registers have been introduced in the computation loop in order to simulate parallelism (it is necessary to avoid modifying a location before it has been used by all its neighboring nodes); on the other hand, a single evolution operator evaluator is sufficient (Fig.A.1). This evaluator is generally in the form of a read-write look-up table, so that evolution rules can be modified easily. The first realization was the cellular automata machine (CAM) built at MIT /28/. This is a general purpose cellular automata machine computing the evolution of a  $256 \times 256$  lattice at the U.S. television field rate. CAM uses 4 bits/node, so that lattice gas simulations need grouping sites by four, reducing the resolution to  $128 \times 128$ , which is insufficient for most hydrodynamic simulations. A more recent realization is the "Reseau d'Automates Programmables" (RAP) built at the ENS (Paris) /29/ which updates  $512 \times 256$  16-bit sites fifty times per second. RAP is quite similar to CAM, but its architecture is slightly different in that it moves results rather than parameters, which renders RAP more efficient at handling lattice gas rules. RAP updates 6.5 Msites/sec which compares favorably with the 1.2 Msites/sec rate obtained with the FPS-164 vector processor. Both CAM and RAP

rely on an external (micro) computer for defining the rules, introducing the initial conditions, and performing the final averaging to obtain macroscopic physical quantities. A 1024x1024 RAP-2 version, currently under development, uses 8 locked processors, each one roughly equivalent to RAP-1. Since the processors sweep the lattice in phase, pre-averaging over 2x4 site blocks can be performed continuously on-board; as a result, the transfer rate to the processing computer will be considerably reduced.

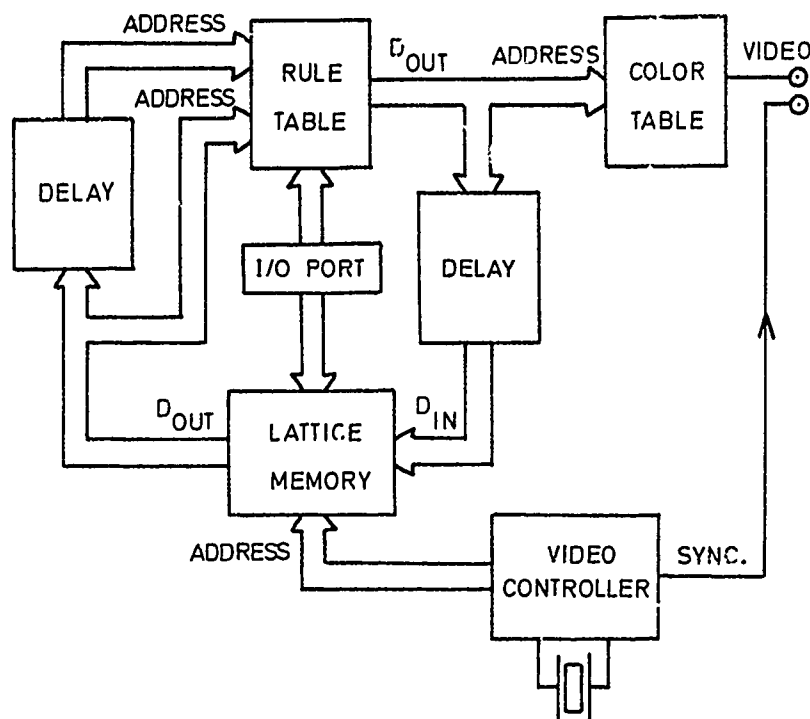


Fig.A.1 : Block diagram of typical cellular automata machine. All timing signals are obtained from a video controller whose addresses outputs scan the whole lattice continuously. The current lattice nodes content is used as an address into a table giving the new state to be written back into that node. Delays are introduced in order to prevent modification of a node before its state is used by all its neighbors. The new state of a node is also transferred to the video output via a color table. The content of this table is chosen so that only relevant states are shown in any desired color. Before starting the computation, the rule table, the color table, and the lattice memory are initialized by a microcomputer via an input/output port (I/O).

## REFERENCES

1. See e.g. J.P. Boon and S. Yip, Molecular Hydrodynamics (Mc Graw Hill, New York, 1980); and P. Résibois and M. DeLeener, Classical Kinetic Theory of Fluids (Wiley, New York, 1977).
2. See the chapters by W.C. Reynolds, and by D. Laurence in this volume.
3. J.P. Hansen, and I.R. McDonald, Theory of Simple Liquids (Academic Press, London, 1976).
4. C. Trozzi and G. Cicotti, Phys. Rev. A **29**, 916 (1984); E. Meiburg, "Direct Simulation Techniques for the Boltzmann Equation", Göttingen (1985), Phys. Fluids, **29**, 3107 (1986); D.C. Rapaport and E. Clementi, Phys. Rev. Lett. **57**, 693 (1986); L. Mannon, G.C. Lie, and E. Clementi, preprint entitled "Molecular Dynamics Simulation of Flow Past a Plate" (1986); M. Mareschal and E. Kestemont, preprint entitled "Experimental Evidence for Convective Roll in Finite Two-dimensional Molecular Models" (1987).
5. See e.g. J.O. Hirschfelder, C.F. Curtiss, and R.B. Bird, The Molecular Theory of Gases and Liquids (Wiley, New York, 1954) chapter 7.
6. S. Wolfram, Theory and Applications of Cellular Automata (World Scientific, Singapore, 1986).
7. J. Hardy, O. de Pazzis, and Y. Pomeau, Phys. Rev. A **13**, 1949 (1976).
8. N. Margolus, T. Toffoli, and G. Vichniac, Phys. Rev. Lett. **56**, 1694 (1986).
9. U. Frisch, B. Hasslacher, and Y. Pomeau, Phys. Rev. Lett. **56**, 1505 (1986).
10. U. Frisch, D. d'Humières, B. Hasslacher, P. Lallemand, Y. Pomeau, and J.P. Rivet, to appear in J. Stat. Phys. (1987).
11. See e.g. ref. /5/, chapter 11.
12. D. d'Humières, P. Lallemand, and U. Frisch, Europhys. Lett. **2**, 291 (1986); see also S. Wolfram, J. Stat. Phys. **45**, 471 (1986).
13. J.P. Rivet, to be published in C.R. Acad. Sci. Paris (1987).
14. See e.g. D.R. Nelson, and B.I. Halperin, Science, **229**, 233 (1985).
15. M. Hénon, to appear in J. Stat. Phys. (1987).
16. d'Humières, P. Lallemand, and T. Shimomura, Los Alamos Report LA-UR-85-4051 (1985).
17. J.P. Rivet, and U. Frisch, C.R. Acad. Sci. Paris, **302**, 11 (1986).
18. U. Frisch and J.P. Rivet, C.R. Acad. Sci. Paris, **303**, 1065 (1986); J.P. Rivet, to appear in J. Stat. Phys. (1987).
19. D. d'Humières and P. Lallemand, Physica **100A**, 337 (1986).
20. A. Noullez and P. Lallemand, private communication.
21. D. d'Humières and P. Lallemand, C.R. Acad. Sci. Paris, **302**, 983 (1986).
22. D. d'Humières, Y. Pomeau, and P. Lallemand, C.R. Acad. Sci. Paris, **301**, 1391 (1985).
23. J.B. Salem and S. Wolfram, in reference /6/, p.362.
24. B. Nennich and S. Wolfram, "Cellular Automaton Fluids : Preliminary Results on Two-dimensional Hydrodynamic Simulations" (1986).
25. P. Lallemand, private communication.
26. P. Lallemand and d'Humières, private communication.
27. P. Clavin, D. d'Humières, P. Lallemand and Y. Pomeau, C.R. Acad. Sci. Paris, **303**, 1169 (1986); P. Clavin, P. Lallemand, and Y. Pomeau, J. Fluid Mech. (1987); d'Humières, P. Lallemand, and G. Searby, preprint entitled "Numerical Experiments on Lattice Gases : Mixtures and Galilean Invariance"; P. Clavin, P. Lallemand, Y. Pomeau, and G. Searby, preprint entitled "Simulation of Free Boundaries in Flow Systems : a New Proposal Based on Lattice-Gas Models".
28. T. Toffoli, Physica **100D**, 195 (1984).
29. A. Clouqueur and D. d'Humières, to appear in J. Stat. Phys. (1987).



REPORT DOCUMENTATION PAGE			
1. Recipient's Reference	2. Originator's Reference	3. Further Reference	4. Security Classification of Document
	AGARD-R-755	ISBN 92-835-0430-5	UNCLASSIFIED
5. Originator	Advisory Group for Aerospace Research and Development North Atlantic Treaty Organization 7 rue Ancelle, 92200 Neuilly sur Seine, France		
6. Title	SPECIAL COURSE ON MODERN THEORETICAL AND EXPERIMENTAL APPROACHES TO TURBULENT FLOW STRUCTURE AND ITS MODELLING		
7. Presented at			
8. Author(s)/Editor(s)	Various		9. Date August 1987
10. Author's/Editor's Address	Various		11. Pages 264
12. Distribution Statement	This document is distributed in accordance with AGARD policies and regulations, which are outlined on the Outside Back Covers of all AGARD publications.		
13. Keywords/Descriptors	<p>Turbulent flow, Mathematical models,</p> <p>Simulation, Fluid dynamics, Not furnished, 1/87</p>		
14. Abstract	<p>The Special Course on Modern Theoretical and Experimental Approaches to Turbulent Flow Structure and its Modelling was sponsored by the AGARD Fluid Dynamics Panel and the von Kármán Institute and presented at the von Kármán Institute, Rhode-Saint-Genèse, Belgium on 16-20 March 1987.</p> <p>The Course discussed the large-eddy concept in turbulence modelling and techniques for direct simulation. A review of turbulence modelling was presented along with physical and numerical aspects and applications. A closure model for turbulent flows was presented and routes to chaos by quasi-periodicity were discussed. Theoretical aspects of transition to turbulence by space-time intermittency were covered. The application to interpretation of experimental results of fractal dimensions and connection of spatial temporal chaos was reviewed. Simulation of hydrodynamic flow by using cellular automata was discussed. <i>Keywords:</i></p>		

<p>AGARD Report No.755 Advisory Group for Aerospace Research and Development, NATO SPECIAL COURSE ON MODERN THEORETICAL AND EXPERIMENTAL APPROACHES TO TURBULENT FLOW STRUCTURE AND ITS MODELLING Published August 1987 264 pages</p> <p>The Special Course on Modern Theoretical and Experimental Approaches to Turbulent Flow Structure and its Modelling was sponsored by the AGARD Fluid Dynamics Panel and the von Kármán Institute and presented at the von Kármán Institute, Rhode-Saint-Genèse, Belgium on 16-20 March 1987.</p> <p>P.T.O.</p>	<p>AGARD-R-755</p> <p>Turbulent flow Mathematical models Simulation Fluid dynamics</p>	<p>AGARD Report No.755 Advisory Group for Aerospace Research and Development, NATO SPECIAL COURSE ON MODERN THEORETICAL AND EXPERIMENTAL APPROACHES TO TURBULENT FLOW STRUCTURE AND ITS MODELLING Published August 1987 264 pages</p> <p>The Special Course on Modern Theoretical and Experimental Approaches to Turbulent Flow Structure and its Modelling was sponsored by the AGARD Fluid Dynamics Panel and the von Kármán Institute and presented at the von Kármán Institute, Rhode-Saint-Genèse, Belgium on 16-20 March 1987.</p> <p>P.T.O.</p>	<p>AGARD-R-755</p> <p>Turbulent flow Mathematical models Simulation Fluid dynamics</p>
<p>AGARD Report No.755 Advisory Group for Aerospace Research and Development, NATO SPECIAL COURSE ON MODERN THEORETICAL AND EXPERIMENTAL APPROACHES TO TURBULENT FLOW STRUCTURE AND ITS MODELLING Published August 1987 264 pages</p> <p>The Special Course on Modern Theoretical and Experimental Approaches to Turbulent Flow Structure and its Modelling was sponsored by the AGARD Fluid Dynamics Panel and the von Kármán Institute and presented at the von Kármán Institute, Rhode-Saint-Genèse, Belgium on 16-20 March 1987.</p> <p>P.T.O.</p>	<p>AGARD-R-755</p> <p>Turbulent flow Mathematical models Simulation Fluid dynamics</p>	<p>AGARD Report No.755 Advisory Group for Aerospace Research and Development, NATO SPECIAL COURSE ON MODERN THEORETICAL AND EXPERIMENTAL APPROACHES TO TURBULENT FLOW STRUCTURE AND ITS MODELLING Published August 1987 264 pages</p> <p>The Special Course on Modern Theoretical and Experimental Approaches to Turbulent Flow Structure and its Modelling was sponsored by the AGARD Fluid Dynamics Panel and the von Kármán Institute and presented at the von Kármán Institute, Rhode-Saint-Genèse, Belgium on 16-20 March 1987.</p> <p>P.T.O.</p>	<p>AGARD-R-755</p> <p>Turbulent flow Mathematical models Simulation Fluid dynamics</p>

<p>The Course discussed the large-eddy concept in turbulence modelling and techniques for direct simulation. A review of turbulence modelling was presented along with physical and numerical aspects and applications. A closure model for turbulent flows was presented and routes to chaos by quasi-periodicity were discussed. Theoretical aspects of transition to turbulence by space/time intermittency were covered. The application to interpretation of experimental results of fractal dimensions and connection of spatial temporal chaos was reviewed. Simulation of hydrodynamic flow by using cellular automata was discussed.</p> <p>ISBN 92-835-0430-5</p>	<p>The Course discussed the large-eddy concept in turbulence modelling and techniques for direct simulation. A review of turbulence modelling was presented along with physical and numerical aspects and applications. A closure model for turbulent flows was presented and routes to chaos by quasi-periodicity were discussed. Theoretical aspects of transition to turbulence by space/time intermittency were covered. The application to interpretation of experimental results of fractal dimensions and connection of spatial temporal chaos was reviewed. Simulation of hydrodynamic flow by using cellular automata was discussed.</p> <p>ISBN 92-835-0430-5</p>
<p>The Course discussed the large-eddy concept in turbulence modelling and techniques for direct simulation. A review of turbulence modelling was presented along with physical and numerical aspects and applications. A closure model for turbulent flows was presented and routes to chaos by quasi-periodicity were discussed. Theoretical aspects of transition to turbulence by space/time intermittency were covered. The application to interpretation of experimental results of fractal dimensions and connection of spatial temporal chaos was reviewed. Simulation of hydrodynamic flow by using cellular automata was discussed.</p> <p>ISBN 92-835-0430-5</p>	<p>The Course discussed the large-eddy concept in turbulence modelling and techniques for direct simulation. A review of turbulence modelling was presented along with physical and numerical aspects and applications. A closure model for turbulent flows was presented and routes to chaos by quasi-periodicity were discussed. Theoretical aspects of transition to turbulence by space/time intermittency were covered. The application to interpretation of experimental results of fractal dimensions and connection of spatial temporal chaos was reviewed. Simulation of hydrodynamic flow by using cellular automata was discussed.</p> <p>ISBN 92-835-0430-5</p>

3105  
9

# AGARD

NATO OTAN

7 rue Ancelle • 92200 NEUILLY-SUR-SEINE

FRANCE

Telephone (1)47.33.57.00 • Telex 610 176

## DISTRIBUTION OF UNCLASSIFIED AGARD PUBLICATIONS

AGARD does NOT hold stocks of AGARD publications at the above address for general distribution. Initial distribution of AGARD publications is made to AGARD Member Nations through the following National Distribution Centres. Further copies are sometimes available from these Centres, but if not may be purchased in Microfiche or Photocopy form from the Purchase Agencies listed below.

### NATIONAL DISTRIBUTION CENTRES

#### BELGIUM

Coordonnateur AGARD — VSL  
Etat-Major de la Force Aérienne  
Quartier Reine Elisabeth  
Rue d'Evere, 1140 Bruxelles

#### CANADA

Defence Scientific Information Services  
Dept of National Defence  
Ottawa, Ontario K1A 9K2

#### DENMARK

Danish Defence Research Board  
Ved Idraetsparken 4  
2100 Copenhagen Ø

#### FRANCE

O.N.E.R.A. (Direction)  
29 Avenue de la Division Leclerc  
92320 Châtillon

#### GERMANY

Fachinformationszentrum Energie,  
Physik, Mathematik GmbH  
Kernforschungszentrum  
D-7514 Eggenstein-Leopoldshafen

#### GREECE

Hellenic Air Force General Staff  
Research and Development Directorate  
Holargos, Athens

#### ICELAND

Director of Aviation  
c/o Flugrad  
Reykjavik

#### ITALY

Aeronautica Militare  
Ufficio del Delegato Nazionale all'AGARD  
3 Piazzale Adenauer  
00144 Roma/EUR

#### LUXEMBOURG

See Belgium

#### NETHERLANDS

Netherlands Delegation to AGARD  
National Aerospace Laboratory, NLR  
P.O. Box 12C  
2600 AC Delft

#### NORWAY

Norwegian Defence Research Establishment  
Attn: Biblioteket  
P.O. Box 25  
N-2007 Kjeller

#### PORTUGAL

Portuguese National Coordinator to AGARD  
Gabinete de Estudos e Programas  
CLAFIA  
Base de Alfragide  
Alfragide  
2700 Amadora

#### TURKEY

Milli Savunma Bakanlığı  
ARGE Daire Başkanlığı  
Ankara

#### UNITED KINGDOM

Defence Research Information Centre  
Kintigern House  
65 Brown Street  
Glasgow G2 8EX

#### UNITED STATES

National Aeronautics and Space Administration (NASA)  
Langley Research Center  
M/S 180  
Hampton, Virginia 23665

THE UNITED STATES NATIONAL DISTRIBUTION CENTRE (NASA) DOES NOT HOLD STOCKS OF AGARD PUBLICATIONS, AND APPLICATIONS FOR COPIES SHOULD BE MADE DIRECT TO THE NATIONAL TECHNICAL INFORMATION SERVICE (NTIS) AT THE ADDRESS BELOW.

### PURCHASE AGENCIES

National Technical  
Information Service (NTIS)  
5285 Port Royal Road  
Springfield  
Virginia 22161, USA

ESA/Information Retrieval Service  
European Space Agency  
10, rue Mario Nikis  
75015 Paris, France

The British Library  
Document Supply Division  
Boston Spa, Wetherby  
West Yorkshire LS23 7BQ  
England

Requests for microfiche or photocopies of AGARD documents should include the AGARD serial number, title, author or editor, and publication date. Requests to NTIS should include the NASA accession report number. Full bibliographical references and abstracts of AGARD publications are given in the following journals:

Scientific and Technical Aerospace Reports (STAR)  
published by NASA Scientific and Technical  
Information Branch  
NASA Headquarters (NIT-40)  
Washington D.C. 20546, USA

Government Reports Announcements (GRA)  
published by the National Technical  
Information Service, Springfield  
Virginia 22161, USA



Printed by Specialised Printing Services Limited  
40 Chigwell Lane, Loughton, Essex IG10 3TZ

ISBN 92-835-0430-5